50 Jahre
1956 - 2006

GKSS
FORSCHUNGSZENTRUM
in der HELMHOLTZ-GEMEINSCHAFT
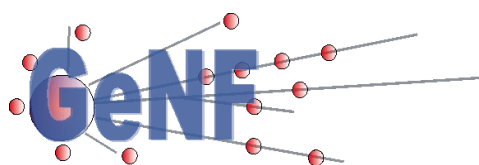
GeNF – Experimental Report 2006

GeNF
Geesthacht Neutron Facility

Editors:

P. K. Pranzas
A. Schreyer
R. Willumeit

HELMHOLTZ
| GEMEINSCHAFT

wissen
schafft
nutzen

GeNF – Experimental Report 2006

Editors:

P. K. Pranzas
A. Schreyer
R. Willumeit
(Institute of Materials Research)

GKSS 2007/6

GeNF – Experimental Report 2006

Philipp Klaus Pranzas, Andreas Schreyer, Regine Willumeit (Editors)

326 pages with 251 figures and 20 tables

Abstract

At the Geesthacht Neutron Facility GeNF about 212 experiments were performed in 2006 by GKSS and by or for external users, partners or contractors. In most cases the measurements were performed and analysed in cooperation by the guests and by the GKSS staff or by the permanent external user group staff. The activities, which are based on a proposal procedure and on the in house R&D program, are reported in 71 contributions in the present annual experimental report for the year 2006. The contributions may contain one or also several combined experiments.

During 2006 the GKSS research reactor FRG-1 achieved an operation time of 197 days at the full 5 MW reactor power providing a neutron flux of ca. $1.4 \cdot 10^{14}$ thermal neutrons/ cm^2 s. The cold neutron source was available during the complete operation time.

The focus of the in house R&D work at GeNF instruments was the characterisation of nanostructures in engineering materials, the analysis of stresses and textures in welds and technical structures at ARES-2, TEX-2, DCD and SANS-2, the structural investigation of hydrogen containing substances such as polymers, colloids and biological macromolecules at SANS-1 as well as the characterisation of magnetic thin films at PNR, NeRo, POLDI and RÖDI. The thoroughly upgraded residual stress diffractomer ARES-2 went in full operation in spring 2006 as well as the new neutron tomography device at GENRA-3. The installation of modern experiment control hardware and software based on LabView was completed on all designated instruments.

In the appendices I and II the experimental reports of REFSANS at FRM II are attached as well as of the GKSS outstation HARWI-II at DESY. Both instruments started full operation in 2006.

Jahresbericht 2006 über die Experimente an GeNF

Zusammenfassung

An der Geesthachter Neutronenforschungseinrichtung GeNF wurden von GKSS und von oder für externe Nutzer, Partner oder Auftraggeber etwa 212 Experimente in 2006 durchgeführt. In den meisten Fällen wurden die Messungen gemeinschaftlich von den Gastwissenschaftlern und GKSS Personal vorgenommen und ausgewertet. Die Experimente, die in der Regel über das Antragsverfahren und über das GKSS eigene F&E-Programm abgewickelt wurden, werden in diesem Jahresbericht in Form von 71 Experimentierberichten dargestellt. Dabei können die Berichte einzelne Experimente oder auch mehrere zusammengefasst beschreiben.

Während 2006 erreichte der Forschungsreaktor FRG-1 197 Volllasttage bei 5 MW und bei einem Fluß von $1{,}4 \cdot 10^{14}$ thermischen Neutronen je cm^2 und s. Die kalte Neutronenquelle war während der gesamten Betriebszeit verfügbar.

Der Schwerpunkt der GKSS eigenen Forschungsarbeiten lag in 2006 im Bereich der Charakterisierung von Nanostrukturen in Werkstoffen, der Analyse von Eigenspannungen und Texturen in Schweißverbindungen und technischen Strukturen an ARES-2, TEX-2, DCD und SANS-2, im Bereich der Strukturanalyse von wasserstoffhaltigen Substanzen wie Polymere, Kolloide und Biomolekülen an der SANS-1 sowie im Bereich der Charakterisierung magnetischer Schichtstrukturen an PNR, NeRo, POLDI und RÖDI. Im Frühjahr 2006 wurde nach gründlichem Umbau das Eigenspannungsdiffraktometer ARES-2 eingeweiht, ebenso wie die Neutronentomographie-Einrichtung an Genra-3. Die Umstellung aller infrage kommenden Instrumente auf die neue Hard- und Software basierend auf Labview wurde weitestgehend abgeschlossen.

In Anhängen werden die Experimentberichte von REFSANS am FRM II sowie von der jungen GKSS Außenstation HARWI-II bei DESY aufgelistet. In 2006 wurde an beiden Instrumenten der Messbetrieb aufgenommen.

CONTENTS

S. *Gürel, A. Braccini, I. Martin, B. Müller*
Micro-Architecture of Scaffolds for Bone Tissue Engineering

J. Müssig, G. Cescutti, D. Hegemann, M. Hossain, T. Donath, F. Beckmann
Microstructure and Orientation of Natural Fibres in Composites investigated
by X-ray Microtomography

S.A. Klapp, H. Klein, C.E. Tomaeseo, L. Raue, W.F. Kuhs, T. Lippmann
Preparation for characterisation of natural gas hydrate reservoirs by high energy
synchrotron radiation

R. Zettler, J.F. dos Santos, T. Donath, J. Herzen, F. Beckmann, D. Lohwasser
Removing the guess work from material flow and deformation mechanics associated
with the FSW of Aluminium and ist alloys through application of micro-computer
tomography and dedicated metallurgical techniques

R.V. Martins, T. Fischer, A. Schreyer
Residual stress analyses in laser beam welded butt joints made from sheets of Al alloy
AA6056

*M. Ney, M. Neudert, T. Beleites, A. Kluge, F. Beckmann, T. Douglas, R. Bernhardt,
D. Scharnweber, T. Zahnert*
SRµCT, a useful technique to localize a new type of titanium implant in a specimen of a
middle ear

*S. Irsen, B. Leukers, H. Seitz, S. Schwanitz, L. Olde Damink, F. Beckman, J. Herzen,
B. Müller*
Synchrotron radiation-based micro computed tomography for the analysis of 3D-printed
and collagen-coated scaffolds for bone replacement

A Roos, J.F. dos Santos, T. Donath, J. Herzen, F. Beckmann
Validation of Diffusion Processes by µCT of Marker Material in new Friction based Hybrid
Friction Diffusion Bonding (HFDB) Process

K. Nusser, T. Sonnleitner, F. Beckmann, G.J. Schneider, D. Göritz
X-Ray Tomography of Silica in Rubber

F. Witte, J. Fischer, M. Störmer, N. Hort
3D characterization of beta-phases in AZ91D by synchrotron-radiation based
microtomography

F. Fierz, B. Leukers, S. Irsen, Ö. Degistirici, F. Beckmann, B. Müller
3D-printed hydroxyapatite scaffolds with centrally aligned channel

H.-A. Crostack, J. Nellesen, G. Fischer, F. Beckmann
3D-Quantification of Strain and Displacement in MMCs utilizing SR-based
Microtomography

A. Ghanbari-Siahkali, S.F. Nielsen, F. Beckmann, T. Donath, J. Herzen
Investigation of Polyolefin insulation for Offshore Application by X-Ray Microtomography

T. Lippmann
Charge density of Pyrite, FeS_2

T. Leisegang, T. Weißbach, T. Lippmann, M. v. Zimmermann, P. Paufler, D.C. Meyer
Electron density determination and topological analysis of $HoNi_2B_2C$

*C.B. Johansson, J. Lindblad, H. Sarve, R. Bernhardt, F. Beckmann, J. Herzen,
G. Borgefors, D. Scharnweber*
Imrpoving the knowledge of integration of mecical devices in bone; a comparison
of 3D SRµCT data to histomorphometrical data obtained on cut and ground sections

B. Müller, M. Germann, A. Andronache, D. Jeanmonod, A. Morel
Determination of the distortion in histological slices of human brain tissue using synchrotron radiation based micro computed tomography

M. Nickel, J.U. Hammel, T. Donath, F. Beckmann
Elastic energy load into spicule reinforced extracellular matrix of the sponge *Tethya wilhelma*? − Evidence from synchrotron radiation based x-ray microtomography

B. Müller, F. Beckmann, J. Herzen, R. Glückert, C. Jolly, A. Schrott-Fischer
Intensity-based segmentation of cochlear implant within the human inner ear

P. Michalik, M. Nickel, J.U. Hammel, T. Donath, F. Beckmann
Internal anatomy of dwarf spiders based on SRμCT

M. Dalstra, P.M. Cattaneo, T. Donath, J. Herzen, F. Beckmann
Microtomography of a human jaw segment at the newly rebuilt W2 beamline

F. Neues, A. Ziegler, T. Donath. J. Fischer, F. Beckmann, M. Epple
Mikrotomographie an Biomineralien

A. Lareida, F. Beckmann, A. Andronache, W. Freysinger, A. Schrott-Fischer, R.Glückert, B. Müller
Morphology of the endolymphatic space in the murine cochlea uncovered by micro computed tomography using synchrotron radiation

M. Kuehbacher, B. Gruenewald, G. Falkenberg, T. Donath, J. Herzen, F. Beckmann, A. Kyriakopoulos
Neuroimaging with Synchrotron-based Methods

G. Taton, T. Rok, E. Rokita, A. Wrobel, F. Beckmann, T. Donath, J. Fischer, P. Thor
Study of renal calculi structure

T. Kleinteich, A. Haas
Transformations of the vertebrate skull: How are skull anatomy and function correlated with the reproductive mode in caecilians (Lissamphibia: Gymnophiona)?

G. Taton, T. Rok, E. Rokita, Z. Tabor, M. Karwala-Szytula, F. Beckmann, T. Donath, J. Fischer
3D Bone Architecture

T. Donath, F. Beckmann, A. Schreyer
Automated Data Reconstruction for X-ray Microtomography

PREFACE

GeNF Operation

The Geesthacht Neutron Facility (GeNF) is operated as an open facility for external users for about 2/3 of the available beam time and it is used for GKSS in house research within its materials science programme for the remaining 1/3. The external users come either from national and international scientific research institutions, universities and industry, or they own and operate experiments at GeNF as permanent external partners.

The beam time allocations for GeNF instruments are established on the base of a continuous proposal procedure which can react in a flexible and fast way on new proposals. Proposals can be submitted at any time. In 2006 about 212 experiments were performed at GeNF by or for external users, partners or contractors as well as for the in house research programmes. A part of these activities – mainly the part of external use based on proposals – is reported in the present annual experimental report for the year 2006. In many cases several experiments are concentrated in one experimental report.

Operation of FRG-1

In 2006 the FRG-1 was operated routinely interrupted by the two planned major shut downs in January/February and in July. The total FRG operation time was 207 days providing neutrons, of these it ran for 197 days at its full power of 5 MW providing a neutron flux of ca. $1.4 \cdot 10^{14}$ thermal neutrons / cm^2 s. The cold neutron source was always available during FRG operation.

GeNF Instruments

The current set of instruments at GeNF is shown in Fig. A and listed in table A. The available sample environment equipment is listed in table B.

In 2006 the installation of modern experiment control hardware and software based on LabView was completed on all designated instruments. The upgraded spectrometer ARES-2 and the new neutron tomography device at GENRA-3 were completed in spring 2006. In October 2006 the official approval for the upgrade of the Cold Neutron Source was obtained. This upgrade - yielding in a flux increase of 60 % – will be finished in spring 2007.

The focus of the GKSS in-house research at GeNF is the characterisation of nanostructures, textures and residual stresses in materials at the instruments ARES-2, TEX-2, DCD and SANS-2, the structural investigation of hydrogen containing substances such as polymers, colloids and biological macromolecules at SANS-1 as well as the characterisation of magnetic and polymer thin films at PNR, NeRo, POLDI and RÖDI.

The small-angle scattering and reflectometry instrument REFSANS of GKSS at the Heinz Maier-Leibnitz (FRM II) reactor started in full operation in 2006. More details can be found in the reports in appendix I. GKSS started also the construction of the small-angle scattering instrument SANS-1 at FRM II together with the Technical University of Munich (TUM). Furthermore, GKSS, HMI and TUM operate the residual stress and texture instrument STRESS-SPEC together at the FRM II.

At the new HARWI-II beamline at the synchrotron storage ring DORIS at DESY in Hamburg 39 experiments in the fields tomography, residual stress and texture research were performed in addition to commissioning. In 2006 the High-Energy Materials Science project at the PETRA III storage ring at DESY started as well and the basic design of this synchrotron beam line was fixed. For details see the reports in appendix II.
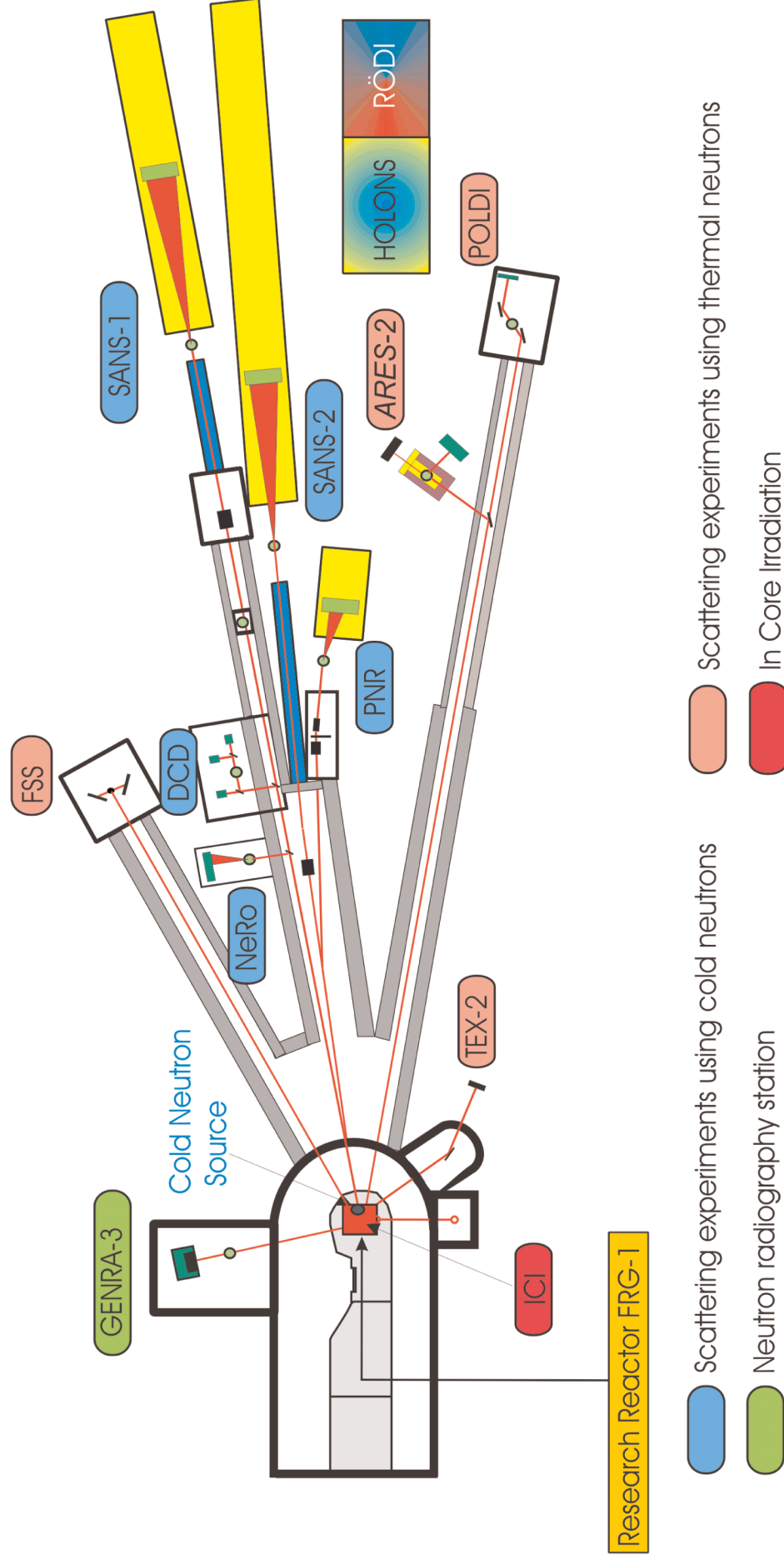
Figure A: Arrangement of the Instruments at GeNF

Table A: **List of GeNF Instruments**

Instrument	Short Instrument Description /Main Tasks	Characteristic Data	Operator / Local Contact
SANS-1	Small Angle Neutron Scattering using cold non-polarised/polarised neutrons primarily to investigate molecular biology, colloids and polymers	$\Phi_{max} = 8 \cdot 10^5$ cm^{-2} s^{-1} (coll.2 m, λ=0.82 nm) $\Delta\lambda/\lambda = 0.1$ (λ = 0.82 nm) Particle sizes: 2 - 80 nm 2-D position-sens. ^{3}He- detector	GKSS / Regine Willumeit Vasyl Haramus
SANS-2	Small Angle Neutron Scattering using cold non-polarised/polarised neutrons to characterise precipitates, clusters, interfaces, grain sizes, magnetic structures etc. in materials (metals, polymers, colloids a.o.)	$\Phi_{max} = 2 \cdot 10^7$ cm^{-2} s^{-1} (coll.1 m,λ=0.5nm) $\Delta\lambda/\lambda = 0.1$ Particle sizes: 1 - 100 nm 2-D position-sens. ^{3}He- detector	GKSS / Melissa Sharp Helmut Eckerlebe P. Klaus Pranzas
DCD	Double Crystal Diffractometer for ultra small angle neutron scattering (USANS) using non-polarised cold neutrons to characterise large creep pores, fatigue and sintering cavities, precipitates, voids, bubbles, etc. in materials	$\Phi \approx 0.5 \cdot 10^3$ cm^{-2} s^{-1} $\Delta\lambda/\lambda = 1 \cdot 10^{-5}$ (λ = 0.443 nm) Particle sizes: 30 nm - 24 µm 3 x ^{3}He- detectors	GKSS / Melissa Sharp P. Klaus Pranzas
ARES	Diffractometer for the Analysis of REsidual Stresses in specimens with technical sizes (up to 100 kg) using thermal non-polarised neutrons	$\Phi \approx 3 \cdot 10^5$ cm^{-2} s^{-1} (perfect Si-Monochr.) $\Delta d/d \approx 4 \cdot 10^{-3}$ take-off angle: 57° - 120° 2-D position-sens. ^{3}He- detector	GKSS / Peter Staron
FSS	Time of flight Fourier Strain Spectrometer to investigate residual stresses in specimens with technical sizes using thermal neutrons	$\Phi = 5.5 \cdot 10^6$ cm^{-2} s^{-1} timing res. ca. $4 \cdot 10^{-3}$ (λ = 0.1 - 0.4 nm) Analyser: 2 x 3072 TOF channels 2 detector banks (90° & 270°)	CAU - Universität Kiel / Hans-Georg Priesmeyer
NeRo	Neutron Reflectometer to study magnetic and other surfaces, layers, thin films and membranes using cold non-polarised/polarised neutrons with high resolution	$\Phi = 5 \cdot 10^4$ cm^{-2} s^{-1} (standard collimation) $\Delta\lambda/\lambda = 0.02$ (λ = 0.433 nm) 2-D position-sens. ^{3}He- detector, ^{3}He-pencil counter	GKSS / Dieter Lott
PNR	Polarised Neutron Reflectometer for the study of magnetic and non-magnetic surfaces, layers, thin films and membranes using cold non-polarised or polarised neutrons with high flux	$\Phi_{nonpol} = 1 \cdot 10^5$ cm^{-2} s^{-1} $\Phi_{nonpol} / \Phi_{pol} = 3 / 1$ $\Delta\lambda/\lambda = 0.05$ ($\lambda \geq 0.635$ nm) 2-D position-sens. ^{3}He- detector	GKSS / Danica Solina

Table A: **List of GeNF Instruments** (continued)

Instrument	Short Instrument Description /Main Tasks	Characteristic Data	Operator / Local Contact
RÖDI	X-ray (RÖntgen) DIffractometer to investigate residual stresses, textures and thin films	Seifert XRD 3003 PTS Heavy load goniometer	GKSS / Peter Staron
TEX-2	Four circle neutron TEXture diffractometer to characterise textures in metallic, ceramic and geologic materials using thermal non-polarised neutrons	$\Phi = 0.3 - 2\cdot10^6$ cm^{-2} s^{-1} take-off angle: 17° - 57° (in 10°-steps) λ-range: 0.08 – 0.27 nm ^{3}He-single detector, 2-D position-sens. ^{3}He- detector 300 x 300 mm	TEXMAT - Technische Universität Clausthal / Heinz-Günter Brokmeier
POLDI	POLarised DIffractometer; 3-D depolarisation analysis is used to investigate magnetic properties and correlations in magnetic materials; additional time of flight option in non-polarised mode	$\Phi_{max} = 0.8\cdot10^5$ cm^{-2} s^{-1} (polarized) take-off angle: 10° < 2 Θ_M < 65° λ-range: 0.1 nm - 0.36 nm ^{3}He-single detector	GKSS / Jochen Fenske Dieter Lott
HOLONS	HOLOgraphy and Neutron Scattering to investigate the properties in functional materials of photonics (e.g. photopolymers and photorefractive crystals) and to study light-induced changes simultaneously by light and neutron diffraction	holographic setup in SANS-2: angular resol.$\leq$ 0.01°, angul.setting acc = 0.001° resol.$\leq$ 0.01°, angul.setting acc = 0.001° lasers (excitation & diffract.): Ar$^+$-laser (single&multi line mode: 25 W /visible, 5.5 W / UV), HeNe-lasers (green, red)	Universities of Vienna and Osnabrück / Romano Rupp
GENRA-3	GEesthacht Neutron RAdiography facility for non-destructive analysis of materials by static and dynamic imaging	Φ_{therm} / Φ_{epi} = 1.4$\cdot10^6$ / 8$\cdot10^3$ [cm^{-2} s^{-1}] image: 15 x 15 to 45 x 45 cm^2 max. size of specimen: 100 x 200 cm^2	GKSS / P. Klaus Pranzas Jürgen Vollbrandt
GBET	Geesthachter Boron- capture (Einfang) Therapy originally designed to study cell cultures in tumours with enriched boron; now available as a cold neutron irradiation facility	$\Phi = 1.6\cdot10^8$ cm^{-2} s^{-1} (λ_m= 0.6 nm) irrad. area : 30 x 40 mm^2 E_m = 2.3 meV	GKSS / Hans-Ulrich Ruhnau
ICI	In Core Irradiation - service for industry and others, different core positions, pneumatic dispatch system available	Φ_{therm} = 2 to 8$\cdot10^{13}$ cm^{-2} s^{-1} Φ_{fast} = 0.02 to 0.06 Φ_{therm} max. sample size: 40 mm$\varnothing$ x 100 mm	GKSS / Wolfgang Knop

Table B: **GeNF Sample Environment**

Instrument	Cryostat	Magnets	Temp. Conditioning	Other Devices
SANS-1	^{3}He / ^{4}He – Cryostat: horizontal dilution-refrigerator with NMR sample coil and microwave source: T-range: 120 mK - RT; NMR: 106 and 16 MHz; Microwave: tunable: 68 to 74 GHz sample dimension: 2,8 x 17 x 19 mm^3 (optimum design for NMR coil), NMR is made for ^{1}H and ^{2}H resonance in 2.5 Tesla continuous wave mode;	2.5 Tesla magnet	heater up to 80 °C	
SANS-2	• several refrigerator cryostats, temp.-range: 4 - 475 K flexible operation in various instruments	• **B-E 25**: up to 2 Tesla with closed cycle refrigerator (T: 8 - 300 K) • **B-E 15**: up to 1.5 Tesla with closed cycle refrigerator (T: 4 - 475 K) • **B-E 10**: up to 1 Tesla with closed cycle refrigerator (T: 4 - 475 K), alternative furnace (T: 300 - 900 K) • **superconducting magnets:** up to 5 Tesla with longitudinal (T: 8 - 300 K) or vertical field (T: 4 - 280 K) • **electro magnet:** > 0.9 Tesla	heater (electric) / cooler (thermostat liquid circuit): T-range: -30 - 400 °C vacuum or inert gas atmosphere furnaces (temperatures up to 1000°C)	- side detector for measurements at large angles - sample container for big samples - lasers
DCD			heater up to 80 °C	Sample changer with up to 6 positions
ARES	refrigerator cryostat Model Leybold RGD 210, temp.-range: 12 - 475 K flexible operation in various instruments		furnace (up to 700°C)	Eulerian cradle (with x, y, z tables), load frame

Table B: **GeNF Sample Environment** (continued)

Instrument	Cryostat	Magnets	Temp. Conditioning	Other Devices
FSS	refrigerator cryostat Model Leybold RGD 210, temp.-range: 12 - 475 K flexible operation in various instruments		heater (up to 1000 °C)	- stress rig max. force: 30 t
PNR	• refrigerator cryostat Model Leybold RGD 210, temp.-range: 12 - 475 K • refrigerator cryostat Model ARS DE 210 SE, temp.-range: 4 - 300 K flexible operation in various instruments	• **electro magnet:** up to 0.9 Tesla	• heater / cooler (thermostat liquid circuit): T-range: -30 - 250 °C	
NeRo	• refrigerator cryostat Model Leybold RGD 210, temp.-range: 12 - 475 K • refrigerator cryostat Model ARS DE 210 SE, temp.-range: 4 - 300 K flexible operation in various instruments	• **electro magnet:** up to 0.9 Tesla • **superconducting magnet:** up to 5 Tesla with closed cycle refrigerator (T: 8 - 300 K) suitable for polarised neutrons	• 2 x vacuum furnaces: T-range: RT - 200 °C - one especially. for annealing purposes under PC control • heater / cooler (thermostat liquid circuit): T-range: -30 - 250 °C	- 2D-analyser for measurements of magnetic diffuse reflectivity
TEX-2				- loading device: range of cycling load: tension up to 1.5 t, compression up to 2.0 t, - sophisticated set of sample holders
POLDI	- refrigerator cryostat T > 10 K	DC magnetic field < 160 A/cm pulsed field < 6.5 kA/cm		

		GeNF
GKSS FORSCHUNGSZENTRUM in der HELMHOLTZ-GEMEINSCHAFT	**EXPERIMENTAL REPORT**	**GeNF SANS-1**

Small-angle scattering instrument SANS-1

Short Instrument Description:

The small angle neutron scattering instrument SANS-1 using cold non-polarised/polarised neutrons serves primarily to investigate molecular biology, colloids and polymers.

Local Contact:

Dr. Regine Willumeit
Phone/Fax : +49 (0)4152 87 – 1291 / +49 (0)4152 87 – 1356
e-mail: regine.willumeit@gkss.de

Dr. Vasyl Haramus
Phone/Fax : +49 (0)4152 87 – 1290 / +49 (0)4152 87 – 1356
e-mail: vasyl.haramus@gkss.de

Schematic view of SANS-1:
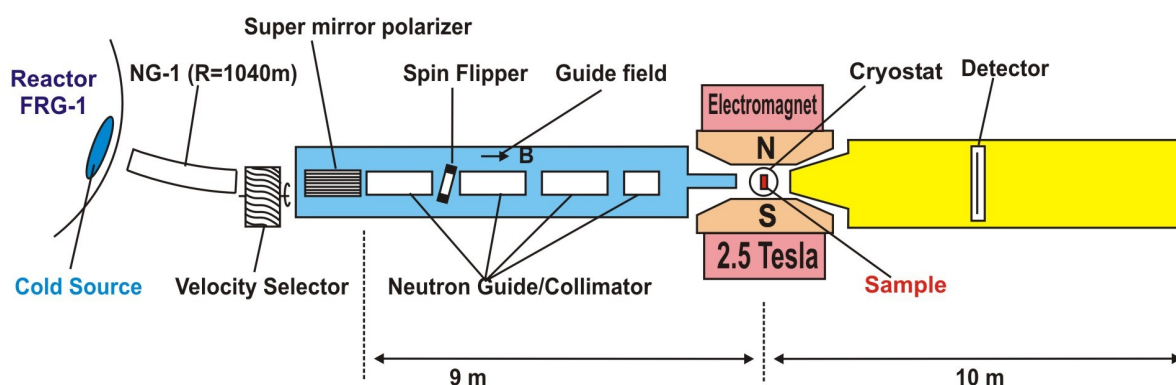
Instrument Details:

Beamline:	Beamline 8 - NG-1, radius of curvature R = 1040 m, cross section 3 x 4 cm^2, cold neutrons
Monochromator	helical slot selector
Wavelength range behind polariser and selector:	$\geq$ 0.45 nm;
Wavelength resolution	$\Delta\lambda / \lambda$ = 0.1 (λ = 0.82 nm)
Length L of collimation:	2 m, 4 m, 6 m, 8 m, 10 m
Flux at specimen:	Φ = 0.05 - 8·10^5 cm^{-2} s^{-1} see table

Instrument Details (continued)**:**

Range of momentum transfer:	$0.05 \leq Q \leq 3$ nm^{-1}
Distance sample to detector:	0.7 m $\leq$ d ≤ 9.7 m

<u>Detector:</u>
    active area:
    effective pixel size:
    background:
	2-dim position-sensitive ^{3}He-counter
	    55 **x** 55 cm^2
	    0.7 x 0.7 cm^2
	    1 cps

<u>Polarized target station:</u>	dilution refrigerator (120 mK) 2.5 T C-shaped electro-magnet microwave emitter (68 - 74 GHz) NMR circuit for protons and deuterons selective nuclear spin depolarisation
<u>Other sample environment</u>	thermostat (5 °C to +80 °C) automatic sample change

Flux of non-polarized cold neutrons at the sample position:

length of collimator [m]	2	4	6	8	10
Φ **[**10^3 n cm^{-2} s^{-1}**]** (λ= 0.82 nm)	**800**	**480**	**160**	**95**	**50**

Variable contrast study of coexisting fluorocarbon-rich and hydrocarbon-rich micelles

Proposer: **Mats Almgren[1]**, [1]Uppsala University, Uppsala, Sweden
Co-Proposers: **Jiang Nan[1]**

Experimental Team: **Vasyl Haramus[2]**, [2]GKSS

User Group Leader: **Mats Almgren[1]**

Date(s) of Experiment: 23rd–28th April 2006, 23rd–30th August 2006

Objectives

Mixtures of fluorocarbon and hydrocarbon surfactants in aqueous solution either assemble to form mixed micelles, or to form coexisting populations of hydrocarbon-rich and fluorocarbon-rich micelles. In earlier experiments (May 2004, August 2005) we have shown that contrast variation SANS results give strong support for the demixing of micelles into hydrocarbon-rich and fluorocarbon-rich populations in solutions containing a fluorinated and a normal cationic surfactant. This is the first time such a demixing have been verified by SANS studies[3,4]. We have now extended the measurements to two systems. (1) $C_8F_{17}C_2H_4C_5D_5NCl$ plus $C_{12}H_{25}C_5H_5NCl$ that according to other reports makes only mixed micelles, but still non-ideally mixed, and (2) an ideally mixed system, SDS + SDS-d25, i.e. SDS mixed with its fully deuterated analog.

Experiment

Mixtures of surfactants form micelles in aqueous solution. The mixed micelles range from ideal mixtures (e.g. deuterated and non-deuterated forms of the same surfactant) to strongly non-ideal, as in mixtures of normal and fluorinated surfactants. It was realized early on (in the 1960, Mysels, Murkerjee and others) that in the latter case a very curious situation could result, where two types of micelles coexists in one and the same solution, one rich in the fluorinated component the other with mainly hydrogenated component. It has since shown difficult to unambiguously proove that such a situation prevails. Some specific demonstrations of the simultaneous presence of two types of micelles have been made for a few systems, but no general study that is fully satisfactory. Conflicting results have often resulted from different methods, used by different researchers.

SANS with contrast variation by using D2O/H2O mixtures for solvent would, at a first glance, appear as ideally suited for such studies: one solvent mixture would make one type of micelles invisible, another the other type of micelles, and a scattered intensity would remain for the demixed system at the nominal match point for the mixed surfactants, where the scattering would all but disappear for an ideally mixed system. Only few studies[1-3] of this kind have been made prior to our series of measurements.[4,5] The early studies seemed to suggest that the systems selected all contained mixed micelles. On a closer inspection of the results, however, in the light of our later findings, it appears that this conclusion is maybe not inescapable.

In the second of our published papers,[4] we presented a simplified theory for the intensity as a function of the contrast:

$$\frac{d\Sigma}{d\Omega}(0) = n_m V_m^2 \left[\sigma^2 (\rho_{FS} - \rho_{HS})^2 + (\bar{\rho} - \rho_S)^2 \right] \qquad (1)$$

It is assumed that we have a distribution of composition over globular, non-interacting micelles of equal size (or, if there is a size polydispersity, that it is not coupled to the composition variation). The width of the composition distribution is given by σ, ρ stands for the scattering length density, subscripts HS for hydrogenated surfactant, FS fluorinated surfactant, S for solvent, and the bar designates the nominal matchpoint for the surfactant mixture, n_m is the number density of micelles, and V_m the dry volume of a micelle. Besides the width of the composition distribution – which is the only information about the distribution that can be obtained from the scattered intensity at zero angle – the micelle aggregation number and the scattering length density at the minimum are determined. $\frac{d\Sigma}{d\Omega}(0)$ was obtained from an IFT analysis of scattering results for q ≥ 0.02 Å^{-1}, obtained using low concentrations of surfactants (to reduce volume interactions) and a salt concentration of 0.2.M to surpress electrostatic interactions.

We used this procedure for the systems 50mM $C_{12}PC$ + 50mM HFDePC in 0.20M NaCl at 25°C, and 35 mM SDS + 35 mM SDS-d25 in 0.20 M NaCl at 25°C.

Achievements and main results
Figure 1 presents the typical variation of zero q intensity with the scattering length density of the solvent (expressed as mole fraction of D_2O in the solvent mixture), and the fit of these values to eqn. (1). In this case the minimum of parabola is close to zero (indeed slightly negative).
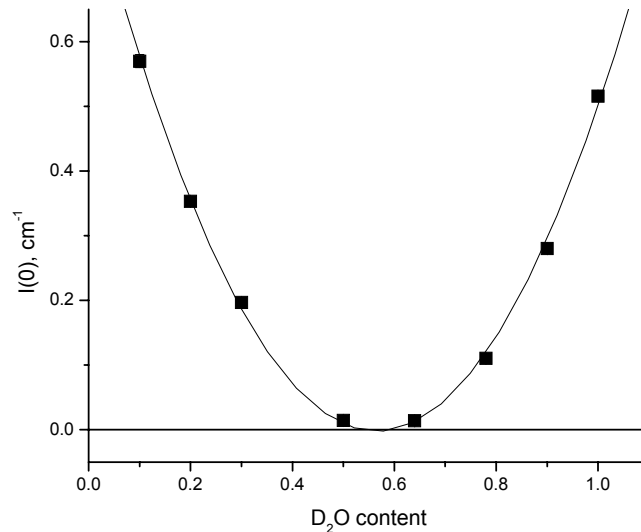
Figure 1: I(0)=$\frac{d\Sigma}{d\Omega}(0)$, obtained from an IFT analysis, for mixtures of 35 mM SDS and 35mM SDS-d25 in 200mM NaCl, fitted to eqn. 1.

In Table 1 we have collected all results for all systems studied in this way.

Table 1: Aggregation number, width of micelle composition distribution, and match point for the systems studied.

System	N_{agg}	σ	$\overline{\rho}$	$\overline{\rho}_{calc}$
C_{16}TAC + HFDePC 25°C	76	0.33	0.35	0.35
C_{16}TAC + HFDePC 60°C	54	0.20	-	0.35
C_{16}PC + HFDePC 25°C	71	0.39	0.38	0.375
C_{16}PC + HFDePC 60°C	54	0.22	0.37	0.375
C_{12}PC + HFDePC 25°C	47	0.22	0.46	0.42
SDS + SDS-d25 25°C	78		0.57	0.59

The results from the first two systems have been published.[4,5] The width of the composition distribution decreases with increasing temperature, as expected, but it is still much larger than the value for ideal mixing, σ = 0.1 for N_{agg} = 50. Even when there is no clear demixing into two micelles populations there is a broadening of the composition distribution. Note that σ must always be smaller than σ = 0.5, the value for complete demixing into pure micelles of the two components. A square distribution of compositions from 0 to 1 – which is the broadest unimodal distribution – would have σ = 0.289.

The results thus indicate that all the mixed systems of hydrogenated and fluorinated surfactants have non-ideal, broad micelle compositions, and that they are probably bimodal for the C_{16} systems at 25°C. In order to verify that other factors that contribute to a scattered signal at the match point have not been overlooked, we have also studied an ideal system, composed of SDS and its deuterated analog. The results give a slightly negative minmum value of the parabola, Figure 1, but the expected value at the minimum for an ideal mixing ($\approx$ 0.017 cm^{-1} in this case) would fell well within the error limits. It appears almost imposible to attain a precision that allows a precise determination of σ^2 for such a system.

The C_{12}PC + HFDePC system in the Table shows a too large difference between calculated and observed values of the scattering length density (in the table expressed as the mole fraction D_2O in the solvent mixture) at the matchpoint. This is probably caused by a difference in the micelle size coupled to the composistion variation, and to a relatively large difference between the size of the two surfactants.

References
[1] Burkitt, S. J.; Ottewil, R. H.; Hayter, J. B.; Ingram, B. T., Colloid Polym. Sci. **265**, 1987, 628.
[2] Caponetti, E.; Chilura Martino, D.; Floriano, M. A.; Triolo, R., Langmuir **9**, 1993, 1193.
[3] Pedone, L.; Chilura Martino, D.; Caponetti, E.; Floriano, M. A.; Triolo, R., J. Phys. Chem. B. **101**, 1997, 9525.
[4] Almgren, M.; Garamus, V., J Phys. Chem. B **109**, 2005, 11348.
[5] Kadi, M.; Hansson, P.; Almgren, M.; Bergström, M.; Garamus, V., Langmuir **20**, 2004, 3933.
[6] Nordstierna, L.; Furó, I.; Stilbs, P., J. Am. Chem. Soc. **128**, 2006, 6704.

![GKSS logo] GKSS FORSCHUNGSZENTRUM in der HELMHOLTZ-GEMEINSCHAFT	**EXPERIMENTAL REPORT**	**GeNF SANS-1**

Analysis of Bilayer Thickness of Lipid Cubic Phases with Large and Normal Water Channels	
Proposer: **Co-Proposers:**	**Angelina Angelova,** Genevieve Lebas, CNRS, Universite de Paris 11, Chatenay-Malabry, France Genevieve Lebas, CNRS,
Experimental Team:	**Vasyl Haramus,** GKSS Wilhelm Müller, GKSS, Borislav Angelov, GKSS
User Group Leader:	Angelina Angelova, CNRS
Date(s) of Experiment:	29th April–2nd May 2006 and 7th–16th August 2006

Objectives

We measured the small angle neutron scattering (SANS) from the lipid monoolein (1-monooleoyl-rac-glycerol, MO) in excess of phosphate buffer of deuterated water (D2O) at different temperatures using a 2D detector in the Q range from $4 \ 10^{-3} - 3 \ 10^{-1} \ A^{-1}$. The sample showed bicontinuous cubic phases with normal water channels and a partial spontaneous ordering. The cubic phases with large water channels (D_{large}) have been observed after addition of the detergent octylgrlucoside (n-octyl-beta-D-glucopyranoside, OG) to MO, i.e. in the monoolein/octylglucoside/water system. Tree samples were studied at different molar ratio of MO to OG and different temperatures in order to find the outlines of the region of stability of D_{large}. Measurements of the scattering from pure OG at different concentrations we also made.

A second group of measurements have been done with MO samples that contain small amount of proteins such as albumin, hemoglobin, trypsinogen, myoglobin, transferrin, alpha chimotrypsinogen A, cytochrome C, or hystone. The objective was to examine the effect of these proteins on scattering behaviour of MO cubic phase[1,2].

Experiment

The measurements have been done at the SANS1 beamline of the FRG-1 research reactor. We have used one setup. The measurements were done in series of 4 or 5 samples within two weeks. The temperature for MO/OG samples were changed from 15 to 65 °C within 5 °C step.

Achievements and Main Results

The fig. 1 below shows images obtained from the 2D SANS1 detector. A sample containing only MO were used as a reference. It scattering correspond to normal water channels and it is presented on the first row.The second row is scattering from a sample MO/OG. The molar ratio between MO and OG was chosen to be close to the critical value for the induction of a nonlamellar-to-lamellar phase transition in MO, which was estimated in our previous work[2]. This allowed us to observe the large water channels. The last row is scattering from MO/histone sample. Histone is the chief protein of chromatin. It acts as spool around which DNA winds and it plays a role in gene regulation.
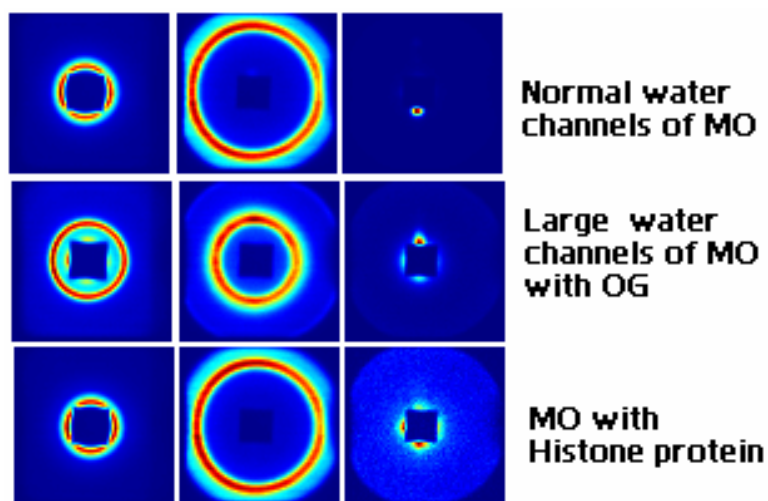
Figure 1: Selected SANS images obtained at room temperature from solutions of monoolein (MO) with different additives.
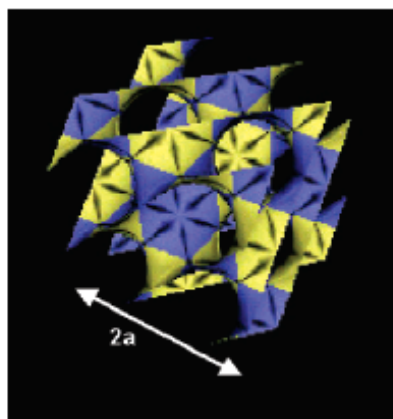
Figure 2: The unit cell of double diamond lattice of monoolein. The {6,4} tilling of curved hexagons is shown in yellow and blue.

This study contributes to the development of controlled drug delivery systems, biosensors, and nanostructured fluid biomaterials[3] and to the elucidation of the intermediate states during membrane fusion[4].

References
[1] Angelov, B., Angelova, A., Papahadjopoulos-Sternberg, B., Lesieur, S., Sadoc, J.-F., Ollivon, M., Couvreur, P., J. Am. Chem. Soc. **128**, 2006, 5813.
[2] Angelov, B.; Angelova, A.; Ollivon, M.; Bourgaux, C.; Campitelli, A., J. Am. Chem. Soc. **125**, 2003, 7188.
[3] Marrink, S. J.; Tieleman, D. P., J. Am. Chem. Soc. **123**, 2001, 12383.
[4] Conn, C.E.; Ces, O.; Mulet, X.; Finet, S.; Winter, R.; Seddon, J.M.; Templer, R.H., Phys. Rev. Lett. **96**, 2006, 108102.

GKSS FORSCHUNGSZENTRUM in der HELMHOLTZ-GEMEINSCHAFT	EXPERIMENTAL REPORT	GeNF SANS-1

The incorporation of oils used as adjuvants for drug solubilisation by copolymer micelles

Proposer:	**Terence Cosgrove[1]**
Co-Proposers:	**Melissa Sharp[1]**
	[1]University of Bristol, Bristol, UK
Experimental Team:	**T. Cosgrove[1], M. Sharp[1], B. Foster[1], M. Quintero[1], V. Haramus[2]**
	[2]GKSS Research Centre
User Group Leader:	**T. Cosgrove[1]**
Date(s) of Experiment:	10th–16th May and 4th–11th July 2006

Objectives

The main objectives of this work are to quantify the swelling of Pluronic type block copolymer micelles by a series of adjuvants, which may be used to aid drug delivery in the pharmaceutical industry[1]. Two adjuvants have been used as part of this study, benzyl benzoate and benzyl alcohol. Benzyl benzoate was studied in detail previously elsewhere, while benzyl alcohol was the focus of the experiments carried out at GKSS. In addition, for comparison purposes, toluene was also used. Small-angle neutron scattering with the use of contrast matching allows for the detailed study of the structure of the swollen micelles.

Experiment

Three different Pluronics have been investigated and their properties are summarised in the table below.

Pluronic	$(EO)_m(PO)_n(EO)_m$		Molecular weight
	m	N	
P85	26	40	4,600
P105	37	56	6,500
F127	99	65	12,600

The block copolymers were swollen by the incorporation of the low molecular weight organic compounds benzyl alcohol and toluene. The current experiments add to the body of data that has already been collected on these systems by PFG-NMR at Bristol.

The samples run at GKSS were 10% Pluronic solutions with concentrations of benzyl alcohol varying between 2 and 7 %. Also toluene was added at concentrations of 1 and 2%. The samples were run off-contrast, at the adjuvant contrast and at the ethylene oxide contrast. These measurements were carried out at 25°C, 30°C and 37°C. Four detector distances were used, 0.7, 1.8, 4.5 and 9.7 m, with a neutron wavelength of 8.1 Å, leading to a Q-range of approximately 0.005-0.25 Å^{-1}.

The data obtained at the adjuvant contrast and the off-contrast data was fitted to the Pedersen model[2], while the data at the ethylene oxide contrast was fitted to a simple hard spheres model.

Achievements and Main Results

The scattering curves obtained for 10 w/w % Pluronic P85 with added benzyl alcohol obtained at 25°C are shown in Figure 1. The samples were run with the adjuvant contrast matched to the solvent and the data was fitted to the Pedersen model[2]. From the fitting procedure we find that the aggregation number of the polymer chains in the micelles increases from 25 to 33 upon the addition of benzyl alcohol. It is also found that the fraction of polymer micellised increases from 0.5 to 0.89. Finally it was found that the radius of the core of the micelle increased from 42 Å to 56 Å.

The results from the pulsed-field gradient NMR experiments, which give the diffusion coefficients of the different components in the system, showed that the benzyl alcohol diffuses more than an order of magnitude faster than the polymeric micelles. Contrast matching was therefore used to determine where in the system the benzyl alcohol was present, by matching the polymer to the solvent. The scattering curves obtained at this contrast are shown in Figure 2. The results show that benzyl alcohol is present within the polymeric micelles. The data at this contrast is fitted to a simple hard spheres model, and a radius of 30 Å and 40 Å are obtained for the two benzyl alcohol concentrations studied.

Similar results are achieved with the other Pluronic block copolymers studied. The interpretation of the data obtained at higher temperatures is still underway, but the micellisation behaviour appears to change radically, specially at the higher benzyl alcohol concentrations used.
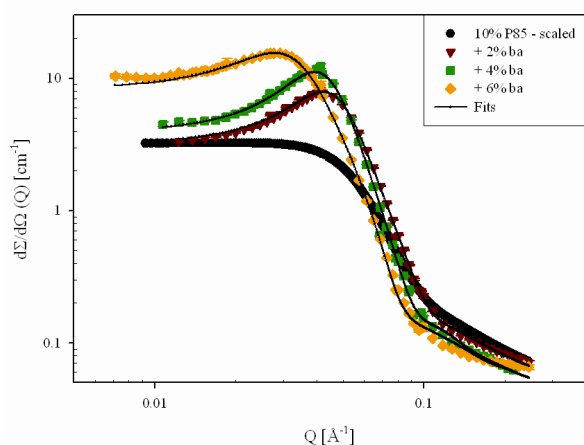
Figure 1: Scattering intensity as a function of the scattering vector for 10 w/w % P85 with the addition of benzyl alcohol at 25°C. The samples were run with the benzyl alcohol contrast matched with the solvent. The data has been fitted to the Pedersen model[2].
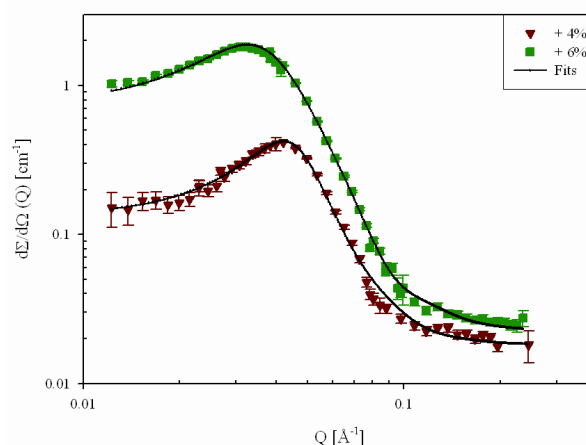
Figure 2: Scattering intensity as a function of the scattering vector for 10 w/w % Pluronic P85 with the addition of benzyl alcohol at 25°C. The samples were run with the polymer contrast matched with the solvent. The data has been fitted to a simple hard spheres model.

References

[1] Wang, L.; Venkatraman, S.; Kleiner, L. *Journal of Controlled Release* **99**, 2004, 207.
[2] Pedersen, J. S.; Gerstenberg, M. C. *Macromolecules* **29**, 1996, 1363.

![GKSS logo] GKSS FORSCHUNGSZENTRUM in der HELMHOLTZ-GEMEINSCHAFT	**EXPERIMENTAL REPORT**	**GeNF SANS-1**
Domain formation in lipid raft mixtures		
Proposer: **Co-Proposers:**	**H. Heerklotz[1],** [1]Biocenter, Basel, Switzerland **T. Gutberlet[2],** [2]PSI, Villigen Switzerland	
Experimental Team:	**Vasyl Haramus[3],** [3]GKSS	
User Group Leader:	**H. Heerklotz**[1]	
Date(s) of Experiment:	27th March–2nd April 2006	

Objectives

Biological membranes are supposed to contain functional domains (lipid rafts) made up in particular of sphingomyelin (SM) and cholesterol (Cho), glycolipids, and certain proteins. It has been the basic assumption of numerous biochemical studies that the application of the detergent Triton at 4°C allows the isolation of these rafts as a detergent-resistant membrane fraction (DRM). However, microcalorimetric measurements have revealed that this assumption is not justified and that Triton may even induce the formation of DRMs in homogeneous membranes. The changes of the domain properties due to the presence of Triton were monitored in vesicles of mixtures of POPC, egg SM, and Cho at different Triton concentrations [1]. The results were discussed in terms of liquid disordered (ld) and -ordered (lo) bilayer and micellar (mic) phases, and the typical sequence encountered with increasing Triton content or decreasing temperature was found to be ld, ld + lo, ld + lo + mic, and lo + mic. Recently the structure of a ternary model raft lipid mixture of unlabelled SM, Cho and DOPC or POPC (1:1:1) multilamellar vesicles was studied by SANS [2]. The results were interpreted in terms of the existence of microdomains at low temperatures. Pencer et al. have described the domain formation in unilamellar vesicles of mixtures of DOPC, DPPC and Cho (1:1:1) using chain-deuterated DPPC [3] but did not study the effect of the detergent. In the present SANS measurements at GKSS, the quaternary system of POPC-SM-Cho (1:1:1) at different Triton content and temperatures was investigated using POPC with a deuterated palmitoyl chain at various contrasts. The study aimed at providing an independent, structural proof for the statement that Triton changes the domain structure in so-called lipid raft mixtures.

Experiment

Model lipid mixtures of POPC-SM-Cho (1:1:1) at different Triton content and temperatures, in particular at 0, 0.1, 1.0 and 4.0 molar ratio of Triton per PC in the model system and at temperatures of 12, 37 and 60°C, covering all possible assumed phase states were measured at SANS1 at GKSS. The contrast of solvent towards the lipid mixture was varied using three solvent mixtures with fractions of D_2O of 12, 24 and 36%, respectively, matching the scattering length density of the (1:1:1) mixture with chain deuterated POPC-d31 at 24% D_2O. Figure 1 shows the scattering curves for mixture of POPC-d31-SM-Cho (1:1:1) at 0.1 molar ratio of Triton content at 12, 24 and 36% D_2O at 12 °C. A first data analysis by fitting of the structure factor of a unilamellar vesicle was performed with the sasfit programme at PSI.
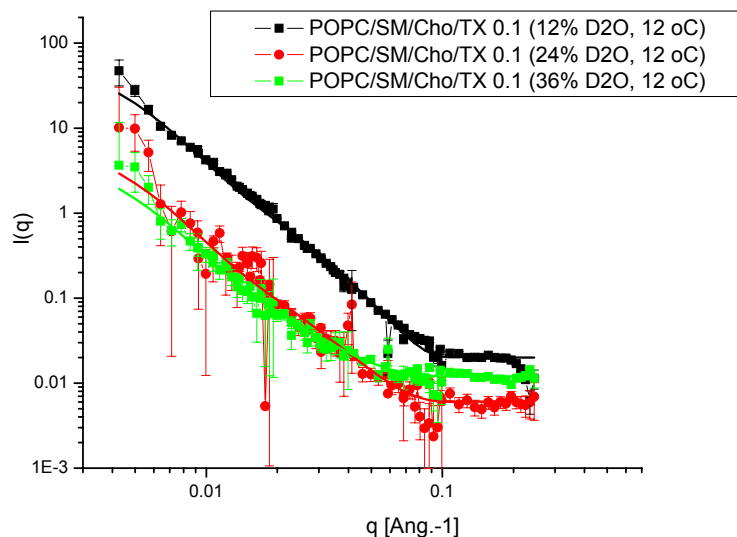
Figure 1: Scattering intensity as a function of scattering vector for samples of POPC-d31-SM-Cho (1:1:1) at 0.1 molar ratio of Triton content at 12, 24 and 36% D_2O at 12 ^{o}C, solid lines are the fit by the structure factor model.

Achievements and Main Results

The measurements provided clear evidence for the presence of a non-homogeneous density distribution within the lipid bilayer of the unilamellar vesicles. For a homogeneous membrane density in a single shell model of a unilamellar vesicle, no scattered intensity of the structure factor should be visible when the scattering length density of the solvent nominally matches the lipid bilayer scattering density. For the POPC-d31-SM-Cho (1:1:1) mixture this is the case for a 24.1 % D_2O solution (red curve in Fig.1). The parameters used in the fitting of the structure factor assumed a radius of the vesicle of 13.3 nm and a bilayer thickness of 5.64 nm and a LogNorm distribution function of the particle distribution. The model used for that purpose is, however, not applicable for determining the domain size and/or distribution of the domains in the bilayer system. This goal is currently pursued in collaboration with J. Pencer, Chalk River Lab., in order to resolve the main issue of the research project.

References

[1] H. Heerklotz, Biophys. J., **83**, 2002, 2693.
[2] C. Nicolini et al., PCCP, **6**, 2004, 5531.
[3] J. Pencer et al., Eur. Phys. J. E, **18**, 2005, 447.

![GKSS FORSCHUNGSZENTRUM in der HELMHOLTZ-GEMEINSCHAFT]	**EXPERIMENTAL REPORT**	**GeNF SANS-1**

A SANS study of polyfluorene beta phase in solution		

Proposer: **Co-Proposers:**	**Matti Knaapila**[1], [1]Department of Physics & Durham Nanomaterials UIC, University of Durham, South Road, Durham DH1 3LE, UK
	Laszlo Almasy[2] **and Andy Monkman**[1], [2]Research Institute of the Solid State Physics (Budapest, Hungary)
Experimental Team:	**Matti Knaapila**[1] **& Vasyl Haramus**[2], [2]GKSS Forschungszentrum
User Group Leader:	**Matti Knaapila**[1]
Date(s) of Experiment:	23rd–30th November 2005

Objectives

Polyfluorenes are a specific class of electroluminescent polymers. Structurally, they are so called hairy rods consisting of a rodlike backbone with flexible side chains. Two most important polyfluorenes are PFO with two linear octyl side chains and PF2/6 with two branched ethylhexyl side chains per each repeat unit. In solid state, PF2/6 is helical showing nematic or hexagonal structure. Besides hexagonal structure of helices, PFO can take a linear shape resulting in a coexistent interdigitated lamellae or zig-zag type structure, so called beta phase. It is further observed that there is a phase transition from two phase (alpha plus beta) system to pure alpha phase at 80 $^{\circ}$C. The control of these phases is interesting because beta phase domains act as energy traps resulting in the emission quench. The idea of this work was to study how the beta phase emerges in the selected solutions.

Experiment

The samples contained PF2/6 and PFO as well as side chain deuterated PFO, all both in deuterated toluene and deuterated methyl cyclohexane (MCH). The samples were studied using SANS at Geesthacht (SANS-1). Q-range of about 0.003-0.3 Å^{-1} was used. Experiments followed the standard procedures of SANS.

Achievements and Main Results

We clarified on the nanoscale structure and solvent induced phase behavior of PF2/6 and PFO, in good and bad (poor) solvents; deuterated toluene and deuterated MCH at 20 $^{\circ}$C. Arguments based on the scaling of the scattering intensity with q, fitting to rodlike and sheet-like models and indirect Fourier transform (IFT) methods indicated that PF2/6 adopts a rodlike conformation in both solvents. The rodlike objects of PF2/6 are 70-90 nm long and are proposed to contain predominantly only a single chain (diameter of the order of 1 nm) indicating dissolution down to the molecular level. The rods are thinner in MCH than in toluene. In contrast, PFO shows rodlike structure in toluene but clear sheet-like structures in MCH (Figure 1), this latter observation indicating dissolution down to "colloidal" level. The rodlike structure is composed predominantly by individual chains adopting dominantly a conformational isomer C_{α}. The sheet-like objects (characteristic size of 100 nm and thickness of 2-3 nm) are instead suggested to comprise of a layer of 1-3 chains and contain conformational isomer C_{β}, of those chains observed in the so called beta-phase (or beta sheets) in the solid state. The observed phenomena were not found to depend on concentration over the concentration regime 5-10 mg/mL [1].
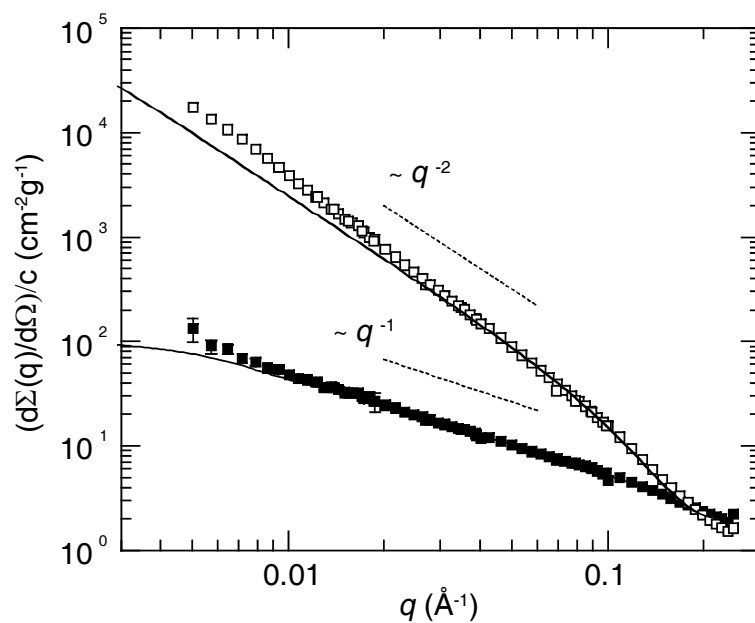
Figure 1: SANS data of PFO in toluene-d_8 with concentration of 10 mg/mL (solid squares) and in MCH-d_{14} (open squares). Solid lines are, respectively, the fits of the data based on the models of rodlike and disk-like objects. Dashed lines show the -1 and -2 decays for comparison.

References

[1] M. Knaapila, V. M. Garamus et al., *Macromolecules* **39**, 2006, 6505.

![GKSS logo] GKSS FORSCHUNGSZENTRUM in der HELMHOLTZ-GEMEINSCHAFT	**EXPERIMENTAL REPORT**	**GeNF SANS-1**

<table>
<tr><td colspan="2">SANS investigation of nanoporous alumina membranes</td></tr>
<tr><td>Proposer:</td><td>Vasyl Ryukhtin[1], Jan Saroun[1]
[1]Nuclear Physics InstituteAcademy of Sciences of the Czech Republic, 25068 Rez near Prague, Czech Republic</td></tr>
<tr><td>Co-Proposers:</td><td>Ivan Turkevych[2], [2]National Institute for Materials Science, Nanomaterials Lab., 3-13 Sakura, Tsukuba, Ibaraki 305-0003, Japan</td></tr>
<tr><td>Experimental Team:</td><td>Vasyl Haramus[3], [3]GKSS</td></tr>
<tr><td>User Group Leader:</td><td>Vasyl Ryukhtin[1]</td></tr>
<tr><td>Date(s) of Experiment:</td><td>2nd–8th April 2006</td></tr>
</table>

Objectives

Aluminum anodization [1] is one of the most controllable self-organized processes yielding vertically aligned uniform cylindrical pores, which can be considered as nano-beakers representing confined space for either self-assembly or synthesis of nanomaterials. Recently, nano-porous anodic alumina (PAA) has been used to make a wide variety of diverse nano-structures, ranging from semiconductor quantum dots and magnetic nanowires to field-effect arrays of carbon nanotubes.

The most important feature of the porous anodic alumina is the high aspect ratio of nanopores, which creates an excellent opportunity for the fabrication of long and more importantly monodisperse nanowires inside the long pores. However the straightforward characterization of the thick templates by microscopical methods such as SEM or AFM cannot provide excessive information about their properties in a bulk. SANS could be very useful and even unique tool for investigations of porous ceramics [2], it enables non-destructive studies of bulk samples and can provide viable information about their structure complimentary to the SEM analysis.

Experiment

SANS spectra measured at samples with different length of pores (Lp) are shown in Fig. 1. Fabrication of these samples was interrupted on the beginning (Fig. 1a, Lp=15.5 µm) and on finishing (Fig. 1b, Lp=55 µm) of the second step of anodization. The lengths of pores were estimated by SEM images taken from break of the samples.
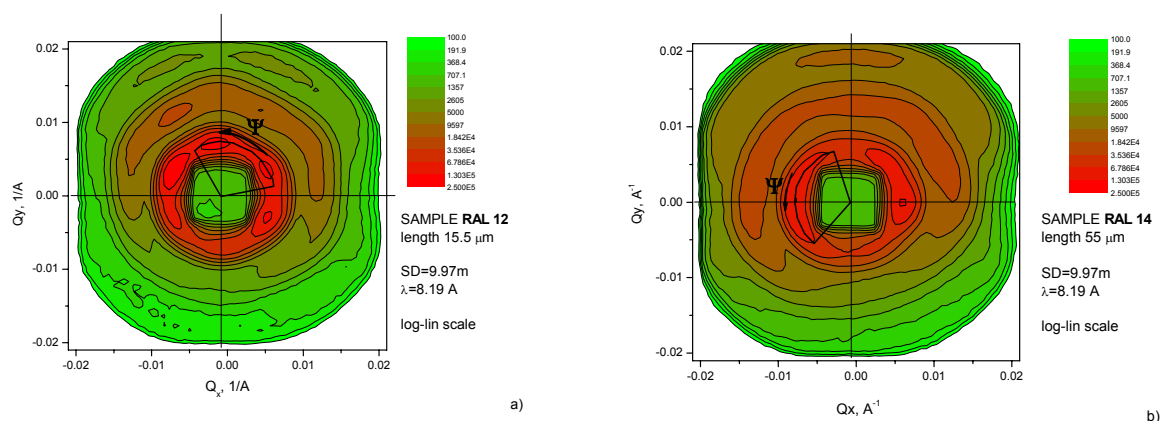
Figure 1: SANS pattern measured on PAA sample at sample-detector distance SD=9.7 m.

Achievements and Main Results

Smearing of hexagonal peaks with increasing of Lp can be seen directly in Fig. 2. Random orientation of these domains leads to smearing of scattering pattern thus it become almost isotropic. Fully isotropic pattern were not observed in our case. This says that domains – regions with highly oriented pores are not randomly oriented indeed but have mutual correlation in sample plane. Moreover, borders of the domains do not "growth" parallel to the axes of pores but curve during the anodization and growing. The sections of two neighboring peaks (see Fig. 2) were taken in dependence on azimuthal angle Ψ at fixed scattering angle $|Q_{10}|=0.0062$ Å^{-1} as it shown in correspondent 2D patterns (see Fig. 1). It can be seen that these neighboring peaks (Fig. 2a) overlap due to smearing (Fig. 2b) with increasing length of pores.
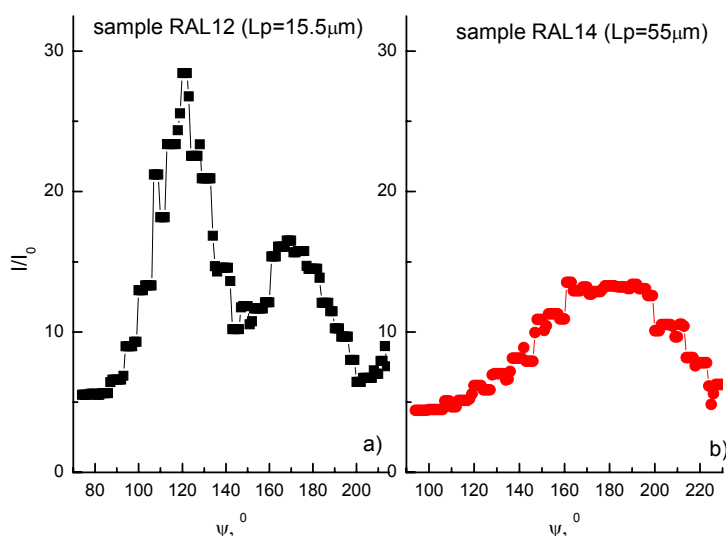
Figure 2: Sections of 2D SANS spectra taken for Q=0.0062 A^{-1} for azimuthal range $\Delta\Psi = 120^0$ covering the two main reflections.

Position of the main peaks in Q-space (Q_x, Q_y) permits determination of interporous distance by simple equation $d_{10}=2\pi/|Q|$ (where $Q=(2\pi/\lambda)\cdot\sin(\theta/2)$ is momentum-transfer vector, θ – scattering angle). The position of first order peaks is clearly seen at $|Q_{10}|=0.0062$ Å^{-1} for these samples. It corresponds to SEM estimation of d_{10} of about 100 nm. Secondary peaks are weaker, however, are detectible at $2*|Q_{10}|$ position. Third and further reflection are smeared by instrumental curve and can not be detected on a background of Porod's tails. However, numerical estimation of volume fraction of pores by these SANS data has no sense in this case since the total scattering intensity is highly dependent on accuracy of sample installation.

SANS results measured on highly ordered nanoporous alumina membranes showed the presence of mutual correlation between domains. It was observed for the samples with initial stage of porous growing. SEM can not provide us by such information due to limited image size. However, it was impossible to obtain pore's size characteristics from SANS because the signal of single pores was much weaker then peaks from porous ordering.

References

[1] J. P. O'Sullivan, G. C. Wood, Morphology and mechanisms of formation of porous anodic films on aluminum, *Proc. R. Soc. London* A **317**, 1970, 511.
[2] A. J. Allen, Characterization of ceramics by X-ray and neutron small-angle scattering, Journal of the American Ceramic Society, **88**, 2005, 1367.

GKSS FORSCHUNGSZENTRUM in der HELMHOLTZ-GEMEINSCHAFT	**EXPERIMENTAL REPORT**	**GeNF SANS-1**

SANS investigations of the porosity in superplastically deformed ceramics

Proposer:	**Vasyl Ryukhtin[1], Pavel Strunz[1]** [1]Nuclear Physics Institute, Academy of Sciences of the Czech Republic, 25068 Řež near Prague, Czech Republic
Co-Proposers:	**Yoshinobu Motohashi[2]** [2]Ibaraki University, Faculty of Engineering, Research Center for Superplasticity, Hitachi, Ibaraki, 316-8511 Japan
Experimental Team:	**Haramus Vasyl[3]**, [3]GKSS Forschungszentrum
User Group Leader:	**Vasyl Ryukhtin[1]**
Date(s) of Experiment:	25th–29th September 2006

Objectives

Ceramics are very attractive materials for industrial applications due to their unique physical properties. Discovering of superplasticity effect in yttria-stabilised tetragonal zirconia polycrystals (Y-TZP) has triggered an extensive international research on ceramics superplasticity in last fifteen years. Cavitation is closely connected with important mechanisms of superplastic deformation (SPD) in ceramics. The cavities formed in the ceramics influence their mechanical, electrical and thermal properties. Generally, cavities and/or cracks in conventional ceramics propagate in a direction perpendicular to the axis of an applied tensile stress. In contrast to conventional ceramics, the cavitation mode in 3Y-TZP (with 3 mol% of yttria) is similar to that in metallic systems where cavities grow and align in parallel to applied stress. Regarding to porosity in ceramics, small-angle neutron scattering (SANS) is very important technique, since it is a non-destructive method, which can be applied directly to the specimens without any further sample preparation [1].

Our recent SANS results have demonstrated two qualitatively different cavitation regimes [2]. In a case of so called high stress regime, a new type of flat pores transversal to the tension axis was observed, in addition to the usually present slightly prolate cavities.

The formation of flat cavities during high strain-rate superplastic deformation in 3Y-TZP, found by means of SANS for the first time ever, can be formed even at very early stage of SPD, *i.e.*, just in the yielding period of the tensile deformation. If so, the actual yield stress must have been higher than the observed one. This fact may affect the discussion of the mechanism of SPD in ceramics. The experimental aim was done for proving this statement.

Experiment

Samples were measured *ex-situ*. SPD of the specimens were carried out under constant strain rate at temperature T=1450 ^{0}C. True strain varies from 0 % to 30 % for different samples. Specimens were installed vertically during the SANS experiment, *i.e.* strain direction is vertical as well. Incident beam was defined by rectangular cadmium aperture of size 2x10 mm^2 in order to avoid of refractions from sides of samples.
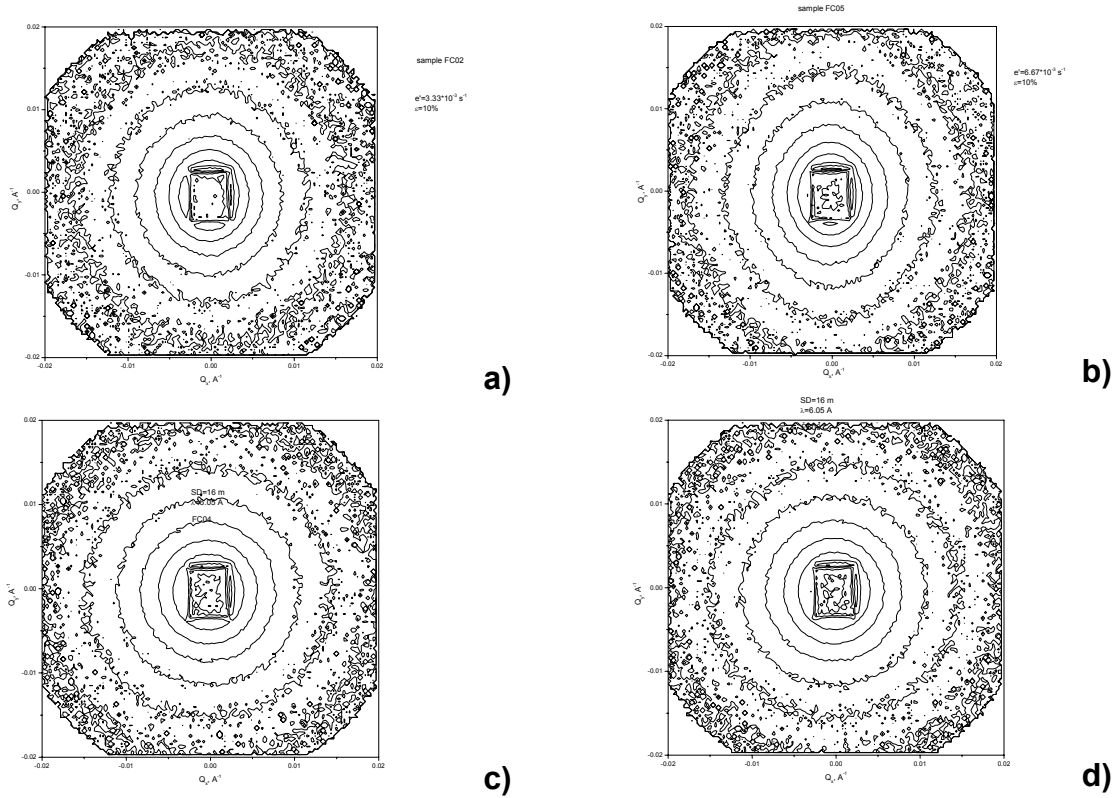
Figure 1.: Scattering from the Y-TZP specimens deformed at (a) e'= 3.33×10^{-3} s^{-1} and (b) e'= 6.67×10^{-3} s^{-1} up to true strain of e=10% with (c) e'= 3.33×10^{-3} s^{-1} and (d) e'= 6.67×10^{-3} s^{-1} up to e=0% (at yield point) at temperature T=1450 ^{0}C.

Achievements and Main Results

2D SANS scattering patterns are shown in Fig. 1. Slight anisotropy can be observed for the both samples even at so small deformation (e=10%). Deformation conditions for these two samples were the same with exception of strain rate.

Anisotropy is oriented vertically in the both cases but aspect ratio is slightly higher for material deformed at deformation rate e'= 6.67×10^{-3} s^{-1} (see Fig. 1b) than for that deformed at two times lower deformation rate e'= 3.33×10^{-3} s^{-1}. Such orientation says about presence of cavities and fine cracks oriented perpendicular to applied stress. However, formation of prolate cavities with longer axis parallel to applied stress was not detected at such stages. Scattering for samples deformed just up to yield point are fully isotropic (see Fig. 1c, d). Obviously, there are no the transversal cracks, the scattering arises due to residual porosity which randomly oriented in bulk of the samples.

The measured scattering functions obey the Porod's law, *i.e.* it is proportional to Q^{-4} in whole covered Q-range. Size information of the cavitation in studied materials could be obtained by means of ultra small-angle neutron scattering (USANS) techniques – DBC-SANS and/or DC-SANS.

References
[1] V. Ryukhtin, J. Šaroun, S. Harjo, Y. Motohashi, M. Baron and R. Loidl, J. Appl. Cryst. **36**, 2003, 478.
[2] V. Ryukhtin, J. Šaroun, S. Harjo, Y. Motohashi, A. Wiedenmann, P. Strunz, Physica B **350**, 2004, 1019.

SANS Study of Poly(Glycidol)-Based Analogues to Pluronic Copolymers

Proposer:	**Stanislav Rangelov[1],** [1]Institute of Polymers, Bulgarian Academy of Sciences
Co-Proposers:	**Silvia Halacheva[1]**
Experimental Team:	**Vasyl Haramus[2],** [2]GKSS Forschungszentrum
User Group Leader:	**Stanislav Rangelov[1]**
Date(s) of Experiment:	19th–26th November 2006

Objectives

The aim of the experiments was to complement studies on self-assembly in aqueous solution of amphiphilic copolymers based on poly(glycidol) (PG). The copolymers are considered as analogues to the commercially available and extensively investigated Pluronic, poly(ethylene oxide)-poly(propylene oxide)-poly(ethylene oxide), PEO-PPO-PEO, block copolymers in which the flanking PEO blocks are substituted by blocks of structurally similar PG blocks. The structural formulae of the monomer units of PEO, PPO, and PG are presented in Figure 1.
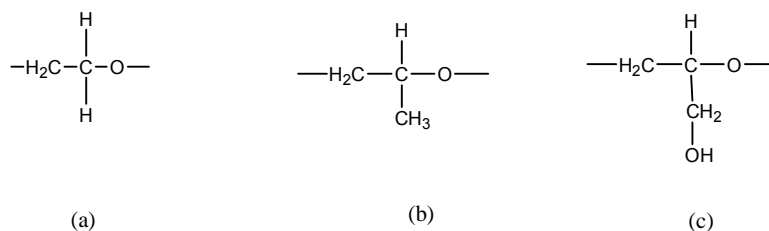
Figure 1: Monomer units of (a) poly(ethylene oxide), (b) poly(propylene oxide), and (c) linear poly(glycidol).

The PG-based analogues form in aqueous solution and above a certain critical concentration larger in both size and aggregation number particles than the corresponding Pluronic copolymers. With the SANS experiments we aimed to parametrize the size of the PPO domains inside the particles and follow possible shape and order-disorder transitions. Four copolymers (see Table 1 for the abbreviations, compositions, PG contents, and molecular weights) were investigated in wide concentration (2 - 33 wt. %) and temperature (15 – 60 ^{o}C) ranges. This is the first time such systems have been investigated by SANS.

Table 1: Abbreviations, composition, poly(glycidol) content, and total molecular weight of the copolymers used in this study. G and PO denote PG and PPO monomer units, respectively.

Abbreviation	Composition	PG content (wt. %)	Molecular weight
LGP63	$(G)_6(PO)_{34}(G)_6$	30	2900
LGP67	$(G)_{26}(PO)_{34}(G)_{26}$	70	5800
LGP68	$(G)_{51}(PO)_{34}(G)_{51}$	80	9500
LGP68+	$(G)_{70}(PO)_{34}(G)_{70}$	84	12400

Achievements and Main Results

Evolutions of scattering curves with copolymer composition and temperature are presented in Figures 2 and 3, respectively. The scattering patterns of the concentrated solutions and high temperatures are characterized by a peak attributed to inter-correlation between PPO domains (right panels of Figures 2 and 3). At lower concentrations and/or temperatures shoulders, rather than peaks, were observed (left panels of Figures 2 and 3).
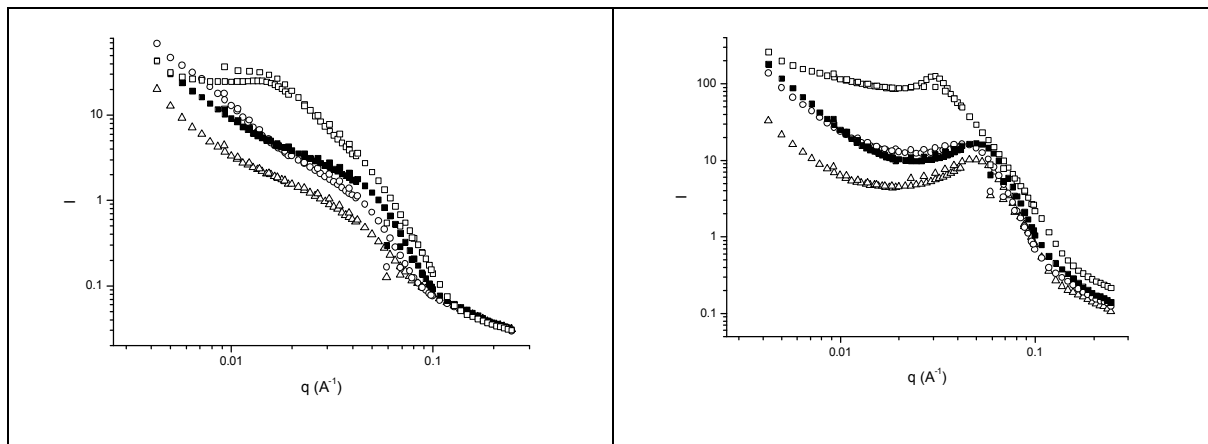
Figure 2: SANS profiles obtained at 40 ^{o}C for 2 (left) and 33 (right) wt. % solutions in D$_2$O LGP63 (squares), LGP67 (closed squares), LGP68 (circles), and LGP68+ (triangles).
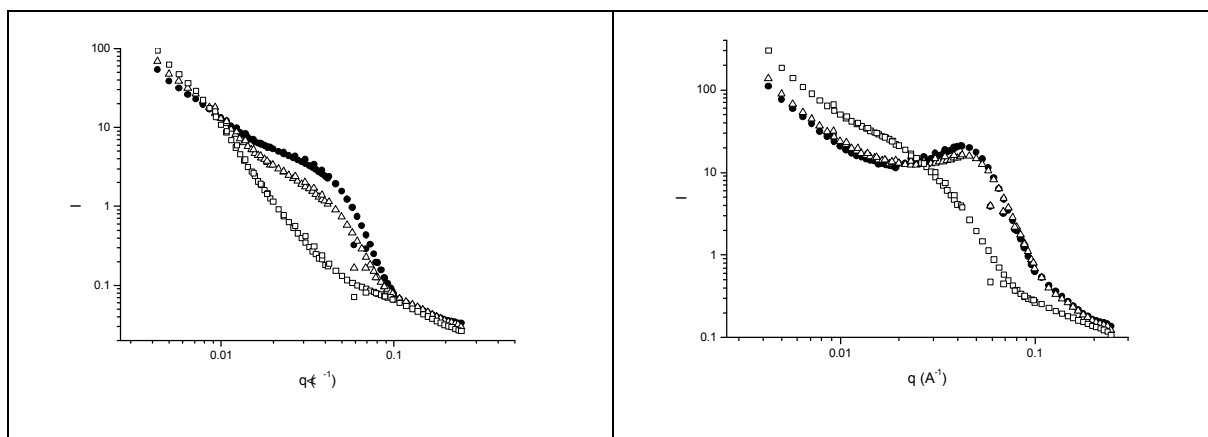
Figure 3: SANS profiles obtained from solutions of LGP68 in D$_2$O at 2 (left) and 33 (right) wt. % and 15 (squares), 40 (triangles), and 60 (closed circles) ^{o}C.

The results from the study are in line with previous results[1] as well as light scattering[2] and rheology[3] data and give insight for the internal structures of the particles. However, before we proceed with data treatment suitable models should be found or constructed. To follow the effect of the PPO block measurements of other series of copolymers that differ from the present one in molecular weight of the middle block would be interesting and accomplish the study.

References

[1] Halacheva, S.; Rangelov, S.; Tsvetanov, Ch., *Macromolecules 39*, **2006**, 6845.
[2] Rangelov, S.; Almgren, M.; Halacheva, S.; Tsvetanov, Ch., *Macromolecules* – submitted.
[3] Halacheva, S.; Rangelov, S.; Tsvetanov, Ch., *Macromolecules* – in preparation.

![GKSS Logo] GKSS FORSCHUNGSZENTRUM in der HELMHOLTZ-GEMEINSCHAFT	**EXPERIMENTAL REPORT**	**GeNF SANS-1**

Investigation of fluorocarbon- and hydrocarbon-rich micelles by SANS		
Proposer:	**Mats Almgren**[1] [1]Uppsala University, Uppsala, Sweden	
Co-Proposers:		
Experimental Team:	**Vasyl Haramus**[2] [2]GKSS Forschungszentrum	
User Group Leader:	**Mats Almgren**[2]	
Date(s) of Experiment:	13th–17th November 2006	

Objectives

Mixtures of fluorocarbon and hydrocarbon surfactants in aqueous solution either assemble to form mixed micelles, or to form coexisting populations of hydrocarbon-rich and fluorocarbon-rich micelles. In earlier experiments (May 2004, August 2005, April 2006, August 2006) we have shown that contrast variation SANS results give strong support for the demixing of micelles into hydrocarbon-rich and fluorocarbon-rich populations in solutions containing a fluorinated and a normal cationic surfactant. This is the first time such a demixing have been verified by SANS studies[1,2]. We have also found that. $C_8F_{17}C_2H_4C_5D_5NCl$ plus $C_{12}H_{25}C_5H_5NCl$ make only mixed micelles, but non-ideally mixed, as expected, and that an ideally mixed system, SDS mixed with its fully deuterated analog, gave no signs on non-ideal broadening of the composition distribution. The present investigation deals with another, much debated fluorocarbon–hydrocarbon surfactant system, namely sodium decyl sulfate mixed with sodium perfluorootanoate. The system was recently subject to a very careful NMR study, indicating no demixing.[3]

Experiment

Mixtures of surfactants form micelles in aqueous solution. The mixed micelles range from ideal mixtures (e.g. deuterated and non-deuterated forms of the same surfactant) to strongly non-ideal, as in mixtures of normal and fluorinated surfactants. It was realized early on (in the 1960, Mysels, Murkerjee and others) that in the latter case a very curious situation could result, where two types of micelles coexists in one and the same solution, one rich in the fluorinated component the other with mainly hydrogenated component. It has since shown difficult to unambiguously proove that such a situation prevails. Some specific demonstrations of the simultaneous presence of two types of micelles have been made for a few systems, but no general study that is fully satisfactory. Conflicting results have often resulted from different methods, used by different researchers.

SANS with contrast variation by using D_2O/H_2O mixtures for solvent would, at a first glance, appear as ideally suited for such studies: one mixture would make one type of micelles invisible, another the other type of micelles, and a scattered intensity would remain for the demixed system at the nominal match point for the mixed surfactants, where the scattering would all but disappear for an ideally mixed system. Only few studies[4-6] of this kind have been made prior to our series of measurements.[1,2] The early studies seemed to suggest that the systems selected all contained mixed micelles. On a closer inspection of the results, however, in the light of our later findings, it appears that this conclusion is maybe not inescapable.

In the second of our published papers,[2] we presented a simplified theory for the intensity as a function of the contrast:

$$\frac{d\Sigma}{d\Omega}(0) = n_m V_m^2 \left[\sigma^2 \left(\rho_{FS} - \rho_{HS} \right)^2 + \left(\overline{\rho} - \rho_S \right)^2 \right]$$

It is assumed that we have a distribution of composition over globular micelles of equal size (or, if there is a size polydispersity, that it is not coupled to the composition variation). The width of the composition distribution is given by σ, ρ stands for the scattering length density, subscripts HS for hydrogenated surfactant, FS fluorinated surfactant, S for solvent, and the bar designates the nominal matchpoint for the surfactant mixture, n_m is the number density of micelles, and V_m the dry volume of a micelle. Besides the width of the composition distribution – which is the only information about this distribution that can be obtained from the scattered intensity at zero angle – the micelle aggregation number and the scattering length density at the minimum are determined. We have used this procedure for the systems in the table.

System	N_{agg}	σ	$\overline{\rho}$	$\overline{\rho}_{calc}$
C_{16}TAC + HFDePC 25°C	91	0.33	0.35	0.35
C_{16}TAC + HFDePC 60°C	65	0.20	-	0.35
C_{16}PC + HFDePC 25°C	89	0.39	0.38	0.375
C_{16}PC + HFDePC 60°C	68	0.22	0.37	0.375
C_{12}PC + HFDePC 25°C	62	0.22	0.46	0.42
SDS + SDS-d25 25°C	78.5	0.005±0.030	0.57	0.59
SdeS + SPFO 25°C	**56**	**0.07±0.024**	**0.41**	**0.42**

The results from the study of the first two systems have been published.[1,2] The width of the composition distribution decreases with increasing temperature, as expected, but it is still much larger than the value for ideal mixing, $\sigma = 0.1$ for $N_{agg} = 50$, as could be expected for a non-ideally mixed system, even if there is no clear demixing into two micelles populations. Note that σ is always smaller than $\sigma = 0.5$, the value for complete demixing into pure micelles of the two components. A square distribution of compositions from 0 to 1 – which is the broadest unimodal distribution – would have $\sigma = 0.289$.

Our earleir results thus indicate that the mixed systems of hydrogenated and fluorinated surfactants have non-ideal, broad micelle compositions, and that they are probably bimodal for the C16 systems at 25°C. In order to verify that other factors that contribute to a scattered signal at the match point have not been overlooked, we also studied an ideal system, composed of SDS and its deuterated analog. The results show a much smaller width of the composition distribution.

Achievements and Main Results
The results from the present study of sodium perfluorooctanoate and sodium decylsulfate in 200mM NaCl, measured at 8 contrasts betqeen $X_{D2O} = 0$ to $X_{D2O} = 1.0$, are given in bold face as the last entry in the table. The results, still tentative since the supplementary NMR studies needed to have full controll of the micelle composition have not yet been completed, indicate that the system is close to ideally mixed. Under theses circumstances the value assigned to the width of the composition distribution is very uncertain, but it shows at least that no broadening from non-ideality effects can be detected. This conclusion agrees with the results

of the detailed study by NMR techniques, giving unprecedent detailed and trustworthy data on micelle composition, variation of free surfactant concentrations etc. Thus, this particular system does not demix, as also verified by our result.

References

[1] Almgren, M.; Garamus, V., J Phys. Chem. B **109**, 2005, 11348.

[2] Kadi, M.; Hansson, P.; Almgren, M.; Bergström, M.; Garamus, V., Langmuir **20**, 2004, 3933.

[3] Nordstierna, L.; Furó, I.; Stilbs, P., J. Am. Chem. Soc. **128**, 2006, 6704.

[4] Burkitt, S. J.; Ottewil, R. H.; Hayter, J. B.; Ingram, B. T., Colloid Polym. Sci. **265**, 1987, 628.

[5] Caponetti, E.; Chilura Martino, D.; Floriano, M. A.; Triolo, R., Langmuir **9**, 1993, 1193.

[6] Pedone, L.; Chilura Martino, D.; Caponetti, E.; Floriano, M. A.; Triolo, R., J. Phys. Chem. B. **101**, 1997, 9525.

![GKSS logo] GKSS FORSCHUNGSZENTRUM in der HELMHOLTZ-GEMEINSCHAFT	**EXPERIMENTAL REPORT**	**GeNF SANS-1**

SANS study of nonionic mixed micelles		
Proposer:	**Jan Skov Pedersen[1]**	
	[1]University of Aarhus, Aarhus, Denmark	
Co-Proposers:	**Petra Bäverbäck[1]**	
Experimental Team:	**Vasyl Haramus[2]**	
	[2]GKSS Forschungszentrum	
User Group Leader:		
Date(s) of Experiment:	26th–30th November 2006	

Objectives

Surfactants are amphiphilic molecules that self-assemble into micelles in water. The structure of the micelles/aggregates is very important for the detergency efficiency and in other industrial applications. Our project aims at identifying any synergetic effects that occur when mixing two non-ionic surfactants with different head group properties; one with a flexible head group, n-dodecyl-hexaethyleneglycol ($C_{12}E_6$), and one sugar-based surfactant with a bulky head group, n-dodecyl-β-D-maltoside ($C_{12}M$). Synergetic effects have already been studied in mixtures of cationic and anionic surfactants [1], and in mixtures of ionic and non-ionic surfactants [2], whereas very little research has been done on non-ionic mixtures.

Experiment

We measured solutions of the two pure surfactants and five mixtures of them in D_2O. The compositions of the mixtures were 15, 30, 50, 70 and 85 mol %. Six total concentrations of about 5, 4, 3, 2, 1 and 0.5 wt % were investigated for each composition.

Achievements and Main Results

Figure 1 shows the scattering curve for the seven surfactant compositions at a concentration of 1 wt % for which the concentration (structure factor) effects are modest. Four different sample-detector distances were used for obtaining the data. The curve is flat at low scattering vector for $C_{12}M$ and the slope increases gradually when the amount of $C_{12}E_6$ is increased. The data thus indicate a transition from globular to worm-like aggregates when going from $C_{12}M$ to $C_{12}E_6$. Already at 15 mol % $C_{12}E_6$ we see a significant change from the pure $C_{12}M$. Further analysis of the data will give us more detailed information on the structure of the micelles as well as their sizes and growth laws at the various compositions. We will analyse the SANS data together with SAXS and light scattering data that we have already measured on the same system. We will employ a self-consistent analysis which takes micelle growth and concentration related interference effects into account [3]. This is expected to provide detailed insight into composition dependence of the structure formation and thus into the synergetic effects of the system.
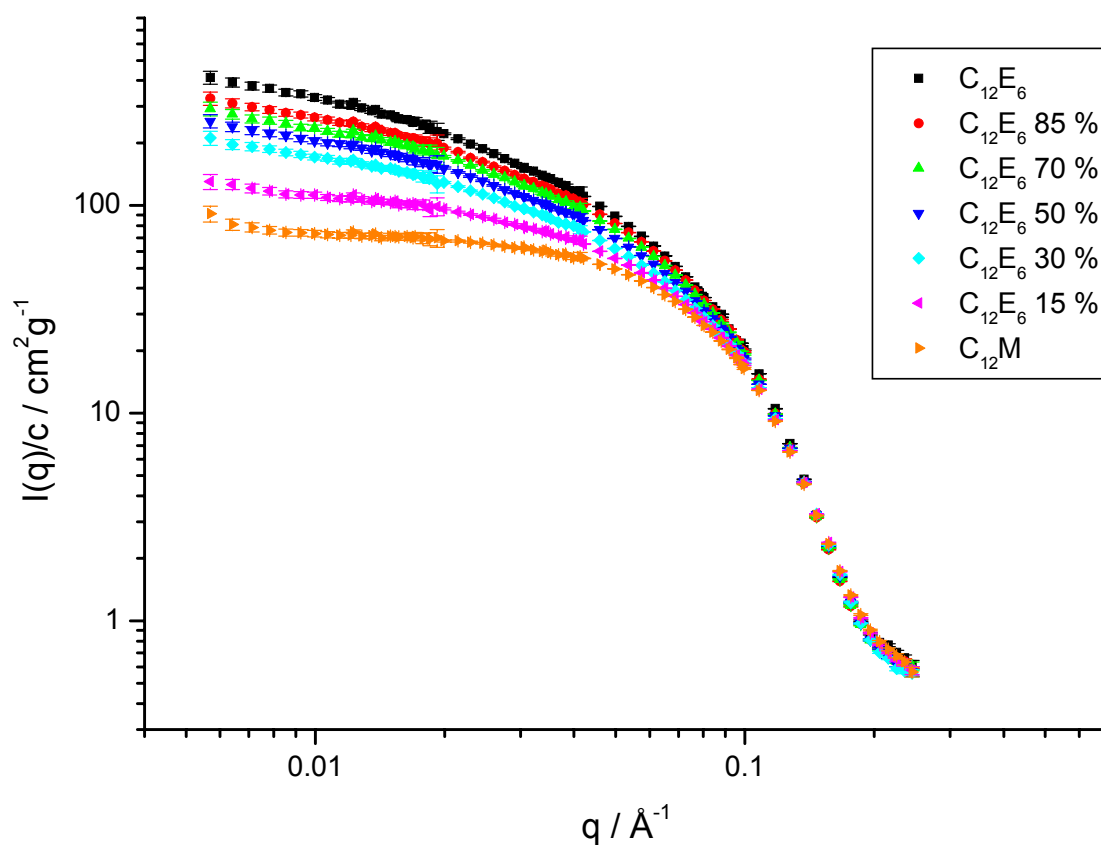
Figure 1: Scattered intensity as a function of scattering vector q for 1 wt % surfactant samples.

References

[1] Bergström LM, Bastardo LA, Garamus VM, A small-angle neutron and static light scattering study of micelles formed in aqueous mixtures of a nonionic alkylglucoside and an anionic surfactant, JOURNAL OF PHYSICAL CHEMISTRY B **109**, 2005, 12387.

[2] Bergström M, Pedersen JS, Formation of tablet-shaped and ribbonlike micelles in mixtures of an anionic and a cationic surfactant, LANGMUIR **15**, 1999, 2250.

[3] Jerke G, Pedersen JS, Egelhaaf SU, et al., Flexibility of charged and uncharged polymer-like micelles, LANGMUIR **14**, 1998, 6013.

![GKSS FORSCHUNGSZENTRUM in der HELMHOLTZ-GEMEINSCHAFT]	**EXPERIMENTAL REPORT**	**GeNF SANS-1**

Structure of Quil A micelles		
Proposer:	**C.C. Müller-Goymann[1]**	
Co-Proposers:	**M.Harms[1], T.Paepenmüller[1]**	
	[1] TU Braunschweig, Inst. f. Pharm. Technologie, Mendelssohnstr. 1, 38106 Braunschweig, Germany	
Experimental Team:	**M.Harms[1], V. Haramus[2]**	
	[2] GKSS Research Centre, Max-Planck-Str. 1, 21502 Geesthacht	
User Group Leader:	**C.C. Müller-Goymann[1]**	
Date(s) of Experiment:	1st–10th December 2005	

Objectives

Pseudo-binary mixtures of Cholesterol (Chol) and Quillaja saponin (Quil A) in buffer were investigated. In these systems worm-like micelles are formed [1]. Previous investigations at SANS revealed that the aggregates become larger with increasing Chol content and developed a superstructure which might be helical.

Since Quil A is a natural product and the composition between lots varies a highly purified Quil A (XQA) as well as a different lot (QA) were used in order to get information about the influence of impurities on the micellar structure.

Experiment

SANS measurements were performed at the SANS1 at the FRG1 research reactor at GKSS Research Centre, Geesthacht, Germany. Wavelength λ was 0.81 nm, and the measured scattering vectors were 0.07<h<2.5 nm^{-1} (with h=4π/λ sinθ). Samples were kept at 25±1°C. Raw spectra were corrected for background scattering from the solvent (TRIS-buffer 140 mM pH 7.4 in D_2O).

Quil A was used in two different purification grades: QA (Accurate Chemical, Westbury, USA) and the highly purified XQA (Isconova AB, Uppsala, Sweden).

Chol was weighted into glass vials and dissolved in chloroform. The solvent was evaporated under vacuum at room temperature for one hour. The resulting film was then hydrated with a solution of either QA or XQA in TRIS-buffer pH 7.4 140mM in D_2O. The samples were stirred at room temperature for 24 hours and filtered through a 0.22 µm membrane filter.

QA micelles
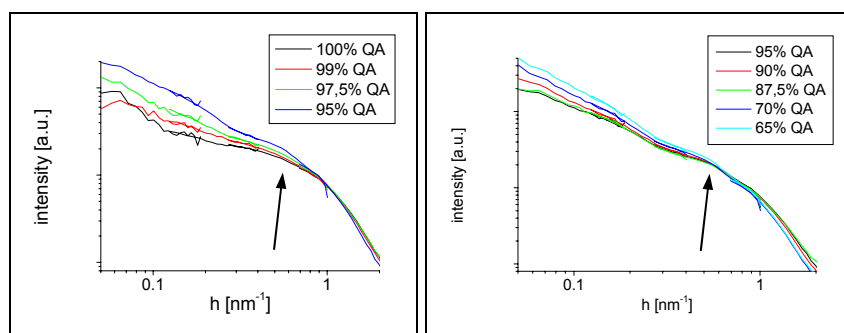
Figure 1: Scattering data of QA micelles with different ratios of QA and Chol (total concentration: 6.7 mg/ml) in TRIS-buffer. (left: 100% QA to 95%; right: 95% QA to 65%; arrow: in text)

Figure 1 shows the results for QA micelles. Pure QA micelles reveal spherical to slightly elongated aggregates. The additional scattering at small angles for pure QA micelles might be attributed to impurities. The micelles grow upon the addition of Chol. This can be observed up to a Chol concentration of 5% (95% QA). At higher Chol concentration the scattering curve does not change that rapidly. A slight increase can be observed at concentrations above 30% Chol (70% QA). The scattering curve shows a small and broad maximum (indicated by an arrow) can be observed in which might again hint at the presence of a helical superstructure of the micelles. The slope at low angles is approx. –1 which hints at the presence of rod-like aggregates. The slope increases at higher concentrations of Chol (30%-35% Chol). This might be an additional hint at the existence of a helical superstructure, since such a structure would result in an increased flexibility of the coil and hence a steeper slope.

This is in accordance with previous measurements (2004), although the increase of the slope at high concentrations of Chol was more pronounced with the latter.

XQA micelles
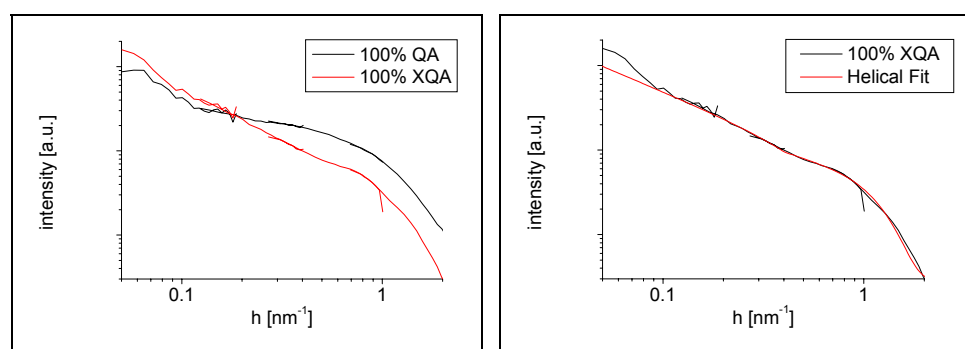
Figure 2: Left: Scattering of 100% XQA micelles compared to 100% QA micelles. Right: Helical Fit of 100% XQA micelles.

In contrast to QA micelles the highly purified XQA micelles consist of large structures in the absence of Chol (Figure 2). This effect can be attributed to the impurities. The saponines in Quil A tend to stack in a rod. If amphiphilic or lipophilic impurities attach to the end of the stacks a prolongation due to the attachment of another Quil A molecule is prevented. Hence impurities can result in the shortening of the stacks. A helical fit [3] to the 100% XQA micelles gave the following results:

- Diameter of spheres   3.82 nm
- Helical pitch   15.6 nm
- Diameter of the helix   2.80 nm

Achievements and Main Results

Independent of the used lot Chol initiates a prolongation of the QA micelles. For both lots a superstructure can be observed which might be of a helical type.

The XQA micelles show a worm-like structure even in the absence of Chol. This leads to the assumption that the impurities in QA result in a shortening of the saponine stacks. A helical fit to the pure XQA micelles was possible.

References

[1] Demana, Davis, Vosgerau, Rades, International Journal of Pharmaceutics **270** (2004), 229.
[2] Lebedev, Baitin, Islamov, Kuklin, Shalguev, Lanzov, Isaev-Ivanov, FEBS Letters **537** (2003), 182.

	EXPERIMENTAL REPORT	**GeNF SANS-1**
GKSS FORSCHUNGSZENTRUM in der HELMHOLTZ-GEMEINSCHAFT		

Investigation of lysozyme aggregation by small angle neutron scattering	
Proposer:	**L. He[1],** [1]Centre for Biomolecular Engineering,University of Queensland, St. Lucia 4072, Australia
Co-Proposers:	**A. Middelberg[1]**
Experimental Team:	**L. He[1],** **V. Haramus[2],** [2]GKSS
User Group Leader:	**A Middelberg[1]**
Date(s) of Experiment:	4th–15th September 2006

Objectives

Protein aggregation is a common phenomenon which occurs both in biological system and bioprocess, and understanding protein aggregation is important for both scientific and technological application. Protein aggregation relates to several diseases such as Alzheimer's and Parkinson's diseases, the spongiform encephalopathy and type II diabetes (Dobson 2001). In bioprocess of protein production, protein aggregation can significantly decrease recovery of proteins, and thus increase the cost of production. Protein aggregation are affected by many factors including the protein hydrophobicity, protein concentration, and solution condition (temperature, pH value, salt concentration). Despite many efforts have been put into this topic, the mechanism of protein aggregation is not well understood so far (Ho and Middelberg, 2003). The aim of this work is to investigate how proteins interact with each other at high concentration and how additives such as amino acids can affect protein aggregation. Hen egg lysozyme was used as a model system in this study.

Experiment

The lysozyme solution was made in 20 mM HEPES buffer prepared from D_2O or H_2O. The salt concentration of samples was controlled by a desalting step using a PD10 column. The small angle neutron scattering experiments were performed on the instrument SANS-1. The range of scattering vectors from 0.007 to 0.25 $Å^{-1}$ was used. In all experiments, the neutron wavelength λ was 8.1 Å with a wavelength resolution $\Delta\lambda/\lambda$ of 10%. The quartz cells (1 mm path length) containing the sample solutions were placed in a thermostatted sample holder. The raw data was corrected for background contribution from the solvent and sample cell by conventional procedures.

Achievements and Main Results

The salt concentration has significant effect on protein interaction. The lypholized lyozyme powder from Sigma contains some residual salt. Thus the salt concentration in the buffer was

increased when the protein powder was added. By using a desalting column, the salt concentration in the sample can be changed back to the same level of the original buffer. As shown in Fig 1, after desalting, the scattering curve of 56 mg lysozyme has a sharper peak than that of the sample without a desalting step. This indicates that electrostatic force plays an important role in lysozyme-lysozyme interaction, and the additional salt can significantly affect this interaction. We have thus performed a desalting step for most samples (except those designed for comparison of salt effect).

The concentration of lyszoyme has been varied from 6 mg/ml to 100 mg/mL to study the concentration dependence of protein aggregation. Aggregation of lyszoyme have been observed at a concentration larger than 70 mg/ml. Interestingly, we have found adding of arginine into the solution can decrease the extent of lysozyme aggregation. The detailed analysis of those data is being currently carried out to reveal its mechanism.
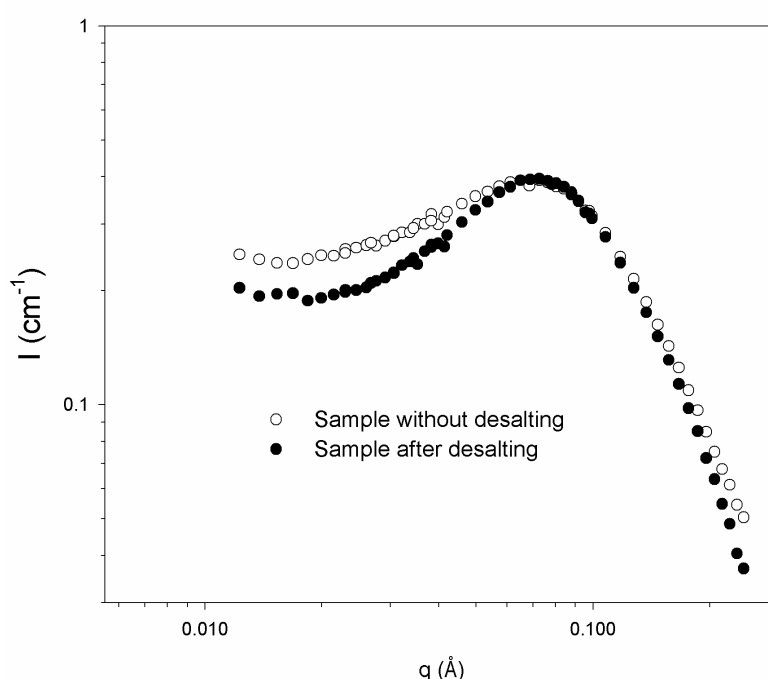
Fig 1: Effect of salt on scattering spectra of lysozyme. (○) 56 mg/mL lysozyme in 20 mM HEPES buffer, D_2O, pD 7.8, prepared directly from protein powders (●) 56 mg/mL lysozyme in 20 mM HEPES buffer, D_2O, pD 7.8, and one desalting step was performed to remove the residual salt from the protein powders.

References

Dobson, C.M. 2001. The structural basis of protein folding and its links with human disease. *Philosophical Transactions of the Royal Society of London Series B-Biological Sciences* **356:** 133-145.

Ho, J.G., Middelberg, A.P., Ramage, P., and Kocher, H.P. 2003. The likelihood of aggregation during protein renaturation can be assessed using the second virial coefficient. *Protein Science* **12:** 708-716.

The study of the topology and fractal properties of xerogels based on SnO$_2$ by SANS		
Proposer: **Co-Proposers:**	**S.V. Grigoriev[1]**, [1] Petersburg Nuclear Physics Institute **G.P. Kopitsa[1]**	
Experimental Team: **User Group Leader:**	**G.P. Kopitsa[1]**, **V.M. Haramus[2]**, [2] GKSS **S.V. Grigoriev[1]**	
Date(s) of Experiment:	15th–29th March 2006	

Objectives

Dioxide (SnO$_2$, cassiterite) is an important material with many technological applications such as photovoltanic devices [1], photosensors [2], transparent conductive electrodes [3], catalysis [4], in lithium ion batteries [5]. Moreover, the cassiterite is used as the component in the solid-sorbent extractants with a high selectivity at radionuclides of cobalt, strontium and transsuranium elements [6]. For achievement of essential characteristics one needs to have the sorbent with a large specific surface and high porosity. The method of sol-gel synthesis is most advanced one [7]. This method allows one to produce the materials in the form of a globular mechanical-strength grains with renewable properties. The goal of this proposal is to study the nanostructure of SnO$_2$-based xerogels and its evolution at different stages of thermal treatment by means of small-angle neutron scattering (SANS).

Experiment

The xerogel tin dioxide SnO$_2$ was prepared from aqueous SnCl$_4$·5H$_2$O solution (1 mol.l^{-1}), precipitated by addition of aqueous ammonia at room temperature as described [7]:

$$SnCl_4 + 4NH_4OH \frac{H_2O}{\Delta} SnO_2 \downarrow + 4NH_4Cl$$
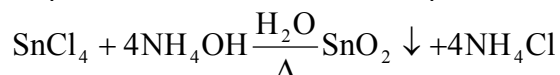
The sol-gel transition was obtained by the partial evaporation of water at T = 373 K till a critical sol concentration of 0.42 mol.l^{-1} of Sn. After gel was washed with distilled water to remove Cl$^-$ and NH$_4^+$ ions, and then isothermally treated during six hours at temperatures from 473 to 1273 K.

Achievements and Main Results

The momentum dependences of the SANS cross section $d\Sigma(q)/d\Omega$ measured for the samples of the xerogel tin dioxide SnO$_2$ are shown in Fig. 1 and 2 on the log-log scale. As is clearly seen in these figures, the increase of the cross sections occurs with the increasing of the annealing temperature T_a.

The studied samples are divided into three groups. The first group consists of the samples with "low" annealing temperature T_a = 373 and 473 K. In this case the scattering is weak and practically does not depend on T_a. Further, the sharp increase of the cross section $d\Sigma(q)/d\Omega$ is observed (Fig. 1) as the annealing temperature T_a increases up to 573 K. From this temperature up to 873 K the scattering increases strongly with the increasing of T_a. The characteristic feature of the curves of $d\Sigma(q)/d\Omega$ at $573 \leq T_a \leq 873$ K is a presence of the maximum in the range q from 0.009 to 0.09 Å^{-1}, which shifts to small-q region as T_a increases. The annealing at "high" temperatures $T_a \geq 973$ K is characterized by both sharp jump of the scattering (Fig. 2.) and the disappearance of the maximum on the curve of $d\Sigma(q)/d\Omega$. Moreover, as is seen from Fig. 2, further growth of T_a results in a weak increase of cross section

$d\Sigma(q)/d\Omega$ only at the low q, while the decrease of the scattering cross-section occurs at $q > 0.01$ Å^{-1}.
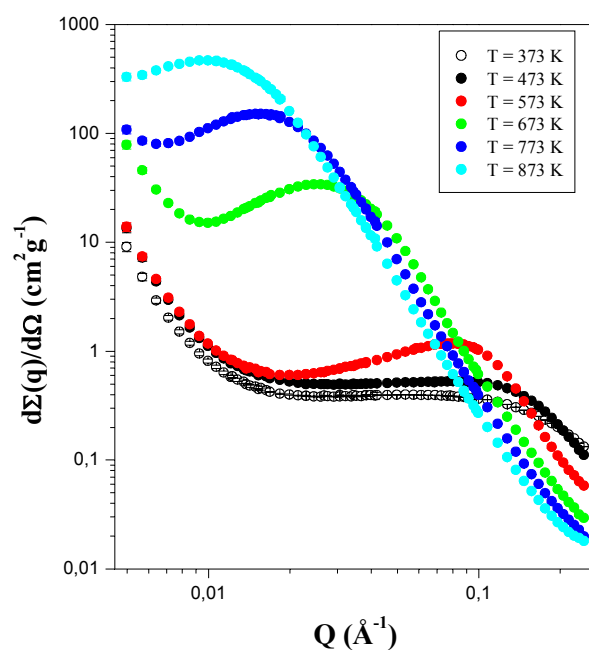
Fig. 1.
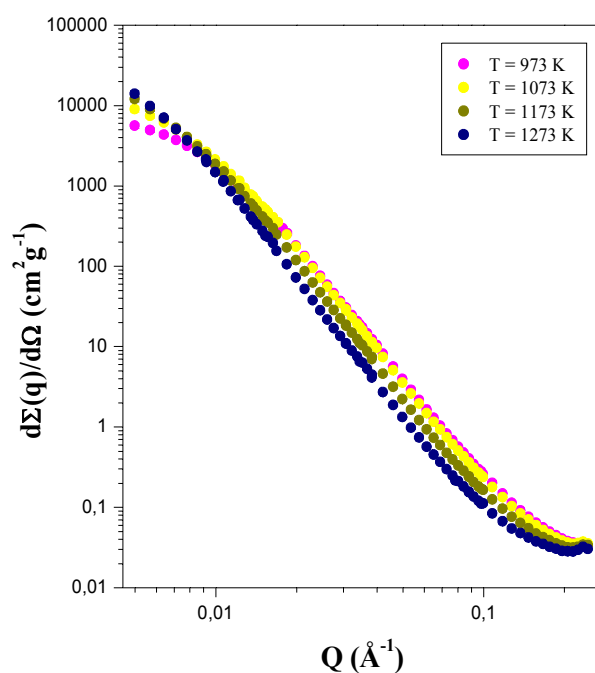
Fig. 2.

References
[1] S.D. Gaal, J.T. Hupp, J. Am. Chem. Soc. 122 (2000) 10956.
[2] J.R. Bellingham, W.A. Philips, C.J. Adkins, J. Mater. Sci. Lett. 11 (1992) 263.
[3] L. Lipp, D. Pletcher, Electrochim. Acta 42 (1997) 1091.
[4] F.M. Del Arco et al., Mater. Sci. Forum 25/26 (1988) 479.
[5] Y. Idota et al., Science 276 (1997), 1395.
[6] L.M. Sharygin et al., Atomic Energy v.91 (2001), 126.
[7] L.M. Sharygin et al., Ion exchange and ionometery. L: LGU, v.5 (1986), 9.

![GKSS logo] GKSS FORSCHUNGSZENTRUM in der HELMHOLTZ-GEMEINSCHAFT	**EXPERIMENTAL REPORT**	**GeNF SANS-1**

Neutron Scattering from Synthetic Stimuli-Responsive Polymers

Proposer: **Co-Proposers:**	**Y.B. Melnichenko[1]**, [1]Oak Ridge National Laboratory, Oak Ridge, TN, USA
Experimental Team:	**G. Rother[1]**, G. Cheng[1], G. Wignall[1], K. Hong[1]
User Group Leader:	**Y.B. Melnichenko[1]**
Date(s) of Experiment:	19th–24th May 2006

Objectives

Biopolymers such as proteins, polysaccharides and nucleic acids are basic components of living organic systems. The concept of cooperative interactions between functional segments of biopolymers has led to attempts to create novel synthetic polymers that are environmentally responsive to various stimuli in a controlled way. The stimuli responsive polymers can undergo significant and reversible changes of their conformation in response to small variation of the environmental conditions. A family of environmental responsible polymers with hydrophobic backbones and hydrophilic side chains has been recently developed at ORNL by J. Mays' group. This class of polymers broadens the family of thermo or pH sensitive polymers and may lead to future applications. The goal of this proposal is to explore the single chain conformation of these polymers in water as well as the mechanism of molecule association as one varies the temperature and concentration.

Experiment

Homopolymer poly [oligo (ethylene oxide) styrene)] with a Mw of 11000g/mol was synthesized at ORNL. The polymers were dissolved in D_2O and kept at room temperature over night before the actual SANS measurement. SANS measurements were carried out at a wavelength of 0.58nm with sample-detector distances of 0.75m, 1.8m and 4.5m. The scattering intensity was reduced to the absolute unit according to established procedures.

Achievements and Main Results

Our preliminary SANS data of 1.0wt.% poly [oligo(ethylene oxide) styrene)] taken in Geesthacht (Germany) have revealed interesting information about the association and phase separation of the polymers in heavy water (Fig. 1). The -3.7 slope at high q suggests a well defined interface. The low q portion of the data at 25^{0}C exhibits an upturn with a slope of -1.8 which suggests the presence of clusters as also found in a PEO/Water system. The solid lines at 25^{0}C and 36^{0}C are the fits to a polydisperse ellipsoid of revolution model with a modified Ornstein-Zernike interaction potential, which is characterized by two radii: short axis R_a and long axis R_b and a correlation length ξ. Ra=14Å, Rb=19Å and ξ=200Å at 25^{0}C and Ra=14Å, Rb=17 Å and ξ=34 Å at 36^{0}C. With increasing temperature, the particles size slightly decreases due to dehydration. The SANS data also suggests that the clusters formed at low temperatures break up and individual ellipsoids are dominating at higher temperatures. At 40^{0}C, which is above the Lower Critical Solution Temperature (LCST), phase separation is expected. The data at three detector-sample distances at 40^{0}C exhibits a kinetic behavior. The counting times for the three distances are 1.7hour (0.7m), 1.4hour

(1.8m) and 2.7hour (4.5m). The decrease in intensity with time indicates that particles are precipitating form the solution.
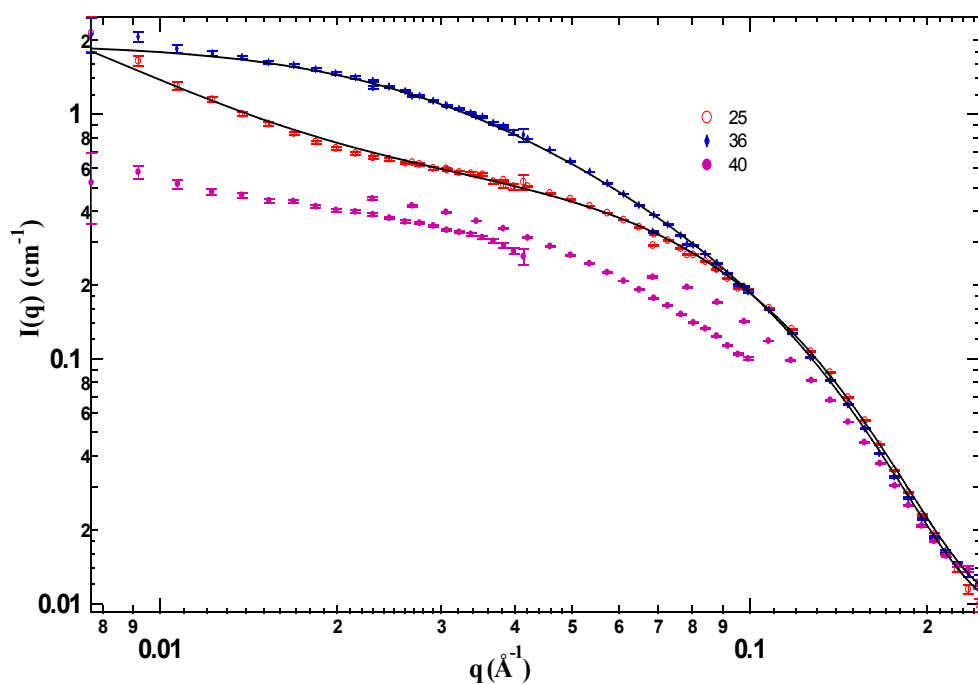
Figure 1:. SANS data of poly[oligo(ethylene oxide) styrene)] in D_2O at 25^0C , 36^0C and 40^0C. The polymer concentration is 1.0wt.%.

![GKSS logo] GKSS FORSCHUNGSZENTRUM in der HELMHOLTZ-GEMEINSCHAFT	**EXPERIMENTAL REPORT**	**GeNF SANS-1**

Small-Angle Neutron Scattering of Bolaform Hydrogelators		
Proposer: **Co-Proposers:**	**Alfred Blume[1],** [1]Institut für Physikalische Chemie, Martin-Luther-Universität Halle-Wittenberg, Halle, Germany **Annette Meister[1]**	
Experimental Team:	**Vasyl Haramus[2],** [2]GKSS	
User Group Leader:		
Date(s) of Experiment:	14th–24th November 2005	

Objectives

We have recently reported on the temperature dependent aggregation behavior of the symmetric long-chain bolaamphiphiles dotriacontan-1, 1'-diyl-bis[2- (trimethylammonio) ethylphosphate] (PC-C32-PC) and dotriacontan-1, 1'-diyl-bis[2- (dimethylammonio) ethylphosphate] (Me$_2$PE-C32-Me$_2$PE) in aqueous suspension.[1,2] These compounds gel water very efficiently at concentrations of 1 mg/ml by forming a dense network of nanofibers. In present experiments the objective was to investigate the shape and size of the aggregates in all possible states at different temperatures.

Experiment

Small angle neutron scattering was used to study the shape and size of bolalipid aggregates depending on the concentration (0.5, 1 and 2 mg/ml), temperature, and pH (5 and 10 for Me$_2$PE-C32-Me$_2$PE). According to the observed phase transition temperatures from calorimetric investigations[1,2], selected temperatures have been studied for each sample in the range between 20 and 75°C. Data analysis by Indirect Fourier Transformation (IFT) was performed at $q > 0.02$ Å^{-1} where the effects of intermicellar interactions are negligible. This yields the scattering at zero angle ($d\Sigma(0)/d\Omega$) and the radius of gyration (Rg) without any presumptions regarding particle size and shape. Figure 1 shows the scattering curves for Me$_2$PE-C32-Me$_2$PE at pH 5 (1 mg/ml) at 20, 50, and 75°C.
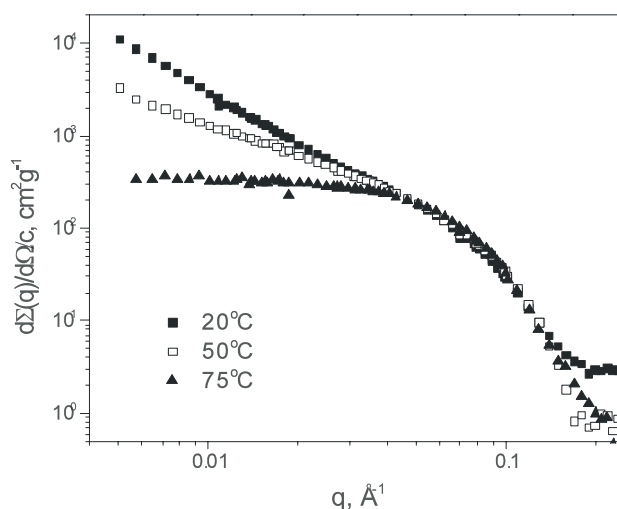
Figure 1: Scattering intensities as a function of the scattering vector for Me$_2$PE-C32-Me$_2$PE (pH 5) at 20, 50, and 75°C.

Achievements and Main Results

SANS data analysis enables us to follow even small changes in the shape and size of the bolalipid aggregates (diameter, contour lengths, stiffness, cross section, aggregation number) and gives important information especially at high temperatures, which are not easily accessible by cryo-transmission electron microscopy (see Table 1).

bolalipid	pH	T / °C	radia / Å	$N_{agg,sphere}$ $N_{unit,rod}$ per 1 Å	shape
PC-32-PC		25	21.35	1.09	short rods (circular cross section)
PC-32-PC		45	23.33	1.2	rods
PC-32-PC		60	31.7	77.46	spherical micelles
Me2PE-32-	5	20	26.0	1.07	flexible chains, elliptical cross section
Me2PE-32-	5	50	23.05	1.01	stiff rods
Me2PE-32-	5	75	34.08	79.11	spherical micelles
Me2PE-32-	10	20	26.59	49.45	spherical micelles
Me2PE-32-	10	50	27.11	52.43	spherical micelles
Me2PE-32-	10	75	24.01	44.4	spherical micelles
PC-26-PC		20	19.09	0.979	stiff rods, circular cross section
PC-26-PC		35	24.53	52.44	spherical micelles
PC-26-PC		75	21.56	33.31	spherical micelles

Table 1: Selected SANS-results of measurements performed with 1mg/ml bola-suspensions.

A comparison of the observed aggregate shapes from these SANS measurements with cryo-TEM measurements[2] shows some discrepancies. These different observations indicate the importance of scattering data. Probably, the fibers in the micrographs are due to the quenching procedure during the preparation of the cryo-TEM samples.

References

[1] K. Köhler, G. Förster, A. Hauser, B. Dobner, U. F. Heiser, F. Ziethe, W. Richter, F. Steiniger, M. Drechsler, H. Stettin, A. Blume *J. Am. Chem. Soc.* 2004, *126*, 16804-16813.
[2] K. Köhler, A. Meister, G. Förster, B. Dobner, S. Drescher, F. Ziethe, W. Richter, F. Steiniger, M. Drechsler, G. Hause, A. Blume *Soft Matter* 2006, *2*, 77-86.

Small-Angle Neutron Scattering of Bolaform Hydrogelators (II)

Proposer: **Co-Proposers:**	**Alfred Blume[1],** Institut für Physikalische Chemie, Martin-Luther-Universität Halle-Wittenberg, Halle, Germany **Annette Meister[1]**
Experimental Team:	**Vasyl Haramus[2]**, [2]GKSS **Simon Drescher[1]**
User Group Leader:	
Date(s) of Experiment:	18th–22nd September 2006

Objectives

We have recently reported on the temperature dependent aggregation behaviour of the symmetric long-chain bolaamphiphiles dotriacontan-1,1'-diyl-bis[2-(trimethyl-ammonio)ethylphosphate] (PC-C32-PC) and dotriacontan-1,1'-diyl-bis[2-(dimethyl-ammonio)ethylphosphate] (Me$_2$PE-C32-Me$_2$PE).[1,2,3] These compounds gel water very efficiently already at concentrations of 1 mg·ml^{-1} by forming a dense network of nanofibers. In the meantime, a new synthetic strategy for symmetric bolaamphiphiles was developed in our group, so that bolaamphiphiles with shorter hydrocarbon chain spacers (C22 to C30) are now accessible.

The objective of our SANS experiments was to investigate the temperature dependent aggregation behaviour of these compounds and the shape and size of the formed aggregates.

Experiment

We used small angle neutron scattering (SANS) to study the shape and size of the bolaamphiphile aggregates at different temperatures and aggregates using combinations of various bolaamphiphiles with different chain lengths. According to the observed phase transition temperatures from DSC-measurements, selected temperatures were studied in the range between 10 and 70°C. Data analysis by Indirect Fourier Transformation (IFT) was performed at q > 0.02 Å^{-1} where the effects of intermicellar interactions are negligible. This yields the scattering at zero angle (dΣ(0)/dΩ) and the radius of gyration (R$_g$) without any presumptions regarding particle size and shape.

Main Results

SANS data analysis enabled us to follow even small changes in shape and size of bolaamphiphile aggregates (radii, cross section, aggregation number, mass) formed by a suspension of pure bolaamphiphiles and also by mixtures of bolaamphiphiles with different hydrocarbon chain lengths. Particularly at high temperatures, where cryo-transmission electron microscopy is not possible, we could obtain information on the aggregate structure (see Table 1).

For the short-chained PC-C24-PC we could investigate three different states (indicated in the DSC-curve of Fig. 1A by arrows), particularly the high temperature structure at 55°C. For bolaamphiphiles with longer chain lengths this was not possible due to the significantly higher transition temperatures.[2] Figure 1B shows the scattering curves for PC-C24-PC (1mg·ml^{-1}) at 10, 20, and 55°C.
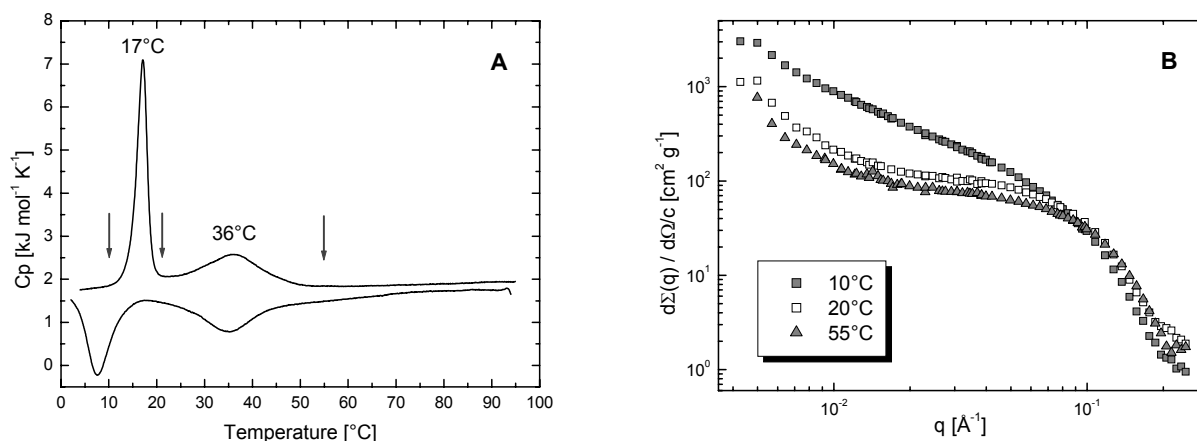
Figure 1: (A) DSC curve of an aqueous suspension of 1 mg·ml^{-1} PC-C24-PC. Arrows indicate temperatures of SANS measurements. (B) Scattering intensities as a function of the scattering vector for PC-C24-PC (1 mg·ml^{-1}) at different temperatures.

Furthermore we investigated the shape and size of aggregates formed by mixtures of bolaamphiphiles with different hydrocarbon chain lengths. According to cryo-TEM images we find a tolerance limit for the formation of fibers: a mixture of PC-C32-PC and PC-C26-PC in equal molar ratio forms fibers. The scattering curve (Fig. 2) from this mixture shows only small differences compared to curves from its single components.

On the other hand, in the mixture of PC-C32-PC with PC-C24-PC the difference in chain length is larger and prevents the formation of fibers. Instead, large aggregates with a diameter of about 240 Å are observed.
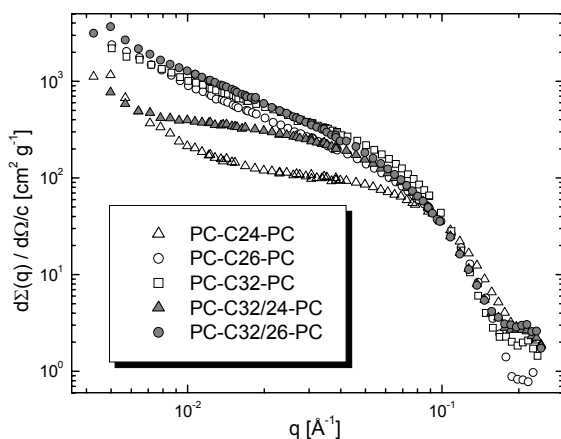
Figure 2: Scattering intensities of the bolaamphiphiles PC-C24-PC and PC-C26-PC and mixtures with PC-C32-PC.

Table 1: Selected SANS-results of measurements – 1 mg·ml^{-1} bolaamphiphile.

bolalipid	T [°C]	radia [Å]	N$_{agg}$ [Å^{-1}]	M, M$_L$ [g], [g·cm^{-1}]	shape
PC-C24	10	20.73	0.73	8.49×10^{-14}	a)
	20	24.37	31.55	3.90×10^{-20}	b)
	55	21.82	22.97	2.84×10^{-20}	c)
PC-C24/32	20	44.53	88.43	1.18×10^{-19}	d)
	42	27.63	46.53	6.20×10^{-20}	c)
	70	24.79	34.29	4.57×10^{-20}	c)
PC-C26/32	20	23.76	1.01	1.29×10^{-13}	a)
	55	27.50	45.88	6.25×10^{-20}	c)

a) fibers
b) micelles and some large aggregates
c) small micelles
d) no fibers – aggregates with d = 240Å

References

1 K. Köhler, G. Förster, A. Hauser, B. Dobner, U. F. Heiser, F. Ziethe, W. Richter, F. Steiniger, M. Drechsler, H. Stettin, A. Blume *Angew. Chem. Int. Ed.* **2004**, 43, 245-247.
2 K. Köhler, G. Förster, A. Hauser, B. Dobner, U. F. Heiser, F. Ziethe, W. Richter, F. Steiniger, M. Drechsler, H. Stettin, A. Blume *J. Am. Chem. Soc.* **2004**, *126*, 16804-16813.
3 K. Köhler, A. Meister, G. Förster, B. Dobner, S. Drescher, F. Ziethe, W. Richter, F. Steiniger, M. Drechsler, G. Hause, A. Blume *Soft Matter* **2006**, *2*, 77-86.

GKSS FORSCHUNGSZENTRUM in der HELMHOLTZ-GEMEINSCHAFT	EXPERIMENTAL REPORT	GeNF SANS-1
Micellar structure of glycolipid mixtures		
Proposer:	**Götz Milkereit[1], Sven Gerber[2], Vasyl Haramus[1]** [1] GKSS Research Centre	
Co-Proposers:	[2] Universität Hamburg, Inst. f. Organische Chemie, Martin-Luther-King-Platz 6, 20146 Hamburg	
Experimental Team:		
User Group Leader:	**Götz Milkereit**	
Date(s) of Experiment:	22nd–24th June, 28th June–1st July, 15th–20th August 2006	

Objectives

We continued our experiments on the investigation of mixed micellar system that consist of glycolipid amphiphiles. In this work we focused on the effect of the anomeric linkage of the alkyl chain to the carbohydrate headgroup. We investigated the α- and β-anomere of the glycolipid dodecyl D-maltoside (figure 1). The properties in solution were investigated by surface tension measurements and small-angle neutron scattering (SANS).

The two anomers α and β have identical hydrophilic-lipophilic balances but significant differences in molecular architecture. The chain is in the axial (α-anomer) or equatorial position (β-anomer) with respect to the polar carbohydrate headgroup.
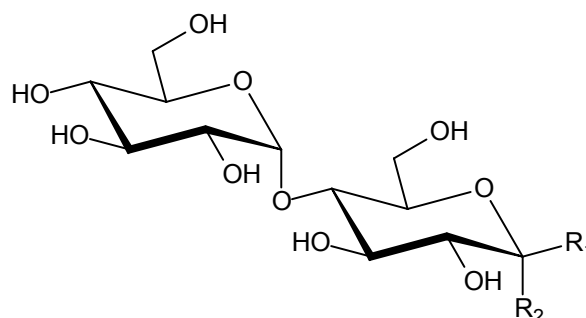
Mal-α-C12:   R$_1$ = H, R$_2$ = OC$_{12}$H$_{25}$

Mal-β-C12:   R$_1$ = OC$_{12}$H$_{25}$, R$_2$ = H

Figure 1: Investigated compounds: Dodecyl-α-D-maltoside (**Mal-α-C12**) and dodecyl-β-D-maltoside (**Mal-β-C12**).

Experiment

Figure 2 shows the CMC values of the mixtures together with the theoretical curve for the CMC's of an ideal mixing of surfactants which was calculated within the regular solution theory (RST).

It is easy to see that the experimental values of the CMC are significant higher than the values expected for an ideal mixing, this points on demixing in the system **Mal-α-C12** / **Mal-β-C12**. It can be expected that the parameters f_1 and f_2 are higher than 1 and the corresponding parameter β ($f_1 = \exp\beta(1-x_1)^2$ and $f_2 = \exp\beta x_1^2$), calculated within RST, which is related to an interaction between surfactants in mixed micelles, is positive [1,2].
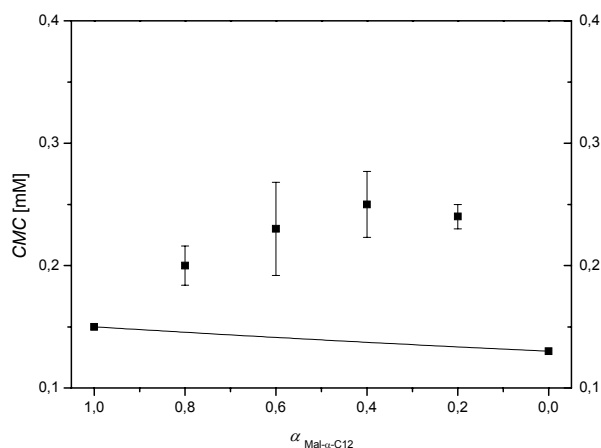
Figure 2: CMC as a function of lipid composition of **Mal-α-C12** and **Mal-β-C12** mixtures (symbols) and ideal mixing curve (solid line). α is the molar fraction of **Mal-α-C12**.

Table 1: Results from surface tension measurements and parameters of β and x_1 obtained for different compositions of **Mal-α-C12/Mal-β-C12** mixtures in D_2O.

$\alpha_{Mal-\alpha-C12}$	*CMC* [mM]	β	$x_{1,Mal-\beta-C12}$
1	0.15		
0.8	0.20	4.5	0.69
0.6	0.23	2.3	0.27
0.4	0.25	2.8	0.67
0.2	0.24	7.54	0.32
0	0.13		

SANS experiments were performed in D_2O at 25 °C. Different fraction of α anomer (0.75, 0.50, 0.25) at a fixed concentration (1 mg/mL) were investigated. SANS data together with fits are shown in figure 3. Scattering data were analyzed by model independent Indirect Fourier Transformation (IFT) method.
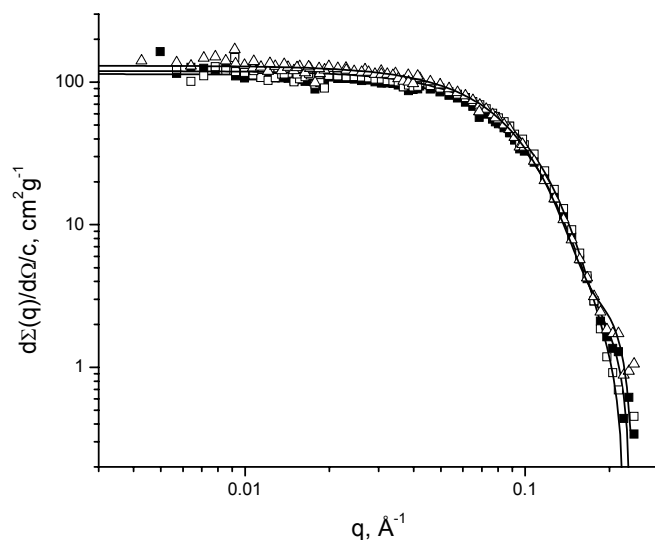
Figure 3: Small-angle neutron scattering data from solutions of **Mal-α-C12/Mal-β-C12** in D_2O for different molar fractions, α = 0.75 (filled squares), α = 0.5 (open squares), α = 0.25 (open triangles).

Results from SANS data analysis are shown in table 2, together with values taken from the literature [3] for the pure compounds. Analysis of the scattering data of the solutions points on the formation of spherical micelles (D_{max} = 60 Å), which slightly increase in size with increasing molar fraction of the β-anomer.

Achievements and Main Results

The mixing of the anomers of dodecyl-D-maltoside leads to antagonistic interaction in micelle formation, as can be seen from the surface tension measurements (parameter β is positive, a maximum in the plot of the CMC vs. composition of mixture). SANS analysis reveals the formation of only spherical micelles, which slightly increase in size and mean aggregation number with increasing molar fraction of **Mal-β-C12**. The formation of larger (elliptical) micelles, as observed for pure **Mal-β-C12** solutions [3] is suppressed by addition of **Mal-α-C12** even in a small molar fraction of α = 0.25 for **Mal-α-C12**.

Table 2: Results of fitting from SANS data by IFT analysis for different molar fractions of **Mal-α-C12**/**Mal-β-C12** (α - molar fraction of **Mal-α-C12**, R_g - Radius of gyration, R - total radius, M_{app} - appearent molar mass , N_{agg} - mean aggregation number). Values for α = 1 and α = 0 are taken from Ref. [3]

$\alpha_{Mal-\alpha-C12}$	Rg	R [Å]	c [mg/mL]	M_{app} [g/mol]	N_{agg}
1		24	10		75
0.75	18.1	23.5	1	3.7×10^4	74
0.5	18.6	24.2	1.1	4.0×10^4	78
0.25	19.3	25.1	1	4.3×10^4	85
0		34.4 (Rt, ε = 0.5)	10		132

References

[1] J. Clint, *J. Chem. Soc., Faraday Trans I*, 71, **1975**, 1327-1334.
[2] P.M. Holland, *Adv. Colloid Interface Sci.*, 26, **1986**, 111-129.
[3] C. Dupuy, X. Auvray, C. Pepitas, I. Rico-Lattes, A. Lattes, *Langmuir*, 13, **1997**, 3965-3967.

![GKSS FORSCHUNGSZENTRUM in der HELMHOLTZ-GEMEINSCHAFT]	**EXPERIMENTAL REPORT**	**GeNF SANS-1**
	SANS contrast variation in ferrofluids as polydisperse multicomponent superparamagnetic systems	
Proposer: **Co-Proposers:**	**M.V. Avdeev[1]**, [1]FLNP, JINR, Dubna, Russia **A.V. Feoktystov[1]**	
Experimental Team:	**Vasyl Haramus[2],** [2]GKSS	
User Group Leader:	**M.V. Avdeev[1]**	
Date(s) of Experiment:	26th November–5th December 2006	

Objectives

The organic non-polar magnetic fluid (magnetite dispersed in benzene and stabilized by single layer of myristic acid) was studied by the SANS contrast variation. The new approach of basic functions for polydisperse multicompnonet and superparamagnetic systems [1] was applied. The approach is the development of the classical method [2]. It employs the fact that in comparison with systems of monodisperse and non-magnetic particles for polydisperse and magnetic particles there is a residual scattering intensity around the effective match point, which can be reliably treated. Now, the effective match point takes the form:

$$\bar{\rho}_e = <\bar{\rho}V_c^2> / <V_c^2>,\qquad(1)$$

and the scattering intensity can be written as

$$I(q) = \tilde{I}_s(q) + \Delta\tilde{\rho}\tilde{I}_{cs}(q) + (\Delta\tilde{\rho})^2\tilde{I}_c(q),\qquad(2)$$

$$\Delta\tilde{\rho} = \bar{\rho}_e - \rho_s.\qquad(3)$$

where $\Delta\tilde{\rho}$ is the modified contrast and $\tilde{I}_c(q)$, $\tilde{I}_s(q)$, $\tilde{I}_{cs}(q)$ are the modified basic functions.

The expressions for integral parameters of the scattering (intensity in zero angle, radius of gyration, Porod volume) as a function of the modified contrast are also changed. For example, the behavior of the radius of gyration as a function of the modified contrast:

$$\tilde{R}_g^2 = (\frac{<V_c^2 R_c^2>}{<V_c^2>} + \frac{A}{\Delta\tilde{\rho}} - \frac{B}{(\Delta\tilde{\rho})^2})/(1 + \frac{D}{(\Delta\tilde{\rho})^2}),\qquad(4)$$

where R_c is the radius of gyration related to the whole particle shape and A, B, D are the parameters, differs qualitatively from the classical expression:

$$R_g^2 = R_c^2 + \alpha/\Delta\rho - \beta/(\Delta\rho)^2,\qquad(5)$$

with parameters α, β. Particularly, Eq.4 has limit $-B/D$ at $\Delta\tilde{\rho} \to 0$. The similar qualitative difference can be found for the Porod volume as a function of contrast.

So, the given method allows us to exclude the effect of magnetic scattering and obtain the additional information about the particles in ferrofluids. Such parameters like A, B, D in Eq.4 can also be used to check out particle models. The given experiment is the first step in the detailed study of possibilities and limits of the proposed approach.

Experiment

The initial magnetic fluid on D-benzene (CFATR, Romania) with the magnetite volume fraction of 6 % was diluted down to 0.8 % with different mixtures of D- and H-benzene with variation of D-benzene in the final solution from 10 to 100 %. Measurements were made at

twelve points over this interval. The special attention was given to the vicinity of the match point estimated as ~35 % of D-benzene.

Achievements and main results

The obtained scattering curves for different contrasts are presented in Fig.1. The intensity at zero angle and visible squared radius of gyration as obtained from the Guinier approximation to these curves are shown in Fig.2. The effective match point is determined as 33.7 % of D-benzene, which corresponds to the scattering length density of 2.58×10^{10} cm^{-2}. The fit of Eq. (4) to the experimental data results in squared radius of gyration R_c^2 = 1670 ± 20 Å^2, or R_c = 40 ± 3 Å. Taking into account the quasi-spherical shape of particles one obtains for the characteristic radius of the whole particle the value of 52 Å, which is consistent with the previous results obtained for this type of magnetic fluids with the use of polarized neutrons [3]. The detailed analysis of other parameters, as well as the treatment of modified basic functions is in progress.
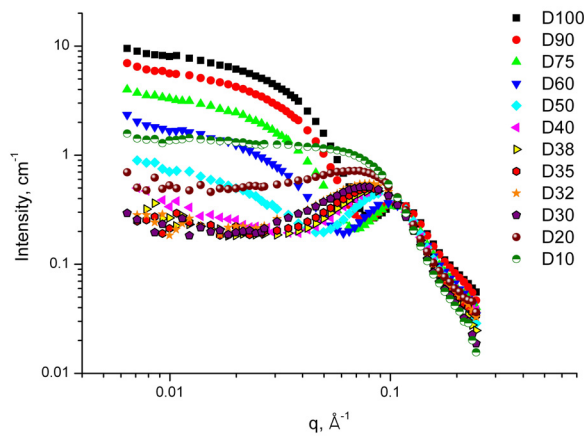
Fig.1: Scattering curves obtained during the SANS contrast variation for 0.8 % ferrofluid magnetite/myristic acid/benzene. In the sample names the content of deuterated benzene is indicated.
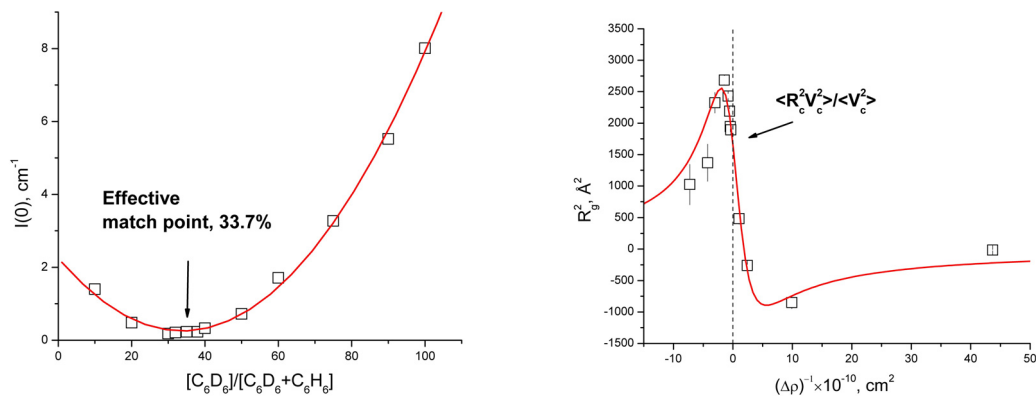
Fig.2: Integral parameters of the SANS curves as a result of the contrast variation. (Left) Intenisty at zero angle as a function of the content of deuterated benzene in the carrier. Line shows the fit to the parabolic dependence. (Right) Squared visible radius of gyration as a function of the inversed modified contrast. Line is a result of fitting with (4).

References

[1] M.V.Avdeev, J. Appl. Cryst. 40 (2007), to appear.

[2] H.B.Stuhrmann, In: Small-angle X-ray scattering, Eds. O.Glatter, O.Kratky, London: Acad. Press, 1982.

[3] M.V.Avdeev, D.Bica, L.Vékás, O.Marinica, M.Balasoiua, V.L.Aksenov, L.Rosta, V.M.Garamus, A.Schreyer, J. Mag. Mag. Mater. (2007), to appear.

![GKSS logo] GKSS FORSCHUNGSZENTRUM in der HELMHOLTZ-GEMEINSCHAFT	**EXPERIMENTAL REPORT**	**GeNF SANS-1 / SANS-2 / DCD**

Morphology of Polyolefin-Nanotube Composite Materials		
Proposer: **R.G. Alamo[1]**, [1]Oak Ridge National Laboratory, Oak Ridge, TN,USA		
Co-Proposers: **G.D. Wignall[1]**, G. Rother[1], Y.B. Melnichenko[1]		
Experimental Team: **G. Rother[1]**, G. Cheng[1], V. Haramus[2], P. K. Pranzas[2], **H. Eckerlebe[2]**, [2]GKSS		
User Group Leader: **G. Rother[1]**		
Date(s) of Experiment: 16th–19th May 2006		

Objective

The incorporation of carbon nanotubes (CNTs) into polymer matrices is presently an active field of research, based on the assumption that the impressive physical, thermal, and electrical properties of CNTs have the potential to improve the properties of polymers [1]. However, the true potential of the nanotubes has not yet been realized and to do so for applications in thermoplastic-nanofiller composites, we need to analyze the microstructure of such polymers, to provide information for the design of processing operations [2]. However, one impediment for their use in such applications is the difficulty of achieving an effective dispersion [3]. The coagulation method has recently been introduced and shows promise for achieving a uniform dispersion of carbon nanotubes in the polymer matrix [4]. Small angle scattering neutron scattering (SANS) techniques are ideal for investigating the structure of CNTs and have been used extensively to characterize the state of dispersion in various aqueous suspensions [3,5-7]. Scattering profiles varying as Q^{-1}, indicating isolated rod-like structures, have been observed for both single-wall [5] and multi-wall [7] CNTs. However, the application of such techniques to study the state of dispersion in CNT-polymer composites is only just beginning [8], and to our knowledge such techniques have not been systematically applied to explore the structure of CNT-polymer composite materials.

Experiment

First SANS experiments have been performed at the FRG1 reactor at GKSS, Geesthacht. All samples were measured at room temperature (T=298 K) . We performed measurements at the SANS1 instrument at sample detector distances of 1m, 2.3m, 4.8 m and 10 m and appropriate collimation settings. The neutron wavelength was λ=0.8 nm with a wavelength spread of $\Delta\lambda/\lambda$=10%. The neutron beam had a diameter of 10 mm. Measured intensities were corrected for sample transmission, background and detector efficiency. Absolute cross sections were calculated by comparison with the incoherent scattering of vanadium. For further analysis the scattering from the empty polymer has been subtracted from the scattering signals in order to to obtain the net signal of the CNT dispersion.

Data have also been taken at the SANS2 machine with neutron wavelengths of λ=0.58 nm and λ=1.16 nm (wavelength spread $\Delta\lambda/\lambda$=10%) and a sample detector distance of 21 m. Additional data for the very low Q –range have been taken at the DCD instrument for selected samples.

Achievements and Main Results

he residual scattering from Multiwall (MW) CNTs of different concentrations is shown in figure 1. For a polyolefin matrix (e.g. polypropylene or polyethylene), the neutron scattering cross section is expected to be small, due to the low SLD of the polymer (~ -0.3 x 10^{10} cm^{-2}). Thus, the scattering from density fluctuations due to the density difference (~ 10%) between the crystalline and amorphous regions, which produces a strong signal in the small-angle X-ray scattering (SAXS) patterns, should be minimal, due to the low overall SANS-SLD.

However, we found significant scattering from both polypropylene (PP) and polyethylene (PE) matrices (e.g. fig. 2 for PE with a similar magnitude for PP), which we believe is due to impurities (e.g. catalyst residues, additives etc.). Thus any scattering heterogeneity with a positive SLD will have strong contrast with the overall SLD of the matrix, which is close to zero. Despite this, the net scattering from the MW-CNTs is positive, after subtracting the PP matrix, and shows power law decay $[I(Q) \sim Q^{-n}]$ over a large Q-range with an exponent, $n \approx 3$. For single-wall (SW) CNTs, the net scattering is negative, due to the errors involved in subtracting such a large background from the PE matrix.

Figure 1: Residual scattering from a range of concentrations of MW-CNT in iPP, after subtracting the matrix signal.
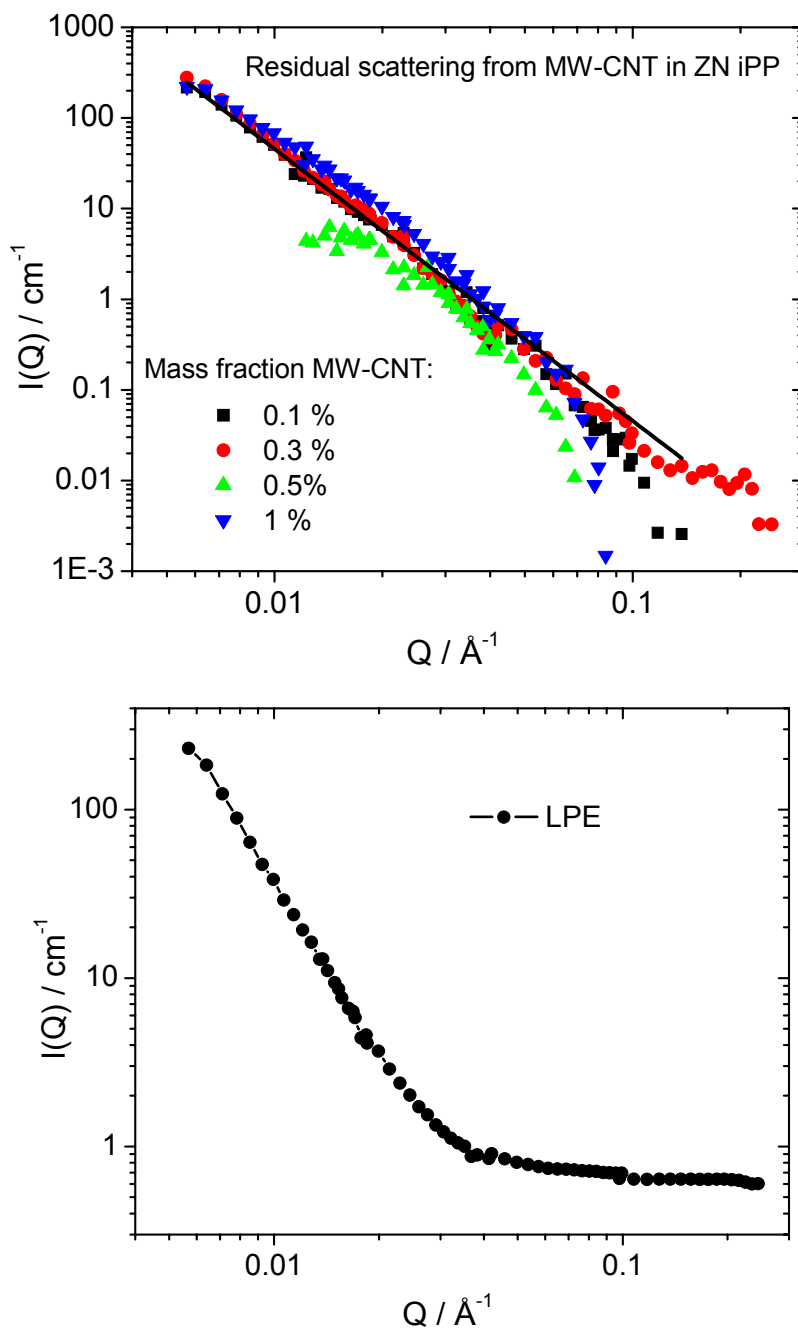
Figure 2: SANS scattering pattern of the LPE matrix.

References

[1]   E. M. Moore et al., *J. Appl. Polym. Phys.,* 93, 2926 (2004)].

[2]   L. Valentini et al., *J. Appl. Polym. Sci.,* 87, 708 (2003)].

[3]   H. Wang et al., *Nano Letters,* 4, 1789 (2004)].

[4]   L. Du et al., *J. Polym. Sci., Polym. Phys.,* 41, 3333 (2003).

[5]   W. Zhou et al., *Chem. Phys. Lett.,* 384, 185 (2004).

[6]   K. Yurekli et al., *J. Am. Chem. Soc.,* 126, 9902 (2004).

[7]   D. W. Schaefer et al., *Chem. Phys. Lett.,* 375, 369 (2003).

[8]   J. Berriot et al., *Polymer*, 44, 4909 (2003).

GKSS FORSCHUNGSZENTRUM in der HELMHOLTZ-GEMEINSCHAFT	**EXPERIMENTAL REPORT**	**GeNF SANS-2**

Small-angle scattering instrument SANS-2

Short Instrument Description:

Small angle neutron scattering using cold non-polarised/polarised neutrons is a powerful tool for investigating the structure of matter in the range between 1 and 100 nm. It is a non destructive method for a wide range of application in:
- Metal physics (precipitates, clusters, interfaces, grain boundaries,...)
- Materials science (defects, porosity,....)
- Nanocrystalline materials (grain size, magnetic structures,...)
- Polymers and polymer systems (blends, mixtures, structure and morphology,...)
- Biology (viruses, proteins,...)
- Complex liquids (microemulsions, colloids, liquid crystals,...)

Local Contact:

Melissa Sharp
Phone/Fax : +49 (0)4152 87 – 1209 / +49 (0)4152 87 – 1338
e-mail: melissa.sharp@gkss.de

Helmut Eckerlebe
Phone/Fax : +49 (0)4152 87 – 1202 / +49 (0)4152 87 – 1338
e-mail: helmut.eckerlebe@gkss.de

Dr. P. Klaus Pranzas
Phone/Fax : +49 (0)4152 87 – 1326 / +49 (0)4152 87 – 41326
e-mail: pranzas@gkss.de

Schematic View of SANS-2:

Instrument Details:

Beamline:	beamline 8 - cold neutron guide NG-2, radius of curvature R = 900 m, cross section 3 x 4 cm^2
Monochromator:	helical slot velocity selectors (Dornier)
Wavelength range at sample position:	0.3 to 2.0 nm
Wavelength resolution:	$\Delta\lambda/\lambda$ = 0.1 (2 additional velocity selectors with $\Delta\lambda/\lambda$ = 0.05 and 0.2 available)
Length of collimation:	max. 16 m (2 m elements)
Flux at sample position:	Φ_{max} = 2·10^7 cm^{-2} s^{-1} (1 m collimation, λ = 0.5 nm)
Range of momentum transfer:	0.01 ≤ q ≤ 3 nm^{-1} (small-angle scattering) q ≤ 25 nm^{-1} (wide-angle scattering with 2. detector)
Distance sample to detector:	1.0 m ≤ d ≤ 22 m optional 2. detector for wide angles: d = 1 m

Detector:
    active area:
    resolution:
    background:
	2-dim position-sensitive ^{3}He-counter
	    50 x 50 cm^2
	    0.25 x 0.25 cm^2
	    < 0.5 cps

Supplementary equipment:	- several electro-magnets up to 2.0 T (horizontal and vertical fields) - superconducting magnets up to 5.0 T - several cryostats (4 - 400 K) - furnace (-30 °C to +400 °C, atmospheric condition, inert gas and vacuum) - linear translation, rotary, tilting and lift tables (freely programmable sample position) - "HOLONS": holographic combined with SANS setup (see table A)
Special features:	- Sample environment space is variable from a few mm up to 2500 mm - User-friendly software for data reduction and evaluation running on PC (SANDRA a. o.)

GKSS	**EXPERIMENTAL REPORT**	**GeNF** **SANS-2**

Characterization of precipitates in a high-strength low-alloy steel

Proposer: **Co-Proposers:**	**H. Leitner**, [1]Montanuniversität Leoben, Franz Josef-Str. 18, 8700 Leoben, Austria **H. Clemens,** [1] **P. Staron,** [2]GKSS
Experimental Team:	**M. Bischof[1], P. Staron[2], P.K. Pranzas[2]**
User Group Leader:	**H. Clemens[1]**
Date(s) of Experiment:	April 2005

Objectives

Precipitates in the size range from nanometres to microns are affecting the mechanical and thermo-physical properties of steel. In the present study a high-strength low-alloy (HSLA) steel containing Ti, Nb, and V is investigated in the as-rolled and different annealed conditions. The combination of modern transmission electron microscopy (TEM) and small-angle neutron scattering (SANS) enables the analysis of precipitates in the nanometre region, which are relevant for the strength of the steel.

Experiment

For several years there has been the demand for hot-rolled strip steel with yield stresses above 700 MPa. The driving force for this development is the aim to reduce component-weight, especially in mobile applications, while the requirements for easy processing, i.e. cold-forming and weldability, have to be preserved. Due to the small size of involved strengthening precipitates the traditional metallographic techniques are of limited use.

SANS was used for the study of changes in particle size distributions as a function of the annealing condition. As the matrix of the investigated steel is ferromagnetic, it was magnetized to saturation by a magnetic field of 2 T. Then the nuclear cross sections can be measured parallel to the applied magnetic field, while the sum of nuclear and magnetic cross section can be measured perpendicular to the field. As the precipitates are nonmagnetic, the ratio of magnetic and nuclear scattering cross section can be analysed additionally.

A total of 6 samples of a HSLA steel with 95.6% Fe and 0.17%C were measured in the as-rolled state and after annealing treatments for 35 min at temperatures between 300 °C and 700 °C. After hot-rolling the material under investigation exhibits a martensitic microstructure resulting in a hardness of about HV2=508. Subsequent annealing treatments at temperatures between 250 °C and 500 °C lead to a considerable decrease in strength (HV2=476 at 250 °C and HV2<400 at 500 °C), which is attributed to tempering of martensite. Annealing at temperatures of about 600 °C leads to a plateau or peak in hardness (HV2=400), followed by a sharp drop (HV2<330) when the material is annealed above 650 °C. The task is to correlate these changes in the mechanical properties with changes in the particle size distribution.
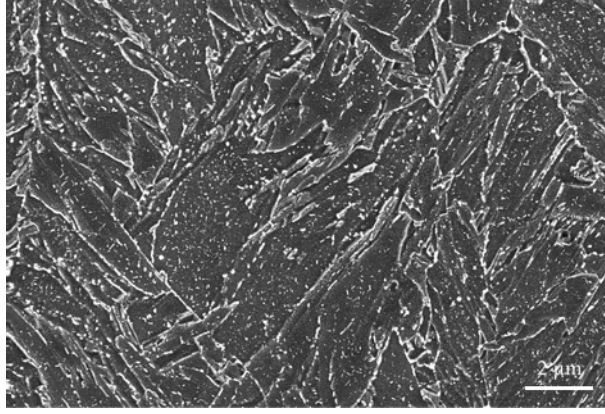
Fig. 1: SEM image of a sample annealed for 35 min at 610 °C.
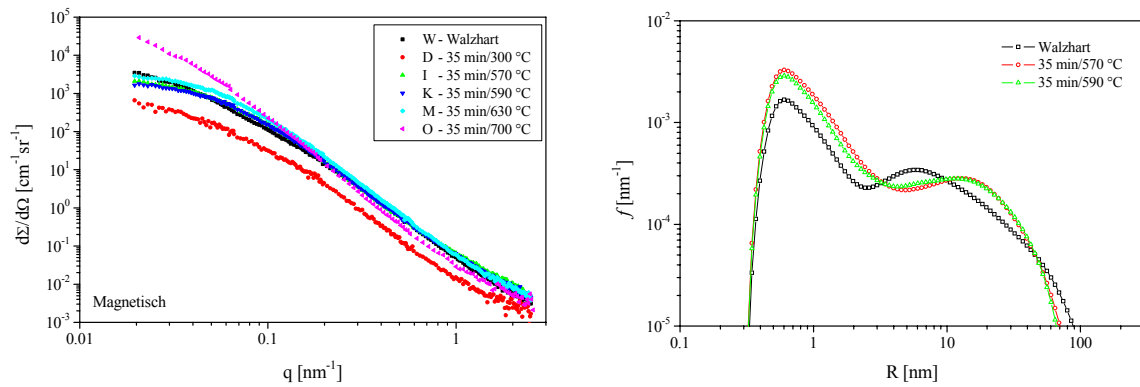
Fig. 2: Measured magnetic scattering cross section (left) and corresponding particle size distributions.

Achievements and Main Results

There are significant changes in the SANS cross sections with the annealing state (Fig. 2). Especially, there is a large drop at the rather low annealing temperature of 300 °C; its origin is not yet fully clear. Most likely the drop is due to annealing effects and the sample tempered at 300 °C can serve as a reference sample. Then, possibly by chance, the particle size distribution shows only small changes from the as-rolled state to annealed states at 570 °C or 590 °C (Fig. 2). There is a bimodal size distribution of particles with sizes of 1 nm and 20-40 nm with a total volume fraction of approximately 1%. At 700 °C the particles grow larger with a reduced number density (coarsening), which seems to correspond to the above mentioned drop in hardness. A careful analysis of the SANS data in combination with electron microscopy results and mechanical data will contribute to a more detailed picture of the strengthening mechanism in the investigated HSLA steel.

72

Investigation of the magnetic structure of the ferromagnet ZrZn$_2$

Proposer:	**Stephanie Pouget[1]**, [1]6 rue Jules Horowitz 38043 Grenoble Cedex FRANCE
Co-Proposers:	**Sergey Grigoriev[2]**, [2]PNPI, Gatchina, St-Petersburg, 188300, RUSSIA
	Niels van Dijk[3], [3]Delft University of Technology, Mekelweg 15, 2629 JB Delft, The Netherlands
Experimental Team:	**Niels van Dijk[3], Sergey Grigoriev[2],**
	Helmut Eckerlebe[4], [4]GKSS Forschungszentrum
User Group Leader:	**Sergey Grigoriev[2]**
Date(s) of Experiment:	1st–7th November 2005

Objectives

In 1958, Matthias and Bozorth [1] discovered that despite being made from non magnetic elements, ZrZn$_2$ becomes ferromagnetic at low temperature. This compound crystallizes in the C15 cubic Laves structure, and the 4d orbitals of the Zr atoms (which form a diamond structure lattice) are responsible for the magnetic behaviour. This behaviour is characterized by a rather low Curie temperature T$_C$= 28.5 K, compared to other ferromagnetic metals, and a weak saturation moment of 0.17 μ_B. Some 40 years later, superconductivity at ambient pressure was observed at T ~ 0.3 K in the ferromagnetically ordered phase of ZrZn$_2$ [2]. This came after the discovery of superconductivity in UGe$_2$, below 1 K, and within a limited pressure range [3], which had provided an unanticipated example of coexistence of superconductivity and ferromagnetism. The electronic pairing mechanism needed for superconductivity is believed to be magnetic in origin for both materials.

Muon spin rotation measurements have recently been performed on a ZrZn$_2$ sample, which again gave unexpected results [4,5]. The measured coherent muon signal at helium temperature cannot be explained by a normal ferromagnetic structure, but it could be explained by the presence of a long-range magnetic modulation. We propose to check this hypothesis by looking for low Q magnetic satellites and investigating their temperature dependence.

Experiment

1. Sample

The polycrystalline sample ZrZn$_2$, a tablet of 1.2 mm in thickness and 8 mm in diameter, has been studied. The sample is the same as used for investigations [4,5].

2. Small-angle neutron scattering

Small-angle neutron scattering (SANS) measurements were carried out with the instrument SANS-2 at the Geesthacht Neutron Facility (GeNF). Neutrons with a mean wavelength of λ = 0.58 nm and a wavelength spread of $\Delta\lambda/\lambda$ = 10% were used. Detector distances up to 10 m were used with appropriate collimations to cover scattering vectors q from 0.03 nm^{-1} to 2.5 nm^{-1} ($q = 4\pi\sin(\theta)/\lambda$ where 2θ is the scattering angle). The scattering intensity was measured in the temperature range from T = 10 K The magnetic contribution to the scattering

was extracted as $I_m(q) = I(q,T) – I(q,T =60$ to T = 60 K. The external magnetic field **H** from 1 to 900 mT was applied. K). The polarization-dependent cross-section was measured also in so-called, "inclined" geometry, when the magnetic field is inclined at the angle $\varphi = 45^o$ with respect to the incident beam **k**. This geometry allows one to observe the left-right asymmetry in SAPNS pattern that originate from the interaction of the neutron spin with the chiral dynamical excitations, i.e. with the spin waves. It is separated from other contributions as the asymmetric part of the polarization dependent scattering: $\Delta I(\theta) = [I_+(\theta)+I_-(-\theta)-I_+(-\theta)-I_-(\theta)]$, where $I_+(\theta)$ and $I_-(\theta)$ are intensities with the polarization directed along and opposite to the field.

Achievements and Main Results

Q-dependence of SANS intensity is presented in Fig.1 for two different temperatures T = 10 K and T = 25 K. We calculated the integral scattering intensity over the whole q-range: $I_{int} = 2\pi\int I(q)qdq$. The temperature dependence of I_{int} is shown in Fig.2. The magnetic field suppresses this scattering (Fig.3). This scattering is attributed to inelastic scattering, i.e. to spin waves. The polarization-dependent cross-section was measured in the inclined geometry and integrated over q ($\Delta I_{int} = 2\pi\int\Delta I(q)qdq$) is plotted in fig.4 as a function of the magnetic field at T = 25 K. The scattering is observed in the range of fields 0 < H < 100 mT. The interpretation of the results obtained is in progress.
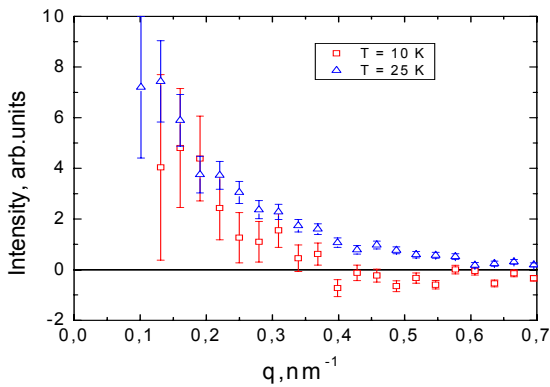
Fig. 1:   Scattering Pattern at 10 and 25 K.
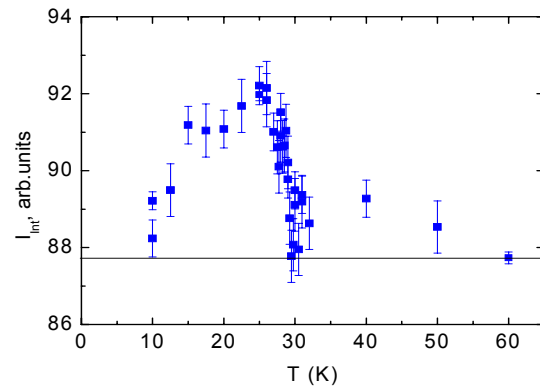
Fig. 2:   Temperature dependence of I_{int}.
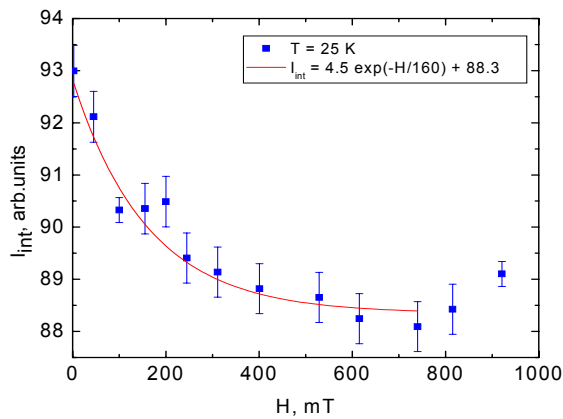
Fig. 3: Magnetic field dependence of I_{int}.
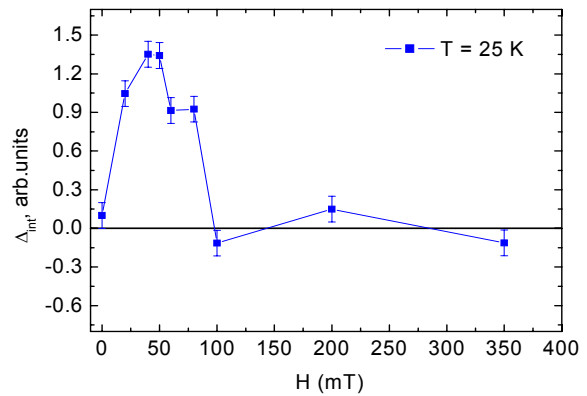
Fig. 4:   Magnetic field dependence of the polarization-dependent cross-section.

References

[1] Matthias B.T. and Bozorth R.M., Phys. Rev. **109**,604 (1958).

[2] C. Pfleiderer, M. Uhlarz, S.M. Hayden, R. Vollmer, H.v. Lohneysen, N.R. Bernhoeft, and G.G. Lonzarich, Nature (London) **412**, 58 (2001).

[3] S. S. Saxena, P. Agarwal, K. Ahilan, F.M. Grosche, R.K.W. Haselwimmer, M.J. Steiner, E. Pugh, I.R. Walker, S. R. Julian, P. Monthoux, G.G. Lonzarich, A. Huxley, I. Sheikin, D. Braithwaite, and J. Flouquet, Nature (London) **406**, 587 (2000).

[4] P. Dalmas de Réotier and A. Yaouanc, J. Phys.: Submitted to Condens. Matter (2005).

[5] P. Dalmas de Réotier and A. Yaouanc, J. Phys.: Condens. Matter **9**, 9113 (1997).

![GKSS FORSCHUNGSZENTRUM in der HELMHOLTZ-GEMEINSCHAFT]	**EXPERIMENTAL REPORT**	**GeNF SANS-2**

Domain structure in FEP polymer based electrolyte membranes for fuel cells	
Proposer:	**Günther Scherer[1]**, [1]PSI, Switzerland **Selmiye Alkan Guersel[1]**
Co-Proposers:	**Urs Gasser[1]**, **K. Mortensen[2]**, [2]Risø Denmark
Experimental Team:	**Urs Gasser[1]**, **K. Mortensen[2]** **P. K. Pranzas[3]**, [3]GKSS, Germany
User Group Leader:	**Günther Scherer[1]**
Date(s) of Experiment:	11th–15th September 2006

Objectives

The project aims for making low cost polymer membranes for PEM fuel cells by new design and synthesis as based on detailed insight into the structural properties. Small angle neutron scattering is an ideal method being sensitive to the relevant length scale, having good contrast for the material components applied, and providing the possibility to use contrast variation for more detailed structural investigations.

Experiment

SANS experiments were performed on samples of poly(tetraflouroethylene–*co*-hexaflouropropylene), FEP, to which polystyrene, PS, was grafted by irradiation induced methods. The films were further crosslinked using divinyl benzene (DVB). While most studies were performed at the SANS instrument, few additional measurements were done at the double crystal diffractometer (DCD) to reveal properties at even larger length scale than probed by SANS. At SANS-2 distances between sample and detector of 1, 3, 9 and 21 m and a wavelength λ of 0.58 nm ($\Delta\lambda/\lambda$=0.1) were used to cover the range of scattering vector q between about 0.01 nm^{-1} and 2 nm^{-1}. Scattering data were corrected for sample transmission and detector response and normalized by monitor counts. Additional studies have been done using SANS facilities at respectively PSI and NIST.

Achievements and Main Results

The main subject of the present study was to use contrast variation to verify that the FEP-PS membranes are predominantly a two-phase system.

Figure 1 shows two examples of contrast variation studies, using water mixtures of H_2O and D_2O. The two series are of cross-linked PS grafted FEP polymers. The blue data points represent the results of H_2O swollen membranes, the purple has 50% H_2O/50% D_2O, the green has 25% H_2O/75% D_2O and the red data represent 100% D_2O.

The results are dominated by two features, a scattering term with maximum at low-*q* and a correlation peak interpreted as resulting from the dominating domain structure of i) a crystalline FEP phase and ii) a phase of water swollen PS-grafted amorphous FEP.
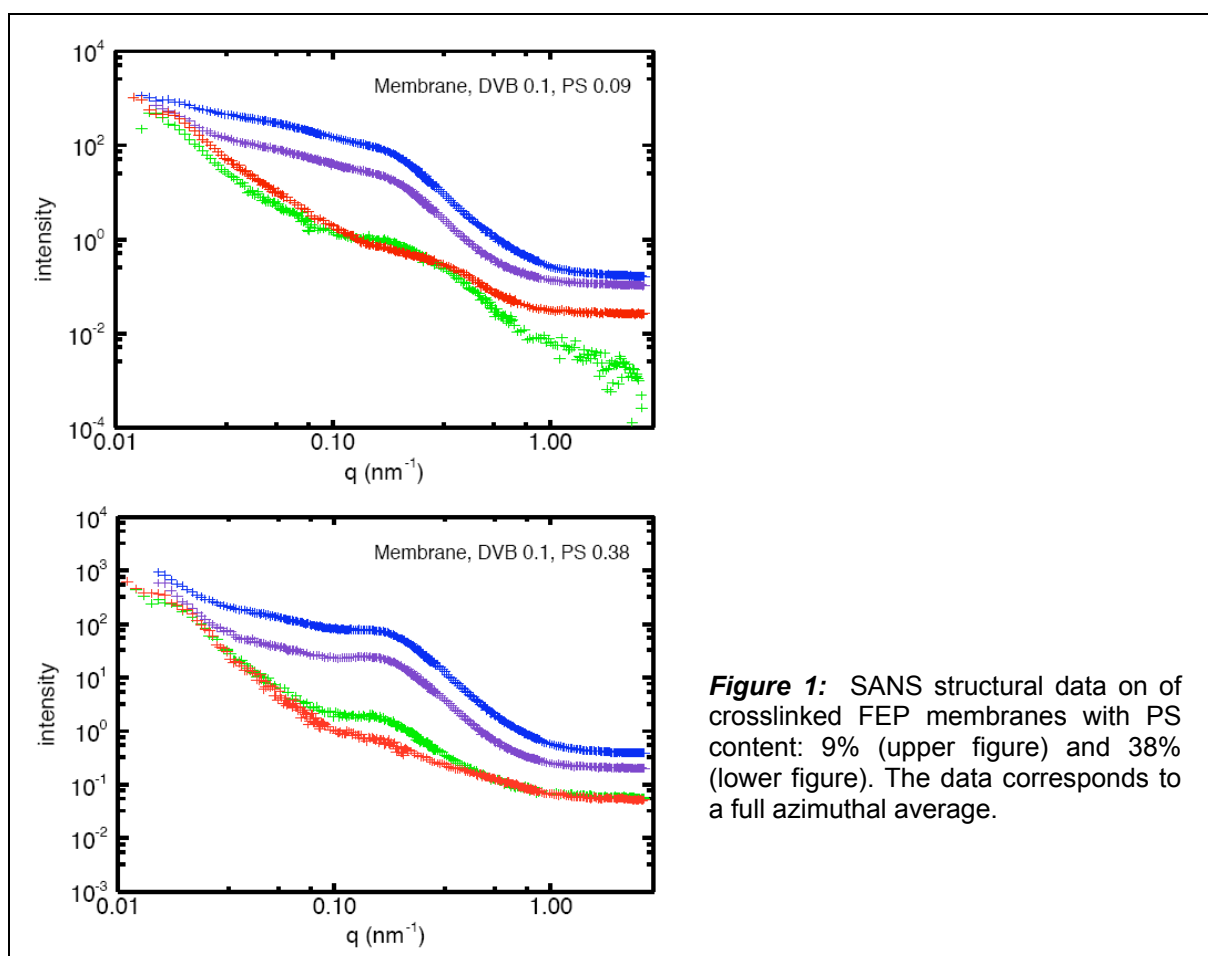
Figure 1: SANS structural data on of crosslinked FEP membranes with PS content: 9% (upper figure) and 38% (lower figure). The data corresponds to a full azimuthal average.

The low-q intensity appears rather independent of water content, while the correlation peak shows a regular dependence on the water mixture.

The match-point of PS/FEP polymer is calculated to occur near 100% D_2O, in good agreement with the results. Both data series show a vanishing correlation peak in the 100% D_2O swollen membrane, and only the low-q scattering contribution is left.

These data conclude that the membranes are dominated by a two phase structure of FEP and water-swollen PS/FEP. But an additional structural feature is clearly apparent, which is not a part of the overall two phase membrane structure.

GKSS FORSCHUNGSZENTRUM in der HELMHOLTZ-GEMEINSCHAFT	EXPERIMENTAL REPORT	GeNF SANS-2

Field-dependent experiments to characterise the precipitates in a high-speed steel		
Proposer:	**Michael Bischof** [1]	
Co-Proposers:	**Elisabeth Eidenberger** [1]	
	[1]Montanuniversität Leoben, Departmentment of Physical Metallurgy and Materials Testing, Leoben, Austria	
	Peter Staron [2], [2]GKSS	
Experimental Team:	**Michael Bischof[1], Elisabeth Eidenberger[1], Peter Staron[2], Helmut Eckerlebe[2], Gerhard Kozik[2], Klaus Pranzas[2]**	
User Group Leader:	**Michael Bischof** [1]	
Date(s) of Experiment:	March 2006	

Objective

Small-angle neutron scattering (SANS) is a widely used method for characterizing chemical or magnetic inhomogenities of materials within the size range of approximately 1 – 100 nm. In the field of steel research it can be used to determine particle-size distributions as well as corresponding volume fractions.

Usually, an external magnetic field of about 2 T is applied on the sample in order to remove all magnetic domain boundaries and a simple two-phase-model [1] is applied in order to interpret the measured SANS data in terms of particles embedded within an entirely homogenous, magnetically saturated matrix.

However, the theory of micromagnetics [2] predicts deviations from the perfectly aligned spin state whenever disordering forces appear which give rise to torques on the magnetic moments. Such forces may be due to, e.g., the magnetocrystalline anisotropy of the individual crystallites, or to the magnetoelastic anisotropy which is associated with the long-range strain fields of dislocations. As a result, in this case magnetic SANS arises not only from variations in the magnitude but also from variations in the orientation of the magnetization, which, as shown in [3], may evolve on a length scale of a few nm up to about 100 nm.

In the same study [3] a method was introduced to extract the so-called "residual scattering" from magnetic-field-dependent SANS measurements on pure Ni and Co samples. The residual scattering is the contribution which is relevant for the analysis of particle scattering. Therefore, it is of great interest to investigate the question whether the same method can be applied for martensitic steels in order to extract information on the particle microstructure from SANS experiments.

Experiment

In our experiment, steel samples containing small amounts of carbide-forming elements as well as Ni and Al have been exposed to different continuous or isothermal heat treatments in the temperature range between 450°C – 750°C. The heat-treated samples have been analyzed by SANS measurements at different external magnetic fields and the residual scattering contribution has been obtained for nuclear as well as for magnetic scattering curves. Two sets of samples were analyzed. One set, consisting of two samples, was annealed for different times at 610°C after quenching, while another set, consisting of three samples, was continuously heated to a specific target temperature at a heating rate of 20 K/min and subsequently quenched to room temperature. Additionally, one sample was analyzed in the as-quenched state. Details on the heat treatments of the samples can be found in Tab. 1.

Table 1: *Nomenclature and heat treatments of the samples used in this study. All samples have been hardened similar to sample A prior to the described heat treatments. λ stands for the quenching parameter and is the time (in seconds) the sample needs to cool down from 800°C to 500°C, divided by a factor of 100.*

sample	heat treatment
A	hardened: 30 min/990°C + quenching (λ0.3)
I-30	as A + isothermal annealing, 30 min/610°C + quenching (λ0.3)
I-1000	as A + isothermal annealing, 1000 min/610°C + quenching (λ0.3)
C-550	as A + continuous heating to 550°C + quenching (λ0.3)
C-600	as A + continuous heating to 600°C + quenching (λ0.3)
C-750	as A + continuous heating to 750°C + quenching (λ0.3)

SANS measurements were performed using unpolarized neutrons with a wavelength of 0.58 nm and a wavelength spread of 10 %. The 1 mm thick, disc-shaped samples with a diameter of 5 mm were mounted on a Cadmium aperture with a diameter of 3 mm. Samples A, C-550, C-600 and C-750 were magnetized close to saturation at 5 different external fields H_a (956, 1040, 1187, 1404, and 1740 mT). The field direction was horizontal and normal to the incident neutron beam. For samples I-30 and I-1000, 4 different fields (956, 1404, 1740 and 1960 mT) were used. Scattered neutrons were detected by a position-sensitive detector with a resolution of 256×256 pixels. Since no sharp features were present in the scattering curves, this resolution was reduced to 64x64 pixels during post-processing of the data, leading to a reduced scattering of the data points. Three distances between detector and sample (3 m, 9 m and 21 m) with appropriate collimation of the neutron beam were used to cover scattering vectors q ranging from 0.02 nm^{-1} to 0.5 nm^{-1}. Measured intensities were corrected for sample transmission, background scattering and detector efficiency.

The nuclear cross section was measured at α = 0 and π while the sum of nuclear and magnetic cross sections was measured at angles of $\pi/2$ and $3\pi/2$, where α is the azimuthal detector angle and α = 0 denotes the horizontal and, consequently, the field-parallel direction. The SANS data reduction was carried out using the SANDRA software tool provided by GeNF. For the separation of the residual scattering ($d\Sigma_R/d\Omega$) and the field-dependent micromagnetic scattering ($d\Sigma_M/d\Omega$) a computer program was written, which performs a linear regression on the basis of a least-square algorithm to a set of data points $d\Sigma/d\Omega$ over R (see Fig. 1). R is the micromagnetic response function which is defined in [3].
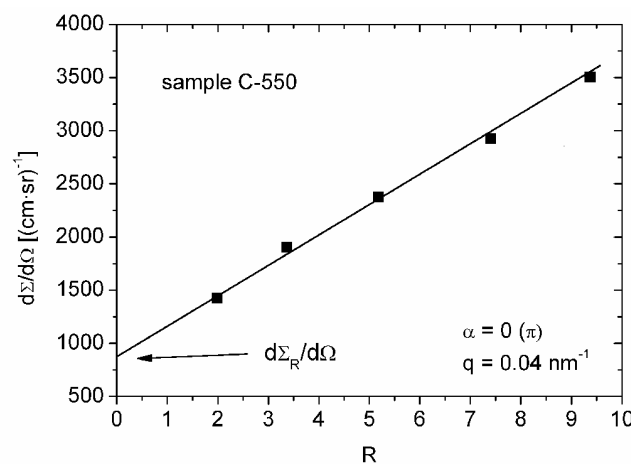
Figure 1: *Measured differential scattering cross section dΣ/dΩ for sample C-550 (see Tab.1) at different magnetic fields versus the micromagnetic response function R(q, H$_a$). Data are for α = 0 (π) and q = 0.04 nm^{-1}. Values of μ$_0$·H$_a$ in order of decreasing R: 956, 1040, 1187, 1404, and 1740 mT. The solid line is the best straight-line fit.*

Achievements and Main Results

Fits to the experimental SANS cross sections of samples A and I-1000, recorded at different applied magnetic fields, as well as $d\Sigma_R/d\Omega$ and $d\Sigma_M/d\Omega$ are displayed in Fig. 2. $d\Sigma_M/d\Omega$ is displayed for the field of 1740 mT. In a classical SANS data evaluation $d\Sigma/d\Omega^{\parallel}$, which is the measured cross section in the field-parallel direction, is expected to correspond to the nuclear cross section. The as-quenched sample (sample A) shows a strong dependence of $d\Sigma/d\Omega^{\parallel}$ on the applied magnetic field (Fig. 2a). The residual scattering cross section is significantly smaller than the experimental cross section, even at the largest applied field of 1740 mT. It is obvious that at the largest field the strength of the spin-misalignment scattering is of the same order of magnitude as the residual scattering.

The field dependence of $d\Sigma/d\Omega^{\parallel}$ for sample I-1000 is much smaller (Fig. 2b)). In this case, the contribution of spin-misalignment scattering to the experimental scattering curves is about one order of magnitude smaller than the residual scattering.

Figs. 2c) and 2d) display $d\Sigma/d\Omega^{\perp}$, which is measured in the field-perpendicular direction; it represents the sum of magnetic and nuclear cross sections. Obviously, the influence of the field-dependent spin-misalignment scattering is much smaller for these scattering curves. Even for sample A, $d\Sigma_M/d\Omega^{\perp}$ is one order of magnitude smaller than $d\Sigma_R/d\Omega^{\perp}$ and for sample I-1000 the factor is about 100.
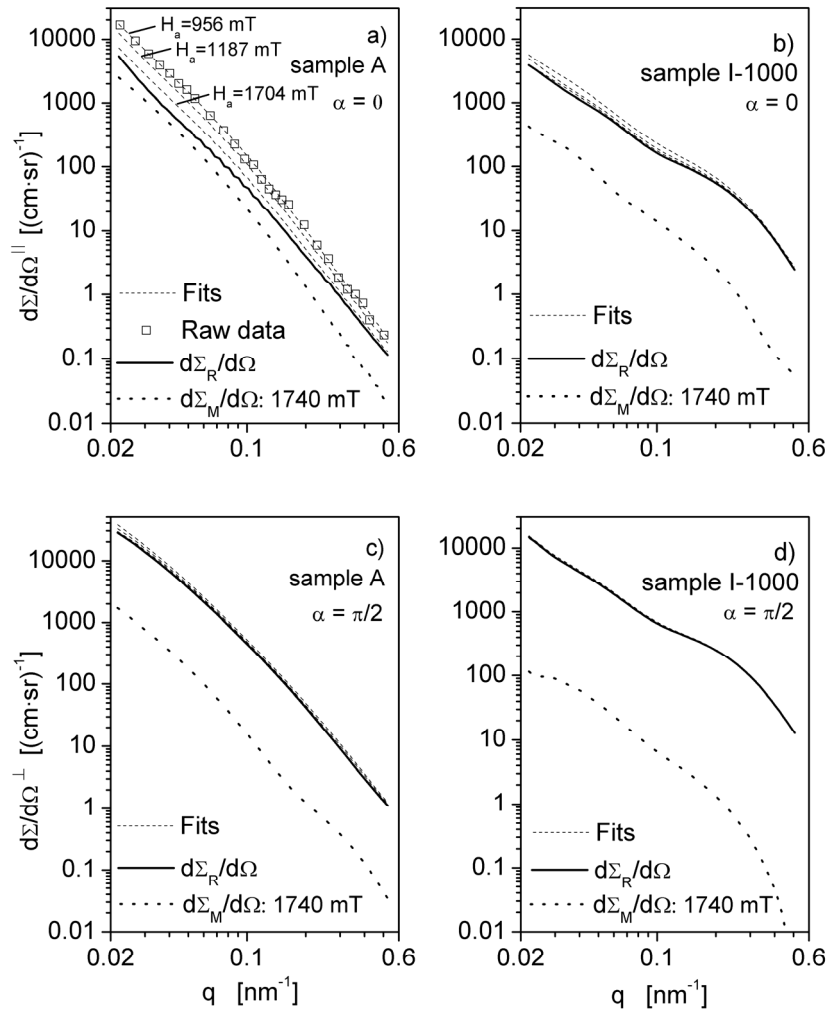
Figure 2: *Fits to the measured $d\Sigma/d\Omega$ of samples A and I-1000 at different applied magnetic fields (dashed lines). Data for $\mu_0 \cdot H_a$ = 956, 1187 and 1740 mT is displayed. The solid line represents $d\Sigma_R/d\Omega$ and the dotted line $\Sigma_M/d\Omega$.. Data originate from sectors parallel (a ,b) and perpendicular (c, d) to the external field . The open symbols in a) are the measured raw data of sample A at the lowest H_a. The corresponding errors are similar to the size of these symbols.*

In the course of our experiment it has turned out that an additional field-dependent scattering contribution is present which cannot be explained by classical theories including the theory of micromagnetics considered above. According to Michels et al. [4] the additional scattering may be understood as a result of dipolar stray fields around the individual particles which are due to the jump in M_S at the interface between matrix and particles. The component of this stray field, which is locally perpendicular to the magnetization of the matrix acts as a torque and, therefore, is responsible for spin disorder in the local vicinity of particles.

The value of this additional scattering, $d\Sigma_D/d\Omega$, is zero at $\alpha = 0$, $\pi/2$, π, and $3\pi/2$, owing to the dependency $d\Sigma_D/d\Omega \sim \sin^2\alpha \cdot \cos^2\alpha$ [4]. This coincides with the sectors of interest for the evaluation of nuclear and magnetic scattering curves. Maxima in $d\Sigma_D/d\Omega$ are expected to be at $\pm\pi/4$ and $\pm 3\pi/4$ relative to the direction of the external magnetic field, leading to a clover-leaf-shaped anisotropy of the scattered intensity distribution on the detector. However, experimentally observed maxima are in the region $\pm 30\text{-}40°$ and $\pm 140\text{-}150°$ (Fig. 3). This can be understood as due to the superposition of dipolar scattering and scattering from the inhomogeneous magnetic anisotropy of the matrix, which shifts the observed maxima in $d\Sigma_D/d\Omega$ to smaller angles α.

Sample I-1000 shows a strong clover-leaf-shaped anisotropy on the detector. Figure 3a) depicts the scattered intensity on the detector when the data recorded at the highest applied field, 1740 mT, is subtracted from the data recorded at 470 mT. At 1740 mT the spin-misalignment scattering is assumed to be small and is used as an approximation to $d\Sigma_R/d\Omega$. The difference data is, therefore, an approximate representation of the field-dependent contributions $d\Sigma_M/d\Omega$ and $d\Sigma_D/d\Omega$ at one particular field, in this case 470 mT. The anisotropy as seen in Fig. 3a) is most pronounced at rather low fields. Figure 3b) shows the difference image for 956 mT, revealing that at this field the clover-leaf-shaped anisotropy is strongly washed out when compared to Fig. 3a). At applied fields higher than 956 mT, clover-leaf-shaped features are no longer observed. Due to this fact and due to the occurrence of intensity maxima of $d\Sigma_D/d\Omega$ on the detector away from the sectors of interest for the data processing used here, $d\Sigma_D/d\Omega$ is found as negligible for the analysis of the scattering data in terms of particle scattering [5].
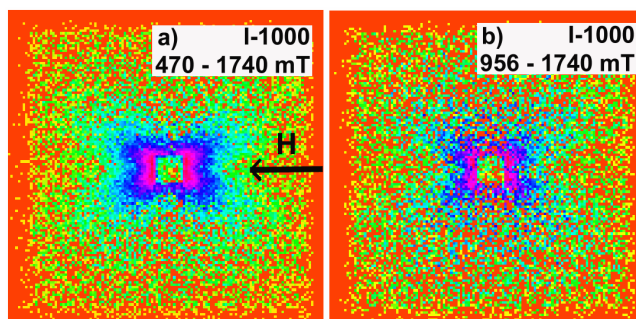
Figure 3: Intensity distributions on the two-dimensional area detector. a) Difference intensity between data measured at 470 mT and data measured at 1740 mT for sample I-1000. b) Difference-intensity data, 956-1740 mT, for sample I-1000.

References

[1] Kostorz G. Application of neutrons in materials science. In: Kostorz G, Herman H, editors. Treatise on Materials Science and Technology, vol.15: Academic Press, 1979. p.227.

[2] Brown WF. Micromagnetics: John Wiley & Sons, New York, 1963.

[3] Weissmüller J, Michels A, Barker JG, Wiedenmann A, Erb U, Shull RD, Phys rev B 2001;63:214414

[4] Michels A, Vecchini C, Moze O, Suzuki K, Pranzas PK, Kohlbrecher J, Weissmüller J, submitted to Phys rev B

[5] Bischof M, Staron P, Michels A, Granitzer P, Rumpf K, Leitner H, Scheu C, Clemens H, submitted to Acta Mat

![GKSS logo] **GKSS** FORSCHUNGSZENTRUM in der HELMHOLTZ-GEMEINSCHAFT	**EXPERIMENTAL REPORT**		**GeNF SANS-2**

Combining SANS experiments with polarized and unpolarized neutrons to study precipitates in steels	
Proposer:	**M. Bischof**, [1]University of Leoben, Department of Physical Metallurgie and Materials Testing, Leoben, Austria
Co-Proposers:	**E. Eidenberger**[1] **P. Staron,** [2]GKSS
Experimental Team:	**E. Eidenberger[1], H. Eckerlebe[2], P. Staron[2]**
User Group Leader:	**H. Clemens**[1]
Date(s) of Experiment:	3rd–4th April 2006

Objectives

Precipitates contribute a lot to the high toughness and strength at elevated temperatures of tool steels and therefore knowledge of their formation kinetics is fundamental for optimizing these properties. In their recently published work Bischof et al. [1] determined the influence of spin-misalignment scattering on the scattering cross section of tool steels. It was shown that in some cases field-dependent SANS measurements are needed to interpret scattering curves correctly. In the current experiments the effect of using polarized neutrons for SANS on tool steels shall be surveyed.

Experiment

The precipitation behaviour of a tool steel (K011) and a recently developed Fe-Co-Mo alloy (S903) is investigated. This novel material is strengthened by intermetallic precipitates of the so-called μ-phase. The nominal compositions of both materials are given in Tables 1 and 2, respectively.

Table 1: Nominal composition of K011 (wt%).

C	Cr	Mo	Ni	V	Co	Al	Si	Mn	Fe
0.3	2.4	2.5	6.5	0.26	1.18	2.6	1.18	0.23	balance

Table 2: Nominal composition of S903 (wt%).

Mo	Co	Fe
15	25	balance

Four detector distances (1 m, 3 m, 9 m and 21 m) were used with appropriate apertures and collimators to cover scattering vectors q from 0.02 nm^{-1} to 2 nm^{-1}. The measurements were performed using polarized neutrons at a wavelength of λ=5.8 nm and a wavelength spread of $\Delta\lambda/\lambda$=10%. The neutron beam impinging on the samples had a diameter of 4 mm. The samples were magnetized to saturation in a field of 2 T. Measured intensities were corrected for sample transmission, background and detector efficiency. The nuclear cross sections were measured at azimuthal detector angles of α=0° and 180°, while the sum of nuclear and magnetic cross section was measured at angles of α=90° and 270°, where α is the angle between the scattering vector and the magnetization. The scattered intensity was averaged over sectors of 25° around the given mean angles. Absolute cross sections were calculated

by comparison with the incoherent scattering of vanadium. The detector resolution was reduced to 128x128 pixels prior to analysis.

Table 3: Notation and heat treatments of the samples used in this study. λ stands for the quenching parameter and is the time (in seconds) the sample needs to cool down from 800 °C to 500 °C, divided by a factor of 100.

sample	heat treatment
A	hardened: 30 min/990 °C + quenching (λ0.3)
I-1000	as A + isothermal annealing, 1000 min/610 °C + quenching (λ0.3)
A_N2	as A , quenching (λ0.3) in liquid nitrogen
S903 LG	homogenised
S903 540°C	as S903 LG + continuous annealing to 540 °C + quenching (λ0.3)
S903 615°C	as S903 LG + continuous annealing to 615 °C + quenching (λ0.3)
S903 675°C	as S903 LG + continuous annealing to 675 °C + quenching (λ0.3)
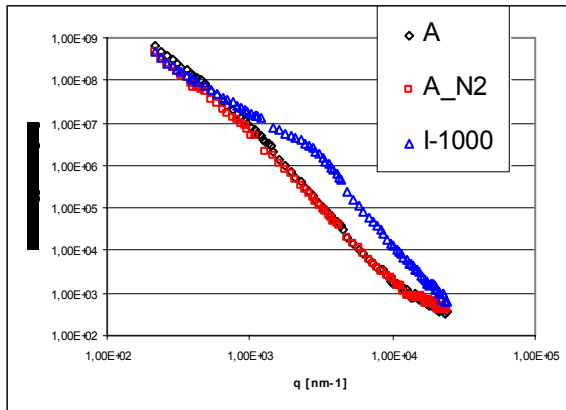
Fig. 1: Sum of nuclear and magnetic scattering of the K011 samples A, A_N2 and I-1000.
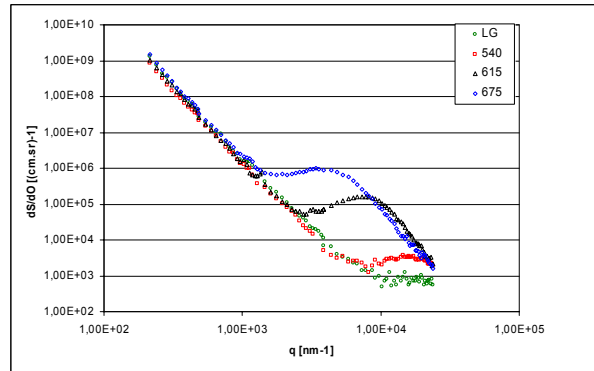
Fig. 2: Sum of nuclear and magnetic scattering of the alloy S903. The effect of different heat treatments is shown.

Achievements and Main Results

The shape of the K011 curves is in good agreement with earlier measurements using unpolarized neutrons of Bischof et al. [2]. All samples contain large primary carbides, the heat treated sample (I-1000) shows additional scattering due to small secondary carbides. Quenching in liquid nitrogen leads to slight changes in the small-*q* range.

Heat treatments after homogenization of S903 lead to precipitation of an intermetallic phase (Fig. 2). The curves exhibit a pronounced maximum due to interparticle interference. Larger structures are also present in the samples, but they do not change during the heat treatments. The shift of the maximum to lower *q* values indicates coarsening of the precipitates.

The data had been collected for checking the potential benefits of polarized neutrons for the analysis of steel; however, data analysis is not yet completed. Possible advantages of the use of polarized neutrons for SANS from steel have to be discussed in detail. In addition, a

quantitative analysis of precipitates has to be made. Also, the effect of spin-misalignment has to be quantified.

Further investigations with SANS are going to be performed on additional samples of S903 to cover a wider range of heat treatment conditions. Additionally, in-situ experiments with SANS or SAXS are planned to thoroughly study the precipitation and decomposition behaviour of the alloy.

References
[1] M. Bischof, P. Staron, A. Michels, P. Granitzer, K. Rumpf, H. Leitner, C. Scheu, H. Clemens, "The influence of spin-misalignment scattering on the SANS data evaluation of martensitic age-hardening steels", Acta Mat., accepted.

[2] M. Bischof, S. Erlach, P. Staron, H. Leitner, C. Scheu, and H. Clemens, "Combining Complementary Techniques to study Precipitates in Steels", Z. Metallkd.,96, No. 9, 1074-1080 (2005).

Characterisation of coherent Cu precipitates in Fe-Cu model alloys		
Principal Proposer:	**M. Parlog**[1]	
Co-Proposer:	[1]Fraunhofer-Institut für zersörungsfreie Prüfverfahren, IZFP **P. K. Pranzas**[2] [2]GKSS Research Centre	
Experimental Team:	**M. Parlog**[1]**, P. K. Pranzas**[2]	
User Group Leader:	**P. K. Pranzas**[2]	
Dates of Experiment:	April 2006, Sept 2006	

Objectives

The precipitation hardening of binary Fe-Cu and ternary Fe-Cu-Ni alloys by thermal aging at 500 °C was investigated by using Small Angle Neutron Scattering (SANS). Cu precipitates are coherent with the Fe matrix if they are smaller than 5 nm. In this size range all Cu particles are spherical. SANS is an ideal tool to investigate structures in the nanometer sizw range. The aim of the present experiment was the determination of size, coherency, number density and volume fraction of coherent Cu precipitates in Fe-Cu alloys.

Experiment

For the present study Fe-Cu samples with Cu content between 0.3 and 1.7 wt.% were manufactured. In order to get Fe-Cu alloys containing small and coherent copper precipitates, the specimens were solution treated at 850 °C for 2 hours, quenched into water and in two steps thermally aged at 500 °C under the following conditions:

Table 1: Thermal ageing time for producing coherent Cu particles

wt.% Cu	0.3	0.65	1.0	1.4	1.7
1 thermal ageing stage [h]	25	12	3.5	2.17	0.83
2 thermal ageing stage [h]	35	14	6.5	3.5	1.17

Both Fe-Cu-Ni samples were thermal aged as long as the Fe-0.65wt.% Cu sample.

SANS measurements were carried out with the instrument SANS-2 at the Geesthacht Neutron Facility (GeNF) by using selector-monochromated neutrons with a mean wavelength of λ = 0.58 nm and a wavelength spread of $\Delta\lambda/\lambda$ = 10%. The samples were magnetized to saturation in a field of 2 T. Four detector distances (1 m, 3 m, 9 m, 21 m) were used together with appropriate collimation to cover scattering vectors of magnitude q from 0.02 nm^{-1} to 2.5 nm^{-1}.

Achievements and Main Results

SANS measurements showed that after the first thermal ageing stage the Fe-Cu and Fe-Cu-Ni samples contain Cu precipitates with a mean radius of 0.7-1.2 nm and after the second stage of the thermal ageing Cu precipitates with a mean radius of 1.2-1.6. In this size range all Cu precipitates are spherical and coherent with the α-Fe matrix.

Fig. 1 shows that the Cu particles number density increases with rising Cu content. It can be also observed that between the first and second thermal ageing the Cu particles number density tends to decrease.
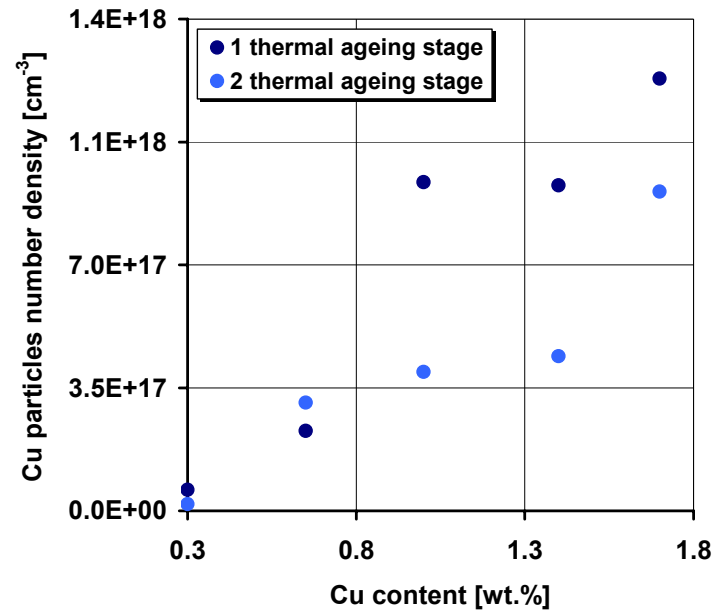
Fig. 1: Number density of Cu precipitates in Fe-Cu alloys assuming spherical precipitates.

Fig. 2 shows that also the volume fraction of coherent Cu particles increases with growing Cu content. This behaviour is caused by an increasing possibility of nucleation with rising Cu content, because the diffusion ways, which have to be crossed by the Cu atoms for Cu precipitates' nucleation, are shorter. Between the first and the second thermal ageing stages the Cu particles volume fraction for all samples increases.
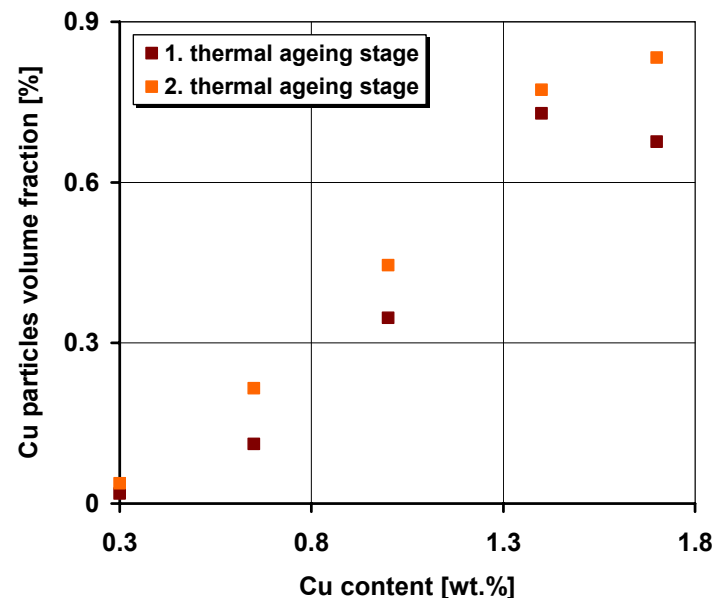
Fig. 2: Volume fraction of Cu precipitates in Fe-Cu assuming spherical particles.

In case of the Fe-Cu-Ni samples it was observed that the cu particles number density decreases with increasing Ni content. The increase of the thermal ageing time yielded also in that case to a decrease of the Cu particles number density.

The second stage of the thermal ageing corresponds to hardness value near to the maximum hardening. That study showed that even in the vicinity of the maximum hardening the Cu particles are still coherent.

![GKSS FORSCHUNGSZENTRUM in der HELMHOLTZ-GEMEINSCHAFT]	**EXPERIMENTAL REPORT**	**GeNF SANS-2**

Magnetic Structure and Anisotropy of Nanocrystalline Terbium		
Proposer:	**Balaji Gopalan[1]**	
	[1]Institute for Nanotechnology, Forschungszentrum Karlsruhe	
Co-Proposers:	**Jörg Weißmüller[1,2], Andreas Michels[2], P. Klaus Pranzas[3]** [2]Fachrichtung Technische Physik, Universität des Saarlandes [3]GKSS Forschungszentrum, Geesthacht	
Experimental Team:	**Balaji Gopalan[1], Jörg Weißmüller[1,2], Frank Döbrich[2], Helmut Eckerlebe[3]**	
User Group Leader:	**Jörg Weißmüller[1,2]**	
Date(s) of Experiment:	July 2006	

Objectives:

In nanocrystalline ferromagnets the alignment of the magnetic moment along the crystallographic easy axes is highly non-uniform due to grain boundaries [1]. Such microstructure greatly influence its macroscopic properties. In that light, it is of importance and interest to study the magnetic microstructure and anisotropy of nanocrystalline terbium (Tb) by magnetic small-angle neutron scattering (SANS), a technique that has the potential to resolve the magnetic microstructure in the bulk and in the nanoscale regime [1].

The interesting feature is the high magnetocrystalline anisotropy of Tb which force the magnitude of magnetization vector to be different along a and c axis even in the paramagnetic regime. Also in a polycrystalline Tb, it can be expected a misalignment between the magnetic moments by two ways: inter and intra grains. We aim to investigate the misaligned spin structure in nanocrystalline material in magnetic saturation and the magnitude of the magnetic anisotropy both in ferromagnetic and in the paramagnetic regime. The extremely high anisotropy of ferromagnetic Tb is reflected in a strongly anisotropic susceptibility tensor in paramagnetic Tb. The hypothesis was that SANS can detect this, since the material (at $T > T_C$ = 218 K) reacts to a magnetic field H by developing a magnetization which varies from grain to grain, according to the local orientation of the main axis of the susceptibility tensor.

Experiment:

These are nanocrystalline (fully dense polycrystalline metal with grain size in the nm-regime, prepared by in-situ consolidation of nanoparticles in UHV) disks 8 mm diameter, 0.3 mm thick. Three samples with 25 nm, 50 nm, and coarse grained (>>100nm) grain sizes were investigated at different applied fields and temperatures. Unpolarized neutrons with a wavelength of 0.6 nm at the GKSS SANS-2 machine and a cryomagnet with the field perpendicular to the beam was used in our experiments

Achievements and Main Results:

Figures 1-3 show the field-dependent SANS measured at T = 260 K for 25, 50 and D >> 100 nm samples respectively (the corresponding parameters are mentioned inside the figures). Obviously, the data bear out the expectation, SANS signal increases with increasing H. Figure 1 also shows a naive fit (the solid lines), using

$$d\Sigma/d\Omega(q_i, H_j) = d\Sigma/d\Omega|_{nuc}(q_i) + S_{mag}(q_i) M^2(H_j)$$

89

with the nuclear scattering, $d\Sigma/d\Omega|_{nuc}$ (due to, typically, residual porosity in the samples) and the magnetic scattering function, S_{mag}, at each q fit parameters, and with $M(H)$ measured by magnetometry. At low q, the scattering increases with the applied field, presumably due to static (in coarse grained material) structure in the spin system which is promoted by the field. It is seen that the grain size dependence looks right, smaller field-induced magnetic structures at smaller grain size, practically no response in a coarse-grained material. At high q, the scattering is suppressed by application of a magnetic field, and we tend to attribute it to dynamic fluctuations. This results in a crossover of the field dependent scattering curves. Interestingly, this cross-over is found irrespective of T, down to $T = 5$ K in the ferromagnetic regime (Figure 4), it shifts to lesser q as T decreases. A detailed experiments performed over a range of temperatures and fields for all the samples covering higher q values will throw light on the magnetic behaviour of these systems.
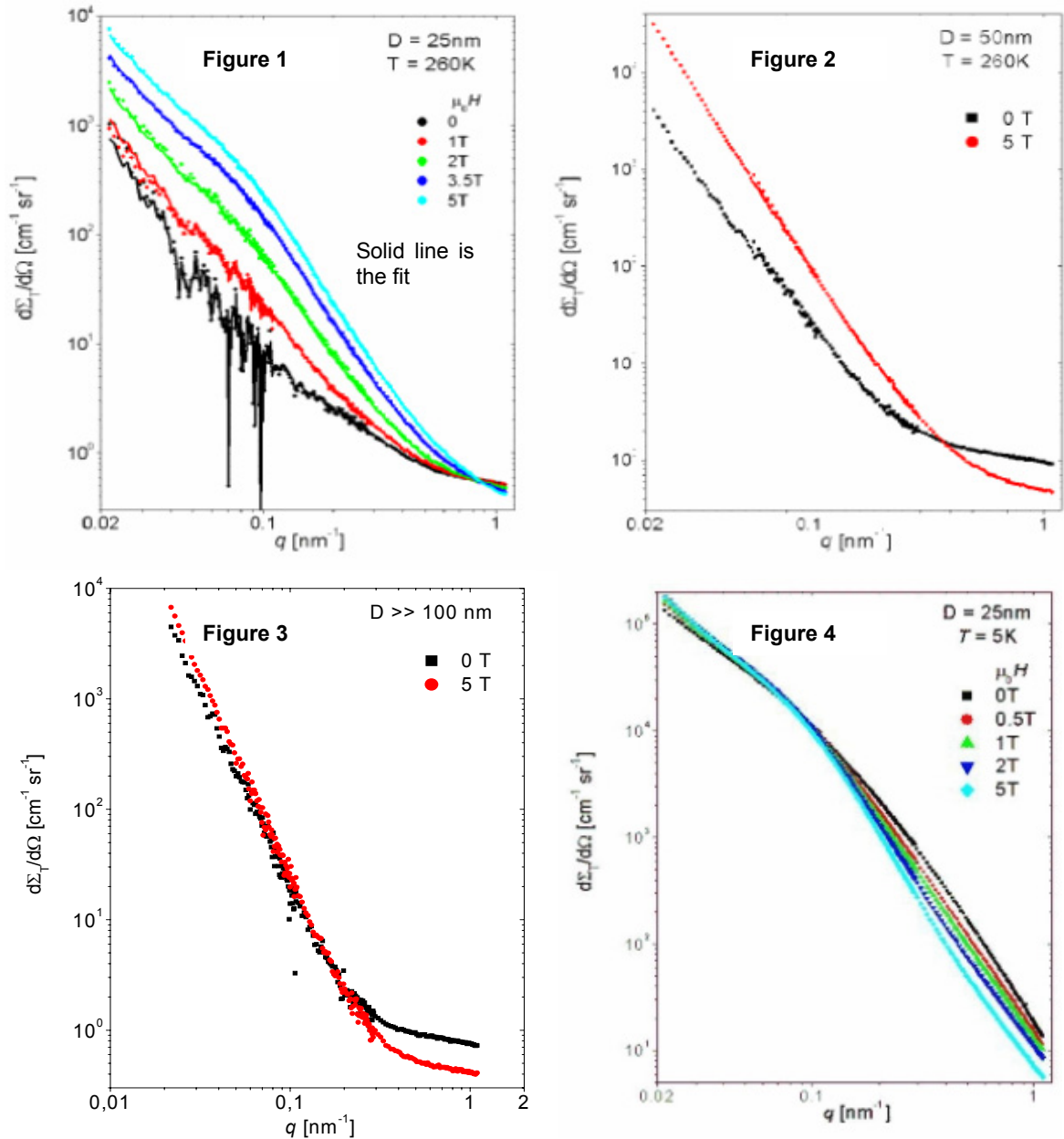
References

[1] J. Weissmüller, A. Michels, J. G. Barker, A. Wiedenmann, U. Erb, and R. D. Shull, Phys. Rev. B **63**, (2001) 214414.

Characterization of precipitates in laser beam welded Al sheets

Proposer: **Co-Proposers:**	**P. Staron, W.V. Vaidya** [1]GKSS
Experimental Team:	**P. Staron**[1]
User Group Leader:	
Date(s) of Experiment:	12th–17th May 2006

Objectives

The heat treatable Al alloy AA6056 is being considered as one of the candidate alloys for laser beam welded airframes [1]. The alloy contains Mg and Si to form, e.g., Mg_2Si precipitates. Precipitate size distributions in different regions of a laser beam weld that have experienced different temperatures during welding were studied for different starting materials. In addition, changes due to post-weld heat treatments were studied.

Experiment

Al sheets with thicknesses of 3.2 mm and 6 mm and a size of 200 mm × 300 mm with a laser beam weld were used. Sheets with initial temper T4 and T6, and sheets with additional post-weld heat treatments T6 and T78 were measured. The fusion zones were approximately 2 mm wide, thus, a slit of size 2 mm × 10 mm was used with the long edge parallel to the weld. Measurements in the fusion zone and in the base material were done. The slit width was reduced to 1 mm for one scan across the weld with higher resolution. The wavelength was 5.7 Å. Four detector distances and corresponding collimations were used to cover a q-range from 0.03 to 3 nm^{-1}. Detector images were azimuthally averaged.
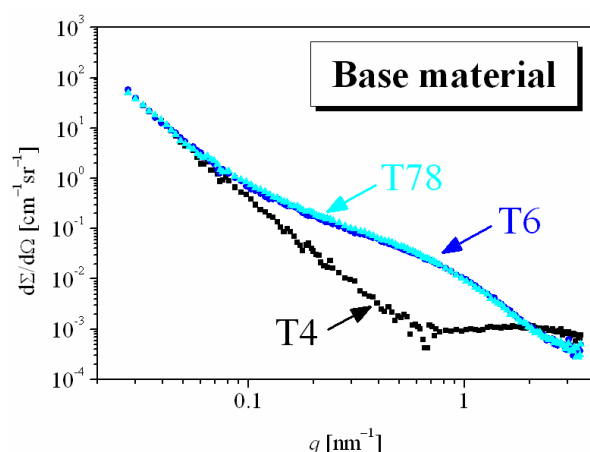
Fig. 1: Scattering curves for different tempers T4, T6, and T78.
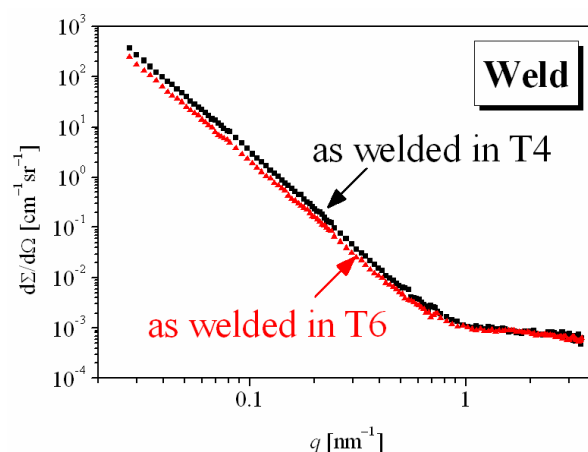
Fig. 2: Scattering curves for weld material for different starting conditions (T4, T6).
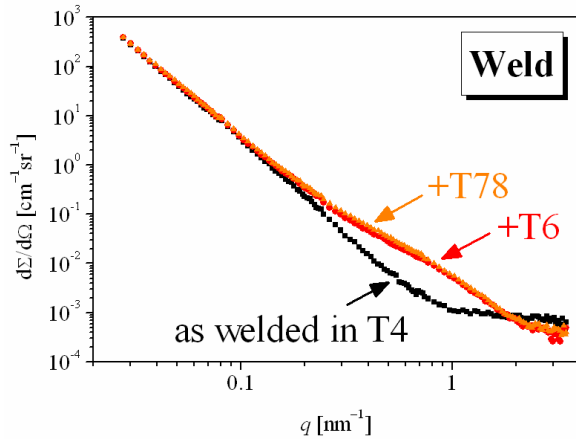
Fig. 3: Scattering curves for the weld for different post-weld heat treatments, T6 and T78.
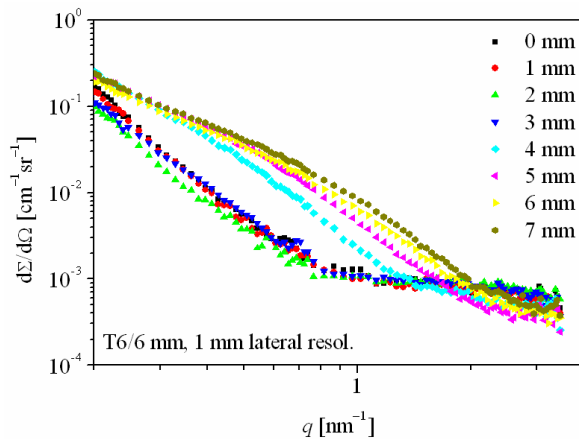
Fig. 4: Scattering curves as a function of the distance from the weld.
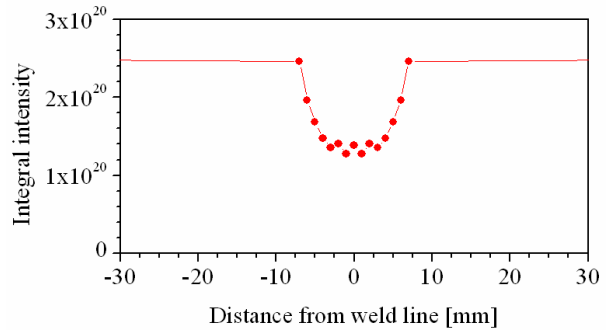
Fig. 5: Integral intensity of the scattering curves shown in Fig. 5 (symmetry assumed).

Achievements and Main Results

A comparison of the different base materials (T4, T6, and T78) shows the general influence of the different heat treatments (Fig. 1). The material with the solution treatment T4 contains no precipitates while the peak-hardness treatment T6 produces precipitates in the nanometre size range. The overaging treatment T78 does not change the precipitate distribution much. In the weld, however, the situation after welding is nearly the same for both starting tempers T4 and T6 (Fig. 2). The post-weld heat treatments T6 and T78 lead to a recovery of precipitates in the weld (Fig. 3), although a comparison with Fig. 1 shows that either the volume fraction or the chemical composition or both of them are different. SANS with a spatial resolution of 1 mm is possible as Fig. 4 shows. From the integral intensity of these curves the width of the heat affected zone can be determined (Fig. 5).

References

[1]   K.-H. Rendigs, Mater. Sci. Forum 242 (1997) 11-24.

GKSS FORSCHUNGSZENTRUM in der HELMHOLTZ-GEMEINSCHAFT	EXPERIMENTAL REPORT	GeNF SANS-2

Characterization of CP-Ti Processed by Equal Channel Angular Process using SANS		
Proposer:	**R. Lapovok[1], D.Tomus[1]**	
	[1]Materials Engineering Department, Monash University, Australia	
Co-Proposers:	**Y. Estrin[2], T. Lowe[3]**	
	[2]Institut fur Werkstoffkunde und Werkstofftechnik, TU Clausthal, Germany, [3]Los Alamos National Laboratory, USA	
Experimental Team:	**D.Tomus[1], K. Pranzas[4]**	
	[4] GKSS Research Centre	
User Group Leader:	**D.Tomus[1]**	
Date(s) of Experiment:	August 2006	

Objectives

Equal Channels Angle Process (ECAP) was employed to severe plastic deform Ti-commercial pure (CP). The nucleation of voids by ECAP is a controversial issue as was revealed by some authors using TEM and SEM techniques. These techniques are destructive methods and provide information only on the small areas. In order to obtain a general view about the microstructure, the size and the distribution of the voids possible induced during the ECAP, the SANS method was employed.

Experiment

Small-Angle Neutron Scattering (SANS) allows the characterization of the structure with size between 1 and 100 nm. A monochromator with 22000 rpm was used and correspond to a wavelength of 0.58 nm. The neutron beam had 7 mm diameter. The specimens used for SANS measurements had cylindrical shape with 10 mm diameter. The ECAP parameters employed to process the samples are listed in Table 1. The ECAP experiments were made at 350°C and various back pressure were employed.

Table 1. Characteristics of ECAP samples

Sample	Main Pressure (MPa)	Back Pressure (MPa)	Passes	Route
As-received (no ECAP)	-	-	-	-
15-0-1p	1800	-	1	-
15-0-4p-RA	1800	-	4	RA
15-0-4p-RB	1800	-	4	RB
15-4000-4p-RA	1800	175	4	RA
15-4000-4p-RB	1800	175	4	RB

In addition, the as-received samples and 15-0-4p-RB were measured at the centre and the edge using 3mm aperture size of the neutron beam.

Achievements and Main Results

In the range of 5-20 nm the volume fraction scattering structure evolve from 4.1×10^{-6} to 6.8×10^{-6} cm^{-1} as shown in Fig. 1(a). It has to be mentioned that this scattering structure is

present in all samples (as-received, ECAP one pass and 4 passes). In the range of 20 – 400 nm the as-received samples exhibit larger volume fraction of scattering structure of 3 x 10^{-6} cm^{-1} and this value decrease due to ECAP process to 1.2 x 10-6 cm^{-1}, trend that suggested that the scattering structure was refined. The number distribution of the scatter structure is plotted in Fig. 1 (b). It can be observed that the maximum density of particles of 6.3 x 10^{12} correspond to a range size of 5-20 nm for all the samples regardless the ECAP process parameters.
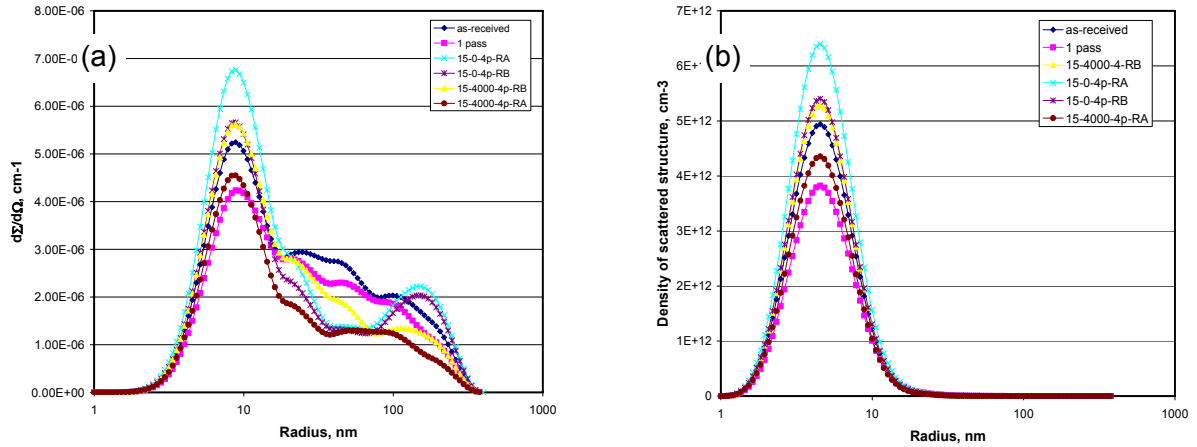
Fig. 1: Volume fractions and number density distribution of scattering structure assuming spherical particles.

The following measurements were focused on the microstructure changes across transversal section of the billet. Two samples were considered for these measurements. One samples was Ti-CP without ECAP and one with ECAP having MP=1800 MP, BP=0, 4 passes by route RB at 350 °C. The scattering pattern in the center of the sample is uniform whereas the scattering transform from circular shape into elliptical at the edge of the billet. Figure 2 shows the curves of each plot correspond to the measurement at the center and at 3.5 mm distance shifted to the edge. It can be seen in Fig. 2 (a) that the scattering structure with a radius of 10 nm exist in the almost the same amount in analyzed locations, center and edge. This demonstrates that at the edge of the billet the scattering structure change from spherical shape to elliptical one with radii of 10 and 45 nm. Figure 2 (b) shows that density of scattering structure with 4.5 nm is larger on the edge of the billet with 1.5 x 10^{12} cm^{-3}. Here a much larger density of scattering with elliptical shape of 5 x 10^{13} cm^{-3} than the scattering structure with the spherical shape of 5 x 10^{12} cm^{-3}. The microstructure along cross-section of the billet evolves from spherical shapes with 10 and 160 nm in the center to the elliptical shape with radii of 10 and 45 nm close to the edge.
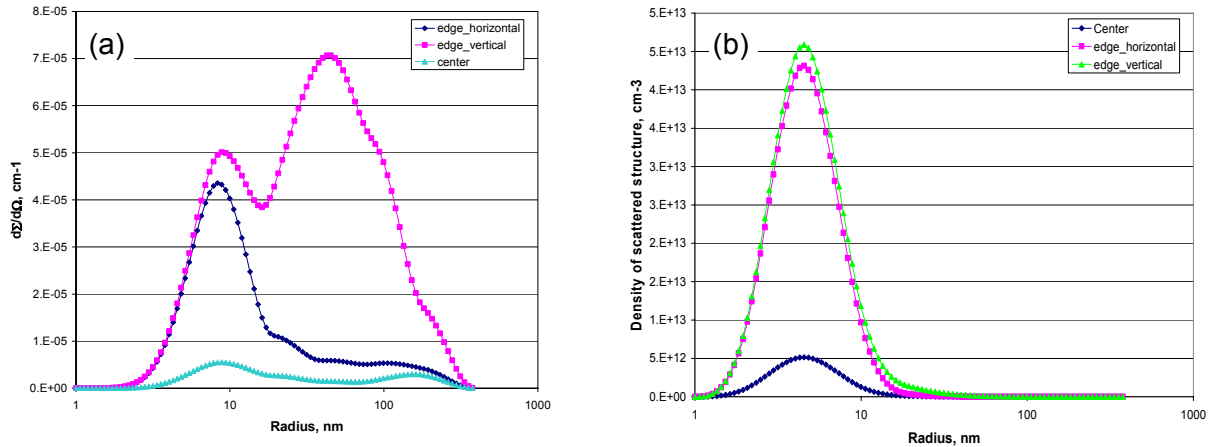
Fig.2: Size (a) and density (b) distribution of the scattering structure of Ti-CP processed by ECAP with no back pressure after 4 passes by route RB at center and the edge of the billet.

GKSS FORSCHUNGSZENTRUM in der HELMHOLTZ-GEMEINSCHAFT	**EXPERIMENTAL REPORT**		**GeNF SANS-2**
Precipitates in a carbon-doped TiAl alloy			
Proposer: Co-Proposers:	**R. Gerling, P. Staron,** GKSS		
Experimental Team:	**P. Staron**		
User Group Leader:			
Date(s) of Experiment:	3rd–4th April 2006		

Objectives

The influence of carbon additions on the microstructure and tensile properties of Nb containing γ-TiAl alloys was investigated. Carbon additions can produce strengthening precipitates in the nanometre size range, but it is not yet known if this also occurs in the Nb containing alloys currently under investigation. A strengthening effect of carbon additions is proven in these alloys, but it is still an open question if solution strengthening or particle strengthening (or a mixture of both) is the responsible mechanism. Similar measurements had been performed before in a γ-TiAl alloy without Nb [1].

Experiment

The two investigated alloys were Ti-45Al-5Nb without and with the addition of 0.5 at% C. Both alloys were studied in the as-rolled state and after a primary annealing treatment (Table 1). The samples were cut from rolled sheet with a thickness of 1.2 mm. The total material thickness in the beam was 2.4 mm. The size of the samples was 15 mm × 15 mm, the cross section of the beam was 9 mm. The wavelength was 5.7 Å. Four detector distances were used to cover a q-range from 0.02 to 2.5 nm^{-1}. Carbon containing perovskite particles are expected to form in the carbon doped samples.

Table 1: List of samples.

Sample	Alloy	Description
WH2	Ti-45Al-5Nb	as rolled
PA2	Ti-45Al-5Nb	primary annealed, 2 h/1050 °C
WH4	Ti-45Al-5Nb-0.5C	as rolled
PA4	Ti-45Al-5Nb-0.5C	primary annealed, 2 h/1050 °C

Figure 1 shows the azimuthally averaged scattering cross section of all four samples. In the as-rolled state both samples exhibit strong small-angle scattering in the observed q-range, while after the annealing treatment this small-angle scattering contribution is largely reduced. On the other hand, the intensity at very small q-values increased by a factor of 5 after annealing. A possible explanation for this behaviour could be particle coarsening.

The SANS signal of the carbon doped sample after annealing (PA4) is only slightly higher than that of the sample without carbon addition (PA2) for 0.05 nm^{-1} < q < 0.5 nm^{-1}. This can either be due to a small difference in scattering length density between matrix and precipitate or to a small precipitate volume fraction.
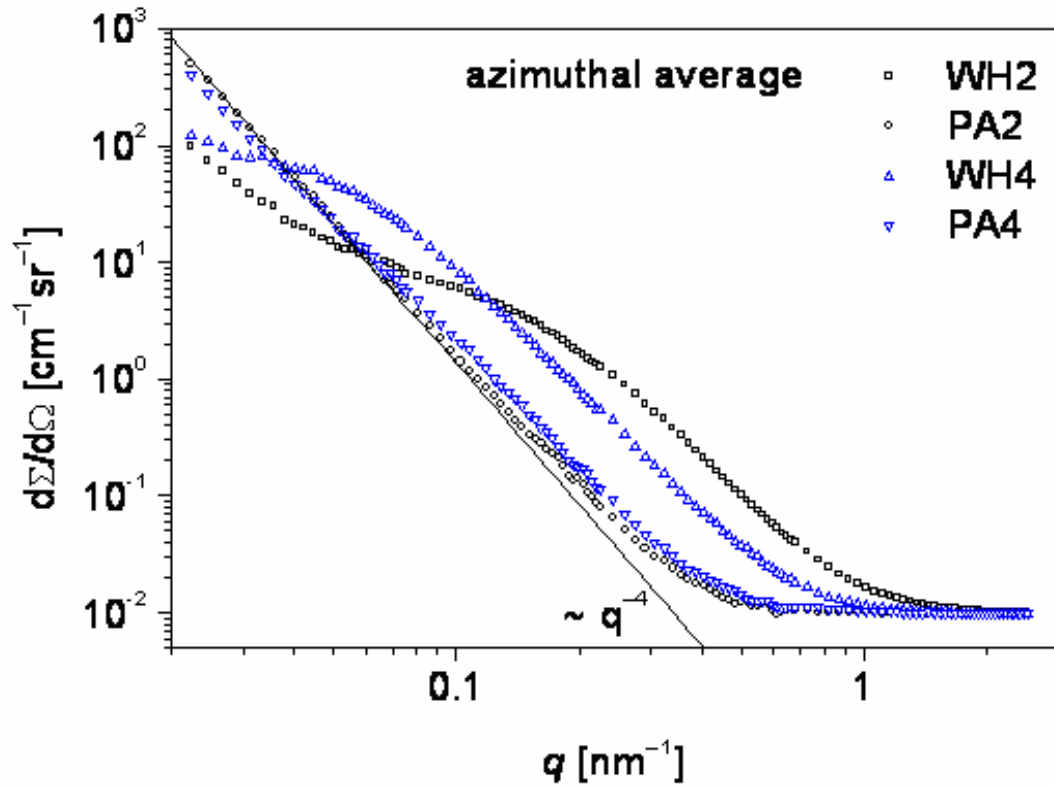
Fig. 1: Azimuthally averaged SANS scattering curves of the four samples.

Achievements and Main Results

In both alloys – with and without carbon addition – there seem to be particles present in the as-rolled state that coarsen during the subsequent annealing treatment at 1050 °C. Therefore, it is not clear whether the relatively small difference in the SANS intensity between the two alloys in the annealed state is due to small carbon containing precipitates. In a next step transmission electron microscopy investigations will be carried out using the samples PA2 and PA4 in order to detect carbon containing precipitates. If this is the case, dimension and shape data can be used for a further evaluation of the SANS data.

References
[1]   P. Staron, U. Christoph, F. Appel, H. Clemens, Appl. Phys. A 74 (2002) S1163–S1165.

![GKSS FORSCHUNGSZENTRUM in der HELMHOLTZ-GEMEINSCHAFT]	**EXPERIMENTAL REPORT**	**GeNF SANS-2**

The study of topology and fractal properties of Zr, Zn, Ce and Fe-based xerogels by SANS		
Proposer: **Co-Proposers:**	**S.V. Grigoriev[1]**, [1]Petersburg Nuclear Physics Institute, Gatchina, 188300 Russia **G.P. Kopitsa[1]**, **V.K. Ivanov[2]**, [2]Institute of General and Inorganic Chemistry, Moscow, 199991 Russia	
Experimental Team: **User Group Leader:**	**G.P. Kopitsa[1]**, **V.K. Ivanov[2]** **P. Klaus Pranzas[3]**, [3] GKSS Forschungszentrum **S.V. Grigoriev[1]**	
Date(s) of Experiment:	24th September–2nd October 2006	

Objectives

The goal of this proposal is to study the peculiarities of fractal nanostructures, formation during synthesis of Zr, Zn, Ce and Fe-based xerogels by use of soft chemistry methods, and its evolution at different stages of synthesis by means of small-angle neutron scattering (SANS).

Recent studies of the structural organization of nanosystems (in particular, colloid systems) have shown that many of them possess surface or volume fractal properties, i.e. self-similarity of structural elements [1,2]. It was also established is that fractal parameters, namely fractal dimension and self-similarity range, may determine physical and chemical properties of the nanomaterials, including reactivity, catalytic activity, sorption capacity etc. [1-3].

Thus, formation of fractal structures during aggregation of nanoparticles in colloid solutions is a very common phenomenon. Numerous examples indicate that variation of conditions of synthesis permits to affect the mechanism of aggregation thus allowing to obtain colloids with given fractal dimension [2]. Unfortunately, information on the further change of fractal properties of colloid particles upon removal of solvent and formation of nanostructured solid state products is quite poor. Most of the papers devoted to this problem deals with study of fractal properties of supercritically-dried silica aerogels and, in some cases, several other aerogels and cryogels [4-6], while fractal characteristics of xerogels were investigated only in a few works [7]. On the other hand, results of our preliminary experiments [8] indicate that fractal properties seems to be quite a common feature of xerogels. Because of this, the study of the subatomic structure of xerogels at various stages of the synthesis and the determination of conditions of fractal structures formation are important from both a basic and application-oriented standpoints. It is nessesary to emphasize that most reliable data on fractal characteristics of solids can be obtained by small angle scattering of light, X-rays and neutrons [9].

Experiment

1. Sample

Five series of the samples of Zr, Zn, Ce and Fe-based xerogels, prepared by sol-gel method, and its evolution at different stages of synthesis were studied. The samples were kept in quartz cells with a path length of 1 mm.

2. Small-angle neutron scattering.

The SAPNS experiment was performed at the SANS-2 scattering facility of FRG-1 research reactor in Geesthacht (Germany), which operates in near point geometry using neutrons with

the wavelengths $\lambda = 5.8$ and 11.6 Å ($\Delta\lambda/\lambda$=0.1). The range of momentum transfer $8\cdot10^{-4} < q < 2.4\cdot10^{-1}$ Å^{-1} was obtained using four sample-to-detector distances (1, 3, 9 and 21.7 m). The scattered neutrons were detected by a position sensitive detector with 256x256 pixels. The measured data were calibrated by the incoherent scattering of vanadium and corrected for the sample transmission, background scattering (from the quartz cell) and detector response. The resulted data were processed by the software of SANDRA.

Achievements and Main Results

The momentum dependences of the SANS cross section $d\Sigma(q)/d\Omega$ measured for the samples of the amorphous xerogel ZrO_2 with different acidity *pH* of medium are shown in Fig. 1 on the log-log scale. As is seen in this figure for all sample, the $d\Sigma(q)/d\Omega$ behave as q^{-n} at $q <$
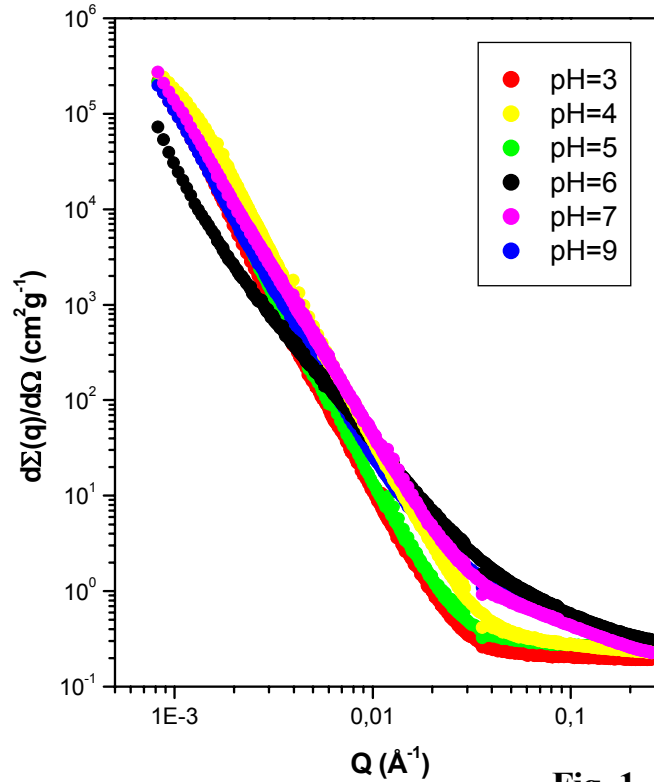
Fig. 1.

$q \approx 0.025$ Å^{-1}. It was found that the exponent *n* is close to 4 for the samples with *pH* = 3, 4 and 5 and equal to 3.6 and 3.4 for the samples with *pH* = 7 and 9, respectively. It means that in these amorphous xerogels the transition from porous structure with practically smooth interface ($D_S \approx 2$) to the surface fractal with D_S = 2.3 и 2.6 is observed with the increase *pH* of medium. It verify results obtained in our early work [10] for the amorphous ZrO_2 xerogels with *pH* =2.95, 7.09 and 9.05. However, in the case of the sample with *pH* = 6 the exponent *n* was equal to 2.6. It correspond to the scattering on the volume fractal with the dimension D_V = 2.6. The reason of it remains undecided now.

The momentum dependences of the SANS cross section $d\Sigma(q)/d\Omega$ measured for series of the CeO_2 xerogels with different annealing temperatures T_a are shown in Fig. 2 on the log-log scale. As is clearly seen in this figure, the increase of the cross sections occurs with the increasing of the annealing temperature T_a. It correspond to the behavior of the attenuation of the incident neutron beam $I(q=0)/I_0$, which decreases with the increasing of T_a and is inversely proportional to integral scattering cross section. It indicates that the fluctuations of the
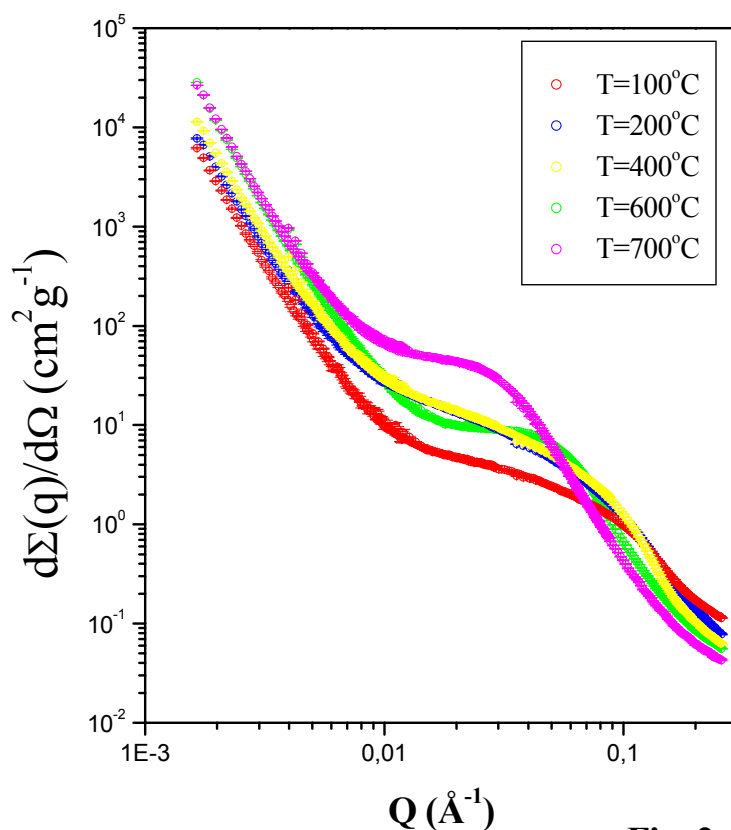
Fig. 2.

nuclear density in the xerogel CeO_2 increase with the increasing of T_a. At once this increase is visibly uneven and depend on the annealing temperature T_a.

The treatment of the data for samples of Zn and Fe-based xerogels and interpretation of all obtained data are in progress.

References

[1]   A. Harrison. Fractals in chemistry. Oxford University Press, 1995. 90 p.
[2]   W.G. Rothschild. Fractals in Chemistry. Wiley-Interscience, 1998, 231 p.
[3]   Fractals in Physics. Ed. by L. Pietronero and E.Tosatti. Elsevier B.V., 1986. p. 638.
[4]   D. R. Vollet, D. A. Donatti, A. Ibañez Ruiz, W. C. de Castro // J. Non-Cryst. Solids. 2003. V. 332. p. 73-79.
[5]   A.A.Vertegel, S.V. Kalinin, N.N. Oleynikov, Yu.D. Tretyakov // J. Non-Cryst. Solids. 1995. V. 181. p. 146-150.
[6]   R.F. Reidy, A.J. Allen, S. Krueger // J. Non-Cryst. Solids. 2001. V. 285. P. 181-186.
[7]   W.L. Huang, S.H. Cui, K.M. Liang et al // J. Phys. Chem. Solids. 2002. V. 63. p. 645-650.
[8]   O.S. Polezhaeva, V.K. Ivanov, was presented at Topical Meeting of the European Ceramic Society, June 27 –29, 2006, Saint-Petersburg, Russia.
[9]   P.W. Schmidt (1995). *Modern Aspects of Small-Angle Scattering*, edited by H. Brumberger, Netherlands: Kluwer Academic Publisher. pp. 1 -56.
[10] G.P. Kopitsa, V.K. Ivanov, S.V. Grigoriev, P.E. Meskin, O.S. Polezhaeva and V.M. Haramus // JETP Letters. 2007. V.85(2), p. 132.

Investigation of the magnetic structure in $Fe_{1-x}Co_xSi$

Proposer:	**Sergey Grigoriev[1]**, [1]PNPI, Gatchina, St-Petersburg, RUSSIA
Co-Proposers:	**Dirk Menzel[2]**, [2]Technische Universität Braunschweig, Germany **Alexey Okorokov[1]**, **Vadim Dyadkin[1]**
Experimental Team:	**Sergey Grigoriev[1]**, **Vadim Dyadkin[1]** **Helmut Eckerlebe[3]**, [3]GKSS Forschungszentrum, Geesthacht
User Group Leader:	**Sergey Grigoriev[1]**
Date(s) of Experiment:	November 2006

Objectives

The cubic B20-type of mixed crystal $Fe_{1-x}Co_xSi$ orders below T_C in a one-handed spin helical structure with a small propagation vector $k < 0.025$ Å^{-1} [1-4]. At present it is widely recognized that in analogy to the magnetic structure of MnSi [5,6] and FeGe [7], the helicity is induced by an antisymmetric Dzyaloshinskii-Moriya (DM) exchange interaction caused by the lack of a centre of symmetry in the arrangement of magnetic atoms Fe and Co [8,9,10]. The AE interaction and cubic anisotropy are extremaly weak in these compounds $Fe_{1-x}Co_xSi$ and the spiral wavevector k is almost randomly oriented. Its direction can be changed by an applied magnetic field. The SANS experiments are aimed to study the spin structure of $Fe_{1-x}Co_xSi$ under applied field at $T < T_C$.

Experiment

1. Sample
The single crystals $Fe_{1-x}Co_xSi$ were chosen for the study with $x = 0.1, 0.15, 0.2, 0.5$ (at%). The samples were discs with a thickness of 1 mm and a diameter of 10 mm.

2. Small-angle neutron scattering
Small-angle neutron scattering (SANS) measurements are carried out with the instrument SANS-2 at the Geesthacht Neutron Facility (GeNF). Neutrons with a mean wavelength of $\lambda = 0.58$ nm and a wavelength spread of $\Delta\lambda/\lambda = 10\%$ were used. Sample - Detector distances of 10 m (for $x = 0.1, 0.15$), 8 m (for $x = 0.2$), 16 m (for $x = 0.5$) were used with appropriate collimations to cover scattering vectors q from 0.06 nm^{-1} to 0.6 nm^{-1} ($q = 4\pi/\lambda \cdot sin(\theta/2)$ where 2θ is the scattering angle). The scattering intensity is measured in the following way: (i) zero field cooling from the paramagnetic state to the temperature of interest; (ii) uprising field from $H = 0$ to the field value of interest; (iii) descending field from H_{max} to $H = 0$. Using these principles the Bragg peak intensity was studied at different values of the x concentration of Co and at different values of magnetic field and temperatures.

Achievements and Main Results
Figure 1 shows maps of the SANS intensities for four different samples $Fe_{1-x}Co_xSi$ and $x = 0.10$ (a) , $x = 0.15$ (b), $x = 0.20$ (c), and $x = 0.50$ (d) at $T \approx 9$ K. A weak magnetic field of $H \sim 1$ mT was applied horizontally in the plane of the

detector. It is clearly seen from Fig.1a that in $Fe_{0.90}Co_{0.10}Si$ the spiral wavevector **k** is oriented along the axis [1 0 0], which is 25 deg inclined to the field direction. In $Fe_{0.85}Co_{0.15}Si$ (Fig.1b) the spiral wavevector **k** is oriented along the [1 0 0] and [0 1 0] axes, which are inclined at 35 deg and 55 deg to the field direction, respectively. The Bragg peaks are, however, strongly smeared, having a clear tendency to form a ring of a radius |**k**|. In $Fe_{0.80}Co_{0.20}Si$ (Fig.4c) the spiral wavevector **k** is almost randomly oriented and the scattering looks like a ring of the intensity. In $Fe_{0.50}Co_{0.50}Si$ (Fig.4d) the spiral wavevector **k** is oriented along the weak field of 1 mT and the scattering intensity is concentrated into two Bragg spots with **k**||**H**. Thus a clear tendency in the spiral orientation is observed with increase of Co concentration. The anisotropic exchange and crystallographic anisotropy play a dominating role in the orientation of the spiral wavevector **k** for compounds with small concentrations of Co. For concentrations of $x \sim 0.1$ the substitution of Co does not break the preferable anisotropy axes <100>. The concentration increase of the substituted atoms up to $x \sim 0.2$ results in a local disorder and, therefore, lead to the random orientation of **k**. Further increase of the Co concentration results in full suppression of the anisotropy so that a weak magnetic field of 1 mT prevails at the anisotropic energy and orients **k** along the field for $x = 0.5$. Thus one concludes that the anisotropy is suppressed with the increase of Co concentration.

The typical magnetic field behavior of the spiral structure of these compounds is shown in Fig.2. As an example, the sample with $x = 0.2$ at $T = 10$ K has been chosen. When a weak magnetic field $H \leq 50$ mT is applied in an arbitrary direction, the randomly oriented spirals remain frozen in spite of the applied field. The scattering intensity is formed as a half of a ring on the map due to the fact that the polarized neutrons with P || H were used (Fig. 2a). When the field H
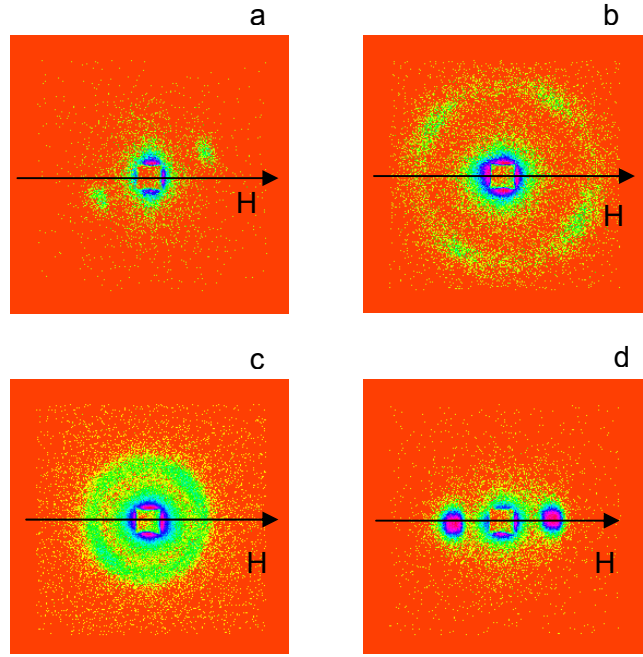
Fig.1: The concentration evolution of Bragg peaks. (a) $x = 0.1$; (b) $x = 0.15$; (c) $x = 0.2$; (d) $x = 0.5$
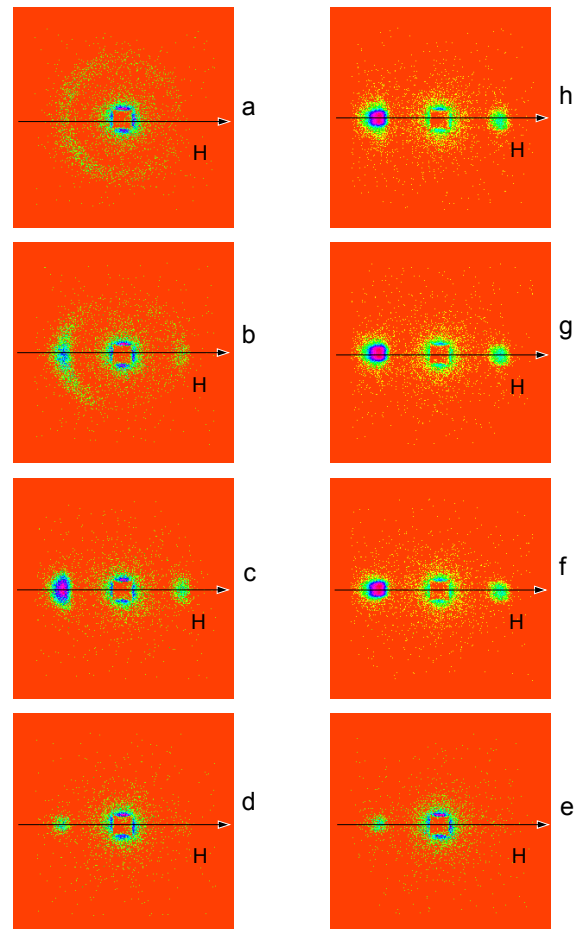
Fig.2: The scattering in the applied magnetic field. (a, h) $H = 1$ mT; (b, g) $H = 50$ mT; (c, f) $H = 100$ mT; (d, e) $H = 170$ mT.

increases above H_{c1} the randomly oriented domain structure transforms into the single domain sample. The ring of the intensity transforms into spots laying on the field axis (Fig. 5 b, c). With further increase of the field above H_{c2} = 175 mT the reflections along the field vanishes that is the helix transforms into the induced ferromagnet (Fig. 5 d). Upon decrease of the field H to zero value the sample remains a single domain showing a large hysteresis in the scattering intensity (Fig.2 e, f, g, h). Particularly, the ring does not appear at small magnetic fields.

The magnetic field dependence of the peak intensity at T = 10 and 35 K for $Fe_{0.80}Co_{0.20}Si$ are shown in Fig.3. The intensity is constant below the first critical field H_{C1}, then it shows maximum and decreases to zero at the second critical field H_{C2}. The deep minimum near H_{in} is observed close to T_c. It is attributed to the existence of a so-called A-phase. We believe that the spiral
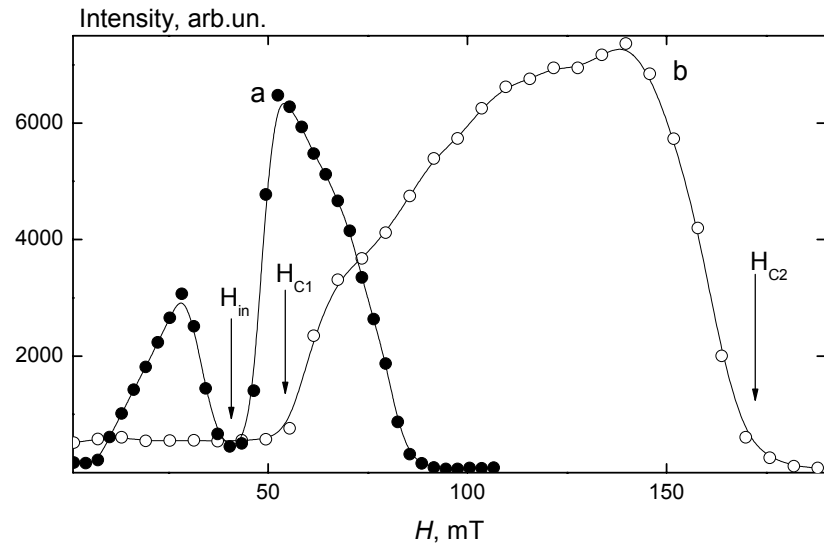
Fig.3: The magnetic field dependence of the peak intensity at T = 35 K (a) and T = 10 K (b).

magnetic domains reorient from $k \parallel H$ to $k \perp H$ and intensity (for $k \parallel H$) decreases almost to zero value. This effect is caused by presence of a gap in the spin wave spectrum. A detailed treatment of the data are required to make a conclusion about driving forces of the magnetic system of $Fe_{1-x}Co_xSi$.

References
[1]   J. Beille, J. Voiron, M. Roth, Solid State Commmun. **47** (1983) 399.
[2]   J. Beille, J. Voiron, F. Towfiq, M. Roth, Z.Y. Zhang, J.Phys.F: Met.Phys. **11** (1981) 2153.
[3]   K. Ishimoto, H. Yamaguchi, Y. Yamaguchi, J. Suzuki, M. Arai, M. Furusaka, Y. Endoh, J.Magn.Magn.Mat. **90&91** (1990) 163.
[4]   K. Ishimoto, Y. Yamaguchi, J. Suzuki, M. Arai, M. Furusaka, Y. Endoh, Physica B **213&214** (1995) 381.
[5]   Y. Ishikawa, K. Tajima, D. Bloch and M. Roth, Solid State Commmun. **19** (1976) 525.
[6]   Y. Ishikawa, G. Shirane, J.A. Tarvin, M. Kohgi, Phys. Rev. B **16** (1977) 4956.
[7]   B. Lebech, J. Bernhard, T. Freltoft, J. Phys. Condens. Matter **1**, 6105 (1989).
[8]   I.E. Dzyaloshinskii, Zh. Eksp. Teor. Fiz. **46** (1964) 1420.
[9]   P.Bak, M.H.Jensen, J.Phys. **C13**, L881 (1980).
[10] D. Nakamishi, A. Janase, A. Hasejawa, M. Kitaoka, Solid State Commun. **35** (1980) 995.

Proposer:	**Kirill Napolskii[1],**	
Co-Proposers:	**Natalia Grigoryeva[2],**	
	[1]MSU, Moscow, Russia, [2]SPSU, St-Petersburg, Russia	
Experimental Team:	**Natalia Grigoryeva[2], Kirill Napolskii[1],**	
	Helmut Eckerlebe[3],	
User Group Leader:	**Sergey V. Grigoriev[1]**	
	[3]GKSS Forschungszentrum, Geesthacht	
Date(s) of Experiment:	June 2006	

Objectives

Nanomaterials have attracted a great attention in the last decade because of their numerous applications in industry. Today, advanced technologies require preparation of nanosystems with specified size and morphology of particles. From a technological point of view, the special role in creation of the components for nano-technology belongs to high-quality nanostructures and nanocomposites with detached, strongly anisotropic, and regularly ordered nanoparticles. The aluminum oxide is considered to be a potential matrix for the preparation of such nanocomposites and, in particular, as a promising candidate for data storage devices. Here, not only the size control of individual nanoparticles is important, but also their mutual disposition in the mesostructure formed by the alumina template as well as their structural anisotropy provoking the strong anisotropy of the physical properties in the whole system. Our experiments were aimed to investigate the structural properties of the Anodic Aluminum Oxide (AAO) Al_2O_3 matrix. Electron microscopy and atomic force microscopy have been widely used to achieve direct imaging of the pores in the aluminum oxide matrix. However, these methods cover only local areas at the surface of sample, which may not be representative of the whole assemble. Our strategy, therefore, has been to carry out a detailed study of mesoporous alumina by means of small angle neutron scattering (SANS) technique.

Experiment

1. Samples. Anodic aluminum oxide membranes formed by two-step anodization technique or nanoimprint technology are well-known to possess uniform pore structure with hexagonal arrangement of cylindrical channels. High purity aluminum foil was annealed at 550°C in air in order to remove the mechanical stress and enhance the grain size in the metal. The anodization was carried out in two-electrode cell. After first anodization for 24 hours the alumina film was selectively etched away. After the second anodization and an oxidation during 50-100 hours oxide layers with a thickness between 90 and 180 µm were obtained. Enlargement of pores diameter was carried out by chemical etching of porous films in 0.3 M oxalic acid at 30°C for 2.5 and 5 hours. The obtained samples were denoted as AA_0h (as-prepared sample without pore widening), AA_2.5h, and AA_5h, respectively.

2. Small-angle neutron scattering. SANS measurements were carried out on the instrument SANS-2 at the Geesthacht Neutron Facility (GeNF). Neutrons with a wavelength of λ = 0.58 nm and a wavelength spread of $\Delta\lambda/\lambda$ = 10% were used. Detector-to-sample distances up to 17 m was set with the appropriate collimation to cover scattering vectors q from 0.03 nm^{-1} to 0.18 nm^{-1}. The samples of the total square of order of 0.5 cm^2 were homogeneously illuminated by the neutron beam. Samples were oriented that pores were directed parallel to the incident beam. In this case of the scattering from the structure with a large period, this geometry allows one to observe diffraction peaks in a range of small-angle

scattering, provided that the Bragg condition is fulfilled: 2d sin(θ_B/2) = λ, or q = 2π/d, where d is the interplane distance and θ_B is the scattering angle. Although the Bragg condition can only be fulfilled for one satellite, due to relatively large mosaic of the structure, the sample can be oriented such that many Bragg reflections are observed.

Achievements and Main Results.

A typical scattering pattern for such systems is shown in Fig.1. The 6-spots pattern of the first order reflections is observed. The second and third order reflections are also well visible. The positions of the reflections are identified using the formula for the regular two-dimensional hexagonal structure of nanopores oriented parallel to the incident neutron beam:

$$d_{hk0} = \frac{\sqrt{3}a}{2\sqrt{h^2 + hk + k^2}}.$$

The reflections are somewhat elongated demonstrating that the samples consists of the system of domains misoriented with respect to each other to the angle of order of 5 degrees. We suppose that a relatively large number of defects leads to this noticeable mosaic of the sample. Nevertheless, several orders of well-distinguished reflections observed in the experiment shows unambiguously a high degree of ordering over the whole sample with the square of order of 0.5 cm^2.

The q-dependence of the SANS intensity is shown in Fig.2 for AA_0h, AA_2.5h, and AA_5h matrices. The scattering intensity was radially averaged over the whole 2D pattern. It is seen that the scattering function is composed of the Bragg reflections and of the diffuse small-angle scattering. The analysis of the positions of the reflections gives the value of the interpore distance a $\approx$ 104 $\pm$ 3 nm. The diffuse small angle scattering stems, firstly, from the inhomogeneity of the form of individual pore and, secondly, from the imperfectness of the superstructure itself. This scattering increases with the chemical treatment: the wider the pore the bigger the diffuse scattering. On the other hand, this treatment does not change the position of the Bragg reflection (10) what makes clear that the matrix was not destroyed by the treatment. At the same time the width of the Bragg reflection (10) increases with the treatment. The quantitative analysis of the data is in progress.
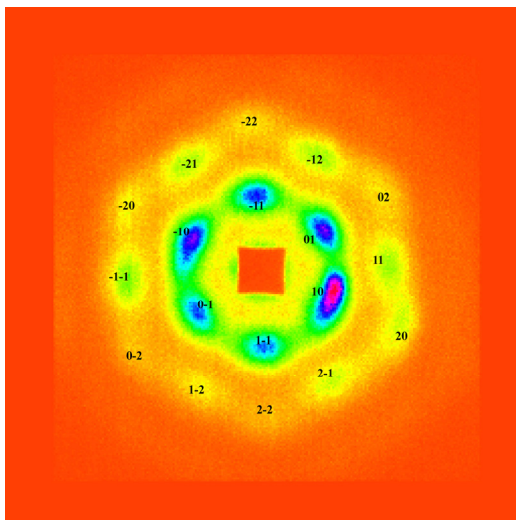
Fig.1: Typical scattering pattern of the anodic aluminum oxide membranes
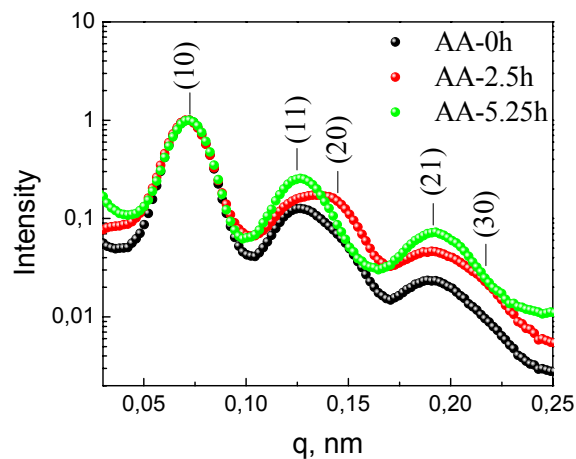
Fig.2: q-dependence of the SANS intensity for AA_0h, AA_2.5h, and AA_5h matrices

GKSS FORSCHUNGSZENTRUM in der HELMHOLTZ-GEMEINSCHAFT	**EXPERIMENTAL REPORT**	**GeNF SANS-2**

Polarized SANS study of the magnetic and temperature behaviour of nickel nanoparticles embedded into Al$_2$O$_3$ matrix		
Proposer: **Co-Proposers:**	**Sergey V. Grigoriev**[1], [1] PNPI, Gatchina, St-Petersburg, RUSSIA **Natalia A. Grigoryeva**[2], [2]SPSU, St-Petersburg, RUSSIA **Andrei A. Eliseyev**[3], [3]Moscow State University, Moscow, RUSSIA	
Experimental Team: **User Group Leader:**	**Natalia A. Grigoryeva**[2]**, P. Klaus Pranzas**[4]**, Helmut Eckerlebe**[4]**,** [4]GKSS Forschungszentrum, Geesthacht **Sergey V. Grigoriev**[1]	
Date(s) of Experiment:	June 2006	

Objectives

Nanomaterials have attracted a great attention in the last decade because of their numerous applications in industry. Today, advanced technologies require preparation of nanosystems with specified size and morphology of particles. At least for another period of ten years the main branch of industry of the information carriers will rely upon magnetic information storage. From a technological point of view, the special role in creation of the components for magnetic information storage belongs to high-quality nanostructures and nanocomposites with detached, strongly anisotropic, and regularly ordered magnetic nanoparticles. The aluminum oxide is considered to be a potential matrix for the preparation of magnetic nanocomposites and as a promising candidate for data storage devices. It has been estimated that a bit density several times greater than that currently possible could be achieved from this type of composite material. Here, not only the size control of individual nanoparticles is important, but also their mutual disposition in the mesostructure formed by the alumina template as well as their structural anisotropy provoking the magnetic anisotropy of the metal nanoparticles in the pores. At present we performed detailed SANS examination of anodic aluminum oxide (AAO) membranes with different pore diameters and AAO-based nickel nanocomposites. It should also be noted that in case of intercalation of magnetic materials inside the pores, neutron scattering brings us information on the magnetic properties of nanocomposites.

Experiment

1. Samples. Sample Anodic aluminum oxide membranes formed by two-step anodization technique or nanoimprint technology are well-known to possess uniform pore structure with hexagonal arrangement of cylindrical channels. High purity aluminum foil was annealed at 550°C in air in order to remove the mechanical stress and enhance the grain size in the metal. The anodization was carried out in two-electrode cell. After first anodization for 24 h alumina film was selectively etched away. After second anodization and oxidation times between 50 and 100 h oxide layers with thicknesses between 90 and 180 µm were obtained. Enlargement of pores diameter was carried out by chemical etching of porous films in 0.3 M oxalic acid at 303K for 2.5, 5 and 7 h. The obtained samples were denoted as AA_0h (as-prepared sample without pore widening), AA_2.5h, AA_5h and AA_7h.

Electrochemical experiments were carried out in three-electrode cell at room temperature. The counter electrode was a Pt wire and the reference electrode – saturated Ag/AgCl electrode connected to the cell via a Luggin capillary. The obtained nanocomposites of Ni/AAO were denoted as AA_th_Ni_l, where t – pore widening time in 0.3M (COOH)$_2$ at 303K; l – calculated length of Ni nanowires in micrometers.

Electron microscopy and atomic force microscopy have been widely used to achieve direct imaging of the nickel nanowires in the aluminum oxide matrix. But these methods cover only local areas of the sample which may not be representative of the whole nanowires assemblies, and do not give any information about the magnetic behaviour of the nanocomposite. Our strategy, therefore, has been to carry out a detailed study of nickel nanowires within mesoporous alumina using polarized SANS technique.

2. Small-angle neutron scattering. The structure and magnetic properties of the samples described above have been studied by polarized SANS with the instrument SANS-2 at the Geesthacht Neutron Facility (GeNF) in Geesthacht, Germany. The beam of polarized neutrons with initial polarization $P_0 = 0.96$, wavelength $\lambda = 0.58$ nm ($\Delta\lambda / \lambda = 0.1$) and divergence of 1.0 mrad was used. The scattered neutrons were detected with a two-dimensional position–sensitive detector with 256×256 pixels. Samples were oriented such that pores were directed parallel to the incident beam. The magnetic field (0 and 850 mT) was set to be either perpendicular or parallel to the incident beam to reveal the magnetic properties of the system.

A typical scattering pattern for such systems is composed of the diffuse small-angle scattering and the Bragg peak observed as a ring on the detector (Fig.1). This ring is observed instead of a 6 spots pattern, which is expected for the hexagonal structure, and corresponds to the scattering on the regular two-dimensional superstructure of nanopores oriented parallel to the incident neutron beam. A large number of defects lead to a multidomain structure in the sample and results in the isotropic distribution of the scattering intensity in a ring. The diffuse small–angle scattering stems, firstly, from the inhomogeneity of the form of the individual pores/nanowires and, secondly, from the imperfectness of the superstructure itself. Since it is difficult to distinguish between these two sources of the diffuse scattering, we assumed for the sake of simplicity that two types of scattering (diffuse scattering and small–angle diffraction) are independent. In general, the cross-section of polarized neutrons for magnetic samples consists of nuclear (N) and magnetic (M) contributions, as well as a nuclear-magnetic (NM) interference scattering. The scattering intensity for the two polarizations, oriented parallel (+) or antiparallel (-) to the external magnetic field **H**, are given as:

$$I^{\pm}(q) = F_N^2(q) + [F_M^2(q)\mathbf{m}_{d\perp}^2 \pm 2\langle \mathbf{P}_0\mathbf{m}_{d\perp}\rangle F_N(q)F_M(q)] +$$
$$+\Phi_N^{2*}\Lambda(q\text{-}q_B) + [\Phi_M^2\mathbf{m}_{B\perp}^2 \pm 2\langle \mathbf{P}_0\mathbf{m}_{B\perp}\rangle\Phi_N\Phi_M]\Lambda(q\text{-}q_B) \qquad (1)$$

Here, q is the modulus of the scattering vector, $q = 4\pi\sin(\theta/\lambda)$, where θ is half the scattering angle, F_N and F_M are the nuclear and magnetic form factors describing diffuse small–angle scattering, and Φ_N and Φ_M are those describing Bragg reflection, $\Lambda(q)$ is the resolution function of the experimental setup. **m** is the unit vector along the magnetization and $\mathbf{m}_\perp = \mathbf{m} - (\mathbf{m}\ \mathbf{e})\ \mathbf{e}$ with $\mathbf{e} = \mathbf{q}/q$. The symbols d and B in subscript refer to the magnetizations attributed to the diffuse scattering and Bragg scattering, respectively. One can assume that $\mathbf{m}_B = \langle \mathbf{m}\rangle$ is the magnetization ascribed to one nanowire but averaged over the whole sample while $\mathbf{m}_d$ is the part of the local magnetization related to the imperfect parts of the nanowires and in rough approximation: $\mathbf{m}_d = \mathbf{m} - \langle \mathbf{m}\rangle$.
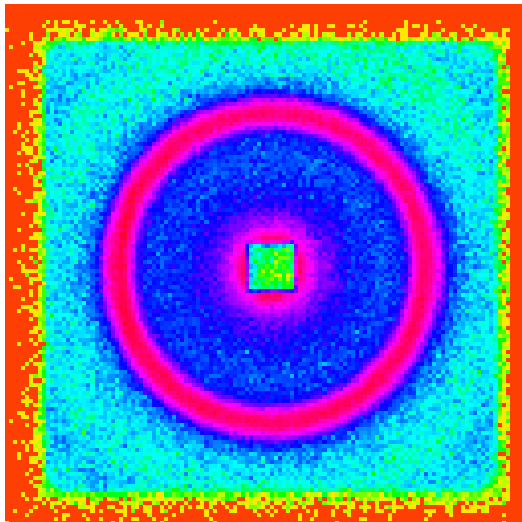
Fig.1
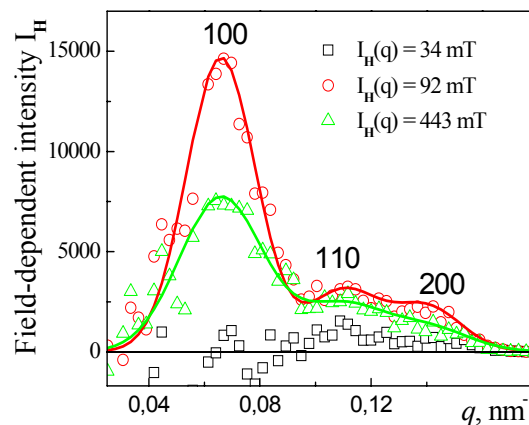
Fig.2

We determine the total (nuclear and magnetic) scattering as: $I(q) = \frac{1}{2}(I^-(q,\alpha) + I^+(q,\alpha)) = I_N + I_M$. The polarisation dependent part of the scattering is determined as the difference $\Delta I(q) = (I^-(q,\alpha) - I^+(q,\alpha)) = I_{NM}$. There are two important features concerning the pure magnetic scattering and the interference scattering. Firstly, the amplitude of the magnetic scattering for Ni is much smaller than that of nuclear scattering. Therefore the nuclear scattering is much

stronger than the magnetic one. On the other hand, the interference scattering $\Delta I(q)$ is linear with respect to the magnetic form factors, while the pure magnetic scattering contribution to $I(q)$ is quadratic. In this case the function $\Delta I(q)$ is much more sensitive to the parameters of the magnetic subsystem and we use this fact as an advantage of the polarized neutron scattering as compare with nonpolarized one. Secondly, the interference scattering is proportional to $\langle P_0 m_\perp \rangle$, i.e. to the average magnetization projected to the external magnetic field, since $P_0 \parallel H$. The pure magnetic scattering is proportional to $\langle m_\perp^2 \rangle$, which brings different information in case $m_\perp$ is not collinear to H. This case is of special interest in investigations of strongly anisotropic systems.

Achievements and Main Results

The q momentum transfer dependence of the SANS intensity was measured for three different AAO matrices with nickel (AA_0h, AA_5h (t_{anod}=100 h), and AA_5h (t_{anod}=150 h) with different treatment and pore's diameter (D $\approx$ 28 nm, 50 nm and 75 nm, respectively), in order to characterize a degree of ordering for the pore system. Since the scattering intensity from the samples was isotropically distributed for both diffuse scattering and Bragg reflection and to sake of the statistics of the magnetic scattering, the data were radially averaged over the whole 2D pattern. Indeed, the magnetic scattering is of order of a few percent of the nuclear one and anisotropic nature of the magnetic contribution has been neglected in this study.

The magnetic properties of the sample AA_5h (t_{anod}=100 h) with Ni were studied in dependence on the external magnetic field applied perpendicular to the incident beam and to the long axis of the nanowires. The pure magnetic contribution to the scattering, or, the field–induced scattering, was extracted as $I_H(q) = I(q,H) - I(q,0)$. This quantity is shown in Fig. 2 for different values of the magnetic field. It should be noticed that in this treatment not only the nuclear contribution is subtracted but also the magnetic diffuse scattering. Nevertheless the Bragg reflections from the magnetic superstructure are perfectly revealed by this treatment. The intensity of the Bragg reflections increases with the magnetic field. This scattering is attributed to the formation of the magnetic structure composed of the magnetic nanowires.
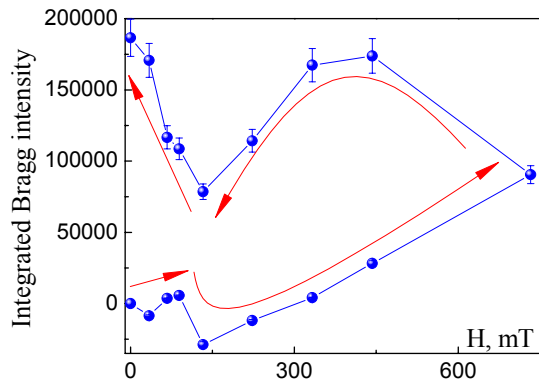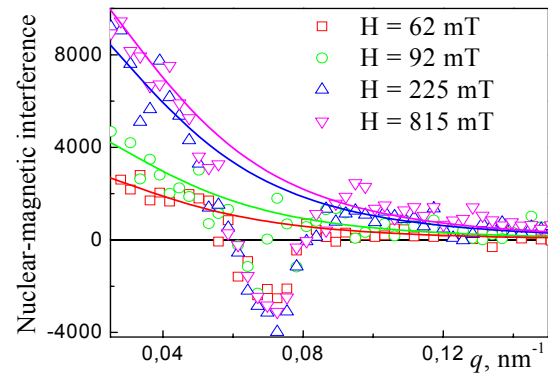
Fig. 3   **Fig. 4**

The scattering intensity was integrated over the Bragg peak and plotted as a function of the magnetic field (Fig. 3). The measurements reveal a large hysteresis in field dependent part of the cross-section $I_H(q)$. This type of behaviour under magnetic field applied perpendicularly to nanowires is quite typical and was observed in the samples with Fe embedded in the silicon oxide [1]. This complex behaviour is caused by interplay of the Zeeman energy (interaction between the magnetic moment and the field) and the large structural anisotropy.

The interference term shows the correlations existing in system between nuclear and magnetic objects and as was shown above it is proportional to the average magnetization of the system. The nuclear-magnetic interference $\Delta I(q)$ is observed over the whole q-range under study (Fig.4). The two types of contributions to the interference scattering, the diffuse small angle scattering and Bragg reflection, appeared to have opposite signs. We fitted the diffuse contribution using the function $I(q) = A(q^2 + R_d^{-2})^{-2}$ where R_d is a characteristic size of the inhomogeneities and A is a constant. The interference contribution into the Bragg peak was obtained by subtracting the experimental points from the extrapolated values.

The integrated interference intensity averaged over the Bragg contribution is shown as a function of the field in the Fig. 5. As well seen this quantity first increases linearly with field at H < 150 mT and then tends to saturates at H > 300 mT. No hysteresis is observed for this interference contribution upon increase and consequent decrease of the magnetic field. The interpolated values of the diffuse interference contribution averaged over the whole q-range demonstrates the similar magnetic field dependence but of the opposite sign. It is interesting to compare the magnetic field behaviour of the magnetic cross-section I_H (Fig.5) and that of the interference scattering ΔI (Fig.6). The interference scattering reflects the behaviour of the average magnetization projected to the magnetic field applied perpendicularly to the long axis of the nanowires. The magnetic cross-section is connected to the autocorrelation function of the magnetization, which reflects the degree of the coherence of the magnetization in different nanowires over the whole sample. The difference between figures demonstrates that the magnetization process proceeds in a much more complex way than it is observed in a simple magnetization measurement using standard methods of magnetometry.

Fig. 5
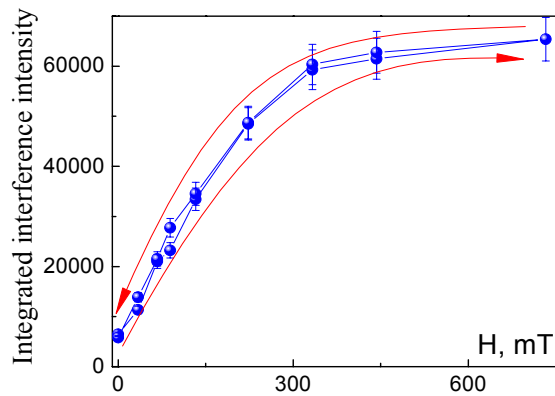
Fig. 6
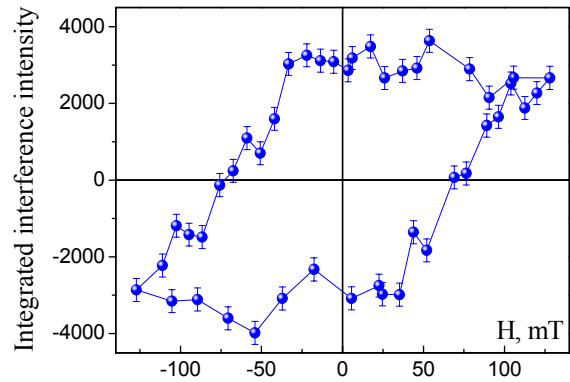
To show the strong magnetic anisotropy of the sample, we applied the external magnetic field parallel to the long axis of the nanowires. It is worth noting that no change for the pure magnetic contribution I_H (q) was detected within error bars, while the interference term changed significantly. The interference scattering is composed again of the two types of contributions of opposite signs, similar to the case shown in Fig.4. The integrated interference intensity averaged over the Bragg contribution is shown as a function of the field in the Fig. 6.

A large hysteresis is observed upon increase and consequent decrease of the magnetic field with the coercive field equal to 75 ± 3 mT. The magnetic system is fully magnetized at H ~ 100 mT and it stays frozen upon decrease of the field up to the negative values of 35 ± 3 mT. Again the magnetic behaviour of the magnetic cross-section I_H is different from that of the interference scattering. The comparison of Fig.5 and Fig.6 shows that there is a big difference in the magnetization process of the sample for the field applied parallel to the long axis of nanowires or perpendicular to it. The additional details of the magnetization process may be extracted from the behaviour of the pure magnetic contribution into the scattering.

In conclusion, the study demonstrates possibilities of polarized SANS for investigation of the structure and magnetic properties of two-dimensional spatially ordered system of ferromagnetic nanowires. The importance of the study is related to the fact that this system is a promising candidate for high-density data storage devices.

References

1. Grigorieva, N.A., Grigoriev, S.V., Okorokov, A.I., Eckerlebe, H., Eliseev, A.A., Lukashin, A.V. & Napolskii, K.S. (2005). Physica E. 28(3), 286-295.

GKSS FORSCHUNGSZENTRUM in der HELMHOLTZ-GEMEINSCHAFT	**EXPERIMENTAL REPORT**	**GeNF SANS-2**

Polarized SANS study of the topology constrained magnetic structure of Ni inverted photonic crystal	

Proposer: **Co-Proposers:**	**Kirill Napolskii[1],** [1]MSU, Moscow, Russia **Natalia Grigoryeva[2],** [2]SPSU, St-Petersburg, 198504, Russia
Experimental Team: **User Group Leader:**	**Natalia Grigoryeva[2], Kirill Napolskii[1],** **Helmut Eckerlebe[3],** [3]GKSS Forschungszentrum, Geesthacht **Sergey V. Grigoriev[4],** [4]PNPI, Gatchina, St-Petersburg, Russia
Date(s) of Experiment:	November 2006

Objectives

Photonic crystals (PCs), the materials with a periodic modulation of dielectric constant, have recently received great attention due to a number of promising applications, such as high-performance light emitting diodes, low-threshold lasers, optical waveguides with sharp bends and all-optical microchips [1]. Ones of the most intensively studied photonic crystals are artificial opals consisting of submicron monodisperse microspheres packed in a face-centered cubic cell. Another important class of photonic crystals is inverse opals, which can be synthesized by filling the voids of opal templates with suitable structure-forming precursors and subsequent removing the initial microspheres to leave three-dimensional ordered porous materials. This templating technique is very flexible and can be applied for the preparation of inverse photonic crystals based on metals, nonmetals, oxides, semiconductors and polymers. Single crystal neutron diffraction is a powerful tool for visualization and analysis of crystalline structures of atomic and molecular crystals. Despite the analogy of self-assembled photonic crystals and ordinary crystals, similar laser diffraction experiments on artificial opals were reported only in a few works. The laser diffraction was demonstrated to be very efficient to determine the orientation and to characterize the ordering of photonic crystal films. The significant limitation of laser diffraction method is that the diffraction patterns can be observed only if the laser wavelength is less than photonic crystal lattice period. Inverted photonic crystals, due to the preparation complexity of their well-ordered samples by templating methods, are significantly less investigated than artificial opals, and to date there are no reported experiments on diffraction studies in inverse opals with rather small diameter of the spheres (less than 400 nm).

Experiment

1. The sample. The Ni PC films with an inverse opal structure were prepared using a templating technique. For template preparation, monodisperse polystyrene microspheres with relative standard deviation less than 5% were synthesized by emulsifier-free emulsion polymerization of styrene using potassium persulfate as initiator. Colloids were centrifuged and re-dispersed in distilled water by ultrasonication. Colloidal crystal films made of 450 nm polystyrene microspheres were grown onto polished Cu substrates by the vertical deposition method [2].

Electrochemical crystallization of nickel in the voids between the spheres was carried out in three-electrode cell at room temperature. The counter electrode was a Pt wire and the reference electrode – saturated Ag/AgCl electrode – connected to the cell via a Luggin capillary; 0.1 M $NiCl_2$, 0.6 M $NiSO_4$, 0.1 M H_3BO_3 and 4 M C_2H_5OH solution was used for potentiostatic Ni deposition at $E_d = -0.85$ V versus reference electrode. In order to obtain free-standing Ni structure onto Cu substrate the polystyrene microspheres were dissolved in toluene.

2. Small-angle neutron scattering. SAPNS measurements were carried out on the instrument SANS-2 at the Geesthacht Neutron Facility (GeNF). A polarized neutron beam with polarization P_0 = 0.95, a mean wavelength of λ = 1.16 nm and a wavelength spread of $\Delta\lambda/\lambda$ = 10% was used. The Sample - Detector distance of 21.5 m was used with the appropriate collimation to cover scattering vectors q from 0.005 nm^{-1} to 0.06 nm^{-1}. An external magnetic field (0 to 135 mT) was applied in the horizontal plane and either parallel or perpendicular to the incident beam. We determine the total (nuclear and magnetic) scattering ($I(q) = I^+(q) + I^-(q)$) and the polarization dependent part of the scattering ($\Delta I(q) = I^+(q) - I^-(q)$) where $I^+(q)$ and $I^-(q)$ are the intensities for neutrons polarized parallel (+) and anti-parallel (-) to the magnetic field. The field-dependent scattering intensity is extracted as $I_H(q) = I(q,H) - I(q,0)$.

Achievements and Main Results

According to the SEM observations all synthesized samples possess an ordered porous structure with uniform spherical pores (Fig. 1). Cross-section SEM images reveal a face-centered structure of spherical pores in a nickel framework (Fig. 1c). The average center-to-center distance between close-packed voids is 450 nm, suggesting no structure shrinkage during the fabrication process.

A typical SANS diffraction pattern is shown in Fig. 2, demonstrating several clearly resolved sets of hexagonally arranged reflections. In similar laser diffraction experiments the patterns were interpreted considering each layer of close-packed spherical voids in PC as an individual two-dimensional (2D) diffraction grating [3]. We can introduce a 2D basis shown in Fig. 1b. For the considered geometry the interplanar spacing (d_{hk}) can be calculated as:

Fig. 1: Low (a) and high (b) magnification SEM images of Ni inverse opals; (c) cross section SEM image.

$$d_{hk} = \frac{\sqrt{3}a}{2\sqrt{h^2 + hk + k^2}}.$$

The analysis of the peak positions of the diffraction pattern gives the values of $d_{hk} = 2\pi/q_{hk}$ corresponding to the interplanar distance a $\approx$ 450 nm. The obtained value is in good agreement with the SEM picture.

Meanwhile, high-order diffraction maxima can be seen in q-dependences of the neutron intensity *I(q)* for certain directions. For instance, q-dependence in the [110]-direction demonstrates diffraction peaks at $q_{11} \approx$ 0.028 nm^{-1} and $q_{22} \approx$ 0.056 nm^{-1} (Fig.3). This result differs from the common laser diffraction experiments, in which the first order reflections in diffraction patterns are usually observed [3, 4]. It is worthwhile to note that although the sample with a large area of about 1 cm^2 was homogeneously illuminated by the neutron beam, the diffraction pattern, typical for the single crystal, was recorded in the experiment, suggesting the high degree of coherence of the PC's structure on a macroscale.

Fig. 2: Typical experimental SAPNS diffraction pattern from Ni PC. The square in the center marks a beam-stop, white circles shows theoretical diffraction pattern.
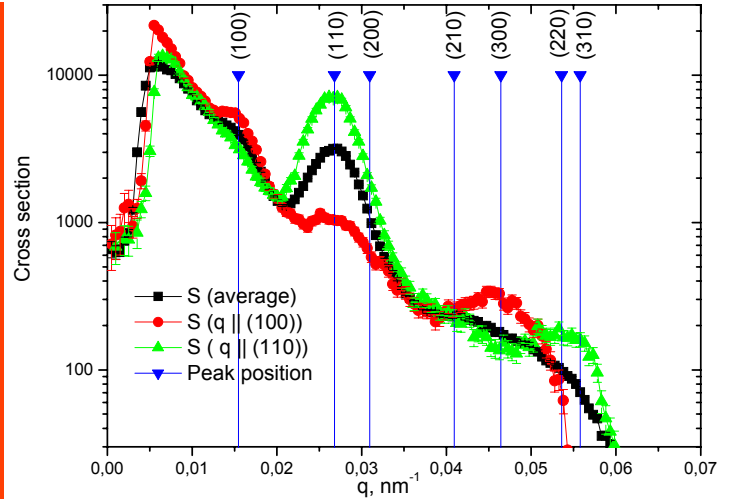
Fig. 3: SAPNS intensity profile from Ni PC in [11] direction.

The significant polarization dependent part of scattering $\Delta I(q)$ is detected in this experiment demonstrating that the nuclear and magnetic structures are well-correlated (Fig. 4a). The two types of contributions to the interference scattering are clearly seen: the diffuse small angle scattering and Bragg reflection. The latter dominates at the former one.

The pure magnetic contribution to the scattering $I_H(q)$, also referred to as field induced scattering, was extracted and shown in Fig. 4b. The scattering consists again of two contribution: diffuse SAS and Bragg reflections. The diffuse SAS decreases, while the reflections increase with the applied field. It is interpreted as a transition from multi to single domain magnetic structure at H > 50 mT. The quantitative analysis of the data is in progress.
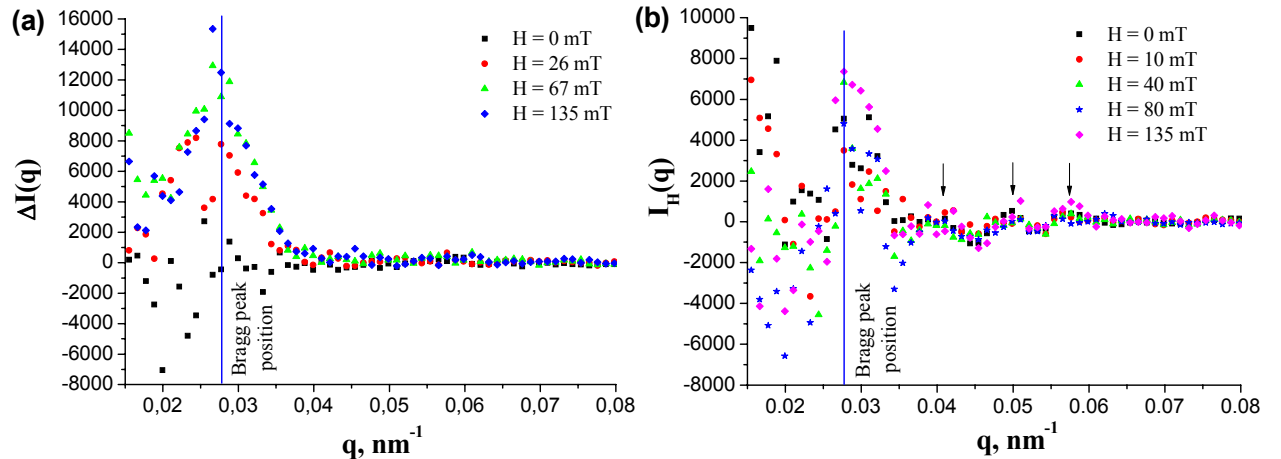
Fig. 4: Q-dependence of the nuclear – magnetic interference (a) and magnetic contribution to the scattering $I_H(q)$ (b).

References

[1] P.V. Braun, P. Wiltzius // Nature 402 (1999), 603.

[2] P. Jiang et. al. // Chem. Mater. 11 (1999) 2132.

[3] Amos R.M. et. al. // Phys. Rev. E 61 (2000) 2929.

[4] Yu.A. Vlasov et. al. // Nature 414 (2001) 289.

SANS study of structure of anodic titanium oxide films

Proposer:	**Kirill Napolskii**[1], [1]MSU, Moscow, Russia
Co-Proposers:	**Natalia Grigoryeva**[2], [2]SPSU, St-Petersburg, 198504, Russia

Experimental Team:	**Natalia Grigoryeva**[2], **Kirill Napolskii**[1],
	Helmut Eckerlebe[3], [3]GKSS Forschungszentrum, Geesthacht
User Group Leader:	**Sergey V. Grigoriev**[4], [4]PNPI, Gatchina, St-Petersburg, Russia

| Date(s) of Experiment: | November 2006 |

Objectives

Porous titanium oxide films have attracted great attention in the last decade because of their unique properties (wettability, sensory and optical properties, biological compatibility, high catalytic activity) and numerous applications in industry.

For preparation of thin oxide films the different synthetic approaches are used, for example: dip- or spin-coating, electrophoresis, precipitation from gas phase, etc. One of the promising method for preparation of porous TiO_2 films is anodic oxidation of Ti. Anodic titanium oxide films formed by anodization technique are well-known to possess uniform pore structure with nanotubes directed perpendicular to the film surface and a narrow pore size distribution. The use of different electrolytes, voltages and variable anodic oxidation time allows one to adjust a pore diameter, an interpore distance and a film thickness. For example TiO_2 films with thickness of 7 micrometers and pore diameter of about 65 nm were synthesized in glycerol electrolyte containing 0.5% ammonium fluoride at 20 V.

Several works reported investigation of organization of TiO_2 nanotubes formed during anodization process, however, most of them involve only electron microscopy or scanning probe microscopy studies, where local structures can only be seen. Our experiments were aimed to investigate the structural features of the anodic titanium oxide TiO_2 by means of small angle neutron scattering (SANS) technique.

Experiment

1. Samples. Titanium foil (0.25 mm thick, >99% purity) was used as the starting material for TiO_2 film preparation. Prior to anodization this Ti foil was mechanically polished to a mirror state and cleaned once again with acetone and deionized water. The anodization of the pretreated Ti foils was carried out in two-electrode cell in 0,5% NH_4F in glycerol (99% purity) or 0,5% NH_4F in glycerol with addition of 0.25% natrium dodecyl sulfate ($C_{12}H_{25}OSO_3Na$, 99% purity) solutions. All preparation experiments were carried out at 0°C in order to reduce the rate of TiO_2 dissolution in fluoride acid. The regime of electrochemical oxidation consisted of two steps: a potential ramp to the anodization voltage required with a sweep rate of 0.2V·s^{-1} and subsequent anodization at constant potential for 15 hours. We used different anodization potentials from 10V to 30V in steps of 5V. After the anodization the samples were cleaned with deionized water and dried in air.

2. Small-angle neutron scattering. SANS measurements were carried out on the instrument SANS-2 at the Geesthacht Neutron Facility (GeNF). Neutrons of a wavelength of λ = 0.58 nm and a wavelength spread of $\Delta\lambda/\lambda$ = 10% were used. Detector-to-sample distance up to 21.5 m was used with appropriate collimation to cover scattering vectors q from 0.03 nm^{-1} to 0.3 nm^{-1}. The samples with an area of order of 0.5 cm^2 were

homogeneously illuminated by the neutron beam. Samples were oriented such that pores were directed parallel to the incident beam on order to provide the Bragg condition fulfilled: $2d \sin(\theta_B/2) = \lambda$, or $q = 2\pi/d$, where d is the interplane distance and θ_B is the scattering angle.

Achievements and Main Results

Typical SANS diffraction pattern is shown in Fig. 1, demonstrating several resolved concentric circle reflections. The second order reflections are not well visible without radial averaging and background subtraction that is caused by low thickness of the films and, therefore, low statistics. The scattering intensity was radially averaged over the whole 2D pattern. The q-dependence of the SANS intensity for the sample prepared at 25V (TiO$_2$_25V) and sample anodized at 20V in electrolyte with surfactant (TiO$_2$_ls_20V) after background subtraction is shown in Fig. 2 and 3, respectively. As can be seen the obtained q-dependence of SANS intensity consist several sets of Bragg reflections interpreted in terms of hexagonal and tetragonal packing of the pores.

The positions of the reflections are identified using the formulas for the regular two-dimensional hexagonal (1) and tetragonal (2) structures of nanopores:

$$d_{hk} = \frac{\sqrt{3}a}{2\sqrt{h^2 + hk + k^2}} \quad (1) \qquad\qquad d_{hk} = \frac{a}{\sqrt{h^2 + k^2}} \quad (2)$$
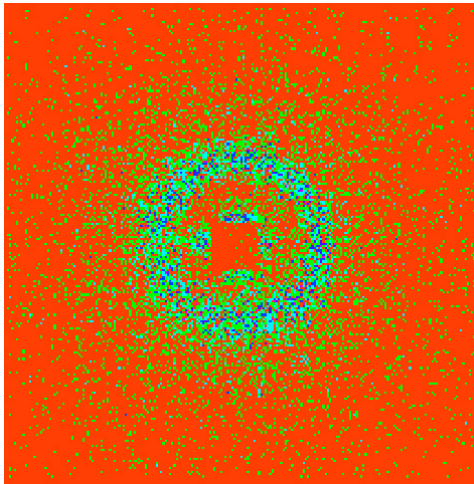
Fig.1

The analysis of the positions of the reflections allows us to determine the symmetry of local surrounding in porous structure and gives the value of the interpore distance *a* (see table 1).

Conclusions about the symmetry of the porous structure have been done from ratio of d_{10}/d_{11}, where {10}- and {11}-diffraction maximum are the first two peaks observed in the spectra. The analysis of the position of diffraction maxima of higher than {11} orders (in region from 0.15 to 0.20 nm^{-1}) is restricted due to its low intensity and high width of the peaks.

It was found that samples anodized at voltage lower than 20 V possess tetragonal porous structure, because this structure has ratio $\dfrac{d_{10}}{d_{11}} \approx 1.5$ (about $\sqrt{2}$).

In the contrary, anodization of the titanium at potentials higher than 20 V corresponds to the formation of hexagonal packed porous structure ($\dfrac{d_{10}}{d_{11}} \approx 1.7 \approx \sqrt{3}$). Addition of sodium dodecyl sulphate into electrolyte (TiO$_2$_ls_20V) leads also to formation of hexagonal porous structures of TiO$_2$. Besides the interpore distance depends on the voltage applied for TiO$_2$ film formation: the higher the anodization potential, the larger interpore distance is formed.

Table 1. Structural parameters of anodic TiO$_2$ porous films.

Sample	q_{10}, nm^{-1}	d_{10}, nm	q_{11}, nm^{-1}	d_{11}, nm	$\dfrac{d_{10}}{d_{11}}$	Symmetry	a, nm
TiO$_2$_10V	0,168	37,4	0,259	24,3	1,540	tetragonal	37,4
TiO$_2$_15V	0,1	62,8	0,154	40,8	1,540	tetragonal	62,8
TiO$_2$_20V	0,08	78,5	0,12	52,4	1,500	tetragonal	78,5
TiO$_2$_ 25V	0,071	88,5	0,12	52,4	1,690	hexagonal	102,2
TiO$_2$_30V	0,064	98,2	0,107	58,7	1,672	hexagonal	113,4
TiO$_2$_ls_20V	0,065	96,7	0,118	53,2	1,815	hexagonal	111,7

Fig.2

Fig.3

117

Spin-wave dynamics in Invar alloy studied by
small-angle polarized neutron scattering

Proposer: **Co-Proposers:**	**Sergey V. Grigoriev[1]**, [1]PNPI, Gatchina, St-Petersburg, Russia **Sergey V. Metelev[1]**
Experimental Team: **User Group Leader:**	**Alexey I. Okorokov[1]**, **Helmut Eckerlebe[2]**, [2]GKSS Forschungszentrum, Geesthacht **Sergey V. Grigoriev[1]**
Date(s) of Experiment:	November 2006

Objectives

Spin-wave (SW) dynamics in Invar FeNi alloys has been investigated in connection with the problem of so called 'hidden excitations' [1,2]. The idea of hidden excitations stems from the observation that conventional spin waves with a stiffness $D(T)$ can not explain the temperature variation of the magnetization $M(T)$. Recently an existence of the "forbidden" mode was found at the invar composition of FeNi system [3,4]. The authors concluded that this mode has a magnetic origin. Furthermore it arises from a dynamic modulation of the magnetic moments associated with the comprehensive strain in the phonon excitations. Although the existence of this mode may be able to account for anomalous thermal variation of the magnetization, the origin of this mode is not understood yet. It is well known that the magnetic ordering temperature T_c in FeNi decreases strongly with applied pressure leading to the quantum phase transition at P = 70 kbar. On contrary, the introduction of carbon into the system results in increase of T_c what is considered as a "negative pressure effect". We propose to study the change of the spin wave dynamics for FeNi system under the pressure. The investigation of the dynamics under applied pressure with use of the neutron scattering technique is strongly restricted due to the limited amount of the sample into a pressure cell and an unwanted deformation, which the pressure cell may produce onto the sample orientation. At present we have performed a preliminary experiment showing the sensitivity of the polarized SANS in inclined geometry of the magnetic field.

Experiment

The polarized SANS experiments were carried out at the instrument SANS-2 at the Geesthacht Neutron Facility (GeNF). The plate of invar alloy $Fe_{65}Ni_{35}$ ($40\times10\times1$ mm^3) has been used as a sample. A polarized beam of neutrons with an initial polarization of $P_0=0.9$, the neutron wavelength $\lambda=5.8$ Å ($\Delta\lambda/\lambda=0.1$) and a divergence of 1.0 mrad was used. The scattered neutrons were detected by a 256×256 position sensitive detector. The detector-to-sample distance of 6.5 m was used with an appropriate collimation to cover an angular range of $\pm$ 40 mrad. The sample was magnetized parallel to its long dimension by an electromagnet. The external magnetic field was applied at an angle of $\varphi=35^o$ with respect to the incident beam. In this geometry the inelastic contribution to scattering attributed to the anti-symmetrical part of the scattering can be separated from the other scattering processes. We considered two contributions to the scattering: the total magnetic scattering $\Sigma I(q) = I^+(q) + I^-(q)$, and the polarization dependent part of the scattering $\Delta I(q) = I^+(q) - I^-(q)$. Here $I^+(q)$ and $I^-(q)$ are the scattering intensities for neutrons polarized parallel (+) and anti-parallel (-) to the magnetic field. The procedure of the extraction of the parameters (the spin wave stiffness coefficient **D**, the damping parameter γ_0 and the dipolar energy ω_0**<S>**) is described in [5,6]. The intensity was measured at the room temperature and at different magnetic field H = 100, 132, 175, 210 mT.

Achievements and Main Results

Fig.1 a and b show the anti-symmetrical ΔI and symmetrical ΣI parts of the magnetic scattering in the **k-H** plane as a function of the scattering angle θ for magnetic field H=132 mT at T=293 K. Both symmetric and antisymmetric scattering contributions are concentrated mostly within the cut-off angle θ_C. This implies that both contributions are caused by spin waves. The cut-off angle depends on the magnetic field as [7]: $\theta_C(H)^2 = \theta_0^2 - g\mu H \theta_0/E$, where θ_0 is inversely proportional to the SW stiffness $\theta_0 = h^2/(2 D m_n)$. In the vicinity of the cut-off angle, the scattering is smeared by the SW damping Γ_q. Fig.2 represents the magnetic field dependence of θ_C^2. As seen from this figure, the experimental data of θ_C^2 obey the linear behavior in accord to the prediction of the theory for ordinary ferromagnets [7]. The value of D obtained from the data is equal to 93.7 meV A^2. The ratio $R(\theta) = \Delta I(\theta) / \Sigma I(\theta)$ is maximal in the vicinity of the cut-off angle and reaches the value of 35 %. This number shows the sensitivity of the method of the inclined geometry in polarized SANS: 1/3 of the scattered neutrons are of use in determination of the spin wave stiffness.

Fig.1 a

Fig.1 b

Fig.2
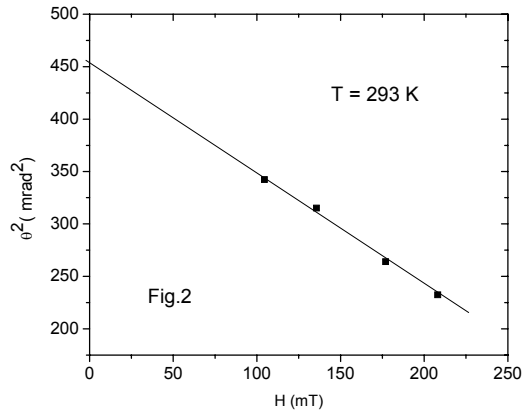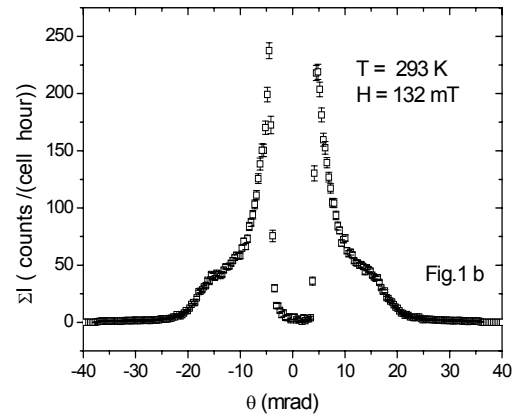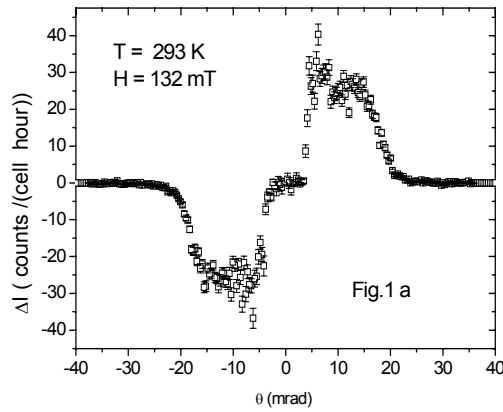
References:

1. Y. Ishikawa, S. Onodera, K. Tajima, J.Magn.Magn.Mat. 10 (1979) 183

2. S. Onodera, Y. Ishikawa, K. Tajima, J.Phys.Soc.Jap. 50 (5) (1981) 1513

3. P.J. Brown, I.K. Jassim, K.-U. Newmann, K.R.A. Ziebeck, Physica B 161 (1989) 9

4. P.J. Brown, B. Roessli, j.G. Smith, K.-U. Newmann, K.R.A. Ziebeck, J.Phys.:Condens.Matter 8 (1996) 1527

5. S.V. Grigoriev, S.V. Maleyev, V.V. Deriglazov, A.I. Okorokov, N.H. van-Dijk, E. Bruck, J.C.P. Klaasse, H. Eckerlebe, G. Kozik, Applied-Physics-A-Materials-Science-Processing A74 (2002) 719

6. V. Deriglazov, A. Okorokov, V. Runov, B. Toperverg, R.Kampmann, H. Eckerlebe, W. Schmidt, W. Lobner, Physica B 181-182 (1992) 262

7. S.V. Maleyev, Zh.Eksp.Teor.Fiz. 48 (1965) 1448

![GKSS logo] GKSS FORSCHUNGSZENTRUM in der HELMHOLTZ-GEMEINSCHAFT	**EXPERIMENTAL REPORT**	**GeNF SANS-2**

Low temperature properties of the helix structure in MnSi

in the critical field regime

Proposer:	**Sergey Grigoriev**[1], [1]PNPI, Gatchina, St-Petersburg, RUSSIA
Co-Proposers:	**Alexey Okorokov**[1],
Experimental Team:	**Sergey Grigoriev**[1],
	Helmut Eckerlebe[2], [2]GKSS Forschungszentrum, Geesthacht
User Group Leader:	**Sergey Grigoriev**[1]
Date(s) of Experiment:	June 2006

Objectives

The weak itinerant ferromagnet MnSi with the spin helicity induced by an antisymmetric Dzyaloshinski-Moriya (DM) exchange interaction attracted much attention in the last few years. Although some details in its properties had been already clarified the magnetic behaviour of MnSi under applied magnetic field is still puzzling. In particular, it is known that the spiral multi-domain structure transforms into a single domain in a weak magnetic field H_{C1} of order of 100 mT at T << T_c and that the conical phase appears. It is also known that the cone angle decreases as the field increases and the induced ferromagnetic state appears at H_{C2} ~ 600 mT. However, the nature of the magnetic field transition at H_{C2} was not studied yet. The simple phenomenological theory predicts smooth second order transition to the ferromagnetic state. On the other hand, a careful consideration shows that the spin wave spectrum becomes unstable at H < H_{C2} but close to H_{C2}. This can lead to the first order phase transition at H_{C2}. The polarized SANS experiments were aimed to study the spin structure of MnSi under applied field at low temperature and thus to examine this new theory.

Experiment

1. Sample. The single crystal MnSi was chosen for the study. The sample was a disc with a thickness of 1.5 mm and a diameter of 15 mm. The crystallographic mosaic and orientation of the sample was tested on the X-ray diffractometer Rödi at GKSS (Germany). The average value of the FWHM over all measured reflections is 0.25^o.

2. Small-angle neutron scattering. Small-angle neutron scattering (SANS) measurements were carried out with the instrument SANS-2 at the Geesthacht Neutron Facility (GeNF). Neutrons with a mean wavelength of λ = 0.58 nm and a wavelength spread of $\Delta\lambda/\lambda$ = 10% were used. Sample - Detector distance of 4 m was used with appropriate collimations to cover scattering vectors q from 0.06 nm^{-1} to 0.6 nm^{-1} (q = $(4\pi/\lambda)\sin(\theta/2)$ where 2θ is the scattering angle). The field ranged from 0 to 800 mT was directed along [1 1 1] axis. The magnetic structure of MnSi has a complicated irreversible behavior at H$\neq$0. Therefore, it is important that the scattering intensity is measured in the following way: (i) zero field cooling from the paramagnetic state to the temperature of the interest; (ii) increasing field from H = 0 to the field value of the interest; and (iii) the magnetic field direction is fixed with respect to the sample in the rocking scan experiment. Using this principles the rocking curves of the Bragg peak (111) were taken at different values of the field at T = 15 K, 28.0 K and 28.5 K.

Achievements and Main Results

The rocking curves are well fitted by the Gauss function with the integral intensity A, the center of the Gaussian φ_c, and its HWHM, or mosaic of the helix structure. The field dependence of the integral intensity A is shown in Fig.1. It is small at low H, then it increases sharply at H_{C1} and has a well-pronounced minimum at H_{ins} = 160 mT. It decreases again diminishing to zero at H_{C2} = 400 mT for the temperatures close to T_C = 29.0 K. At low temperatures ($T < T_C$) the integral intensity A shows a long exponential decay from 400 mT to 550 mT, while it decreases to zero. This behavior of A contradicts to the simple phenomenological theory mentioned above with $A \sim \sin^2\alpha = (H_{\parallel} / H_{C2})^2$, where $H_{\parallel}$ is the an applied field parallel to the helix wavevector **k**.
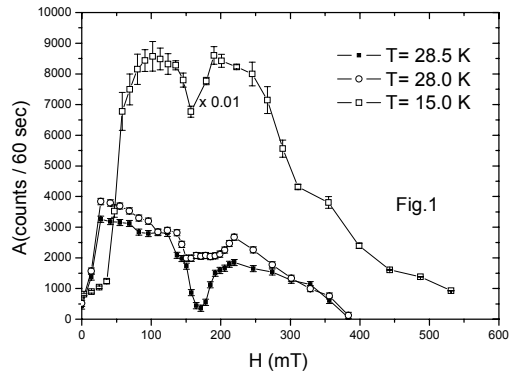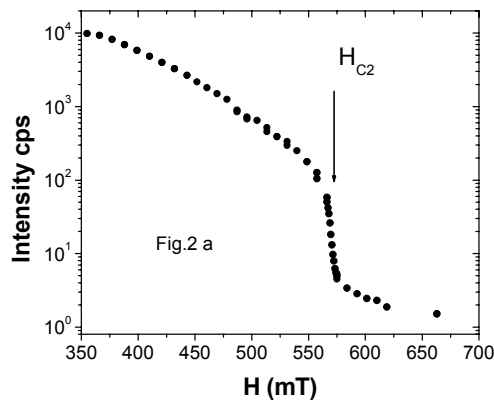
To specify the behavior of the helix near H_{C2} the intensity and the polarization of the Bragg reflection (111) were measured in detail and are plotted as a function of the field in Fig. 2a and Fig. 2b, respectively. The polarization is constant and is equal to 1 in the whole field range H < H_{C2}. The abrupt change of the intensity and polarization at H_{C2} shows that the transition to the ferromagnetic state is sharp, again in contradiction to the simple classical theory, which predicts the second order transition. Thus we show that behavior of the spin system in MnSi in the critical field region H ~ H_{C2} is not trivial and requires additional theoretical and experimental studies.

Fig.1

Fig.2 a

Fig.2 b
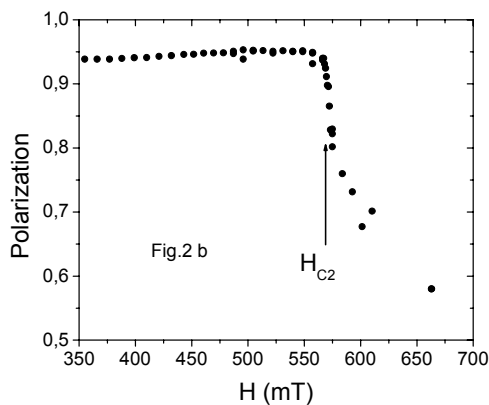
References
[1] S.V. Maleyev, Phys. Rev. B **73** (2006) 174402.

![GKSS logo] GKSS FORSCHUNGSZENTRUM in der HELMHOLTZ-GEMEINSCHAFT	**EXPERIMENTAL REPORT**	**GeNF SANS-2**

The investigations of the topology and magnetic properties of the Co nanocomposites in the alumo-silicate mesoporous matrix		

Proposer: **Co-Proposers:**	**Sergey V. Grigoriev**[1], [1] PNPI, Gatchina, St-Petersburg, RUSSIA **Natalia A. Grigoryeva**[2], [2]SPSU, St-Petersburg, RUSSIA
Experimental Team: **User Group Leader:**	**Natalia A. Grigoryeva**[2]**, Klaus Pranzas**[3]**, Helmut Eckerlebe**[3]**,** [3]GKSS Forschungszentrum, Geesthacht **Sergey V. Grigoriev**[1]
Date(s) of Experiment:	June 2006

Objectives

Modern information technologies require development of novel high-density data storage devices due to colossal growth of digital information volume. The special role in creation of the components for such devices belongs to high-quality nanostructures and nanocomposites with detached, and strongly anisotropic, and regularly ordered magnetic nanoparticles. At present, the most promising matrices for high-density data storage devices are mesoporous aluminosilicate (MAS) sieves. These matrices have highly ordered uniform pore structure with maximal anisotropy constants and could be considered as one-dimensional (1D) systems. A novel variant of synthesis of ordered magnetic nanowires in the mesoporous aluminosilicate matrix was used for these investigations. The method is based on the introduction of a hydrophobic metal compound (cobalt carbonil), into the hydrophobic part of the as-prepared mesoporous aluminosilicate-surfactant composite [1]. To provide better crystallinity of the metal nanowires the additional annealing in the hydrogen flow was performed. Obtained samples were denoted as Co-MAS-T, where T = 300, 400 and 500K.

Experiment

Polarized Small-Angle Neutron Scattering (SANS) measurements were carried out with the instrument SANS-2. An external magnetic field (0 to 300 mT) was applied in the horizontal plane and perpendicularly to the incident beam. Temperature was changed from 10K to 300K. We determine the total (nuclear and magnetic) scattering ($I(q) = I^+(q) + I^-(q)$) and the polarization dependent part of the scattering ($\Delta I(q) = I^+(q) - I^-(q)$), where I+(q) and I-(q) are the intensities for neutrons polarized parallel (+) and anti-parallel (-) to the magnetic field.

Achievements and Main Results

The isotropic ring of the neutron intensity is observed for powder samples of mesoporous silica matrix with metal containing nanowires. This ring corresponds to the scattering on the regular two-dimensional structure of nanopores. In the data analysis the intensity was radially averaged over the range from 0° to 360°.

As powder samples consist of many randomly oriented particles, the contribution to the scattering is strongly dependent on their orientation. Obviously the particles with pores oriented parallel to the neutron beam, make the major contribution to the diffraction ring with six reflexes for each mesoporous crystallite, the particles oriented perpendicularly to the beam give two low-intensity reflexes, while nearly no contribution should be observed for other crystallites due to mismatch of the Bragg conditions for these orientations. We suppose that the magnetization inside the nanowires is oriented along the cylinder generatrix, and, therefore, it is parallel to the neutron beam for the particles contributing to the Bragg

reflection. The field-dependent and temperature-dependent scattering intensity was extracted as $I_H (q) = I(q,H) - I(q,0)$ and $I_T (q) = I(q,T) - I(q, 300 \text{ K})$, respectively. We summarized the scattering intensity over the Bragg peak and small angle region, and plotted the integral cross section as a function of the field in the range from -300 mT to +300 mT at T = 300 K (Fig.1).
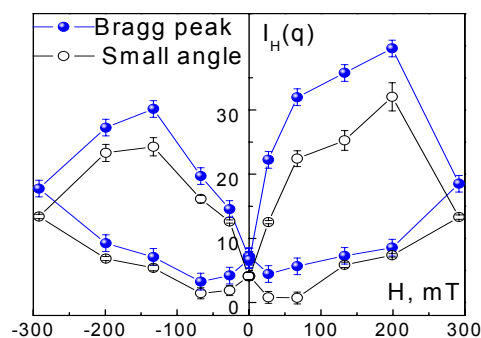
Fig. 1
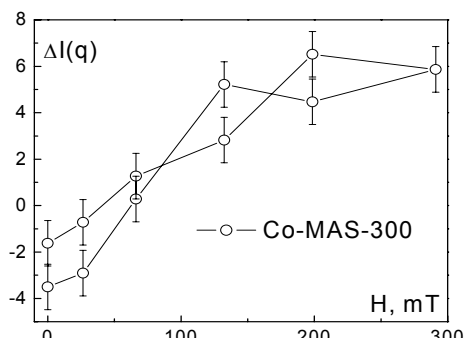
Fig. 2

The measurements reveal a large hysteresis in field dependent part **H**(*q*) of the cross-section.

As the magnetic field (perpendicular to the neutron beam and to the nanowires) increases from 0 to 300 mT, the intensity of the Bragg reflection increases slightly. This is attributed to the rotation of the magnetization inside nanowires from the direction along the wire to the direction perpendicular to it. As a result, at the magnetic field 300 mT we get the ensemble of nanowires with the magnetic moments oriented perpendicular to the anisotropy axis. A decrease of the magnetic field leads to the coherent rotation of the magnetic moments of the whole ensemble toward the anisotropy axis (parallel to the beam), and therefore, to the further increase of the Bragg reflection. This coherency is decreased at the magnetic field smaller than 150 to 100 mT by thermal fluctuations and dipole interactions. The magnetization of nanowires becomes randomly oriented again and the intensity of the Bragg reflection decreases.

The nuclear-magnetic interference $\Delta I(q)$ is observed in the small *q*-range only but no interference is visible at the Bragg peak. The interference term shows the correlations existing in system between nuclear and magnetic objects and it is proportional to the average magnetization of the system. The absence of the interference in the Bragg peak shows that the nuclear and magnetic periodic structures are spatially incoherent. At the same time, nuclear and magnetic contrasts are correlated for individual nanowires. The field dependence of the integral interference cross-section for small q is presented in Fig. 2. It is interesting that it shows no hysteresis.

References.
1. A.S. Vyacheslavov, A.A. Eliseev, I.V. Kolesnik, A.V. Lukashin, P. Goernert, Yu. V. Maksimov, I.P. Suzdalev, Yu.D. Tretyakov, Progress in solid state chemistry (2005) in print.

		GeNF
GKSS FORSCHUNGSZENTRUM in der HELMHOLTZ-GEMEINSCHAFT	**EXPERIMENTAL REPORT**	**GeNF** **SANS-2/DCD**

SANS/USANS investigations of light weight metal hydrides	
Proposer:	**Martin Dornheim**
Co-Proposers:	**P. Klaus Pranzas**
Experimental Team:	**P. Klaus Pranzas, Ulrike Bösenberg, Helmut Eckerlebe**
User Group Leader:	**P. Klaus Pranzas**
Date(s) of Experiment:	18th–24th April 2006

Objectives

Light weight metal hydrides are the favoured materials for hydrogen storage in mobile application. Nanocrystalline MgH_2 is due to its availability and high gravimetric storage capacity with 7.6 wt% of special interest. The sorption properties could be significantly influenced by the addition of metal-oxide catalysts. However, the influences of microstructure, e.g. grain and particle sizes, and distribution of different additives on kinetic properties have hardly been investigated until now. The aim of this work is to characterize structural changes of high energy ball-milled MgH_2 with different oxide additives in micro and nano quality and with variation of milling time.

Besides pure MgH_2 also the novel MgH_2-based Reactive Hydride Composites (RHC) are under investigation. In these composites an additional exothermic reaction between the decomposition products of the hydrides occurs during the endothermic desorption. If the formation of this new compound is exothermic, the total reaction enthalpy is lowered and the reaction should therefore proceed at lower temperatures [1]. First investigations with SANS have been performed on the system of $2LiBH_4+MgH_2 \leftrightarrow 4\ H_2+ 2LiH+MgB_2$. For a better understanding of the sorption properties in these materials knowledge of the microstructural properties is of utter importance.

Experiment

The MgH_2 samples were milled in a Fritsch P5 planetary ball mill using steel tools with a ball to powder ratio of 10:1. As additives commercially available micro- and nanocrystalline Fe_2O_3, Cr_2O_3 and Al_2O_3 were used with an initial particle sizes of 50 µm and 75 nm (µ- and nano) respectively. One sample with nano-Cr_2O_3 was milled with ceramic tools. The powder was milled for 200 hours and samples also taken in between after 1, 2, 10 and 50 hours.
The RHC were milled in a Spex 8000 Mixer Mill using hardened steel tools with a ball to powder ratio of 4:1. Different hydrogenation states were produced in a Sievert's type apparatus.

The powders were measured at the instruments SANS-2 and DCD at room temperature in quartz cuvettes with a thickness of 1mm. At SANS-2 distances between sample and detector of 1, 3, 9 m (λ= 0.58 nm) and 21 m (λ= 0.58 nm and 1.16nm, $\Delta\lambda/\lambda$=0.1) were used to cover the range of scattering vector q from 0.009 nm^{-1} and 2.4 nm^{-1}. Scattering data were corrected for sample transmission and detector response and normalized by monitor counts. The

differential scattering cross section was obtained by calibration with a vanadium reference sample.

Ultra small-angle neutron scattering (USANS) measurements were carried out at the double-crystal diffractometer DCD to detect particle sizes up to 24µm. The used wavelength of 0.443 nm resulted in a range of scattering vector q from 10^{-5} to 10^{-2} nm^{-1}.

Achievements and Main Results
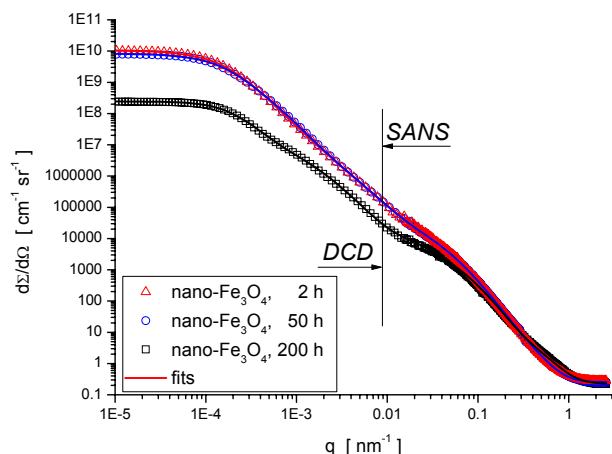
Figure 1: *SANS/USANS curves of MgH$_2$ samples with nano- Fe$_2$O$_3$ additives after 2, 50 and 200h of milling.*
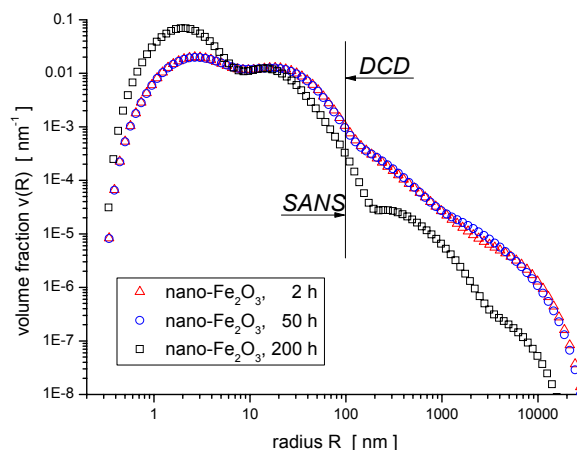
Figure 2: *Volume fraction distributions corresponding to the SANS/USANS curves of figure 1.*

Figure 1 shows an example of combined SANS/USANS curves of MgH$_2$ with an addition of nano-Fe$_2$O$_3$ after milling times of 2, 50 and 200 hours using ceramic vials and balls. The scattering curves after 2 and 50 hours of milling show little difference, therefore the particle-size-distributions in figure 2 for these two samples are very similar.

A significant effect of 200 hours of milling is already visible in the scattering curves in figure 1. The measured intensity for q values smaller than 0.01 indicates a lower fraction of particles with the corresponding particle size larger than 200 nm. This is even better visible in the calculated particle size distributions in figure 2. The curve of the sample after 2 hours of milling shows a significantly higher volume fraction for very small radii of about 2 nm. The volume fraction at larger radii above 100nm is considerably smaller than after shorter milling times. This was different in case of the addition of µ-Fe$_2$O$_3$. If µ-Cr$_2$O$_3$ was added this milling time effect could already be observed after much shorter milling times, such as 50 hours. For Cr$_2$O$_3$ the effect of milling on the particle size has been recorded in previous measurements [2].

In figure 3 three examples for the SANS curves of milled RHC are presented, synthesized in the desorbed state and in the hydrided state with and without 5 mol% of additive. A tendency of the material in the dehydrided state to a larger amount of smaller particles can be observed. Also the addition of the additive appears to increase the amount of smaller particles.

This tendency can also be observed in the scattering curves obtained from the DCD-instrument, see figure 4. The material milled in the dehydrided state scatters more strongly in the q-range of 0.003-0.03 nm^{-1} than in the material milled in the hydrid state. This, again,

indicates a larger volume fraction of large particles in the dehydrogenated state. Due to the large scattering length density differences (SLDD) of the different hydrogenation states as well as the high absorption and incoherent scattering of the samples, a quantitative evaluation of the scattering curves is difficult.
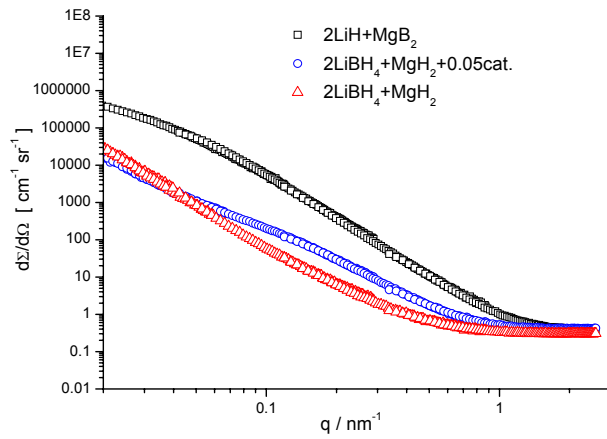
Figure 3: *SANS curves of RHC synthesized in the dehydrogenated and hydrogenated state by high-energy ball milling.*
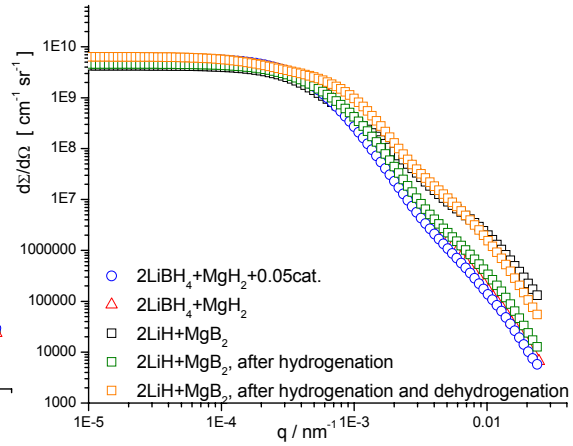
Figure 4: *DCD curves of milled RHCs in different hydrogenation states.*

First evaluations of the scattering curves for the RHC-samples are currently in progress. Due to the complexity of the material additional information of the microstructure obtained by X-ray diffraction and electron microscopy is necessary to apply suitable models.

References

[1]   G. Barkhordarian, T. Klassen, R. Bormann, int. Patent application, Publ. Co. WO2006063627

[2]   P.K. Pranzas, M. Dornheim, D. Bellmann, K.-F. Aguey-Zinsou, T. Klassen, A. Schreyer, *Physica B* 385-386 (2006), 630-632.

Double crystal diffractometer DCD

Short Instrument Description:

The double crystal diffractometer for ultra small angle neutron scattering (USANS) uses non-polarised cold neutrons to characterise in materials large creep pores, fatigue and sintering cavities, precipitates, voids, bubbles, etc. with particle sizes in the range between 100 nm and 24 μm in diameter.

Local Contact:

M. Sharp
Phone/Fax : +49 (0)4152 87 – 1209 / +49 (0)4152 87 – 1338
e-mail: melissa.sharp@gkss.de

Dr. P. Klaus Pranzas
Phone/Fax : +49 (0)4152 87 – 1326 / +49 (0)4152 87 – 41326
e-mail: pranzas@gkss.de

Schematic View of DCD:

A: neutron guide NG-1
B: deflecting crystal
C: monochromator crystal
D: analyzer crystal
E: sample
F: ^{3}He neutron detectors
G: collimator tube
H: electronic autocollimator
J: diffractometer bench
K: shielding
L: slit diaphragm
M: channel-cut crystals
N: granite table
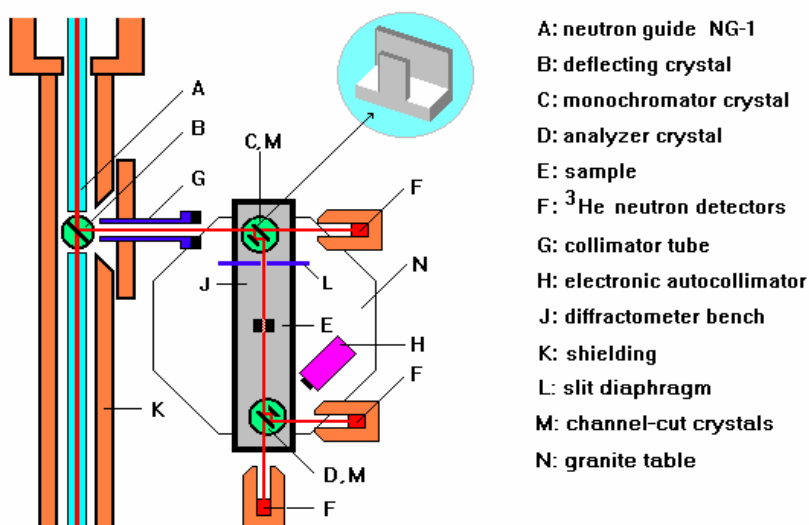
Instrument Details:

Beamline:	beamline 8 - cold neutron guide NG-1, max. beam cross section 30 x 40 mm^2
Deflecting crystal:	Si(111), Si(311), mosaic spread 0.1 mrad
Monochromator / analyser:	channel-cut perfect Si crystals
Wavelength resolution	$\Delta\lambda/\lambda$ = 1·10^{-5} (λ = 0.443 nm)
Max. flux at deflecting crystal	Φ = 2.3 x 10^8 cm^{-2} s^{-1}
Flux at sample position:	$\Phi \approx 500$ cm^{-2} s^{-1} (Si(111), λ = 0.443 nm) $\Phi \approx 180$ cm^{-2} s^{-1} (Si(311), λ = 0.232 nm)
Range of momentum transfer:	1·10^{-5} nm$^{-1} \leq Q \leq$ 5·10^{-2} nm^{-1}
Detectors:	three ^{3}He-detectors
Control of crystal alignment:	electronic autocollimator, angular resolution < 0.05 μrad
Sample environment:	thermostat (5 °C to +80 °C) automatic sample change electro magnet with field up to > 0.9 T

![GKSS FORSCHUNGSZENTRUM in der HELMHOLTZ-GEMEINSCHAFT]	**EXPERIMENTAL REPORT**	**GeNF DCD**
Magnetic USANS investigations of **spin-misalignment fluctuations in Nanoperm (Fe$_{89}$Nb$_6$B$_{10}$)**		
Proposer:	**A. Michels**	
Co-Proposers:	**C. Vecchini, O. Moze, K. Suzuki, P. K. Pranzas,** **J. Weissmüller**	
Experimental Team:	**C. Vecchini, O. Moze, P. K. Pranzas, J. Weissmüller**	
User Group Leader:	**A. Michels**	
Date(s) of Experiment:	March 2006	

Objective

The objective of this experiment was to determine the magnetic-field-dependent characteristic length scale of spin-misalignment fluctuations in the prototypical nanocomposite soft magnet Nanoperm (Fe$_{89}$Nb$_6$B$_{10}$) by means of ultra small-angle neutron scattering (USANS).

Experiment

The USANS measurements were carried out at ambient temperature at the DCD camera using an incident wavelength of λ = 4.43 Å with a bandwidth $\Delta\lambda/\lambda$ = 1.0 $\times$ 10^{-5}. We were able to install an electromagnet into the DCD setup, which allowed us to apply a magnetic field of up to 900 mT to the sample. The direction of the applied magnetic field was perpendicular to the momentum-transfer vector.

Achievements and Main Results

The figure below shows the USANS intensity I as a function of the modulus q of the scattering vector at different applied magnetic fields. For q-values below about 0.0003 nm^{-1} the USANS signal does practically not depend on the applied field, an observation which suggests the absence of a significant change of magnetic scattering contrast at the smallest momentum transfers. On the other hand, the relatively strong field dependence of the scattering at the higher q-values demonstrates the existence of long-range magnetization fluctuations in Nanoperm with a characteristic length scale in the μm-range. This result is qualitatively consistent with our previous investigations on nanocrystalline Ni, Co and Tb [1,2], which have provided evidence that magnetic correlations in nanomagnets evolve on length scales of up to 100 nm.
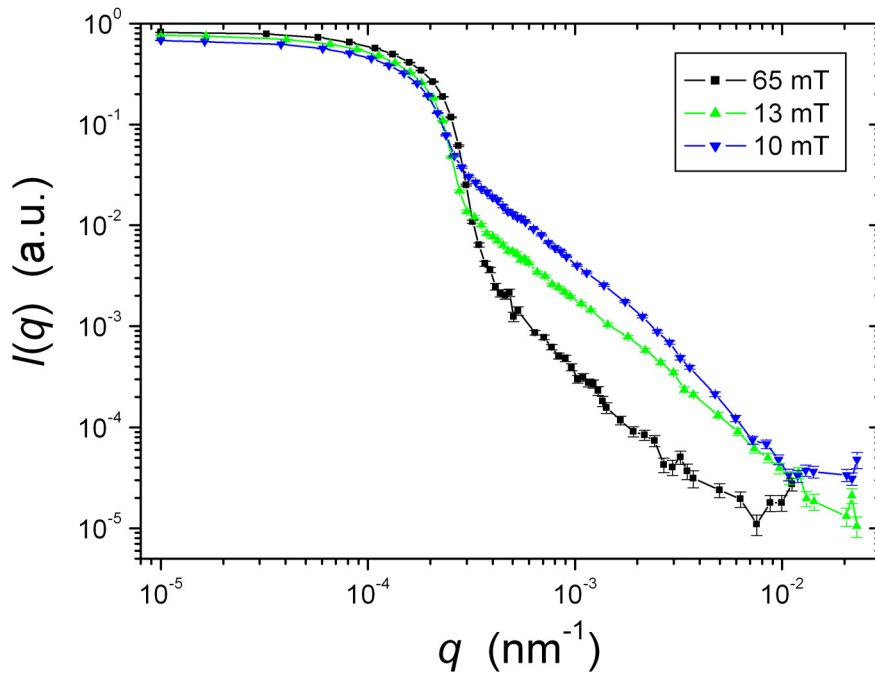
Figure 1: USANS intensity $I(q)$ of the alloy Nanoperm at different applied magnetic fields (see inset).

References

1. J. Weissmüller, A. Michels, D. Michels, A. Wiedenmann, C. E. Krill III, H. M. Sauer, R. Birringer, Phys. Rev. B **69**, 054402 (2004).

2. A. Michels, R. N. Viswanath, J. G. Barker, R. Birringer, J. Weissmüller, Phys. Rev. Lett. **91**, 267204 (2003).

![GKSS logo] GKSS FORSCHUNGSZENTRUM in der HELMHOLTZ-GEMEINSCHAFT	**EXPERIMENTAL REPORT**	**GeNF DCD**

U-SANS analysis of NiTi shape memory alloys treated by Impulse Electric Current Treatment		
Proposer:	**Dr, Giuliani, A.**	
Co-Proposers:	**Dr, Fiori, F.**	
	Prof, Dutkiewicz, J.	
Experimental Team:	**Dr. Giuliani, A.**	
	Dr. Calbucci, V.	
User Group Leader:	**Dr. Giuliani, A.**	
Date(s) of Experiment:	28th–31th August 2006	

Objective

We were interested in the investigation of fine structure changes in NiTi intermetallics as a result of high-density impulse electric current treatment (IECT). For steels, the fragmentation of structure (mosaic blocks), precipitating of tiny carbides with their migration from borders and pores / defects annihilation take place after IEC treatment: as a result, the enhancement of mechanical properties occurs. With the present experiment, we verified for the first time, these effects using U-SANS on NiTi shape memory alloys (SMA) produced by 3 different processing routes, namely (1)metal Injection moulding, (2) Combustion synthesis, (3) mechanical alloying and hot compaction.

Experiment

USANS was performed at the Double Crystal Diffractometer (DCD) instrument at the Geesthacht Neutron Facility (GeNF) (D) on NiTi samples before and after the IECT treatment. The DCD was equipped with triple-bounce channel-cut perfect Si crystals (Bellmann et al., 1998). Using the (111) reflection, the full width at half-maximum (FWHM) of the RC is about 2.6×10^{-4} nm^{-1} at a wavelength of $\lambda = 0.44$ nm.

DCD was used in the present work to analyse shape, size distribution and volume fraction of precipitates and pores and the effect of the IEC treatment on them.

A particle size distribution n(R) shall be defined in the radius interval [Rmin, Rmax]. It can be written as a linear combination of m basic size distributions $n_i(R)$ with coefficients xi:

$$N(R) = \sum_{i=1}^{m} x_i n_i(R) \tag{1}$$

Cubic B-splines are chosen for the basic size distributions ni(R). With such a set of basic functions, an arbitrary smooth function can be approximated (Glatter, 1977, 1980).

The basic size distributions are normalized and the basic volume distributions for spherical particles (we assumed that NiTi pores are spheres) $v_i(R)$ define the volume contained in each basic distribution V_i:

$$V_i = \int_{R_{min}}^{R_{max}} v_i(R) dR \tag{2}$$

We numerically treated both the samples (IEC treated and untreated) with a model based on two phases: the NiTi phase and another phase corresponding to the pores. This model is

called **two-phase model** and it is based on the assumption of the presence of particles (pores) with a size distribution N(R), embedded in a homogeneous matrix (polidispersion). The Master equation of such model is the following (e.g. Guinier & Fournet, 1955; Fedorova & Schmidt, 1978; Kostorz, 1979):

$$\frac{d\Sigma}{d\Omega} = (\Delta\rho)^2 \int_0^\infty N(R)V^2(R)|F(QR)|^2\, dR \tag{3}$$

where:

$$|F(\mathbf{Q})|^2 = \frac{1}{V_p^2}\left|\int_{V_p} e^{i\mathbf{Q}\cdot\mathbf{r}}\, dv\right|^2 \tag{4}$$

is called Form Factor and represents the nuclear contrast between the two phases. In our case, as previously mentioned, we considered the sphere-model form factor, being the pores approximately of spherical shape.

Achievements and Main Results
At the moment we already characterized, for the first time according to our review, the microstructure of NiTi SMA produced by Metal Injection Moulding (MIM), before and after the high-density impulse electric current treatment (IECT). The analysis of data obtained on NiTi samples produced by combustion synthesis or by mechanical alloying and hot compaction is under processing and will be completed in the next week.
Ultra-Small Angle Neutron Scattering (U-SANS) Analysis was performed on the samples because we basically verified, by this technique, pores size dimension variation before and after the IECT in the dimensional range between 100 nm and 45 microns.

In NiTi samples produced by MIM we obtained the following results : while for pores with diameter smaller than 3-5 μm the IECT was demonstrated to cause coalescence phenomena, in pores with diameter bigger than 5 μm the IECT was found to be responsible of an opposite behavior similar to what happens for steels, where fragmentation of the structure, precipitating of secondary phases and pores / defects annihilation take place after IECT.

References

[1] Conrad H (1998). Some effects of an electric field on the plastic deformation of metals and ceramics, Mat Res Innovat; 2:1–8.
[2] Sprecher AF, Mannan SC, Conrad H (1986) Acta Metall 34: 1145.
[3] Conrad H, Sprecher AF (1989) The electroplastic effect in metals. In: Nabarro FRN (ed) Dislocations in solids, chapt 43. Elsevier Science Publ BV, p 499.
[4] Cao W, Sprecher AF, Conrad H (1991) The electroplastic effect in niobium in high temperature niobium alloys. In: Stephens JJ and Ahmed I (eds) High temperature niobium alloys. TMS, Warrendale, PA, p 27.
[5] Cao W, Conrad H (1995) Effect of stacking fault-energy and temperature on the electroplastic effect in FCC metals. In: Chu S et al. (eds) Micromechanics of advanced materials. TMS, Warrendale, PA, p 225.
[6] Cao W, Lu X, Sprecher AF, Conrad H (1990) Superplastic behaviour and microstructure of 7475 Al deformed in an external electric field. In: McNelly T, Heikkenean H (eds) Superplasticity in aerospace II. TMS, Warrendale, PA, p 269.
[7] Cao WD, Lu X, Sprecher AF, Conrad H (1990). Mater Sci Engr. A;138:247.
[8] Conrad H, Cao W, Lu X, Sprecher AF (1991). Mater Sci Engr. A;138:247.
[9] Lu XP, Cao W, Sprecher AF, Conrad H (1992). Jnl Mater. Sci.; 27:2243.
[10] Cao WD, Lu XP, Conrad H (1996). Acta Mater.; 44:6976.
[11] Hwang SL, Chen IW (1990). J Amer. Ceram. Soc.; 73:3269.
[12] Bellmann, D., Klatt, M., Kampmann, R. &Wagner, R. (1998). Physica B, 241±243, 71±73.
[13] Glatter, O. (1977). J. Appl. Cryst. 10, 415±421.
[14] Guinier, A. & Fournet, G. (1955). Small-Angle Scattering of X-rays. New York: Wiley.
[15] Kostorz, G. (1979). In Treatise on Materials Science and Technology, Vol. 15, Neutron Scattering, edited by G. Kostorz & H. Herman. New York: Academic Press.

USANS investigations of organized nanostructures of diblock copolymers in immiscible solvents	
Proposer:	**Ryukhtin Vasyl**[1], [1] Nuclear Physics Institute, Academy of Sciences of the Czech Republic, 25068 Řež near Prague, Czech Republic
Co-Proposers:	**Stepanek Petr**[2], **Tuzar Zdenek**[2] [2] Institute of Macromolecular Chemistry, Heyrovský Sq. 2, 16206 Prague 6, Czech Republic
Experimental Team:	**Pranzas Klaus**[3], [3] Forschungszentrum Geesthacht, Postfach 1160, D-21494 Geesthacht, Germany
User Group Leader:	**Pranzas Klaus**[3]
Date(s) of Experiment:	18th September–1st October 2006

Objectives

Block and graft copolymers in applicable solvents can form various microstructures and thus influences properties of the whole studied system, *e.g.*, they can stabilize particles of colloidal dimensions or "compatibilize" immiscible homopolymers. Such systems found numerous applications in many sectors of industrial technology. The long-range-ordered nanostructures have been found in the solutions of diblock copolymers in two partially miscible solvents. Such self-ordered nanostructures are formed by periodically arranged domains of solvents, stabilized by the block. Our recent investigation of such systems by small-angle neutron scattering (SANS) has shown that the ordered structure has either a hexagonal or cubic symmetry with period of 60-110 nm. The long range periodic structure is limited in extend, typically it consists of grains that have an expected size of about several μm, as was estimated by birefringence measurements on similar systems. The grains (of typical size of several μm) can neither be observed by dynamic light scattering (relaxation time of the grains is too large) nor be detected by birefringence measurements as described for polymer melts, because in this case the two used solvents are isorefractive and the resulting structure is not birefringent.

Our previous USANS investigations of the solutions with hexagonally ordered microstructure has shown strong dependence of grains structure on temperature and cooling regime. The presented USANS experiment was aimed to describe microstructure of grains in the cubically ordered solutions.

Experimental

We have measured on DCD-SANS the scattering functions of several polymer systems consisting of the mixture (deuterated) d-CX (10%-20%) and DMF (6%, 8.2% and 10.1%) and the diblock copolymer poly(styrene-b-butadiene) (SB (16-79), c=20 %) at room temperature (~21 ^{0}C), 30 ^{0}C and 40 ^{0}C. The measurements were carried out at wavelength 4.43 Å.

Results

USANS data were fitted by model of log-normal distribution of incoherent spheres by means of SASProfit [1] program based on indirect Fourier Transformation method (see Fig. 1). Volume-weighed size distributions obtained from data fitting are shown in Fig. 2. However, scale of the size distribution is not in absolute units but in arbitrary since exact scattering length contrast can not be defined for such material. Moreover, the scattering contrast can be depended on temperature. Nevertheless, it does not influence on the results of mean sizes of the studied grains.
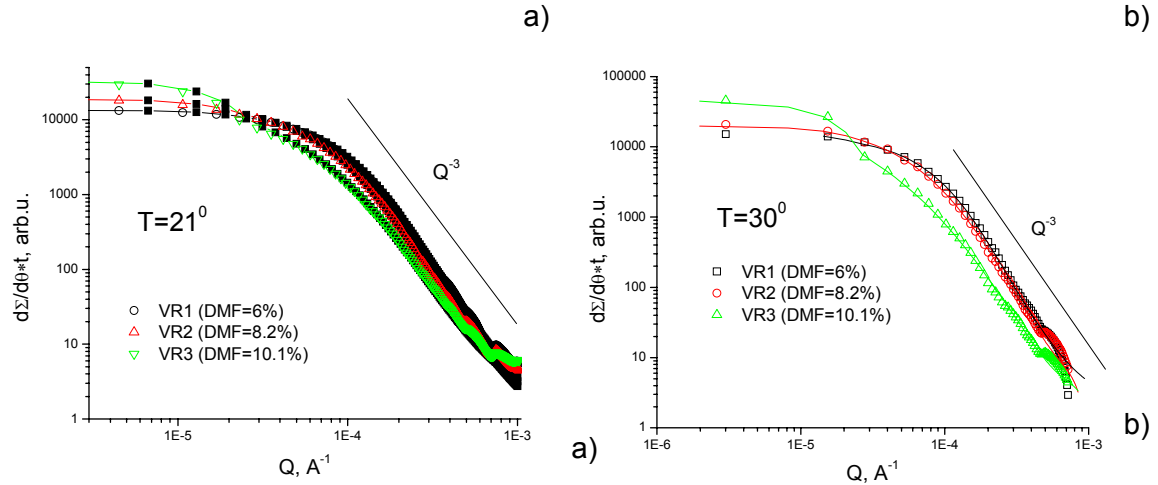
Fig. 1: Scattering functions with fitted models (lines) measured at room temperature (a) and 30 ^{0}C (b).
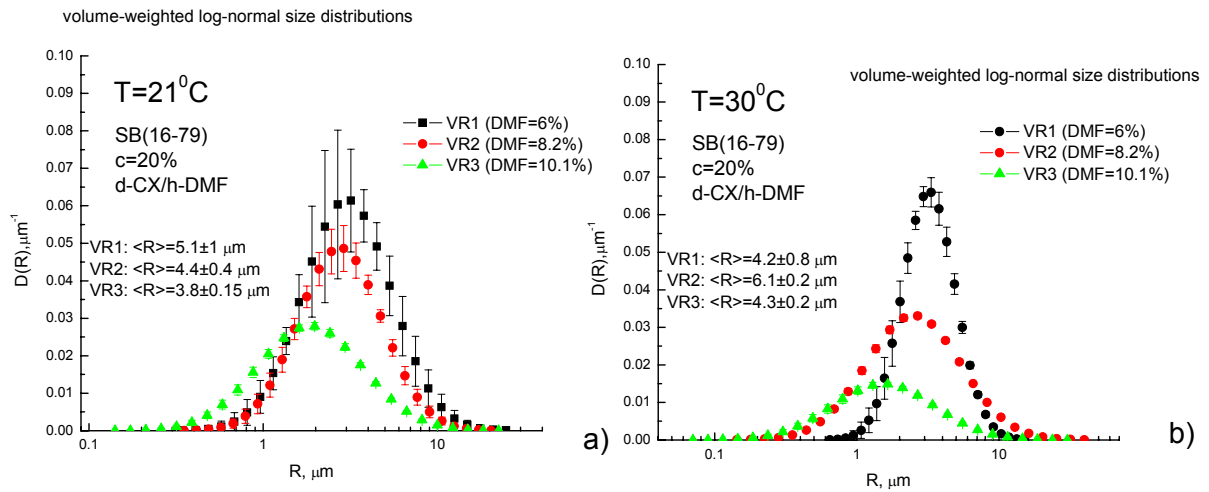
Fig. 2:. Volume-weighted size distributions for measurements at room temperature (a) and 30 ^{0}C (b).

The obtained size distributions are rather wide (see Fig. 2). Mean sizes of the grain are about 4-6 μm for the samples. There is no systematic dependence of the sizes on temperature. However, the position of maximum slightly shifts toward smaller values with increasing concentration of DMF for all temperatures.

Conclusions

The formation of the grains in the diblock copolymers in partially miscible solvents was studied by USANS. It was shown that the mean size of the grains is almost independent on temperature for solutions with cubic microstructure in contrast to hexagonal ordered ones [2]. We can conclude that studied grain microstructure in these solutions is more stable with temperature in comparison with hexagonally ordered solution.

References

1. P. Stepanek, F. Nallet, Z. Tuzar and Nirez, Macromolecules, 38, 3426-3431 (2005)
2. V. Ryukhtin, P. Stepanek, Z. Tuzar, K. Pranzas, USANS investigations of solutions of diblock copolymers in partially miscible solvents. Physica B 385-386 (2005) 762-765.

![GKSS FORSCHUNGSZENTRUM in der HELMHOLTZ-GEMEINSCHAFT]	**EXPERIMENTAL REPORT**	**GeNF PNR**
	Reflectometer for polarised neutrons PNR	

Short Instrument Description

The polarised neutron reflectometer is used to study magnetic and non-magnetic surfaces, layers, thin films and membranes using cold non-polarised or polarised neutrons with high flux.

Local Contact:

Dr. Danica Solina
Phone/Fax : +49 (0)4152 87 – 1373 / +49 (0)4152 87 – 1338
e-mail: danica.solina@gkss.de

Schematic View of PNR:
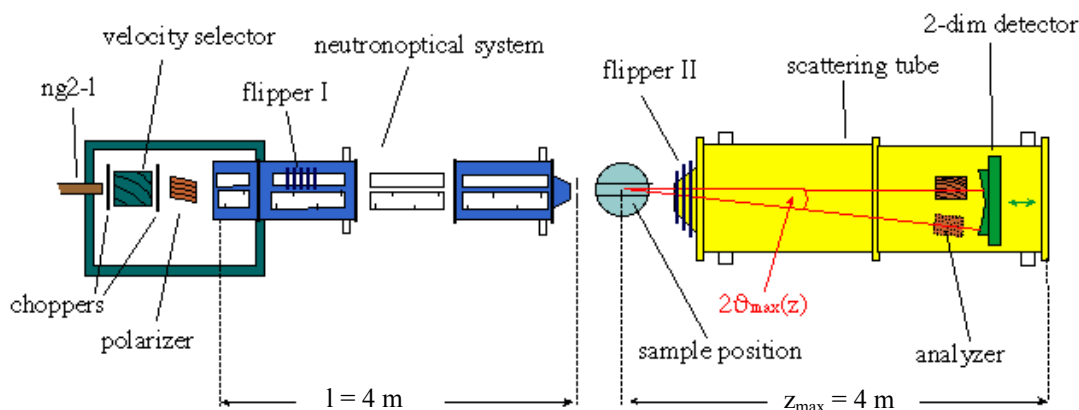
Instrument Details:

Beamline:	beamline 8 (NG-2I), cross section 30 x 40 mm^2
Monochromator:	helical slot selector
Wavelength:	$\lambda \geq 0.635$ nm
Wavelength resolution:	$\Delta\lambda/\lambda = 0.05$
TOF equipment:	2 choppers, to be used if a resolution better than 0.05 is required
Polariser:	transmission polariser
Analyser	set of bent supermirrors
Spin flipper:	hf-flipper
Collimation lengths:	4 m
Flux at sample position: (beamsize: 0.5 x 40 mm^2)	$\Phi_{nonpol} = 1 \cdot 10^5$ cm^{-2} s^{-1} (unpolarised) $\Phi_{pol} = 3 \cdot 10^4$ cm^{-2} s^{-1} (polarised neutrons)
distance sample-detector:	3 m to 4 m
angular range:	$0° \leq 2\theta \leq 8°$
Detector:	2-dim position-sensitive ^{3}He-counter
Ancillary equipment:	- refrigerator cryostats – temp.-range: 4 – 475 K - electro magnet up to 0.9 T with closed cycle refrigerator (8 - 300 K) suitable for polarised neutrons

GKSS FORSCHUNGSZENTRUM in der HELMHOLTZ-GEMEINSCHAFT	EXPERIMENTAL REPORT	GeNF-PNR

Report on the measurement of a D7-type supermirror on PNR

Principal Proposer: A. Wildes [1]; [1]ILL
Experimental Team: A. Wildes and D. M. Solina
Date(s) of Experiment: April 2006

Scientific Objective

An m = 2.8, D7-type Fe/Si polarizing supermirror in a saturating field should have neutron spin-flip reflectivities that are equal and negligible. Such a sample can therefore be used to calibrate the polarizing efficiency of the different elements on a neutron reflectometer. When this was attempted on the D17 reflectometer at the ILL, a strange effect was seen. It appeared that the spin-flip reflectivities were equal and zero below the m = 2.8 cut-off, however above the cut-off one of the spin-flip reflectivities became finite. In order to test the observations, a short experiment was performed at the PNR instrument at the GKSS, using polarization analysis.

Experimental Technique

The instrument was configured with polarization analysis and a field was applied to the sample by means of an ADAM-style electromagnet. The sample was subjected to a field of ~1000 Oe, which is believed to make the sample mono-domain. A diagram of the instrument configuration is shown in Figure 1.
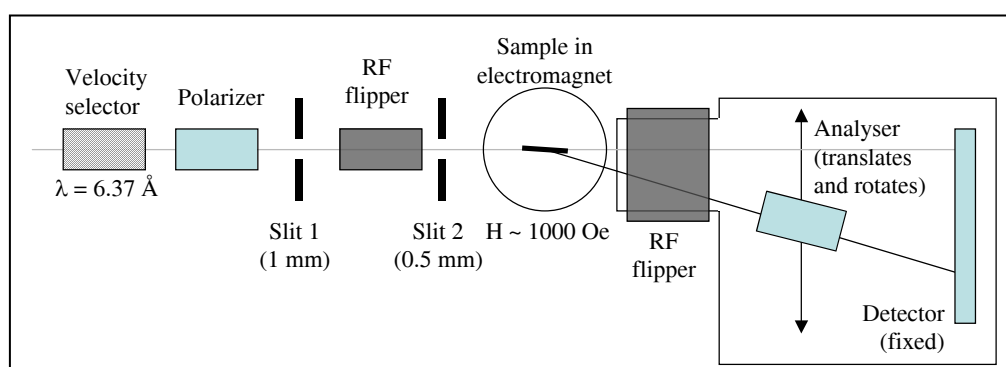
Figure 1: Schematic showing the experimental set up for the PNR experiment.

Results and Preliminary Conclusions

The instrument polarizing efficiency was calibrated using standard methods [1]. Measurements of the main beam gave correction terms:

ϕ = -0.939 +/- 0.003 (NOTE, ϕ is NEGATIVE because the polarizer and analyser are CROSSED)
F1 = 0.9883 +/- 0.0008
F2 = 0.979 +/- 0.008

On measuring the supermirror, the efficiencies of the polarizer and the analyser could be separately determined to be:

P = 0.978 +/- 0.001
A = 0.0095 +/- 0.002.

Two sets of measurements were performed: a series of measurements with no analysis; and a series of measurements with analysis.

The measurements without analysis showed a strong specular peak with significant off-specular scattering. The measurements are shown in Figure 2. Missing, however, was scattering that could be explained by the gain or loss in energy of a neutron that has undergone spin-flip scattering in a field. This is evidence that there is no strong specular spin-flip scattering coming from the sample.
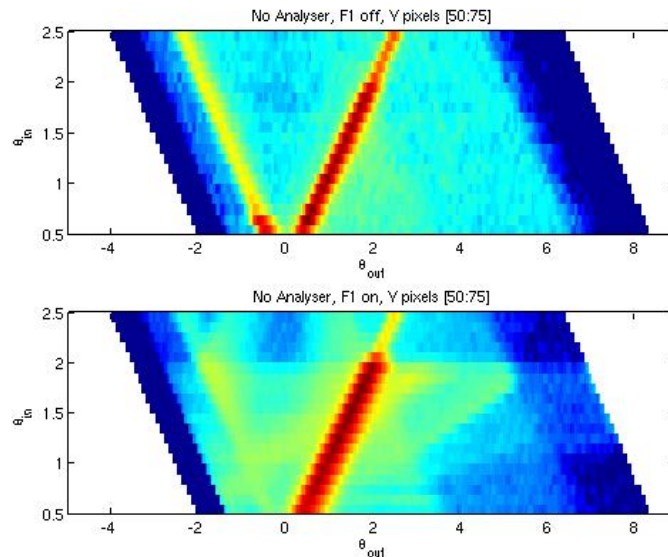
Figure 2: The measurements made without analyser, integrated between y-pixels 50:75 and plotted as a function of θ_{in} / θ_{out}.

Measurements with the analyser, corrected for the polarizing efficiency of the instrument, are shown in Figure 3. There are two points to note: the first is that the spin flip data is everywhere equivalent, thus contradicting the observation on D17; the second is that the spin flip data is less than zero below the supermirror cut off. This is unphysical, and can be directly attributed to an error in estimating the value of ϕ – if ϕ is too small, the data will be overcorrected and can appear to be negative. This is particularly likely if the cross-sections are zero, as was expected for the supermirror. Increasing the value of ϕ by 3% is enough to make the spin flip scattering equal zero for all θ.
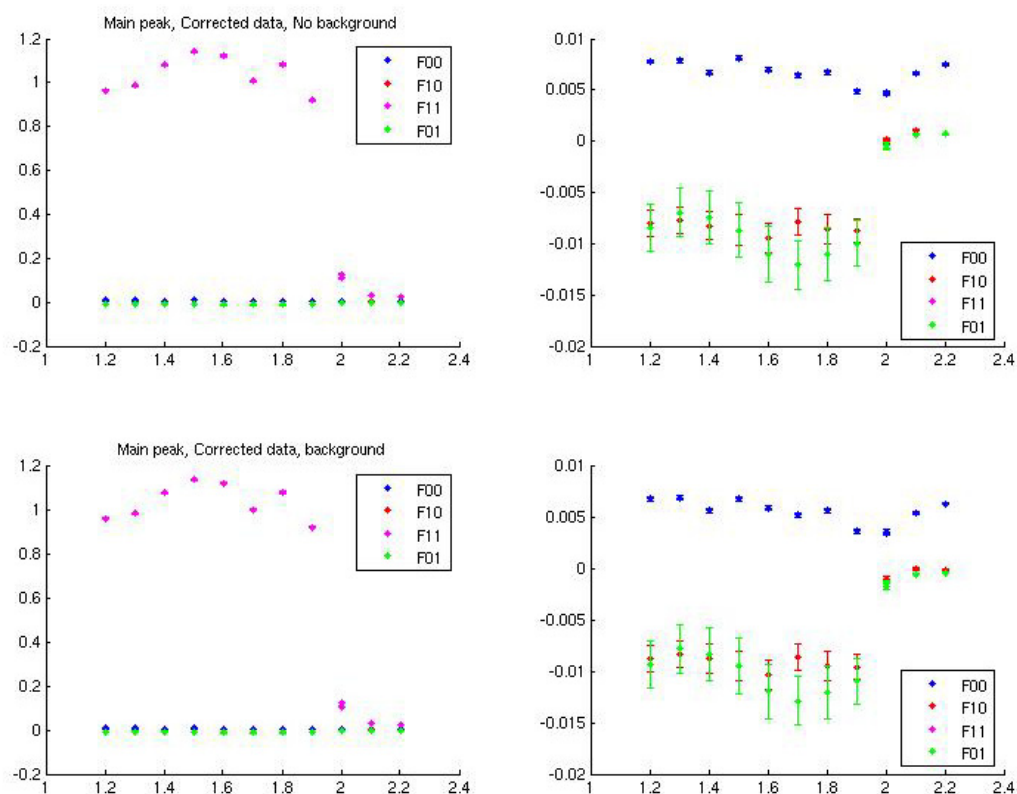
Figure 3: The data with polarization analysis, corrected for polarization inefficiency. The data are shown on both a log scale (left) and a linear scale (right).

Following these results, the D17 instrument was closely looked at and a design flaw was discovered in the first flipper. Plans are now being developed to rebuild this device in combination with further improvements to the D17 primary spectrometer.

References

[1] A. R. Wildes, Neutron News **17(2)** (2006) p. 17

Neutron reflectometer NeRo

Short Instrument Description

The Neutron Reflectometer NeRo is designed for measurements of thin film systems including polymer and magnetic systems using cold non-polarised / polarised neutrons with high resolution.

Local Contact:

Dr. Dieter Lott
Phone/Fax : +49 (0)4152 87 – 1372 / +49 (0)4152 87 – 1338
e-mail: dieter.lott@gkss.de

Schematic View of NeRo:
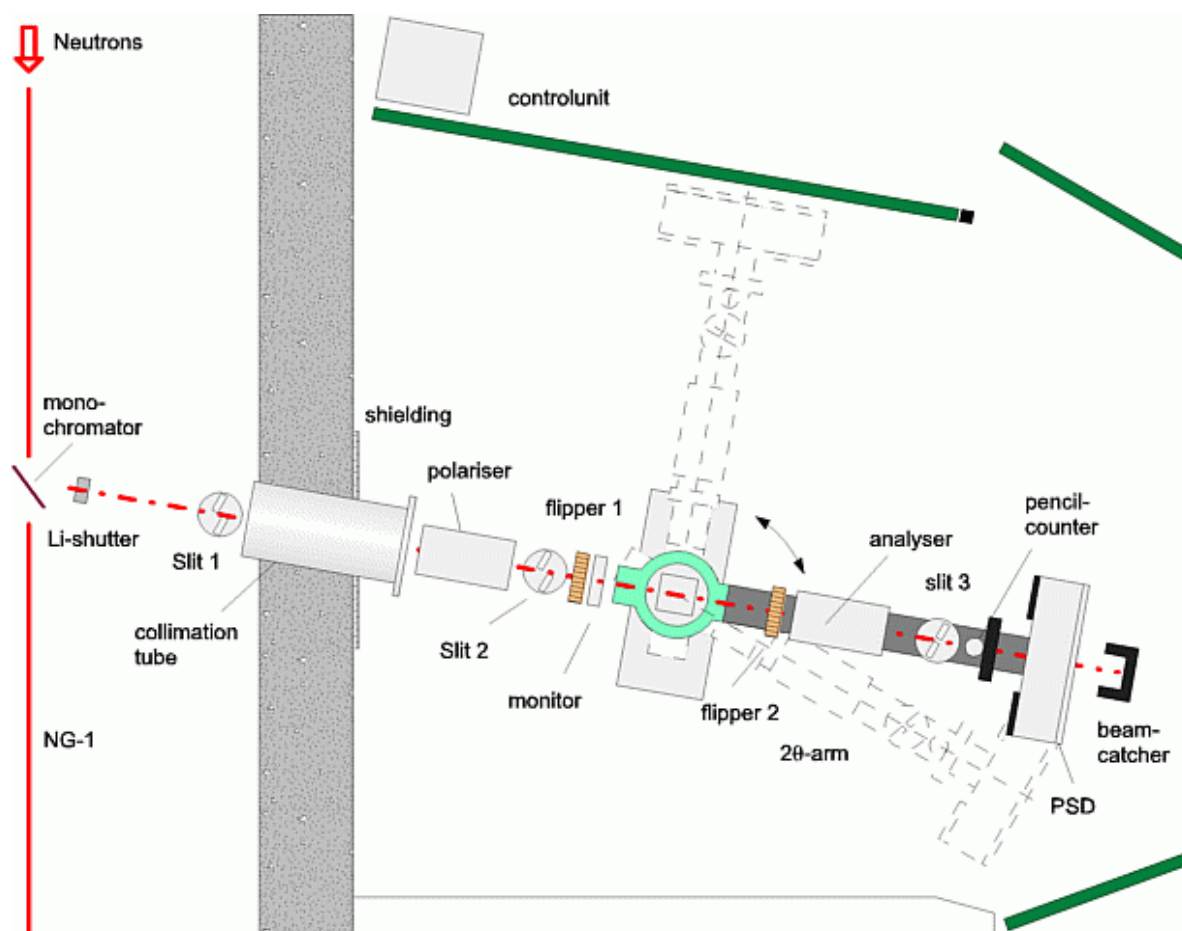
Instrument Details:

Beamline:	beamline 8 (NG-1)
Wavelength:	λ = 0.433 nm;
Wavelength resolution	$\Delta\lambda/\lambda$ = 0.02
Angular range	-20° ≤ θ ≤ 100°
Flux at sample position:	$\Phi = 5 \cdot 10^4$ cm^{-2} s^{-1} (unpolarised, standard collimation)
Detectors:	2-dim position-sensitive ^{3}He-counter ^{3}He pencil counter
Polarisation equipment:	Transmission polariser / analyser 2D-analyser: super-mirror stack for measurements of magnetic diffuse reflectivity 2 Mezei-flippers
Ancillary equipment:	Several refrigerator cryostats - temp.-range: 4 - 475 K electro magnet with field up to 0.9 T cryo-magnet with field up to 5 T

Neutron reflectometry on complex coacervate core micelles adsorbed to the solid-liquid interface		
Proposer:	**Roland Steitz**	
Co-Proposers:	**Ilja Voets, Gerhard H. Findenegg**	
Experimental Team:	**Roland Steitz, Ilja Voets, Wiebe de Vos, Ari de Keizer**	
User Group Leader:	**Roland Steitz**	
Date(s) of Experiment:	8th–16th May 2006	

Objectives

Coating surfaces with polymer brushes has been a topic of great scientific interest for many years. One of the most important applications is antifouling, which can be used for instance in medicine (contact lenses, implants), membrane technology (water purification) and cleaning.

Complex coacervate core micelles (C3Ms), also known as polyion complex micelles or block ionomer micelles, spontaneously physisorb on a variety of surfaces [1]. They form from (i) a diblock-copolymer with an anionic block and a water-soluble neutral block, and (ii), a cationic homopolymer, or (iii), a diblock-copolymer with a cationic block and a water-soluble neutral block under the right mixing conditions in aqueous solution (see Fig. 1).

It is expected that the coacervate core attaches to the surface, while the neutral polymer blocks stick out into the solution. To render a surface antifouling, one would simply dip it into a C3M solution. C3M layers were shown to be very good anti-fouling agents (decrease of >95% adsorption of lysozyme on silica).
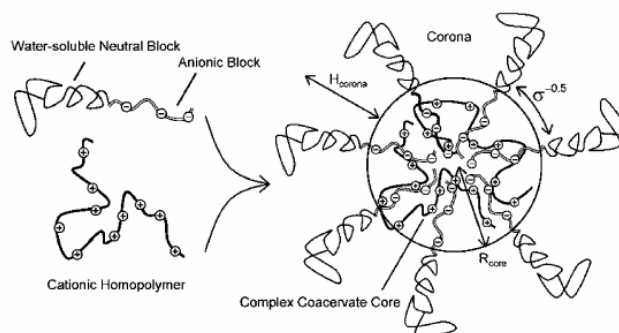
Fig. 1: Formation of C3Ms in aqueous solution. Taken from [1]

The formation of adsorbed layers of C3Ms (2 - 4 mg/m^2) on hydrophobic and hydrophilic substrates was revealed by optical reflectometry [1]. Light scattering experiments on C3M-coated silica beads indicated a thickness of the coating of ca. 250 Å [1], while preliminary AFM experiments did not indicate any surface structures, suggesting that a homogeneous layer was formed.

Experiment

Complex coacervate core micelles were produced by mixing aqueous solutions (0.1g/l, 10mM NaNO$_3$, pH=7.2) of (i) P(BNH$_3$Cl)$_{65}$-P(EO)$_{212}$ (20.2 kDa) and (ii) P(BCOOH)$_{65}$-P(EO)$_{212}$ (19.8 kDa) at a mixing fraction of polymer (i) to total polymer (i+ii) of 0.482. The (premixed) solution was brought into contact with the substrate surface in a flow cell designed for neutron reflectivity studies at the solid-liquid interface [2].
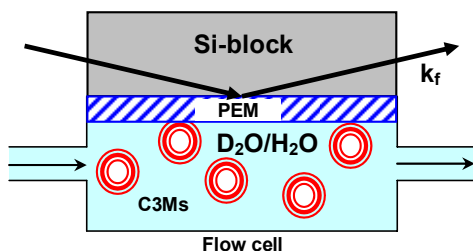
Fig. 2: Sketch of the exp. setup.

The incident monochromatic neutrons (λ = 4.34 Å) impinged on the solid-liquid interface through a silicon single crystal block (80 x 50 x 15 mm^3) which formed the basis of the substrate (Fig. 2). Experiments were conducted on a silicon block coated with a thin polyelectrolyte multilayer, Si/PEI/(d-PSS/PAH)$_6$ from the respective polyelectrolytes PEI (polyethyleneimine), d-PSS (deuterated polystyrene sulfonate) and PAH (poly-allyl-hydrochloride). A coating of approximately 300 Å thickness was prepared by "layer-by-layer" deposition [3] on the silicon single crystal.

Polyelectrolyte multilayers (PEMs) absorb substantial amounts of water [4]. The scattering length density (SLD) of the coatings and of the water phase can thus be matched by using appropriate mixtures of D_2O and H_2O, and in this way the polyelectrolyte/water interface can be made invisible to the impinging neutrons in the absence of the adsorption layer.

Achievements and Main Results

Figure 3, top curve, shows the reflectivity of the Si/PEM/D_2O interface with well pronounced Kiessig oscillations. Those fringes originate from partial reflection at the Si/PEM and PEM/D_2O interface, respectively. From a series of subsequent experiments the match point condition was found at 82.6 vol-% D_2O + 17.4 vol-% H_2O or SLD = $5.16 \cdot 10^{-6}$ Å^{-2}. Consequently, the reflectivity curve of the PEM layer against the indexed-matched water (IMW) did not show any Kiessig oscillations (Fig. 3, middle curve). It was only after incubation with a diluted disperison of C3Ms in indexed-matched water that the Kiessig oscillations in the spectrum could be retrieved, see Fig. 3, bottom curve. The latter result is a clear signature of the C3M adsorption layer

Fig. 3: Neutron reflectivity from the Si/PEM/D_2O, Si/PEM/IMW, and Si/PEM/C3M/IMW interface. Curves are offset on the y-axis by factors of 10.

formed at the PEM/liquid interface. First analysis employing a single box model yielded a thickness of the adsorbed C3M layer of 33 Å with a scattering length density ($5.16 \cdot 10^{-6}$ Å^{-2}) lower than that of PEM and indexed-matched water. The thickness of the C3M layer was about 8 times smaller than that as seen by light scattering experiments, d = 250 Å [1]. However, the applied one-box model cannot distinguish between collapsed coacervate part and diluted, heavily water-swollen brush part of the C3M adsorption layer. Hence, it is most likely that this model is exclusively sensitive to the adsorbed coacervate sub-layer. Further analyis taking into account additional results obtained from different contrasts and refined models are under way.

References

[1] van der Burgh et al., Colloids and Surfaces A, 242, 167-174 (2004).
[2] Howse et al., J. Chem. Phys. 116, 7177 (2002).
[3] G. Decher, Science 277, 1232 (1997).
[4] Steitz et al., Colloids and Surfaces A. 163, 63-70 (2000).

![GKSS logo] GKSS FORSCHUNGSZENTRUM in der HELMHOLTZ-GEMEINSCHAFT	**EXPERIMENTAL REPORT**	**NeRo**

Neutron reflectometry on a thin epitaxial Ni film on Si(100) substrate		

Principal Proposer:	W. Kreuzpaintner[1] [1] GKSS Forschungszentrum GmbH, Max-Planck-Straße 1 21502 Geesthacht
Experimental Team:	W. Kreuzpaintner[1], D. Lott[1]
Date(s) of Experiment:	16th October 2006

Introduction

In the last decades the growth of thin metallic films on silicon substrates has been widely studied [1, 2, 3]. Amongst these metals the ferromagnetic elements are of particular interest because the low defect epitaxial growth of these elements on a silicon substrate could hold the key to a comprehensive use of magnetic properties in electronic devices like non-volatile Magnetic Random Access Memory (MRAM) or devices which utilize spininjection. Especially the epitaxial growth of Ni appears problematicas only twinned growth on Si could be observed so far, leading to an unwanted anisotropy in the magnetic properties [4].

Although, in general it is assumed that epitaxial growth can only be achieved by low energy adsorbates and low deposition rates, the epitaxial growth of Ni on Si by means of magnetron sputtering was found to allow for the deposition of low defect thin epitaxial Ni films. For this the deposition process is stopped after an initial nickel seed and then continued with readjusted deposition parameters.

During the optimisation of the deposition parameters, the epitaxial and structural properties of the Ni film were studied using out-of plane and in-plane x-ray diffraction (XRD) and x-ray reflectometry (XRR), giving information about the layer structure and epitaxial realtionship which was found to be Ni[110]||Si[100].

Of particular interest was the continuity of the magnetic properties, as the layer was deposited in 2 steps, which was found did not influence the continuity of the crystalline structure, but the effect of the interruption during the deposition process on the magnetic structure was unknown and needed to be investigated by a depth sensitive technique.

Hence, we here report on a neutron reflectivity investigation which -- complementarilly to the results gained by x-ray methods -- addresses the magnetic continuity of the deposited Ni film.

Experimental

For the experiment a (by x-ray methods) pre-characterized thin epitaxial Ni layer with a total thickness of 75 nm which was deposited in 2 steps as described above, was analysed by polarised neutron reflectometry.

Measurements were performed at room temperature for the as-deposited Ni film without any previously applied external field in the range of 0.01 Å⁻¹ to 0.09 Å⁻¹ in Q_z. The measurements were repeated in an applied external magnetic field of 70 mT parallel to the film surface, which was sufficient to saturate the magnetic moments in the Ni film.

Results and discussion
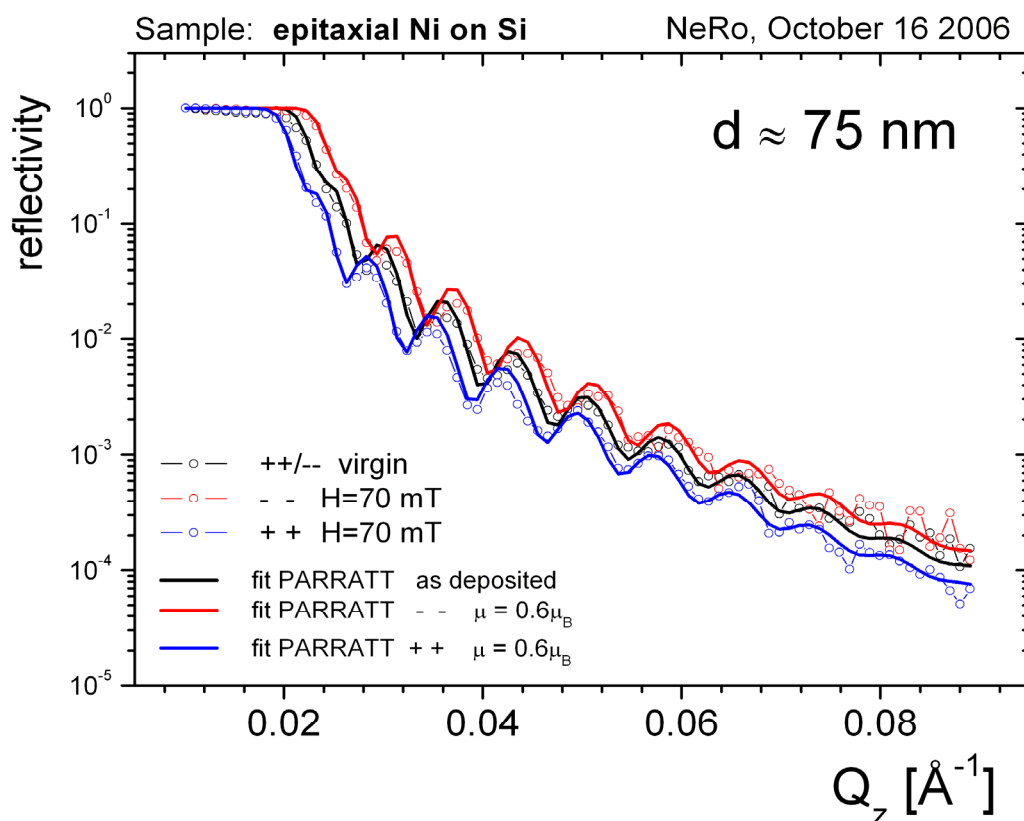
Figure 1: Neutron reflectivity curves from the epitaxial Ni film on Si substrate.

Figure 1 shows the reflectivity of the Si/Ni/Air interfaces with well pronounced Kiessig oscillations for all three measurements. The oscillations correspond to a film thickness of about 75 nm. Due to the contribution of the magnetic moments to the scattering length density, a shift in the reflectometry curve for spin up and spin down polarisation towards lower or higher values in Q_z is observable. By fitting the experimental results to theoretical models using the PARRAT32 1.5.2 software package, it was found that the magnetic layer was fully magnetized to a thickness which is equivalent to the structural thickness of the Ni film. The magnetic momentum of the Ni layer could be determined as $\mu = 0.6 * \mu_B$.

Combining these results with the results gained by x-ray diffraction and reflectometry it can be concluded that neither the structural nor magnetic properties of the epitaxial Ni-layer are influenced by stopping the deposition process after a Ni seed layer before continuing with the deposition of the remaining Ni to its final thickness.

References

[1] Chin-An Chang. *Magnetocrystalline anisotropy of (100) face-centered cubic Co structures deposited on Cu/Si(100).* Applied Physics Letters, 58(16):1745–1747, April 1991.

[2] Chin-An Chang, Joyce C. Liu, and Joseph Angileilo. *Epitaxy of (100) Cu on(100) Si by evaporation near room temperatures: In-plane epitaxial relation and channeling analysis.*
 Applied Physics Letters, 57(21):2239–2240, November 1990.

[3] Yang-Tse Cheng, Yen-Lung Chen, M. M. Karmarkar, and Wen-Jin Meng. *Epitaxial growth of Fe films on Si(111) substrates.* Applied Physics Letters, 59(8):953–955, August 1991.

[4] L. Wray and M. Prutton. *The Structure of Nickel and Cobalt Films on the (111) Surface of n-type Silicon.* Thin Solid Films, 15:173–180, 1973.

![GKSS logo] GKSS FORSCHUNGSZENTRUM in der HELMHOLTZ-GEMEINSCHAFT	**EXPERIMENTAL REPORT**	**GeNF NeRo**

Field-induced chirality of the spiral spin structure in Dy/Y multilayer system		
Proposer:	**Yury Chetverikov[1]**, [1]PNPI, Gatchina, St-Petersburg, Russia	
Co-Proposers:	**Sergey Grigoriev[1],** **Alexey Okorokov[1],**	
Experimental Team:	**Yury Chetverikov,** **Dieter Lott[2],** [2]GKSS Forschungszentrum	
User Group Leader:	**Sergey Grigoriev**	
Date(s) of Experiment:	5th–19th November 2006	

1. Objectives. The nature of the planar helical - paramagnetic phase transition in dysprosium and holmium has attracted much attention both from a theoretical and experimental point of view. In our previous work [1] we used the advantages of polarized neutrons to study the critical chirality of the Dy/Y multilayer system. As shown in [2, 3], the differential cross section for the elastic neutron scattering from the magnetic helix below T_N can be represented as:

$$\sigma_{el}(q) = [r\ S\ F(q)/2]^2 \{1 + (\mathbf{q\hat{c}})^2 + 2(\mathbf{qP_0})(\mathbf{q\hat{c}})(n_L - n_R)\}\ \Delta_{\mathbf{q+k}} \qquad (1)$$

where r = 0.54 x 10^{-12} cm, $\mathbf{\hat{c}} = [\mathbf{S_1} \times \mathbf{S_2}]/S^2$; $\mathbf{q} = \mathbf{q}/q$; $\mathbf{k}$ magnetic helix wavevector and $\Delta_{\mathbf{q\pm k}} = [(2\pi)^3/V]\ \delta(\mathbf{q \pm k})$, and V is the volume of the low-level cell. The cross section depends on the mutual orientation of the $\mathbf{P_0}$ and $\mathbf{\hat{c}}$. When $\mathbf{P_0} \parallel \mathbf{\hat{c}}$, then the scattering is fully polarized at $\mathbf{q} = \pm \mathbf{k}$. When $\mathbf{P_0} \perp \mathbf{\hat{c}}$, then the scattering is fully depolarized at $\mathbf{q} = \pm \mathbf{k}$. n_L and n_R are the population numbers of the left and right handed helixes and $n_L + n_R = 1$. The polarization independent part of the magnetic scattering is proportional to the square of the staggered magnetization $<\mathbf{S_z}>^2$ while the polarization dependent part of this scattering is proportional to the average chirality $<\mathbf{C}> = [\mathbf{S_{R1}} \times \mathbf{S_{R2}}]$. In the previous experiment [1] we had found non-equal helix domain population numbers in the system. It was also found that the critical exponents of the helical - paramagnetic phase transition for staggered magnetization β is equal to *0.40* and the average chirality $\beta_C = 1.02$. From the difference $\beta_C - 2\beta = 0.22$ it is clear that the critical behavior for the average chirality deviates from that for the staggered magnetization. Our findings are in agreement with those found in [4].

The phenomenon of the non-equal spiral domain population could stem from the several sources. The first one is the stress in multilayer structure, which leads to a torsion deformation of the superlattice. It is known that such a deformation may create non-equal domain population [4]. The second one is the random statistical distribution of the right- and left-handed domains, so that $\Delta n = n_L - n_R \sim (n_L^2 + n_R^2)^{1/2}$. The third one is Dzyaloshinskii-Moria interaction on the surfaces of the multilayer structure. The present experiment was aimed to establish what is the force stabilizing the system with non-equal spiral domain population. The other aim, related to the first one, was to determine the origin of the difference $\beta_C - 2\beta = 0.22$. According to Kawamura hypothesis [5] the difference $\beta_C - 2\beta = 0.22$ suggests that chirality is a component of the order parameter independent of the staggered magnetization. In this case it is assumed that $\Delta\sigma(T) \sim <C>$, just as it was done in [4], and the difference in domain population $\Delta n = n_L - n_R$ is temperature independent. There is an alternative explanation if one assumes the temperature scaling of the population number difference Δn. In this case $\Delta\sigma(T) \sim S^2(T) * \Delta n(T)$ where $S^2(T) \sim \tau^{2\beta}$, while $\Delta n(T) \sim \tau^{\beta_C - 2\beta}$. The change of Δn suggests that the domain topology (its size and, perhaps, its shape) changes with temperature.

2. Sample. The sample is a superlattice of the layer sequence $Y_{50\,nm}[Dy_{4.3\,nm}/Y_{2.8\,nm}]_{350}/Y_{234\,nm}/Nb_{200\,nm}Al_2O_3$(substrate), which was grown along the c-axis of the hcp-structure of Dy and Y, the same as used in [6]. The anisotropy of the crystal fixes the direction of the magnetic spirals *k* along the *c*-axis. In this Y/Dy superlattice, a coherent helical phase occurs at $T<T_N$, and extends over several bilayers. It is supposed that a helical spin density wave is induced by the charge wave of the Y conduction electrons but not by the scalar Ruderman-Kittel-Kasuya-Yosida coupling between the Dy planes on either side of the Y layer.

3. Experimental Technique. The experiments were carried out at the NeRo reflectometer of FRG-1 research reactor in Geesthacht (Germany). A polarized beam of neutrons with the initial polarization of $P_0=0.95$, the neutron wavelength $\lambda=4.33$ Å ($\Delta\lambda/\lambda=0.02$) was used. The scattered neutrons were detected by the position sensitive detector (PSD) with (256x256) pixels. The multilayer sample was oriented in such a way that the c-axis was set almost perpendicular to the incident beam. This geometry allows one to observe neutron diffraction peak from incommensurate helix structure. The polarization followed the direction of the guide magnetic field of order of 1 mT, which was applied perpendicularly to the incident beam and perpendicularly to multilayer surface (along c-axis). The additional magnetic field **H** from 10 to 900 mT could be applied, when necessary, perpendicularly to the incident beam and parallel to multilayer surface. The scattering intensity was measured in the temperature range from T=100 to T=200 K for two incident polarizations $I(\pm P_0)$ along and opposite to the guide magnetic field.

4. Results. The magnetic Bragg peak is observed at |**q**| (2.6 nm^{-1} (q || c) below TN = 166 K and its intensity increases with decreasing temperature. This result is in good agreement with our previous measurements [1]. The rocking scans of the Bragg peak were taken at different temperatures and different values of the magnetic field. After ZFC to T=150 K the intensity integrated over the Bragg peak is shown in Fig. 1a as a function of the rocking angle (for two incident polarizations I((P0). The rocking scans are well fitted by the Lorentzian centered at (c and with a relatively large width showing a large dispersion in the helix orientation. The q-dependence of the intensity for two polarizations $I(\pm P_0)$ taken at $\omega = \omega_c$ is shown in Fig.1b. It has a Gaussian distribution of the intensity centered at |**q**| $\cong$ 2.63 nm^{-1} with a width $\Delta q \cong 0.09$ nm^{-1}. The coherent length of the helix domain extracted from the width is in the order of $2\pi/\Delta q \cong 70$ nm.

For our experiment (**P**$_0$ || **ĉ**) the scattering intensity with a certain polarization is in accordance with Eq.(1) attributed to one of two types of the helix domains: left- or right-handed ones. The non-zero difference between two intensities $I(+P_0)$ and $I(-P_0)$ demonstrates the existence of the non zero average chirality in the sample i.e. there is a non equal population of the left- and right- handed domains. This difference is near the maximum of the peak intensity in the order of 10% (see Fig.1a and 1b). The difference is also noticeable in the widths of the rocking curves. The more populated domains have a smaller width (for 2-3 %) both in q- and ω dependence. This means that more populated domains are bigger in size and better ordered.
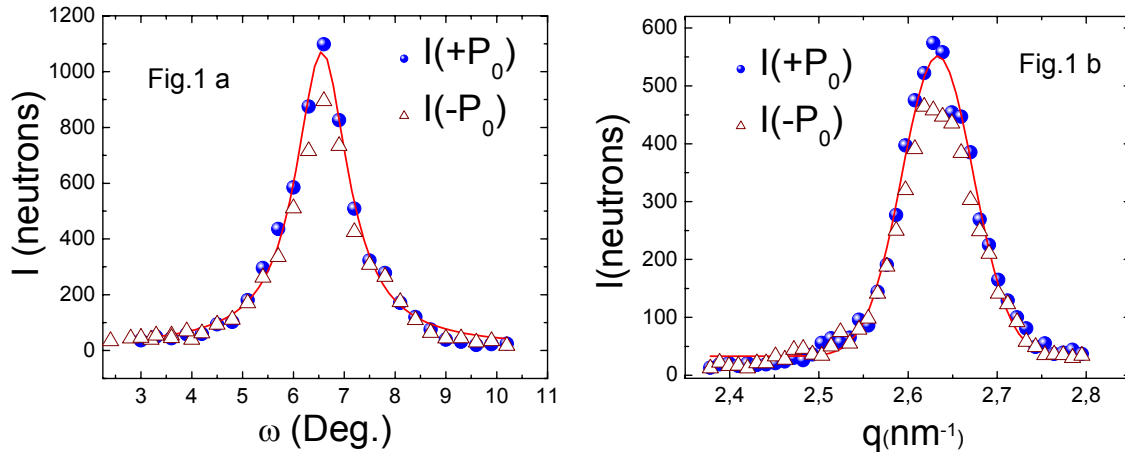
For the comparison of the two contributions to scattering due to the left- and right- handed helix domains we introduce the ratio $R_D=(I(-P_0) - I(+P_0))/(I(-P_0) + I(+P_0))$, where $I(+P_0)$ and $I(-P_0)$ are q-integrated intensities at $\omega = \omega_c$. Figure 2a shows the value of R_D for different temperature and magnetic field treatment. For Zero Field Cooling (ZFC – red symbols) R_D is negative and decreases from zero at T above T_N to negative 0.1 at low temperature. Fitting of R_D to the scaling function of $\tau=(T_N – T)/T_N$ gives the value $\beta_C-2\beta=0.22$ in good agreement with the previous experiment on SANS2 [1]. It should be noticed that thermocycling (heating and cooling through the critical temperature range in zero field) has no effect on the value of R_d.

Fig.2 a

Fig.2 b
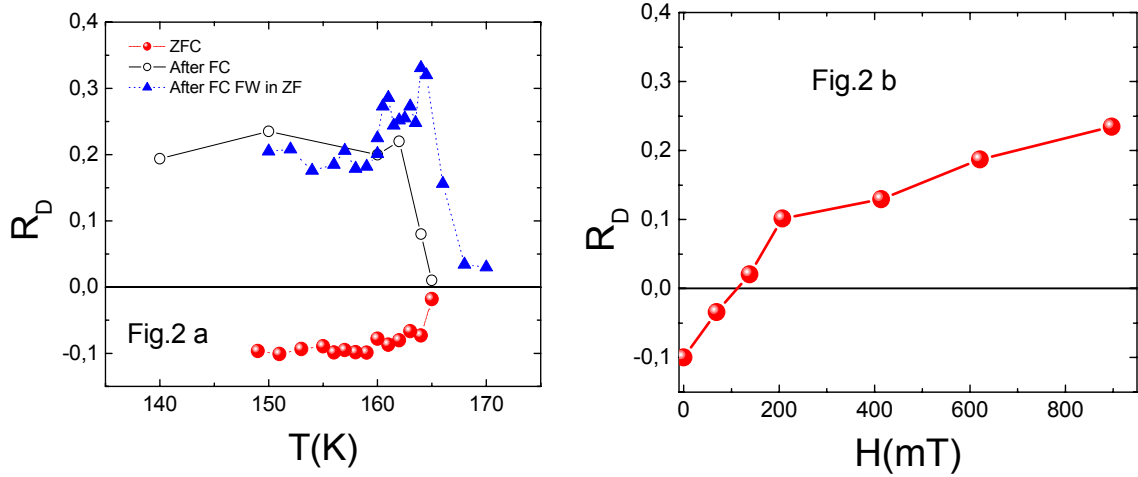
The main result of the present experiment is the fact that R_D depends on the temperature/magnetic-field prehistory. The sample, being cooled to a certain T in a field **H**=900 mT applied along the sample plane (**H** $\perp$ **ĉ**) and measured in a small guide field (**H** || **P**$_0$ || **ĉ**), gives R_D value of the opposite sign as in the ZFC experiment. Now R_d is zero above T_N and positive (+0.2) below T_N (Fig. 2 a open symbols). An even more intriguing behavior of R_D is observed for measurements after FC (**H**=900 mT) to 150 K with the subsequent heating in zero field (Fig.2 a blue symbols). R_d is constant in the range from 150 to 160 K, and increases then as temperature approaches T_N. After a maximum at T_N, it decreases to zero in the paramagnetic range. Furthermore, the value R_d depends on the strength of the magnetic field applied along the sample plane in the FC procedure but it does not depend on the direction ($\pm$) of the field. Figure 2b gives R_D as a function of the field in the FC procedure to T=150 K. It is clear that the magnetic field applied upon cooling is able to change R_D and repopulate the left- and right-handed domain structure.

In conclusion, we have observed for the first time the field-induced chirality in the Y/Dy multiplayer system.

References

[1] S. V. Grigoriev A. I. Okorokov, Yu. O. Chetverikov et al. JETP Letters vol. 83 No. **11** (2006) 478.

[2] S. V. Maleev, V. G. Bar'yakhtar, and R. A. Suris, Fiz. Tverdogo Tela **4** 3461 (1962) [Sov. Phys. Solid State **4**, 2533 (1962)].

[3] M. Blume, Phys. Rev. **130**, 1670 (1970).

[4] V.P.Plakhty, W.Schweika, Th. Bruckel, J. Kulda, S.V. Gavrilov, L.-P.Regnault, D. Visser, Phys.Rev.B **64** (2001) 100402(R).

[5] H. Kawamura, Phys.Rev.B **38** (1988) 4916.

[6] Ross W. Erwin, J.J. Rhyne, M.B.Salamon, J.Borchers, S. Sinha, R. Du, J.E. Cunningham, C.P. Flynn, Phys.Rev.B **35** (1987) 6808.

Polarized neutron reflectivity study of composite heterosructures GaAs / granular film SiO$_2$ with Co nanoparticles		

Proposer:	**Yury Chetverikov[1]**, [1]PNPI, Gatchina, St-Petersburg, Russia
Co-Proposers:	**Natalia Grigoryeva[2],** [2]SPSU, St-Petersburg, Russia

Experimental Team:	**Natalia Grigoryeva[2],** **Dieter Lott[3],** [3]GKSS Forschungszentrum
User Group Leader:	**Sergey Grigoriev[1]**

Date(s) of Experiment:	20th–29th November 2006

1. Objectives

The interest in ferromagnet/semiconductor (FM/SC) interfaces is increasing due to the possibility of employing these structures as spin injectors of polarized electrons in SCs [1–3]. Transfer of spin-polarized electrons (spin injection) from a magnetic contact into a nonmagnetic SC is intended for use in spintronic devices such as spin transistors, sensors and magnetic memory cells [4, 5]. It is noticed that the spin injection depends on a potential barrier formed at the interface. Although significant progress has been made, the efficient spin injection has not been achieved and the highly efficient spin injection into SCs at room temperature is the actual problem. This problem can be resolved by using FM/SC heterostructures with an accumulation electron layer in the SC at the interface. The exchange interaction between d (f) electrons in the FM at the interface and electrons in the SC polarizes electrons in the accumulation layer. This interaction forms a potential barrier for spin-polarized electrons injected from the FM. Recently a new phenomenon was observed [6]: the giant injection magnetoresistance in Gallium-Arsenide/Granulated-Film heterostructures with nanosize cobalt inclusions. The room temperature magnetoresistance values appeared to be two orders of magnitude higher than maximum values of magnetoresistance achieved up to now in magnetic tunnel junction structures and metal multilayers. The magnetoresistance effect is observed in the temperature range [200 - 350 K] and depends on an applied magnetic field. It is suggested that the magnetoresistance effect is due to the ferromagnetic layer in the granular film SiO$_2$ (Co) and due to the accumulation layer with polarized electrons formed in the semiconductor near the interface. In our investigation we study this composite heterosructures using polarized neutron reflectometry.

2. Samples

Composite heterosructure GaAs / granular film SiO$_2$ with Co nanoparticles was prepared by the magnetron sputtering. The average size of the ferromagnetic Co particles was determined from the small-angle X-ray scattering measurements: 2.5 - 5 nm. The thickness D of the granular film SiO$_2$ (Co) is equal to 47 nm and the thickness of the GaAs is 0.4 mm.

3. Experimental Technique

The experiments were carried out at the NeRo reflectometer of FRG-1 research reactor in Geesthacht (Germany). A polarized beam of neutrons with an initial polarization of P$_0$=0.95, the neutron wavelength λ=4.33 Å ($\Delta\lambda/\lambda$=0.02) was used. The scattered neutrons were detected by a position sensitive detector (PSD) with (256x256) pixels. The sample was set in a standard position to measure the reflectivity from the granular film of SiO$_2$ with Co on the GaAs substrate. The polarization followed the direction of the magnetic field (from 1 to 900 mT), which was applied perpendicularly to the incident beam and parallel to film surface. The reflected intensity was measured in the temperature range from T=100 to T=450 K for two incident polarizations I($\pm$P0) along and opposite of the guide magnetic field.

4. Results

Typical reflectivity profiles from the sample taken with the polarized neutron beam at T = 120 K are shown in Fig. 1 for the applied magnetic field H = 14 and 346 mT. The data were taken after the remagnetization process i.e. after application of a magnetic field of 900 mT in opposite direction. It is clearly seen that the granular film SiO_2 (Co) is magnetized resulting in a splitting of the reflectivity curves measured with polarization up (+) and polarization down (-). Furthermore the splitting has the opposite signs for the reflectivity curves carried out at small and large magnetic fields indicating the presence of a hysteresis in the magnetization. The splitting $\Delta I = I(+P0) - I(-P0)$ was measured at the angle $2\theta = 0.3$ degree as a function of the magnetic field at different temperatures (Fig.2). The hysteresis curves obtained are characterized by the coercive force HC and by the saturation value of the splitting at large fields ΔI_{SAT}, which is an analogue of the saturation magnetization. Both value H_C and ΔI_{SAT} decreases with increasing temperatures. The temperature dependence of HC (see Fig.3) shows three temperature regimes corresponding to different states of the magnetic layer: (i) the ferromagnetic state below 200 K, the superparamagnetic state above 360 K and the intermediate state between 200 K and 360 K. The intermediate state can be described by the percolative model with the percolative length ranging from l_p (size of the particle) at T = 360 K to the infinitely large value at T = 200K. It is important to note that the intermediate state is related to the giant magnetoresistance effect observed in the temperature range from 200 to 350 K [6] and maybe even determines it.

Fig.1

Fig.2

Fig.3
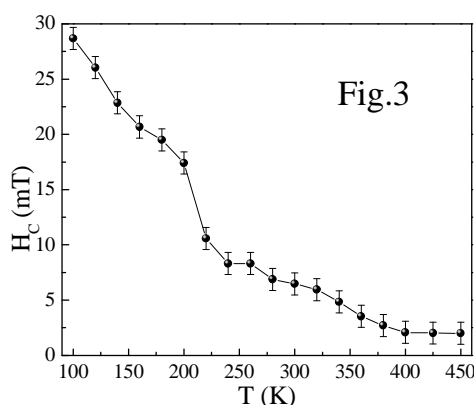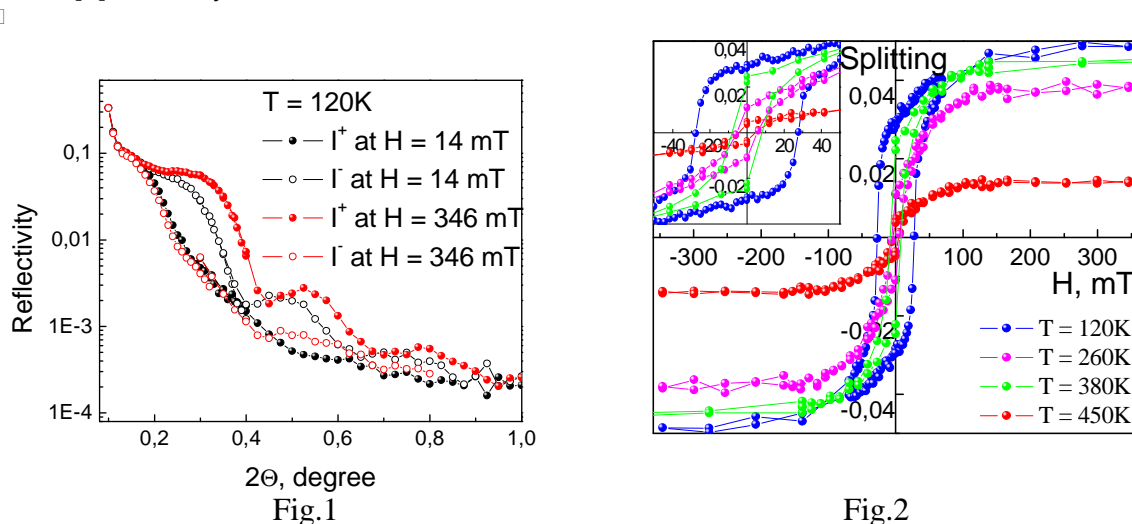
References

[1] I. Zutic, J. Fabian and S. Das Sarma Rev. Mod. Phys. 76 (2004) 323.

[2] B. P. Zakharchenya and V. L. Korenev, Phys. Usp. 175 (2005) 603.

[3] R. Bertacco, M. Riva, M. Cantoni, F. Ciccacci, M. Portalupi, A. Brambilla, L. Duo, P. Vavassori, F. Gustavsson, J.-M.George, M. Marangolo, M. Eddrief and V.H. Etgens, Phys. Rev. B 69 (2004) 054421.

[4] S. A. Wolf, D.D. Awschalom, R.A. Buhrman, J.M. Daughton, S. von Molnar, M.L. Roukes, A.Y. Chtchelkanova and D.M. Treger, Science 294 (2001) 1488.

[5] G. Schmidt, J. Phys. D: Appl. Phys. 38 (2005) R107.

[6] L. V. Lutsev, A. I. Stognij, and N. N. Novitskii, JETP Letters 81(10) (2005) 514.

Diffractometer for the analysis of residual stresses ARES-2

Short Instrument Description:

Diffractometer for the analysis of residual stresses ('strain scanner') in specimens with technical sizes (up to approx. 200 kg) using thermal neutrons. Starting from the ground with a dance floor a completely new sample stage and detector mounting was installed in 2006, significantly improving the capability of handling large samples.

Local Contact:

Dr. Peter Staron
Phone/Fax : +49 (0)4152 87 - 1208 / +49 (0)4152 87 - 1356
E-mail: Peter.Staron@gkss.de

Schematic View of ARES-2:
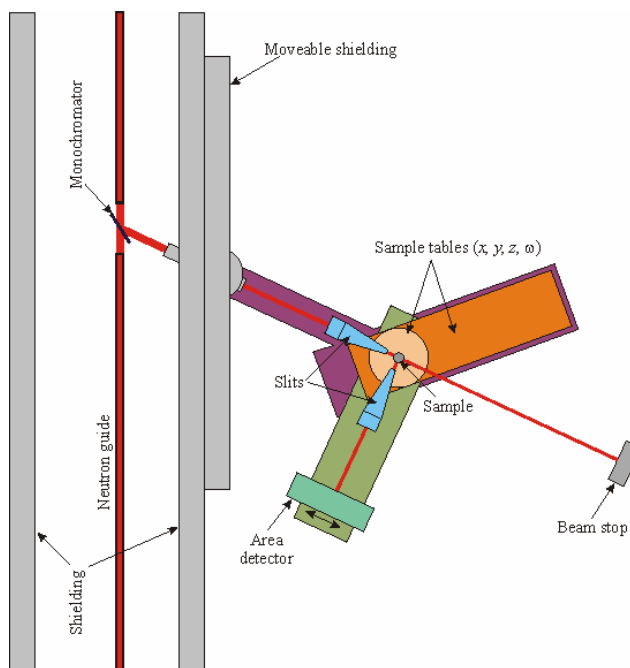
Instrument Details:

Location at FRG-1:	beam line 7; thermal neutron guide (cross section 42 × 90 mm^2, supermirrors on top and bottom wall)
Monochromator:	elastically bent perfect Si monochromator, Si (311), double focussing
Take-off angle:	57° to 120°, continuously selectable
Wavelength:	λ = 0.16 - 0.23 nm (with Si 311)
Flux at sample position:	$\Phi \approx 5\cdot10^5$ cm^{-2} s^{-1}
Sample movements:	x, y, z (range 400 mm), Ω
Detector:	^{3}He area detector (300 mm × 300 mm)
Sample environment:	Eulerian cradle (with x, y, z tables), load frame, furnace
Software:	PC programs for data reduction and analysis available

![GKSS logo] GKSS FORSCHUNGSZENTRUM in der HELMHOLTZ-GEMEINSCHAFT	**EXPERIMENTAL REPORT**	**GeNF ARES-2**

Re-commissioning of ARES after major upgrade		
Proposer: **Co-Proposers:**	**P. Staron,** [1]GKSS	
Experimental Team:	**P. Staron[1], H.-U. Ruhnau[1]**	
User Group Leader:	**-**	
Date(s) of Experiment:	9th–24th May 2006	

Objectives

In 1999 ARES had been built using parts of an older diffractometer for enabling a variation of the wavelength. As a consequence, the available space under the beam was rather limited and no large specimens could be mounted for strain measurements. Therefore, these old parts of the diffractometer were replaced with completely new components. The monochromator (double focussing perfect Si, elastically bent) and its housing was not changed.

Experiment

For extending the space under the beam to a maximum, a fork-lift device for vertical positioning was constructed (Fig. 1). The vertical movement is performed with a heavy linear table with a travel range of 400 mm. Only the "fork" with a relatively small height is under the beam at the position of the sample. The fork has a length of about 90 cm and carries two perpendicular linear tables with travel ranges of 400 mm. This relatively large travel range makes sample positioning easy and enables a placement of more than one sample, depending on the size of the samples. The two linear tables are mounted on a goniometer for rotating the axes of sample movement. The sample stage in the current state is designed for samples of a mass up to 200 kg.

An area detector with an active area of 300 mm × 300 mm is used at ARES-2. It is mounted on a large goniometre with a detector arm. The goniometre has an angle encoder for precise positioning of the detector.

The whole sample stage is placed on air cushion feet for changing the monochromator take-off angle. There is a laser and a video camera for positioning purposes. An open Eulerian cradle with integrated x, y, and z-tables is available.

Measurements

The size of the gauge volume defined by two 2.8 mm wide slits was measured by scanning it with a 1 mm thick Cu wire in 0.5 mm steps. The slits were at a distance of 90 mm from the wire. The Cu-220 reflection was recorded with an area detector at an angle of about 79.8° (Fig. 2). The size of the gauge volume, determined from the width at half maximum intensity (solid contour line in Fig. 2), is 3.1 mm (incoming side) × 2.9 mm (detector side). The beam is broadened on the incoming side by the divergence of the beam coming from the focussing monochromator. Broadening on the detector side is minimal because of the perfect Si crystals in the monochromator.

Summary and Outlook

After the upgrade of ARES larger samples can be measured. Accordingly, the travel ranges of the linear tables for sample positioning have been extended to 400 mm. Next optimization steps will cover the monochromator and the detector for increasing the primary and recorded neutron intensity.
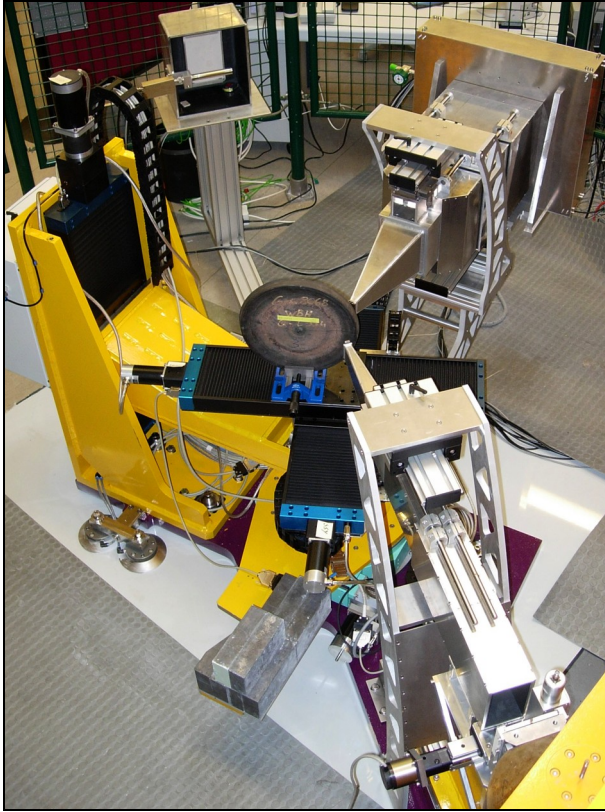
Fig. 1: Photograph of ARES-2.
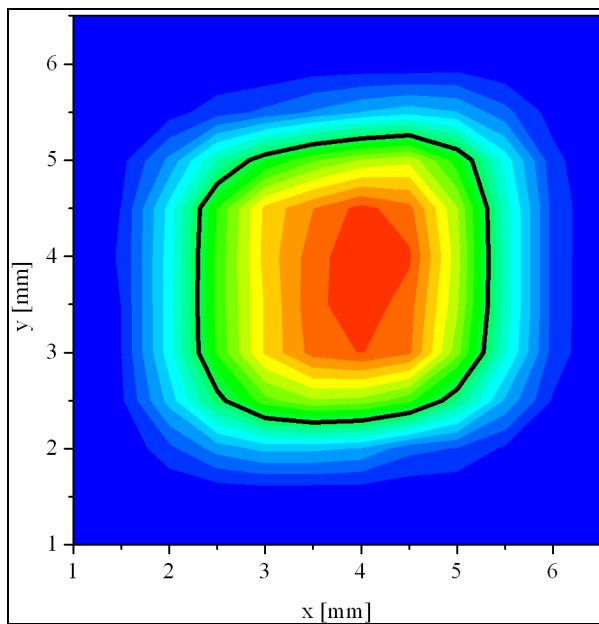
Fig. 2: Intensity distribution within the gauge volume formed by two 2.8 mm wide slits at a distance of 90 mm. The beam comes from the bottom, the diffracted beam goes to the right.

![GKSS logo] GKSS FORSCHUNGSZENTRUM in der HELMHOLTZ-GEMEINSCHAFT	**EXPERIMENTAL REPORT**	**GeNF ARES-2**

Strain measurements in tool steel rods		
Proposer: **Co-Proposers:**	**C. Redl,** [1]Böhler Edelstahl GmbH, Kapfenberg, Austria; **P. Staron,** [2]GKSS	
Experimental Team:	**P. Staron**[2]	
User Group Leader:		
Date(s) of Experiment:	27th November–06th December 2006	

Objectives

A feasibility study of residual stress analyses in specimens made of the tool steel 1.2343 produced by Böhler Edelstahl GmbH was performed. Two rods with a length of 200 mm and a diameter of 20 mm were used for this study. One rod was quenched, the other was in an annealed state.

Experiment

Scans were performed along a diameter in both samples using the (211) reflection of the α phase. 1 mm slits with a height of 30 mm were used for measurements of radial and hoop strains. The slit in the incoming beam was set to 1 mm × 1 mm for measurements of axial strains, leading to a bad counting statistics for the rod thickness of 20 mm and a material path length of 28 mm. It was observed that the reflection from the quenched rod was extremely broadened to a width of 1.9° while the width of annealed iron was only 0.4° (Fig. 1). The peaks of the annealed rod are also broadened, but to a lesser width of 0.7°.
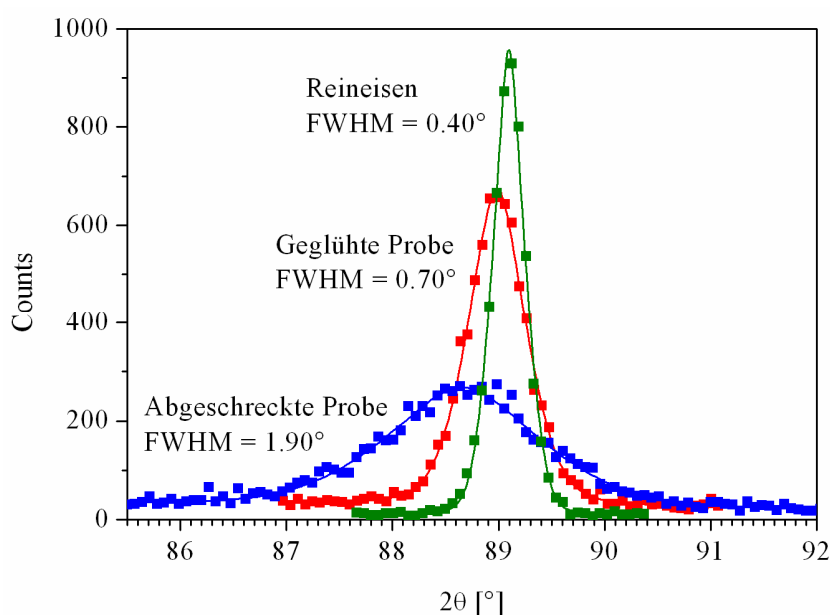
Fig. 1: Typical measured (211) reflections for annealed pure iron ("Reineisen"), the annealed steel rod ("Geglühte Probe"), and the quenched steel rod ("Abgeschreckte Probe"). The fitting lines were calculated using the Pseudo-Voigt function.
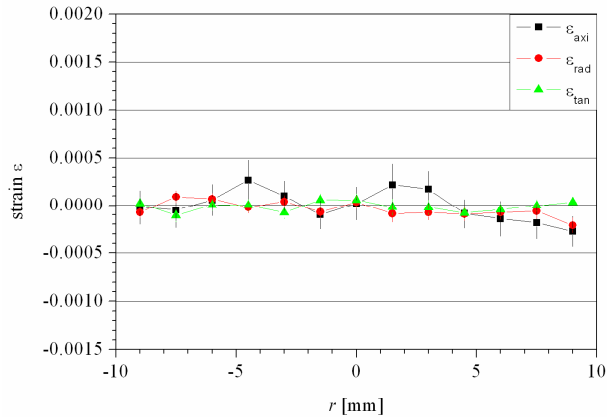
Fig. 2: Strains measured in the annealed steel rod.
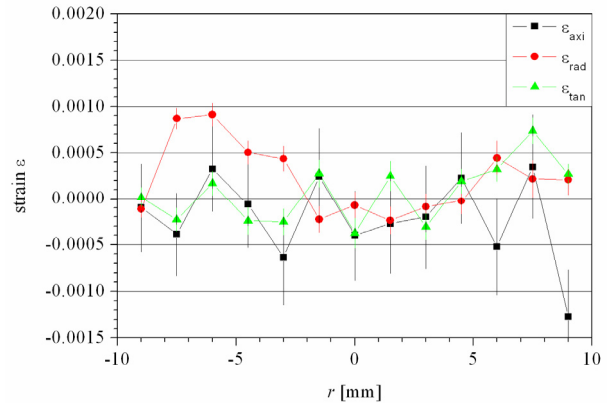
Fig. 3: Strains measured in the quenched steel rod.

As expected, measured strains in the annealed rod are very small (Fig. 2). On the other hand, the strains in the quenched rod are larger (Fig. 3). Besides the fact that the errors in the axial strains are large due to the small slit size, also the shapes of the radial and hoop strain distributions are rather irregular. A possible reason could be the influence of micro segregation leading to fluctuations in the chemical composition on a microscopic scale. This problem could possibly be overcome by use of larger slits, i.e. a reduced spatial resolution, leading to integration over those fluctuations over a larger volume, or by use of small reference samples cut out of the specimen under investigation at the exact positions of strain measurements, in which macro stresses relax, or a combination of both. The presence of micro segregation is supported by the fact that an analysis of the peak width in terms of micro strains after Stokes and Wilson failed, because the peak width seems to be much too large to be explained by elastic strains only. As a consequence, changes in the local chemical composition seem to be present and the microstructure of this steel seems to exhibit inhomogeneities. In fact, micro segregation of Cr and Mo in this steel is well known and Böhler also produces special (remelted) steel qualities with reduced micro segregation and enhanced micro homogeneity.

Achievements and Main Results
The feasibility of residual stress analyses in the steel 1.2343 seems to be given, although it is complicated by a strong peak broadening, especially in quenched material. An inhomogeneous microstructure could require relaxing the spatial resolution in favour of a better integration over fluctuations in the chemical composition.

162

	EXPERIMENTAL REPORT	GeNF ARES-2
GKSS FORSCHUNGSZENTRUM in der HELMHOLTZ-GEMEINSCHAFT		

Residual stress in a CT specimen made of a Cu bronze

Proposer: **Co-Proposers:**	**J. Heerens, P. Staron,** [1]GKSS
Experimental Team:	**P. Staron**[1]
User Group Leader:	
Date(s) of Experiment:	10th–20th November 2006

Objectives

Residual stresses in a CT sample for fatigue crack testing of dimensions 13.5 mm × 98 mm × 100 mm made of a cast Cu bronze containing approximately 9 wt% Al and additions of Mn, Fe, and Ni were investigated. The aim was to check if residual stresses are present in such a sample, which could possibly influence the results of a fatigue crack test.

Experiment

Strains in three perpendicular directions were measured in the sample using the (311) reflection of the Cu-rich α phase with an fcc structure (Fig. 1). In order to retain a sufficient spatial resolution in the through-thickness direction, a gauge volume with a nominal size of 2 mm × 2 mm × 10 mm was used. However, the material proved to be coarse-grained so that the sample was rocked around a vertical axis by ±2° in steps of 1° for increasing the number of grains contributing to the diffracted intensity. As a demonstration of the effect, integral intensity and peak position were recorded for a rotation of the sample by 90° in steps of 0.5° (Figs. 2 and 3). As a conclusion, ±2° seems not to be enough to achieve good grain statistics in this material with the chosen gauge volume.

The peak intensity also shows strong variations with the location through the thickness of the sample (Fig. 4). The residual strains determined form such data were small (Fig. 5). A plane stress state was assumed for calculating d_0 from the measurements.
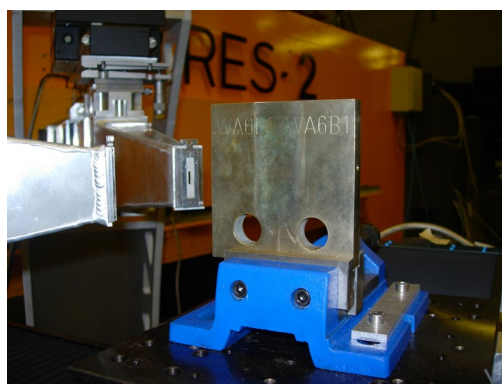
Fig. 1: Photograph of the sample.
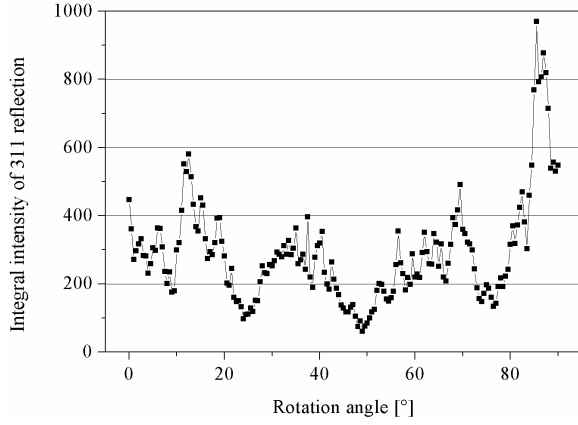
Fig. 2: Integral intensity as a function of the sample rotation angle for a gauge volume size of 30 mm^3.
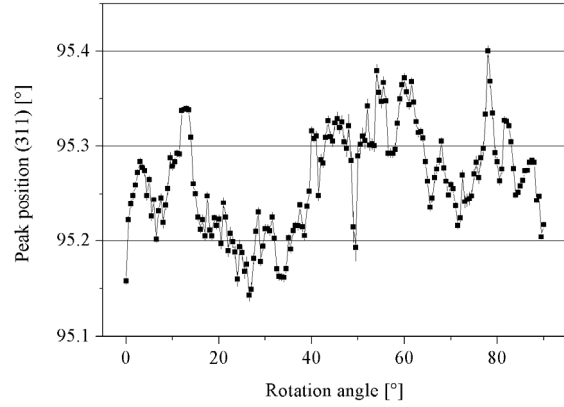
Fig. 3: Peak position as a function of the sample rotation angle for a gauge volume size of 30 mm^3.
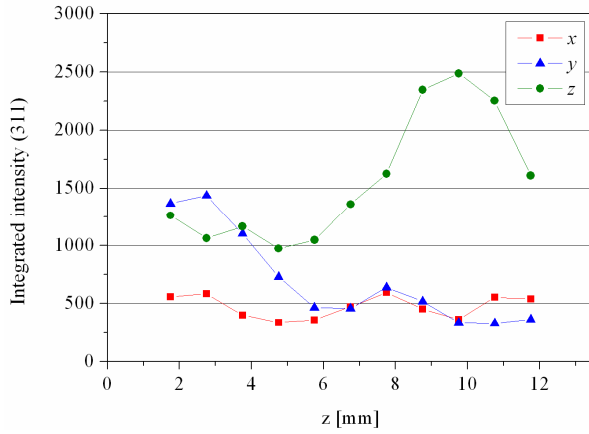
Fig. 4: Peak intensity through the thickness of the sample.
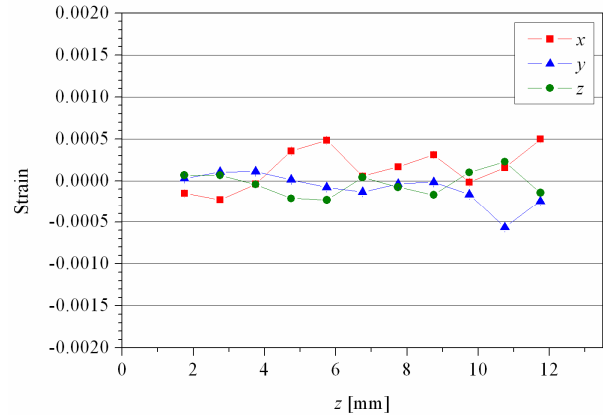
Fig. 5: Strain through the thickness of the sample.

Achievements and Main Results

Residual stress analysis in the investigated Cu-bronze is possible, however only with relaxed spatial resolution due to the large mean grain size of the material. In order to retain sufficient spatial resolution the sample should be rotated for several degrees during each measurement for increasing the number of diffracting grains. Residual stresses seem to be small in the studied sample.

<table>
<tr><td>GKSS
FORSCHUNGSZENTRUM
in der HELMHOLTZ-GEMEINSCHAFT</td><td>**EXPERIMENTAL REPORT**</td><td>**GeNF
ARES-2**</td></tr>
</table>

Residual stress in a steel specimen with a friction stir point weld	

Proposer: **Co-Proposers:**	**M. Piza,** [1]PETROBRAS, Brasil**; P. Staron,** [2]GKSS
Experimental Team:	**P. Staron**[2]
User Group Leader:	
Date(s) of Experiment:	18th–22nd August 2006

Objectives

Residual stresses in a 30 mm thick ferrite steel sample with a point weld were determined. The investigated sample had a size of 140 mm × 200 mm. A point weld using a rotating rod had been applied in the middle of the sample, resembling a repair weld.

Experiment

The investigated material is an unalloyed structural ferrite steel of grade S355 J2 G3 (old name: BS 4360 Gr 50D), corresponding to the German St 52-3 (DIN17100). The (211) reflection of the α phase was measured at an angle of about 89° using a wavelength of 1.64 Å from a Si (311) monochromator. Since stress gradients are present in all three directions, a cubic gauge volume was used for strain scanning. Because of the large sample thickness of 30 mm with a material path length of 42 mm, a large gauge volume with a nominal size of 5 mm × 5 mm × 5 mm was used. This spatial resolution is sufficient because the stress gradients around the weld cover a relatively large region. The grain size of base materials and weld was small enough to make sure that a large number of grains is included within the gauge volume. 28 points were measured along four 60 mm long lines in different depths, starting at the weld centre (Fig. 1).
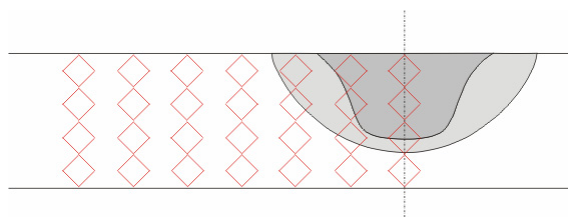
Fig. 1: Sketch of the cross section of the 30 mm thick sample with point weld and heat affected zone. The positions and approximate size of the 28 measured volumes are indicated.

The stress-free lattice parameter was determined from the assumption of a plane stress state. Significant variations of d_0 from the base material into the weld were found. Later, the so calculated d_0 values shall be checked by small samples cut out of the specimen.

Positive strains in radial and hoop direction are present in the weld (Fig. 2). There are systematic variations with the distance from the weld centre as well as with the depth.
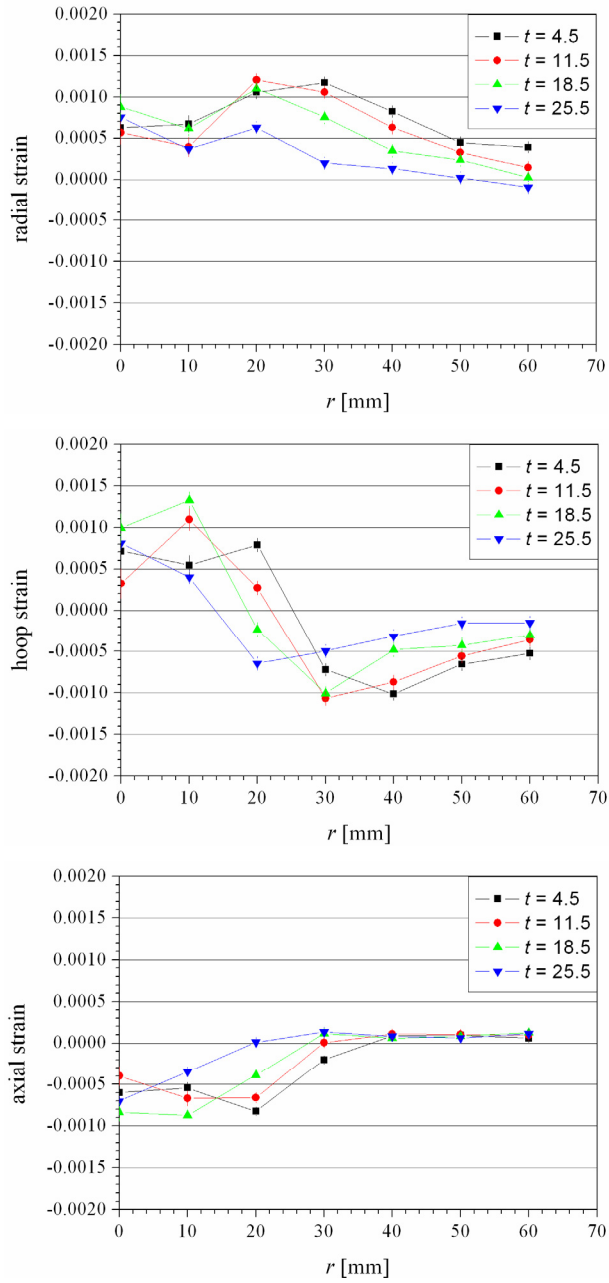
Fig. 2: Measured strains in different depths *t* (given in mm).

Achievements and Main Results

Significant tensile stresses are present in the weld zone of the investigated steel samples. The width of the tensile stress zone approximately corresponds to the width of the weld and heat affected zone.

![GKSS FORSCHUNGSZENTRUM in der HELMHOLTZ-GEMEINSCHAFT]	**EXPERIMENTAL REPORT**	**GeNF ARES-2**

| **The Effect of Pocketing on Residual Stresses in LB welded T-joint Al sheets** |||

Principal Proposer:	**M. Koçak, F.S. Bayraktar** GKSS Abt. WMF
Experimental Team:	**Funda Seniz Bayraktar, P. Staron** GKSS
Date(s) of Experiment:	22nd June–10th August 2006, 22nd–26th September 2006

1 Introduction

Residual stresses are an inescapable consequence of manufacturing and fabrication processes such as quenching, welding, forging, and machining operations. They can also be introduced into components as a result of deformation and creep during use or due to the different response of particles and matrix in a multiphase material. It is known that residual stresses in weldments are due to hindered shrinkage in the weld metal and its adjacent base metal during cooling when the yield strength and modulus of elasticity of the material are stored to their higher values at lower temperatures. The magnitudes of weld residual stresses can often be a high proportion of the yield or proof strength depending on the joint configuration and welding process. High residual stresses in regions near the weld may promote brittle fracture, fatigue, or stress corrosion cracking.

Welding of aluminium alloys is considered an essential long-term alternative to riveted structures for high-strength aerospace alloys because of their high strength/weight ratio. Thus, the retention of good post-weld microstructures and properties, and the control of residual stress and distortion are essential. Among the fusion welding methods, laser technology (LBW) appears to be the most promising solution for structural 6XXX aerospace alloys due to its high level of specific power and the limited area involved [1].Since weight reduction is very important in aerospace applications, pocketing (decreased thickness area) (Fig.1b) is being applied to the skin component of aircraft structures. If pocketing is applied after welding process, the residual stresses amount and distribution may be changed due to relaxation or addition of stresses during machining process.

2 Experimental

The investigated specimens were laser beam welded T-joint configurations with a 4.5 mm thick Al alloy grade 6156 base plate (skin) with the dimension of 400×625 mm^2 and 2 mm thick Al alloy grade 6013 T part (clip). The effect of pocketing on residual stresses was investigated. The specimens are shown in Fig. 1.

a)   b)
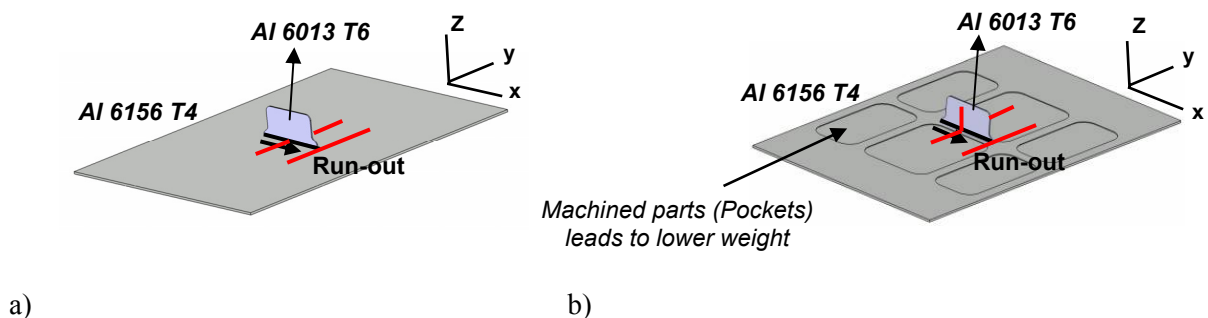
Figure1: Schematic illustration of the specimens; a) without pockets and b) with pockets

Internal strain measurements of both specimens have been performed at 17 points along 56 mm long scan lines (red lines in Fig. 1a and 1b) in the mid-thickness of a plate using neutron diffraction. Measurements in the clip have been performed only for specimen B at 10 points at the mid-clip position along a scan line pointing in the z-direction. Zero position is mid-clip position for the base plate and weld end for the clip.

Neutrons of 0.16427 nm wavelength from an elastically bent perfect Silicon (311) monochromator were used. Strain measurements in three perpendicular directions were performed. For measurements in the base plate a matchstick-like gauge volume of nominal size $2\times2\times10$ mm^3 was used for measurements of y and z strains for improving the intensity [2]. A cubic gauge volume size $2\times2\times2$ mm^3 was used for measurements of x strains, because large stress gradients are expected in the y direction. In order to increase the number of diffracting grains for the small gauge volume, the latter gauge volume was shifted by 2.5 mm in x direction during the measurement. Therefore, approximately the same volume as in the two other directions is analysed. The grain size of the material proved to be small enough to ensure a good grain statistics even with the small gauge volume of approx. 8 mm^3. However, for the measurements in the mid-clip position of the base plate and in the clip of specimen with pocket a matchstick-like gauge volume of nominal size $1\times1\times30$ mm^3 was used for measurements of y and z strains and a gauge volume size $1\times1\times2$ mm^3 was used for measurements of x strains; the gauge volume was shifted by 2.5 mm in x direction during the measurement. The Al (311) diffraction peak was recorded with an area detector at an angle of about 84° [2]. The elastic modulus E=70 GPa and Poisson number ν=0.33 were used for calculation of stresses [4].

For the determination of a triaxial stress state, the knowledge of the unstrained lattice parameter d_0 (or the peak position θ_0) at each measured point inside the sample is required. As the lattice parameter can change e.g. with the solute content (Vegard's law [5]), or, more generally, with the chemical composition of the material, d_0 can depend on the heat input the material has experienced during welding. Therefore, proper reference material is required for the determination of the stress-free lattice parameter d_0. For this purpose a reference sample will be cut out of specimens, in which macroscopic stresses can relax. Up to now a plane stress state was assumed. From the condition σ_z=0, d_0 can be calculated for each point except those points in and close to the weld. For the latter points, d_0 was interpolated.

3 Results

The results showed that:

in both specimens at mid-clip and run-out positions tensile longitudinal stresses appear with a peak value of about 150 MPa (Fig. 2);

in the specimen with pockets both at mid-clip and run-out positions tensile transverse stresses appear with a peak value of about 75 MPa; these stresses were significantly higher than in the specimen without pockets;

there is a maximum of longitudinal tensile stress in the heat affected zone of the clip reaching up to about 200 MPa (Fig. 3c);

a)   b)
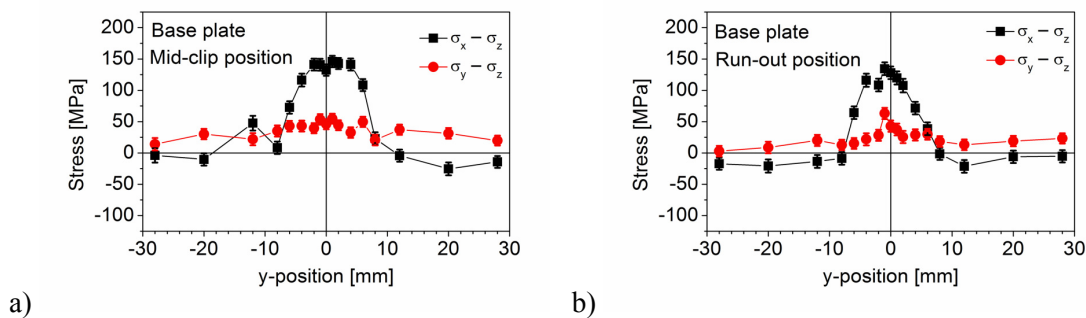
Figure 2: Residual stress results of the specimen without pockets at a) mid-clip position b) run-out position of the base plate.
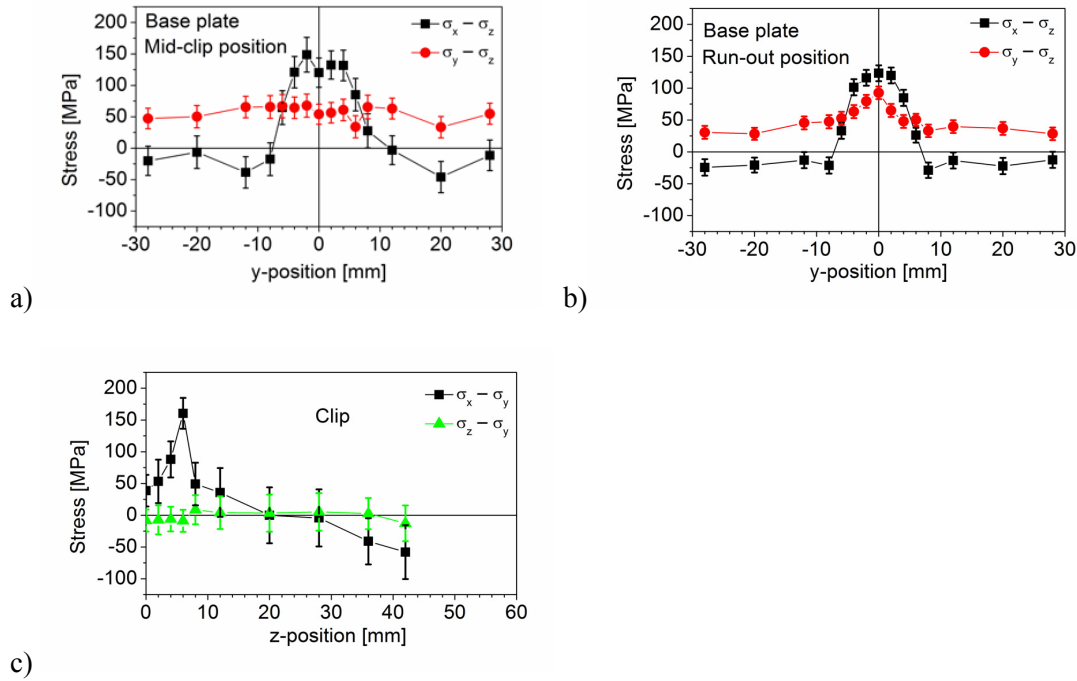
Figure 3: Residual stress results of the specimen with pockets at a) mid-clip position of the base plate, b) run-out position of the base plate and c) in the clip.

References

M.N. James, D.J. Hughes, Z. Chen, D.G. Hattingh, P.J. Webster, "Residual stresses and fatigue performance", 11th International Conference on Fracture (ICF), Turin (Italy), March 20-25, 2005.

L. Pintschovius, V. Jung, E. Macherauch, O. Vöhringer, Materials Science Engineering 61 (1983) 43-50.

V. Hauk, "Structural and Residual Stress Analysis by Nondestructive Methods", Amsterdam, Elsevier (1997).

H.G. Priesmeyer, in "Measurement of residual and applied stress using neutron diffraction", (eds. M.T. Hutchings and A.D. Krawitz), NATO ASI series E 216 (1992) 277-284.

![GKSS logo] GKSS FORSCHUNGSZENTRUM in der HELMHOLTZ-GEMEINSCHAFT	**EXPERIMENTAL REPORT**	**GeNF ARES-2**

The Effect of Socket Width on Residual Stresses in LB welded T-joint Al sheets		
Principal Proposer:	**M. Koçak, F.S. Bayraktar** GKSS Abt. WMF	
Experimental Team:	**Funda Seniz Bayraktar, P. Staron** GKSS	
Date(s) of Experiment:	26th September–8th November 2006	

1 Introduction

Residual stresses are an inescapable consequence of manufacturing and fabrication processes such as quenching, welding, forging, and machining operations. They can also be introduced into components as a result of deformation and creep during use or due to the different response of particles and matrix in a multiphase material. It is known that residual stresses in weldments are due to hindered shrinkage in the weld metal and its adjacent base metal during cooling when the yield strength and modulus of elasticity of the material are stored to their higher values at lower temperatures. The magnitudes of weld residual stresses can often be a high proportion of the yield or proof strength depending on the joint configuration and welding process. High residual stresses in regions near the weld may promote brittle fracture, fatigue, or stress corrosion cracking.

Welding of aluminium alloys is considered an essential long-term alternative to riveted structures for high-strength aerospace alloys because of their high strength/weight ratio. Thus, the retention of good post-weld microstructures and properties, and the control of residual stress and distortion are essential. Among the fusion welding methods, laser technology (LBW) appears to be the most promising solution for structural 6XXX aerospace alloys due to its high level of specific power and the limited area involved [1].Since weight reduction is very important in aerospace applications, pocketing (decreased thickness area) (Fig.1b) is being applied to the skin component of aircraft structures. If pocketing is applied after welding process, the residual stresses amount and distribution may be changed due to relaxation or addition of stresses during machining process. The distance of the pockets to the weld region (socket) may have also effect on residual stresses.

2 Experimental

The investigated specimen was laser beam welded T-joint configurations with a 3.2 mm thick Al alloy grade 2139 base plate (skin) with the dimension of 400×625 mm^2 and 2 mm thick Al alloy grade 6013 T part (clip). The specimen is shown in Fig. 1. The effect of socket width on the pocketed sample (decreased thickness area) on residual stresses was investigated. Whereas the socket width is 11 mm, that for the previous sample measured was 20 mm.
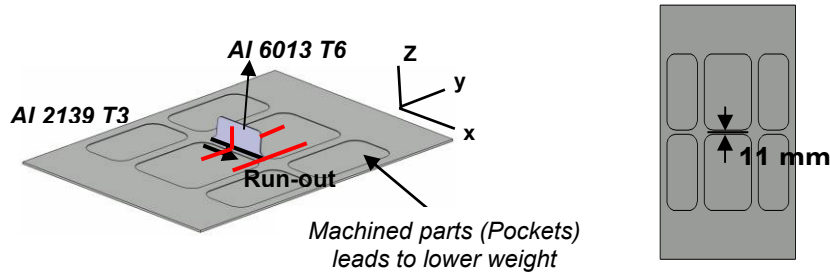
a)

Figure1: Schematic illustration of the specimen

Internal strain measurements of both specimens have been performed at 25 points along 120 mm long scan lines (red lines in Fig. 1) in the mid-thickness of a plate using neutron diffraction. Measurements in the clip have been performed only for specimen B at 12 points at the mid-clip position along a scan line pointing in the z-direction. Zero position is mid-clip position for the base plate and weld end for the clip.

Neutrons of 0.16427 nm wavelength from an elastically bent perfect Silicon (311) monochromator were used. Strain measurements in three perpendicular directions were performed. For measurements for run-out position in the base plate a matchstick-like gauge volume of nominal size 2×2×10 mm^3 was used for measurements of y and z strains for improving the intensity [2]. A cubic gauge volume size 2×2×2 mm^3 was used for measurements of x strains, because large stress gradients are expected in the y direction. In order to increase the number of diffracting grains for the small gauge volume, the latter gauge volume was shifted by 2.5 mm in x direction during the measurement. Therefore, approximately the same volume as in the two other directions is analysed. The grain size of the material proved to be small enough to ensure a good grain statistics even with the small gauge volume of approx. 8 mm^3. However, for the measurements in the mid-clip position of the base plate and in the clip of a specimen a matchstick-like gauge volume of nominal size 1×1×30 mm^3 was used for measurements of y and z strains and a gauge volume size 1×1×2 mm^3 was used for measurements of x strains; the gauge volume was shifted by 2.5 mm in x direction during the measurement. The Al (311) diffraction peak was recorded with an area detector at an angle of about 84° [2]. The elastic modulus E=70 GPa and Poisson number ν=0.33 were used for calculation of stresses [4].

For the determination of a triaxial stress state, the knowledge of the unstrained lattice parameter d_0 (or the peak position θ_0) at each measured point inside the sample is required. As the lattice parameter can change e.g. with the solute content (Vegard's law [5]), or, more generally, with the chemical composition of the material, d_0 can depend on the heat input the material has experienced during welding. Therefore, proper reference material is required for the determination of the stress-free lattice parameter d_0. For this purpose a reference sample will be cut out of specimens, in which macroscopic stresses can relax. Up to now a plane stress state was assumed. From the condition σ_z=0, d_0 can be calculated for each point except those points in and close to the weld. For the latter points, d_0 was interpolated.

172

3 Results

The results showed that:

a) at mid-clip and run-out positions tensile longitudinal stresses appear with a peak value of about 160 MPa (Fig.2a and b);

b) at mid-clip position tensile transverse stresses appear with a peak value of about 70 MPa; these stresses were significantly higher than at the run-out position (Fig.2a and b);

c) there is a maximum of longitudinal tensile stress in the heat affected zone of the clip reaching up to about 225 MPa (Fig. 2c);

d) in comparison with the values of the specimen with wide socket, the specimen with narrow socket has almost the same tensile stress values at the mid-clip and run-out position of the base plate, however higher tensile stresses occur in the clip (the peak value was almost 165 MPa in the specimen with wide socket). In addition lower compressive stresses were determined at the run-out position of the base plate of the specimen with narrow socket. (See the stress graphics of the specimen with wide socket (Fig.2a,b and c) in the previous report)
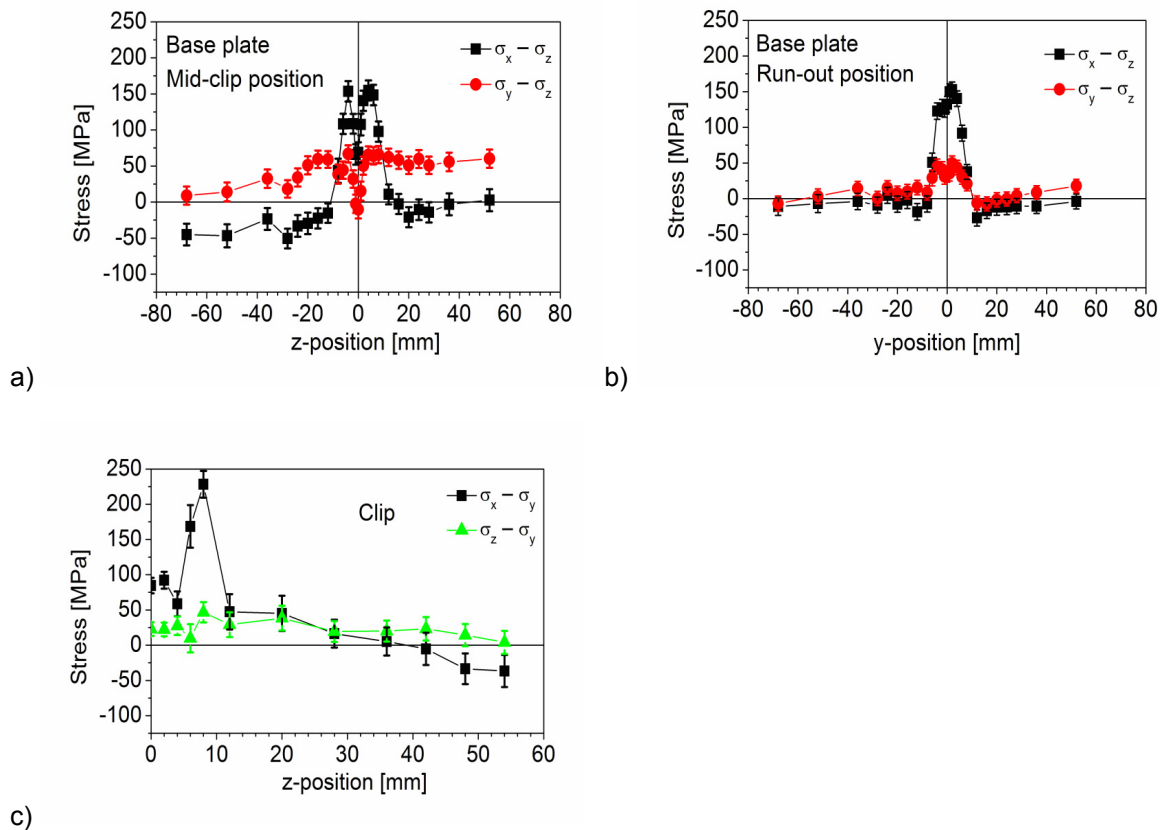
a)

b)

c)

Figure 2: Residual stress results of the specimen with pockets at a) mid-clip position of the base plate, b) run-out position of the base plate and c) in the clip.

References

(1) M.N. James, D.J. Hughes, Z. Chen, D.G. Hattingh, P.J. Webster, "Residual stresses and fatigue performance", 11th International Conference on Fracture (ICF), Turin (Italy), March 20-25, 2005.

(2) L. Pintschovius, V. Jung, E. Macherauch, O. Vöhringer, Materials Science Engineering 61 (1983) 43-50.

(3) V. Hauk, "Structural and Residual Stress Analysis by Nondestructive Methods", Amsterdam, Elsevier (1997).

(4) H.G. Priesmeyer, in "Measurement of residual and applied stress using neutron diffraction", (eds. M.T. Hutchings and A.D. Krawitz), NATO ASI series E 216 (1992) 277-284.

![GKSS logo] GKSS FORSCHUNGSZENTRUM in der HELMHOLTZ-GEMEINSCHAFT	**EXPERIMENTAL REPORT**	**GeNF ARES-2**
	Determination of stress-free lattice parameters in laser beam welded Al alloy T-joint	
Principal Proposer:	**M. Koçak, F.S. Bayraktar** GKSS Abt. WMF	
Experimental Team:	**Funda Seniz Bayraktar, P. Staron** GKSS	
Date(s) of Experiment:	16th–22nd September 2006	

1 Introduction

It is known that residual stresses in weldments are due to hindered shrinkage in the weld metal and its adjacent base metal during cooling when the yield strength and modulus of elasticity of the material are stored to their higher values at lower temperatures. High residual stresses in regions near the weld may promote brittle fracture, fatigue, or stress corrosion cracking. Welding of aluminium alloys is considered an essential long-term alternative to riveted structures for high-strength aerospace alloys because of their high strength/weight ratio. Thus, the retention of good post-weld microstructures and properties, and the control of residual stress and distortion are essential. Among the fusion welding methods, laser technology (LBW) appears to be the most promising solution for structural 6XXX aerospace alloys due to its high level of specific power and the limited area involved [1].

For the determination of a triaxial stress state, the knowledge of the unstrained lattice parameter d_0 (or the peak position θ_0) at each measured point inside the sample is required. As the lattice parameter can change e.g. with the solute content (Vegard's law [2]), or, more generally, with the chemical composition of the material, d_0 can depend on the heat input the material has experienced during welding. Therefore, proper reference material is required for the determination of the stress-free lattice parameter d_0. For this purpose a reference sample was cut out of a specimen, in which macroscopic stresses can relax.

2 Experimental

The investigated specimen was cut as comb-like structure from laser beam welded T-joint with a 6 mm thick Al alloy grade 6056 T6 base plate (skin) and 2 mm thick Al alloy grade 6013 T part (clip). The specimen is shown in Fig. 1.
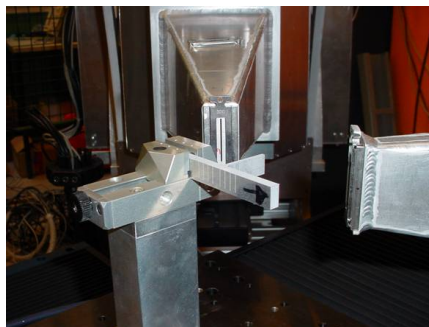
Figure 1: The specimen

175

Internal strain measurements of both specimens have been performed at 16 points along 50 mm long scan in the mid-thickness of a plate using neutron diffraction. Measurements in the clip have been performed only for specimen B at 11 points at the mid-clip position along a scan line pointing in the z-direction. Zero position is mid-clip position for the base plate and weld end for the clip.

Neutrons of 0.16427 nm wavelength from an elastically bent perfect Silicon (311) monochromator were used. Strain measurements in three perpendicular directions were performed. For measurements in the base plate a matchstick-like gauge volume of nominal size 1*1*10 mm^3 was used for measurements of y and z strains. A cubic gauge volume size 1×1×2 mm^3 was used for measurements of x strains (parallel to the weld line). In order to increase the number of diffracting grains for the small gauge volume, the latter gauge volume was shifted by ±2.5 mm in x direction during the measurement. Therefore, approximately the same volume as in the two other directions is analysed. The grain size of the material proved to be small enough to ensure a good grain statistics even with the small gauge volume of approx. 2 mm^3. The Al (311) diffraction peak was recorded with an area detector at an angle of about 84° [2].

3 Results

Figure 2 shows the measured lattice parameters. It can be seen that, firstly, there are significant variations of the lattice parameter in the weld, and, secondly, there are significant differences for the three directions. The latter could possibly be due to the presence of microstresses. These results have to be confirmed by additional measurements and will then be used for the calculation of residual stresses in the weld from the data measured before cutting of the reference sample.

a)   b)
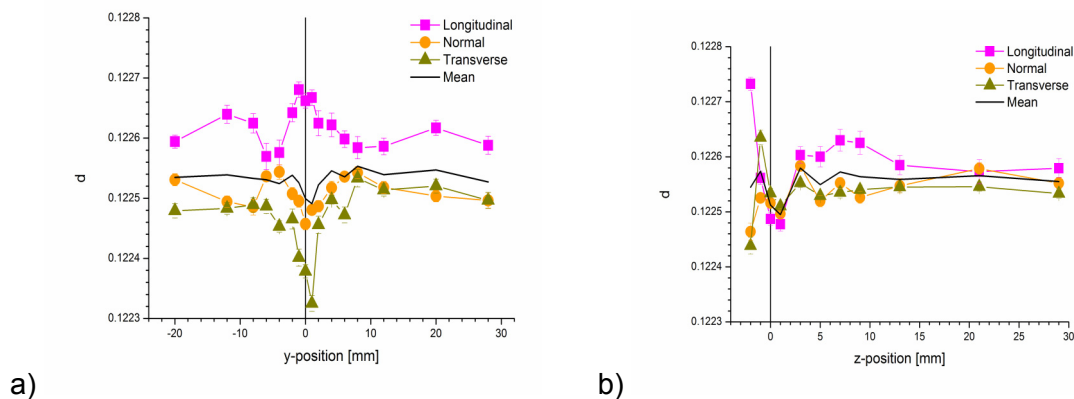
Figure 2: Lattice parameter values of the specimen a) mid-clip position of the base plate, b) in the clip.

References

(1) M.N. James, D.J. Hughes, Z. Chen, D.G. Hattingh, P.J. Webster, "Residual stresses and fatigue performance", 11th International Conference on Fracture (ICF), Turin (Italy), March 20-25, 2005.

(2) H.G. Priesmeyer, in "Measurement of residual and applied stress using neutron diffraction", (eds. M.T. Hutchings and A.D. Krawitz), NATO ASI series E 216 (1992) 277-284.

	EXPERIMENTAL REPORT	**GeNF**
GKSS FORSCHUNGSZENTRUM in der HELMHOLTZ-GEMEINSCHAFT		**ARES-2**

Residual stresses in friction welded rods, part 1: Al/Al joint	
Proposer: **Co-Proposers:**	**V. Luzin**, [1]GKSS; **S. Lenser**, [2]TU Clausthal **P. Staron**[1]
Experimental Team:	**V. Luzin[1], P.Staron[1]**
User Group Leader:	
Date(s) of Experiment:	6th–21st June, 10th–17th August 2006

Objective

Friction welding is a solid-state welding technique that can be used to join cylindrical parts. Application of this welding process to produce a joint involves pressing of one rotating part against a second part in the axial direction, which remains stationary. Heat produced by friction between the two parts in contact creates conditions for forming a high performance weld. In this way, joints between dissimilar materials can be produced which cannot by other welding techniques.

The integrity and quality of weld and the life span of the welded component are dependent on the conditions in which the weld is created. These conditions are affected by process parameters such as the rotational speed and deceleration regime, contact pressure, and the thermal and mechanical properties of the materials welded. The stress distribution in the weld is affected by these conditions and is believed to be a driving force for crack initiation and propagation, a potential cause of engineering component failure.

Experimentally, little is known about the residual stresses in rotary friction produced welds or about the stress distribution type and the stress formation mechanism. A consideration of the thermo-mechanical properties can be used to explain some aspects of the stress formation in the weld. For example, stress in a weld made from two dissimilar materials may be generated from vastly different thermal expansion coefficients of the materials. When welding similar materials, other factors become important, such as a high temperature gradient across and along the welding caused by specific temperature distribution or the cooling regime, which depend on the heat conductivity of the welded materials and sample size.

Materials and samples

Two pairs of materials were used, Al/Al and Ti/Al. The use of different materials may allow the elucidation of different sources of stress and the mechanism of stress formation. In both cases, two-part rod-like samples were fabricated, of diameter 24 mm. Results on the Al/Al sample is presented in this report (see [1] for results on Ti/Al sample).

Aluminium, if not coarse-grained, is a good candidate for stress measurement using neutrons because of its small neutron attenuation. The half-attenuation length in aluminium is $d_{\frac{1}{2}}(Al) = 67\ mm$, for titanium is $d_{\frac{1}{2}}(Ti) = 12\ mm$ and for steel is $d_{\frac{1}{2}}(Fe) = 6\ mm$. Given the sample size and half-attenuation lengths, measurement of the non-aluminium parts is expected to be challenging. Another feature of aluminium is its near isotropy of the elastic properties. Hence, although texture is present in the sample, the isotropic elastic constant provides very good approximation for description of the generally anisotropic material.

Grade AA7020-T6 Zn-Mg aluminium alloy was used. Alloys of this series are usually of high strength and of good machining properties, hence they are used as materials for structural elements in many different applications, including the airspace industry. Such alloys are heat-treatable, naturally age-harden, and are known to be unsuitable for welding. Despite overcoming the general problems with the successful welding of the aluminium alloy, processes occurring in the heat-affected zone (HAZ) at elevated temperatures impose additional complications for stress determination - stress-free lattice parameters can be changed as a result of additional heat treatment during welding. For this reason, two sets of measurements were necessary for precise stress determination, one for stressed samples and another for stress-free samples.

Experiment

The neutron stress measurements were performed at the neutron stress diffractometer ARES-2. A monochromatic neutron beam of wavelength λ = *1.642 Å* was used (monochromator stetting: Si(311), $2\theta_M$ = *87°*), providing almost 90°-geometry ($2\theta_B \approx$ *84°*) for the measured Al(311) reflection. Considering the sample dimensions, the number of measurements, and the time necessary for stress determination, a 2×2×2 mm³ gauge volume was chosen.

Aluminium samples were machined from the same rolled thick aluminium sheet, with the rolling direction (RD) as the axis of the rods, and the normal and transverse directions (ND, TD) perpendicular to the axis (Fig. 1a). Mutual orientation of the two halves was lost or was not controlled during production and welding. Texture measurements [2] were carried out on both halves after sample production allowing reconstructing of the parental coordinate system (ND, RD, TD), inherited from the rolling process, with respect to the cylindrical coordinate system used in stress measurements (see Fig. 1b)
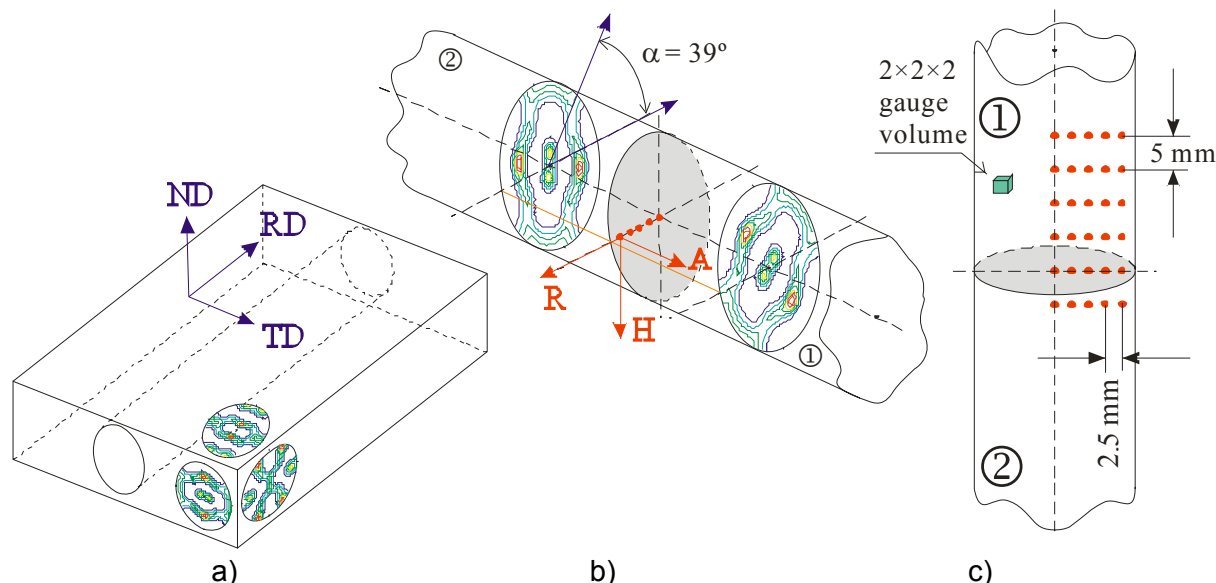
Figure 1: a) Orientation of the cylinder machined from aluminium rolled sheet in the coordinate system of the rolling process ((111) pole figure is used as an indicator of texture). b) Misorientation of the two sample halves in the cylinder coordinate system. c) Experimental mesh (red dots) and illustration of the size of the gauge volume.

Cylindrical sample symmetry assumes an axisymmetrical residual stress distribution, with the principal axes defined as axial (A), hoop (H) and radial (R). The sample symmetry suggests that the stress distribution is fully defined when measured in one plane which cross-sectioning sample along the cylinder axis. The two halves of the Al/Al sample were considered to be identical in regard to the stress distribution, so that one quarter of this

178

cross-section was used with the experimental mesh shown in Fig. 1c. (One additional row of measurement points was measured to check the symmetry of the two parts.)

The three principal directions, R, H, A, were measured in each of the 30 mesh points resulting in 90 individual measurements. The average measurement time was about 30 min per point, resulting in d-spacing accuracy within 1×10^{-4} Å.

Because of the ambiguity concerning d_0-values, they were experimentally measured using a specially designed comb-like sample produced by EDM (electric discharge machining). In this way, exactly the same measurement points were allowed to be measured a second time in the stress-relieved sample. Experimental conditions were kept the same for both series of measurements, before and after sample destruction.

Achievements and Main Results

Stresses were recalculated from the measured d-spacings using the (isotropic) diffraction elastic constants of the Al(311) reflection, $S_1(311) = -5.16\,\text{GPa}$ and $\frac{1}{2}S_2(311) = 19.57\,\text{GPa}$.

Three principal stress components were reconstructed assuming axial symmetry, resulting in zero shear components.

Fundamental to this study is the variation of d_0-value across the sample. Fig. 2a shows that variations in d_0-values are of the same order of magnitude as variations due to stress (data along the cylinder axis is shown as an example). D_0-values were obtained from the analysis of the stress relieved sample data when all stresses became zero in LSM (number measured strains was 3 and number of unknowns was 1). The d_0-value map (shown in Fig. 2b) provides experimental evidence that a certain material transformation occurred in HAZ during welding.
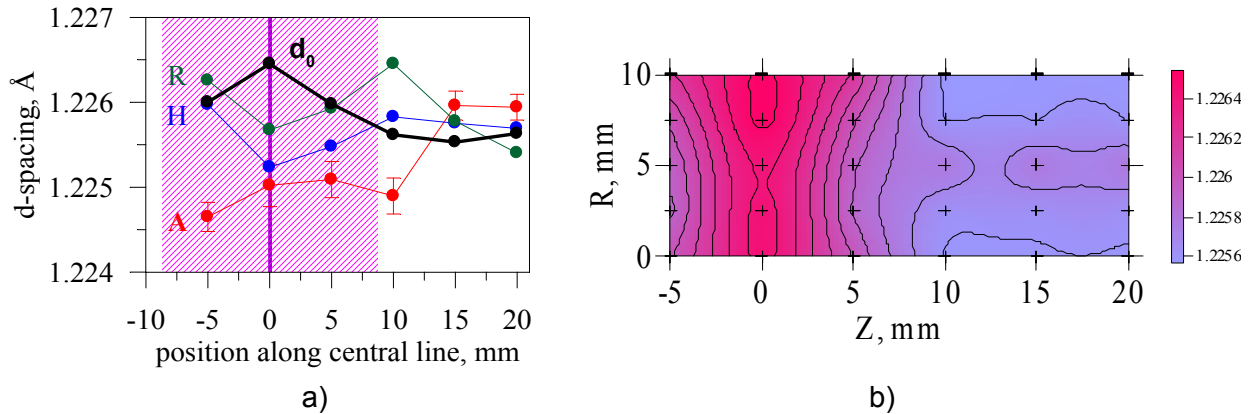
Figure 2: a) Example of the measured d_0-value and d-values along the central line in the axial, hoop, and radial directions. b) Experimentally determined map of d_0-value from stress-free sample.

On the basis of the determined d_0-values, strains and stresses in the stressed sample (before destruction) were calculated using Hooks law (in tensor form):

$$\sigma_i = \frac{1}{\frac{1}{2}S_2}\left(\varepsilon_i - \frac{S_1}{\frac{1}{2}S_2 + 3S_1}\left(\varepsilon_a + \varepsilon_h + \varepsilon_r\right)\right), \qquad \varepsilon_i = \frac{d_i - d_0}{d_0}, \qquad i = a, h, r.$$

As a result of these calculations, maps of all measured components are plotted in Fig. 3. The same formula was used as a basis for recalculation of the uncertainties of the stress values from uncertainties of the strain values using error propagation. The typical uncertainty was approximately 30 MPa, arising in part from neutron counting statistics (~15 MPa), and in part from grain size variation (~25 MPa).

A few observations concerning the reported stress measurement results are noteworthy. Firstly, friction welding of the aluminium rods results in the formation of a core of compressed material in the center of the welding. It has a near-spherical shape and extends

approximately 5-7 mm from the center. From the fundamental principal of elasticity theory, this zone of compression must be balanced by other regions of compression (in some generalized sense) so that all balance conditions are fulfilled. Two of these zones are located roughly at (R=7, Z=7) and (R=0, Z=12). The available balance conditions were checked, and found to be fulfilled within errors.
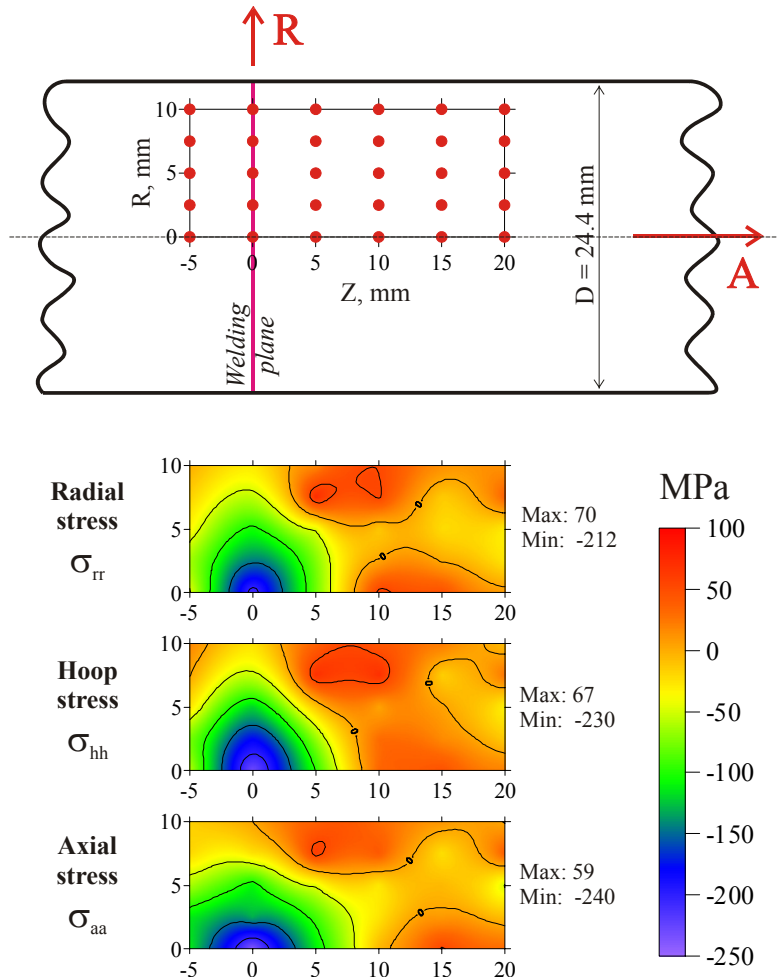
Figure 3: Maps of the three measured stress components.

The existence of the compressed core cannot be explained simply in terms of a sample quenching effect when the sample is cooled down uniformly. For any bulk sample that is simply quenched, the stress inside this sample is tensile – as the middle of the sample cools, it undergoes a thermal contraction under constrains imposed by the outer regions of the sample which solidify first. Thus, an explanation of the observed stress distribution here must arise from a more complex interplay of thermo-mechanical quantities (heat flux, pressure, temperature) and material properties which have very inhomogeneous distributions [1].

References
[1] V. Luzin et al., "Residual stresses in friction welded joints, part 2: Ti/Al joint", this volume.
[2] S. Lenser et al., "Initial texture of base materials of friction welded rods (AA7020-T6; Ti6Al4V)", this volume.
[3] Z. Lindemann, K. Skalski, W. Wlosin'ski, and J. Zimmerman, "Thermo-mechanical phenomena in the process of friction welding of corundum ceramics and aluminium", Bulletin of the Polish Academy of Science: Technical Sciences, Vol. 54, No. 1, 2006, pp. 1-8.

![GKSS logo] GKSS FORSCHUNGSZENTRUM in der HELMHOLTZ-GEMEINSCHAFT	**EXPERIMENTAL REPORT**	**GeNF** **ARES-2**

Residual stresses in friction welded rod, part 2: Ti/Al joint		
Proposer: **Co-Proposers:**	V. Luzin, [1]GKSS; **S. Lenser**, [2]TU Clausthal; **P. Staron**[1]	
Experimental Team:	**V. Luzin**[1], **P.Staron**[1]	
User Group Leader:		
Date(s) of Experiment:	6th–21st June, 10th–17th August 2006	

Objective

In the first part of this residual stress research [1] the join made by friction welding of two aluminium rods was investigated. It was found that mechanism of the residual stress formation in this case depends in a rather complex manner on temperature, thermal flux, pressure distributions and material properties (e.g. d_0-value, thermal conductivity) in the area adjacent to the weld.

Welding of dissimilar materials further complicates picture of the residual stresses introducing an additional mechanism of stress formation – the thermal expansion coefficient (CTE) discrepancy. A simple estimation to evaluate the order of magnitude of this effect can be done based on thermo-elasticity theory. In order to simplify this analysis, the join of the two dissimilar thin discs (instead of rods) can be considered in an approximation of the plane stress state. In case of aluminium-titanium joint (with CTE, correspondingly,

$\alpha(Al) = 22 \times 10^{-6} \, K^{-1}$ and $\alpha(Ti) = 8.6 \times 10^{-6} \, K^{-1}$), calculations give an approximate stress in the aluminium $\sigma_{rr} = \sigma_{\vartheta\vartheta} = 200 \, \text{MPa}$ ($\sigma_{zz} = 0$) at temperature drop of $\Delta T = 150^\circ C$.

Also, while in welding of Al/Al rods thermo-mechanical quantities and properties were symmetric about the weld plane, in welding of dissimilar materials we expect different distributions in the two different parts (for example, see Fig. 1, from [2]).
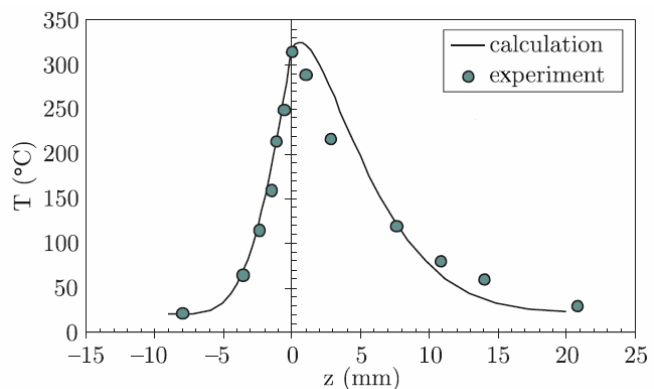
***Figure** 1: Lateral temperature distribution on the surface sample made by friction welding of Al_2O_3 and Al after welding completion.*

Materials and samples

Geometrically the sample of two welded rods of Ti and Al studied in this part of the project was very similar to the Al/Al sample which was measured earlier - it had a diameter of 24 mm. Aluminium alloy was of the same grade, AA7020-T6, and titanium alloy Ti6Al4V (wt%), was used as the second part of the welded component. This alloy is the most widely used titanium alloy (more then 50% of the world Ti usage) because of its excellent mechanical properties: strength, formability, wear and fatigue resistance, and toughness. Like Al7020, Ti6Al4V is popular material in airspace industry (e.g. turbine engine blades) though it is not very easily welded.

For the neutron residual stress measurements titanium presents a number of potential problems. It has approximately 10% (volume fraction) of the bcc β-phase in addition to hcp α-phase, so for proper stress experiment it would be necessary to measure the second phase too. Secondly, titanium is much less transparent for neutrons then aluminium, the half-attenuation length is more then five times smaller. Thirdly, titanium is elastically anisotropic so isotropic approximation of the material would be not very accurate. Thus, only aluminium part was investigated with all precautions against potential gradient of d_0-value around the welding area. This problem was addressed by measuring the Al part twice – intact and after EDM (electric discharge machine) cutting to a comb-like structure, stress-relieved sample, from which we can determine the d_0-value distribution.

Experiment

The neutron stress measurements of this sample were performed at the neutron stress diffractometer ARES-2 in the same experimental conditions as for the Al/Al sample [2]: neutron wavelength $\lambda = 1.642$ Å, , $2\theta_B \approx 84°$ for the Al(311) reflection, $2\times2\times2$ mm^3 gauge volume.

Aluminium part was machined from a rolled thick aluminium sheet (RD is the axis of the rods, see Fig. 1a). The axis of the titanium rod is the natural extrusion direction, ED (Fig. 1a). Mutual orientation of the two halves and the relation to the material processing coordinate system (ND, RD, TD or ED) was determined measuring texture in the two halves (Fig. 2b) [3].

a)   b)   c)
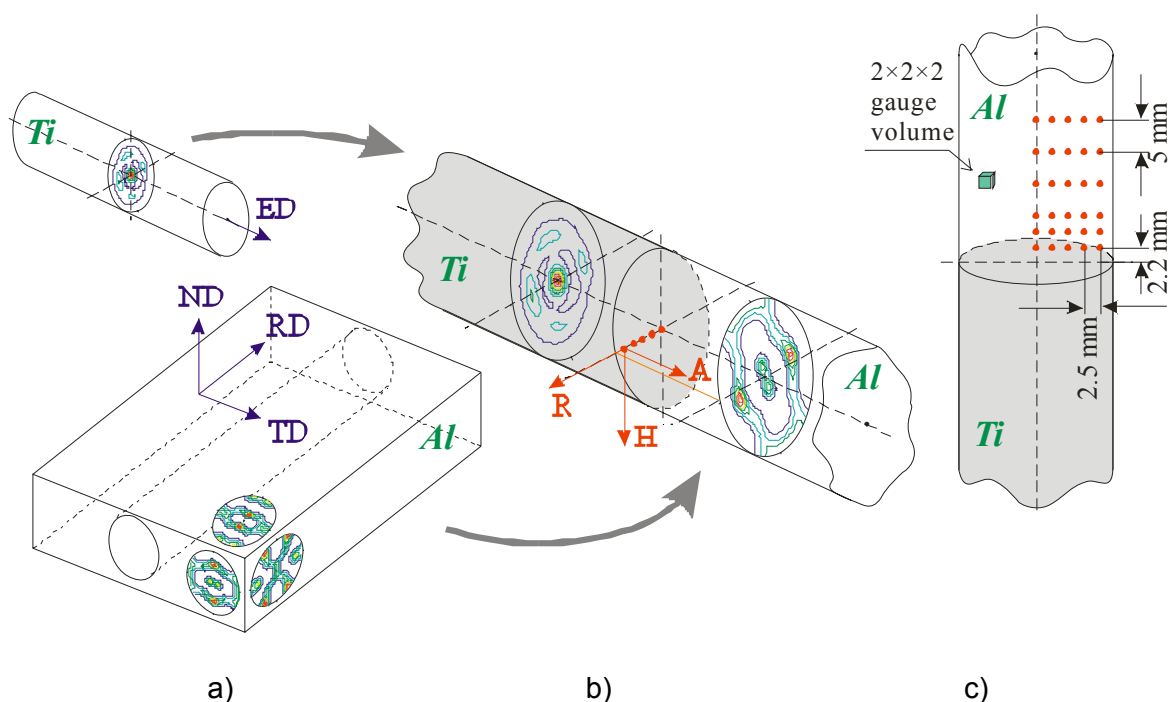
Figure 1: a) Orientation of the first rod machined from aluminium rolled sheet in the coordinate system of the rolling process and the second rod machined from extruded rod stock (Al(111) and Ti(100) pole figures are texture indicators) a) b) Misorientation of the two sample halves in the cylinder coordinate system. c) Experimental mesh (red dots, shown partially) and illustration of the size of the gauge volume.

The experimental mesh in Al part is shown in Fig. 1c. The three principal directions, R, H, A, were measured in each mesh point. The average measurement time was about 30 min per point providing accuracy of d-spacings within 1×10^{-4}. After cutting off the comb-like, stress-relieved sample, measurements were carried out second time in the same locations in order to find out distribution of the d_0.

Achievements and Main Results

Stresses were recalculated from the measured d-spacings using (isotropic) diffraction elastic constants of the Al(311) reflection, $S_1(311) = -5.16\,\text{GPa}$ and $\frac{1}{2}S_2(311) = 19.57\,\text{GPa}$. Three principal stress components were accounted assuming axial symmetry, resulting in zero shear components.

Fig. 2 illustrates the variations in d_0-values determined from the analysis of stress-relieved sample indicating that apparent changes take place in HAZ during welding.
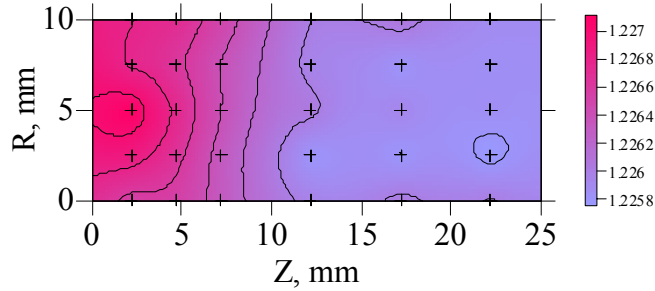
Figure 2: Experimentally determined map of d_0-value from stress-free sample.

Using these experimentally determined d_0-values, strains and stresses in the sample before destruction were calculated. Maps of all measured components are plotted in Fig. 3.
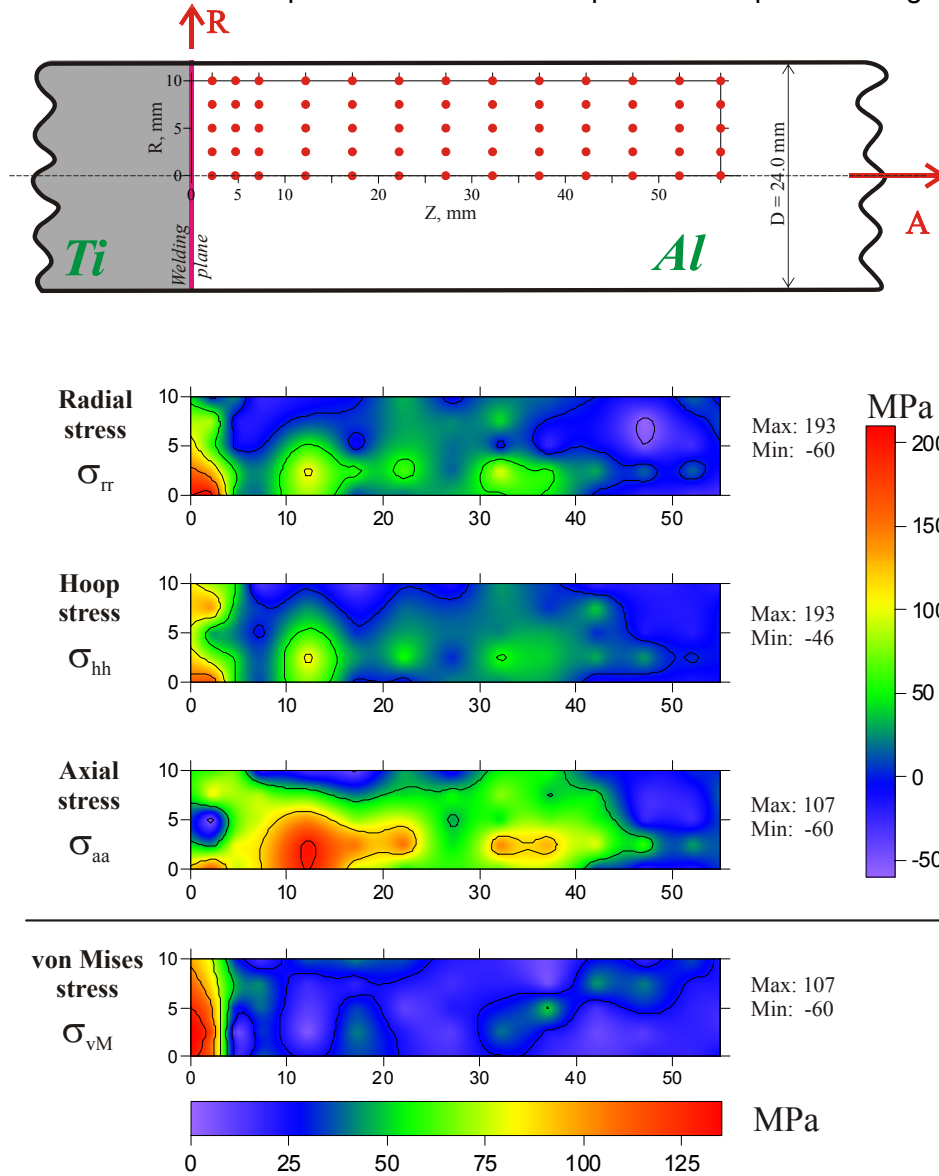
Figure 3: Maps of the three measured stress components and von Mises stress.

As one would predict, the highest stresses are found in the interface of the two materials. A zone at (Z=0, R=0) is the main feature of the stress distribution. There, the radial/hoop stress reaches some 200 MPa, which agrees in sign and value with predictions, while the axial stress is nearly zero. Other features are less defined. Some of them are caused by specific stress redistribution in 3D sample and some of them are simply due to the fact that statistical uncertainties were of the order of 30 MPa (mostly due to grain size variations).

The main feature of the obtained stress distribution in the center of the Ti/Al weld, which is uniquely different from that in the Al/Al sample, can be explained by the two materials CTE mismatch. However, the 3D stress distribution pattern has a complex structure which, to be fully explained, would require solution of the thermo-mechanical problem in 3D. Overall performance of the weld in terms of stresses must be good since the maximum value of the stresses (e.g. maximum von Mises stress is of about 120 MPa) well below the critical values, 0.2% Proof Stress and Ultimate Tensile Stress (which are, correspondingly, 360 MPa and 400 MPa).

References
[1] V. Luzin et al., "Residual stresses in friction welded joints, part 1: two Al rods", this volume.
[2] Z. Lindemann, K. Skalski, W. Wlosin'ski, and J. Zimmerman, "Thermo-mechanical phenomena in the process of friction welding of corundum ceramics and aluminium", Bulletin of the Polish Academy of Science: Technical Sciences, Vol. 54, No. 1, 2006, pp. 1-8.
[3] S. Lenser et al., "Initial texture of base materials of friction welded rods (AA7020-T6; Ti6Al4V)", this volume.

Short Instrument Description
The four circle neutron texture diffractometer is used to characterise textures in metallic, ceramic and geologic materials applying thermal, non-polarised neutrons.

Local Contact:
Prof. Dr. Heinz-Günter Brokmeier
Phone/Fax:+49 (0)4152 87 – 1207/+49 (0)4152 87 – 1338
e-mail: brokmeier@gkss.de

Schematic View of TEX-2:
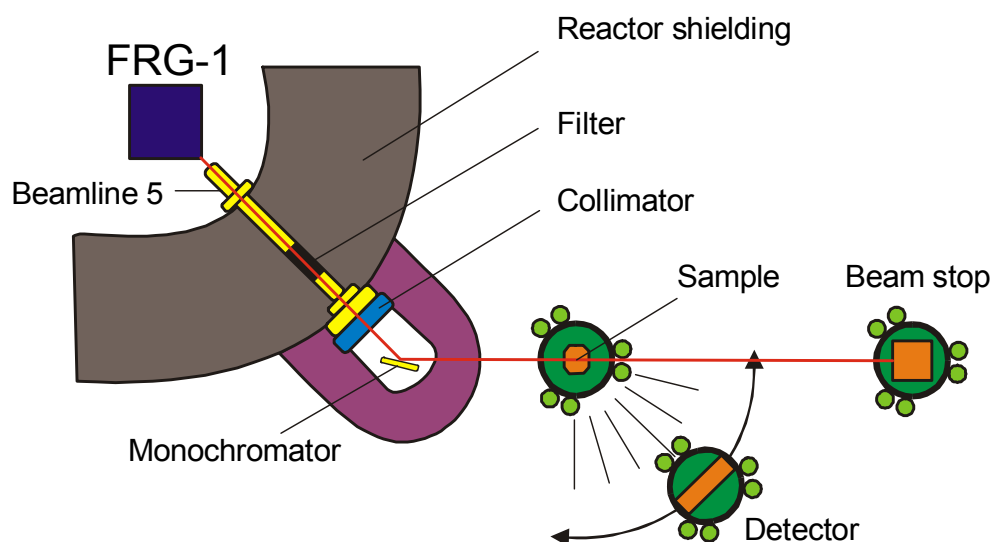
Instrument Details:

Location at FRG-1:	beamline 5, thermal neutrons maximum beam cross section: 45 x 45 mm^2
Primary collimation:	30', 42', 51'
Monochromator:	Cu (111), Cu (200), PG (002)
Take-off angle:	17.2°, 27.2°, 37.2°, 47.2°, 57.2°
Wavelength range:	λ = 0.08 – 0.27 nm (in steps)
Flux at sample position:	Φ = 0.3 - 2·10^6 cm^{-2} s^{-1}
Angular range	Φ: -360° to +360° X: -360° to +360° Ω: -46° to + 46° 2Φ: -60° to +90°
Detector:	^{3}He- single detector 2 - D position - sensitive ^{3}He - detector 300 x 300 mm

Instrument Details (continued)**:**

Sample geometries (standard):	cube 10 mm edge, sphere 15-20 mm $\varnothing$
	cylinder 10-15 mm $\varnothing$, 10-15 mm high
(various):	e.g. wires, tubes, tensile samples
Distances: sample ^{3}He detector	65 - 160 cm
sample 2-D - detector	60 - 120 cm
Sample environment:	- loading device: range of cycling load:
	tension up to 1.5 t, compression up to 2.0 t,
	- sophisticated set of sample holders

![GKSS logo] GKSS FORSCHUNGSZENTRUM in der HELMHOLTZ-GEMEINSCHAFT	**EXPERIMENTAL REPORT**	**GeNF TEX-2**

Experiment title		
Mineral fabric in clay sediments: new results from TEX-2 analysis		
Proposer:	**Massimo Mattei,** Università Roma TRE, Dipart. di Scienze Geologiche	
Co-Proposers:	**Francesca Cifelli,** Università Roma TRE, Dipart. di Scienze Geologiche	
Experimental Team:	Sabine Lenser , Bernd Schwebke	
User Group Leader:	Prof. Heinz-Günter Brokmeier	
Date(s) of Experiment:	28th November–7th December 2005, 26th–30th April 2006	

Objectives

The aim of this research project is to use an integrated approach of magnetic and mineral fabric analyses to study grain scale and regional deformation pattern in weakly deformed sediments, where macroscopic evidence of deformation is not detectable.

Several geological studies demonstrated that magnetic fabric analysis is a suitable method to detect deformation in fine-grained sediments, such as clays, that generally don't show pervasive tectonic structures at outcrop scale and where the standard method of structural analysis cannot be used. In particular, the study of the Anisotropy of Magnetic Susceptibility (AMS) on these clays demonstrated that, even if they are not deformed at the mesoscale, they are influenced by the tectonic setting and the magnetic fabric shows a well defined correlation with the regional tectonic structures. However, a clear correlation between the acting deformation and the origin of such magnetic fabric, which is pervasively found in clay sediments from deformed sedimentary basins, is not yet well understood.

Our idea is to use neutron texture analysis (using TEX-2) to evaluate the spatial distribution of those minerals responsible for the observed magnetic fabric and to correlate the preferred orientation of such minerals (and, therefore, their magnetic fabric) with the tectonic deformation acting in the sedimentary basin. This approach allows gaining insight into the deformational processes that lead to the development of a tectonic magnetic lineation in sedimentary basins.

Experiment

Starting from encouraging and interesting preliminary results from neutron pole figure measurements, using TEX-2 (see GeNF – Experimental Report 2003, pg. 93-94), a new set of measurements was carried out on 16 clays samples taken from another geological area, the Moroccan Rif. Due to the large availability of different-shaped specimens holders of the TEX-2, measurements can be done on the standard paleomagnetic cylinder used for magnetic analysis. As a consequence, specimen preparation is not necessary, avoiding possible artifact texture arising from cutting and polishing. Moreover, the texture can be compared directly to the magnetic fabric.

Previous X-ray diffraction scans identified chlorite as the principal iron-bearing mineral in studied sediments. The density distributions of the chlorite c-axes (perpendicular to basal plane) obtained by TEX-2 measurements are presented as contoured plots.

Achievements and Main Results

Representative pole figures measurements are shown in Fig. 1. The orientation distributions of the poles to the chlorite basal planes were evaluated by the means of the multiples of random distribution (m.r.d.) values. The observed chlorite fabric is well defined in most of the specimens. The basal planes of chlorite (orthogonal to the c-axis) describe a well-defined mineralogical foliation, sub-parallel to the bedding plane. In some cases, the c-axes of the chlorite grains tend to show a girdle distribution around the bedding plane sometimes with several maxima implying kinking of the chlorite basal planes. This spatial configuration imaged by AMS and neutron pole figure measurements, reflects basin scale deformation processes. The integrated approach of magnetic and mineral fabric investigations may therefore represent a valid tool to study strain mechanism on the grain scale and regional deformation pattern in weakly deformed sediments, even if macroscopic evidence is not visible in field observations. Results indicate that neutron diffraction analysis represent a unique tool for mineral fabric investigation in clays. In fact the high penetration of neutron beam makes this method particularly suitable in detecting the mineral fabric in such sediments whose original mineral texture may be easily modified by specimen cutting and polishing.
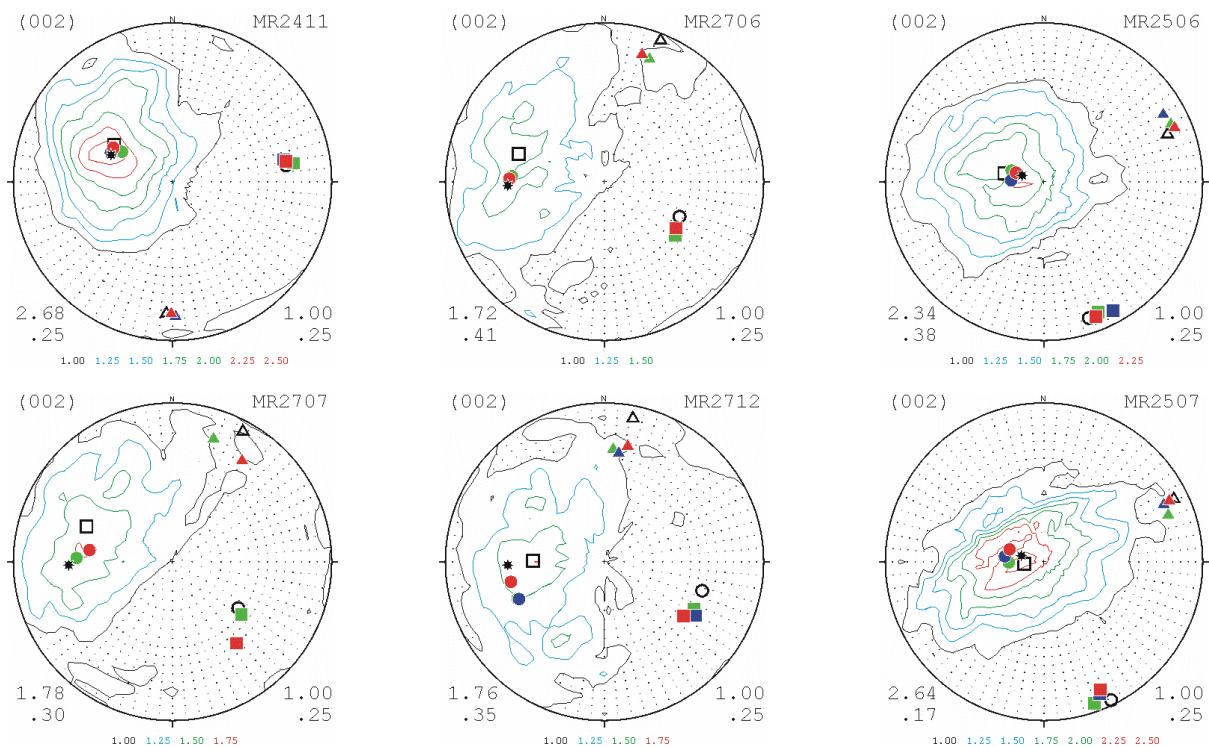
Fig. 1: Pole figures of chlorite basal planes of some representative samples measured by Tex-2. Plots are contoured in multiples of random distribution (m.r.d.) with contour interval of 0.25 m.r.d., above 1 m.r.d. Maximum and minimum m.r.d. values are expressed in the lower left of each plot. The principal directions of the orientation tensor, HFP (high-field paramagnetic), AMS at low temperature and AMS at room temperature tensors are represented with white, green, red, and blue symbols, respectively. Squares, triangles, and circles represent the maximum, intermediate and minimum directions, respectively. Data are shown on equal-area, lower hemisphere projections plotted in geographical coordinate system.

![GKSS Logo] GKSS FORSCHUNGSZENTRUM in der HELMHOLTZ-GEMEINSCHAFT	**EXPERIMENTAL REPORT**	**GeNF TEX-2**

	Texture Development in Mg-Si Alloys under ECAP Processing with Different Deformation Routes	
Proposer:	W. M. Gan [1,2], M. Y. Zheng[1], K. Wu[1] 1-School of Marerials Science and Engineering, Harbin Institute of Technology, China	
Co-Proposers:	H. -G. Brokmeier[2,3], B. Schwebke[2,3] 2-GKSS-Forschungszentrum, Max-Planck Strasse1, Geesthacht Germany; 3- Institute for Materials Science and Engineering, TU-Clausthal, Germany	
Experimental Team:	TEX-2	
User Group Leader:	H. -G. Brokmeier	
Date(s) of Experiment:	May, 2006	

Objectives

Magnesium is attractive for the light weight structural applications due to its low density. However, Mg alloys are easily shown anisotropy after deformation because of its h.c.p crystallography structure which has limited slip system. Researches show that Mg-Si alloys have a high potential as a heat resistant alloys because of the existence of the Mg2Si second phase which has high melting point and hardness, but the coarse and in-homogeneous distribution of the Mg_2Si greatly affected its mechanical property [1, 2]. Equal channel angular pressing (ECAP) is effective to refine the grain size of Mg alloys as well as the second phase [3, 4]. Besides the grain size refinement, texture modification also plays an important role [3, 5, 6]. Texture developed during ECAP processing is various with different processing routes.

The aim of the present study is to investigate the texture evolution of the ECAPed Mg-Si alloys which is closely related to the deformation mechanism; and further to provide the experimental data to help the simulation of the ECAP processing.

Experiment

The cast Mg-3.26wt%Si alloys was prepared by normal casting method, and then hot rectangular extruded. ECAP processing of the as-cast and as-extruded Mg-Si alloys were carried out with R_A, R_{Bc} and R_C route from 1 pass to 8 passes. Bulk samples with a dimension of 6X12X12 mm^3 cut from the centre part of the ECAPed specimen were measured by neutron diffraction at the 4-circle diffractormeter TEX-2. Sample's coordination system is defined as shown in Fig. 1. Four complete pole figures (10.0), (00.2), (10.1), (11.0) were measured by the combination of the reflection and transmission methods. ODFs were calculated by serious method with an expansion degree L_{max} =22 [7].

Achievements and Main Results

The recalculated complete (00.2) and (10.0) pole figures of the ECAPed as cast and as extruded Mg-Si are shown in Fig. 2. As for the cast alloys, basal planes tilted at about 20°to the extrusion direction after 1P. With further route A processing, the basal pole position has not changed a lot, while the pole intensity was increased. Basal planes have a degree of about 10° to the extrusion direction after 4P route Bc processing; and the intensity went down from 1P to 4P, then tended to be stable for the next pass. With route C, two strong intensity points occurred in pole figure; while after 8P, there exited nearly a typical rolling texture in the ECAPed samples.

As for the extruded alloys, after 4P and 8P route A processing, the basal planes were reoriented with inclination of about 22°and 15° to the extrusion direction, respectively. Different textures were obtained by route Bc, there were two strong positions in pole figures. By route C, similar texture was obtained as the cast alloys which the basal planes in most grains were almost parallel to the extrusion direction.

Variation of the maximum intensity in each pole figure with the processing pass for different routes is shown in Fig. 3. It can be found that for both alloys, route Bc has the lowest pole density in each pole figure. The pre-existed texture has a great effect on the texture evolution for the fist few passes; while texture tended to be similar after 4P except that much higher intensity obtained for as-cast alloys. Texture component was formed at first few passes, then tended to be stable with the next passes processing.

The unique texture formed during ECAP processing is attributed to the accumulative effect of the typical 45°shear deformation after each pass processing [5, 6].
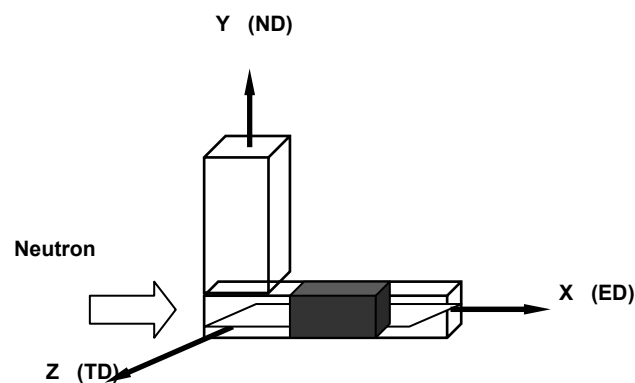
Fig.1: Definition of the coordination system fort the texture measurement.
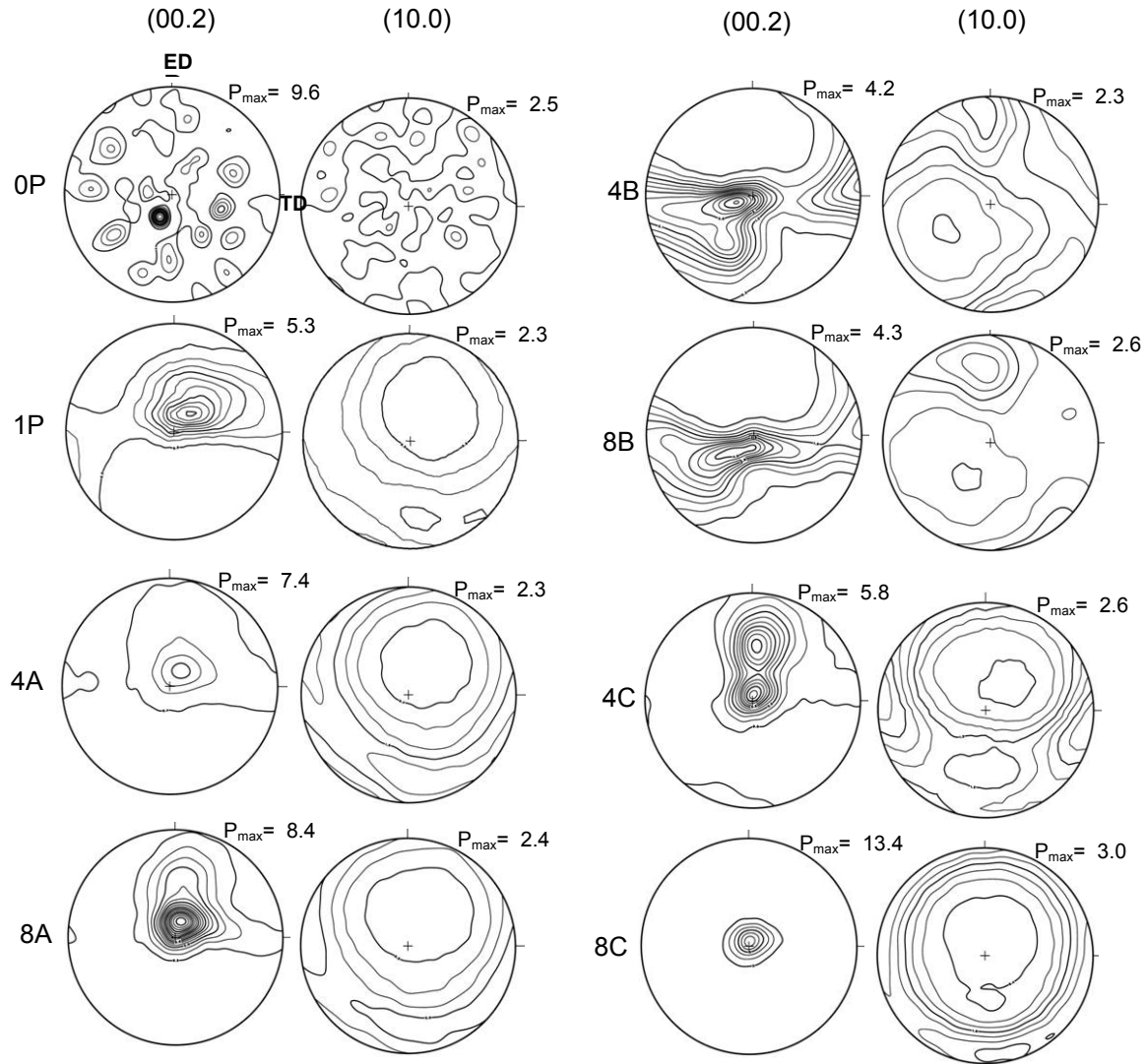
Fig. 2: Recalculated (00.2) and (10.0) pole figures of the ECAPed cast Mg-Si alloys by different routes. The extrusion axis is to the top.
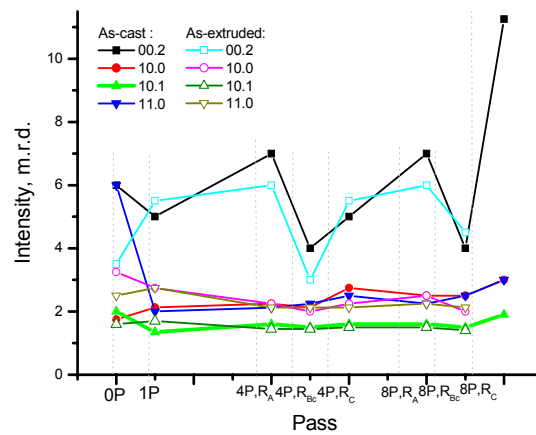
Fig. 3: Maximum intensity variations in pole figures with the processing pass for different routs.

Publications related to the experiment

[1] W. M. Gan, M. Y. Zheng, K .Wu, H.-G. Brokmeier, B. Schwebke, A. Schreyer, K. U. Kainer. Texture Development in Different Routes ECAP Processed Mg-Si Alloys by Neutron Diffraction. Proceedings of the 7th International Conference on Magnesium Alloys and their Applications. Dresden, Germany. Edited by K. U. Kainer, Wiley-VCH, 2006, P 529-534.
[2] W. M. Gan, M. Y. Zheng, K. Wu, H.-G. Brokmeier, B. Schwebke, A. Schreyer, K. U. Kainer. Neutron studies on the texture evolution of the ECAPed Mg-Si alloys. German Conference for research with Synchrotron Radiation, Neutrons and Ion Beams at large Facilities 2006. 04-06 Oct., Hamburg.

References

[1] M. Mabuchi, K. Higashi, *Acta Mater*. 1996, 44, 4611-4618.
[2] B. Bronfin, M. Katsir, E. Aghion, *Mater. Sci. & Eng*. 2001, A30: 246-50.
[3] A. Yamashita, Z. Horita, T. G. Langdon, *Mater. Sci. & Eng.* 2001, A300: 142-147.
[4] W. J. Kim, S. I. Hong, Y. S. Kim, S. H. Min, H. T. Jeong, J. D. Lee, *Acta Mater.* 2003, 51 3293-3307.
[5] S. R. Agnew, P. Mehrotra, T. M. Lillo, G. M. Stoica, P. K. Liaw, *Mater. Sci. & Eng.* 2005, A408: 72-78.
[6] H. K. Lin, J. C. Huang, T.G. Langdon, *Mater. Sci. & Eng.* 2005, A402: 250-257.
[7] Brokmeier H. -G.. Textures and Microstructures. 1999, 13-33.

GKSS FORSCHUNGSZENTRUM in der HELMHOLTZ-GEMEINSCHAFT	EXPERIMENTAL REPORT	GeNF TEX-2

Texture of hematite ore deformed to high strains in torsion

Proposer:	**H. Siemes**
	Institut für Mineralogie und Lagerstättenlehre, RWTH-Aachen
Co-Proposers:	**E. Rybacki**
	Geoforschungszentrum Potsdam, Germany
Experimental Team:	**B. Schwebke**
User Group Leader:	**H.-G. Brokmeier**
	Institut für Werkstoffkunde und Werkstofftechnik, TU Clausthal
Date(s) of Experiment:	28th November–7th December 2006

Objectives

Textures of naturally deformed hematite ores:

The microstructure and crystallographic preferred orientation (texture) of banded iron ores from the Iron Quadrangle in Minas Gerais, Brazil and from other localities was the objective of numerous publications, e.g. Quade et al. 2000, Rosiere et al. 2001, Bascou et al. 2002. Two (0003)-pole figures from Iron Quadrangle are presented in Fig. 1a and Fig 1b.

Experimental procedure:

Torsion experiments were performed on hematite ore from the Sishen Mine, South Africa, comprising a modal composition of 99.5 % hematite with varying fine grain sizes and a very weak texture (Fig. 1c). The specimens (10 mm length, 15 mm diameter) were deformed by means of a HTP-torsion apparatus (Paterson & Olgaard, 2000) at the GFZ, Potsdam.

Measurement, Achievements and Main Results

The preferred orientation was measured by means of neutron diffraction (Brokmeier et al. 1998, Jansen et al. 2000) on small prismatic samples of 2.5 x 2.5 x 10 mm^3 (Fig. 3c) close to the periphery of the deformed specimens (the volume of strongest shear strain).

Experimental textures depending on temperature:

A first series of tests on a very fine grained hematite ore was run with a constant strain rate in the temperature range 800°C to 1000°C up to a shear strain between γ = 4.4 and γ = 4.6. The pole figures of the basal plane show an elliptical maximum close to the pole of the shear plane in the center of the figure. The density of the maximum increases slightly with increasing temperature as shown in Fig. 2

Experimental textures depending on shear strain:

A second series of tests on a somewhat coarser hematite ore was run at 1000°C with a constant strain rate, but to different shear strains. The pole figure resulting from high shear strain (γ ~ 4) in Fig. 3b reveals again a high concentration of poles (6.4 m.r.d) in the center but with lower density as the comparable pole figure of fig 2c (10.3 m.r.d.). This seems to be the effect of the difference in grains sizes. The pole figure resulting from low shear strain (γ ~ 1) shows a girdle with a maximum density of 1.5 m.r.d. distant from the pole of the shear plane.

Experimental textures depending on shear strain-rate:

A third series of tests again on a somewhat coarser hematite was run in the temperature range 750°C to 950°C up to a shear strain of γ ~ 1 but applying different strain rates. All three pole figures reveal a low maximum density between 1.8 m.r.d. and 2.3 m.r.d. also far away from the pole of the shear plane.

Conclusions

Strain shear deformation of hematite results in a recrystallized polygonal microstructure, which is well known from naturally deformed hematite ores. The high sheer strain experimental pole figures strongly resemble pole figures of naturally deformed iron ores. Additional experiments varying temperature, total strain, strain rate, and e.g. grain size of hematite are necessary.

Acknowledgements

(0003)-pole figures of naturally deformed hematite ores

1a) Caue Mine, Brazil   1b) Andrade Mine, Brazil   1c) Sishen Mine, South Africa
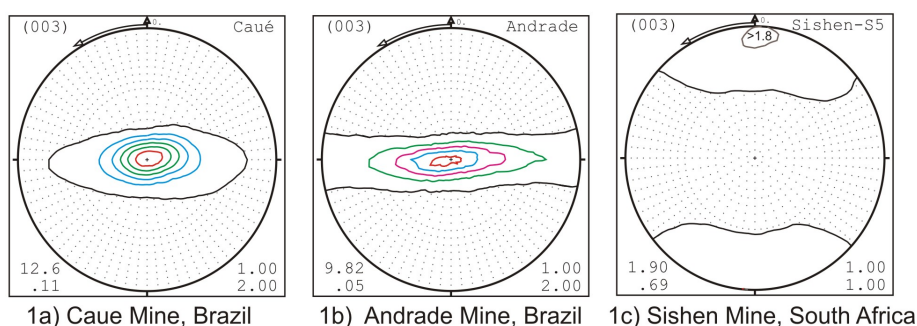
(0003)-pole figures of experimentally deformed hematite ore

variation of temperature

2a) 850°C ~4γ - 4.6*10^{-5}s^{-1} 2b) 900°C ~4γ - 4.6*10^{-5}s^{-1} 2c) 1000°C ~4γ - 4.6*10^{-5}s^{-1}

variation of strain
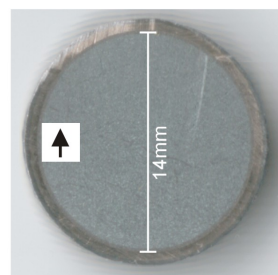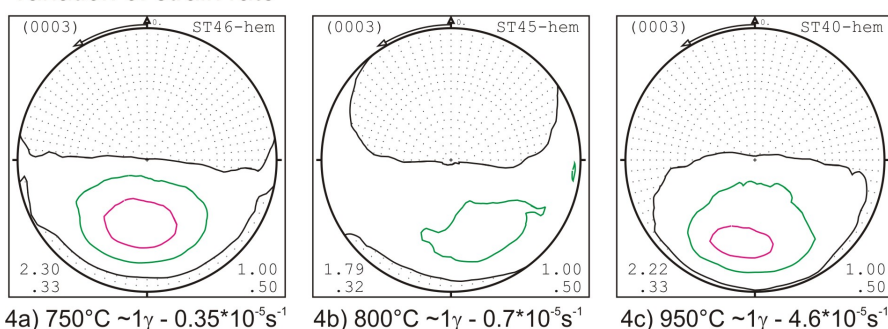
3a) 1000°C ~1γ - 4.6*10^{-5}s^{-1} 3b) 1000°C ~4γ - 4.6*10^{-5}s^{-1} 3c) position and size of the prismatic texture samples

variation of strain rate

4a) 750°C ~1γ - 0.35*10^{-5}s^{-1} 4b) 800°C ~1γ - 0.7*10^{-5}s^{-1} 4c) 950°C ~1γ - 4.6*10^{-5}s^{-1}

References

Siemes, H. et al., Journal of Structural Geology 25 (2003)1371-1391.

![GKSS logo] GKSS FORSCHUNGSZENTRUM in der HELMHOLTZ-GEMEINSCHAFT	**EXPERIMENTAL REPORT**	**GeNF TEX-2**

Influence of the aluminium content in magnesium alloys on the texture development of flat bars during extrusion		
Proposers:	**Jan Bohlen, Weimin Gan, Dietmar Letzig** Institut für Werkstoffforschung, GKSS Forschungszentrum	
Experimental Team:	**Weimin Gan, Bernd Schwebke, Heinz-Günter Brokmeier,** Institut für Werkstoffforschung, GKSS Forschungszentrum and Institut für Werkstoffkunde und Werkstofftechnik, TU Clausthal GKSS Forschungszentrum	
Date(s) of Experiment:	6th–23rd June 2006	

Motivation

The mechanical properties of semi-finished products such as extruded profiles are dependent on the microstructure which develops during processing. This especially includes the texture of the profile. It has been shown that there is a direct influence of the texture on the resulting mechanical properties of round bars with a special emphasis on the difference between the tensile and compressive yield stress [1]. Therefore, the texture development during extrusion is of interest for a better understanding of the development of mechanical properties.

Objectives

The objective of these measurements is to analyse the influence of the alloy composition and the process parameter settings on the resulting texture of flat bars. Unlike round bars flat bars do not obey a symmetric forming behaviour perpendicular to the extrusion direction any more. This should have a visible influence on the texture formation during extrusion. The study is focussed on aluminium as an alloying element in magnesium alloys of the AZ-series, such as AZ31, AZ61 and AZ80.

Experiment

Three indirect extrusion trials were carried out using alloys AZ31, AZ61 and AZ80. A flat bar was produced using an initial billet temperature of 300°C. Resulting pole figures are shown in Fig. 1 - 3.
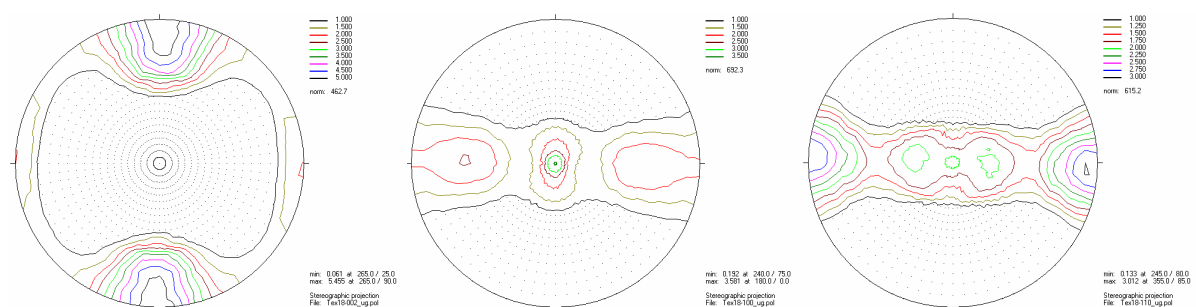
Fig. 1: (00.2)-, (10.0) and (11.0) pole figures of an AZ31 flat bar after indirect extrusion at 300°C (ND = extrusion direction).
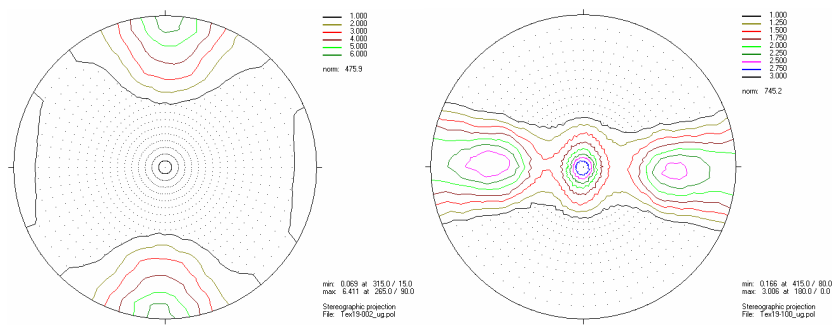
Fig. 2: (00.2)-, and (10.0) pole figures of an AZ61 flat bar after indirect extrusion at 300°C (ND = extrusion direction).
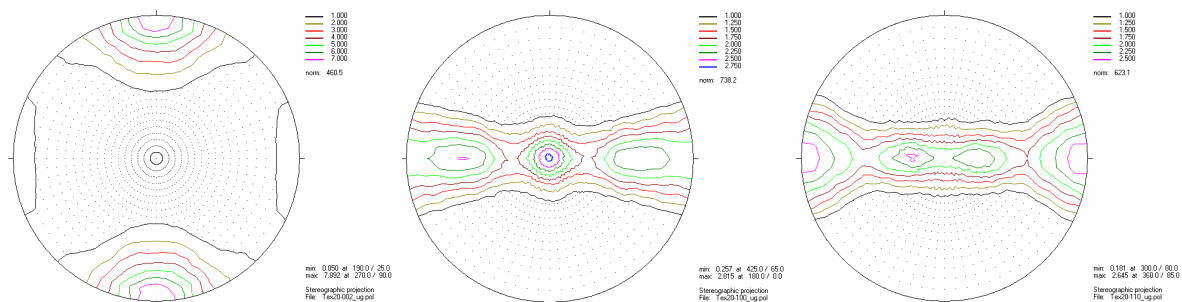
Fig. 3: (00.2)-, (10.0) and (11.0) pole figures of an AZ80 flat bar after indirect extrusion at 300°C (ND = extrusion direction).

Achievements and Main Results

Unlike the symmetric <10.0> fibre texture or <10.0>-<11.0>-double fibre texture of extruded round bars, the texture of flat bars is more complex [2]. In principle, this original texture of extruded profiles is still found with basal planes mainly oriented perpendicular to the extrusion direction as it can be seen best in Fig 1 for AZ31. It is again notable, that the intensity of this texture component decreases with increasing content of aluminium as described earlier for round bar extrusions [1]. However, a further texture component occurs with basal planes mainly oriented parallel to the larger surface plane of the extrudate. This texture component increases in intensity with increasing content of aluminium. It compares well to a typical sheet texture component of magnesium alloys where also basal planes are mainly oriented parallel to the sheet plane.

References

[1]   J. Bohlen, J. Swiostek, H.-G. Brokmeier, D. Letzig, K. U. Kainer, Magnesium Technology 2006,
[2]   J. Bohlen, D. Letzig, GeNF Experimental Report 2005, GKSS Forschungszentrum, p.165-166.

GKSS FORSCHUNGSZENTRUM in der HELMHOLTZ-GEMEINSCHAFT	**EXPERIMENTAL REPORT**	**GeNF TEX-2**

Texture measurements on an ultrafine-grained Al alloy AA6016 produced by accumulative roll bonding		
Proposer:	**Werner Skrotzki**	
	Institut für Strukturphysik, Abteilung Metallphysik, Technische Universität Dresden, D-01062 Dresden	
Co-Proposer:		
Experimental Team:	**S. Lenser, B. Schwebke**	
	IWW – TEXMAT, Clausthal University of Technology	
User Group Leader:	**Heinz-Günter Brokmeier**	
	IWW – TEXMAT, Clausthal University of Technology	
Date(s) of Experiment:	01st–7th November 2006	

Objectives

During recent years, bulk ultrafine-grained (UFG) materials, produced by severe plastic deformation (SPD) and with grain sizes in the range from 100 nm to less than 1 μm, have received considerable scientific attention [e.g. 1]. Compared to their conventional grain-sized counterparts the UFG microstructure leads, beside many other enhanced properties in UFG-materials, to an extraordanary high strength and enhanced ductility [2]. While much is known about texture formation in SPD materials produced by equal channel angular pressing [e.g. 3], texture measurements on fcc metals subjected to accumulative roll bonding (ARB) are less frequent. ARB is a process where the rolled sheet is cut, polished, brushed, stacked and then roll-bonded (Fig. 1) [4, 5]. By repeating this procedure very high strains have been introduced sucessfully into different metals and alloys, and as a result, significant structural refinement has been achieved. Observations of the structural evolution during ARB have shown the formation of a lamellar structure at high strains, indicating a microstructural evolution similar to that which takes place during conventional rolling [6]. Similarly, texture formation should compare with that of rolling. However, because of repeated stacking of sheets containing a texture gradient characterized by plane strain deformation in the centre and a high portion of shear at the surface, marked differences are expected. Morover, there are small zones heavily treated by brushing in order to accomplish good bonding.

In principal the ARB process may be easily integrated into existing industrial process chains. Thus, from the technological point of view, ARB is a highly promising process with a high light weight construction potential for the automobile and aircraft industry. Because of their significantly higher specific strength sheet like UFG workpieces should allow the production of lighter structural parts and, therefore, due to weight reduction contribute to save ressources.

It is the aim of the present project to study in detail texture formation in the aluminum alloy AA6016 as a function of ARB cycles.
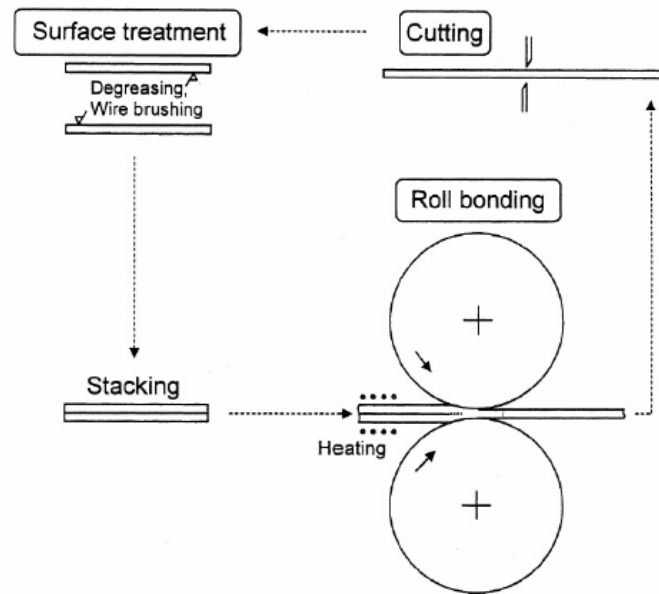
Fig. 1: Principle of the accumulative roll-bonding process [4].

Experiment

In this investigation sheets of the aluminum alloy AA6016 with an original thickness of 1 mm were used. After a recrystallization heat treatment at 520°C for 1h the ARB-process was applied at 230°C to small strips of material, which had a width of 80 - 100 mm and a length of approximately 300 mm. The reduction of the thickness was set nominally to 50% per rolling pass. After each pass (cycle) the surfaces were wire brushed, the sheet was folded at half of the length and the rolling process was repeated (Fig. 1). The number of cycles applied was eight leading to a sheet with 256 bonded layers.

Texture measurements were done by neutron diffraction on a stack of eight sheets with a size of 10 mm x 10 mm. Because of their high penetration depth neutrons allow bulk texture measurements. The orientation distribution function (ODF) was calculated from the measured pole figures (200, 220, 111) by using the harmonic method with a maximum series expansion coefficient of 22 [7].

Achievements and Main Results

The starting texture consists of a strong cube component tending to a <100> fibre parallel to ND and a minor Goss component (Figs. 2 and 3a, c). During ARB this texture breaks down and a texture typical for rolling of face-centred cubic metals with high stacking fault energy develops. The texture is characterized by the β-fibre with the Cu component dominating (Figs. 2 and 3b). Moreover, the rotated cube component forms. This component is typical for simple shear which during rolling takes place in the surface layer of the sheets.

The textures shown are the bulk textures of the entire sheet thickness. Thus, with these textures it is possible to calculate the bulk properties of the ARB sheets. Calculations of the mechanical anisotropy of the sheets are in progress. To find out the spatial distribution of the different texture components as well as texture gradients within the layers of the ARB stack, electron back-scatter diffraction with high area resolution is planned.
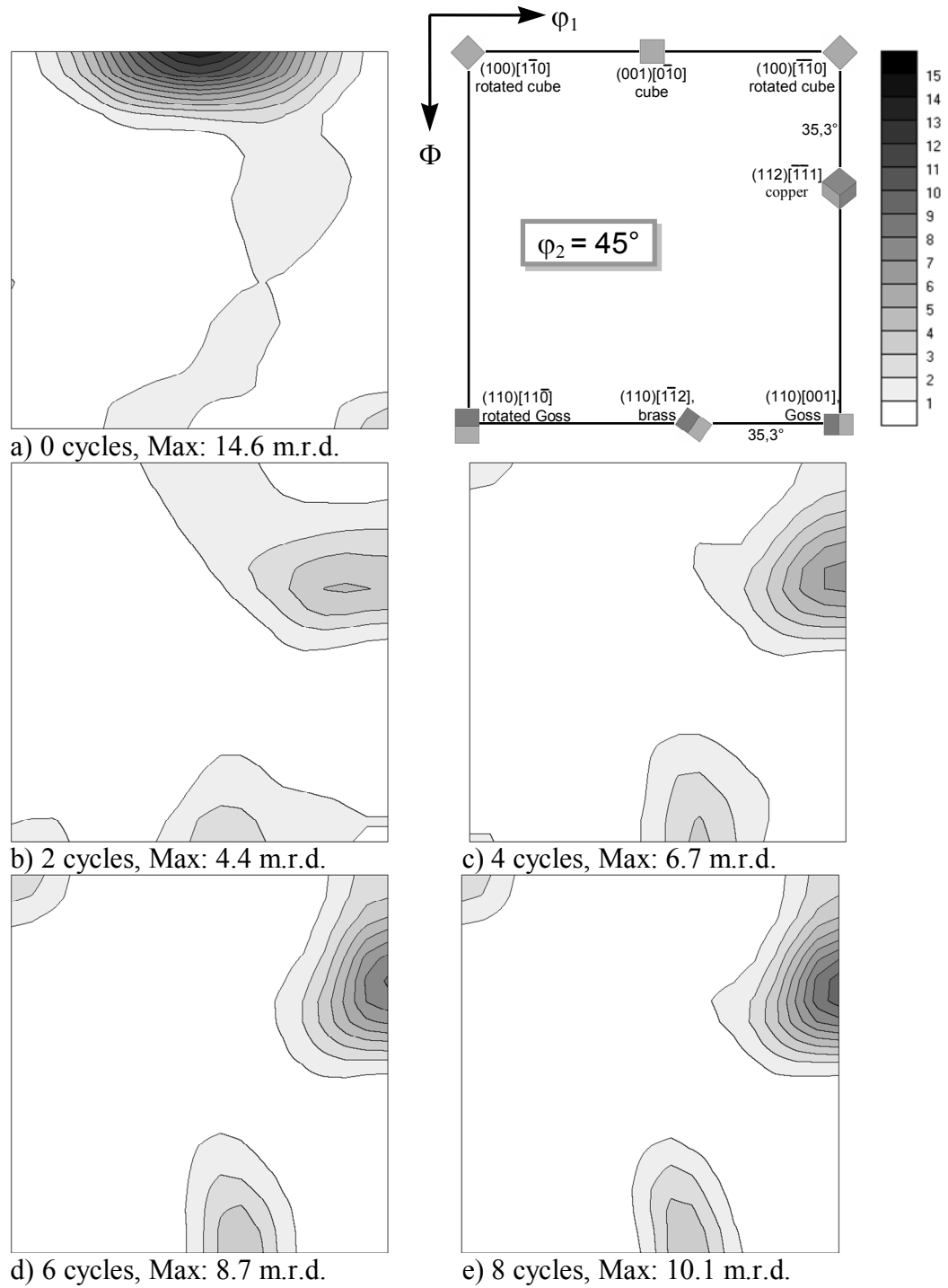
Fig. 2: Texture of ARB AA6016 after (a) 0, (b) 2, (c) 4, (d) 6 and (e) 8 cycles displayed as ODF sections at φ_2 = 45°, intensities are given in multiples of a random distribution (m.r.d.). Keyfigure shows the position of the main texture components.
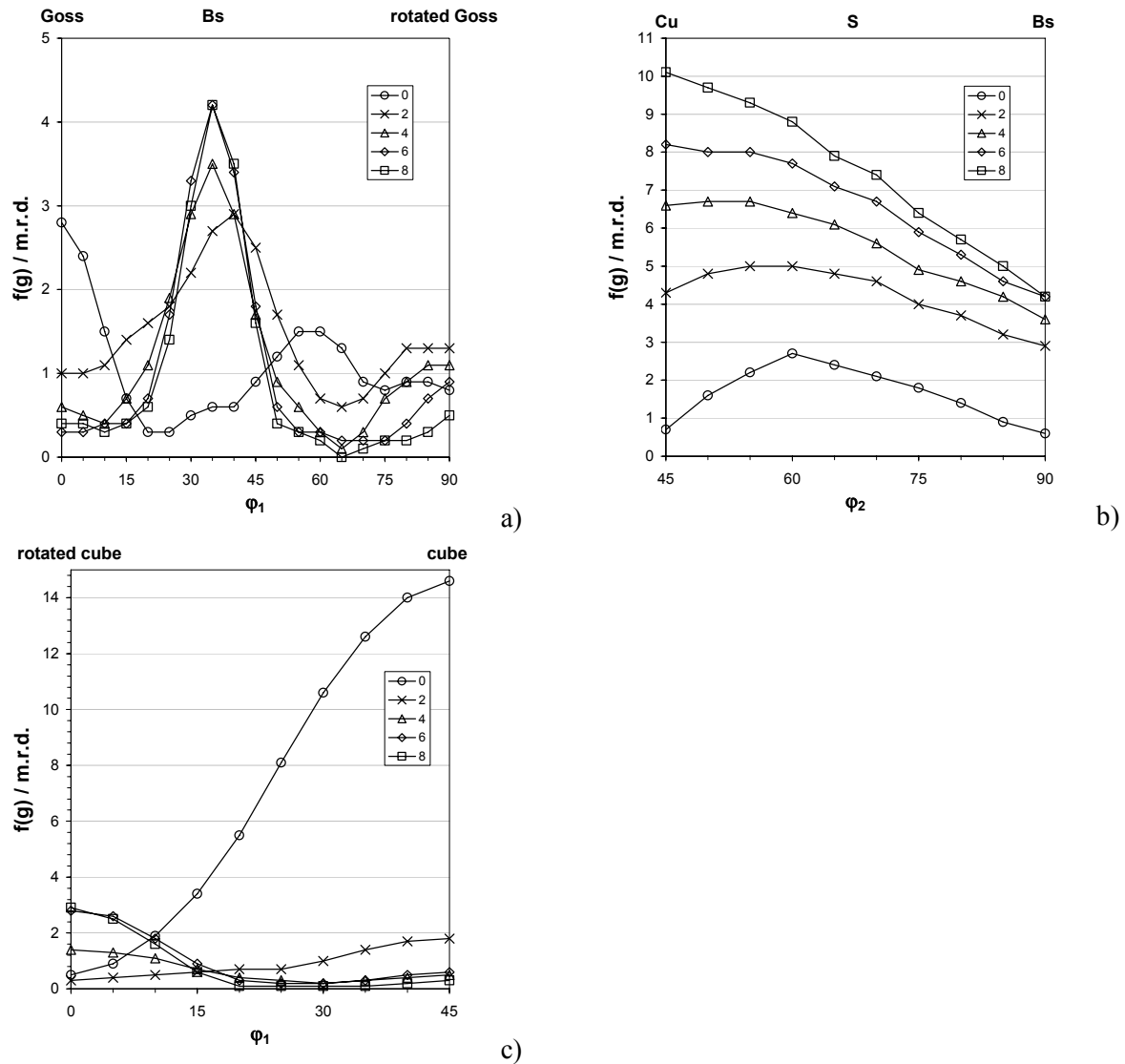
Fig. 3: Intensity along different fibres: (a) α-fibre, (b) β-fibre and (c) ND-fibre.

Acknowledgements

References

[1] Valiev, R.Z., Estrin, Y., Horita, Z., Langdon, T.G., Zehetbauer, M., JOM 58 (2006) 33.

[2] Höppel, H.W., May, J. Göken, M., Adv. Eng. Mat. 6 (2004) 219.

[3] Tóth, L.S., Arruffat-Massion, R., Germain, L., Baik, S.C., Suwas, S., Acta Mater. 52 (2004) 1885.

[4] Saito, Y., Utsunomiya, H., Tsuji, N., Sakai, T., Acta Mater. 47 (1999) 579.

[5] Tsuji, N., Saito, Y., Utsunomiya, H., Tanigawa, S., Scripta Mater. 40 (1999) 795.

[6] Huang, X., Tsuji, N., Hansen, N., Minamino, Y., Mater. Sci. Eng. A340 (2003) 265.

[7] Dahms, M, Eschner, T., Quantitative Texturanalyse durch iterative Reihenzerlegung von Beugungs-Polfiguren (software manual) (1996).

	EXPERIMENTAL REPORT	GeNF Tex-2

Texture development of Mg AZ-80 and Mg-ZK60 extruded at different temperatures

Proposer:	**Muhammad Shahzad, L. Wagner, H.-G. Brokmeier:**
	Institute of Material Science and Engineering - TEXMAT- Clausthal University of Technology
Experimental Team:	**B. Schwebke, Weimin Gan**
	IWW – TEXMAT, Clausthal University of Technology, GKSS
User Group Leader:	**Heinz-Günter Brokmeier:** IWW-TEXMAT, Clausthal University of Technology
Date(s) of Experiment:	22nd September–1st October 2006

Objectives

It is known, that the crystallographic texture plays an important rule for the anisotropy of materials properties in Mg-alloys. Intense investigations were carried out worldwide to overcome this problem, because in practical application different behavior in case of a crush due to the strain direction is unwanted. Of basic interest is the investigation of Mg-alloys with optimized properties. Two important points are the grain size and the grain size distribution. Grain refinement can be done by severe plastic deformation (equal channel angular pressing or accumulative roll bonding) and by alloying elements to form precipitations. The present study deals with a comparison of AZ80 and ZK60 extruded at different temperatures. Due to differences in the grain size one can expect a different texture behavior.

Experiment

Ingot material with coarse grained AZ80 and little finer grained ZK60 was hot extruded in a laboratory extrusion device (HBFG). In the case of 250°C, 300°C and 350°C an extrusion ratio of 46% was realized, while at the lower temperature only an extrusion ratio of 13% could be operated. Before extrusion the ingots were preheated. Thereafter, neutron test samples were cut from each rod, so that cylindrical samples were obtained for a global texture measurement of the averaged crystallographic texture of each cylinder. The instrument TEX-2 at the FRG-1 was adjusted in a way, so that no overlapping reflections occur. The wavelength was 1.24Å obtained by a graphite monochromator. According to a neutron flux of 1x10^6 n/cm²sec, the total counting time for one sample was about 18h. For each sample four pole figures were measured (Mg (10.0), (00.2), (10.1) and (11.0)) to calculate the orientation distribution function (ODF). A windws PC based program of the iterative series expansion method was used for ODF-calucaltion.

Achievements and Main Results

The texture index in figure 1 shows:
- Both ingots ZK60 and AZ80 have a random orientation distribution
- ZK60 has always the sharper texture compared to AZ80
- The two sample deformed at 200°C with an extrusion ratio of 13% show much stronger textures than the others
- With increasing temperature and constant extrusion ration a texture sharpening is observed for both alloys
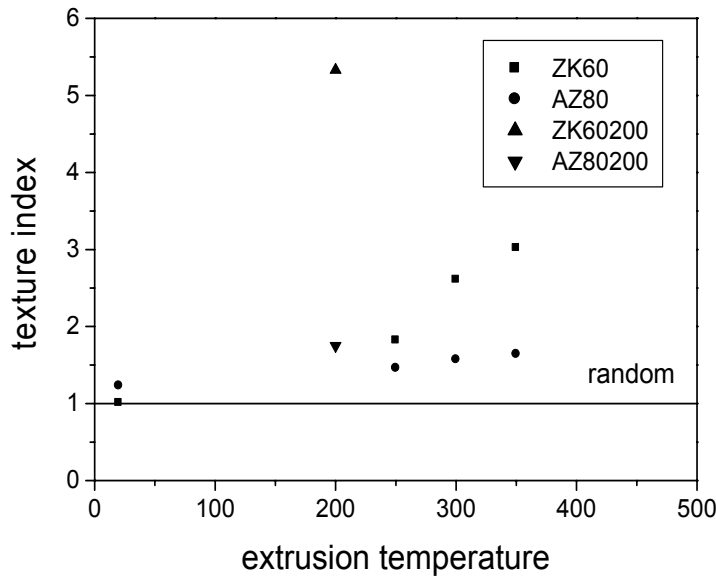
Fig. 1: Texture index

The inverse pole figures in extrusion direction explain on hand all points already mentioned in the interpretation of the texture index and on the other hand that the texture type changes with the extrusion temperature. In figures 2a-c three inverse pole figures for AZ80 at 250°C, 300°C and 350°C are shown. The main orientation H_{max} is in the corner of the (10.0) reflection but is also aligned between (10.0) and (11.0). The 200°C sample which is not shown here has an H_{max} value of 5.5 mrd.
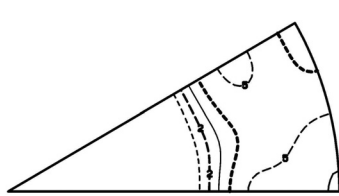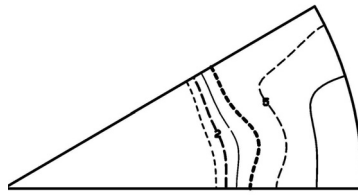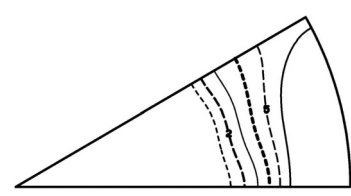
H_{max}= 2.0 mrd	P_{max}= 2.1 mrd	P_{max}= 2.7 mrd
Fig. 2a: AZ80 - 250°C	Fig. 2b: AZ80 - 300°C	Fig. 2c: AZ80 - 350°C

The identical set of inverse pole figures for ZK60 can be seen in figures 3a-c. One can see that the texture is much sharper. Moreover, the main orientation is more concentrated at (10.0). A rather strong texture with H_{max} = 15.3 mrd was analyzed for ZK60 with low extrusion ratio and 200°C extrusion temperature.

H_{max}= 5.5 mrd	P_{max}= 7.4 mrd	P_{max}= 10.1 mrd
Fig. 3a: ZK60 - 250°C	Fig. 3b: ZK60 - 300°C	Fig. 3c: ZK60 - 350°C

![GKSS logo] GKSS FORSCHUNGSZENTRUM in der HELMHOLTZ-GEMEINSCHAFT	**EXPERIMENTAL REPORT**	**GeNF Tex-2**
	Texture measurement of strip cast Mg-alloy	

Proposer:	**H. Palkowski, P. Rucki,:**
	Institut für Metallurgie, Technische Universität Clausthal
Co-Proposer:	**H.-G. Brokmeier**
	Institute of Material Science and Engineering
	TEXMAT- Clausthal University of Technology
Experimental Team:	**B. Schwebke, H.-G. Brokmeier**
	IWW – TEXMAT, Clausthal University of Technology
User Group Leader:	**Heinz-Günter Brokmeier:**
	IWW-TEXMAT, Clausthal University of Technology
Date(s) of Experiment:	10th–18th November 2006

Objectives

Magnesium strips can be produced by Direct Strip Casting (DSC), as demonstrated by Wondraczek and Palkowski [1, 2]. Direct strip casting is a continuous process of a combination of a casting process with a rolling process. An optimized strip production helps to minimize the following processes for a sheet production. The caster used at the Clausthal University of Technology (IMET) is a laboratory device with a casting width of approximately 160 mm. Molten magnesium is fed from the supply system, with a constant melt flow onto a moving belt which is cooled by water from below. Strip thickness is adjusted by melt flow in combination with speed of the cooling belt. During solidification the strip is transported to the roller table by the moving belt. The belt is driven and fixed by two rolls which are rotating synchronous. Among others the strip quality is influenced by the melt flow and the cooling. The texture gradient over the strip thickness is the basic information which can help to optimize the cooling system.

Experiment, Achievements and Main Results

Firstly, X-ray texture measurements were carried out to determine the surface texture on top and bottom of the strip. The result was a rather coarse grained material, so that the grain statistics was insufficient for a pole figure measurement. The pole figures show single spots. In order to increase the grain statistics cubic samples were prepared from three segments. Therefore, the strip was sliced in top-, bottom – and central part. The final cube was about 1cm³. From each sample the Mg (10.0), (00.2), (10.1) and (11.0) pole figures were measured. The results were shown in Figure's 1-3. All three samples show a random texture.

References:

[1] L. Wondraczek; H. Palkowski und H.-G. Brokmeier:
   Walzen von im DSC-Verfahren hergestelltem Magnesiumband
   Metall **9**, 543 – 547, 2005.
[2] Dr. Lutz Wondraczek
   Untersuchungen zur Herstellung von Magnesiumbändern mit dem DSC-Verfahren
   Technische Universität Clausthal 2005

(10.0)   (00.2)

P_{max}= 2.0 mrd P_{max}= 2.1 mrd

Fig. 1: Top of the strip

(10.0)   (00.2)

P_{max}= 2.0 mrd P_{max}= 2.1 mrd

Fig. 2: Central part of the strip

(10.0)   (00.2)

P_{max}= 2.0 mrd P_{max}= 2.1 mrd

Fig. 3: Bottom of the strip

![GKSS FORSCHUNGSZENTRUM in der HELMHOLTZ-GEMEINSCHAFT]	**EXPERIMENTAL REPORT**	**GeNF TEX-2**

Initial texture of base materials of friction welded rods	
(AA7020-T6; Ti6Al4V)	
Proposer:	**Sabine Lenser[1]**
Co-Proposers:	**Heinz-Günter Brokmeier[1]**
	[1]Institute of Material Science and Engineering – TEXMAT, Clausthal University of Technology
Experimental Team:	**Sabine Lenser[1]**
User Group Leader:	**Heinz-Günter Brokmeier[1]**
Date(s) of Experiment:	5th–14th September 2006

Objective

Friction welded joints of similar and dissimilar metals are under investigation because of their considerable advantages for many industrial applications. In addition to improving the performance of many types of equipment, such joints can also save weight and cost, especially in the automobile and aerospace industry. Friction welding is a completely mechanical solid phase process in which heat is generated by friction to produce a high-integrity welded joint between similar or dissimilar metals. In this process one part is held stationary and the other part is rotated by means of a motor which maintains an essentially constant rotational speed. The two parts are brought in contact under axial pressure for a specified period of time with a specific pressure. Finally, rotating power is disengaged from the rotating piece and the axial pressure is increased. When the rotating piece stops the weld is completed. This process can be accurately controlled when speed, pressure and time are closely regulated. Advantages of such joints cover metallurgical as well as physical properties. The main reasons for a superior weld quality are that a bonded joint is formed without using filler metal, flux, or shielding gas, and that the welding temperature is below the melting point of the work material. In addition, the heat affected zone is narrow. Furthermore, for most materials no surface preparation is required. Moreover, this joining process is environmentally clean: no arcs, smoke or flames are generated by clean parts. These advantages make friction welding an interesting method for industrial mass production of similar joints [1].

Experiment

In this report we will describe the results for the base materials of one of the different friction welding combinations. The base materials are AA7020-T6 and Ti6Al4V. The texture measurements were performed on the neutron diffractometer TEX-2 using a wavelength of 1,239 Å. The samples were measured none-destructively. The geometric form of the samples is a rod. The specimens have a length of approx. 180 mm and a diameter of 24 mm. The measurements were done far away from the welding seam and the heat affected zone. For each position complete pole figures were collected. A quantitative texture analysis was performed using the iterative series expansion method up to a degree of Lmax = 22.

Achievements and Main Results

Three complete pole figures, i.e. (111), (200), (220), were collected for AA7020-T6 (figure 1). The rolling direction (RD) is similar with the axis of the rod in the figures 1 and 2
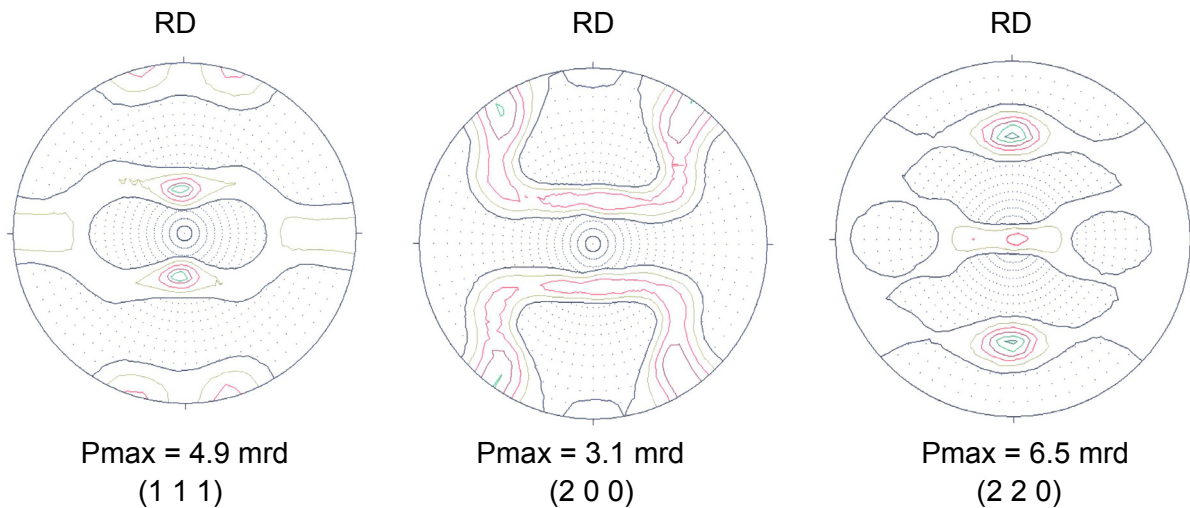
Figure 1: Measured pole figures of Al-alloy

The texture is characterized by a strong Cu component {112} <111> and a strong Brass component {110} <112>. AA7020-T6 shows also an S component {123} <634>. One is able to notice a weak Goss component {110} <001> and a weak cube component {001} <100> furthermore. This characterization is typical for rolling process [2].

Five complete pole figures, i.e. (00.2), (10.0), (11.0), (10.1), (10.2) were collected for Ti6Al4V. Figure 2 presents three representative pole figures.
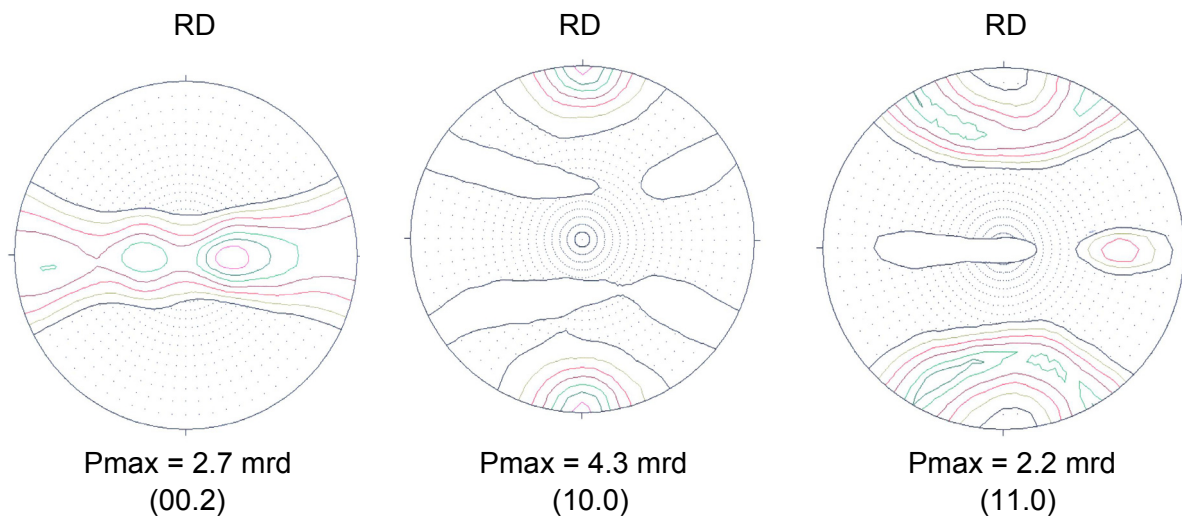
Figure 2: *Part of measured pole figures of Ti6Al4V*

The titanium-alloy is composed of two phases: the main α-phase with hexagonal crystal structure and the bcc β-phase with a small volume fraction. The presented pole figures describe the results of the α-phase [3].

The presented pole figures for AA7020-T6 and Ti6Al4V are typical results of deformation.

Further investigations deal with the texture measurement in the heat affected zone and the welding seam.

References
[1] A. Fuji, Y. Horiuchi and K. Yamamoto, „Friction welding of pure titanium and pure nickel",
      Science and Technology of Welding and Joining; **Vol. 10**, No. 3, 2005, pp. 287-294
[2] G. Wassermann und J. Grewen, "Texturen metallischer Werkstoffe", Berlin: Springer, 1962
[3] A. D. Rollett and S. I. Wright, "Typical textures in metals", Texture and
     Anisotropy, ed. F. Kocks, C. N. Tome and H.-R. Wenk, Cambridge University
     Press, 1998, pp. 181-239

![GKSS logo] GKSS FORSCHUNGSZENTRUM in der HELMHOLTZ-GEMEINSCHAFT	**EXPERIMENTAL REPORT**	**GeNF TEX-2**

Texture of similar friction welded rods		
(AA7020-T6 with AA7020-T6)		
Proposer:	**Sabine Lenser**[1]	
Co-Proposers:	**Heinz-Günter Brokmeier**[1]	
	[1]Institute of Material Science and Engineering – TEXMAT, Clausthal University of Technology	
Experimental Team:	**Sabine Lenser**[1]	
User Group Leader:	**Heinz-Günter Brokmeier**[1]	
Date(s) of Experiment:	9th–17th May 2006	

Objective

Friction welding is a solid state joining process in which heat is generated by friction to produce a high integrity welded joint between similar or dissimilar metals. This established method is new for the light metal Aluminium. This material was considered as none-weldable a long time [1].

Experiment

In this report we will describe the results of two measurements of a similar friction welding combination. The base material is AA7020-T6. The texture measurements were performed on the neutron diffractometer TEX-2 using a wavelength of 1,239 Å. The samples were measured none-destructively. The geometric form of the samples is a rod. The specimens have a length of approx. 180 mm and a diameter of 24 mm. In each case two positions above and below the welding seam were measured. In this report we present the results of two positions above the weld. The measurements were done 56 mm and 14 mm above the welding seam. Pole figures measurements below the weld are performed on the same sample area. From special interest is the modification in terms of the components and the sharpness of the texture.

A quantitative texture analysis was performed using the iterative series expansion method up to a degree of Lmax = 22.

.

Achievements and Main Results

Three complete pole figures, i.e. (1 1 1), (2 0 0), (2 2 0), were collected for each position. The rolling direction (RD) is similar with the axis of the rod.
Figures 1 and 2 shows the measured and the calculated pole figures for (111) and the ODF-sections for phi2 = 0° and phi2 = 45° respectively.

| Pmax = 5.1 mrd | Pmax = 5.1 mrd | Fmax = 10.4 mrd | Fmax = 10.4 mrd |
| measured pole figure | calculated pole figure | ODF-section | ODF-section |
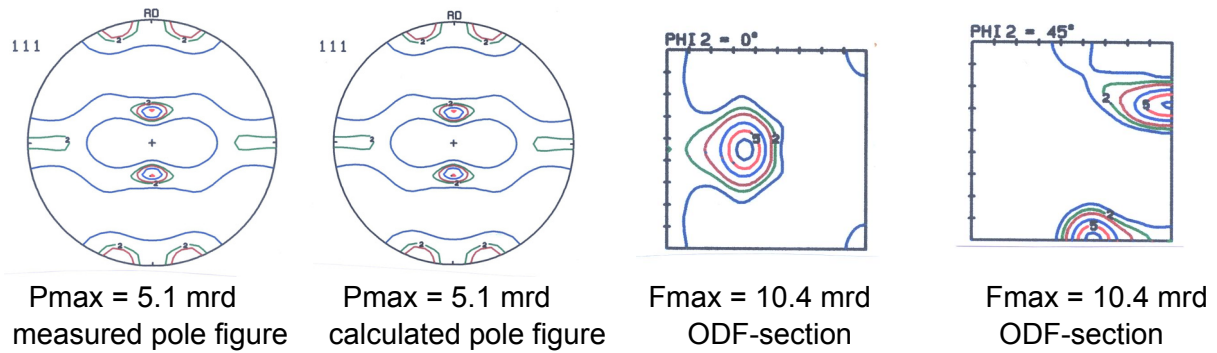
Figure 1: Measured and calculated pole figures (1 1 1); ODF-sections;
sample position 56 mm away from the weld

| Pmax = 6.0 mrd | Pmax = 5.6 mrd | Fmax = 11.2 mrd | Fmax = 11.2 mrd |
| measured pole figure | calculated pole figure | ODF-section | ODF-section |
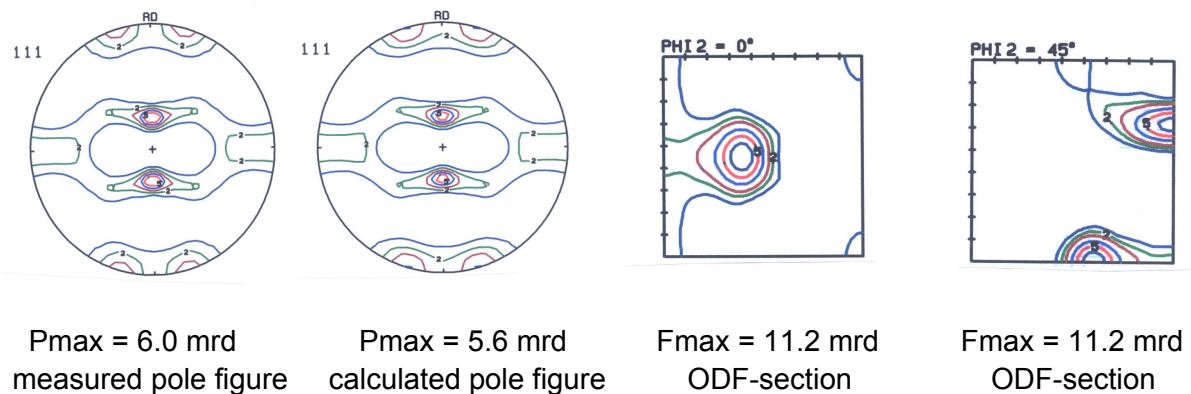
Figure 2: Measured and calculated pole figures (1 1 1); ODF-sections;
sample position 24 mm away from the weld

Figures 1 and 2 present the same texture components for different positions. The sharpness of the texture and the relation between the components of both positions are different.
The texture is characterized by a strong Cu component {112} <111> and a strong Brass component {110} <112>. AA7020-T6 shows also an S component {123} <634>. One is able to notice a weak Goss component {110} <001> and a weak cube component {001} <100> furthermore. This characterization is typical for rolling process [2].

After the welding process are the sample positions of both welding materials to each other equivalent to the positions before the welding process. A comparison of the results is possible in a directly way. The presented results above the weld are compatible with the results below the weld which are not described in this report.

References

[1] A. Fuji, Y. Horiuchi and K. Yamamoto, „Friction welding of pure titanium and pure nickel", Science and Technology of Welding and Joining; **Vol. 10**, No. 3, 2005, pp. 287-294

[2] G. Wassermann und J. Grewen, "Texturen metallischer Werkstoffe", Berlin: Springer, 1962

Texture Investigation of the Friction Stir Welding AZ31

Proposer:	**Rongchang Zeng**
	GKSS-Forschungszentrum, Max-Planck Strasse1, Geesthacht Germany
Co-Proposers:	**Wolfgang Dietzel, Karl Ulrich Kainer**
	GKSS-Forschungszentrum, Max-Planck Strasse1, Geesthacht Germany
Experimental Team:	**B. Schwebke, Weimin Gan**
	IWW – TEXMAT, Clausthal University of Technology, GKSS
User Group Leader:	**Heinz-Günter Brokmeier:**
	IWW-TEXMAT, Clausthal University of Technology

Date(s) of Experiment:	1st–4th May 2006

Objectives

Magnesium alloys have attractive applications as the light structural materials in automobile industry, aerospace etc. The friction stir welding (FSW) has been demonstrated to be a very effective and environmentally attractive method for a wide range of metals and alloys. Magnesium alloys such as AZ31 etc have been demonstrated to be successfully jointed by FSW. The process involves severe plastic deformation in the solid state; there is no melting and metal flow occurs by dynamic recrystallization. Dynamic recrystallization provides the mechanism for solid-state flow in the FSW process and the weld zone is always characterized by a recrystallized, usually equiaxied, small grain structure.

During the stress corrosion cracking (SCC) tests of FSW-AZ31 samples, it was found that the small cracks initiated in the welded zone, and generally propagated and connected together, finally formed several main cracks. However, the interest is that these initial small cracks seem to be parallel each other along a certain direction. Therefore, it is very necessary to investigate the texture of the welded zone and the base material as a comparison.

Experiment

Four pieces of sheet samples cut from the welding region were clipped together for the texture measurement by neutron diffraction at the 4-circle diffractometer TEX-2. Sample's coordination system is defined according to the welding direction. Four complete pole figures (10.0), (00.2), (10.1), (11.0) were measured by the combination of the reflection and transmission methods. ODFs were calculated by serious expansion method with an expansion degree L_{max}=22 [1].

Achievements and Main Results

The matrix alloy has a (0002) fiber texture, which is very typical for the rolling texture of Mg-AZ31. With 9.8 mrd the crystallographic texture is relatively sharp. As for the welding region, basal planes tilted at about 25° to the welding direction, which is due to the shear deformation during high temperature welding. To give a more pronounced interpretation of this 25° angle, one needs a correlation between the welding speed in forward direction. Therefore more samples with varies welding conditions are necessary. The pole intensity of the $(11\bar{2}0)$ was increased, which is related to the DRX during cooling.

References

 [1] Brokmeier H. -G..
      Advantages and Applications of Neutron Texture Analysis
      Textures and Microstructures **33**, 13-33, 1999.

a)   (00.2)   a)   (11.0)

b)   (00.2)   b)   (11.0)
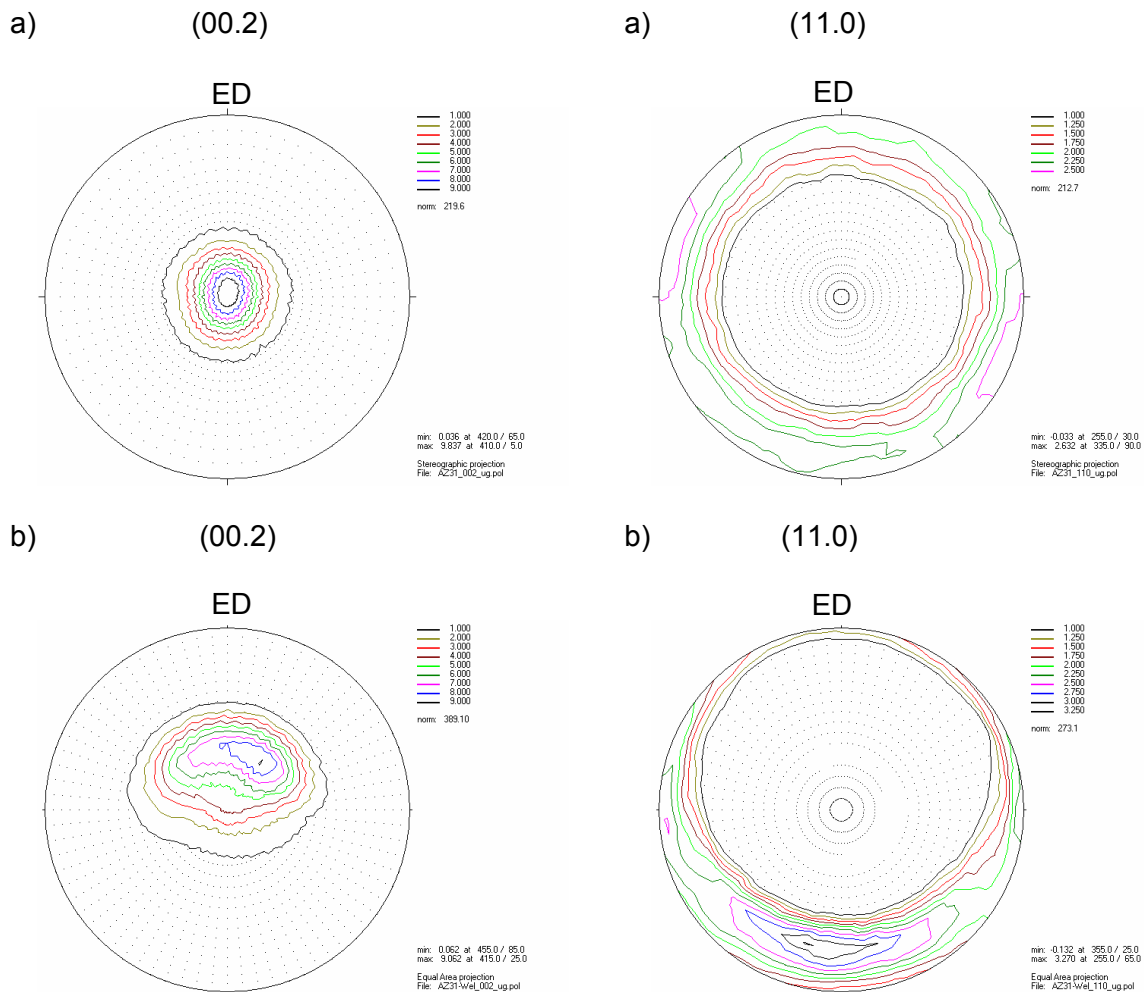
Fig.1: Measured completed pole figures of the (a) matrix alloy and (b) welding region.

![GKSS logo] GKSS FORSCHUNGSZENTRUM in der HELMHOLTZ-GEMEINSCHAFT	**EXPERIMENTAL REPORT**	**GeNF Tex-2**

Absorption influence on the quality of quantitative textures		
Proposer:	**S.- J. Jin:** Institute of Material Science and Engineering - TEXMAT- Clausthal University of Technology	
Co-Proposers:	**Heinz-Günter Brokmeier**: Institute of Material Science and Engineering - TEXMAT-, Clausthal University of Technology	
Experimental Team:	**B. Schwebke, S.-J.Jin** IWW – TEXMAT, Clausthal University of Technology	
User Group Leader:	**Heinz-Günter Brokmeier:** IWW-TEXMAT, Clausthal University of Technology	
Date(s) of Experiment:	19th–25th November 2006	

Objectives

The pole figure measurement is based on intensity measurements of the half of the orientation sphere. An ideal case is a small spherical sample with low absorption and a large beam size with a beam of high penetration power. In such a measurement no corrections are necessary and complete a pole figure with high quality results. In all other cases absorption can play a rule for the quality of the pole figure. The absorption depends on the radiation respectively the effective absorption coefficient, the sample geometry and the scattering angle.

In the case of composite material a very special situation takes place if the absorption coefficients are different, which is normal. It was demonstrated by Bunge [1] that the microstructure is of great importance. Figure 1 shows some microstructures (globular with round particles in a matrix, curling structure and lamellar structure), which have a different ansotropic absorption behavior due to the sample orientation.
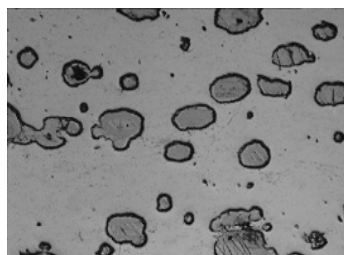
Fig. 1a: Al10-Cu90 (round particles)
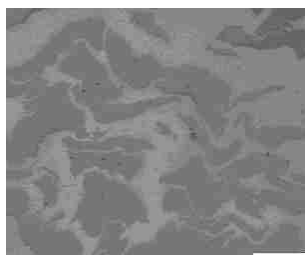
Fig. 1b: Cu50-Nb50 curling structure
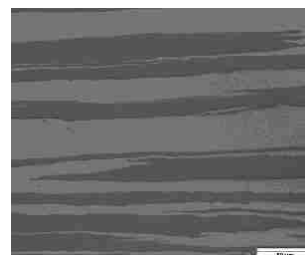
Fig. 1c: Cu50-Nb50 lamellar structure

A project was started to look on extreme cases of two-phase materials as shown in figure 2, to investigate the absorption influence on the quality of measured pole figures using neutron diffraction and high energy X-ray. Both radiations have similar penetration power, but the true absorption is different. We will expect differences in the influence of the absorption on the quality of the non-corrected pole figures.
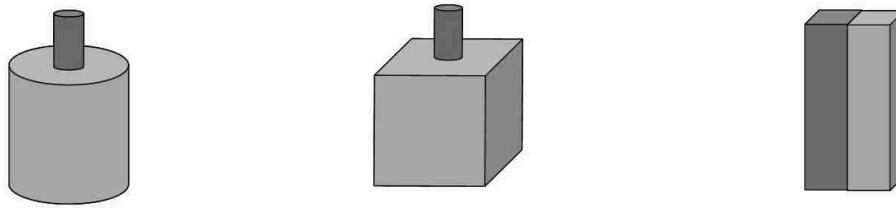
Fig.2: Three types of combinations with different geometries of the two phases

Experiment

A first set of wires were taken from the store:

> Steel wires with 20mm, 10mm, 5mm and 3mm diameter and a gamma-Fe crystal structure;
> Cu wires with 16mm and 10mm;
> Al wires with 20mm, 10mm and 5mm

The wires were cut to test samples with a length corresponding to diameter. In the next step one set of sample were used to prepare composites. Therefore, holes were drilled in Cu16mm, Cu10mm, Fe20mm, Fe10mm and Al20mm with diameters of 3mm, 5mm and 10mm. This second set of samples was not part of the present experiments.

In order to have the whole test sample in the primary beam the beam size varies from sample to sample. Also the different scattering behavior was taken into account so that the total counting time for the different samples (sample volume, neutron scattering length of Fe, Cu and Al) vary. The set of 9 samples was measured with three pole figures each to be able to calculate the orientation distribution function for texture comparison.

Achievements and Main Results

Figure 3 gives the three (110) pole figures of the steel wires. One can see that a wire has not necessarily cylindrical pole figure symmetry. That means, they were processed in a different way than wire drawing or round extrusion.

| 111 | 111 | 111 | 111 |
| P_{max}= 1.4 mrd | P_{max}= 2.3 mrd | P_{max}= 4.2 mrd | P_{max}= 7.1 mrd |
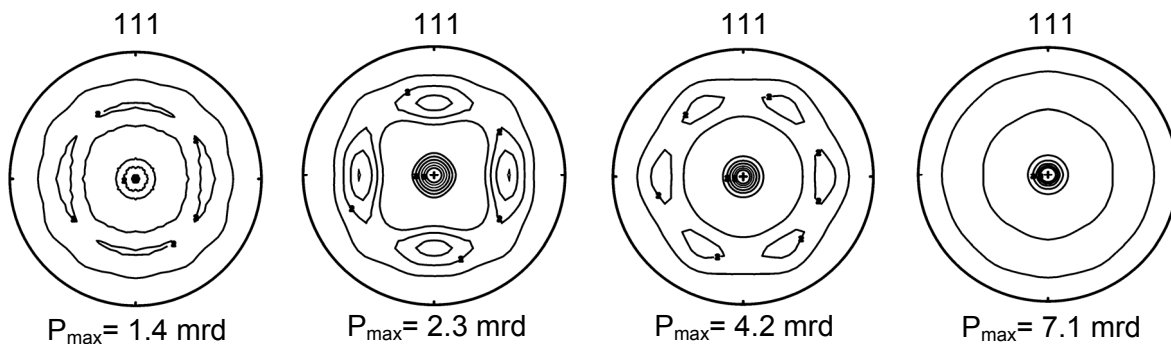
Fig. 3a: Steel 20mm   **Fig. 3a:** Steel 10mm   **Fig. 3a:** Steel 5mm   **Fig. 3a:** Steel 3mm

References

[1] H.-G. Bunge, Anisotropic Absorption in Multiphase Texture Analysis in: Experimental Techniques of Texture Analysis, ed. H.J. Bunge, DGM-Informationsges. Oberursel1986.

GKSS FORSCHUNGSZENTRUM in der HELMHOLTZ-GEMEINSCHAFT	**EXPERIMENTAL REPORT**	**GeNF POLDI**

Polarised diffractometer POLDI

Short Instrument Description:
With the polarised diffractometer 3-D depolarisation analysis is used to investigate magnetic properties and correlations in magnetic materials. With minor modifications a time of flight option in non-polarised mode is additionally available for the purpose of dosemeter calibration.

Local Contact:
Jochen Fenske
Phone/Fax : +49 (0)4152 87 – 1224 / +49 (0)4152 87 – 1338
e-mail: jochen.fenske@gkss.de

Dr. Dieter Lott
Phone/Fax : +49 (0)4152 87 – 1372 / +49 (0)4152 87 – 1338
e-mail: dieter.lott@gkss.de

Schematic View of POLDI:

$$P = \mathcal{D} P_0$$
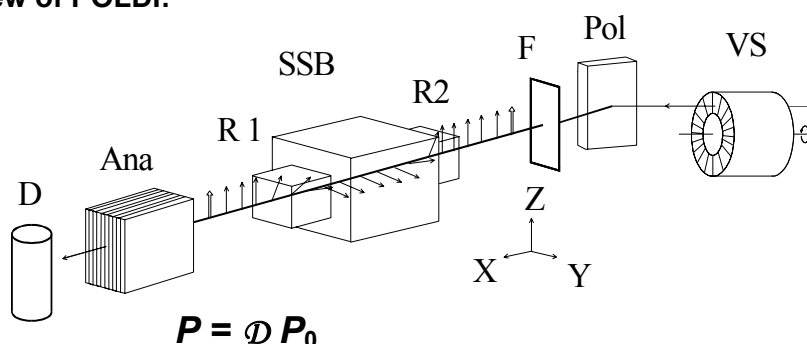
Set-up for full 3-dimensional neutron depolarisation analysis in the transmitted beam

Instrument Details:

Location at FRG-1:	beamline 7, thermal neutrons cross section 10 x 4 cm^2,
Polariser / monochromator (Pol)	Cu$_2$MnA (111), PG(002), Si (311) doubly focussing; helical slot selector (VS)
Take-off-angle:	$10° < 2\,\Theta_M < 65°$
Wavelength:	λ = 0.1 to 0.36 nm, 2nd order suppression by velocity selector (VS)
Flux at sample position:	Φ_{max} = 0.8 ·10^5 cm^{-2} s^{-1} (polarised)
Analyser (Ana):	Co/Ti-supermirror
Overall polarisation:	0.94
3D depolarisation analysis in transmitted beam:	accuracy < 1% for any component of ***D***
Sample environment fitting in the magnetically shielded sample box (SSB) for 3D depolarisation analysis:	- refrigerator T >12 K, - DC magnetic field < 160 A/cm - pulsed field < 8.0 kA/cm - superconducting magnet up to 5.0 T
Detector (D):	^{3}He-counter
Instrument control / data acquisition:	remote internet PC control IEEE bus, serial bus and special interfaces

Investigation of temperature behaviour of the AF-FM transition in $Fe_{50}Pt_{50-x}Rh_x$ thin films

Principal Proposer:	**P. Mani[1], D. Lott[2]** [1] MINT Center, University of Alabama, Tuscalosa, Al, USA [2] GKSS Research Centre, Institute for Material Science
Experimental Team:	**J. Fenske[2], D. Lott[2]**
Date(s) of Experiment:	March 2006

Introduction

In the last years, perpendicular recording has been in the focus of scientific and technological interest in the search for materials to overcome the limitations in storage density of conventional magnetic recording media. Promising media such as FePt, have a high perpendicular anisotropy providing good thermal stability. However, the high anisotropy leads also to high coercivity fields and therefore to high write fields. In order to lower the high coercivity soft magnetic underlayer are needed. A possible candidate for such an underlayer is the $L1_0$ structured $Fe_{50}Pt_{50-x}Rh_x$ film. The bulk system shows an antiferromagnetic (AF) phase at low temperature and ferromagnetic(FM) phase at high temperature [1]. In the low temperature state the AF phase stabilizes the magnetization state of the recording media and at high temperature state the FM phase leads to a strong reduction of the write field [2].

Results and Discussion

With the neutron diffractometer POLDI temperature dependent measurements were performed in a temperature range between 12K and 325K on the $Fe_{50}Pt_{40}Rh_{10}$ film. The out-of-plane scans clearly show the (001/2) peak at about 0.85Å⁻¹ (see Fig.1). The peak intensity decreases with increasing temperature, but is still observable at 325K which was the highest temperature that could be reached with the setup. Additionally, the in-plane (1/200) peak could be detected at about 1.17Å⁻¹ (see Fig.: 2). Similar to the out of plane peak the intensity of the in-plane peak also decreases with increasing temperature but vanishes already at a temperature of about 292K. By fitting the data using the power law, $I(T)^{1/2} = [1 - T/T_c]^\beta$ it could be calculated that the out-of-plane peak vanishes at a temperature of about 329K which is approximately 40K higher than the in-plane peak. Figure 3 shows the temperature dependent intensity curves corrected for illumination effects for both the in-plane and out-of-plane peaks with the corresponding fits. It should be noted that the intensity of the in-plane peak is approximately three times less then the out-of-plane peak intensity.
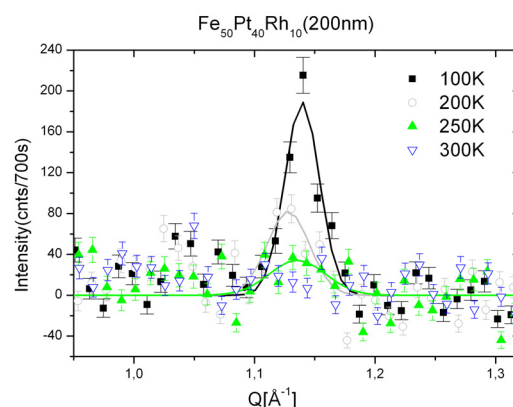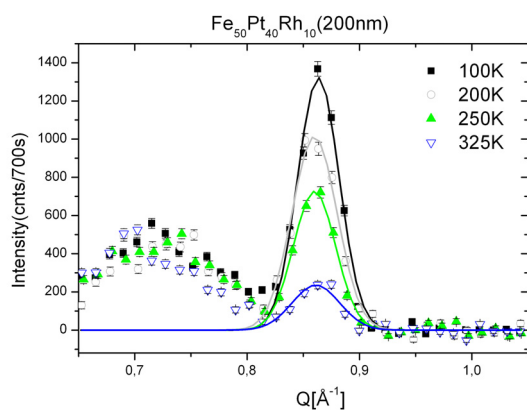
The appearance of both half order peaks shows clearly the presence of an antiferromagnetic configuration of the magnetic moments in the out-of-plane as well as in the in-plane direction. The ratio of the integrated intensity between the out-of plane and in-plane peaks can be explained with a dominantly in-plane orientation of the magnetic moments.

Furthermore the decreasing peak intensity of both peaks with increasing temperature is a possible indication for a reorientation of the magnetic moment with rising temperature and thus an AF-FM phase transition in this system.
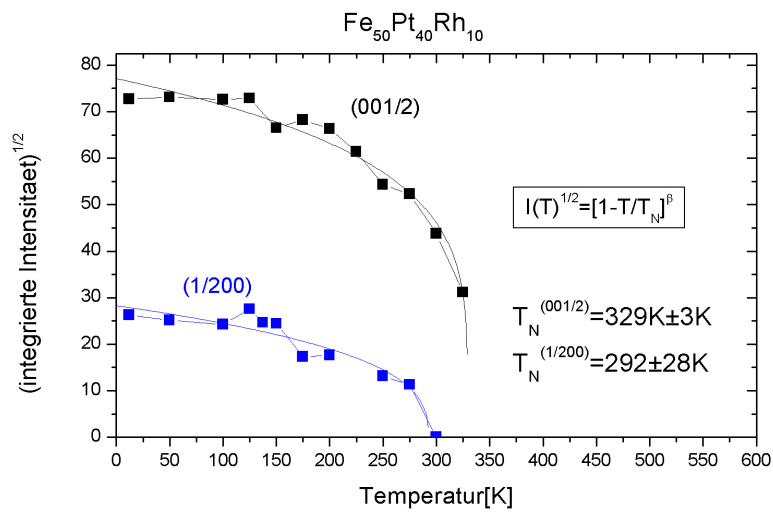
Fig.3: Integrated Peak intensity against temperature

Outlook

Following these measurements, a detailed study of the (002) and (200) peak is planned to examine the possibility of an AF-FM phase transition. Additionally, measurements of $Fe_{50}Pt_{50-x}Rh_x$ films of the same thickness but with different Rh concentration will be performed to examine the temperature behaviour of the samples in the dependence of the composition.

[1]Takizawa, K; Ono, T; Miyajima, H, Journal of Magnetism and Magnetic Materials **226**: 572 Part 1 Sp. Iss. SI MAY 2001
[2]Thiele, J-U, Maat, S, Fullerton, EE, Applied Physic Letters **82** 2859(2003)

Investigation of exchange bias between MnPt and CoFe layers

Principal Proposer:	**D. M. Solina[1],** [1]GKSS Research Centre
Co-Proposers	**Lai, C.-H.[2],** [2]Dept. Phys., Univ. Tsing-Hua, Taiwan
	J. Fenske[1]
	A. Schreyer[1]
Experimental Team:	**J. Fenske and D. M. Solina**
Date(s) of Experiment:	May 2006

Scientific Objective

The phenomena of exchange bias (EB), observed as a shift in the ferromagnetic hysteresis loop owing to pinning of the ferromagnetic layer at a ferromagnetic/ anti-ferromagnetic (FM/AFM) interface is used extensively in the fabrication of magnetic recording media devices. Although EB is used, the exact nature of the coupling is poorly understood, in particular the role of the AFM layer, thus hindering the optimisation of the performance of these devices.

Neutron diffraction is the ideal technique to access information on the moment -structure, - direction, -size and even -domain size. Neutron diffraction studies to investigate the behaviour of the AFM layer have been made on repeat multilayers [1] however, to date, no neutron diffraction studies have been made on the system as it is used in industry i.e. with a single AFM layer (~100 nm) and FM layer. This is primarily owed to the small amount of material available and the difficulty in obtaining a single crystal layer of sufficient quality to give a reflection. After much work on sample optimisation, new samples of EB MnPt/CoFe have been obtained from Taiwan. At GeNF, sample characterisation was carried out on RöDi and POLDI to determine whether the sample was of sufficient quality for further measurements.

Sample

The layer system :CoFe(10 nm)/MnPt (100 nm)/MgO(100) was fabricated using sputter deposition and annealed in field. MnPt is an ordered AFM that requires annealing to transform from the non-magnetic face-centred-cubic phase to the AFM face-centred tetragonal phase shown in Figure 1.
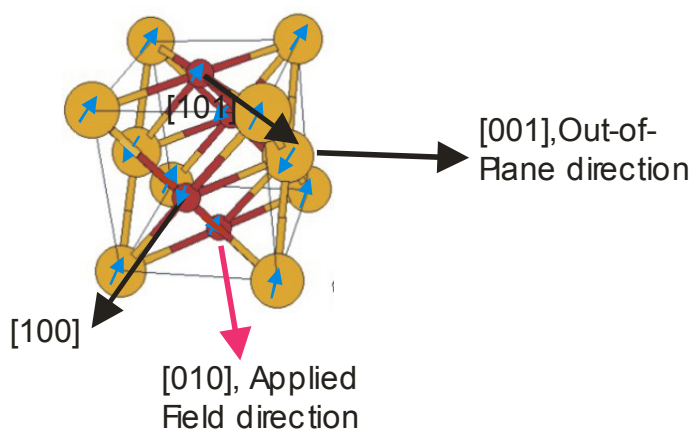
Hysteresis loops show EB occurs in the annealed direction only (figure 2).

Figure 1: Schematic of MnPt structural and AFM moment structure. Yellow: Mn and Red: Pt atoms. Arrows show [001], [100] and [010] plane direction and annealing field direction.
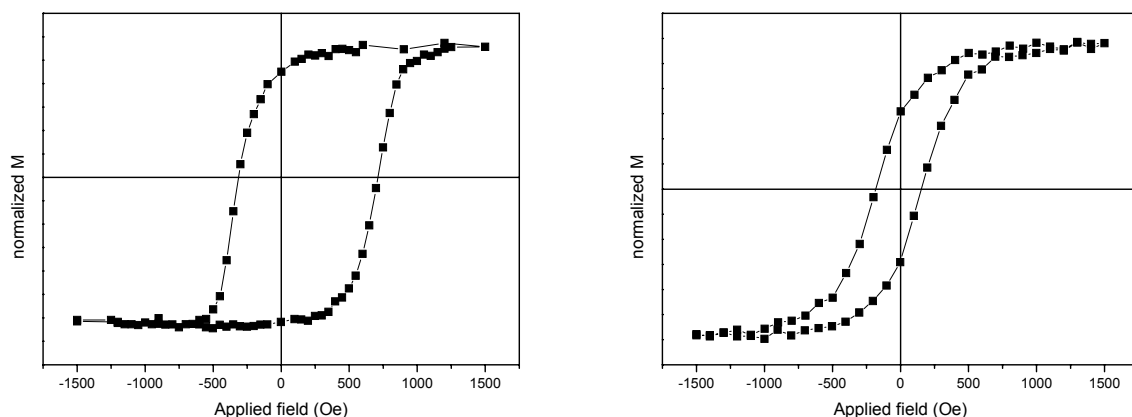
Figure 2: A. Annealed at 350 ℃ for 1 hr - 0°, B. Annealed at 350 ℃ for 1 hr – 90°

Experimental Technique, Results and Preliminary Conclusions

Structural measurements carried out on RöDi in order to determine the quality of the sample show that it is single crystal with well defined in-plane scans and a rocking curve of ~1.3°.

Neutron diffraction measurements for the MgO(002) structural reflection, MnPt(001) superlattice peak, and MnPt(100) and MnPt(101) AFM diffraction peaks were carried out at both room temperature and 12 K on the neutron diffractometer, POLDI. The results are given in figure 3.

As is clearly visible in the figure, both the MnPt(100) and MnPt(101) AFM peaks are present. There is no significant change observed in peak intensity with temperature. This is possibly owed to the fact that MnPt is a high temperature AFM with a Neel temperature of 975±10 K [2]. For a sample of only 100 nm thickness and mosaic spread of 1.3° this is a wonderful result.

These preliminary measurements confirmed that the samples were appropriate for diffraction measurements at a higher intensity source e.g. the ILL. As a result, the sample was used in a test measurement on the ILL instrument IN12 in August and the first polarized measurements on the EB system as used in industry were obtained.
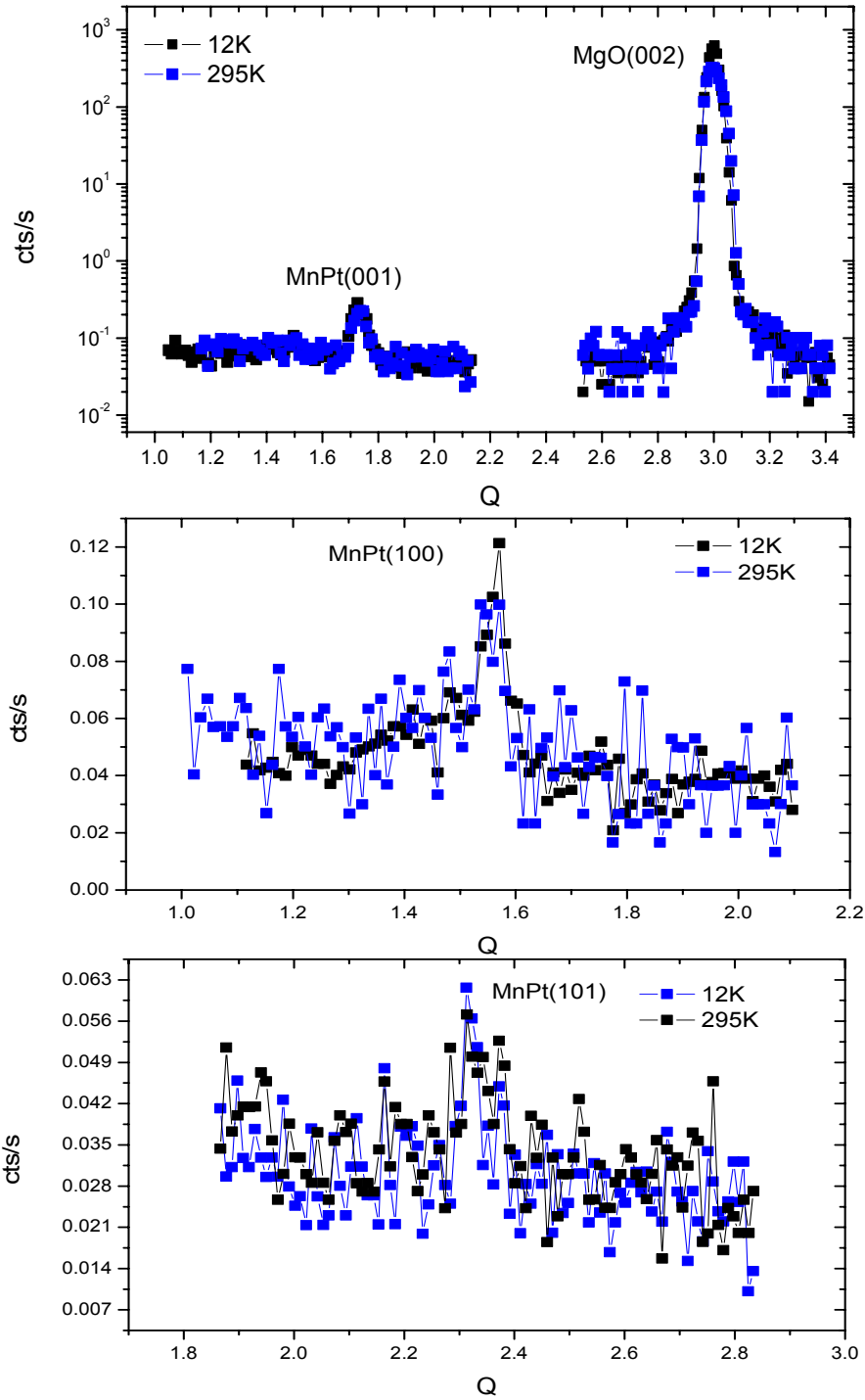
Figure 3: Neutron diffraction results for Top: MgO(002) substrate structural peal and MnPt(001) superlattice peak, Middle: MnPt(100) AFM diffraction peak and Bottom: MnPt(101) AFM diffraction peak at 295 K and 12 K, as indicated in the diagram.

References

[1]   Y. Ijiri et al., Phys. Rev. Lett. **80**, pp. 608-611 (1998).
[2]   E. Kren et al., Phys. Rev. **171**, pp. 574-585 (1968).

Neutron diffraction studies on Dy/Y superlattices

Principal Proposer: A. Grünwald[1,2], A. Wildes[2], W. Schmidt[3], H. Tartakowskaya[4], R.C.C. Ward[5], A. Schreyer[1]

[1] GKSS Forschungszentrum GmbH,Institut for Material Science, Max-Planck Str. 1, D-21502 Geesthacht, GERMANY
[2] Institut Laue-Langevin, Grenoble/FRANCE
[3] Forschungszentrum Jülich, GERMANY
[4] Institut for Magnetism, Kiev/UKRAINE
[5] Oxford University, UK

Experimental Team: D. Lott[1] / J. Fenske[1], A. Grünwald[1,2]

Date(s) of Experiment: July 2006

Introduction:

Diffraction measurements with thermal neutron scattering have been performed on Dy/Y samples on POLDI in preparation for subsequent experiments with inelastic neutron scattering on PANDA (FRM-II, Munich) and on IN12 (ILL, Grenoble).

Investigation of spin excitations in magnetic multilayers is of great interest to understand fundamental properties of solids and magnetic parameters of confined structures and because of modern thin film growth techniques which allow great flexibility in the choice of sample composition. While techniques as Brillouin Light scattering and Ferromagnetic Resonance experiments are limited to specific regions in reciprocal space, Inelastic Neutron Scattering provides, in principle, access to the entire Brillouin zone. In the past we have conducted a series of inelastic neutron measurements on IN12, IN14 (ILL) and on PANDA (FRM-II) on a Dy/Y superlattice system of the layer sequence $Y_{50nm}[Dy_{4.3nm}/Y_{2.8nm}]_{x350}/Y_{234nm}/Nb_{200nm}/Al_2O_3$(substrate) around the Dy/Y(0002-т) reflection [1], showing indications of *discrete* energy levels for spin waves propagating along the surface normal. Bulk Dy has a hexagonal closed packed structure. Below 179 K the magnetic moments order in an incommensurate helix along the crystallographic c-axis and possess a first order phase transition to a ferromagnetic state at 89 K. In Dy/Y superlattices the ferromagnetic phase is suppressed, due to magnetoelastic effects. The helical phase coherence extends over several multilayer periods [2]. In comparison with bulk Dy, in Dy/Y superlattices the Néel temperature decreases slightly with decreasing bi-layer thickness. Bulk Y is non-magnetic and has hexagonal closed packed structure with similar lattice parameters to Dy.

To study the dependence of the spin excitation spectra on the Dy and Y slab thicknesses, new samples with different bi-layer thicknesses, $Y_{25nm}/[Dy_{3nm}/Y_{3nm}]_{x150}/Y_{50nm}/Nb_{50nm}/Al_2O_3$(substrate) and $[Dy_{3nm}/Y_{1.8nm}]_{x150}$, have been grown with MBE methods along the c-axis of Dy and Y. As inelastic measurements are very sensitive to the magnetic structure, here elastic neutron diffraction measurements as a function of temperature have been carried out in advance to exclude from fundamental differences in the magnetic structure of the new samples in comparison with the previous sample.

Experiment:

To verify the magnetic structure and the Néel temperature in the new Dy/Y superlattices, non-polarized, elastic neutron measurements have been performed around the Dy/Y (0002) Bragg peak as function of temperature. The instrument was set up in the standard diffraction mode with 30'-60' collimation around the sample. For the measurements on the $[Dy_{3nm}/Y_{3nm}]_{x150}$ sample the velocity selector was used to discriminate against higher harmonics. The other sample has been measured without selector due to temporary problems with the selector. It turned out, that no disturbing harmonics were measured and thus allowed to also evaluate the data.
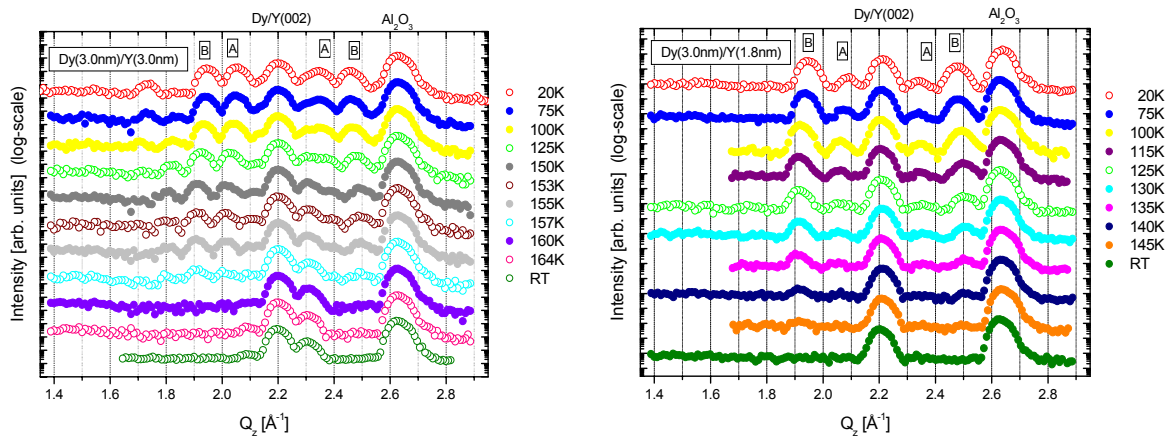
Fig.: Elastic neutron diffraction scans as function of temperature on Dy/Y superlattices around the (002) Bragg peak. The +1/-1 helical magnetic peaks (A) and the corresponding +1/-1 superlattice peaks (B) are indexed, respectively.

Results:

Neutron diffraction scans as function of temperature show on both Dy/Y superlattices the features known from a previous measured sample confirming that the temperature dependent behaviour of the helimagnetic structure is similar. With increasing temperature the helimagnetic peaks and the corresponding superlattice peaks shift further away from the Bragg peak due to an increasing interplane turn angle of the helimagnetic spiral. As expected, the phase transition from the helical phase to the paramagnetic phase occurs at reasonable lower temperature in the sample with less Y in the bi-layer.

References:
[1] A. Schreyer et al., J. Appl. Phys. 87, 5443 (2000)
[2] M.B. Salamon et al., Phys. Rev. Lett. 56, 259 (1986)

GKSS FORSCHUNGSZENTRUM in der HELMHOLTZ-GEMEINSCHAFT	**EXPERIMENTAL REPORT**	**GeNF GENRA-3**

Geesthacht neutron radiography and tomography facility GENRA-3

Short Instrument Description

The Geesthacht neutron radiography and tomography facility serves as an instrument for non-destructive testing and damage analysis of materials and technical structures by static and dynamic imaging. The ability of light elements, e.g. hydrogen or boron, to absorb neutrons allows unique analysis possibilities.

Local Contact:

Dr. P. Klaus Pranzas
Phone/Fax : +49 (0)4152 87 – 1326 / +49 (0)4152 87 – 41326
e-mail: pranzas@gkss.de

Jürgen Vollbrandt
Phone/Fax : +49 (0)4152 87 – 1268 / +49 (0)4152 87 – 1338
e-mail: juergen.vollbrandt@gkss.de

Schematic View of GENRA-3:

Instrument Details:

Location at FRG-1:	beamline 13, thermal neutrons
Collimation ratio:	100 to 300
Flux at sample position:	Φ_{therm} = 1.4·10^6 cm^{-2} s^{-1} Φ_{epi} = 8·10^3 cm^{-2} s^{-1} with 4 cm Bi-filter at position: 2 m from beam exit available filters: 9 cm Bi-filter combined with 10 cm Be 0.2 cm Cd
max. size of specimen:	100 x 200 cm^2
Image:	15 x 15 cm^2 to 45 x 45 cm^2
Detecting: direct imaging indirect imaging	Gadolinium foil: max 14 x 17 inch Gd-scintillation screen connected to an image intensifier video camera transfer material: Indium, Dysprosium
Sample handling	Remote control of specimen, e.g. for scan purposes

Neutron Tomography (NCT) on tyrannosaurid foot at GENRA-3

Proposer:	**Tjard Kusche[1], [1]GeoStudio, Heidmoor**
Co-Proposers:	**F. Beckmann[2], J. Vollbrandt[2], H.-W. Schmitz[2], T. Donath[2], A. Schreyer[2], [2]GKSS**
Experimental Team:	**F. Beckmann[2], J. Vollbrandt[2], H.-W. Schmitz[2]**
User Group Leader:	**Tjard Kusche[1]**
Date(s) of Experiment:	27th–28th April 2006

Objectives

The recently developed setup for Neutron Computerized Tomography (NCT) at GENRA-3 was used to study the 3-dim. bony structure of tyrannosaurid left foot specimen. NCT is the pre-analysing method to find organic remains that could be destoyed through the following preparation.

Experiment

The setup for neutron tomography was installed in the irradiation chamber of GENRA-3 at distance P = 0.5 m in the hutch, resulting in a distance to the source of about 3.5 m. The neutron beam parameters are:

P [m]	0.5
Size [cm^2]	16x16
Flux [$n\,cm^{-2}\,s^{-1}$]	$7.4 \cdot 10^6$
L/D	100

The setup for tomography consists of a 2-dimensional neutron detector and a high precision sample manipulator (s figure 1). A more detailed description of the used setup and components can be found elsewhere [1].
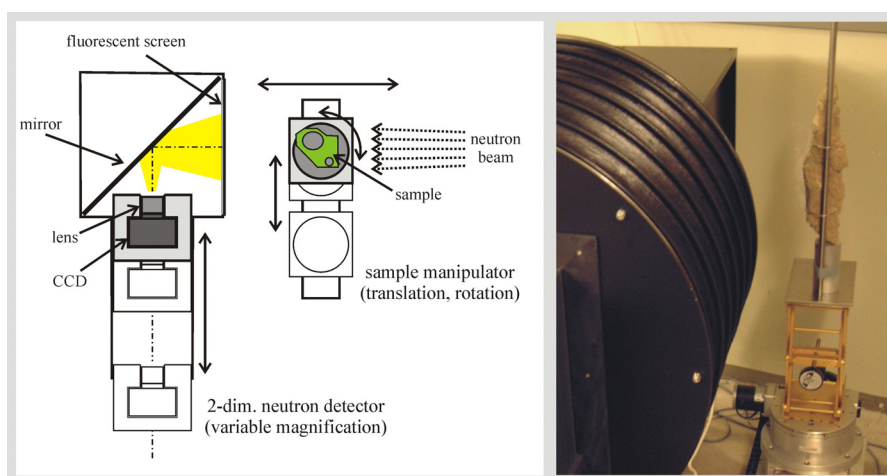
Figure 1: Sketch of the experimental setup for NCT (left). Investigation of the tyrannosaurid foot (right). The sample is installed on the manipulation stage in front of the fluorescent screen
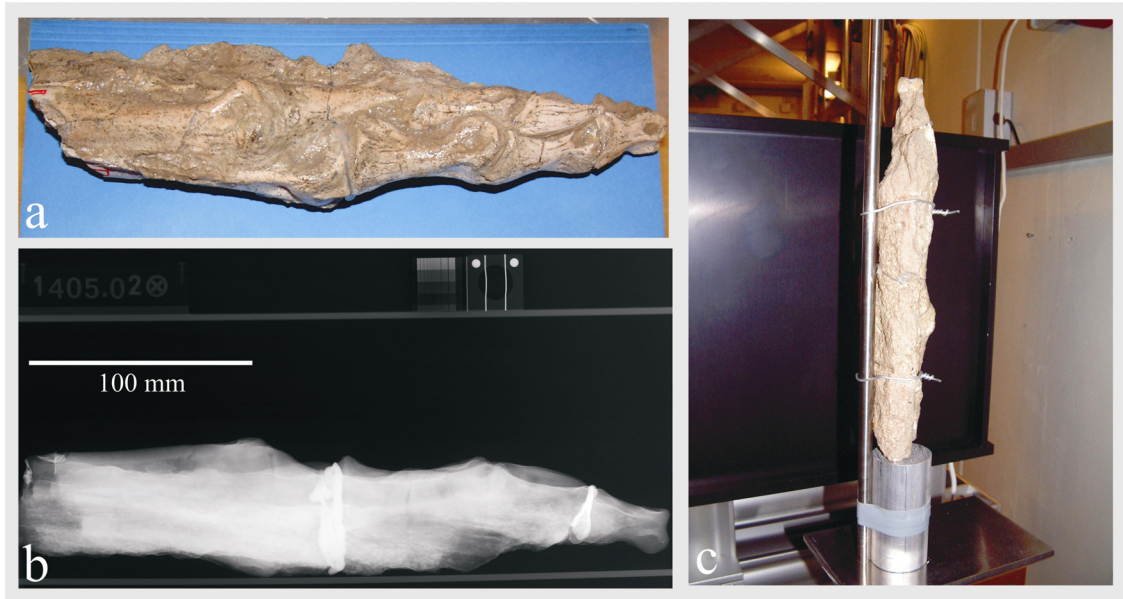
Figure 2a: Optical viewgraph of the tyrannosaurid-foot specimen. ***2b:*** Neutron radiogram using conventional film. ***2c:*** Set up of the sample on the manipuation stage in front of the fluorescent screen.

To perform the tomographical scan the tyrannosaurid foot sample was fixated onto the sample manipulator (s. figure 2). The detector was set to a field of view of about about 135 x 172 mm². During the experiment 30 flat field images (images without sample) and 720 projections at different sample rotation equally stepped between 0 and 2π were taken. The exposure time of each image was 15 seconds. The measurement for a single projection is shown in figure 3. The total scan lasts about 4.9 hours.

For tomographical reconstruction the axis of rotation was carefully aligned by software to be perpendicular to the lines of the projections. These aligned projections then were reconstructed by using the method of backprojection of filtered projections. Each line in the projection yields a reconstructed slice. By stacking all slices we obtain the resulting 3D dataset. To investigate the total sample volume of the tyrannosaurid-foot specimen two tomographical scans were combined resulting in a total reconstructed volume of 497 x 497 x 931 voxels, representing 130 x 130 x 243 mm³.
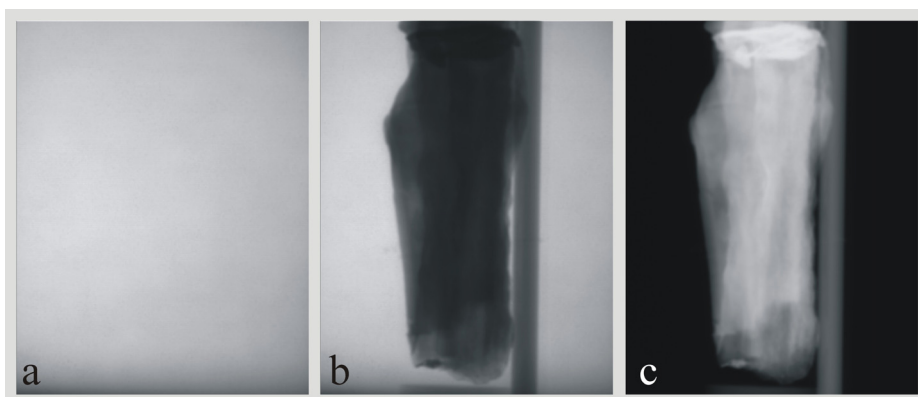
Figure 3: Measurement for a single projection of the tryrannosaurid foot. Images with (a) and without (b) sample were recorded. The resulting attenuation projection is shown in (c). The detector was set to a field of view of about 135 x 172 mm².
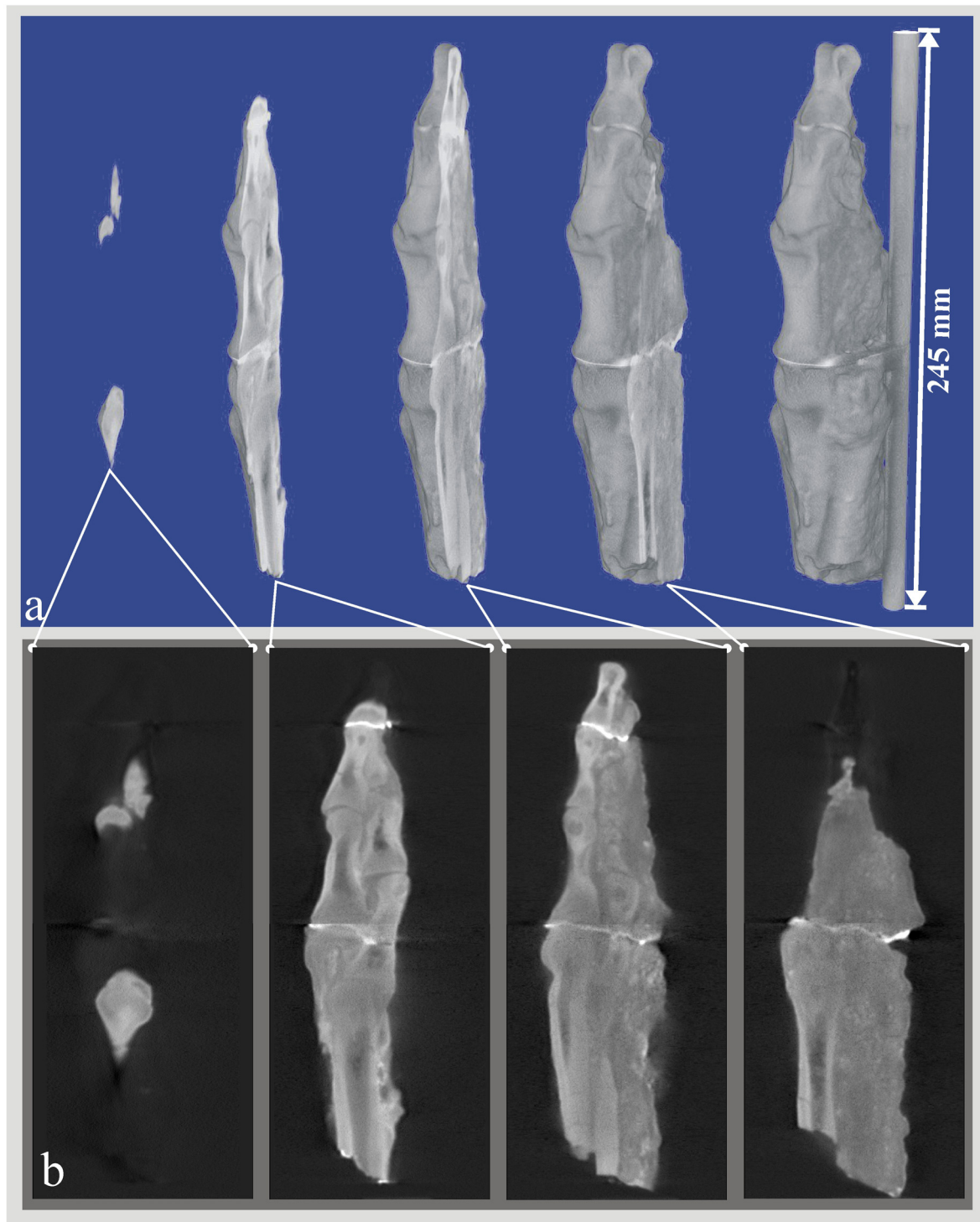
Figure 4: Volume renderings of the reconstructed data set of the tyrannosaurid-foot specimen. The total volume consists of 497 x 497 x 931 voxels, representing 130 x 130 x 243 mm³. In a) the volume is virtually cut in the z/y-direction at different postions in x. The 3D-representation is obtained by the software VGStudioMax, Volume Graphics GmbH, Heidelberg, Germany. In b) the z/y-slices belonging to the vertical cuts in a) are shown (thickness 0.26 mm). The internal bone structure (hollow chambers,bone thickness) is clearly visible. Foot broke through excavation, so the pieces were glued back together.

Achievements and Main Results

The application of NCT at GENRA-3 to the tyrannosaurid-foot sample provides for a high resolution 3D data set representing the internal information of this unique sample. This not only gives new insight to the internal organisation the sample, but allows for obtaining precise and valuable morphological information non-destructively. By the use of specialized software the 3D-volume can be virtually sliced in any direction to reveal the internal bony structure of the specimen (s. figure 4). It is planned to use this method on the complete tyrannosaurid specimen prior to specimens preparation to avoid the damage of very fine and delicate bone structures and possibly present organic ligaments, as for example organic remains of the inner organs, skin, muscles and especially stomach contents. It is possible to find these remains under certain conditions of fossilisation. But in most cases these remains will be destroyed through mechanically preparation, before they are even discovered.

References

F. Beckmann, J. Vollbrandt, T. Donath, H.W. Schmitz, A. Schreyer, "Neutron and synchrotron radiation tomography: New tools for materials science at the GKSS-Research Center", Nuclear Instruments and Methods in Physics Research A 542 (2005) 279-282.

Note:

The following research projects have been supported by the European Commission under the 6th Framework Programme through the Key Action: Strengthening the European Research Area, Research Infrastructures. Contract n°: RII3-CT-2003-505925':

M. Almgren, J. Nan
Variable contrast study of coexisting fluorocarbon-rich and hydrocarbon-rich micelles

A. Angelova
Analysis of Bilayer Thickness of Lipid Cubic Phases with Large and Normal Water Channels

T. Cosgrove, M. Sharp
The incorporation of oils used as adjuvants for drug solubilisation by copolymer micelles

H. Heerklotz, T. Gutberlet
Domain formation in lipid raft mixtures

M. Knaapila, L. Almasy, A. Monkman
A SANS study of polyfluorene beta phase in solution

V. Ryukhtin, J. Saroun, I. Turkevych
SANS investigation of nanoporous alumina membranes

V. Ryukhtin, P. Strunz, Y. Motohashi
SANS investigations of the porosity in superplastically deformed ceramics

S. Rangelov, S. Halacheva
SANS Study of Poly(Glycidol)-Based Analogues to Pluronic Copolymers

M. Almgren
Investigation of fluorocarbon- and hydrocarbon-rich micelles by SANS

J. S. Pederesen, P. Bäverbäck
SANS study of nonionic mixed micelles

H. Leitner, H. Clemens, P. Staron
Characterization of precipitates in a high-strength low-alloy steel

S. Pouget, S. Grigoriev, N. van Dijk
Investigation of the magnetic structure of the ferromagnet $ZrZn_2$

G. Scherer, S. Alkan Guersel, U. Gasser, K. Mortensen
Domain structure in FEP polymer based electrolyte membranes for fuel cells

M. Bischof, E. Eidenberger, P. Staron
Field-dependent experiments to characterise the precipitates in a high-speed steel

E. Eidenberger, M. Bischof, P. Staron
Combining SANS experiments with polarized and unpolarized neutrons to study

A. Michels, C. Vecchini, O. Moze, K. Suzuki, P. K. Pranzas, J. Weissmüller
Magnetic USANS investigations of spin-misalignment fluctuations in Nanoperm ($Fe_{89}Nb_6B_{10}$)

A. Giuliani, F. Fiori, J. Dutkiewicz

U-SANS analysis of NiTi shape memory alloys treated by Impulse Electric Current Treatment

V. Ryukhtin, P. Stepanek, Z. Tuzar

USANS investigations of organized nanostructures of diblock copolymers in immiscible solvents

R. Steitz, I. Voets, G.H. Findenegg

Neutron reflectometry on complex coacervate core micelles absorbed to the solid-liquid interface

M. Mattei, Francesca Cifelli

Mineral fabric in clay sediments: new results from TEX-2 analysis

Appendix I

**Reports of experiments carried out
at the REFSANS instrument at the
Forschungsneutronenquelle Heinz Maier-Leibnitz (FRM II)
in support of internal and external users.**

**These reports were taken from the
FRM II Annual Report 2006.**

(Reprints by courtesy of the Forschungsneutronenquelle
Heinz Maier-Leibnitz (FRM II), Garching)

Surface and buried layers in thin, lamellar diblock copolymer films

Experimental team:
Z. Di[1], C.M. Papadakis[1], L. Willner[2], R. Kampmann[2], M. Haese-Seiller[2], V. Kudryashov[2]
[1]Physikdepartment E13, Technische Universität München
[2]Institut für Festkörperforschung, Forschungszentrum Jülich
[3]FRM-II, Technische Universität München

REFSANS, December, 2006

Local contact: R. Kampmann, M. Haese-Seiller, V. Kudryashov

Diblock copolymers form spontaneously oriented structures in thin film geometry, which may be useful for a number of applications, such as the creation of nanoporous films. The aim of our investigation was to gain detailed information on the lamellar structure in thin diblock copolymer films. In supported films of a poly((d-styrene)-b-butadiene) (dPS-PB) diblock copolymer (molar mass 150 kg/mol), we had previously detected using GISAXS that the lamellae are perpendicular to the substrate [1], in agreement with our results on non-deuterated PS-PB [2,3,4,5]. However, one may anticipate a thin overlayer of PB because of its lower surface tension than dPS or a buried layer of dPS or PB near the substrate surface (Fig. 1). The existence of such layers is important for the accurate calculation of the free energy of the films, which allows the prediction of their orientation [6,7]. Since the neutron contrast between dPS and PB is significantly higher than the X-ray contrast between PS and PB, we attempted neutron reflectometry in order to detect possible buried layers or overlayers.
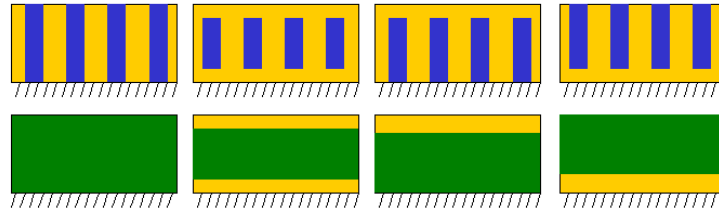
Fig. 1: A few of the possible structures of the film consisting of perpendicular lamellae with an overlayer and/or a buried layer. Blue: dPS, yellow: PB. Green indicates the average scattering length density of dPS-PB which is relevant in the reflectometry experiment. The hatched areas represent the Si substrate.

Films from dPS-PB (molar mass 150 kg/mol) were spin-coated from toluene solution (26 mg/ml) onto a Si wafer with a native oxide layer. The sample size was 3×8 cm^2. Neutron reflectivity curves were measured at the ToF-reflectometer REFSANS. Three incident angles between 1.50 and 3.75° were used. In this way, step widths Δq_z as low as 7×10^{-4} Å^{-1} were obtained. The experimental settings are compiled in Table 1.

Table 1: Experimental settings.

α_i	$\Delta\alpha_i/\alpha_i$	λ_0 [Angstr]	$\Delta\lambda_i/\lambda_i$ $(\lambda < \lambda_0)$	$\Delta q/q$ $(\lambda<\lambda_0)$	$\Delta q/q$ $(\lambda\sim1.5*\lambda_0)$	Measuring time[*] [h]
1,5°	0.018	24	0,02	0,027		13
2,5°	0.019	16	0,02	0,024		45
3,5°	0.014	16	0,02	0,027	0,017	19

For explanation see text. *): without primary beam measurement

The curves obtained are shown in Fig. 2a. A dynamic range of 10^{-6} could be achieved, and a large number (16) of Kiessig fringes related to the thickness of the polymer film could be resolved. A

comparison of the resolution of the Kiessig fringes obtained in the three measurements shows that the higher the incident angle, the better they are resolved (Fig. 2b). This results from the variation of the q-resolution with λ: The highest resolution in wavelength is obtained for $\lambda > \lambda_0$ where λ_0 denotes the wavelength with the highest transmission of the REFSANS chopper (defined by the chopper setting, see Table 1). In the range $\lambda < 0.5\,\lambda_0$, the λ-resolution is decreased, resulting in a reduced resolution of the fringes.

An analysis of the positions of the minima of the fringes in $R \times q_z^4$ (Fig. 2c) shows that in total an excellent number of 16 fringes could be resolved and that the positions of the minima in dependence of the number of the fringe follow very precisely a straight line. From these results, a film thickness of ~1300 Å has been derived. The resolution of REFSANS is thus sufficient to resolve such large film thicknesses. The overall decay of the curve follows approximately a Fresnel law, i.e. the film surface is smooth.
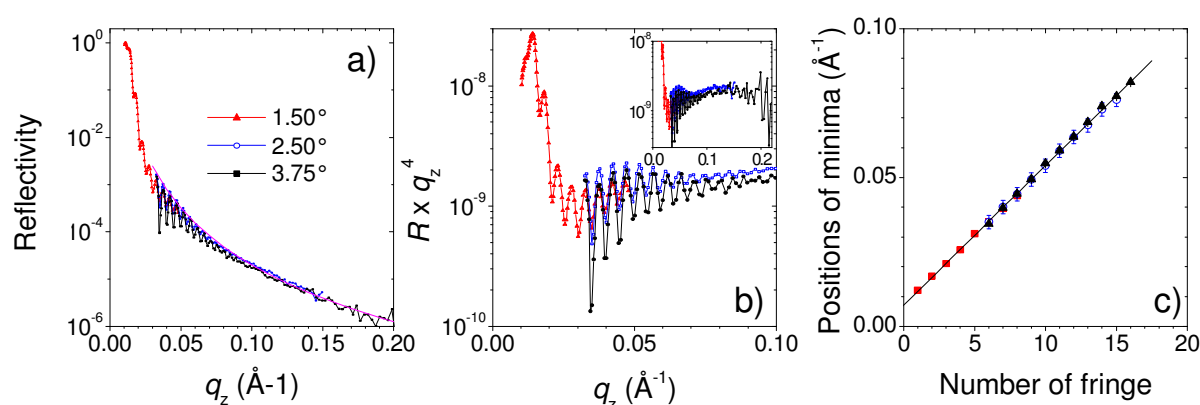
Fig. 2: (a) Reflectivity curve from a thin film of dPS-PB. The different symbols indicate different incident angles. The pink line represents Porod behavior. (b) Reflectivity curve from (a), normalized by the Fresnel law. The inset shows the entire q_z-range. (c) Positions of the minima read off from the curve in (b).

Thin buried or surface layers are expected to give rise to variations of the reflectivity with large periodicities in q_z. From the inset in Fig. 2b, a slight deviation from a horizontal line may be anticipated. In order to identify such layers, i.e. such deviations from the Fresnel law, the measurements should be extended to higher q_z-values, possibly with relaxed resolution in q_z.

We conclude that a thin, supported film of dPS-PB diblock copolymers gives rise to an excellent signal in neutron reflectivity at REFSANS. A large number of Kiessig fringes are resolved, and film thicknesses of more than 1000 Å can be resolved. The precision of the intensity is high enough to detect thin buried or surface layers. Future experiments will focus i) on identifying the optimum conditions for detection of such layers and ii) on GISANS investigations to characterize the in-plane structure.

1. C.M. Papadakis, P. Michelberger, C. Darko, E. Metwalli, S.V. Roth, D. Posselt, D.-M. Smilgies, Annual Report, Hasylab 2005.
2. D.-M. Smilgies, P. Busch, C.M. Papadakis, D. Posselt, *Synchr. Rad. News* **15**, no. 5, p. 35 (2002).
3. P. Busch, D.Posselt, D.-M. Smilgies, D. Posselt, B. Rheinländer, F. Kremer, C.M. Papadakis, *Macromolecules* **36**, 8717 (2003).
4. C.M. Papadakis, P. Busch, D. Posselt, D.-M. Smilgies, *Adv. Solid State Phys.* **44**, 327 (2004).
5. P. Busch, D. Posselt, M.Rauscher, D.-M. Smilgies, C.M. Papadakis, *Macromolecules*, ASAP, 2007.
6. I.I. Potemkin, *Macromolecules* **37**, 3505 (2004).
7. I.I.Potemkin, P. Busch, D.-M. Smilgies, D.Posselt, C.M. Papadakis, *Macromol. Rapid. Commun.*, in the press, 2007.

Time-of-flight GISANS, No. 294

Experimental team:
P. Müller-Buschbaum [1]
[1]TU München, Physik-Department LS E13, James-Franck-Str. 1, D-85748 Garching, Germany

Instrument: REFSANS, 09-14-2006

Local contact: V. Kudryashow, M. Haese-Seiler, R. Kampmann

Grazing incidence small angle scattering (GISAS) overcomes the limitations of conventional small-angle scattering with respect to extremely small sample volumes in the thin film geometry. GISAS experiments require a q_y-resolution which increases the complexity in the experimental realisation. As compared to GISAS measurements with synchrotron radiation, experiments using neutron (abbreviated with GISANS) are still rather rare. Up to now, the largest body of work was performed at the beamline D22 at the ILL (Grenoble). The instruments D22 was most likely operated in the region of highest neutron flux available at wavelengths of typically $\lambda \approx 0.6$ nm (wavelength selector $\Delta\lambda/\lambda = 10$ %) at a distance of 17.7 m between sample and detector. So far no GISANS experiments had been performed in the time-of-flight (TOF) mode. Thus the reported experiment is the first one combing TOF and GISANS.
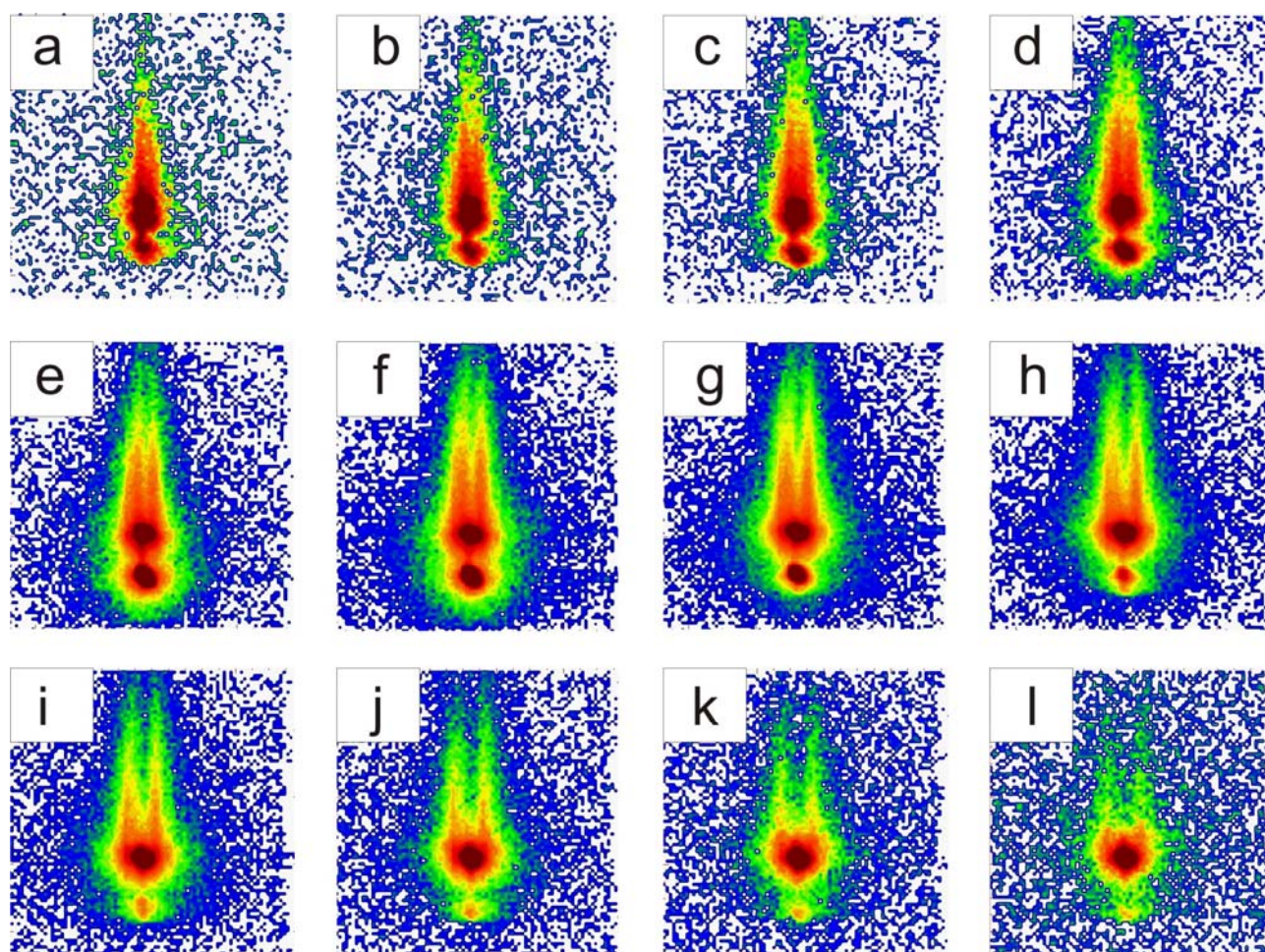
FIGURE 1: *Selection of 2d intensities measured simultaneously in the TOF-GISANS experiment. The corresponding mean wavelengths are a) 4.99, b) 5.52, c) 6.11, d) 6.75, e) 7.46, f) 8.23, g) 9.09, h) 10.03, i) 11.06, j) 12.20, k) 13.45 and l) 14.83 A.*

Time-of-flight GISANS, No. 294

TOF allows for a specular and off-specular scattering experiment, in which neutrons with a broad range of wavelength λ are used simultaneously and registered as a function of their respective times of flight. The necessary pulsing of the beam is realized by a double chopper system. A setting with 5 beams, which are focussed on the detector was chosen. A sample-detector distance of 10.1 m was operated. The scattered intensity is recorded on a two-dimensional (2d) detector without the movement of any motors. On the detector the counts were registered for each spatial pixel (x, y) as a function of TOF in 1024 channels. After integration of the counts for fixed xy area and TOF channel, and the TOF to λ conversion, the scattered intensity is displayed as a function of the out-of plane angle ψ and the exit angle α_f (see fig. 1). Finally, the corrected data set I(ψ,α_f) can also be transformed to I(qy, qz) with the given (constant) angle of incidence $\alpha_i = 0.5°$, where qz denotes the wave vector component perpendicular to the surface and qy the one in the surface in perpendicular to the neutron beam.

Figure 1 pictures the anisotropy of the observed scattering patterns. Different main features are already determined right from the two-dimensional images: The intense specular reflected peak, the Yoneda peak (which position depends on the related λ) and the splitting of the diffuse scattering into two strong Bragg-rods. Due to the different λ each 2d intensity in figure 1 corresponds to a different (qy, qz)-range. Therefore due to the TOF-mode at one fixed incident angle GISANS pattern above the critical angle (fig. 1a-c), at the critical angle (fig. 1d) and below the critical angle of PSd (fig. 1e-l) were recorded.
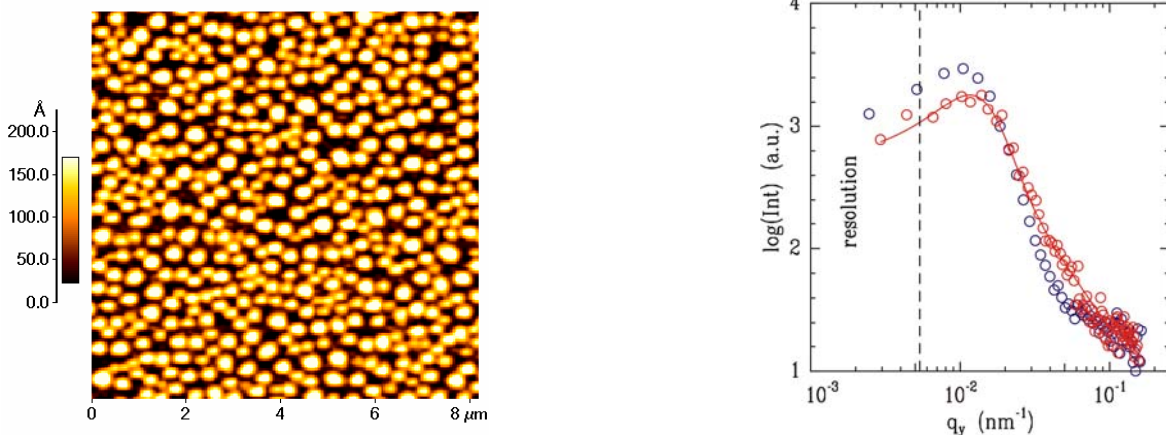
FIGURE 2: (left) AFM image displaying the polymeric nano-dots prepared by dewetting of an ultra-thin PSd film [1]. (right) Comparison between the out-of plane intensity recorded at D22 (blue) and at REFSANS (red) at a selected wavelength of 10 and 9 A, respectively. The solid line is a fit to the data yielding D= 545 nm.

The investigated sample is a polymeric nano-dot structure (see fig. 2) prepared by dewetting of an ultra-thin film of deuterated polystyrene (PSd) on silicon [1]. The nano-dots have a well defined nearest neighbour distance D which causes the observed Bragg-rods at $q_{y,peak}=2\pi/D$. In an out-of plane cut displayed in a double logarithmic presentation (see fig. 2) both Bragg-rods coincide into the strong peak. Figure 2 compares the data obtained using TOF-GISANS with the data collected at a fixed λ in normal GISANS. For the particular selected λ example, differences in the maximum intensity result from different counting times. However, a direct comparison is rather difficult and needs fully to account for the transmission of the chopper in the experimental setting. It is further pointed out that the GISANS performance of REFSANS will significantly be improved by use of the third double-disk-chopper which has been installed in REFSANS after this measurement. Nevertheless, figure 2 shows that REFSANS can be successfully operated in the GISANS geometry. In summary, *the experiment was very successful.*

[1] P.Müller-Buschbaum, E.Bauer, O.Wunnicke, M.Stamm: *Control of thin film morphology by an interplay of dewetting, phase separation and micro-phase separation*; J. Phys. Condens. Matter **17**, S363 (2005)

Sample environment and first reflectivity experiments on a solid-supported membrane at REFSANS

Experimental team:
B. Nickel, K. Seidel, C. Reich, W. Fenzl, J. Rädler
Department für Physik, Ludwig-Maximilians-Universität, München

Instrument: Refsans

Local contact:
R. Kampmann, M. Haese-Seiller, V. Kudryashov
GKSS-Forschungszentrum Geesthacht

Sample environments for biological interfaces. Refsans has been designed to study the structure and function of biological interfaces such as solid-supported membranes and lipid monolayers adsorbed at the air-water interface. For this purpose, we have set up different sample environments which allow for the preparation of such interfaces on site, namely a microfluidic flow cell and a Langmuir trough. Both sample environments allow for a characterization of the biological interface by fluorescence microscopy and neutron scattering. The Langmuir trough available to Refsans users is shown in Fig. (1a). The trough exhibits two movable barriers, a plastic housing, and two windows giving access to the neutron beam impinging on the water surface. The trough is placed on a damping table and it can be moved in height for alignment with the neutron beam. The flow cell for solid supported membranes is shown in Fig (1b). Here, the optical access is realized by making use of a quartz slide, while the neutrons access the interface through the Si support. In order to minimize the volume of the cell, the water film thickness is in the order of 400 microns. In turn, the necessary filling volume of this cell is only about 2.5 ml, allowing to expose the interface to rare biomolecules such as membrane proteins. A quartz window provides the optical access for a fluorescence microscope. This cell design, which has been adapted from a similar setup for synchrotron experiments, is unique for neutrons. It allows preparing complex interfaces step-by-step with optical feedback.
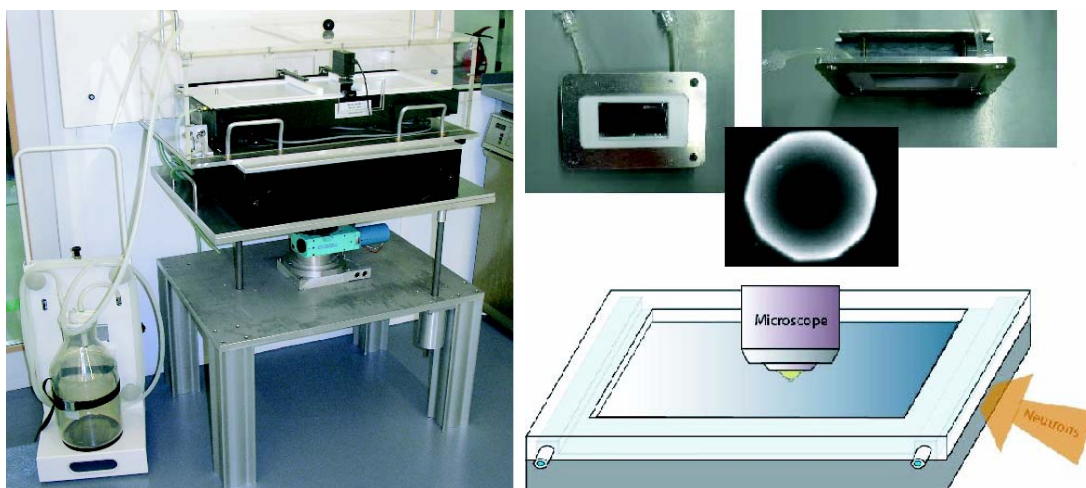
Fig. 1 (a) Langmuir trough for experiments at the air-water interface. (b) Flow cell for the preparation of solid-supported membranes. Fluorescence microscopy and bleaching techniques allow characterizing the interfaces on a micron scale. Neutron reflectivity experiments give access to depth profiles with nanometer resolution, while GISANS experiments will allow to access lateral structures, e.g. segregation phenomena in lipid membranes.

Sample environment and first reflectivity experiments on a solid-supported membrane at REFSANS

Neutron reflectivity from solid supported membranes. A SOPC membrane was deposited by spin-coating. After closing the flow cell, excess lipids were removed by flushing with H_2O. Finally, D_2O was injected and the membrane was measured. Also the bare oxide in contact with D2O prior to the coating was measured as a reference.

Reflectivity measurements at several angles of incidence (α_i= 0.75 deg, 1.50 deg, and 3.75 deg) have been performed. In order to limit the footprint of the neutron beam to the length of the cell, the slit setting before the sample was B2 = 0.7 mm, 1.6 mm, and 3.5 mm, respectively. The chopper system was operated with an angular opening of 6.5 deg and the total flight distance from the first chopper to the detector was 15966.5 mm, while the distance from the sample to the detector was 5000 mm. Two chopper frequencies were used (f = 7.16 Hz for α_i= 0.75 deg and 3.75 deg and 4.76 Hz for α_i=1.5 deg), resulting in a maximal transmission of the chopper system at λ_0= 16 Å and 24 Å, respectively. The reflected intensities were normalized to the direct beam intensity passing straight through the Si block while leaving all other parameters unchanged. Finally, all measurements are merged in a single curve.

The combined reflectivity curves (see Fig. 2) cover an intensity range of 5-6 orders of magnitude and a maximal momentum transfer of 0.1 $Å^{-1}$ was achieved. The results are in good agreement with similar experiments performed at AMOR (PSI) intended to test the flow chamber design. We are confident that the dynamical range and maximal momentum transfer can be further increased in early 2007.
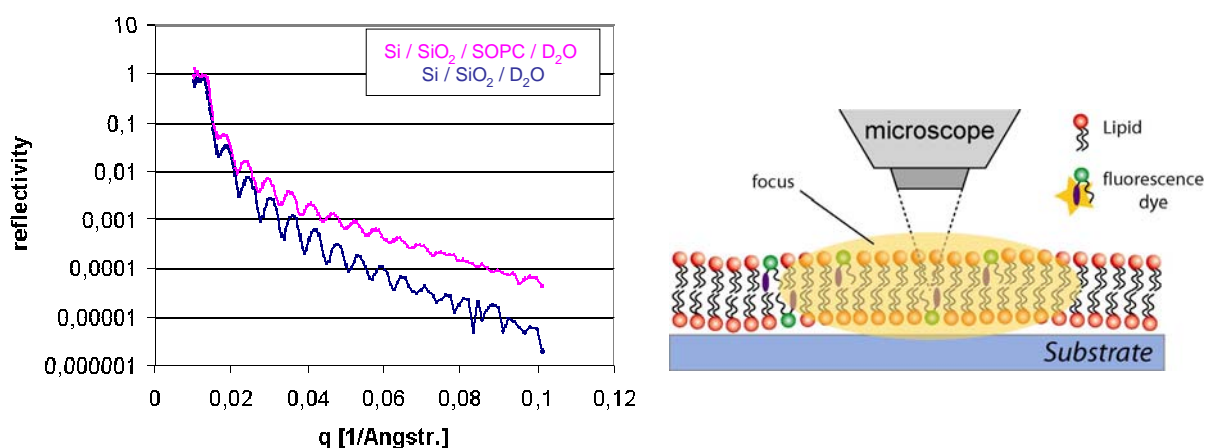
Fig. 2. Neutron reflectivity. (a) The neutron reflectivity obtained from a Si block covered by thermal oxide and in contact with deuterated water is shown as a blue curve. After deposition of a SOPC membrane, the reflected intensity is modified giving rise to the pink curve. (b) Schematic of the setup after membrane deposition.

[1] C. Reich, M. Hochrein, B. Krause, B. Nickel, *A Microfluidic Setup for Studies of Solid-Liquid Interfaces using X-ray Reflectivity and Fluorescence Microscopy,* **Rev. Sci. Inst. 76**, 095103 (2005)

Appendix II

**Reports of experiments carried out
at HASYLAB / DESY by GKSS personnel
and at the GKSS outstation HARWI-II at DESY
in support of internal and external users.**

**These reports were taken from the
HASYLAB Annual Report 2006.**

(Reprints by courtesy of DESY, Hamburg)

Commissioning, new developments and new equipment at the Engineering Materials Science Beamline HARWI II

T. Lippmann, F. Beckmann, R.V. Martins, L. Lottermoser, T. Dose and A. Schreyer

GKSS Forschungszentrum Geesthacht, Max–Planck-Str. 1, 21502 Geesthacht, Germany

As has been reported last year [1] GKSS and GFZ are operating the beamline Harwi II in order to perform engineering materials science and geoscience experiments. With the intention of improving the conditions for performing engineering materials science experiments, i.e. texture and residual strain analysis and microtomography, some new equipment has been installed and tested in 2006, and shall be shortly introduced here.

Commissioning of the first monochromator, which was already installed last year, has been performed. It is a fixed–exit double–Laue–crystal monochromator, which scatters in the horizontal and provides a maximum beam of 10×10 mm^2. Using annealed Si 111 crystals (FWHM: ≈ 6", thickness: 5 mm) a spectrum was recorded at 17 mm gap, which is shown in fig. 1. With respect to the filters in the beamline (10 mm carbon and 1 mm copper) the intensity maximum was found to be $\approx 1.7 \cdot 10^{10}$ photons/sec/mm^2 in the centre of the beam at 75 keV.
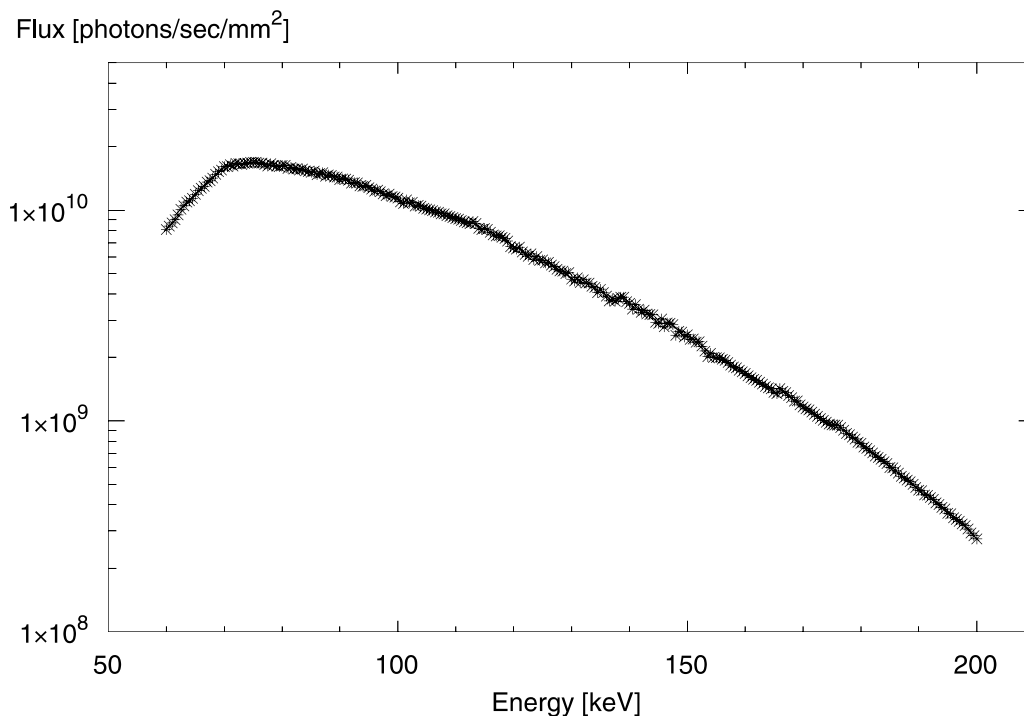
Figure 1: Spectral flux through an aperture of 1×1 mm^2 measured in the optics hutch of HARWI II behind the horizontal monochromator (Si 111 annealed, wiggler gap: 17 mm).

A second fixed–exit monochromator has been built up and installed in the monochromator tank. It uses the vertical scattering geometry and consists of a fixed "first–crystal tower" with crystal changers and a set of three "second–crystal towers". The latter are located on a translation stage parallel to the beam and can be independently moved into the beam. Three sets of monochromator crystals can thus alternatively be aligned and used without breaking the vacuum of the tank. The monochromator is optimized for imaging experiments and offers a beam up to 70 mm in width.

The energy range currently available is 16 to 60 keV, but shall be extended to higher energies in future. Moreover, new crystal bender units are in construction.

Fig. 2 gives an overview of the new monochromator. More details are presented in [2].

The optics hutch equipment was completed by the installation of a beam diagnostics and beam manipulation table. As shown in fig. 3, various components can be aligned using four linear stages perpendicular to the beam, and the whole equipment can be moved 75 cm aside in order to protect it against radiation in cases of white beam experiments. In the shown configuration the table is equipped with

- a large slit system with a maximum aperture of 85 by 85 mm,

- an ionization chamber, which can be used in the vertical monochromator beam,

- a direct beam camera, which can be used in the horizontal monochromator beam,

- two fast shutters for horizontal and vertical monochromator beam, respectively,

- a diode, which is used to monitor high energy photons,

- a filter box, which is equipped with various iron absorbers, allowing selecting iron thicknesses between 0 and 45 mm in 3 mm steps (fig. 4) and

- an evacuated "white beam" tube.
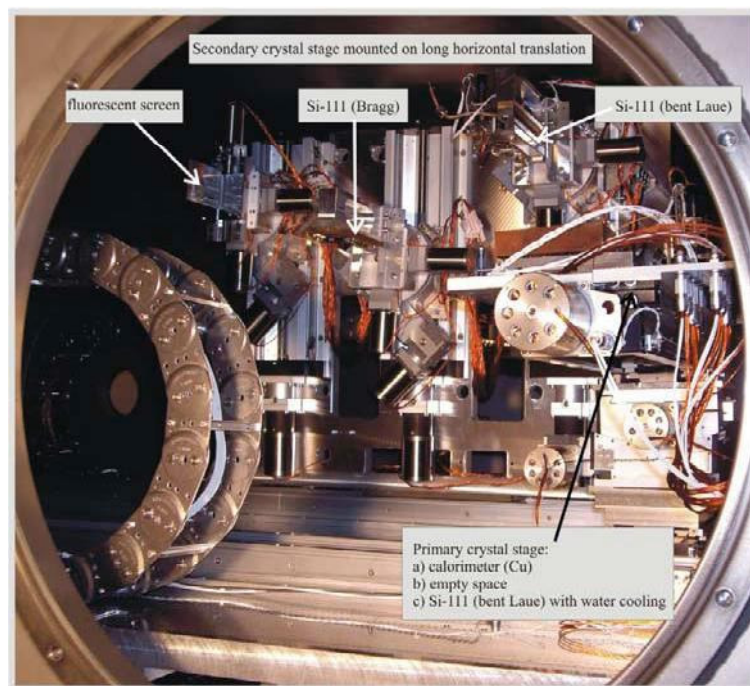
Figure 2: View through a maintenance hatch into the monochromator tank. The first tower of the vertical monochromator carries an additional copper block working as calorimeter. The middle tower of the secondary towers ensemble is moved into the beam. Actual energy setting is 36 keV here. In the foreground, the translation stage of the horizontal monochromator is visible.

Figs. 5 and 6 show photographs of the table.

The shutters are newly constructed and differ from those used at other high–energy beamlines in the lab. Each consists of two separate Densimet blocks, which are independently moved into and out
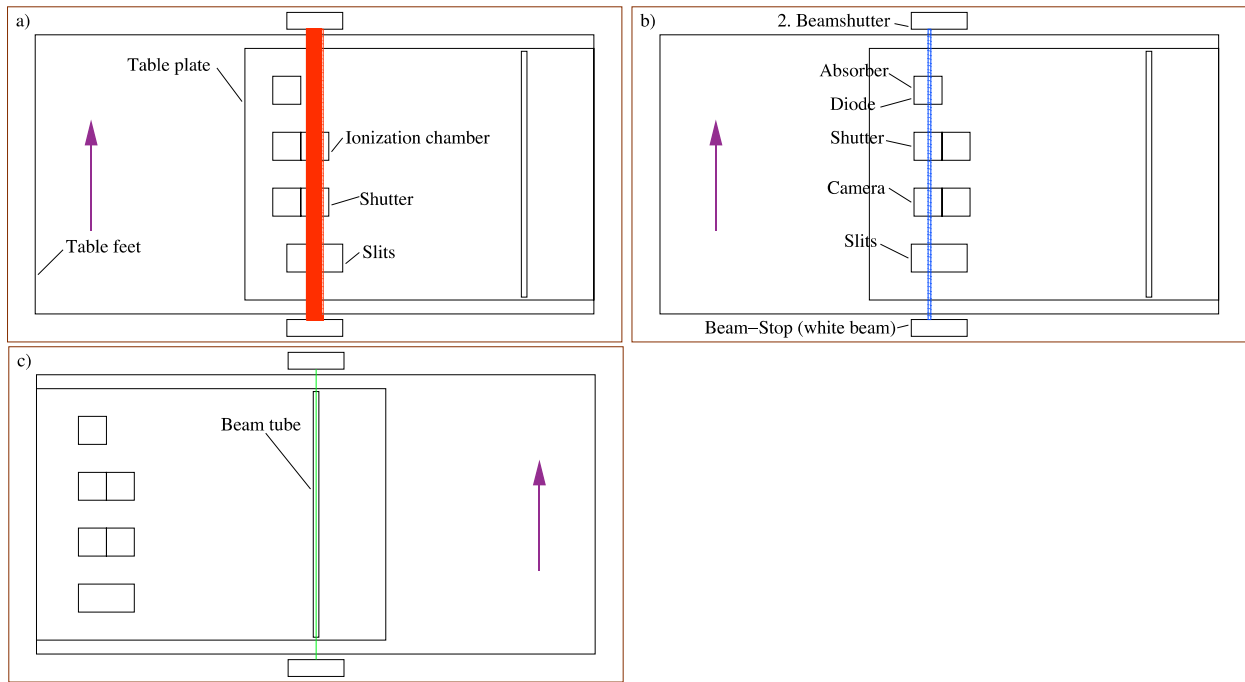
Figure 3: Principle of the operation modes of the diagnostics table. a) Vertical monochromatic beam, b) horizontal monochromatic beam (the table plate is on the right side for both configurations) and c) small fraction of the white beam (the table plate on the left side). The beam–stop for the white beam is located between the monochromator tank and the diagnostics table and the second beamshutter is the last component within the optics hutch.

Figure 4: The interior of the filterbox equipped with 4 different iron absorbers. One slot is still empty. The beam is coming from the right.

of the beam by four pressure cylinders. This design not only allows very fast movements, but also guarantees a homogeneous exposure of the illuminated area. The working principle of the shutters is shown in fig. 7. Since there are two possibilities for the status "shutter closed", the position of each separate block has to be controlled, which at the moment is only done by software, but will in future be carried out using Beckhoff technology.

A detector portal was installed in the experimental hutch I. It consists of a large framework, which covers nearly the whole interior space of the hutch. Two detector carriers equipped with linear travels allow to move two 2D position–sensitive detectors independently to any possible position behind the sample. Numerically, possible locations for the detectors are approximately $0 - 10000$ mm behind the sample, -350 – 1500 mm in height with respect to the vertical beam position and ± 1140 mm with respect to the horizontal beam position. The positioning accuracy is about 100 μm but will be further enhanced in future by the use of encoders.

As an example, fig. 8 shows one of two available gas–multi–wire detectors (manufactured by DENEX), which will be used for residual stress analyses, mounted on one of the two carriers. In fig. 9 a texture experiment was assembled on one of the experiment tables and an image plate scanner (model MAR 345) was positioned behind the sample using the detector portal.
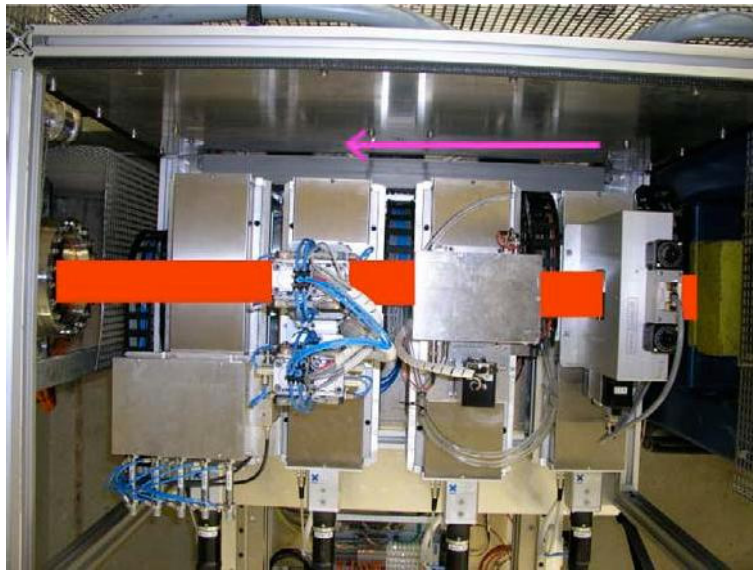
Figure 5: View of the beam diagnostics table from above. The table is aligned for the vertical monochromator beam, and the beam is coming from the right (marked by the arrow). The red bars symbolize the x-ray beam.

Figure 6: Side view of the beam diagnostics table. The beam is coming from the right.

114
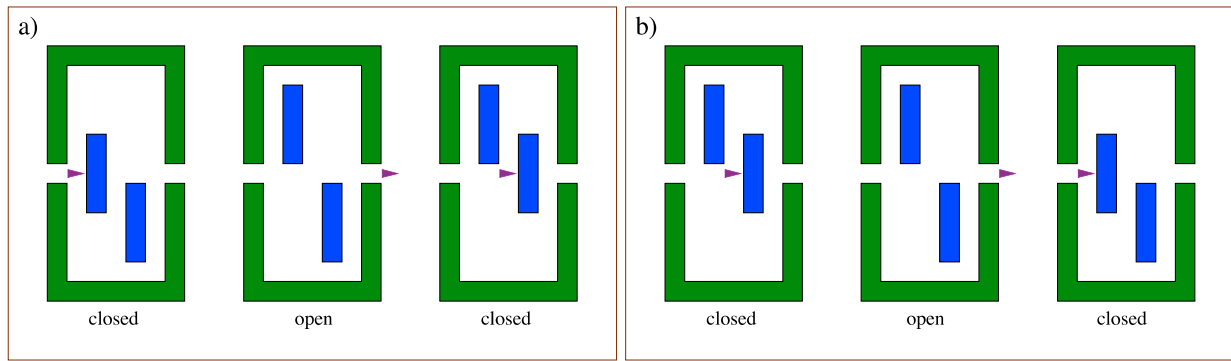
Figure 7: The working principle of the new shutters (vertical cut). Note the two possibilities a) and b) to open the shutter window.

Figure 8: One of the 2D position–sensitive gas–multi–wire photon detectors mounted on one of the detector portal carriers.

In order to perform in–situ residual stress analysis experiments a stress rig was constructed and manufactured by INSTRON. Tab. 1 summarizes the technical parameters and fig. 10 shows the device. It works servo–hydraulically and is equipped with water–cooled clamps. The rig can be used either in–situ or ex–situ, i.e. for long–term experiments.

Height	≈ 2500 mm
Weight	≈ 550 kg
Mechanical load	± 100 kN
Cyclic loading	25 Hz at ± 1 kN
Max. sample length	600 mm
Max. sample thickness	16 mm
Free viewing angle	$\pm 80°$

Table 1: Technical parameters of the stress rig.

115

Figure 9: A diffraction experiment on the experiment table 1 uses an image plate scanner mounted on the detector portal.

Figure 10: The new stress rig shortly after delivery.

References

[1] T. Lippmann, F.Beckmann, R.V. Martins, L. Lottermoser, T. Dose, A. Schreyer, HASYLAB Annual Report 2005.
[2] F. Beckmann, T. Donath, J. Fischer, J. Herzen, T. Dose, L. Lottermoser, R.V. Martins, T. Lippmann, A. Schreyer, this Annual Report.

New developments for tomographic imaging at HARWI II

F. Beckmann, T. Dose, T. Donath, J. Fischer[1], J. Herzen,

L. Lottermoser, R.V. Martins, T. Lippmann, and A. Schreyer

GKSS Research Center Geesthacht, Max-Planck-Str. 1, 21502 Geesthacht, Germany

[1]Hannover Medical School, Anna-von Borries-Straße 1-7, 30625 Hannover, Germany

Since the end of 2002 the GKSS-Research Center Geesthacht has been responsible for running the user experiment for microtomography at DESY. During the construction phase of the HARWI-II beamline attention was given to the optics concept to obtain a high-energy high-flux X-ray beam with a large field of view optimized for materials science applications [1]. Here the new monochromator setup used for imaging applications is described. Furthermore, the new data-management concept and the newly installed computer hardware for microtomography are presented.

Beamline optics

The main components for the beamline optics are the HARWI-II wiggler, the new front-end filter, the monochromator, the beam stop, and the diagnostics table (see figure 1). The design and features of the installed wiggler is presented in detail elsewhere [2]. The main parameters of the wiggler are:

Total length:	4	m	Peak field:	1.91	T
Period length:	110	mm	K:	20.3	
Minimal gap:	14	mm	Critical Energy:	26.7	keV.

To reduce the heat load on the first crystal of the monochromator 3 mm carbon is permanently installed as a high-pass filter. For the use of high photon energies, a 7 mm carbon filter and a 1 mm or 2 mm copper filter can additionally be placed into the beam. The sketch of the filter system is given in the inset of figure 1. A detailed description of the system located in the DORIS-DESY injection tunnel 36 m downstream of the HARWI-II wiggler is given elsewhere [3].
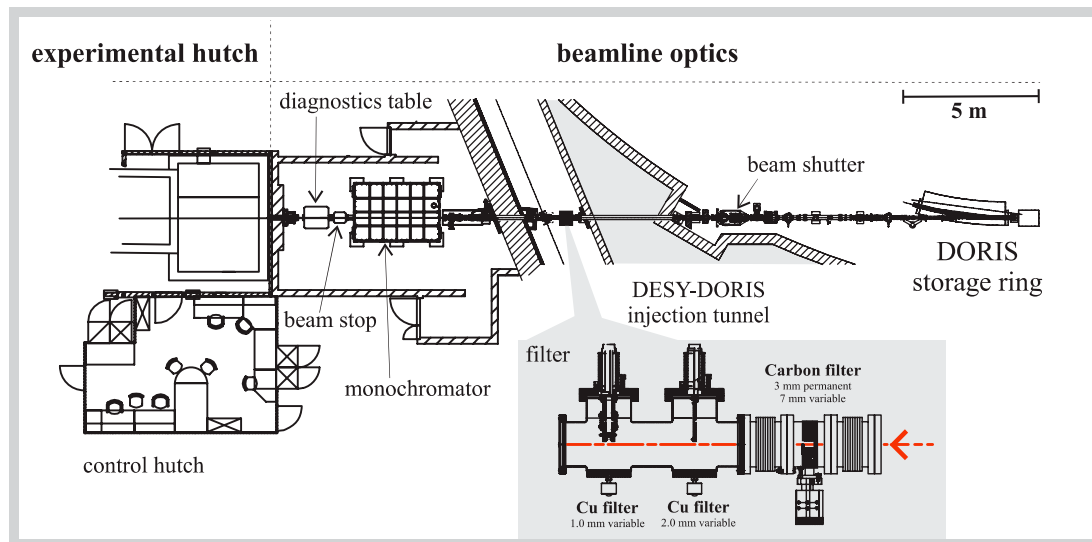
Figure 1: Sketch of the HARWI-II beamline showing the beamline optics. The permanent and optional high-pass filter installed in the DORIS-DESY injection tunnel is shown in the inset. A permanent 3 mm thick carbon filter can be extended by optional 7 mm carbon, 1 mm, or 2 mm copper.
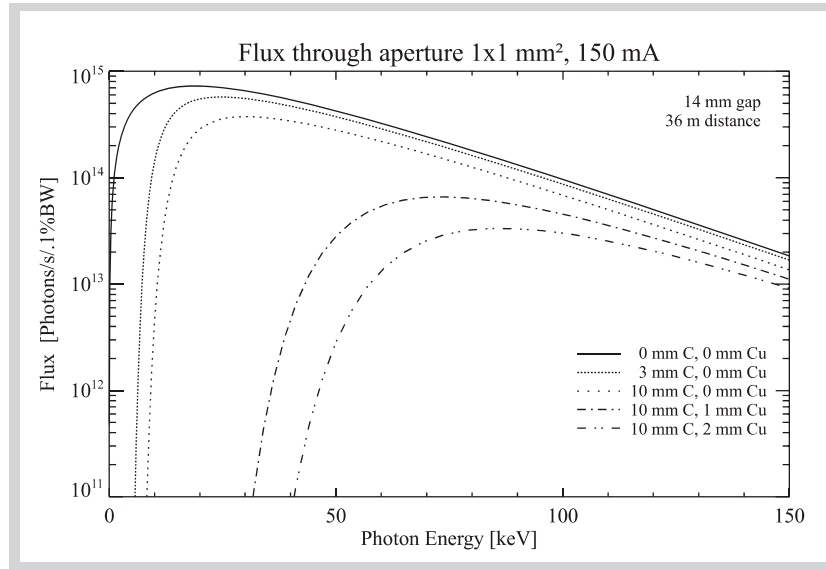
Figure 2: Comparison of the flux of the HARWI-II wiggler at minimal gap of the different filter settings with the unfiltered spectrum at the position of the high-pass filter (36 m distance from the source).

The resulting flux behind the filter system is presented in figure 2. The remaining total power of the white beam (70 x 10 mm²) at minimum gap and minimum filter (3 mm carbon) is about 12.6 kW. To further reduce the heat load on the first crystal, the wiggler gap can be increased. The resulting flux for a gap of 14 mm, 20 mm, and 30 mm is shown in figure 3. By use of different combinations of the filters and wiggler gaps the optimized conditions with respect to photon energy and beam size can be found.
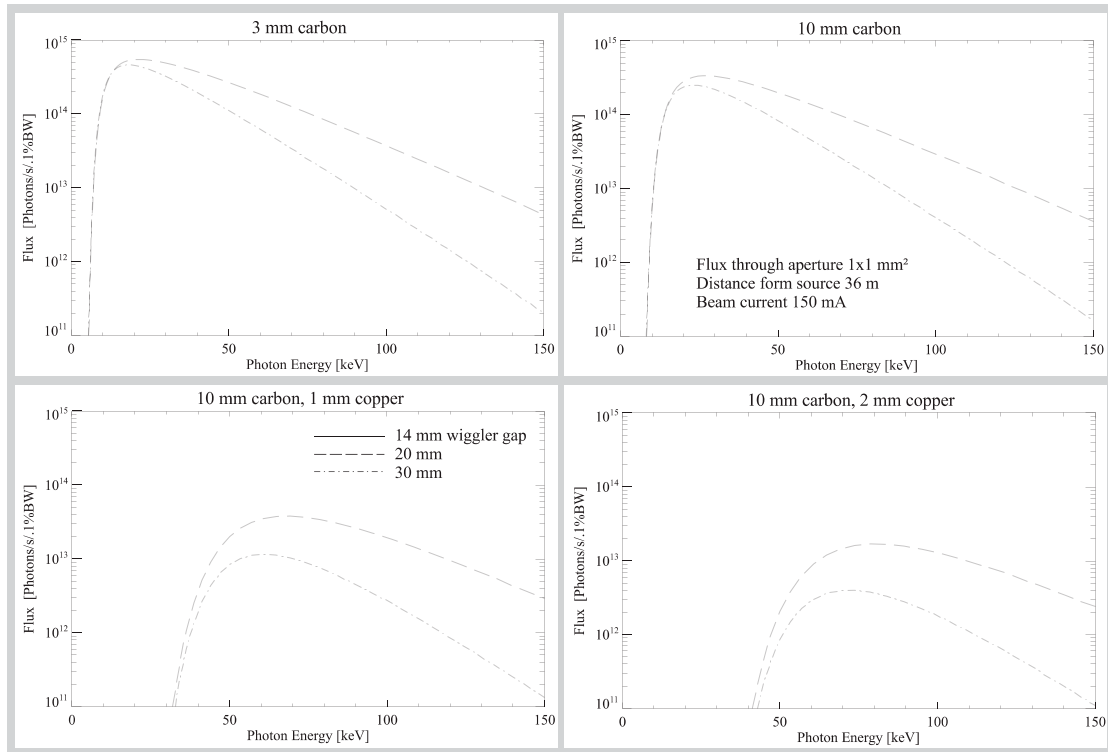
Figure 3: Comparison of the flux for different gaps of the HARWI-II wiggler with respect to different filter settings. Depending on the photon energy range of the monochromator different settings are foreseen. *Left top:* low photon energies (15-25 keV); *right top:* medium photon energies (20-80 keV) and large X-ray beam (70 x 10 mm²); *left bottom:* high photon energies (60 -250 keV) and small X-ray beam (10 x 10 mm²); *right bottom:* high photon energies and large X-ray beam.
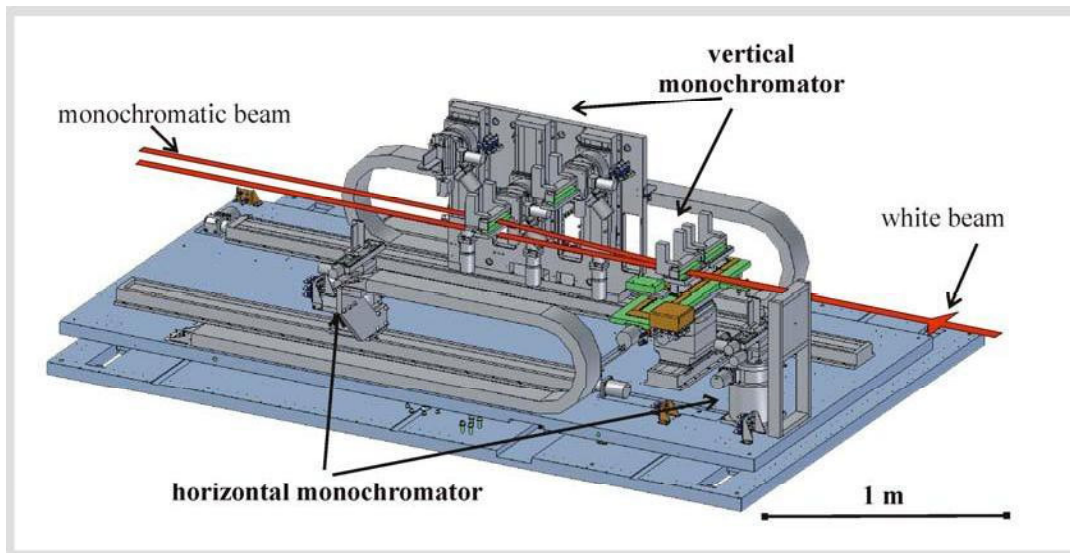
Figure 4: Sketch of the monochromator setup. The user can switch between two different monochromators. The horizontal monochromator in the foreground and the vertical monochromator in the background are placed into the white X-ray beam by moving the upper plate perpendicular to the beam. The monochromator is installed in the monochromator tank in the optics hutch. The tank is of dimension 3 x 2 x 1 m (L x W x H) and can be evacuated to below 10^{-6} mbar.

The concept of the monochromator setup is presented in figure 4. Two different monochromator systems, one reflecting in the horizontal plane, and one reflecting in the vertical plane, are installed. The horizontal monochromator is mainly used for diffraction applications and provide for an X-ray beam with a size of 10 x 10 mm² from 50 to 250 keV. The vertical monochromator is optimized for imaging applications and will deliver an X-ray beam with a size of 70 x 10 mm² and a photon energy range of 15 to 200 keV. Different pairs of crystals with a new design in Laue-Laue and Laue-Bragg geometry will be installed. Furthermore, the bent-Laue crystals are used to increase the energy band path of the reflected X-ray beam.
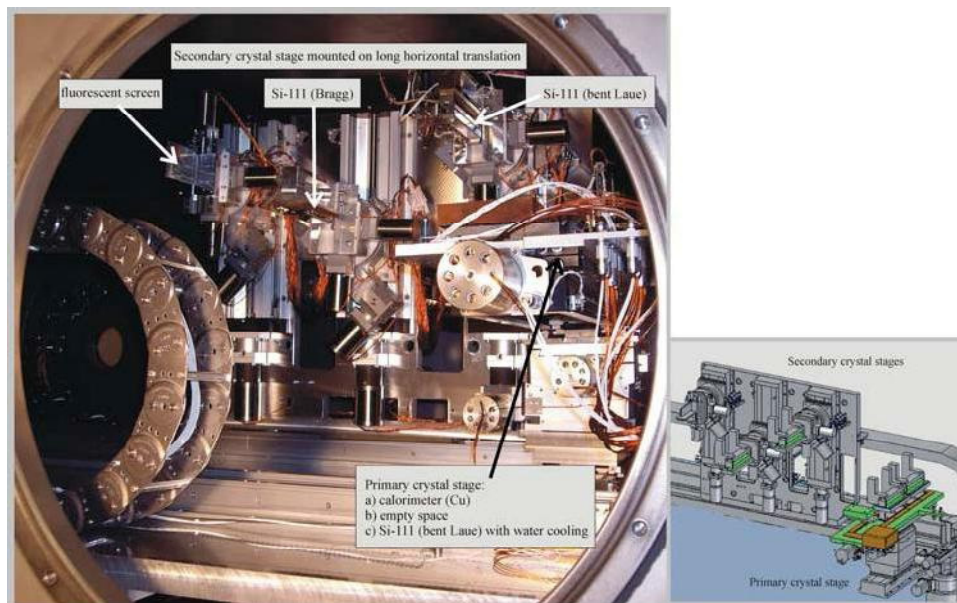
Figure 5: View (left) on the installed vertical monochromator as shown in the sketch (right). The primary crystal stage (right foreground) carries a calorimeter and the first Si crystal. The secondary stage (left background) consists of three stages which allow for combinations of different secondary crystal stages with the first crystal. Here the middle secondary crystal stage is set to a photon energy of 36keV (Si-111). The fixed exit monochromator has an offset of 40 mm.
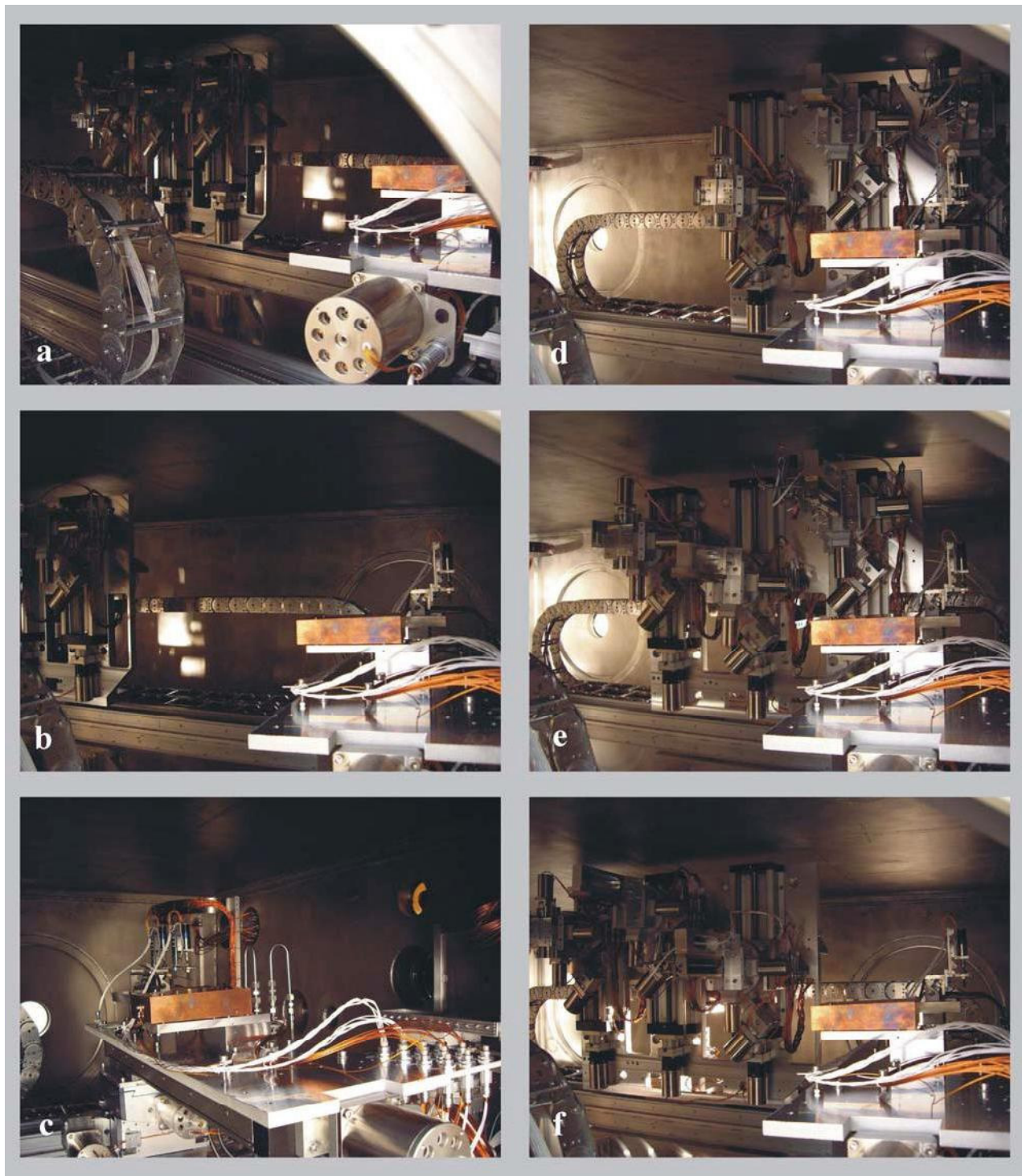
Figure 6: Interior view of the vertical monochromator installed in the vacuum tank. The scheme for the alignment of the monochromator is shown. *a-c:* First the monochromator is aligned relative to the white X-ray beam. Therefore, the secondary crystal stage is placed to its rest position. The calorimeter mounted on the first crystal stage is set into the white beam. After aligning the vertical and horizontal positions of the monochromator the first crystal (Si-111, bent Laue) shown in the background of (c) is moved into the incident white beam. *d-e* The alignment of the fixed exit monochromator (offset 40 mm). In d the fluorescent screen is set to the foreseen position, and the reflection of the first crystal is aligned to the centre of the screen. Then in e the fluorescent-screen stage is replaced by the middle crystal stage (Si-111, Bragg). The bending of the first crystal is then adapted, so that the width of the Rocking curve is minimized. At the end *f* the secondary crystal (Si-111, bent Laue) is used, and the bending of the second crystal is matched to maximise the intensity of the reflection. The photon energy was 36 keV.

In June / July 2006 the vertical monochromator was successfully set up. For the first commissioning phase a fluorescent screen, a Si-111 (Bragg), and Si-111 (bent-Laue) crystal were installed on the secondary crystal stage. The primary crystal stage was equipped with a calorimeter and a water-cooled bent-Laue crystal. Figure 5 shows a view into the monochromator tank revealing the installed monochromator system. Both the sketch and the viewgraph show the same setting. The different steps for alignment of the total system for a photon energy of about 36 keV are presented in figure 6.

For performing microtomography, the microtomography apparatus that was so far mainly used at BW2 was installed onto the lift table in the experimental hutch (see figure 7). The first tomographical scans using the vertical monochromator were successfully performed in July 2006 [4]. Within two weeks of operation 110 tomographical scans were performed in user mode. In the second run for tomography at HARWI II with 3 weeks of user operation another 170 scans were successfully performed using the photon energy range from 16 keV to 64 keV. Due to this huge amount of data the environment for data processing becomes very important. Especially, for running the experiment in user mode it is necessary to directly process the measured data. Therefore, the GKSS decided to renew the hardware for effective data processing.

New data processing chain for microtomography at DESY

For processing of the huge amount of tomographical data a new computing environment was installed by the GKSS at DESY in cooperation with the computer center of DESY. A schematic view of the new computing architecture is shown in figure 8. At beamlines BW2 and HARWI II the control computer of the experiment transmits the data via ethernet to the Sun Fileserver. The Fileserver is connected via fiber channels to the Sun Storage system, which currently have a capacity of 20 TByte. Both the fileserver and storage system are installed at the computer center of DESY. In addition to the fileserver a reconstruction server equipped with 64 GByte RAM and eight dual-core Opterons were set up at the computer center. The 3D-visualization of the tomographic data and the control of the reconstruction process is warrented by a multiprocessor system, which is connected via fiber channels with a 7 TByte RAID system. The backup of the data is supported by a so-called dCache, which is connected to the DESY long-term storage systems. The data exchange to the long-term storage systems is performed automatically and is invisible to the user.

Figure 7: Setup for microtomography at the HARWI-II beamline. The experiment is mounted onto a lift table. The experiment can be lowered by 1.5 m. The pit will then be covered by the shown roof.
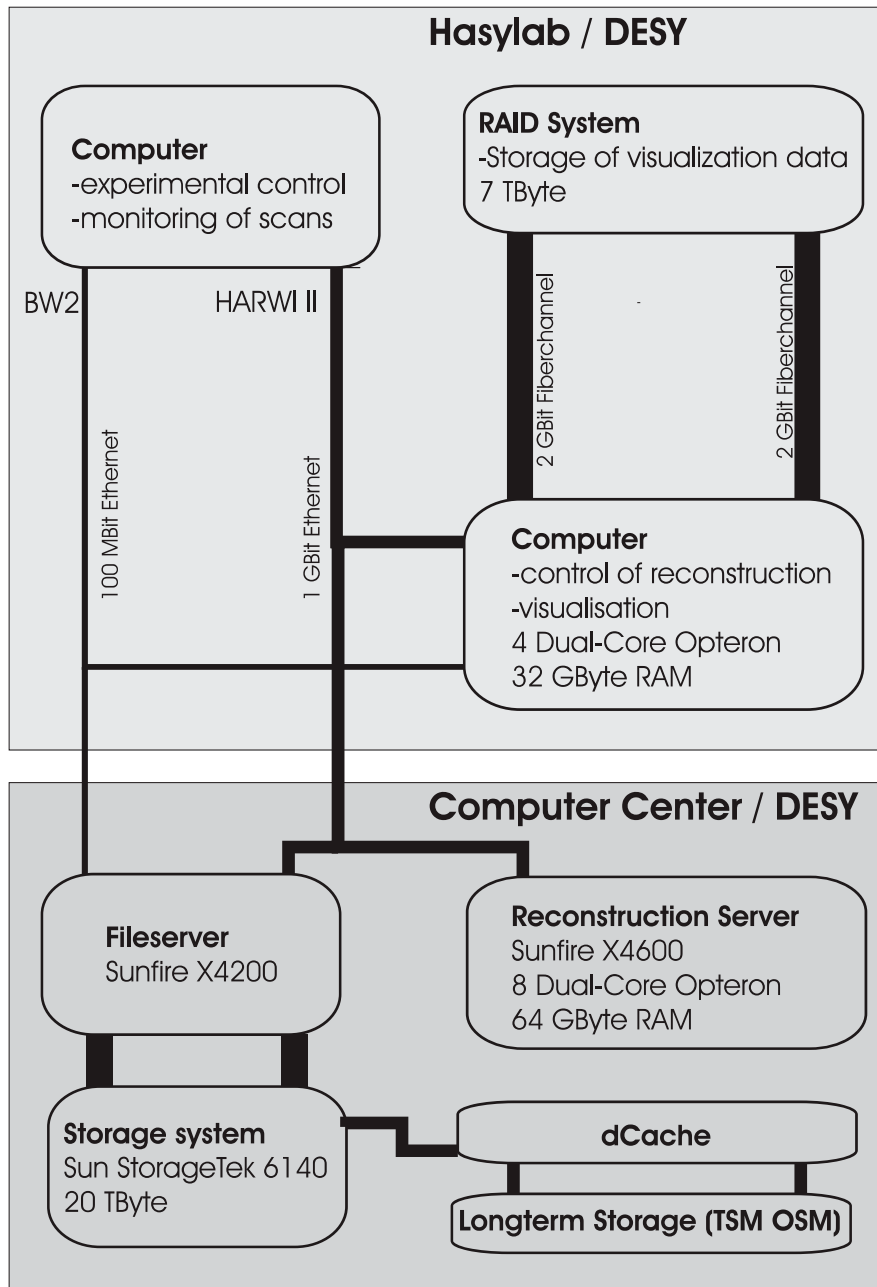
Figure 8: Schematic view of the new computing environment used by the GKSS for running the user experiments for tomograhy at beamlines BW2 and HARWI II at DESY.

References

[1] M. Tischer, L. Gumprecht, J. Pflüger, T. Vielitz, "A New Hard X-ray Wiggler for DORIS III", SRI 2006, Daegu, Korea, AIP Conference Proceedings.

[2] H. Schulte-Schrepping, and U. Hahn, "Hard x-ray wiggler front end filter design", SRI 2006, Daegu, Korea, AIP Conference Proceedings.

[3] F. Beckmann, T. Dose, T. Lippmann, R.V. Martins, and A. Schreyer, "The new materials science beamline HARWI-II at DESY", SRI 2006, Daegu, Korea, AIP Conference Proceedings.

[4] F. Beckmann, T. Donath, J. Fischer, T. Dose, T. Lippmann, L. Lottermoser, R.V. Martins, and A. Schreyer, "New developments for synchroton-radiation based microtomography at DESY", Proc. of SPIE Vol. 6318, 631810, (2006).

Design of the High Energy Materials Science Beamline at PETRA III

N. Schell, R.V. Martins, T. Lippmann, F. Beckmann, H.-U. Ruhnau, R. Kiehn, and A. Schreyer

GKSS-Research Centre Geesthacht GmbH, Max-Planck-Str. 1, 21502 Geesthacht, Germany

The future **H**igh **E**nergy **M**aterials **S**cience Beamline **HEMS** at PETRA III [1] will have a main energy of 120 keV, tunable in the range of 50 to 300 keV, and will be optimized for sub-micrometer focusing with Compound Refractive Lenses (CRLs) and Kirkpatrick-Baez (KB) Multilayer mirrors. Design, construction, operation and main funding will be the responsibility of the Research Center Geesthacht, GKSS. Approximately 70 % of the beamtime will be dedicated to Materials Research, the rest reserved for "general physics" experiments covered by DESY.

The materials science activities will be threefold:

1) Fundamental research will encompass metallurgy, physics, chemistry, biology *etc*. which are more and more merging. First experiments are planned for the investigation of the relation between macroscopic and micro-structural properties of polycrystalline materials, grain-grain-interactions, recrystallisation processes, and the development of new & smart materials or processes. For this purpose a dedicated 3D-microstructure-mapper will be designed.

2) Applied research for manufacturing process optimization will benefit from high flux in combination with ultra-fast detector systems allowing complex and highly dynamic *in-situ* studies of microstructural transformations, e.g. during welding processes. The beamline infrastructure will allow easy accommodation of large user provided equipment (at present an *in-situ* friction stir welding device for measurements at synchrotron radiation sources is currently in the design phase at GKSS).

3) Experiments targeting the industrial user community will be based on well established techniques with standardised evaluation, allowing "full service" measurements. Environments for strain mapping [2] on large structural components up to 1 t will be provided as well as automated investigations of large numbers of samples, e.g. for tomography and texture determination.

After a first workshop in June 2006 in order to address the future user community, the current working design for the beamline (P07 in sector 5 of the future experimental hall) consists of a five meter in-vacuum undulator source (U19-5), an optics hutch, an in-house test facility and two independent experimental hutches working alternately, plus additional set-up and storage space for long-term experiments. Figure 1 shows in the upper part schematically the side and top views of the beamline. In the lower part a 3D-CAD-plot visualizes the working environment and indicates the required experimental possibilities. HEMS should be operational in spring 2009 as one of the first beamlines running at PETRA III.

References

[1] http://petra3.desy.de/beamlines/work_packages/e1036/e1557/index_eng.html
[2] R.V. Martins, V. Honkimäki, Textures & Microstructures 35, 145 (2003)

4.5 m

Laboratories

L1 L2

Optics Hutch
OH

Test Facility
TF

Control TF
EC0

Control Cabin 1
EC1

BL Freeway

Control Cabin 2
EC2

Hall Freeway

Exp. Hutch 1
EH1

Exp. Hutch 2
EH2

Electricity

Gas

Ring
Tunnel

Storage
SP1

Storage
SP2

Maintenance
SP3

BL Freeway

DESY

GKSS

40 m from source

Test Facility (5 m)
- calibration / detector tests
- powder diffraction

Protected setup / storage space
- testing devices
- long term thermo-mechanical treatments

75 m from source

Optics Hutch
(11 m)

control
cabins

90 m from source

**cabin for
maintenance**

1st Experimental Hutch (10 m)

- **general purpose diffractometer**
- high resolution **3D microstructure mapper**
- focussing optics <10 µm (CRLs & KB mirrors)

2nd Experimental Hutch (12 m)

- **heavy duty diffractometer** up to 1 t
- detector robotics
- HR ultra fast **micro-tomography**
- focussing optics <10 µm (CRLs & KB mirrors)
- **SAXS option**
- **space**

GKSS

Figure 1: Design study of the HEMS beamline at PETRA III.

Application of X-ray microtomography in catalysis: A study of shell-impregnated solid catalysts

J.-D. Grunwaldt[1], F. Beckmann[2], and A. Baiker[1]

[1]Department of Chemistry and Applied Biosciences, ETH Zurich, Hönggerberg – HCI, CH-8093 Zürich, Switzerland

[2]GKSS-Research Center, Max-Planck-Str. 1, D-21502 Geesthacht, Germany

Impregnation of pre-shaped metal oxide particles is one of the most applied preparation procedures of industrial heterogeneous catalysts. Different mathematical descriptions of the impregnation step have been developed [1]. However, radial profiles have been seldomly measured in practice [2] and, to our knowledge, no tomographic study using X-ray microtomography has been reported up to now. Only recently, we reported on the application of X-ray absorption tomography to identify the oxidation state distribution inside a catalytic microreactor [3]. The advantage of X-ray microtomography is that it can give non-destructively information on the microstructure [4], e.g. grain size structure, of the pre-shaped catalyst pellets. In addition, element contrast can be achieved, if the X-ray absorption is different. To demonstrate the perspective of this approach, we have determined the microstructure of a commercial 0.5%Pd/Al$_2$O$_3$ catalyst, that we recently successfully applied in alcohol oxidation in supercritical fluids [5]. In addition, a Cu-based catalyst with different impregnation depth was prepared using different impregnation times and a similar kind of Al$_2$O$_3$-pellet (cylindrical shape, cf. ref. [2]).

X-ray microtomography was performed on the differently impregnated alumina pellets with cylindrical shape (3.2 x 3.6 mm) at beamline BW2 at HASYLAB. The photon energy was set to 18 keV and a pixel size of 2.3 μm was used (resulting spatial resolution of about 4 μm). The sample was rotated using the GKSS-stage described in ref. [6]. Fig. 1 shows the results on the 0.5%Pd/Al$_2$O$_3$ catalyst sample (Engelhard 4586). Clearly the microstructure of the alumina pellet with its grains is visible. With a brighter contrast towards the side planes the impregnated part with the palladium constituent is observed. The sharp gradient demonstrates that the front during impregnation has been very sharp, indicating a diffusion-controlled impregnation process. This is in line with electron microscopy (not shown), which however can only give two dimensional information. The present data in Fig. 1 contain the information in three dimensions.
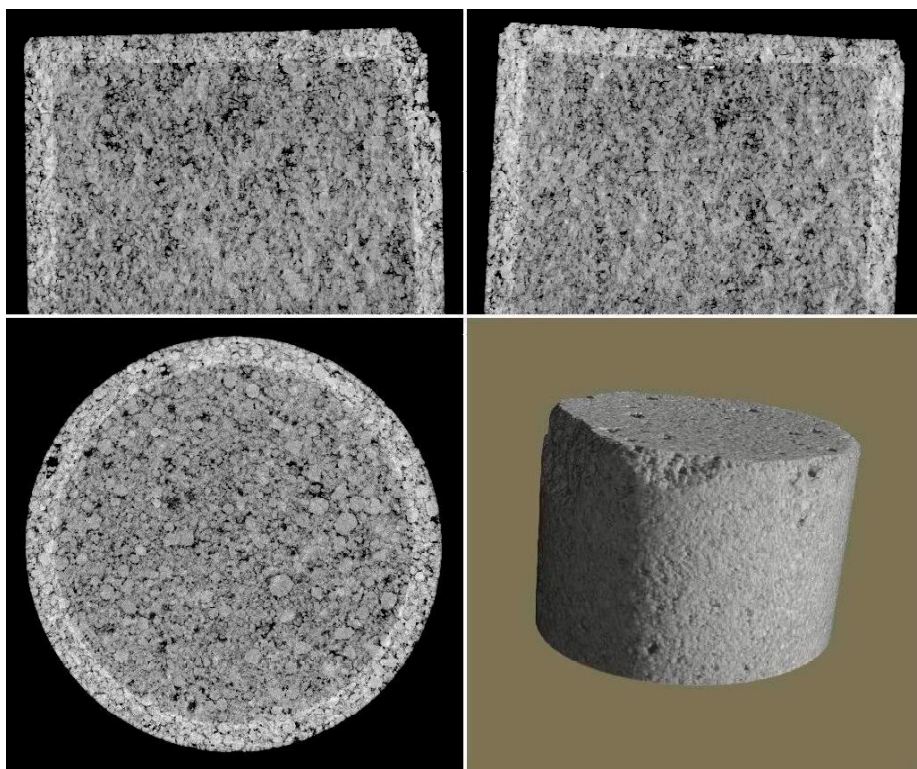
Fig. 1: 3D-reconstruction of 0.5%Pd/Al$_2$O$_3$, shell-impregnated catalyst pellet of cylindrical shape; sample was stuck from one side on the sample holder, field of view: 3.54 mm x 2.36 mm; total reconstructed volume of 3.54 x 3.54 x 2.36 mm^3.

In the same manner, Cu/Al$_2$O$_3$ catalysts, differently impregnated with CuCl$_2$-solution as described in ref. [2] and using alumina pellets of the same shape and size, were investigated. The results are depicted in Figs. 2 and 3.

Whereas the first catalyst was immersed for 1 min, the second one was kept for 10 min in the impregnation solution. The sharp diffusion front moved progressively towards the center of the pellet indicating a shell-progressive behaviour [2]. Interestingly, certain differences can be found (particularly in Fig. 3) for the horizontal and axial direction, indicating some structural anisotropy resulting in a different diffusion behaviour in the two directions.

The presented results allow to determine the progress and shape of impregnation zone without destruction of the pellets and are thus excellently suited for deriving a mathematical description of the diffusion-immobilization process [1,2]. This can be achieved with a series of experiments where the impregnation time is varied. This will allow us to optimize the impregnation process. The use of the technique will also be of further relevance to identify the element distribution (in combination with fluorescence detection) and thus the microscopic structure of heterogeneous catalysts. The strategy can be regarded complementary to micro-Raman and UV-vis, magnetic resonance imaging techniques and the recently described X-ray absorption tomography using a microfocussed beam [3] as well as the detection of oxidation state distributions using an X-ray camera [7]. The latter are more time-consuming since full XANES spectra have to be measured.

Fig. 2: 3D-reconstruction of Cu/Al_2O_3, 1 min with $CuCl_2$-solution impregnated catalyst pellet; field of view: 3.54 mm x 2.36 mm.
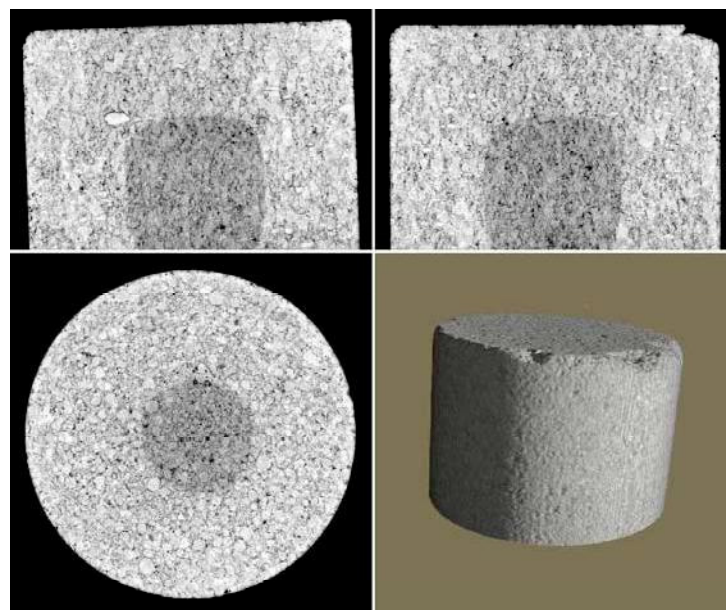
Fig. 3: 3D-reconstruction of Cu/Al_2O_3, 10 min with $CuCl_2$-solution impregnated catalyst pellet; field of view: 3.54 mm x 2.36 mm.

References

[1] A.V. Neimark, L.I. Kheifez and V.B. Fenelow, Ind. Eng. Chem. Prof. Res. Dev. 20, 439 (1981)

[2] A. Baiker and W.L. Holstein, J. Catal. 84, 178 (1983)

[3] C. G. Schroer, M. Kuhlmann, U. T. Hunger, T. F. Günzler, O. Kurapova, S. Feste, F. Frehse, B. Lengeler, M. Drakopoulos, A. Somogyi, A. S. Simionovici, A. Snigirev, I. Snigireva, C. Schug, and W. H. Schröder, Appl. Phys. Lett., 82, 1485 (2003).

[4] F. Beckmann, U. Bonse, T. Biermann, Proc. of SPIE Vol.3772, 179 (1999)

[5] M. Caravati, J.-D. Grunwaldt, and A. Baiker, Catal. Today, 91-92, 1 (2004); J.-D. Grunwaldt, M. Caravati, A. Baiker, J. Phys. Chem. (letter), doi: 10.1021/jp068081u.

[6] F. Beckmann, T. Donath, J. Fischer, T. Dose, T. Lippmann, L. Lottermoser, R.V. Martins, A. Schreyer, Proc. of SPIE Vol. 6318, 631810-1-11 (2006).

[7] J.-D. Grunwaldt, S. Hannemann, C. G. Schroer, and A. Baiker, J. Phys. Chem. B, 110, 8674 (2006)

Computer Microtomographic Investigation of Polyetherimide/Al 2024-T351 Friction Riveted Joints

S. Amancio, J. F. dos Santos, F. Beckmann, A. Schreyer

GKSS Forschungszentrum Geesthacht, Max-Planck-Straße 1, 21502, Germany

The Friction Riveting process is a new patent pending spot joining technique developed by GKSS Forschungszentrum in 2005 [1]. The process is based on mechanical fastening and adhesion bonding associated with frictional heating. Joints are strong achieving in some cases a 100% efficiency compared to the strongest base material [2]. The required joining equipment is simple, being composed by a standard friction welding machine or adapted machine tool equipment. In Friction Riveting the joining partners are composed of metallic rivets (stud) and base elements, which can be made thermoplastic materials or metallic alloys.

There are several possible joint configurations in Friction Riveting. The basic process configuration, the "point-on-plate" joint, where a metallic rivet is inserted and mechanically anchored in a polymeric base element is herein schematically described in Figure 1. In this configuration the metallic rivet is rotated and pressed against the surface of the polymeric base element (see Figure 1.A). During the initial phase the rotating rivet penetrates the polymer forming a very thin layer of molten polymer around its shaft (Figure 1.B) due to frictional heating. When the rivet reaches a certain insertion depth heat input rate becomes much higher than the heating dissipation rate owing to the low polymer's thermal conduction. The most critical point of this phenomenon is found underneath the tip of the rivet, which plasticizes to a softer state. At this point rotation is stopped and forging pressure is applied. As a result plasticized material in the tip of the stud will deform being pushed backwards by the cooler polymeric volume, assuming a paraboloidal geometry (see Figure 1.C). That will help anchoring the stud into the base element after joint consolidation (Figure 1.D).

X-Ray Computer Microtomography, µCT, is a very powerful non-destructive way of qualitatively and quantitatively investigating the microstructural features of a friction riveting joint i.e. its level of deformation at the paraboloidal tip of the rivet, presence volumetric defects associated with thermal degradation, volatiles and thermal shrinkage, etc.. Several section views can be obtained and volume rendered images allow a complete

Figure 1. Schematic representation of the Friction Riveting process for point-on-plate joints in metal-polymer multi-material structures. A) Rotating pin is moved downwards to touch the polymeric base plate. B) Insertion of the rivet into the polymeric base element and formation of a molten polymeric film. C) Deformation of the rivet's plasticized tip resulting in the paraboloidal anchoring pattern. D) Joint is formed after consolidation.
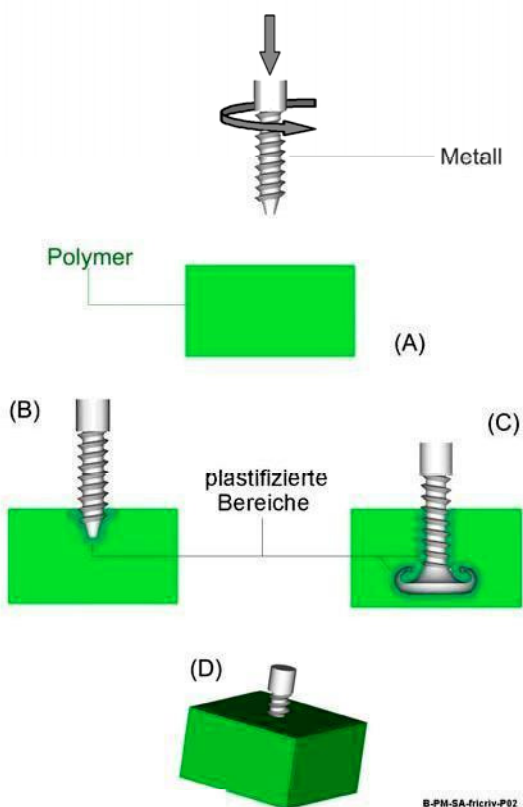
qualitative microstructural analysis. With the aid of image analysis software different volumes can be segmented and quantified. Considering that mechanical performance is directly related to microstructure, µCT-analysis is an important tool to understand this new process. Therefore joining mechanisms can be better comprehended and process optimized, leading to stronger and improved quality joints. Figure 2 presents a volume rendered picture of a friction riveted polyetherimide (green)/Al 2024-T351 (red) joint. In this example the joint was volume-segmented and each segment differentially coloured. Three main segments constitute the joint: the heat affected area in the polymer (in green, Figure 2.D), the thermo-mechanically affected zone in the polymer (in yellow, Figure 2.C) and the deformed anchoring zone of the rivet (in red, Figure 2.E)
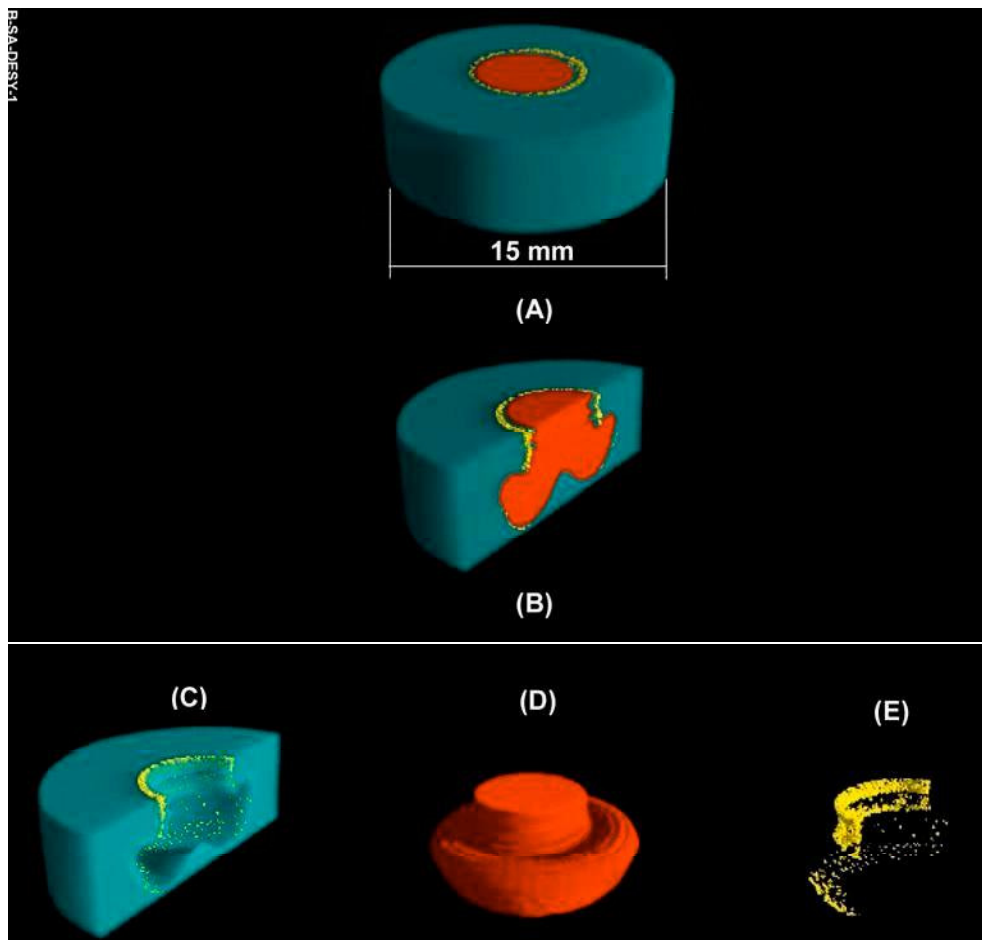
Figure 2. CT volume rendering of PEI-Al 2024-T351 friction rivet joint. A) The total rendered volume. B) A cross sectional cut of the volume in A. C) The heat affected zone in the polymer (green). D) The deformed paraboloidal tip of the rivet. E) The thermo-mechanically affected zone with thermal degraded and volatile defects. The sample was scanned at beamline W2 (HARWI II) using a photon energy of about 36 keV.

References

[1] AMANCIO FILHO, S. T., BEYER, M., DOS SANTOS, J. F., Verfahren zum verbindem eines metallischen Bolzens mit einem Kunststoff-Werkstück. DE Patent Application Nr. 10 2005 056 606.5, 2005.

[2] AMANCIO , S., DOS SANTOS, J. F., Reibnieten: Beitrag zur Entwicklung eines neuen Fügeverfahrens für Kunststoff und Leichtbaulegierungen. In Proc.: Geesthachter Schweißtag'06, Geesthacht, Germany, 22.-23. November 2006.

Damage Mechanisms and LCF Crack Extension in Al2024

R. Braun, D. Steglich and F. Beckmann

GKSS Research Center ,Institute of Materials Research, Max-Planck-Str.1, 21502 Geesthacht, Germany

Micromechanics is a powerful methodology for the investigation and prediction of materials behaviour at the meso/macroscale using characteristics of the microstructure. One of the challenges in micromechanical modelling is the possibility to incorporate the damage processes on the basis of physics and thus to follow the associated progressive degradation of the material. In order to apply this methodology efficiently, detailed information on a materials microstructural features as well as their evolution are required.

Engineering components and structures may be subjected to loading conditions, which can force the material to undergo cyclic plastic flow. The occurrence of plastic deformation and accumulation with cycles is a cause of damage development that, sooner or later, will lead the material to fail. Damage is related to the irreversible processes that occur in the materials microstructure, therefore its presence affects the material constitutive response at meso/macro scale. In the low cycle fatigue (LCF) regime, irreversible microstructural changes take places, in order of increasing strain amplitude, in the following forms: persistent slip bands, rearrangement of dislocation systems into cell structures, and void nucleation and growth at the secondary phase inclusions [1,2]. The latter mechanism is peculiar of high strain amplitudes, for which very short lives are usually expected.

For the modelling of LCF it is essential to describe the damage mechanisms and the resulting crack extension behaviour correctly. In the present study, LCF experiments of notched round bars machined from the technical aluminium alloy Al2024 T351 have been conducted. Some of the tested specimen are later investigated by computer tomography at DESYs Hamburg Synchrotron Radiation Laboratory HASYLAB in order to visualise crack initiating and propagation. Figure 1 depicts the specimens geometry (inner diameter 4 mm, notch radiums 4 mm). All tomographical scans were performed at beamline W2 (HARWI II) using the photon energy of 28 keV.

To avoid the influence of surface roughness on the nucleation of cracks, the specimen has been polished mechanically before testing. The mechanical tests have been performed under strain control in order to be able to stop the experiment without completely braking the specimen. A typical measured load-elongation graph is given in figure 2. This particular test was stopped as the maximum load was decresing significantly, which coincides with a propagating crack starting from the specimen´s surface.
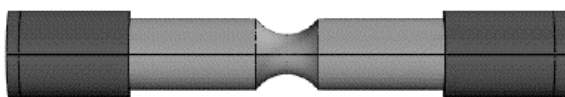
Figure 1: scetch of the specimen under investigation(inner diameter 4 mm, notch radiums 4 mm)
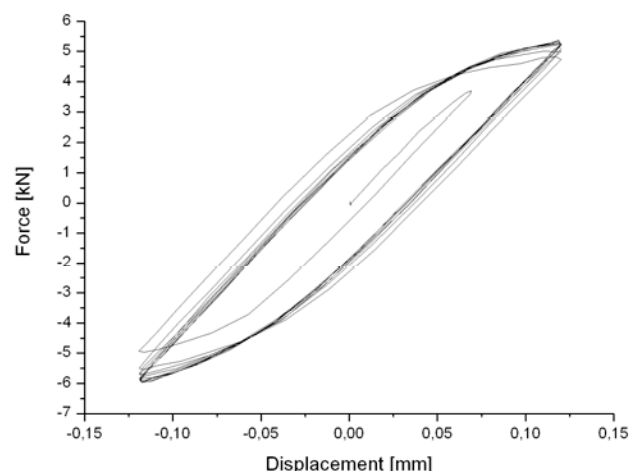
Figure 2: Load-elongation behaviour obtained form the mechanical test

The goals of the this study were to obtain the shape of the cracks inside the specimens and to investigate damage mechanisms. Figure 3 shows a cut of the specimen´s minimum cross section,

where the cracks have been initiated. A crack is visible from the surface of the specimen, see left picture. This discontinuity in the material has been visualised as blue surface in the right picture. Obviously, the crack front is neither a straight line nor it lies in the symmetry plane of the specimen. The crack front follows microstructural features, and probagates in a complex manner.
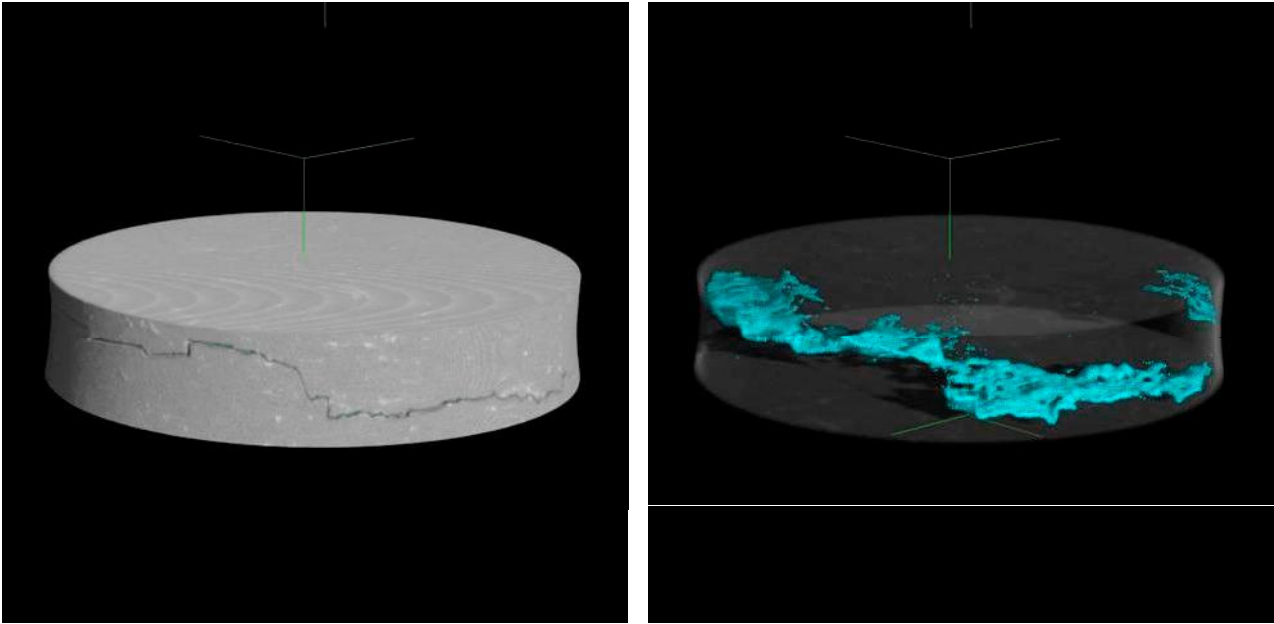
Figure 3: Cut of one specimen, left as a full solid, right semi visible with the cracks appearing in blue (inner diameter 4mm). The volume renderings werd done using the software VGStudiomax 1.2.1, Volume Graphics GmbH, Heidelberg.
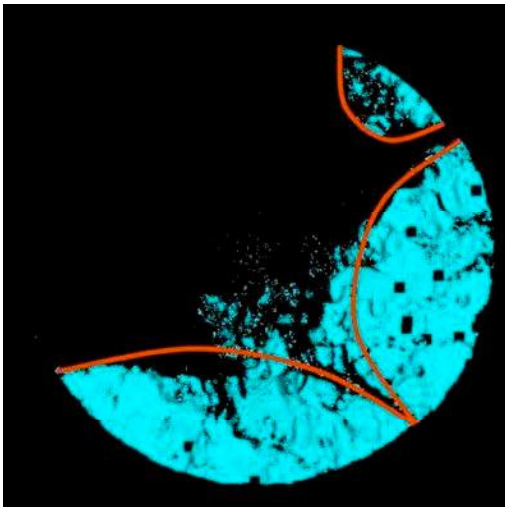
Figure 4: projection of the crack front on the symmetry plane

From the projection of the cracked surface in axial direction it can be seen that at least three initiation sites exist on the surface, indicated by the red lines in figure 4.

References

[1] Klesnil, M. and Lukas, P. Fatigue of Metallic Materials, Elsevier Science Publishers, Amsterdam (1980).

[2] Polak, J. Cyclic plasticity and low cycle fatigue life of metals, Elsevier Science Publishers, Amsterdam (1991).

Determination of Fiber Characteristics using lattice-Boltzmann Methods and μ-Tomography

G. Brenner, A. Al-Zoubi

Institute of Applied Mechanics, TU Clausthal, Adolph-Roemer Str.2A, 38678 Clausthal-Zellerfeld, Germany

The background of the present project is the development of modern manufacturing processes for fiber-reinforced materials. An important technology in the context is resin injection or liquid composite molding (LCM) and variants, such as the resin transfer molding (RTM). The main idea of these manufacturing processes is to inject liquid polymer resin into a mold, that consists of one or several layers of dry textile structures placed into it. In the same assembly the resin is finally cured. The advantage of the process is a high accuracy of the parts and of the surfaces as well as a short processing time. In order to design and to optimize the resin transfer molding, accurate and reliable predictions of the flow and other transport phenomena within the reinforcement material are required. Insufficient knowledge and ability to quantify these transport phenomena is the main reason why - up to now - the design of the molds is mainly based on intuition. Time consuming and expensive test series have to be performed in order to guarantee uniform propagation of the resin front through the textile structure. In order to improve this situation, more reliable and accurate data representing the hydrodynamic characteristics of reinforcement material have to be obtained. In the present project this is achieved by a combination of μ-tomography of real specimen of reinforcement materials such as glass and carbon fibers and subsequent numerical simulations of the impregnation with a viscous flow using the lattice-Boltzman technique.

The hydrodynamic characteristics of dry reinforcement materials are basically determined by the porosity and permeability. Those properties may vary significantly depending on the type of the textile structure as well as the way the material is draped into the mold. As a consequence, large variations of porosity and permeability result, which causes an unpredictable propagation of the resin front in the cavity. Thus, the goal of the present project is to determine a database for permeability of different textile structures and to develop a parameter model to determine the change of permeability depending on geometric features of these structures.
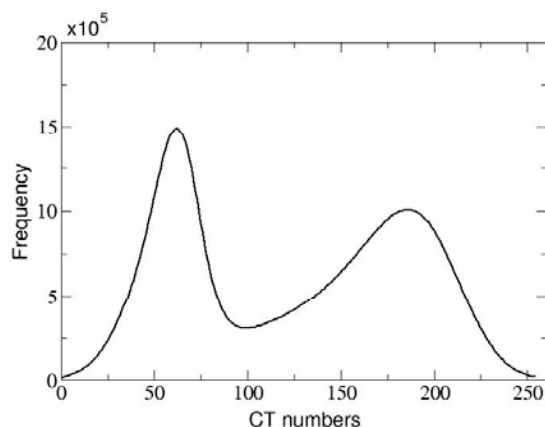
Fig. 1: Distribution of CT Number of carbon fibers in polymer matrix.
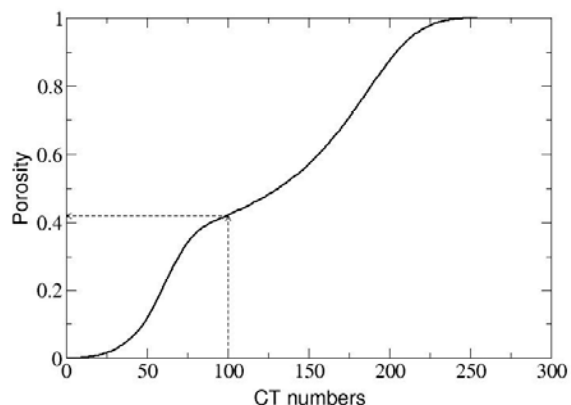
Fig. 2: Porosity of reconstructed geometry.

In order to determine the permeability within a representative elementary volume, its geometry has to be scanned. This has been realized in the present project using μ-tomography at HASYLAB. As a result of the tomographic scan the absorption coefficient is reconstructed along several slices and finally assembled to a three-dimensional array of CT-Number. In the present work the CT-Number

is stored with 8-bit accuracy. Figure 1 shows the frequency of occurrence of CT-Number for a compound of carbon fibers in polymer a matrix. The two peaks of the distribution correspond to the maximum absorption of the carbon components as well as the matrix material.

In order to reconstruct the true geometry of the composite from the CT-data, a threshold value of the CT-Number has to be defined in order to distinct between resin and carbon fiber. The definition of this threshold value has a distinctive influence on the porosity of the resulting geometry, as shown in figure 2. Since the porosity of the present composite is known, this maybe used in order to calibrate the threshold value. Finally, after a binarization a three-dimensional bitmap of the present structure is obtained. This geometry is shown in figure 3.

After reconstruction of the geometry, the lattice-Boltzman method developed in the Institute of Applied Mechanics at TU Clausthal is used to simulate the viscous flow through the compound. The flow is driven by a prescribed pressure gradient in one of the coordinate directions. By measuring the volumetric flow rate, the permeability of the compound can be obtained using Darcy's Law:

$$\boldsymbol{u}_D = -\frac{\boldsymbol{K}}{\mu} \cdot \nabla p$$

Note, that the permeability is a symmetric tensor. For the present compound the components of the permeability tensor are as follows:

$$\boldsymbol{K} = \begin{pmatrix} 15.49 \cdot 10^{-10} & 2.14 \cdot 10^{-16} & 3.38 \cdot 10^{-14} \\ 2.38 \cdot 10^{-14} & 9.98 \cdot 10^{-10} & 1.52 \cdot 10^{-14} \\ 4.62 \cdot 10^{-14} & 3.47 \cdot 10^{-16} & 0.86 \cdot 10^{-10} \end{pmatrix}$$

It is clearly seen that the permeability in the x-direction is different from y-direction as expected, since the fiber is tilted. The permeability in the z-direction is about one order of magnitude smaller than in the in-plane permeability, which is also in accordance to measurements.

The present results indicate, that the lattice-Boltzman technique together with the μ-tomography may be used in order to determine the permeability and the porosity of a fiber reinforced materials very efficiently and with high accuracy.
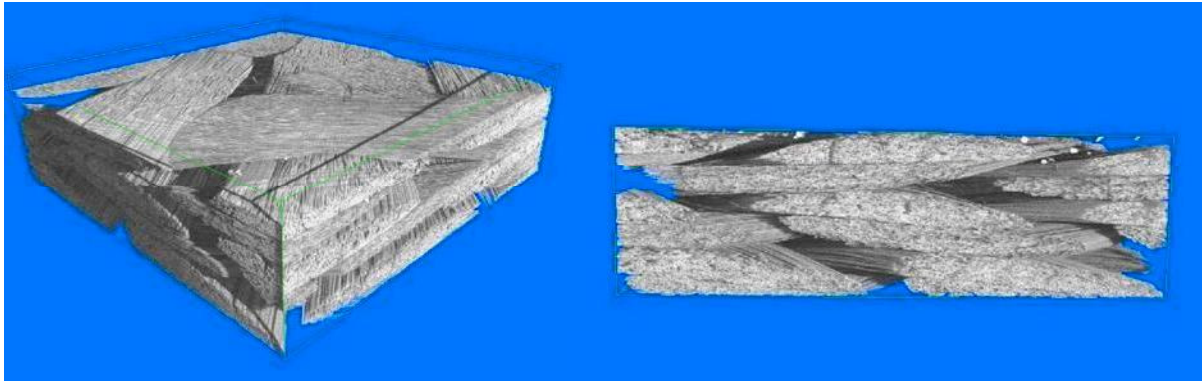
Fig. 3: View of the fiber geometry obtained by μ-tomography.

References

[1] G. Brenner, A. Al-Zoubi: *Application of the Lattice-Boltzmann Method for the Estimation of Permeabilities in Complex Structures, Proceedings of the Parallel CFD Conference*, Palma, 2004.
[2] A. Al-Zoubi: Numerical Simulation of Flows in Complex Geometries Using the Lattice Boltzmann Method, Dissertation, TU Clausthal, 2006.

Image analysis of the microstructure of natural fiber composites

T. Walther[1], T. Donath[2], K. Terzic[3], H. Meine[3], H. Thoemen[1], and F. Beckmann[2]

[1]*Department of Wood Science, Hamburg University, Leuschnerstrasse 91, 21031 Hamburg, Germany*

[2]*GKSS-Research Center Geesthacht, Max-Planck-Strasse 1, 21502 Geesthacht, Germany*

[3] *Department of Computer Science, Cognitive Systems Group, Hamburg University, Vogt-Kölln-Strasse 30,*

22527 Hamburg, Germany

Fiber composites were investigated by x-ray microtomography (μCT) within the research project I-04-100 "Microstructure of Natural Fiber Composites". A number of fiberboard samples with average densities from 300 kg/m^3 up to 1000 kg/m^3 were examined at beamline BW2 at a photon engergy of 12.0 keV. The recorded volume data were further analyzed using 3D image analysis, which enabled a detailed three-dimensional characterization of the fiberboard structure [1].

The developed image analysis routines allow for the segmentation of the tomography data into cell wall material and air regions. Furthermore, air regions inside of the fibers (intra-fiber voids) and outside of the fibers (inter-fiber voids) can be distinguished automatically. Figure 1 shows the volume fraction of the three regions as a function of sample density. The values have been determined from small subvolumes with a size of 256^3 voxels out of the whole μCT data set with a size of 1536×1536×1024 voxels.
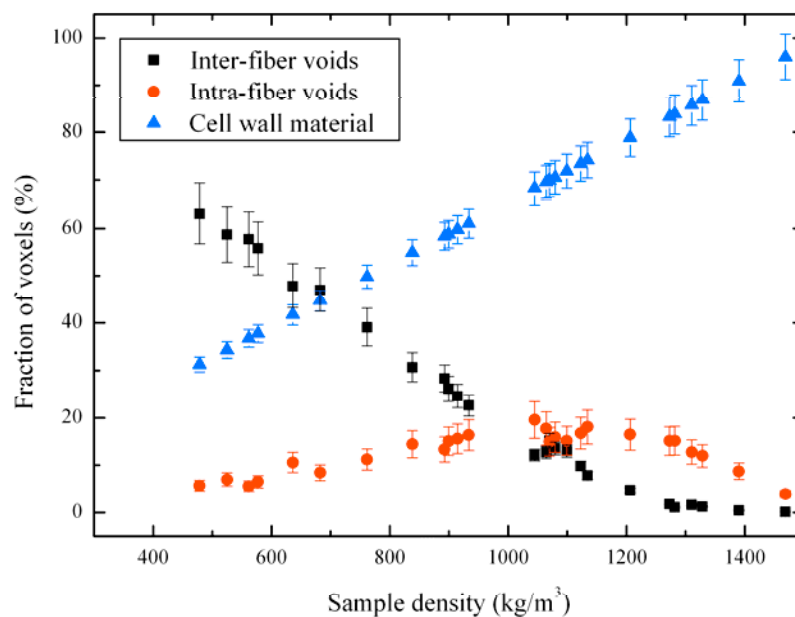
Figure 1: Fraction of voxels belonging to one of the three components in the samples.

The volumes and ratios of cell wall material, intra-fiber voids and inter-fiber voids were calculated by counting voxels within the segmented images. It is clearly visible that the amount of voids decreases with increasing sample density. Of great interest is the region around the density of 1100 kg/m^3, where the amount of intra-fiber voids starts to decrease. This indicates the collapse of fibers caused by the high densification during fiberboard production.

Furthermore, the surface of the fibers was calculated by counting the contact surfaces between the cell wall voxels and the inter-fiber voids. This value is important for the calculation of the resin distribution on the fibers and for the free surface area due to the hygroscopic behaviour of the fiber material.
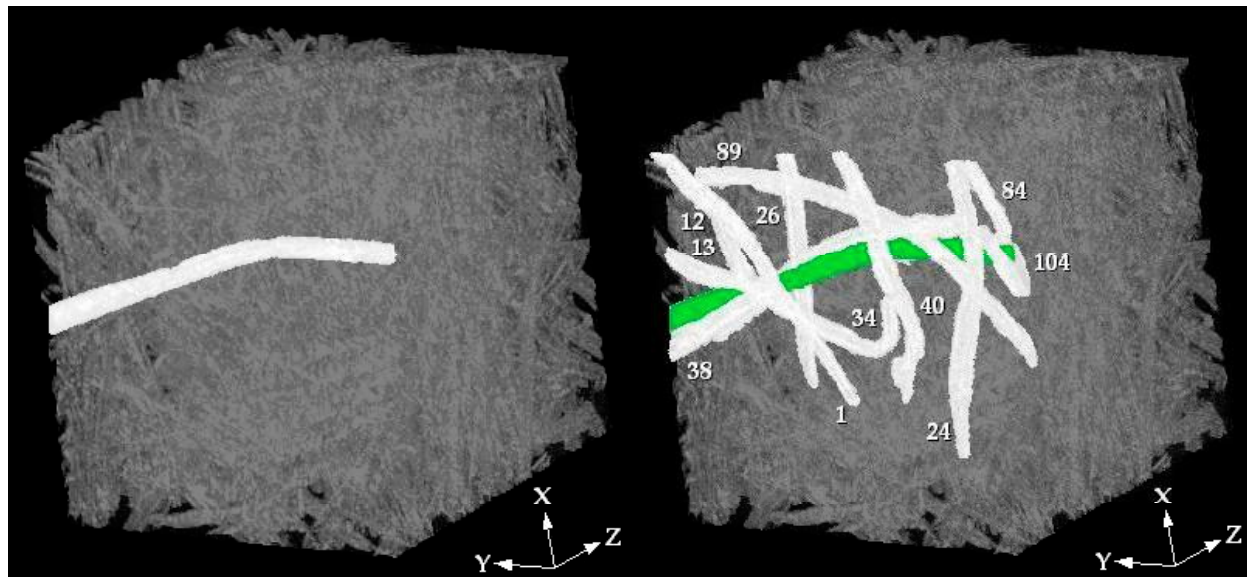
Figure 2: Highlighted fiber in a 300 kg/m^3 MDF volume (Left) and with numbered contacting fibers (Right). The volume has a size of 256^3 voxels with an edge length of 588 µm.

Finally, the orientation of the fibers was obtained by performing a principal component analysis on the segmented intra-fiber voids inside of the fibers. This information was necessary to idenfiy the contact points and the contact area between the fibers. Figure 2 shows a representative example of a selected fiber and its contacting neigbours. The contacting fibers are displayed with their individual numbering, so that each fiber can be handled and characterized separately.

The segmented µCT data was also used for the simulation of the permeability in *x* and *y* direction and for a thermal conductivity simulation in *x*, *y* and *z* direction using software tools of the Fraunhofer Institut für Techno- und Wirtschaftsmathematik (ITWM) in Kaiserslautern [2]. The results of the calculations were close to results gained by laboratory experiments on fiberboard samples [3].

Further investigation is planned to identify and to analyze the distribution of the stained adhesives on the fibers and to enhance the simulation tools for the permeability and the thermal conductivity calculations.

References

[1] Walther, T., Terzic, K., Donath, T., Meine, H., Beckmann, F., Thoemen, H., „Microstructural analysis of lignocellulosic fiber networks", Developments in X-Ray Tomography V, Proceedings of SPIE Volume 6318, CID Number 631812, 13.-17. August 2006, San Diego, California, USA

[2] Schulz, V., Kehrwald, D., Wiegmann, A., Steiner, K., „Flow, heat conductivity, and gas diffusion in partly saturated microstructures", 2. NAFEMS CFD Seminar: Simulation of Complex Flows, Niedernhausen/Wiesbaden, Germany, 25.-26.April 2005, 1-10

[3] Walther, T., Thoemen, H., Terzic, K., Meine, H., „New opportunities for the microstructural analysis of wood fibre networks" Proceedings of the 10th European Panel Products Symposium, Llandudno/Wales, UK, 11.-13.October 2006, 23-32

In vivo corrosion of AZ31 magnesium screws in a sheep model characterized by synchrotron-radiation based microtomography

F. Witte [1], A.A.Kaya [2], R.A. Kaya [3], O.Duygulu [2]

[1]Laboratory for Biomechanics and Biomaterials, Department of Orthopedic Surgery, Hannover Medical School, Anna-von-Borries-Str. 1-7,30625 Hannover, Germany

[2]TUBITAK Marmara Research Center, Materials Institute, Turkey

[3]Neurosurgery Department, SISLI ETFAL State Hospital, SISLI Turkey, Turkey

Light metals such as magnesium alloys gained an increasing interest in transportation and aerospace industries as well as in medical applications as a novel biomaterial during the past years [1-4]. Especially the need for mechanically reliable and degradable implant materials in orthopaedic surgery and neurosurgery promoted the reaserch on degradable metallic implants. The corrosion resistance of magnesium alloys at physiological pH levels is limited. This seemingly disadvantageous feature of magnesium can be used as an advantage in case of degradable implant materials in the field of biomaterial research [4]. Previous studies have shown that magnesium alloys have positive osteogenic effects and are suitable mechanical implant materials for orthopaedic surgery and neurosurgery [4]. Therefore, magnesium screws made of extruded magnesium alloy AZ31 were investigated as cortical screws in a sheep model.

Cortical bone screws were machined from magnesium alloy AZ31 (3 wt% Al-1 wt% Zn) extrusion rod to serve as implant material in this study. Each screw was manufactured individually via machining from an AZ31 extrusion rod of 10mm diameter. Along with magnesium, other traditional screws were also used for comparison such as titanium, hydroxyapatite coated titanium and bioabsorbable polymer. Cortical bone screws were machined according to ASTM standard [ASTM-F543-02: Standard Specification and Test Methods for Metallic Medical Bone Screws. Annual Book of ASTM Standards. Philadelphia, Pennsylvania, USA: American Society for Testing and Materials, (2002)]. These screws were implanted to hip-bones of sheep via surgery. Three months after surgery, these hip-bones were removed from the sacrificed animals. Radiographic examinations were conducted on these hip bones.

Synchrotron-radiation based micro-computed tomography (SRμCT) allows the 3D reconstruction of a specimen from a set of 2D projections using the backprojection of filtered projection algorithm. The SRμCT were performed at beamline HARWI II at Hamburger Synchrotronstrahlungslabor HASYLAB at Deutsches Elektronen Synchrotron DESY (Hamburg, Germany).

The specimens were imaged by microtomography in absorption mode utilizing synchrotron radiation at beamline HARWI II using 30 keV photon energy. Exposed to the parallel synchrotron X-ray beam, the sample was precisely rotated 0.25° stepwise to 180°, and after every fourth step the reference image (projection) was recorded to eliminate intensity inhomogeneities and variations of the X-ray beam.

Due to the size of the bone-screw explants, the explants where scanned in three different hight levels and the reconstructed tomographs were stacked to an entire data-set allowing to characterize the interphase of the screw and the bone at the entry of the screw into the bone and the bone-screw interphase in the cancellous bone.

The results of the microtomography using synchrotron-radiation (SRμCT) showed the 3D orientation of the magnesium screw inside the sheep bone (Fig. 1). While the screw head exhibited severe surface corrosion on the convex areas of the screw head at 3 months post-operatively (deep grey areas, Fig. 1 a; front head area, Fig. 1 b), just minor corrosion attack was observed on the screw head area of the machined hexagonal screw drive (Fig. 1).

The threads of the screw displayed a quite homogeneous corrosion layer (Fig. 1 a) which was thicker on the tip of the threads. Partly direct contact of the screw to adjacent bone tissue was

observed. Cancellous bone formation were observed inside the pitches assuming a good mechanical hold of the magnesium screw, even though the threads were partly corroded. In further studies the screw–bone interphase will be analysed histologically.

The three-dimensional visualization using synchrotron-raditaion based microtomography (SRμCT) enabled us to describe the corrosion morphology of engineered magnesium screws for the application as cortical bone screws in a sheep model.
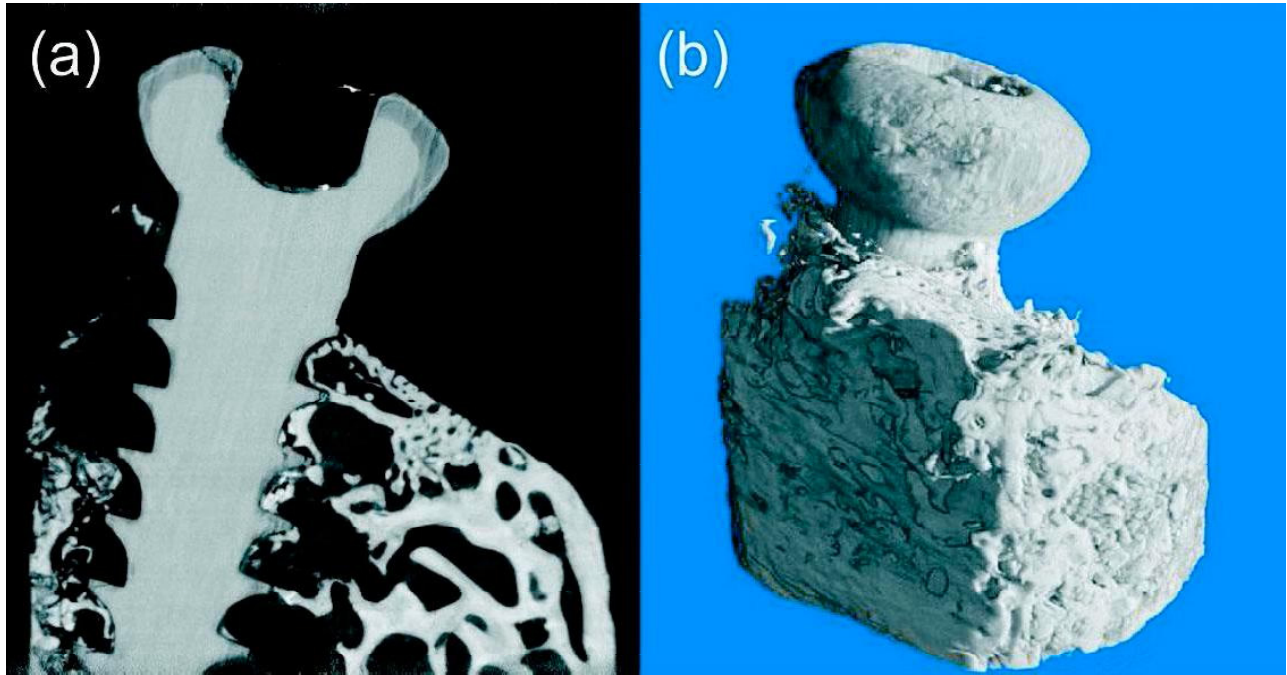
Figure 1: Left image (a) shows a longitudinal section through the 3D reconstructed and stacked data-sets of a AZ31 magnesium screw that was implanted into sheep bone for 3 months. Rigth image (b) shows the external appearance of the same data-set as displayed in the left image (a).

References

[1] S. Schumann, Materials Science Forum 488-489 (2005) 1-8
[2] A. A. Luo, Materials Science Forum 419-422 (2003) 57-66
[3] E. D. McBride, JAMA 111 (1938) 2464-2476
[4] F. Witte et al., Biomaterials 26, (2005) 3557-3563

Lattice strain evolution of the textured AZ31 magnesium alloy

S.B. Yi[1], H.-G. Brokmeier[1,2], P. Spalthoff[1,2], B. Schwebke[1,2] and T. Lippmann[2]

[1]*Institut für Werkstoffkunde und -technik, TU-Clausthal, Agricolarstr. 6, D-38678 Clausthal-Zellerfeld, Germany*

[2]*GKSS-Forschungszentrum, Max-Planck-Str., D-21502 Geesthacht, Germany*

Despite of the advantages of magnesium alloys such as a high specific strength, the poor cold formability is a facing problem for industrial applications of these alloys. The problem is linked with an inadequate number of independent deformation systems. The initial texture and deformation condition play important role in activation of potential deformation systems, e.g. various slip- and twinning modes, and mechanical behaviours [1]. Since magnesium alloys show high plastic anisotropy, i.e. individual grains, depending on their orientation, response differently to the mechanical loading, plastic deformation induces internal strain. It should be noted that the dominant mechanism of internal strain evolution in magnesium is the plastic anisotropy, because magnesium single crystal shows nearly isotropic elastic coefficient and thermal expansion [2]. The residual strain, which has an important meaning in engineering materials, is directly influenced by internal strain. Careful studies on the lattice strain evolution will give meaningful information on the internal strain evolution mechanism as well as on the activity of the deformation systems.

In this report we will shortly describe recent results on the lattice strain evolution during tensile loading of AZ31 (Mg–3Al –1Zn–0.1Mn in wt. %) plate produced by hydrostatic extrusion. For the different initial conditions in terms of the texture, hour-glass shaped tensile samples were prepared in three different directions, i.e. 0°, 45° and 90° to extrusion direction, see Fig. 1 (a). During the continuous tensile straining with constant ram speed, 0.002 mm/sec., Debye-Scherrer rings were repeatedly registered with MAR345 image plate. The experiments were conducted at the HARWI-II beam line. The macroscopic load and displacement were recoded by a load cell and an extensometer.

Fig. 1 (b) shows the stress-elongation (in tensile direction) curves. Each sample shows characteristic behavior which can be explained by different initial texture and the measuring points during uniaxial tension. The lattice strains, $\varepsilon^{hk.l}$, were calculated from the measured inter-planar spacing, $d^{hk.l}$, using the following equation:

$$\varepsilon^{hk.l} = \frac{d^{hk.l} - d_0^{hk.l}}{d_0^{hk.l}}$$
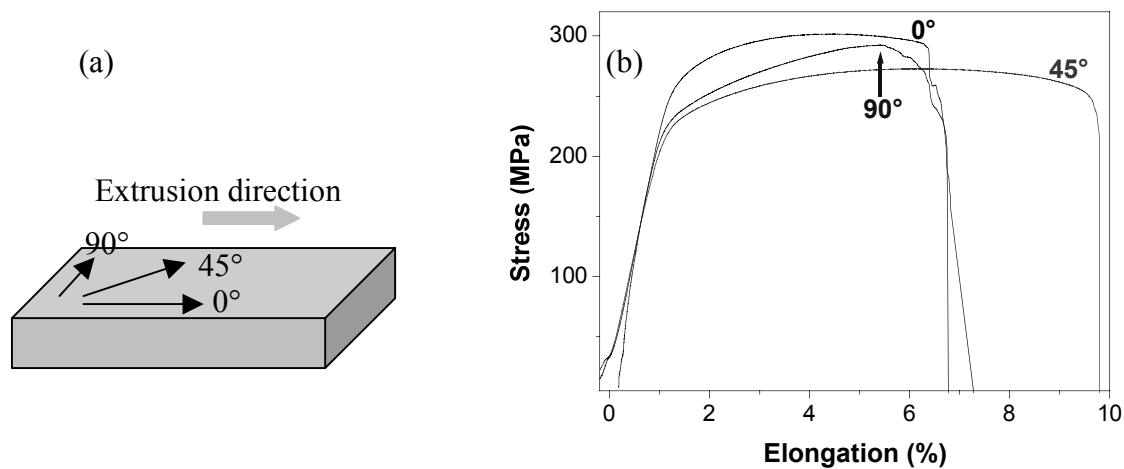
Figure 1: (a) Tensile sample cutting directions. (b) The flow curves by tensile loading of samples.

The reference lattice spacing, $d_0^{hk.l}$, was obtained from the linear fit to the linear elastic response during the initial loading, i.e. at zero stress. Fig. 2 presents, as a preliminary result, the macroscopic load versus lattice strain curves in the tensile loading direction. Because of the strong texture of the extruded plate and different sample cutting direction, there are variations of diffraction peaks which are visible in the tensile loading direction. For example, (00.2) diffraction peak is visible only in the sample cut in 90° to the extrusion direction. Lattice strain on the {10.0} and {11.0} planes were evaluated in all samples, and both show similar behavior, i.e. soft and linear behavior. The {10.1} lattice plane is visible also in all samples, however, this behaves non-linear and harder than the {10.0} and {11.0}. The {10.2} lattice plane shows harder than the above planes, see Fig. 2 (b) and (c). The abnormal behavior of the (00.2) lattice strain is clearly shown in the 90° sample. Firstly, the contraction of the (00.2) lattice spacing is observed at the beginning of the elastic deformation, while other lattice planes show always elongation. Secondly, this plane has very hard behavior in the elastic range, e.g. (00.2) lattice strain is 2 ~ 3 times smaller comparing to other planes. However, the (00.2) lattice strain increases rapidly after the macroscopic yield point.
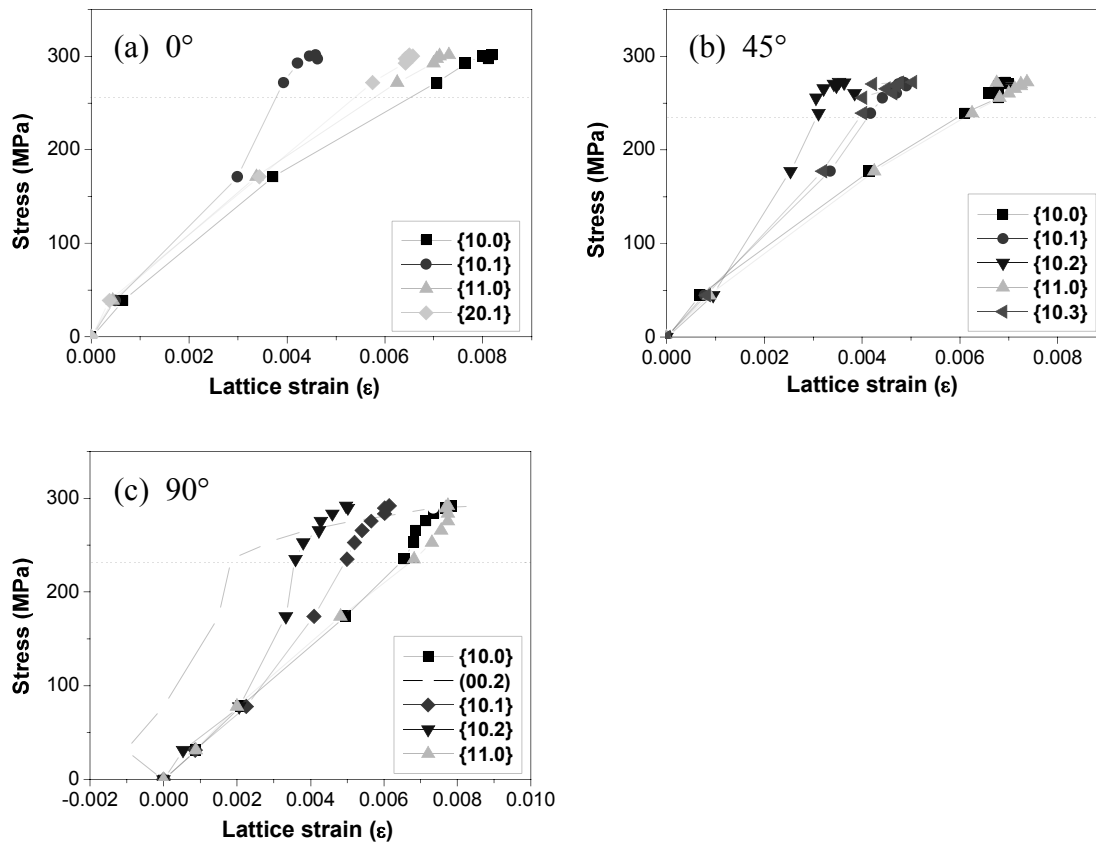
Figure 2: Measured lattice strains during the tensile loading of (a) 0°, (b) 45° and (c) 90° samples. (the horizontal dotted line shows the macroscopic yield point of each sample)

References

[1] S.B.Yi, C.H.J. Davies, H.-G. Brokmeier, R.E. Bolmaro, K.U. Kainer and J. Homeyer, Acta Mater., Vol. 54, 549 (2006)
[2] S.R. Agnew, D.W. Brown, S.C. Vogel, T.M. Holden, Mater. Sci. Forum, Vol. 404-407, 747 (2002)

Micro computer tomographic analysis of miniaturised sensor elements

H. Rahn[1], S. Odenbach[1], R. Baumann[2], S. Fasoulas[2], F. Beckmann[3]

[1]TU Dresden, Professur für Magnetofluiddynamik, 01062 Dresden, Germany
[2]TU Dresden, Professur für Raumfahrtsysteme/-Nutzung, 01062 Dresden, Germany
[3]GKSS, Max-Planck-Str.1, 21502 Geesthacht, Germany

This project supported by the European Space Agency (ESA) deals with the development and application of a new respiratory sensor system (RSS) for human respiratory investigations. The key element for this development is a new miniaturised sensor system that enables a simultaneous in-situ measurement of O_2, CO_2 and volume/mass flow rates. Due to the very fast response times of the sensors, the possibility for a very accurate breath-by-breath analysis is also given [1].

The working principle of the developed gas sensors is based on the ion conductivity of ceramic materials. For ion conducting solid state electrolytes, e.g. yttria-doped zirconia, the conductivity starts at a temperature above 400°C. Therefore, the sensor is heated by an electrical resistance. Corresponding to the used sensor material and electrical circuits either a current or a voltage is measured that is directly dependent to the partial pressure of the specific gas.

The flow rate measurement profits from the high operating temperature of the O_2- or the CO_2-sensor. The digital sensor electronics controls this temperature via a resistor heater to maintain stable operating conditions. Due to the very fast micro-controller, heat losses caused by the gas flow (forced convection) are almost immediately compensated by a corresponding increase in electrical power supply. By measuring the electrical power consumed to keep the sensor temperature constant, the original volume flow rate can be derived (similar to hot wire anemometry).

In the development, miniaturisation and reproducibility are main foci, to achieve an optimal system design and the possibility for serial production. Therefore innovative production methods are integrated into the development process. Screen printing techniques in multi-layer design are used (see. Fig. 1.1).
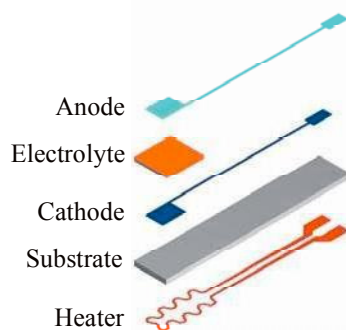
Fig. 1.1: Planar design and multi layer structure of the sensors
(Size: 20 x 3.5 x 0.5 mm)

The different layers have to be sintered to up to 1500°C in specific temperature cycles. Materials, their combinations and mixtures, together with the screen printing and sinter procedures influence the characteristics of the sensor. For a better understanding of these influences, microscopic methods (including cross section analysis), impedance spectroscopy and functional tests have been applied.

A new promising method to analyse the different layers is offered by the means of micro computer tomography (µCT). Due to the high brilliance of the variable energy of the used synchrotron radiation 3-dimensional non destructive imaging of the inner structure of the sensors is possible. The high spatial resolution down to 2 µm allows a sufficient analysis of the layer dimensions, density, porosity and material distribution [2]. Comparisons to the

common examinations as well as new possibilities for failure analysis are given. The results will open new ways for optimizing the production for further sensor developments.

In a first experiment some tests that reveal interesting information about the inner structure of the sensors are available in μCT data sets. In Fig. 1.2 an example of a qualitative density distribution is shown. With the assignment of different colours to corresponding density it is simple to separate the different layers. This is important as some of the used ceramics can not be separated optically (see Fig.1.3). The comparison shown in Fig. 1.3 demonstrates the advantage of μCT with the visualisation of cracks in the ceramic layers.
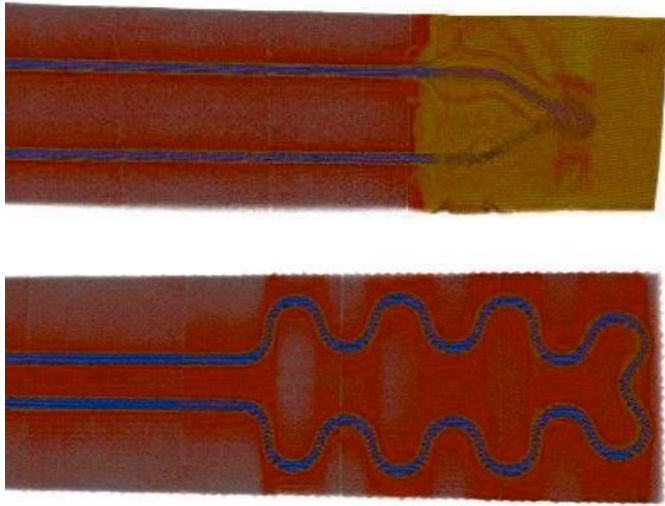
Fig. 1.2: View of the sensor with μCT Data
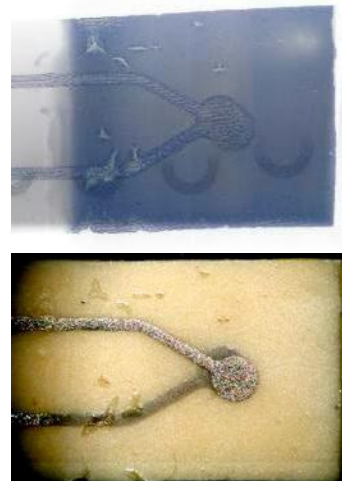
Fig. 1.3: Comparison of μCT view (top) to microscopic view (bottom)

Fig. 1.4: Cross section analysis with μCT Data

Main advantage of the μCT is the non destructive visualisation of cross sections (see Fig. 1.4). With this method it was recognized that the density in the substrate changes beneath the printed layers. This was not observed until now. It might also be possible to estimate the interaction between the materials. In the cross section view the influence of the function ceramics goes deeper than assumed before. The complete substrate is modified beneath the main structure of the sensor, where many layers are stacked. As next sensor design variations will have even more layers, this should be observed in more detailed examinations.

References

[1] Fasoulas S., Baumann R., Gläser M., Gritzner C., Hammer F., Heisig J., Kahle R., Kirschke T., Schmiel T., Völkel M.: Report No. ILR-RSN P 06-07
[2] O. Brunke, S. Odenbach, F. Beckmann (2004) Quantitative methods for the analysis of synchrotron-μCT datasets of metallic foams, European Physical Journal of Applied Physics, 2005. 29: p. 73-81. DOI: 10.1051/epjap: 2004203

Micro-Architecture of Scaffolds for Bone Tissue Engineering

Sarper Gürel[1] , Alessandra Braccini[2], Ivan Martin[2], and Bert Müller[1]

[1]*Biomaterials Science Center, University of Basel, c/o University Hospital, 4031 Basel, Switzerland*

[2]*Departments of Surgery and of Research, University Hospital Basel, 4031 Basel, Switzerland;*

Bone tissue engineering based on porous ceramic scaffolds and autologous cells is a promising approach for treating numerous clinical cases. Scaffold characteristics such as porosity, inter-connectivity and mechanical properties are crucial for optimizing the osteoinductivity of the generated constructs.

In this study, we characterized the micro-architecture of cylindrically shaped hydroxyapatite scaffolds with the diameter of 8 mm and the height of 4 mm. The scaffolds (Engipore; Fin-Ceramica Faenza, Faenza, Italy) have a total porosity of 83% ± 3%. Their size distribution can be described as the following: 22% are smaller than 100 μm; 32% between 100 and 200 μm; 40% between 200 and 500 μm and 6% larger than 500 μm [1]. Qualitatively, this can be seen in Figure 1. Therefore, these scaffolds are appropriate for cell seeding.

The opaque constructs are made visible by the use of synchrotron radiation-based micro computed tomography (SRμCT) in absorption contrast mode. These measurements with a duration of about 2 hours have been carried out at the beamline W 2 using the photon energy of 30 keV. The pixel length corresponded to 4.3 μm. The spatial resolution of 7.4 μm was determined by means of the modulated transfer function. The data were reconstructed by the filtered back projection algorithm taking into account 721 projections. This means that the sample was rotated between 0 and 180° in steps of 0.25°.

Figure 1 shows the 3D representation of the open porous scaffold in red color. It also contains the frontal, sagital, and axial cuts to give the reader a better impression of the pores with their almost perfectly spherical shape. The green color, which represents the embedding material, namely paraffin shows the degree of interconnectivity. Only a very few pores are partially filled. Even more seldom, a pore is totally dark, because the paraffin did not penetrated through. It is planned to quantify the interconnecting canals of the scaffolds by means of sophisticated computer vision tools including component labeling, growing region, dilatation procedures.

Using a perfusion bioreactor system previously developed for cell seeding of 3D scaffolds [2], it is possible to seed, expand, and differentiate bone marrow stromal cells directly in a 3D environment, bypassing the conventional process of monolayer expansion; following ectopic implantation in nude mice, the engineered constructs generated bone tissue more reproducibly, uniformly, and extensively than scaffolds loaded with cells expanded in monolayers [3, 4]. As a future work, the constructs generated and mechanically loaded in vitro will be morphologically characterized. In particular, we are going to use SRμCT to make the extracellular matrix visible, which is produced by the cells and in vitro deposited within the pore network of the ceramic. This challenging task has not yet been achieved.

The optimized scaffolds with interconnected pores, as visualized here, will be seeded with patient-derived cells avoiding undesired immune responses. These vital/avital composites are expected to be promising fillings for cavities, for instance, after tumor resection and trauma.
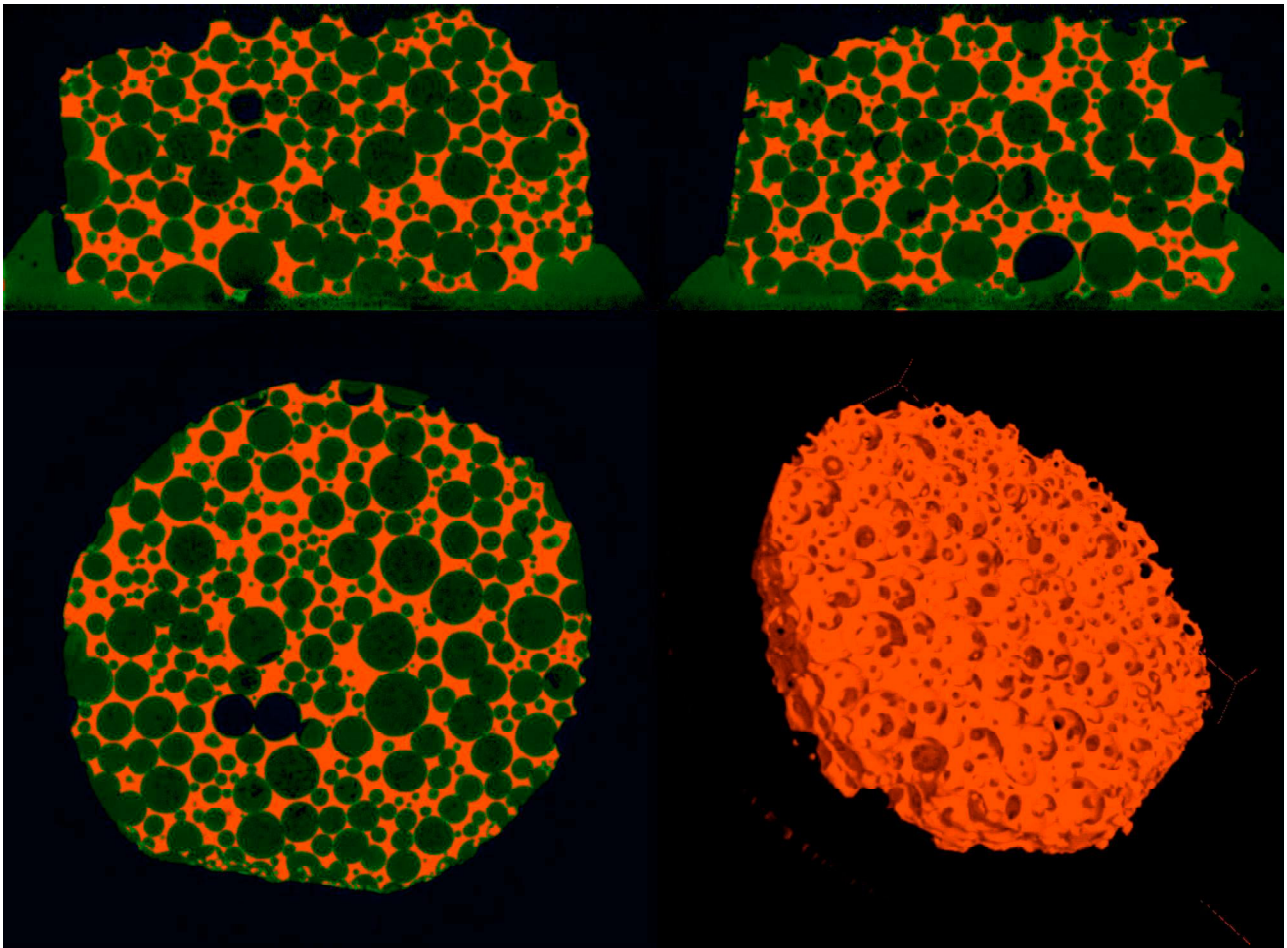
Figure 1: The 3D representation of hydroyapatite scaffold (red colored) shows the interconnected spherical pores together with frontal, sagital and axial cuts, respectively. The interconnectivity is demonstrated by the green color, which represents paraffin, where the scaffold have been embedded. Only a few pores are partially filled or not penetrated (see dark areas inside).

References

[1] www.finceramica.it

[2] D. Wendt, A. Marsano, M. Jakob, M. Heberer, I. Martin, Biotechnol. Bioeng. 84, 205 (2003)

[3] A. Braccini, D. Wendt, C. Jaquiery, M. Jakob, M. Heberer, L. Kenins, A. Wodnar-Filipowicz, R. Quarto, and I. Martin., Stem Cells. 23, 1066 (2005)

[4] B. Müller, M. Riedel, P. J. Thurner, Microsc. Microanal. 12, 97 (2006)

Microstructure and Orientation of Natural Fibres in Composites investigated by X-ray Microtomography

J. Müssig [1], G. Cescutti [1], D. Hegemann [2], M. Hossain [2], T. Donath [3], F. Beckmann [3]

[1] Faserinstitut Bremen e.V. – FIBRE –, Am Biologischen Garten 2, 29359 Bremen, Germany

[2] EMPA, Swiss Materials Science & Technology, Lerchenfeldstrasse 5, 9014 St. Gallen, Switzerland

[3] GKSS-Forschungszentrum, Max-Planck-Strasse 1, 21502 Geesthacht, Germany

The application of materials on the basis of renewable resources becomes particularly interesting. In terms of technical requirements natural fibres are excellently suited for the reinforcement of polymers. There are many possibilities to use natural fibres in technical applications like natural fibre composites or Medium Density Fibreboard (MDF) based on wood fibres [4]. The use of natural fibres for example in fibre-reinforced polymers requires fibres with very specific properties. Many controls of processed fibre products are necessary then to achieve high-quality fibres with the required properties. Scanning techniques are a very cost efficient and reliable method to carry out these controls. Fibre or bundle fineness improves the tensile properties of composites. Together with fibre length the fineness is a critical property for the quality of injection moulded parts. Fibre orientation is another important material property since it plays a key role for the improvement of the mechanical stability of fibre reinforced composites. Fibres isolated from a composite can be used to be image analysed e,g. with Fibreshape system. It determines the width distribution and the orientation of the fibres [3]. Natural fibres are known to undergo a considerable amount of thermal and mechanical degradations during melt mixing of natural fibres with thermoplastics such as polypropylene (PP). A possible method to measure degradation of fibres is to Soxhlet extract fibres and particles out of a PP matrix. An image analysis system can be used for monitoring the geometrical degradation of the extracted natural fibres. Length and width measurements can be realised on the raw and extracted fibres to describe the degradation process. The measured length to width ratios can used in micro-mechanical models to predict the stiffness properties of the injection moulded natural fibre reinforced samples [1]. For a better prediction it would be necessary to measure fibre geometry and orientation inside the composite. According to Walther et al. [4] wood fibre geometry and orientation was measurable in a MDF board using X-ray microtomography (µCT). For X-ray µCT the following materials were used:

- Sample A: Hemp fibres GDE-02 in a Epoxy thermoset resin
- Sample B: Hemp fibres GDE-02 in a Epoxy thermoset resin (ca. 15 % of the embedded hemp fibres were preliminarily sputtered with copper to improve the contrast)
- Sample C: Hard beech wood flour with PP homopolymer injection moulding type and maleic anhydride-polypropylene copolymer [1]
- Sample D: Hard beech wood flour with PP homopolymer injection moulding type [1]

A pilot-plant plasma reactor was used to metallize hemp fibres (Sample B) at Empa, St.Gallen, which is able to treat textiles semi-continuously with a maximum width of 65 cm. The metal deposition process was carried out with a pulsed DC magnetron sputtering (1 kW, 1 Pa). Cu atoms and cluster were ejected from a Cu target by the bombardment of high energy Ar ions and thus yielding Cu films on the fibres fixed on a rotable drum. The fibres were coated twice by turning them in order to deposit homogenous and uniform metal thin films. Thus, approx. 125 nm thick Cu coatings were obtained on the fibres. Using a recently developed fibre coating apparatus at Empa, St.Gallen an even more homogeneous metallization can be expected at a high through-put for future activities within this field.

X-ray µCT was performed on small samples of the natural fibre composites with a dimension of $2 \times 2 \times 5$ mm³ at beamline BW2 at HASYLAB. The synchrotron radiation X-ray µCT-equipment operated by the GKSS was used. The photon energy for the scans was set to 10 keV to match the low absorption of the fibres. Results of this observation are given in Figure 1.

631
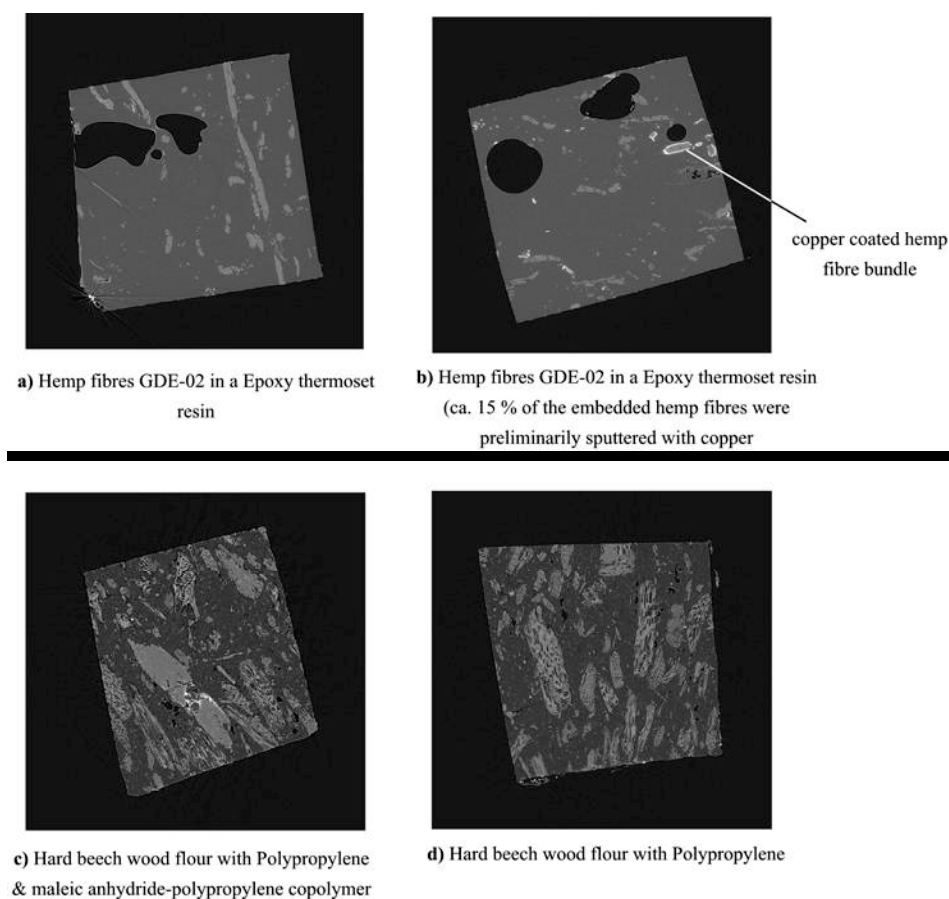
Figure 1: Cross sections (2.90 x 2.90 mm²) from the microtomography data of the natural fibre reinforced plastics with pixel edge length 1.888 µm and spatial resolution 2.96 µm.

The alignment and the distribution of the fibres in the sample are displayed in the cross sections shown in Figure 1. It is possible to determine important geometrical parameters, such as the shape of the fibres, the thickness of the cell walls, and the orientation (see. Figure 1c / 1d). With µCT equipment and the spatial resolution of 2 µm it will be possible to observe element sizes, aspect ratios and orientations. With a comparison of both PP/Wood samples a detailed analysis of coupling agent effects on fibre size and fibrillation will be done in 2007. The nanoporous coating improves the contrast of the fibres noticeably (Figure 1b). Further research on the microstructure of natural fibre composites especially with the view on fibre orientation in the matrix will be done in 2007.

References

[1] **Cescutti, G. / Müssig, J. / Specht, K. / Bledzki, A.K. 2006:** *Injection Moulded Natural Fibre Reinforced PP-Determination of Fibre Degradation by Using Image Analysis and Prediction of the Mechanical Composites Properties.* In: Universität Gh Kassel, Institut für Werkstofftechnik, Kunststoff- und Recyclingtechnik (Hrsg. und Veranst.): 6th Global Wood and Natural Fibre Symposium, Kassel, Germany: 2006, S. B9-1 bis B9-11

[2] **Hegemann, D. / Hossain, M.M. and Balazs, D.J. 2006:** *Nanostructured Plasma Coatings to Obtain Multifunctional Textile Surfaces.* In: Prog. Org. Coat. 2006, doi:10.1016/j.porgcoat.2006.08.027

[3] **Müssig, J. / Schmid, H.G. 2004:** *Quality Control of Fibers along the Value Added Chain by Using Scanning Technique - from Fibers to the Final Product -.* In: Microscopy and Microanalysis, Volume 10, Supplement 2, 2004) (ISSN 1431-9276 .- (2004)10+2;1-U), p. 1332CD - 1333CD

[4] **Walther, T. / Donath, T. / Terzic, K. / Meine H. / Thömen H. and Beckmann F. 2006:** *Microstructural Investigations on Natural Fiber Composites and Medium Density Fiberboard (MDF) .* In: HASYLAB Annual Report 2006, p. 455 – 456.

Preparation for characterisation of natural gas hydrate reservoirs by high energy synchrotron radiation

S.A. Klapp, H. Klein[1], C.E. Tommaseo[1], L. Raue[1], W.F. Kuhs[1] and T. Lippmann[2]

Research Center Ocean Margins, University of Bremen, Klagenfurter Strasse, D-26334 Bremen
[1]Dept. of Crystallography, Geoscience Center at the University of Göttingen, Goldschmidtstr.t 1, D-37077 Göttingen
[2]GKSS Research Center, Max-Planck-Str.1, D-21502 Geesthacht

Natural Gas Hydrate reservoirs in the Gulf of Mexico and in the Black Sea have been characterised by Synchrotron radiation at the new materials beam line HARWI II.

Eight natural samples were investigated in September 2006. Although at that time, only phase fractions could be measured, the results strongly indicate that further attention needs to be paid on those samples. Unfortunately, the instrumentation at the HARWI II did not allow moving detector measurements, otherwise already at that time crystal sizes and grain shapes would have been measured [1][2][3]. Grain Size information are an important tool in characterising gas hydrate reservoirs. Thus determining the age of naturally occurring gas hydrates should be feasible by statistically sufficient grain size investigations. Dating gas hydrates is not possible by any other mean and is of great importance for geosciences. Appropriate grain size or shape identification is difficult and often impossible to obtain by using light or electron microscopy.
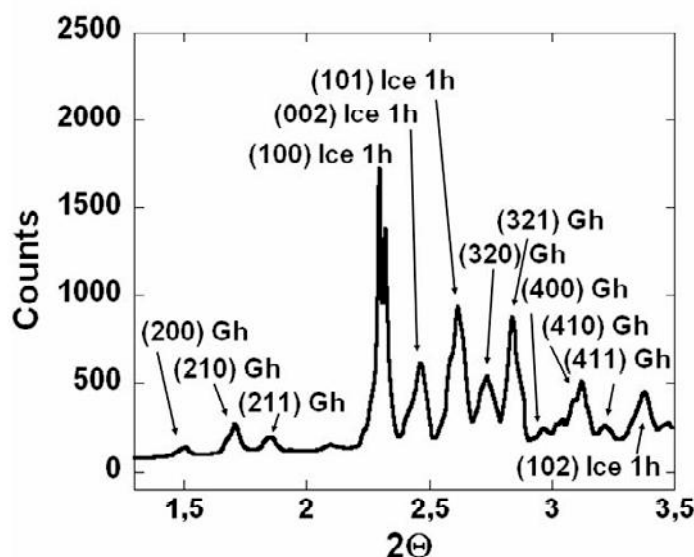
Fig.1: Diffraction diagram of a natural gas hydrate

Recent synchrotron measurements at HARWI II in September 2006 revealed samples both from the Black Sea and the Gulf of Mexico feature structure I (and structure II?) gas hydrate and ice 1h [4][5]. These interesting findings suggest a more complex environment at the sites of sampling than previously anticipated. Our results as well as gas analysis and electron microscopy of the samples are important news for the scientific community. However, the observations need further investigation.

Also, judging from the relative peak intensities in the diffraction diagram (fig. 1) one could assume that the gas hydrate crystals might be textured, which is an issue well worth for further investigation. The two-dimensional diffraction image (fig. 2) shows, however, that the texture plays only a very small role. Apparently the large grain sizes dominate the diffraction diagram.
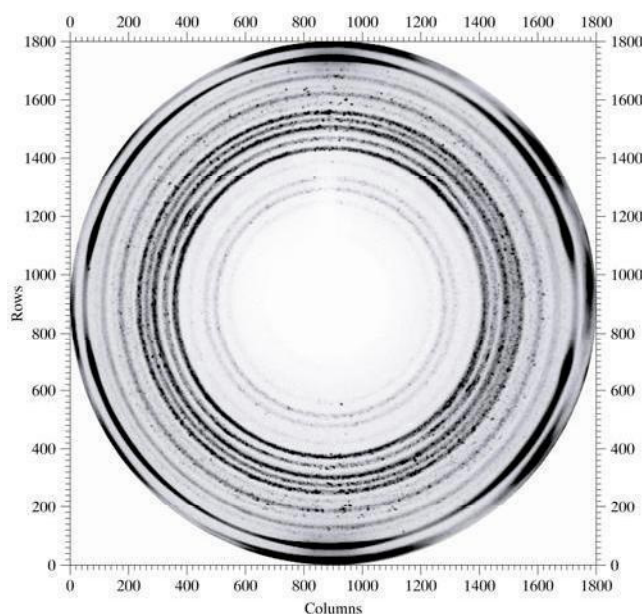
Fig.2: Two-dimensional diffraction image of the gas hydrate in fig.1. Large spots on the Debye-Scherrer-rings originate from large crystallites.

Moreover, gas hydrate crystals have been observed with crystal sizes ranging from 300 μm to 600 μm in natural samples [6]. However, these investigation were merely a test of applying the Moving area detector method [1][2] on gas hydrate samples, even though samples from different geological sites were investigated.

References

[1] L. Wcislak, H. Klein, H.J. Bunge, U. Garbe, T. Tschentscher and J.R. Schneider. Texture Analysis with High-Energy Synchrotron Radiation. J. Appl. Cryst. **35** (2002) 82-95

[2] H.J. Bunge, L. Wcislak, H. Klein, U. Garbe, R. Nowak and J.R. Schneider. Orientation Imaging of Crystals in Polycrystalline Materials. Adv. Eng. Mater. **4** (2002) 300-305

[3] H. Klein, A. Preusser, H.J. Bunge and L. Raue. Recrystallization Texture and Microstructure in Ni and AlMg1Mn1 determined with High-Energy Synchrotron Radiation; Proc. of 2. Int. Conf. on Recrystallization and Grain Growth. Material Science Forum, Vols. 467-470 (2004) 1379-1384

[4] A.Klapproth, E. Goreshnik, D. K. Staykova, H. Klein, and W. F. Kuhs. Structural studies of gas hydrates Can. J. Phys. **81** (2003), 503-518.

[5] D.K.Staykova, W. F. Kuhs, A. N. Salamatin, and T. Hansen. Formation of porous gas hydrates from ice powders: Diffraction experiments and multi-stage model. J. Phys. Chem. B **107** (2003) 10299-10311.

[6] S.A. Klapp, H.Klein and W.F. Kuhs. First Gas Hydrate Crystallite Size Determination using High-Energy Synchrotron Radiation. GRL (submitted).

Removing the guess work from material flow and deformation mechanics associated with the FSW of Aluminium and its alloys through application of micro-computer tomography and dedicated metallurgical techniques

R. Zettler, J. F. dos Santos, T. Donath, J. Herzen, F. Beckmann and

D. Lohwasser[1]

GKSS-Forschungszentrum Geesthacht, Max-Planck-Straße 1, 21502 Geesthacht, Germany

[1]Airbus Deutschland GmbH, 28199 Bremen, Germany

Friction Stir Welding (FSW) is a revolutionary solid state joining technology first patented by The Welding Institute (TWI) of Cambridge, England in 1991 [1]. Over the last decade the FSW process has witnessed an explosive growth in research and industrial application. Often quoted advantages include good strength and ductility along with minimisation of residual stress and distortion. These qualities, particularly when joining aluminium and its alloys are attributed to the solid state nature of the joining process. Thus FSW avoids the necessity of filler wire or shielding gas, and since there is no bulk melting of the parent material, eliminates problems such as hot cracking and or porosity found to occur when fusion welding aluminium and its alloys [2].

Although FSW can list numerous applications across diverse industrial sectors, the technology still cannot be considered a main stream industrial process. This is not because of productivity or quality issues associated with the join, rather because the process is still very much experimentally and not theoretically driven. For this reason FSW has largely remained in the hands of major automotive, ship building and aerospace cooporations capable of financing research intensive and costly process parameter studies. Subsequently, simulation i.e. modelling and visualisation of the material flow/deformation mechanics in relation to processing and geometric parameters (tool and joint geometry) as well as the search for an empirical or workshop formula, which it is hoped can provide the link between parent material properties and suitable process parameters, has aroused significant interest within the scientific community. To date no process model or empirical formula has demonstrated an ability to successfully predict weld parameters for any given material/tool combination, or resultant join properties, or more importantly when onset of flaw formation such as non-bonding and volumetric defects can be anticipated to occur.

The current study builds on work commenced in 2004. Here the global objective has been to develop knowledge that will assist in confident industrialisation of the FSW process, particularly with regard to the fabrication and also repair of aerospace (aircraft) structures. Work has been conducted by the GKSS Forschungszentrum GmbH, in Geesthacht and at the HASYLAB beamline W2, in Hamburg using a variety of techniques including the production of the friction stir welds and their characterisation i.e.metallography, mechanical testing and micro-tomography.

Macrographs, micro-hardness, strain and stress measurements are the common probes for microstructure investigation. All of them however only give selected local information or integrated information of the full sample volume. The first simultaneous depth resolved phase and strain mapping on dissimilar friction stir welded aluminium alloys has been performed by Martins et.al [3] using X-ray synchrotron radiation. In the current investigation X-ray computed microtomography (μCT) has been applied to study the bulk material flow (3-D mapping) within the stir zone of 4mm thick friction stir welded 2024-T351, 6013-T6 and an AlMgSc alloy. Here two contrast giving metallic powders; Cu and Ti-powders (particle size 20-63μm) have been implanted into the workpieces and subsequently friction stir welded such that the welding pin is abruptly stopped in the region containing marker material, Figure 1.
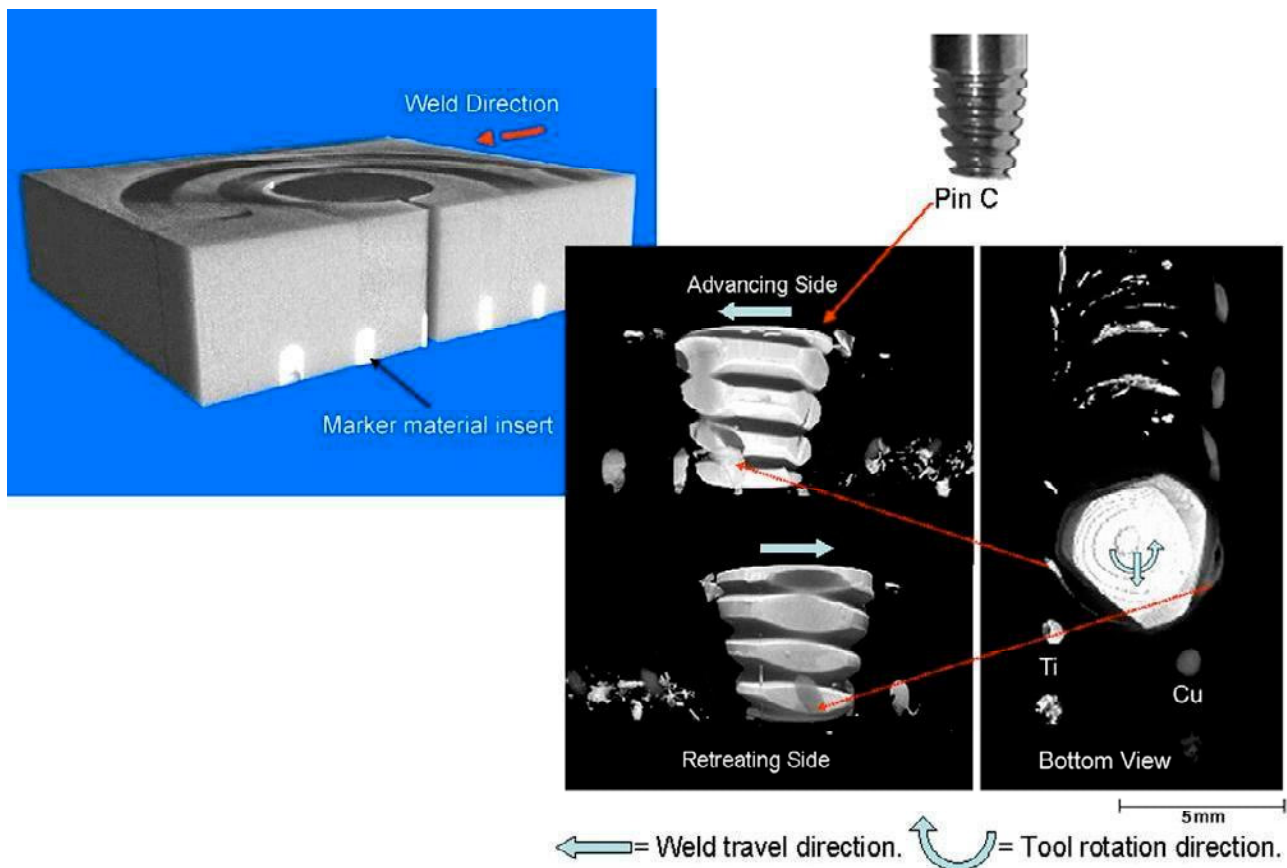
Figure 1: Simultaneous marker material displacement (Cu and Ti) around the frozen in workpiece FSW tool (Pin C – conical and threaded with three equally spaced flats along entire thread length). On the left a volume rendering showing the Aluminium sample (5 mm thickness) and the introduced marker material. On the right the Aluminium is set transparent to reveal the 3D distribution of the marker material around the pin. The tomographical scans were performed at beamline W2 using a photon energy of about 64 keV.

The knowledge gained through investigation of material flow/deformation, microstructure and mechanical properties of the friction stir welded aluminium alloys has enabled answers to be obtained for the following questions:

1. Can all alloys (aluminium) be friction stir welded using a single tool combination?
2. If not, which tool is best suited for a specific alloy and why?
3. Can all alloys be successfully welded using a single set of welding parameters?
4. If not, which parameter is best suited for each alloy and why?

By answering the above four questions this has further allowed for the formulation of an empirical or workshop formula giving guidance as to selection of process and geometric parameters for a given parent material without the need for numerous and costly welding trials. Hence a relationship has been established between base material properties, the selection of welding parameters and suitable tooling for the investigated friction stir welded aluminium alloys.

References

[1] Thomas WM, Nicholas ED, Needham JC, Church MG, Templesmith P, Dawes CJ: International Patent Application No. PCT/GB92/02203 and GB Patent Application No. 9125978.9, (1991)
[2] Katayama S, Matsunawa A, Welding Int. 12, 44-59 (1998)
[3] Martins RV and Honkimäki V, Texture and Microstructures Vol. 35 No. 3/4, 145-152, (2003)

Residual stress analyses in laser beam welded butt joints made from sheets of Al alloy AA6056

R.V. Martins, T. Fischer, A. Schreyer

GKSS-Research Centre, Max-Planck-Str. 1, 21502 Geesthacht, Germany

Advanced welding techniques and the development of new materials play an important role in the pursuit of weight and cost reduction in civil aircraft industries. Examples are the development of new Aluminum alloys such as AA6065 and the Laser Beam Welding (LBW) technology. Advantages of the LBW technology as compared to standard fusion welding are the low material distortion and the high processing speed. However, the welding process leads to residual stresses in the material which could be detrimental to the lifetime and reliability of the component. High energy synchrotron radiation is a suitable probe to investigate non-destructively the stress state by diffraction with an appropriate spatial resolution.

The two samples investigated were CO_2 laser welded butt joints of 3 mm and 6 mm thick sheets respectively. The sheets were made from Aluminum alloy AA6065 in T6 condition. A filler wire made from AlSi12 was used to improve the weld seam properties [1]. Metallographical investigations by optical microscopy showed the expected pancake shaped grains in the parent material with a diameter of up to 300 μm and a thickness of about 60 μm. In the weld seam area a dendritic microstructure was reported by [2]. A Cu powder directly attached to the sample was used as a reference to determine the diffraction peak shifts for the strain measurements. For the measurements of the strain free lattice parameter d_0 a thin slice cut out from the sample was used.

The measurements were carried out at the beamline HARWI II (W2). The monochromatic beam had an energy of 80 keV and a size on the sample of 6 x 0.2 mm^2 which provided a sufficient spatial resolution transverse to the weld seam. The large beamsize parallel to the weld assured better grain statistics. The measurement was done in transmission geometry with the incoming beam parallel to the surface normal. Fractions of Debye-Scherrer rings were recorded with a 30 x 30 cm^2 large gas filled multi-wire area detector placed 7.6 m behind the sample, hereby providing the required high angular sensitivity.
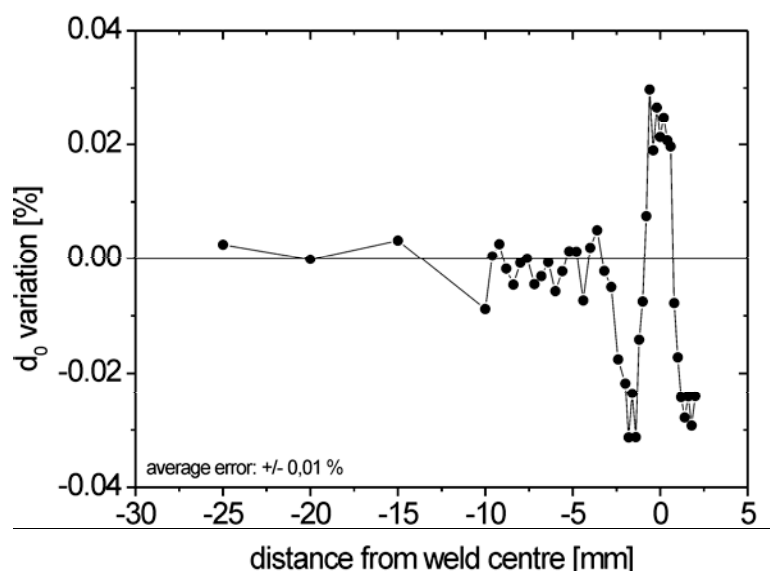
Figure 1: Variation of the strain free lattice parameter d_0 for the Al 311 reflection as a function of the distance from the weld line.

The results shown here relate to the 3 mm thick sample. Figure 1 shows the variation of the strain free lattice parameter as a function of the distance from the weld centre. The largest variations of ±0.03% occur in the weld seam. However, they are so small that their impact on the measured strain is minor. In figure 2 the residual stress distributions are presented for the longitudinal (parallel to the weld) and the transverse direction. For the calculations of the stress the assumptions of a biaxial stress state and an isotropic elastic behaviour were made. Close to the weld seam, at 2.6 mm, high tensile stresses of up to 210 MPa were observed. This corresponds 78% of the materials' yield strength. The present measurements reveal features like the decrease below 50 MPa and the dips at ±10 mm which could not be resolved during previous measurements using neutron diffraction [3]. The transverse stress component exhibits strong oscillations between +20 MPa and -70 MPa. This is attributed to the coarse grain structure which seems to have a stronger impact on the measurement in the vertical scattering direction due to the beam geometry and divergence. Optimisations of the beam parameters will be made in future measurements.
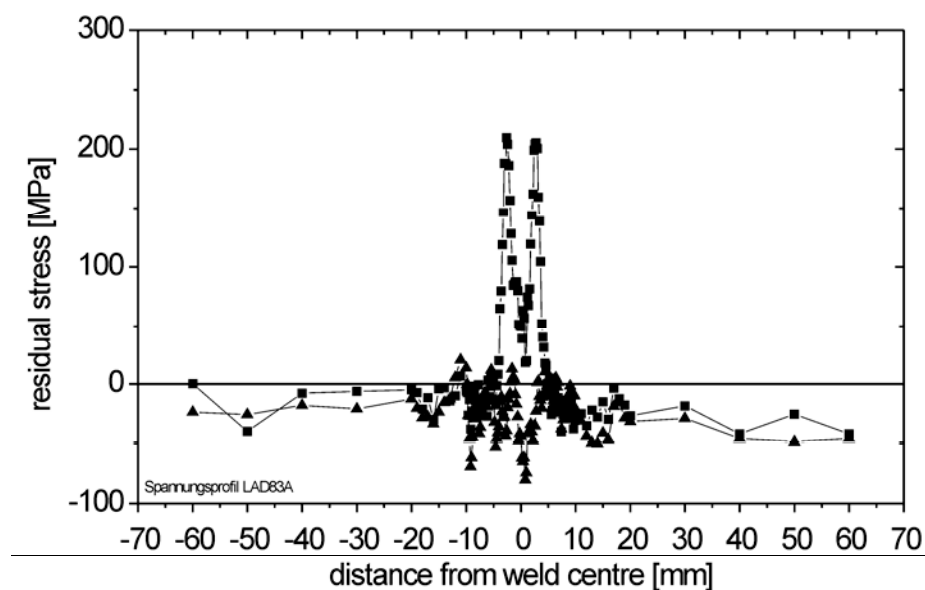
Figure 2: Residual stress distribution in the laser welded Al-sheets in transverse (▲) and longitudinal (■) direction. Calculated from the line shifts of the Al 311 reflection and corrected with the measured d_0 values. Average error: ±20 MPa.

The authors acknowledge P. Staron and W.V. Vaidya for the provision of the samples.

References

[1] R. Braun, Mater. Sci Eng. A426, 250-262 (2006)

[2] D. Fabrègue, A. Deschamps, M. Suery, Mat. Sci. Tech. 21, 1329-1336 (2005)

[3] P. Staron, W.V. Vaidya, M. Koçak, J. Homeyer, J. Hackius, Mat. Sci. Forum Vol. 524-525,. 413-418 (2006)

SRµCT, a useful technique to localize a new type of titanium implant in a specimen of a middle ear

M. Ney[1], M. Neudert[1], T. Beleites[1], Anne Kluge[1], F. Beckmann[2], T. Douglas[3], R. Bernhardt[3], D. Scharnweber[3] und T. Zahnert[1]

[1]Dept. for Otorhinolaryngology, Dresden University, Fetscherstraße 74, 01307 Dresden, Germany
[2]GKSS Forschungszentrum Geesthacht, Institut für Materialforschung, c/o GKSS am DESY, Notkestrasse 85, D-22607 Hamburg, Germany
[3]TU Dresden, Institut für Werkstoffwissenschaft, Max Bergmann Center of Biomaterials, Budapester Str. 27, D-01069 Dresden, Germany

Inflammation processes as well as injuries of the middle ear can be associated with destruction and interruption of the ossicle chain. The consequence is a loss of acoustic transmission that results in hearing loss. To improve hearing there are various middle ear prostheses available to be implanted to bridge the gap in the chain.

Common prostheses are placed into the gap without additional fixation and therefore tend to dislocate which can result in renewed hearing loss. But there is no option to fix them in the way conventional osteosynthesis are fixed, e.g. with screws.

In addition, the development of implants for use in reconstructive middle ear surgery faces numerous problems. Firstly, space in the human middle ear is extremely limited. Secondly implants need to fulfil special acoustic requirements.

The idea of this BMBF-aided research project was to design a prosthesis from titanium according to principles of bio-surface engineering equipped with a biofunctional surface and coated with different growth factors which was able to initiate cell movement and adhesion. The aim was to achieve osseous integration of the implant to restore or improve hearing.

25 sheep underwent middle ear surgery in which the different implants were placed onto the stapes footplate. After a follow-up time of three months animals were sacrificed and the middle ears with the implants inside were explanted for histological examination.
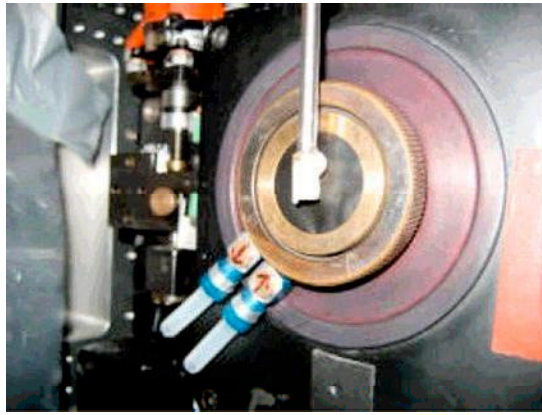
Figure 1: positioning of the specimen in the SRμCT-device

Due to the extremely tiny measurements of the implants used (350 x 550 μm) it was even more difficult to localize the implant in the specimen than expected. As SRμCT is a non-destructive technique, we decided to examine all our specimens using this technique before performing conventional histology, which is a very important step.

Apart from the exact localization of the implant in relation to the stapes footplate we expect to gain additional information on the osteoconductive/osteoinductive potential of the implant surfaces. For that, μCT-results are currently being compared with findings from histology and in particular polychrome labelling which will give additional information on formation of new bone.

References:

[1]   Neudert, M., Simulation of Interacting Forces Between Prostheses and Stapes
        Footplate in Case of Osseointegration. Submitted to JARO 11/06
[2]   Schwager, K., [Scanning electron microscopy findings in titanium middle ear
        prostheses]. Laryngorhinootologie, 2000. **79**(12): p. 762-6
[3]   Turner, A.S., The sheep as a model for osteoporosis in humans. Vet J, 2002. **163**(3): p.
        232-9

Synchrotron radiation-based micro computed tomography for the analysis of 3D-printed and collagen-coated scaffolds for bone replacement

Stephan Irsen[1], Barbara Leukers[1], Hermann Seitz[1], Stefan Schwanitz[1], Leon Olde Damink[2], Felix Beckmann[3], Julia Herzen[3] and Bert Müller[4]

[1]caesar research center, Ludwig-Erhard-Allee 2, 53175 Bonn, Germany
[2]Matricel GmbH, Kaiserstrasse 100, 52134 Herzogenrath, Germany
[3]GKSS-Research Center Geesthacht, Max-Planck-Straße 1, 21502 Geesthacht, Germany
[4]Biomaterials Science Center, University of Basel, c/o University Hospital, 4031 Basel, Switzerland

3D printing is a powerful technology for the fabrication of scaffolds, to be used in tissue engineering, directly from computer data [1]. The key advantage of such a rapid prototyping process is the computer-based design of the scaffold's outer shape and internal structure prior to the fabrication. The data can be artificially created using computer simulation or CAD-software. Alternatively, the data for the initial scaffold can be derived from biological structures for example by means of CT-scans. For the fabrication of bone grafts, hydroxyapatite (HA) is known to be well suited because of its chemical similarity to the mineral part of the human bone. Beside chemical aspects, which are often termed biocompatibility, the porosity is of key importance. Especially an internal open porosity with pore sizes between 100 and 500 µm is helpful for initiating vascularization in the scaffolds after implantation. Synchrotron radiation-based micro computed tomography (SRµCT) was successfully used for the image-based porosity analysis of 3D-printed bone grafts [2]. Another important property of 3D-printed bone grafts is their mechanical stability. Polymer coating seems to be a promising path to enhance the mechanical stability introducing elastic components into the brittle ceramic scaffold. Using natural materials such as collagen for coating, the osteointegration of the scaffold is significantly improved [3]. The aim of the present study was the non-destructive evaluation of 3D-printed and collagen-coated bone grafts, whereby the homogeneity of the collagen coating has been of special interest.

An experimental 3D printer was used for the fabrication of the bone grafts [4]. Hydroxyapatite granules and water-based binder solutions were used as building materials. The scaffolds were fabricated with the spatial resolution of about 100 dpi and a slice thickness of 220 µm. The green bodies were sintered after 3D printing to enhance the mechanical stability. The authors acknowledge the partners at Matricel GmbH, who coated the sintered scaffolds with the mixture of collagen type I and elastin [5]. The samples were directly glued on the stainless steel holder to be fixed on the high-precision rotation stage of the SRµCT experiment. The measurements were carried out at the beamline W 2 using the recently established set-up for absorption contrast tomography. The photon energy was selected to 30 keV. Projections of 1536 x 1024 pixels were recorded in steps of 0.25° between 0 and 180°. The filtered back-projection algorithm provided the tomogram. The applied optical magnification of 2.4 led to the pixel length of 3.7 µm. The spatial resolution, measured by the modulated transfer function [6] corresponds to 6.0 µm.

Figure 1 shows the histogram of the tomography data with a volume of (5.7 x 5.7 x 3.8) mm³. The two peaks representing air and material can be easily separated. Using three Gaussians, the data can be perfectly fitted. The three Gaussians are associated with air, coating, and ceramics. The slice below show is coloured according to the fitted histogram using the crossing points: air – black, coating – red, and HA – white. The collagen coating is homogenously distributed on the surface of the scaffold. It also fills the open micro-pores of the HA, while the macro-pores remain open. The influence of this coating on the mechanical and biological behaviour of the scaffolds will be the topic of further publications. Please note that optical images just yield the outer shape of the scaffold. The tomography data enable us to virtually cut the scaffold in any desired direction as demonstrated by the 3D representation. Here, the air is made transparent, the coating is red-coloured, and the HA is given in white, again according to the histogram. This example elucidates the power of SRµCT in the analysis of opaque composite scaffolds with complex morphologies on different length scales.
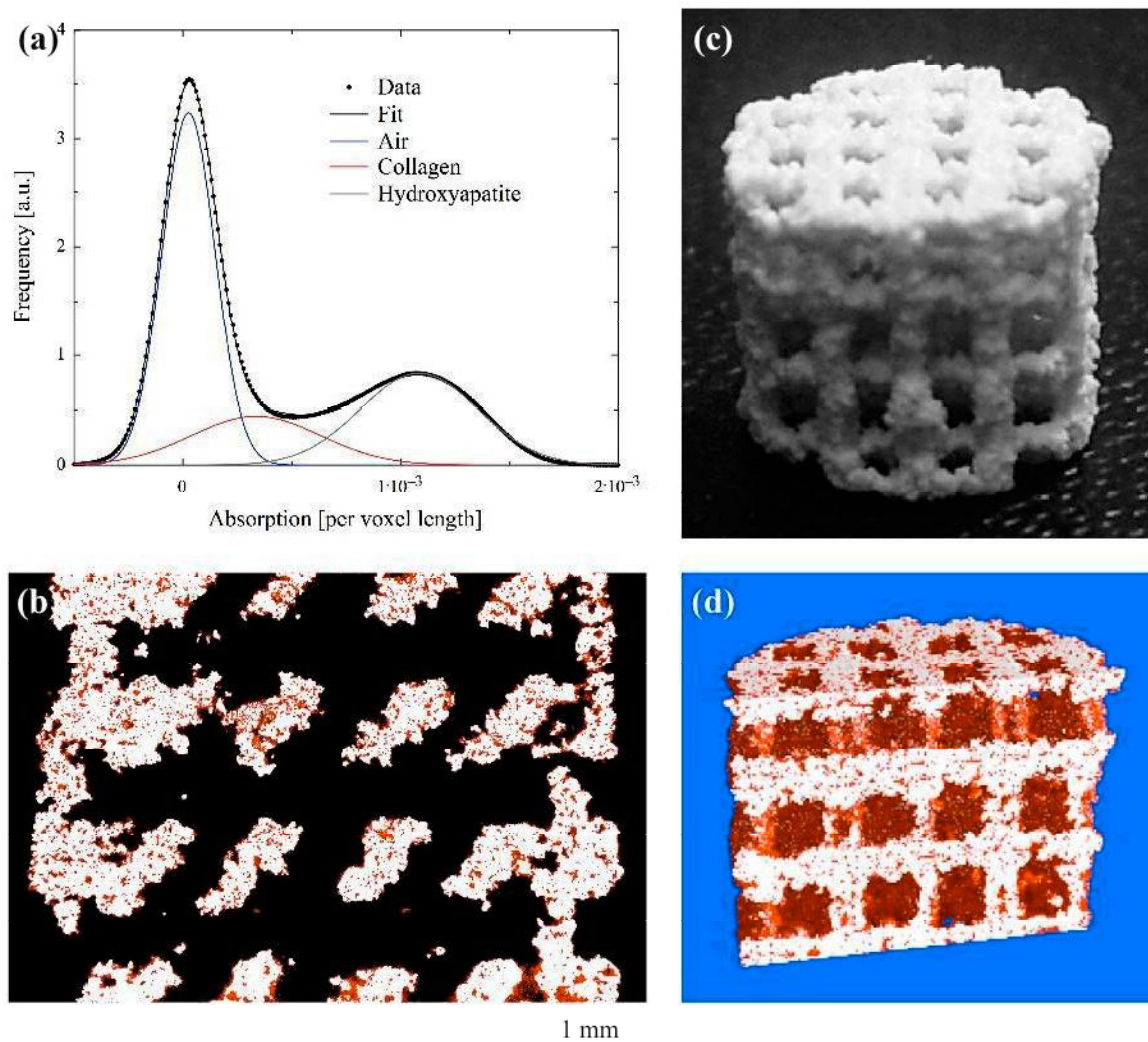
Figure 1: *(a)* The histogram of the acquired tomography data can be perfectly fitted with 3 Gaussians associated with air (blue coloured), collagen (red coloured), and hydroxyapatite – HA (grey coloured). *(b)* The tomographic slice parallel to the rotation axis is coloured according to the histogram using the crossing points of the Gaussians. The collagen covers the HA surface and fills the micro-pores. The larger pores, however, are open. The optical images just can represent the surface of the opaque scaffold *(c)*, whereby the tomography data allow virtually cutting the scaffold in any desired direction, as shown in *(d)*.

References

[1] C.X.F. Lam, X.M. Mo, S.H. Teoh, D.W. Hutmacher, Mater. Sci. Engin. C 20, 49 (2002)

[2] S. H. Irsen, B. Leukers, B. Bruckschen, C. Tille, F. Beckmann, B. Müller and H. Seitz, Proc. SPIE 6318, 631809 (2006)

[3] H. Schliephake, D. Scharnweber, M. Dard, A. Sewing, A. Aref, S. Roessler, J. Biomed. Mater. Res. 73B, 8 (2005)

[4] H. Seitz, W. Rieder, S. Irsen, B. Leukers, C. Tille., J. Biomed. Mater. Res. 74B, 782 (2005)

[5] www.matricel.com

[6] B. Müller, P. Thurner, F. Beckmann, T. Weitkamp, C. Rau, R. Bernhardt, E. Karamuk, L. Eckert, J. Brandt, S. Buchloh, E. Wintermantel, D. Scharnweber, H. Worch, Proc. SPIE 4503, 178 (2001)

Validation of Diffusion Processes by μCT of Marker Material in new Friction based Hybrid Friction Diffusion Bonding (HFDB) Process

A. Roos, J.F. dos Santos, T. Donath, J. Herzen and F. Beckmann

GKSS-Forschungszentrum Geesthacht, Max-Planck-Straße 1, 21502 Geesthacht, Germany

Hybrid Friction Diffusion Bonding (HFDB) was invented and is patent pending by GKSS in 2006 [1]. The HFDB process is a friction based process whereas the underlaying bonding process is diffusion related. The HFDB process essentially relies on frictional heating, axial pressure and thermomechanically recristallised fine grain boundary diffusion. The rotating non consumable HFDB tool touches the surface of the friction partner under axial pressure until the friction partner is heated and plastified. The tool is then traversed along the area to be joined. The workpieces can be either joined in overlap or butt joint configuration. Direction of translating the HFDB tool on top of the underlying workpiece can be selected without restraint. The HFDB process is best suited for connecting metal foils or for welding metal foils on top of structures. Currently metal foils of 0.3mm thickness and less have been welded using HFDB.

A schematic of the HFDB process can be found in Figure 1.
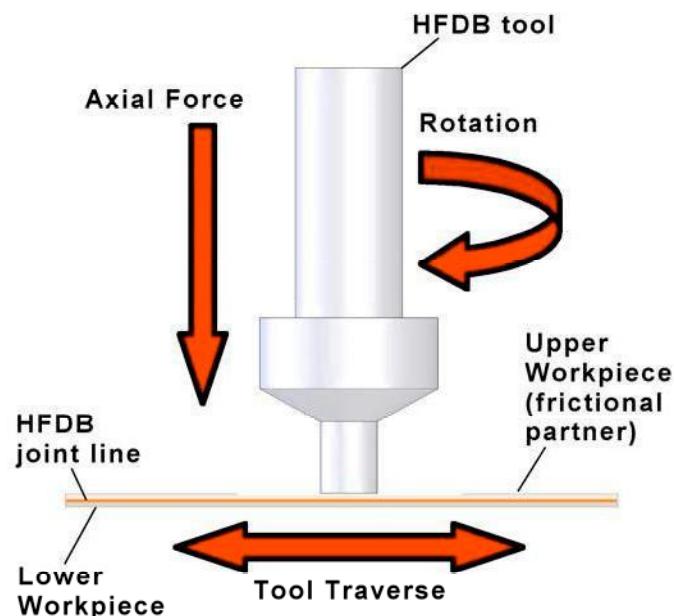
Figure 1: Schematic of HFDB process.

The HFDB tool in conjunction with the processing parameters; axial load or downforce, rotation and travel speed provide the necessary energy input to thermally soften the underlying workpiece material. The HFDB tool consists in general of the shoulder. The shoulder of the HFDB tool produces frictional heat and pressure as well as helps to keep the plastified material in the weld area from being expulsed out of the immediate weld zone. The HFDB tool induces a fine grain in the underlying workpieces through thermomechanically plastic deformation. Grain boundary dominated diffusion through the increased number of grain boundaries of the fine grains leads to a higher diffusion coefficient and therefore to higher diffusion speeds at a given temperature. As a result the diffusion partners can be joined at lower temperatures as for example with conventional diffusion bonding (DB).

A schematic of the HFDB tool can be found in Figure 2.

Figure 2: Schematic of HFDB tool with engraved shoulder.

HFDB alumina welds have shown recristallised fine grain in both workpieces. The weld zone of these welds could not be easily distinguished by common metallographic procedures. To verify the joining mechanism is diffusion related and not dependend on macroscopic mixing of the material, marker material has been introduced into the workpieces. After welding the distribution of the marker material over the joint line has been investigated by µCT technique.

A schematic of the marker material distribution can be found in Figure 3.
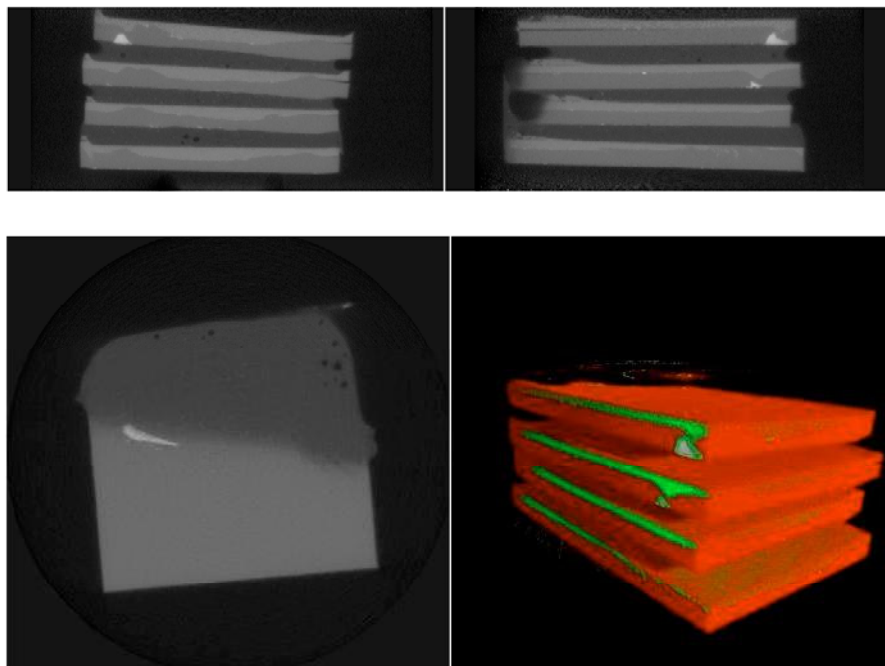
Figure 3: Schematic of marker material distribution using µCT technique;
upper left: front view; upper right: side view; lower left: top view; lower right: 3D view. Each sheet has a thickness of about 1 mm and a size of about 10 x 10 mm². The µCT experiment was performed at beamline W2 (HARWI 2) using a photon energy of about 64 keV.

It can be seen that the marker material is not vertically distributed between the work pieces due to macroscopic mixing. After the initial plastic deformation of the marker material filled holes nearly no further vertical movement of the marker material occurs during the HFDB process. This reinforces the assumption that HFDB of the alumina alloys on hand is diffusion related.

References

[1] A. Roos, J.F. dos Santos, GKSS Patent Application DE 102005045954.4

X-Ray Tomography of Silica in Rubber

K. Nusser[1]*, T. Sonnleitner*[1]*, F. Beckmann*[2]*, G. J. Schneider*[1] *and D. Göritz*[1]

[1] *Institute of Physics, University of Regensburg, 93040 Regensburg (Germany)*
[2] *GKSS Research Center Geesthacht, Max-Planck-Str. 1, 21502 Geesthacht (Germany)*

Silicas are technically important fillers for elastomers with respect to several applications. In such a filler-rubber system the mechanical properties strongly depend on the kind and the concentration of the filler [1, 2, 3]. Despite being cruciable for the adjustment of high performance materials, the exact correlation between the morphology of the filler and the related reinforcement of the material is still unknown.

Up-to-date constitutive models assume that isotropic silica primary particles form fractal clusters, which work as a basic unit for larger cluster structures. These models have been investigated in several scattering experiments [4]. From theory the process of clustering can be infinitely extended. Hence, a hierarchical structure ranging from a few nm up to some mm is generated, which is in general modelled by the mathematical framework of fractals.

In general, on the one hand by means of scattering experiments only a minor part of the hierarchical structure can be investigated, namely objects smaller than $1\,\mu$m. Thus, there is no evidence for the assumptions needed in the constitutive models.

On the other hand microscopic experiments are limited to two dimensional slices of a sample. Thus, the contribution of X-ray computer tomograph experiments of Silicas in rubbers may help to find information on the real structure of silicas in elastomers, and thus to gain new insight into modelling the reinforcement effect.

The experiments were performed using beamline BW2 of the DORIS III storage ring at the synchrotron radiation facility HASYLAB/DESY in Hamburg, Germany. The measurements were carried out at a fixed energy of 9 keV, corresponding to a wave-length of $\lambda = 0.138$ nm. The transmitted intensity was recorded with a two dimensional CCD-detector (pixel size $9\,x\,9\,\mu$m^2, number of pixels 1536 x 1024) [5]. The circular samples were rotated in steps of $0.25°$ from $0°$ to $180°$ to get the transmission pictures needed for a three dimensional reconstruction of the sample in the tomograph. A spatial resolution of less than $3\,\mu$m was obtained. The investigated materials included the elastomer Natural Rubber (NR), filled with various concentrations of silica. Six rubber discs of diameter 3 mm and height 1.2 mm were stuck to each other and attached to the sample holder.

Fig. 1 shows the set up of the samples (left) and a volume rendering of the disc stack (right), where the rubber part is transparent and silica is in white color (high absorption). From bottom to top the loading of silica increases from 2 to 20 vol-%. This fact can be confirmed by the tomographic pictures. Moreover, the dispersion of silica on the accessible length scale is very well visible. The distribution of clusters is quite homogenous. Smaller length scales, however, are unreachable. Consequently a hierarchical structure is not visible.

In summary, the dispersion of silica in elastomers was examined by X-ray tomography for various loadings of silica. For the first time the three dimensional dispersion of silica at μm length scale can be analyzed and hence one gains new insight into material dependent parameters.
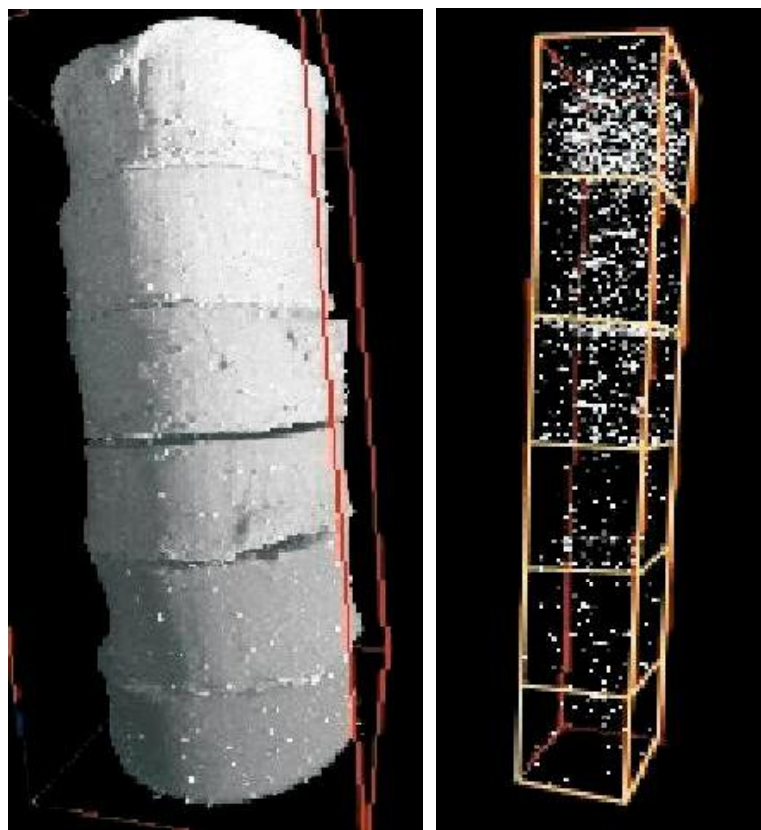
Figure 1: Left: Sample stack of 6 NR discs, filled with different concentrations of silica (from bottom to top: 2, 5, 9, 13, 16, 20 vol-%). A volume rendering of the total reconstructed volume is shown. Right: Volume rendering of the same sample stack with setting the rubber part transparent. Visible are silica clusters in white color.

References

[1] D. Göritz, J. Böhm, In: "Constitutive Models for Rubber II", D. Besdo, J. Ihlemann, R. H. Schuster (Eds.), Balkema (2001).

[2] D. Göritz, G. J. Schneider, Reinforcement with precipitated silica, Kautschuk-Herbst-Kolloquium, Hannover (2004).

[3] P. Maier, D. Göritz, Kautsch. Gummi Kunstst. 49, 18 (1996)

[4] D. W. Schäfer et al., J. Appl. Cryst. 33, 587 - 591 (2000)

[5] F. Beckmann, Microtomography as a User Experiment at Beamlines BW2 and BW5 at HASYLAB, HASYLAB Annual Report (2000)

3D characterization of beta-phases in AZ91D by synchrotron-radiation based microtomography

F. Witte1, J. Fischer1, M. Störmer2, N. Hort2

1Laboratory for Biomechanics and Biomaterials, Department of Orthopedic Surgery, Hannover Medical School, Anna-von-Borries-Str. 1-7,30625 Hannover, Germany

2GKSS Forschungszentrum Geesthacht GmbH, Max-Planck-Strasse 1, 21502 Geesthacht, Germany

Light metals such as magnesium alloys gained an increasing interest in transportation and air & space industries during the past years. Especially the need of reducing weight to increase the payload, to minimize fuel consumption and the emission of the green house gas CO_2 lead to a growing number of applications made out of magnesium alloys [1-9]. Besides the development of alloys that can be used at service temperatures in the range of 150 °C or even more the corrosion properties are of major importance [10]. Especially the corrosion resistance is a limitation to magnesium alloys in transportation and air & space industries.

In contrast to known applications, new research areas focusing on magnesium alloys as biodegradable implants will use an adjusted corrosion behavior to produce a temporary implant material [11]. The mechanical behavior and corrosion resistance of magnesium alloys is determined by its metallurgical factors. The metallurgical factors can influence the corrosion behaviour of any particular magnesium part and is dependent on the combined effects of its chemical composition and its microstructure [12, 13]. High purity (HP) magnesium alloys have been developed in the past to overcome the poor corrosion behavior of commercial magnesium alloys. The content of Fe, Cu and Ni was significantly reduced to a few ppm of these elements in modern magnesium alloys. The modern HP alloys like AZ91D show similar corrosion properties as Cu containing aluminium alloys or mild steels. Besides the influence of impurities like Fe, Cu and Ni, especially the beta-phase ($Mg_{17}Al_{12}$) in magnesium-aluminium alloys are known to influence the mechanical and corrosive properties of the alloy depending on their shape and spatial distribution [10, 12, 13]. Annealing or solution treating at temperatures near 430°C will cause all or part of the beta-phases to dissolve [12, 13].

Synchrotron-radiation based micro-computed tomography (SRμCT) allows the 3D reconstruction of a specimen from a set of 2D projections using the backprojection of filtered projection algorithm. The SRμCT were performed at beamline BW2 at Hamburger Synchrotronstrahlungslabor HASYLAB at Deutsches Elektronen Synchrotron DESY (Hamburg, Germany).

The specimens were imaged by microtomography in absorption mode utilizing synchrotron radiation at beamline BW2 using 16 keV photon energy. Exposed to the parallel synchrotron X-ray beam, the sample was precisely rotated 0.25° stepwise to 180°, and after every fourth step the reference image (projection) was recorded to eliminate intensity inhomogeneities and variations of the X-ray beam.

The results of the microtomography using synchrotron-radiation (SRμCT) showed the 3D orientation of the beta-phases, micro-pores and high density areas of aluminium-manganese particles. The typical microstructure of $Mg_{17}Al_{12}$ precipitates in the form of secondary, lamellar structures can be observed threedimensionally (Fig. 1).

This study showed that SRμCT is an advantageous method for the characterization of the microstructure in magnesium-aluminium alloys. It was successfully demonstrated that Synchrotron-radiation based microtomography (SRμCT) is a three-dimensional, non-destructive method to visualize the microstructure of magnesium alloys. The microstructural changes in magnesium alloy AZ91D according to the processing route were successfully visualized three-dimensionally using SRμCT. SRμCT is able to visualize any network of phases at grain boundary as well as the size and distribution of pores. Therefore, SRμCT gives valuable additional information to explain materials behavior especially in cases where phases on grain boundaries determine properties as it is in the case of corrosion or creep behavior for magnesium alloys.
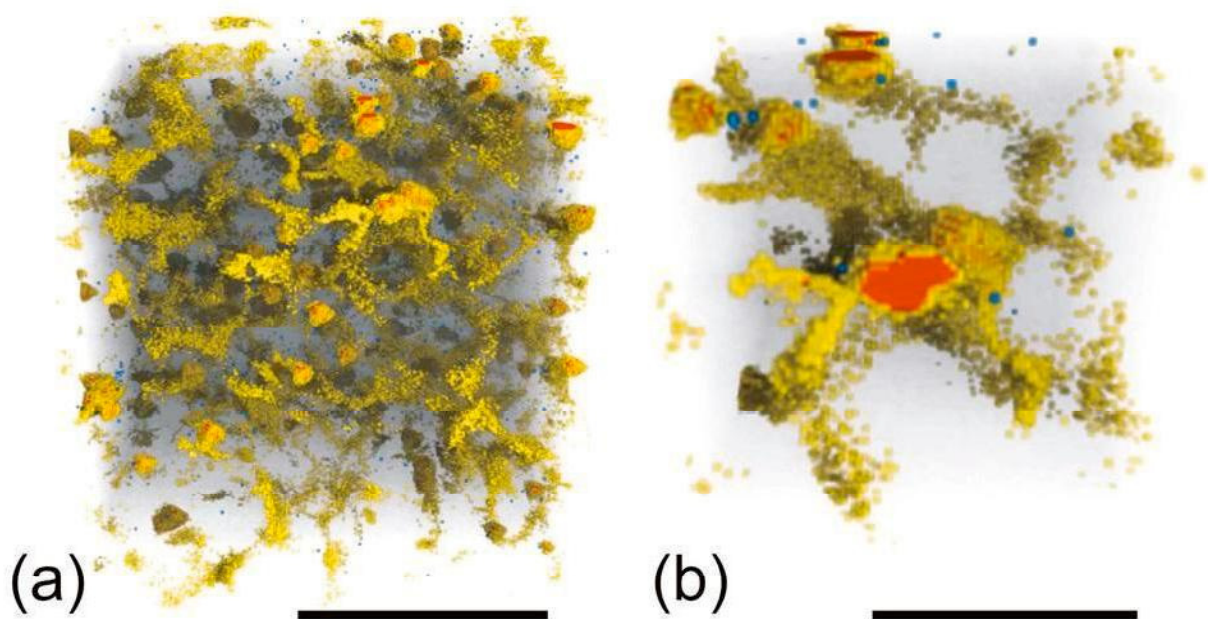
Figure 1: Left 3D reconstruction (a) shows 3D-segmented beta-phases (yellow), pores (blue) and Al-Mn-phases (red) in an as-cast AZ91D. Scale bar = 150 μm. Right 3D reconstruction (b) shows a 3D-magnification of figure 1a, demonstrating the lamellar character of the beta-phases enclosing the Al-Mn-phases in a kind of network. Scale bar = 50 μm.

References

[1] S. Schumann, Materials Science Forum 488-489 (2005) 1-8

[2] H. Westengen et al., Proc. 61st Annual World Magnesium Conference 2004, New Orleans, Louisiana, USA, 33-44

[3] E. Aghion et al., Magnesium Technology 2004, Ed: A. A. Luo, TMS, 2004, 167-172

[4] A. A. Luo, Materials Science Forum 419-422 (2003) 57-66

[5] W. Schneider et al., Proc. 61st Annual World Magnesium Conference 2004, New Orleans, Louisiana, USA, 71-80

[6] K. Pettersen et al., Proc. 5th Int. Conference on Magnesium Alloys and their Applications, Munich, Germany, 2000, 29-34

[7] M. Yang et al., Materials Science Forum 488-489 (2005) 923-926

[8] Communications from the Commission to the Council and the European Parliament: Implementing the Community Strategy to Reduce CO2 Emissions from Cars: Third annual report on the effectiveness of the strategy (Reporting year 2001), COM (2002) 693

[9] US government's Cafe Corporate Average Fuel Economy (CAFE) standards Passenger car and truck, hybrid and alternative fuel vehicle standards, 1975

[10] L. G. Song and A. Atrens, Advanced engineering materials 1999; 1(1):11-32.

[11] F. Witte et al. Biomaterials 2005; 26(17):3557-3563.

[12] M. Avedesian and H. Baker; ASM International, 1999, ISBN 0-87170-657-1.

[13] H. E. Friedrich, B. L. Mordike, Magnesium Technology, Springer, Berlin, 2006, ISBN 3-540-20599-3

3D-printed hydroxyapatite scaffolds with centrally aligned channel

Fabienne Fierz[1,2], Barbara Leukers[3], Stephan Irsen[3], Özer Degistirici[3], Felix Beckmann[4], and Bert Müller[1,2]

[1]*Biomaterials Science Center, University of Basel, c/o University Hospital, 4031 Basel, Switzerland*
[2]*Computer Vision Lab, ETH Zürich, Sternwartstrasse 7, 8092 Zürich, Switzerland*
[3]*Caesar Research Center, Ludwig-Erhard-Allee 2, 53175 Bonn, Germany*
[4]*GKSS-Research Center Geesthacht, Max-Planck-Straße 1, D-21502 Geesthacht, Germany*

Larger bone defects, which could be the result of tumour resection, are a source of fibrous scar formation and make healing difficult or even impossible. Replacing the defect by synthetic bone seeded with progenitor cells may allow further cell attachment, proliferation and finally formation of high quality bony tissue. If autologous bone implants cannot be harvested or surgery on a secondary site should be avoided, the synthetic bone graft seems to be a promising path. This approach allows using patient-derived progenitor cells to be seeded on the 3D-printed scaffold avoiding undesired immune responses.

The design of the open porous 3D scaffolds should fulfil different criteria to ensure cell viability and function. These criteria should include nano-porosity to allow diffusion of molecules for nutrition and signaling, micro-pores to ensure cell migration and capillary formation as well as macro-pores for larger blood vessels. In order to non-destructively determine the 3D morphology of the micro- and macro-pores under in-vitro conditions, we have applied synchrotron radiation-based micro computed tomography (SRµCT). Three different designs termed A, B, and C having a cylindrical shape (diameter 4 mm, height 6 mm) were fabricated layer-by-layer using 3D printing with a dot resolution of 240 µm. Subsequently, the scaffolds were sintered at 1250 °C associated with a shrinking of about 25%. As building material, spray-dried hydroxyapatite granules were employed. Each scaffold was statically loaded with 80 µL cell suspension containing 200'000 multi-potent ectomesenchymal progenitor cells isolated from the human tooth. The cell-scaffold constructs were harvested after 28 days and fixed in paraformaldehyde. SRµCT measurements were carried out in absorption contrast mode at the beamlines BW 2 and W2 using the photon energies of 24 and 30 keV, respectively. The higher photon energy is better suited for the total absorption of the scaffolds. Here, the pixel length corresponds to 4.3 µm and the spatial resolution determined by the modulation transfer function to 7.4 µm [1]. The 3D data are obtained by means of the standard filtered back-projection reconstruction algorithm. The tomograms obtained at two different height levels were combined after reconstruction. For data visualization the software VG Studio Max (Volume Graphics, Heidelberg, Germany) was used.

As shown in Figure 1, the morphology of the test scaffolds is intended to imitate the morphology of the natural bone. A denser outer structure takes over the role of the compacta providing the necessary mechanical stability. The inner part, which exhibits a rather similar structure to the spongiosa, provides a fully interconnected network of channels with diameters between 180 to 700 µm. This central part also contains a channel with a diameter of 700 to 1'000 µm, which forms a network with all micrometer-sized pores. This central channel should serve for different purposes, namely to surgically incorporate existing blood vessels at the acceptor site that promotes further vascularization [2], to avoid the often mentioned problem that bone in-growth does not reach central areas of the scaffold and, finally to enhance the medium flow during the in vitro phase.

The SRµCT data allows investigations with advanced computer vision tools such as distance mapping and component labeling to precisely characterize pore size distribution, interconnectivity and pore morphology. 3D analysis yields more precise values compared to classical histological 2D data treatment. Histological evaluation, on the other hand, reveals vital cells occupying the pore volume. Consequently, SRµCT and histology are complementary.

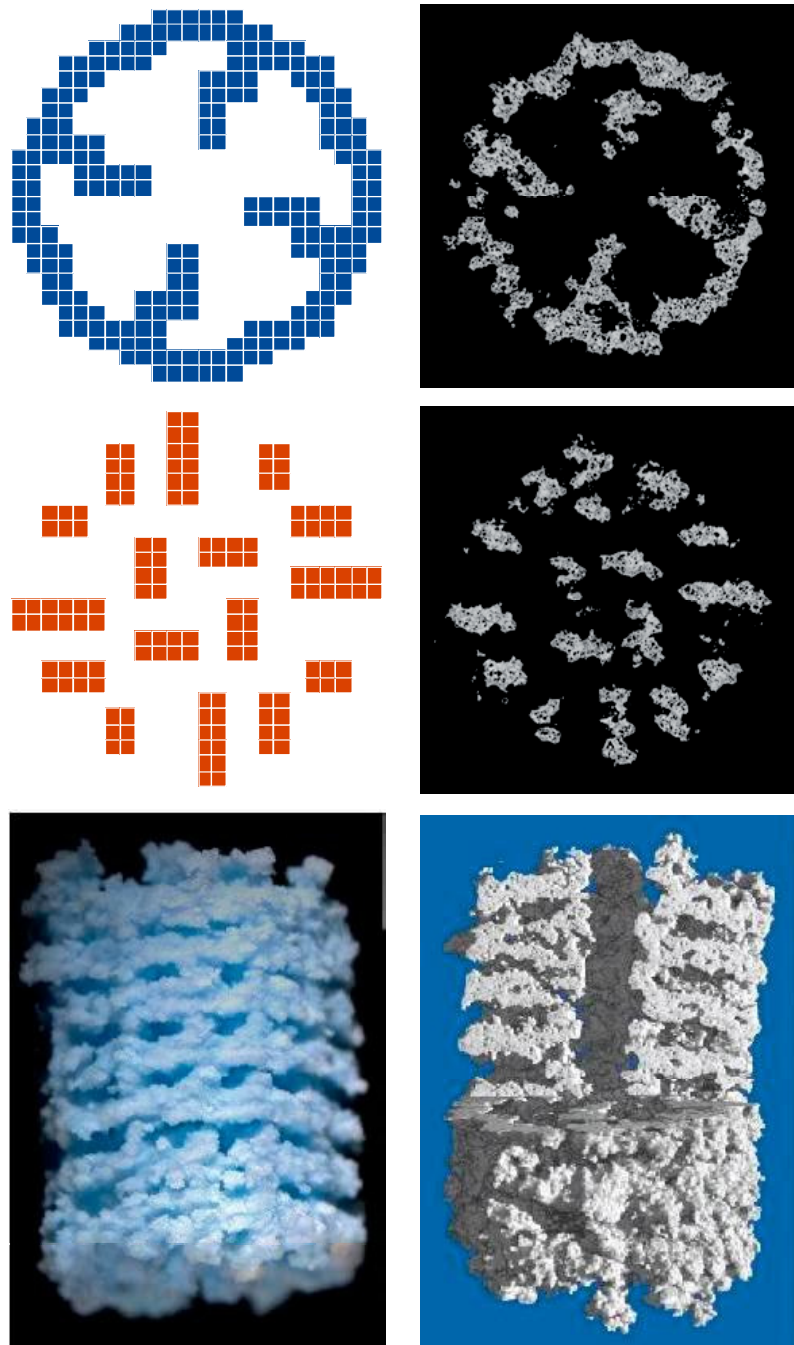Figure 1: The design C is realized by alternating layers (red- and blue-colored). On the right the related slices and a virtual cut from SRµCT data of the sintered structure are given. Optical images just provide the outer shape of the opaque scaffolds, whereby SRµCT leads to any desired insight.

References

[1] B. Müller et al., Proc. SPIE 4503, 178 (2001)

[2] Nakasa et al., J. Biomed. Mater. Res. 75, 350 (2005)

3D-Quantification of Strain and Displacement in MMCs utilizing SR-based Microtomography

H.-A. Crostack, J. Nellesen[1], G. Fischer[1] and F. Beckmann[2]

Lehrstuhl für Qualitätswesen, Fakultät Maschinenbau, Universität Dortmund, D-44221 Dortmund
[1] RIF e.V., Joseph-von-Fraunhofer-Str. 20, D-44227 Dortmund, Germany
[2] GKSS Research Center, Max-Planck-Str. 1, D-21502 Geesthacht, Germany

In order to understand the actual material behaviour under load, the microstructure has to be imaged in the course of loading. With SR-based microtomography this can be done on the mesoscale, i.e. with a spatial resolution in the micrometer range. From the acquired image series the spatial distribution of deformation quantities and damage can be determined. In this way, correlations between microstructural features and peaks in the deformation fields can be found. Additionally, these results can be compared with the findings of FE-simulations that are based on realistic geometric models of microstructure and realistic boundary conditions.
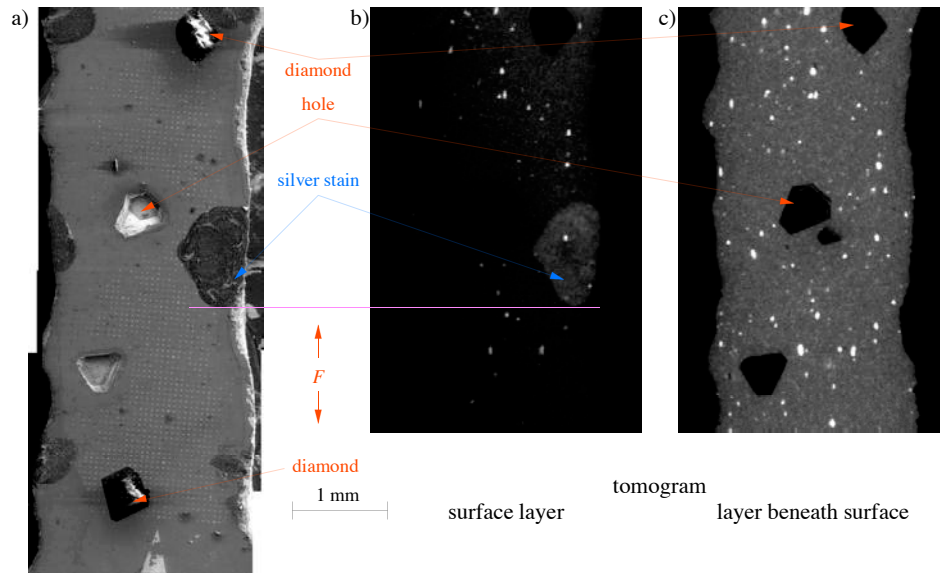
Figure 1: a) SEM-image of the specimen's surface with applied Silver stains, b) surface layer extracted from tomogram revealing Silver stain and c) sub-surface layer of tomogram showing diamond and tungsten carbide particles

In this work, the commercially available composite material Co/WC/Diamond consisting of diamonds and WC particles which are dispersed in a Cobalt matrix was investigated. This material is widely used for rotating tools cutting stone. The typical diameter of the diamonds amounts to 300 μm whereas the mean size of the WC-particles is about a few microns (cf. Fig. 1b). Tiny plain dog bone shaped tensile specimens were prepared from this material by water jet cutting. With the CT-scanner at the HARWI-II beamline the microstructure of the specimen gauge length (cross-sectional area 2 mm^2) was rendered at different stages of plastic deformation using monochromatic photons of 82 keV. A detailed discription of the testing conditions can be found in [1].

From the reconstructed tomograms the strain and displacement fields were calculated by an iterative image correlation technique, which is explained in detail in [1]. In Fig. 2 the colour-coded distributions of the equivalent plastic strain ε_{equ} in different parallel yz-planes are shown. An elevated level of strain can be found in the neighbourhood of diamonds. However, elevated strain values are also visible inside the diamonds. This is due to the fact that the image correlation algorithm averages over three-dimensional regions that have to be adapted to the characteristic microstructural

length given by the distances between WC-particles. In this case, the diamond size has a similar magnitude as this length.

The displacement vectors acting upon a geometric model of the microstrucure in a FE-simulation were also computed by the above mentioned iterative data processing technique. The vectors are visualized in Fig. 3. It can be seen clearly that the vectors have a preferential direction in the global loading direction which mirrors the elongation of the specimen. The FE model consisting of tetrahedral elements was generated starting from a triangle net representing the interface between the center diamond and Co matrix. A cut representation of the mesh can be seen in Fig. 4.
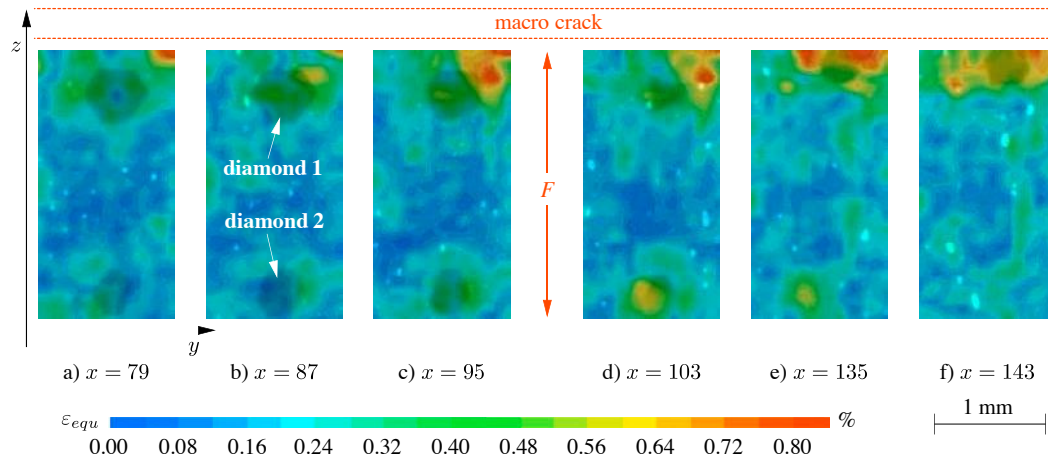
Figure 2: Contour plot of equivalent plastic strain ε_{equ} superimposed on different 2D CT slices through the tomogram given by the x-indices.
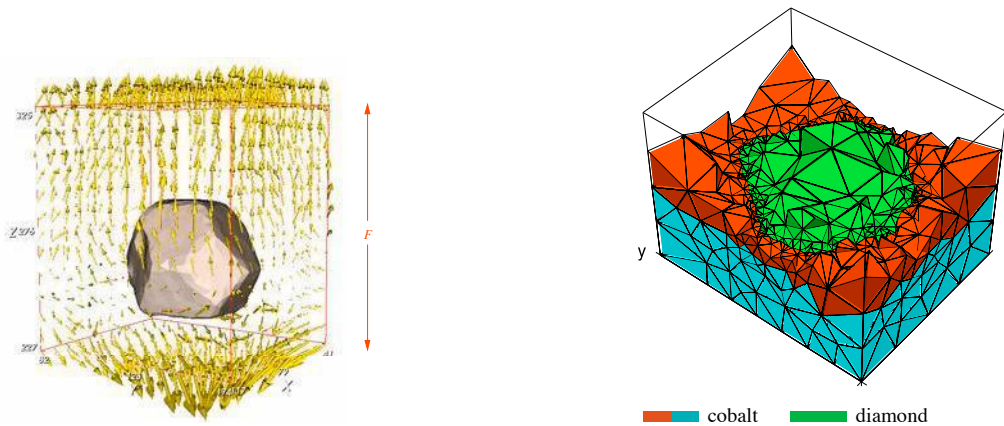
Figure 3: Displacement vectors at the model boundaries

Figure 4: Representation of the cut tetrahedra mesh

References

[1] H.-A. Crostack, J. Nellesen, G. Fischer, S. Schmauder, U. Weber, F. Beckmann, In: Ulrich Bonse (Editor): *Developments in X-ray Tomography V* Bd. 6318, 63181A-1-12 SPIE, Bellingham, WA, 2006

Investigation of Polyolefin insulation for Offshore Application by X-Ray Microtomography

A. Ghanbari-Siahkali, S.F. Nielsen[1], F. Beckmann[2], T. Donath[2], J. Herzen[2]

NKT Flexibles I/S, Priorparken 510 , 2605 Broendby, Denmark

[1] Risø, Materials Research Department, Building 228, Frederiksborgvej 399; 4000 Roskilde, Denmark

[2] GKSS-Research Center, Geesthacht, Germany

Flow assurance including thermal insulation is critical elements in the design and operation of flow lines and risers in deep waters due to a combination of high temperature, high pressures and economic drives for high availability. Hence, durability of the insulation materials directly contributes to maintain a reliable offshore production during its life service (i.e. 20 years). In order to achieve this goal it is vital to have knowledge and understanding of the material physicochemical properties, its stability and limitation in the extreme conditions.

In general, the insulation material consist of two main phases namely polymer and hollow spherical glass filler. The roll of glass filler, here, is to insure sufficient thermal barrier by lowering thermal conductivity of the polymer. Thus, the integrity of glass filler has always been one of important issues during the service. X-Ray microtomography is been reported to be a reliable quantitative analysis method to monitor the insulation materials, which are utilised in offshore industry [1].

For this reason, NKT Flexibles is interested to evaluate the stability of the filler, embedded in polymer matrix under real service conditions (e.g., high pressure, temperature or combination of both in an aqueous media) by means of a non-destructive analysis technique such as X-Ray microtomography.

Figure 1: preliminar X-Ray microtomograph results of reference polyolefine insulation tape with hollow spherical glass filler. The CT experiment was performed at beamline BW2 at Hasylab with a photon energy of 10 keV.

References

[1] V. Sauvant-Moynot, et al., Oilfield Engineering with polymer Conference. London 29-30 March, 1-14 (2006).

Charge density of Pyrite, FeS_2

T. Lippmann

GKSS Forschungszentrum Geesthacht, Max–Planck-Str. 1, 21502 Geesthacht, Germany
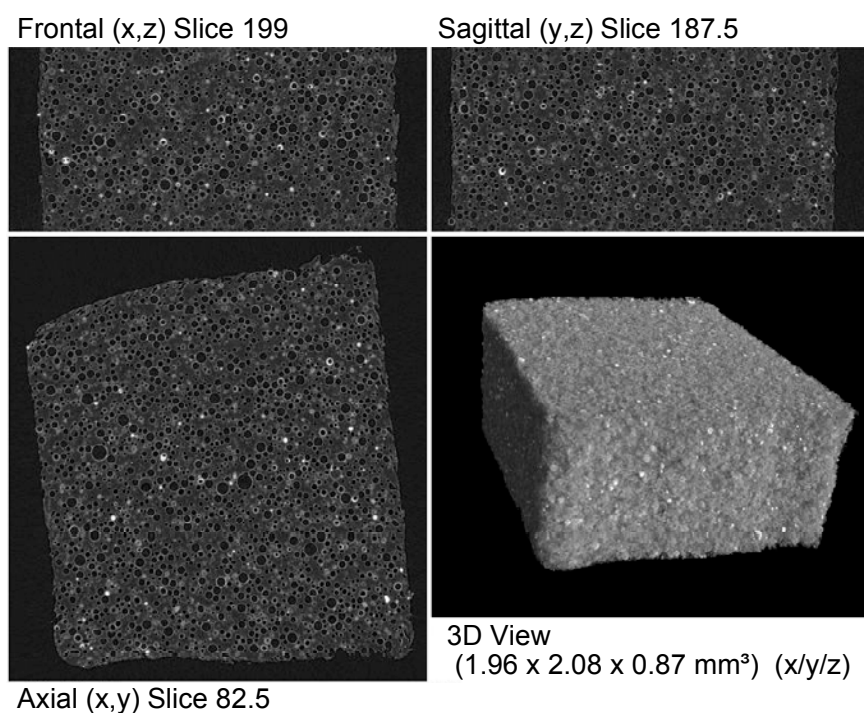
Within the framework of charge density studies of structures, which contain transition metal bonds, most of the investigations were focussed on oxides up to now, e.g. [1, 2]. Studies of sulfides can be regarded as a most welcome addition, not only due to the industrial and economic importance of the materials, but also with respect to the character of the chemical bonds. The choice of pyrite, FeS_2, as the first structure of interest here, was not arbitrary, since it can serve as a reference for future studies of compounds and an appropriate pyrite crystal was available. Pyrite crystallizes in the cubic space group Pa3 (a = 5.417Å, Z = 4). The charge density was studied using high–energy synchrotron radiation of 100 keV provided at beamline BW5. 5580 reflections were recorded (0 $< \sin\Theta/\lambda < 1.3$) and averaged to 317 uniques with an internal consistency of $R_{int} = 0.015$. A multipole model up to the order $l = 4$ was applied both to Fe and S, and the model was refined to R(F) = 0.0083 (wR(F) = 0.0085).
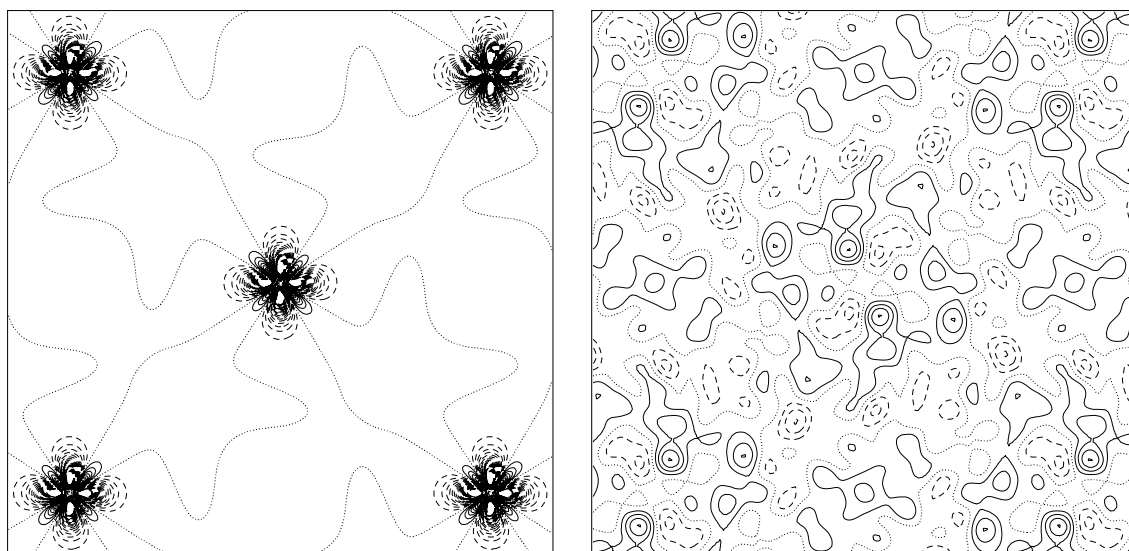
Figure 1: Charge deformation density (spherical parts of the charge density excluded, left) and residual density (right) in a plane containing only iron atoms. Contour lines: 0.1 e/Å^3.

Fig. 1 shows the aspherical part of the charge density and the 'residual density', i.e. the differences between model and experimental data, in a plane, which only contains iron atoms. The 'deformation density', which is related to the valence shells, is located near the iron nuclei and the interatomic regions turned out to be smooth and featureless. The residual density map does not indicate any significant unmodelled density in this plane. Fig. 2 shows density maps of another plane, which is characterized by both iron and sulphur, respectively. Again, the deformation density is concentrated near the nuclei, which is typical for ionic–dominated bonding.

In addition, a topological analysis has been performed in order to determine the interatomic surfaces, which separate the density into local atomic basins. Fig. 3 shows that the basin of the iron cation is of quite cubic shape, whereas the the basins of the sulphur anions have various faces, because they are coordinated by both Fe and S. The integration of the charge density within each basin yielded 24.3 electrons in the Fe basin and 16.85 electrons in the S basin, respectively. Thus, the chemical formula is $Fe^{1.7+}S_2^{0.85-}$, which is a further indication for an ionic–dominated structure. Thus, although pyrite is believed to have a considerable amount of covalent bonding, e.g. [3], the present results indicate ionic–dominated bonding. This discrepancy has to be further investigated.
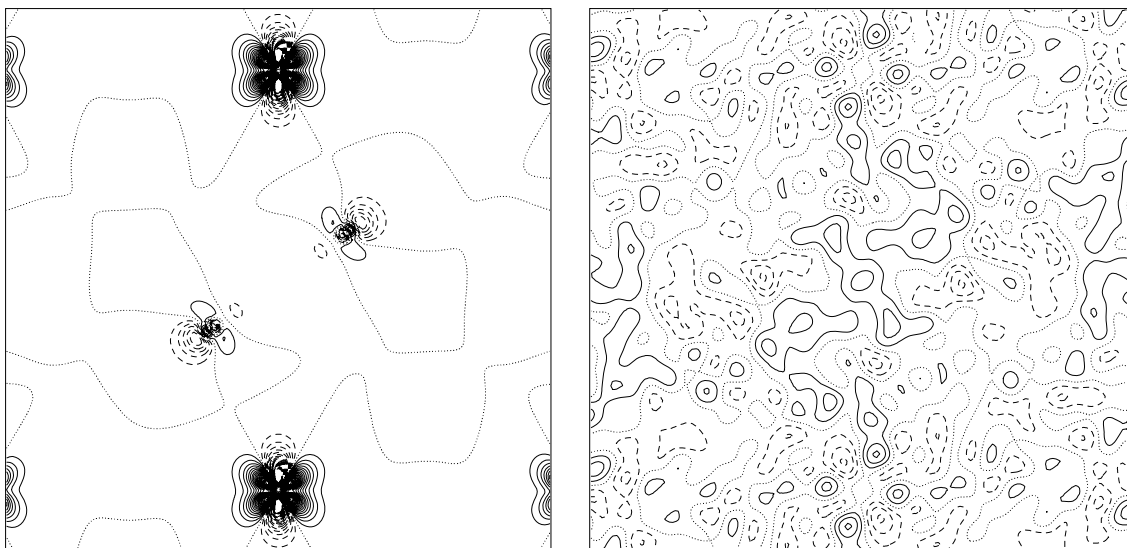
Figure 2: Charge deformation density (left) and residual density (right) in a plane containing both iron and sulphur atoms. Contour lines: 0.1 e/Å^3.
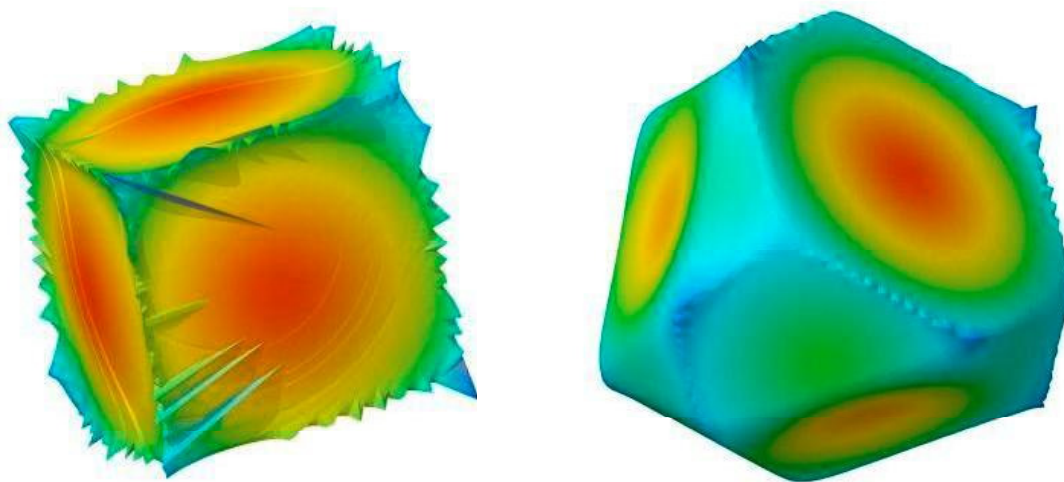
Figure 3: Interatomic surfaces of Fe (left) and S (right) in pyrite.

References

[1] G.V. Gibbs, D.F. Cox, K.M. Rosso, A. Kirfel, T. Lippmann, P. Blaha, K. Schwarz, Phys. Chem. Minerals 32, 114 (2005).

[2] A. Kirfel, T. Lippmann, P. Blaha, K. Schwarz, D.F. Cox, K.M. Rosso, G.V. Gibbs, Phys. Chem. Minerals 32, 301 (2005).

[3] P. Bayliss, Amer. Min. 62, 1168 (1977).

Electron density determination and topological analysis of HoNi$_2$B$_2$C

T. Leisegang, T. Weißbach, T. Lippmann[1], M. v. Zimmermann[2], P. Paufler, D. C. Meyer

Institut für Strukturphysik, Technische Universität Dresden, D-01062 Dresden, Germany
[1]GKSS Forschungszentrum Geesthacht, Max–Planck-Str. 1, 21502 Geesthacht, Germany
[2]Hamburger Synchrotronstrahlungslabor HASYLAB, D-22603 Hamburg, Germany

The homologous series of rare-earth nickel-borocarbides (RENi$_2$B$_2$C) is an interesting system for studying the interplay of magnetism and superconductivity at low temperatures. All known RENi$_2$B$_2$C compounds crystallise in the LuNi$_2$B$_2$C-type of structure [1] which is shown in Fig. 1 for the compound with RE = Ho. Their low-temperature properties depend decisively on the rare-earth element: in the Y, Sc and Lu compounds, superconductivity occurs, whereas the Pr, Nd, Sm, Gd and Tb compounds show ferromagnetic ordering. In the Dy, Ho and Er compounds both properties can coexist. In HoNi$_2$B$_2$C superconductivity occurs at temperatures below $T_c \sim 8$ K. On further cooling an antiferromagnetic phase can be observed at $T_N \sim 6$ K which suppresses superconductivity. At $T \sim 5$ K, the superconductivity recurs accompanied by another antiferromagnetic phase. This is called reentrant behaviour with respect to the superconductivity [2]. It is known that this behaviour is sample-dependent and can be changed, also reversibly, by thermal annealing so that only superconductivity or antiferromagnetic ordering without superconductivity can be obtained. It is presumed that the differing behaviour is mediated by an interchange of atoms, *i. e.* B and C atoms.

The investigations of the current project are focused on the comparison of two different samples, one in the as-grown state, the other one annealed at 1000°C. The crystals were grown by a floating zone melting method [3] at the IFW Dresden. Precise electron densities as well as the exact crystal structure are to be determined. For the collection of high-quality data and to reduce absorption effects, especially by the heavy Ho atoms, high-energy synchrotron radiation is used for single crystal diffraction measurements.
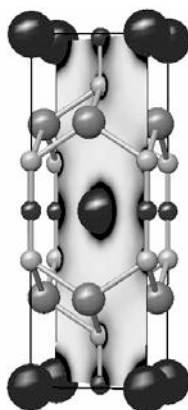
Figure 1: Tetragonal body-centred unit cell with space group symmetry (139) *I4/mmm* of HoNi$_2$B$_2$C with $a \approx 3.519$ Å and $c \approx 10.510$ Å (large dark spheres: Ho, large light spheres: Ni, small light spheres: B small dark spheres: C). Additionally, a section of the electron density ((110)-plane) has been drawn inside.

A first single crystal of HoNi$_2$B$_2$C in the as-grown state was used for single crystal X-ray diffraction measurement at Beamline BW5 at the HASYLAB. The photon energy of 100 keV ($\lambda = 0.12311$ Å) used was selected with a Si-111 monochromator crystal in Laue-geometry. At this energy, the absorption of X-rays in the sample material is drastically lowered (in the order of 1 %). All allowed reflections of the tetragonal body-centred lattice were measured, up to a sin $\theta/\lambda = 1.542$ Å^{-1} (corresponding to 7274 measured reflections). The measured peak profiles show a slight peak broadening due to the crystal mosaicity, making the sample a good approximation of the "ideally imperfect crystal". The data collected are of high quality, as reflected by an internal residual of $R_{int} = 3.57$ % for all reflections. A structure refinement of the data was performed yielding low residuals of $R_1 = 1.67$ %, $wR_2 = 2.23$% indicating a good agreement with the LuNi$_2$B$_2$C-type of structure.

The electron density distribution in the crystalline unit cell will be determined using the maximum-entropy approach [4] and the multipole formalism [5]. An example of a maximum-entropy calculation, the (100)-plane of the unit cell, is shown in Fig. 2, were the difference density (ρ_{MEM}-ρ_{PRIOR}; ρ_{PRIOR} is the electron density of superposed spherical atoms within the unit cell) can be seen. A topological analysis of the electron densities obtained will be performed according to Baders theory [6]. The results are to be compared with theoretical calculations using density functional theory.
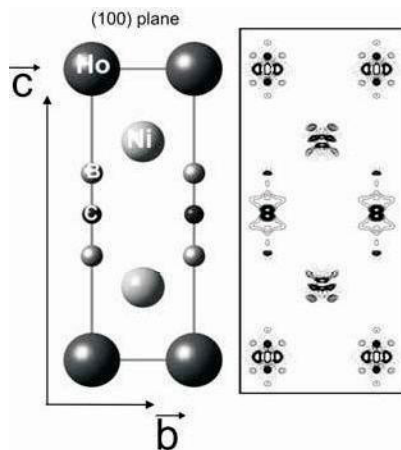
Figure 2: Schematic representation of the (100) plane of the unit cell of HoNi$_2$B$_2$C. Additionally, the corresponding difference electron density (ρ_{MEM}-ρ_{PRIOR}), calculated by the maximum entropy method (MEM) with the program BayMEM [4], is shown. Contour lines drawn are $\Delta\rho = \pm 0.05$ e/Å^3 in the range from 0.05 e/Å^3 to 1.00 e/Å^3, whereas lines correspond to positive and dots to negative electron densities, respectively.

The investigation of another crystal which was annealed at 1000°C is a further objective. A comparison of both crystals should give an insight of the structural changes caused by the annealing process and their interplay with magnetic order and superconductivity.

Acknowledgement

References

[1] T. Siegrist, H. W. Zandbergen, R. J. Cava, J. J. Krajewski, W. F. Peck jr.: The crystal structure of superconducting LuNi$_2$B$_2$C and the related phase LuNiBC. Nature 367, 254-256 (1994).

[2] K. H. Müller, V. N. Narozhnyi: Interaction of superconductivity and magnetism in borocarbide superconductors. Rep. Prog. Phys. 64 943-1008 (2001).

[3] D. Souptel, G. Behr, A. Kreyssig, W. Löser: Growth features of RENi$_2$B$_2$C (RE=Y, Ho, Tb) single crystals. J. Cryst. Growth 276, 652-662 (2005).

[4] S. van Smaalen, L. Palatinus and M. Schneider: The maximum entropy method in superspace. Acta Crystallogr. A 59, 459-469 (2003).

[5] N. K. Hansen and P. Coppens: Testing aspherical atom refinements on small-molecule data sets Acta Crystallogr. A34, 909-921 (1978).

[6] R. Bader: Atoms in Molecules: A Quantum Theory. Oxford □niversity Press, New York (1990).

Improving the knowledge of integration of medical devices in bone; a comparison of 3D SRµCT data to histomorphometrical data obtained on cut and ground sections

C.B. Johansson[1], J. Lindblad[2], H. Sarve[2], R. Bernhardt[3], F. Beckmann[4], J. Herzen[4]
G. Borgefors[2], D. Scharnweber[3]

[1]Department of Clinical Medicine, Örebro University, SE-701 82 Örebro, Sweden.
[2]Centre for Image Analysis, Swedish University of Agricultural Sciences, SE-751 05 Uppsala, Sweden.
[3]Max-Bergmann-Center of Biomaterials, Institute of Materials Science, Dresden University of Technology, D-01062 Dresden, Germany.
[4]Institute for Materials Research, GKSS Research Centre Geesthacht, D-21502 Geesthacht, Germany.

Introduction

Despite the long-term clinical success rate of oral implants there are several questions that still are un-answered. Moreover, there are more complicated cases, i.e., compromised bone beds treated today compared to former days. Research is aiming at improving the osteoconductivity or the biological potential of the medical devices surfaces in various ways in order to speed up the integration. With the "hard-ware" in focus, we are able to technically and controllable mimic the biomaterials related factors whereas the "soft-ware factors" are less controllable.

Retrieval of human biomaterials as well as research animal samples including bone tissue, with subsequent analysis in our laboratories, most often involve sample processing to undecalcified cut and ground sections of 10 µm thickness. One could refer to this as a "destructive technique" albeit it is the "state of the art technique" when one wants to investigate integration of hard biomaterials in bone tissue. Due to the time consuming techniques involved most often only one central section in one plane is prepared from each sample. The section is histologically stained and histomorphometrical analysis of for example bone to implant contact and bone area surrounding the implant is conducted with the aid of semi-quantitative computer-based techniques.

The aim of our research is to try to find, and apply additional techniques that will help us to understand the mechanisms of integration of biomaterials in bone tissue. We will combine *in vivo* biomechanical data with the traditional histomorphometrical data and add the SRµCT data. We foresee that adding various parameters obtained with various techniques would help us to gain the understanding of integration of biomaterials.

Materials and Methods

Bone blocks with screw shaped implants of commercially pure titanium were retrieved from rabbit bone (samples from cortical bone). Two of the animals (samples with spongeous bone) had been *in vivo* labeled with fluorescent dyes (clinical antibioticum). Laboratory processing resulted in embedment of all samples in resin. Most of the samples had an outer diameter of 12 mm whereas the larger samples (spongeous bone beds) had an outer diameter of 16 mm.

All samples were imaged with the SRµCT device of the GKSS at beamline W2 using a photon energy of 64 keV. The tomographical scan was performed by acquiring 720 X-ray attenuation projections equally stepped between 0° and 180°. For the smaller samples the field of view of the X-ray detector was set to 12.2 mm × 8.2 mm (width × height) with a pixel size of 8.0 µm showing a measured spatial resolution of about 17.2 µm. The larger samples were

larger than the field of view of the detector. Therefore a scanning technique was used. The detector was set to a field of view of 9.1 mm × 6.0 mm, pixel size 5.9 µm, and a measured spatial resolution of about 15.6 µm. The rotation axis was then set near the border of the detector and the scan was performed obtaining radiograms between 0° and 360°. Before reconstruction combination of the projection of 0° – 180° and 180° – 360° were built. A filtered back projection algorithm was used to obtain the three-dimensional data of X-ray attenuation for the samples. A slice through a reconstructed data volume can be seen in Figure 1 (left).

Currently

Computer aided analysis of the reconstructed radiographs is ongoing. A preliminary result of segmentation of the data into three classes, implant, bone, and non-bone regions is visualized in Figure 1 (right). A challenge is to see if it possible to separate new bone growth from older bone, in the SRµCT data. Cut and ground sections are under processing resulting in "routine sections" of the implants. The histomorphometrical data of bone area / volumes outside the implants will be compared to "similar slices / sections" in the radiographs. With the samples retrieved from the *in vivo* labeled bone – the aim is to additionally investigate if the fluorescence is still in the bone or if it is faded due to treatment in the W2. If still occurring in the bone tissue, as deduced on unstained cut and ground sections – the aim is to investigate if this information can be observed in the radiographs.
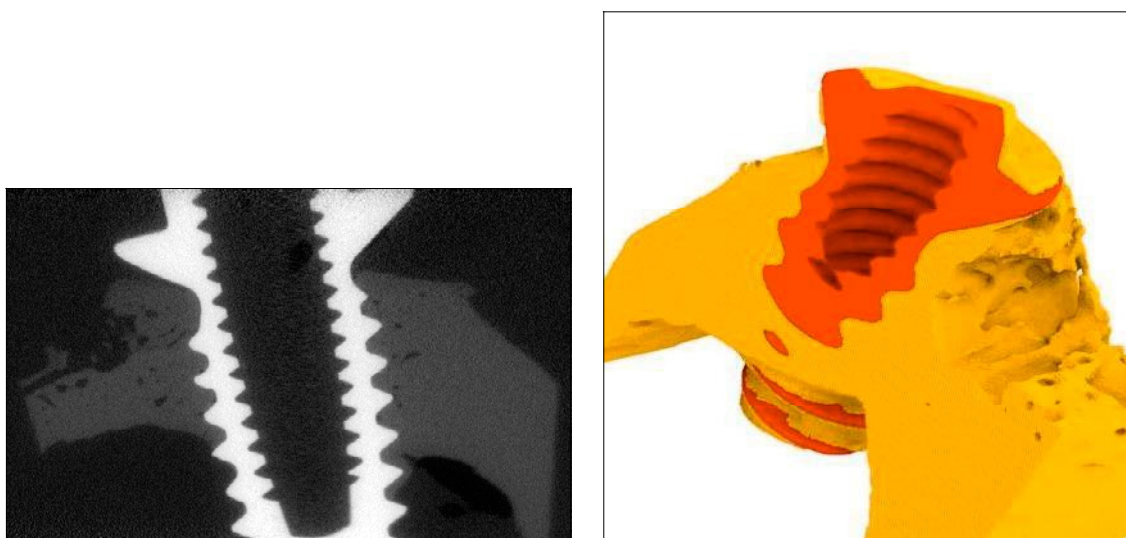

Figure 1: SRµCT image of commercially pure titanium implant inserted in rabbit-tibia bone for 10 weeks. Left: Slice through the reconstructed data. Right: 3D rendering of a preliminary segmentation of the data into implant (red) and surrounding bone material (yellow).

Determination of the distortion in histological slices of human brain tissue using synchrotron radiation based micro computed tomography

Bert Müller[1,2], Marco Germann[1,2,3], Adrian Andronache[2], Daniel Jeanmonod[3] and Anne Morel[3]

[1]*Biomaterials Science Center, University of Basel, c/o University Hospital, 4031 Basel, Switzerland*
[2]*Computer Vision Lab, ETH Zürich, Sternwartstrasse 7, 8092 Zürich, Switzerland*
[3]*Department of Functional Neurosurgery, University Hospital Zurich, Sternwartstrasse 6, 8091 Zürich, Switzerland*

Optical microscopy is the standard method to characterize the morphology of hard and soft human tissues. Especially the high lateral spatial resolution and the functional staining methods enable us to establish relations between local morphology and function on the cellular level and below. The preparation of histological slices leads to deformations often associated with feature dependent swelling and shrinking, especially for soft matter such as brain tissue. These local distortions are believed to be negligible, because they are just in the percentage range. If the tissue of interest should be represented not only in a 2D image but in a 3D fashion, the histological sections have to be registered, a task, which could become difficult, if the distortions are large. Consequently, it is highly desirable to correct the distortions in the images before their registration in 3D space.

Synchrotron radiation based micro computed tomography (SRμCT) is demonstrated to be an appropriate method to generate 3D data that allow correcting the optical images of the histological brain sections and whereby to determine the local strains in the sections. It has been shown [1, 2] that white and grey matter of human brain tissue exhibit slightly different absorption levels even avoiding any kind of staining. Therefore, the registration of the optical images with the tomographic data provides a reasonable estimate for the local strain as the result of the sectioning procedure.

Human brain tissue was conserved in formalin for several years. For the experiments, parts of the tissue (anterior medulla oblongata including the inferior olivary nucleus) were removed and transferred into Eppendorf containers with a volume of 0.5 mL. To avoid drying artefacts, the containers were entirely filled with phosphate buffer. The container was glued onto the holder and fixed on the high-precision rotation stage of the SRμCT experiment. The measurements were performed at the beamline BW 2 using the standard set-up for absorption contrast tomography. Using the double crystal monochromator, the photon energy was selected to 10 keV, where the absorption difference between white and grey matter could be clearly detected. 721 projections of 1536 x 1024 pixels were recorded. Using an optical magnification of 2.22, the pixel length corresponds to 4 μm. The spatial resolution of 6.2 μm was quantified by the use of the modulated transfer function [3].

Subsequent to the SRμCT experiments the tissue was frozen for crygenic cutting. The 30 μm thick slices underwent optical microscopy in bright- and dark-field mode. Depending on the stain applied, the typical features were visualized (see Figure 1) and registered with the tomographic data. Figure 1 shows an example of a bright-field image of a Nissl stained slice. The nuclei, which are also well distinguished in the SRμCT slices [1, 2], are the conglomerated dark dots. The 2D optical images of the histological slices are elastically registered with the corresponding 2D slices of the tomogram using the multi-modal non-rigid registration algorithm presented in [4]. The result of the registration is depicted by the red-coloured arrows which indicate the direction and amplitude of the local strain.

The combination of the corrected optical 2D images and the 3D SRμCT data allows generating a highly precise atlas of the brain or its parts, which is of importance for minimally or non-invasive surgical interventions and teaching purposes.
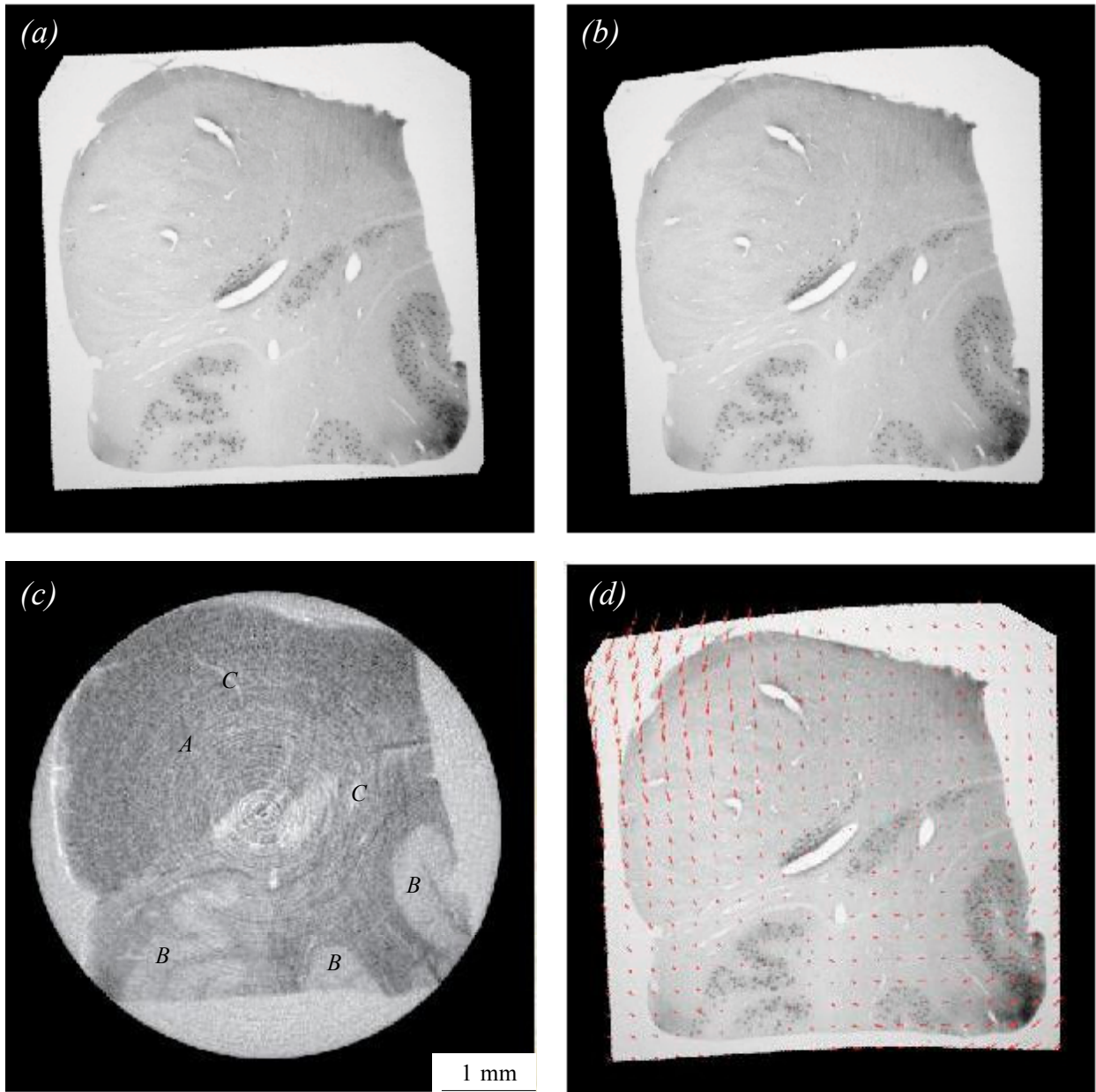
Figure 1: *(a)* The distorted histological slice of brain tissue shows the typical (Nissl-stained) features, i.e. blood vessels as well as the white and grey matter. *(b)* The corrected histological slice can be used, e.g. to rebuild the 3D representation of parts of the brain. *(c)* The letters in the SRμCT slice indicate the white brain tissue – *pyramis* (*A*), the grey matter - *inferior olivary* (*B*), and the blood vessels (*C*). *(d)* The arrows represent the amplitude and direction of the deformation field.

References

[1] M. Germann, F. Beckmann, A. Morel, and B. Müller, HASYLAB Annual Rep. Part I, 1079 (2005)

[2] B. Müller, M. Germann, D. Jeanmonod, and A. Morel, Proc. SPIE 6318, 631803 (2006)

[3] B. Müller et al., Proc. SPIE 4503, 178 (2001)

[4] A. Andronache, Multi-Modal Non-Rigid Registration of Volumetric Medical Images, Ph.D. thesis, ETH-Zurich (2006)

Elastic energy load into spicule reinforced extracellular matrix of the sponge *Tethya wilhelma*? – Evidence from synchrotron radiation based x-ray microtomography

M. Nickel[1], J. U. Hammel[1], T. Donath[2] and F. Beckmann[2]

[1]*Department of Zoology, Biological Institute, University of Stuttgart, Pfaffenwaldring 57, 70550 Stuttgart,Germany*

[2]*GKSS Forschungszentrum, Max-Planck-Str. 1, 21502 Geesthacht, Germany.*

Background

Sponges (Porifera) are sessile, filter-feeding animals, mainly inhabiting the sea. They are an evolutionary ancient, most likely the oldest recent group of multicellular animals. For this reason the understanding of the biology of poriferans is of general interest to biology, since it will allow insights into some primordial aspects of multicellularity. Sponges do not possess a nervous system, nor muscle cells. However, they are capable of showing movement bahaviours, like contraction [1] or body disclocation [2]. These behaviours raise a number of issues, especially of physiological as well as morphological viz. biomechanical nature. The physiological control and integration of these behaviours seems to be mediated by cellular receptor systems, which are specific for a number of neuroactive substances [3, 4]. However the biomechanical fundamentals of these processes are not jet understood. We have characterised the 3-dimensional structure of the tissue, the aquiferous system as well as the siliceous compound skeleton of the sponge *Tethya wilhelma* during previous SR µCT studies at DESY [5]. Especially the quantitative analysis of the skeleton of the closely related species *T. minuta* lead us to the conclusion that the skeleton is formed by superstructures, which are compound materials composed of siliceous spicules as filler particles and collagen as a viscoelastic matrix [6]. One superstructure, in the form of a sphere at the sponge's cortex-choanoderm (filtering tissue) boundary is very prominent, since it is composed by tenthousands of aster-shaped megascleres of around 50 µm diameter, which are embedded into a thick collagen sphere. Without having performed material tests, but in conjunction with similar biomaterals, this superstructer is a particle reinforced extracellular matrix. Such kind of structures show superior material properties in comparison to regular extracellular matrices, eg. a higher tensility, increased strength and a lower stretchability. What happens with this material within the sponge during contraction? Material tests are extremely difficult due to the small size of the animals and correspondingly the even smaller size of the skeletal superstructures. Therefore we aimed at answering the question by comparative investigations on expanded and contracted sponges by SR µCT.

Morphological changes within the megastar-collagen superstructure during sponge contraction

Both, a contracted as well as an expanded specimen of *T. wilhelma* was shok frozen within liquid nitrogen, contrasted by OsO4 and dried. The exact methodology is described elsewhere [5]. The spesimens where imaged performing SR µCT at HASYLAB beamline BW2, using an x-ray-beam of a photon energy of
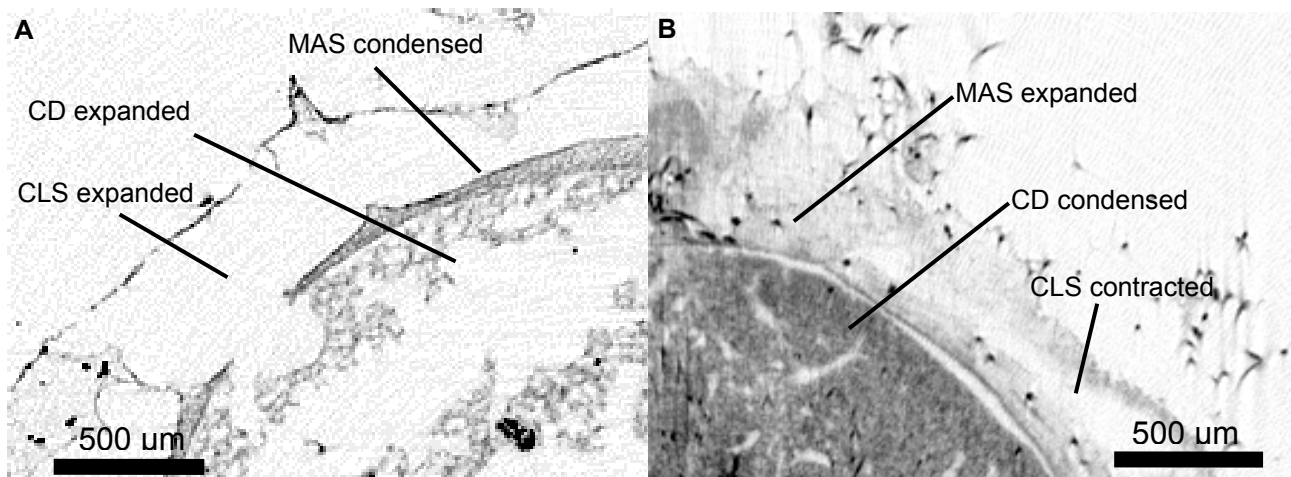
Figure 1: Comparison of two specimen of *T. wilhelma*. Detail of the cortex-choanoderm boundary, shown as reconstructed slice from SR µCT. **A.** Expanded specimen. **B.** Contracted specimen. MAS, megastar-collagene sphere; CD, choanoderm; CLS, cortical lacunar system.
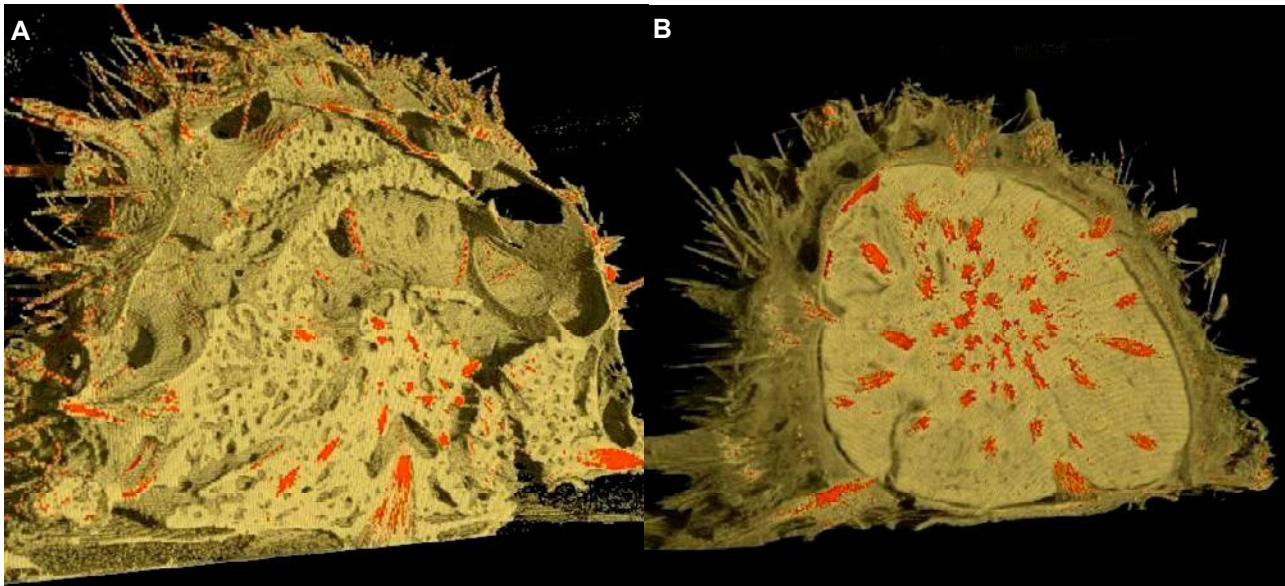
Figure 2: Reconstruction of two specimens of T. wilhelma based on SR μCT data. **A.** Expanded specimen, with homogenous appearance. **B.** Contracted specimen, with clear cortex-choanoderm differentiability. Rendered using VG studio.

14.5 keV, at a final reconstructed pixel size of 5.7 μm. Both, the reconstructed slices (Fig. 1), as well as virtual sections through the 3D-renderings of sponge tissue (Fig. 2) displayed significant differences for the megastar-collagen superstructure between the contracted and the non-contracted specimens. Unexpectedly in the contracted sponge, the megastar-collagen sphere seems to be expanded, while in the expanded sponge the sphere is condensed (Fig. 1). In contrast, the whole filtering sponge core (choanoderm) seems to be condensed in the contracted sponge. Our results provide evidence for viscolelastic strain of the megastar-collagen sphere during contraction. This would mean a load of viscoelastic energy into the superstructure, which subsequently helps to expand the contracted canal structures in the choanoderm core and the lacunar cortex, when the active contraction of the epithelial-like pinacocytes is completed. This hypothesis is supported by previous experiments using *in vivo* x-ray microimaging [7], which clearly showed displacement of skeletal structures during sponge contraction. However, theses structure where slowly and passively reoriented towards the initial state during an ongoing long term contraction of the sponge in this experiment.

Conclusions and Outlook
Combining SR μCT and *in vivo* x-ray microimaging provides first evidence for a repeated load of elastic energy into distinct skeletal superstructures, which represent compound materials. More detailed investigations using SEM, TEM, AFM, but also further SR μCT are necessary to confirm these results. Ideally, *in vivo* SR μCT would allow for more detailed data on this phenomenon. For this purpose the speed of imaging will have to be enhanced. However, with a slight modification of existing methodology, stereologically enhanced *in vivo* x-ray imaging is possible and will be tested within the next project.

References
    [1] M. Nickel, Journal of Experimental Biology, 207, 4515-4524, (2004) link
    [2] M. Nickel, Journal of Experimental Biology, 207, 2839-2846, (2006) link
    [3] K. Ellwanger & M. Nickel, Frontiers in Zoology, 3, 7, (2006) link
    [4] K. Ellwanger, A. Eich & M. Nickel, Journal of Comparative Physiology A, Onlne first (2006), link
    [5] M. Nickel, T. Donath, M. Schweikert & F. Beckmann, Zoomorphology 125, 209-223 (2006), link
    [6] M. Nickel, E. Bullinger & F. Beckmann, Zoomorphology, 125, 225-239 (2006), link
    [7] M. Nickel, J.U. Hammel, T. Donath & F. Beckmann, DESY Annual Report 2005, Part I: 1065-1066 (2005), link

Intensity-based segmentation of cochlear implant within the human inner ear

Bert Müller[1], Felix Beckmann[2], Julia Herzen[2], Rudolf Glückert[3], Claude Jolly [4], and Annelies Schrott-Fischer[3]

[1]Biomaterials Science Center, University of Basel, c/o University Hospital, 4031 Basel, Switzerland
[2]GKSS-Research Center, c/o GKSS at DESY, Notkestrasse 85, 22607 Hamburg, Germany
[3]ORL University Clinics, Medical University Innsbruck, Anichstrasse 35, 6020 Innsbruck, Austria
[4]MED-EL Worldwide Headquarters, Fürstenweg 77a, 6020 Innsbruck, Austria

The cochlear implant is a medical option for individuals with severe to profound sensorineural hearing loss. In this type of hearing loss, hearing aids provide limited benefit because they are designed to amplify sound, but the cochlea is unable to process this sound. A cochlear implant bypasses the non-functioning part of the cochlea and delivers sound signals directly to the hearing nerve. Cochlear implants function by electrically stimulating the sensory cells in the cochlea. Both pre-lingually and post-lingually deafened children and adults can take advantage of these implants. A cochlear implant system has two main parts - the internal and external ones. The internal part consists of the housing for the electronics, the electrode array, and the reference electrode. The external part contains the speech processor with the control unit, the battery pack, and the coil.

Cochlear implantation is a standard therapy with the aim to allow persons afflicted with sensory-neural deafness to experience sound again. Sound perception is restored through electrical stimulation of the nerve and sensory cells. Therefore, the electrode is inserted into the inner ear. The conductive fluids provide the interface with the excitable neural elements [1]. Long electrodes deeply inserted in the scala tympani can stimulate the complete frequency range available in the cochlea. The advantage is due in part by the presence of long nerve fibres in the apical region of the cochlea [2]. The details of the electrical stimulation are complex. They include the shape, frequency, and strength of the waveform used to deliver the charges, the location and design of the electrodes, the tissue impedance and, finally the spiralling geometry of the cochlea.

It is a very difficult task for the medical doctors to acquire data, which allow drawing conclusions on the integration of the electrode within the hardest human bone. Histology does only provide limited information, since the electrode has to be removed before the cutting becomes possible. Therefore, it is the aim of the present study to demonstrate that synchrotron radiation-based micro computed tomography (SRμCT) has the power to non-destructively uncover the implant, the structure of the inner ear, and the temporal bone, simultaneously.

The implant with surrounding tissue was removed 36 hours after the death and fixated in Karnosky solution. Bones needed to be reduced in size for imaging. In order to improve the density resolution of the soft tissues, the entire specimen was stained with 1% OsO$_4$. The fixated explant with the surrounding hard and soft tissue was placed and fixed in a suitable container. It was entirely filled with the fixation solution and glued to the high-precision rotation stage of the experimental setup. The SRμCT measurements were performed at the beamline W 2 (HASYLAB at DESY) using the standard set-up for tomography in absorption contrast mode. The photon energy of 64 keV was selected. The spatial resolution determined by the modulation transfer function corresponded to 20.7 μm at a pixel size of 8 μm [3]. The experiments were carried out with an asymmetric rotation axis and 360° rotation. For reconstruction by means of the filtered back projection in each case two out of the 1441 projections were combined. To obtain the 3D dataset of the entire explant, 3 tomograms each with 1536 x 1024 pixels were combined.

Figure 1 shows the 3D representation of the implant, intensity-based segmented by means of the software VG Studio Max (Volume Graphics, Heidelberg, Germany). In order to make visible the position of the implant within the inner ear, it is represented with the virtually truncated bony tissue. The fully 3D dataset, that was non-destructively obtained, enables us to perform virtual cuts

in any desired direction. Therefore, one can easily recognize the bony structure of the modiolus and the electrode, simultaneously.

With SRμCT in absorption contrast mode, we were able to demonstrate that rather large samples of complex 3D structures such as the metal implant consisting of 12 electrodes in bony tissue can be evaluated with quite high spatial resolution. This resolution allows the detailed analysis of the temporal bone structures of the inner ear and the position of the electrode array. The use of only histological techniques results in artefacts because of the necessary cut of the electrode array [4]. Consequently, SRμCT is a unique technique for characterizing the integration of cochlea implants.
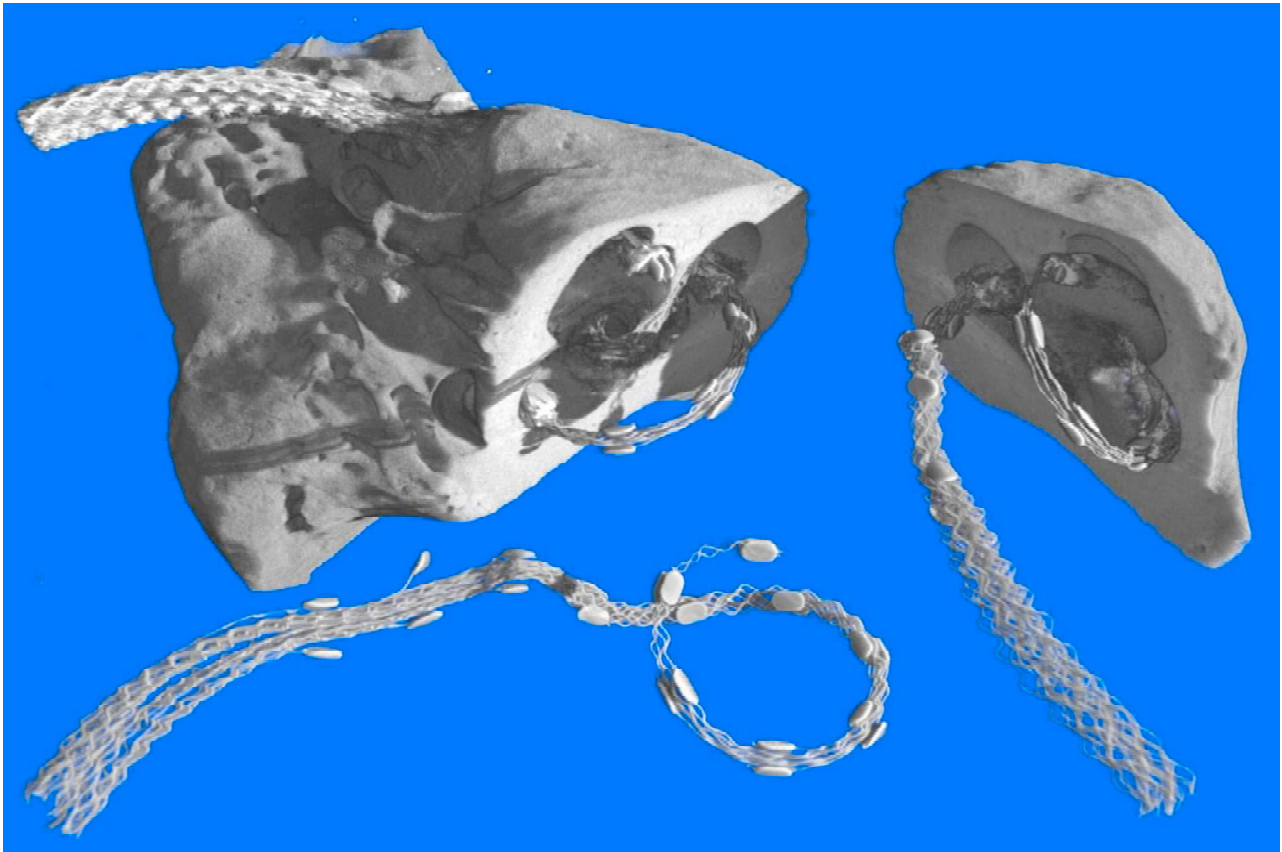
Figure 1: The metallic cochlea implant consists of an array of 12 pairs of electrodes and exhibits a complex characteristic shape, since it follows the cochlea. The implant-tissue interface is of special importance. It is accessible by the SRμCT, which is non-destructive and allows performing histology subsequently. The rather large specimen was hold in liquid during the experiment. Multiple scans were necessary. The 3D representations were produced by means of the software VG Studio Max.

References

[1] C. Arnoldner, W.D. Baumgartner, W. Gstoettner, and J. Hamazavi, Acta Otolaryngol. 125, 228 (2005)

[2] J.B. Nadol Jr. and D.K. Eddington, Adv. Otorhinolaryngol. 64, 31 (2006)

[3] B. Müller et al., Proc. SPIE 4503, 178 (2001)

[4] O. Adunka, M.H. Unkelbach, M. Mack, M. Hambek, Acta Otolaryngol. 124, 807 (2004)

Internal anatomy of dwarf spiders based on SR *µ*CT

P. Michalik[1], M. Nickel[2], J.U. Hammel[2], T. Donath[3] and F. Beckmann[3]

[1]*Zoological Institute and Museum, Ernst-Moritz-Arndt-University, J.-S.-Bach-Str. 11/12, 17489 Greifswald, Germany*

[2]*Department of Zoology, Biological Institute, University of Stuttgart, Pfaffenwaldring 57, 70550 Stuttgart,Germany*

[3]*GKSS Forschungszentrum, Max-Planck-Str. 1, 21502 Geesthacht, Germany.*

Investigation of the internal anatomy of arthropods is mostly based on invasive methods, i.e., sectioning for light and electron microscopy. Due to preparation (fixation) problems resulting from impermeability of the cuticular exoskeleton artefacts are often present and complicate the three-dimensional reconstruction of the internal organization. For example in spiders, the reconstruction of the female genitalia and the male palpal organ is very difficult due to the complexity of the structures, e.g., the convoluted cuticular ducts and surrounding/adjacent tissues that are often complicated to investigate with standard methods. Three-dimensional reconstructions of spider genitalia have only been based on serial sections until now [1], which are very time consuming and difficult due to possible artefacts and preparation problems. Therefore, non-invasive techniques seem to be most useful for observations of the organization of these structures.

In this first analysis, using SR µCT at a photon energies of 8 and 10 keV, we imaged two females of *Oedothorax retusus*, a species of sheet-web spiders (Linyphiidae). We were able to reconstruct and render the outer and inner morphology of the specimens at a final effective pixel sizes of 1.7 to 3.3 µm per pixel (Fig. 1). A main advantage (and reason for choice) of this species is the body size, adult females are only 2-3 mm in length. The female genitalia of this species are of the entelegyne type, i.e., it consists of paired spermathecae and different ducts and is much more complicated in contrast to, e.g., species with haplogyne genitalia [2]. The 3D structure is represented in the dataset (Fig 2A, B), but will have to be segmented for a more detailed investigation. Furthermore, the ovary structure is resolved, too (Fig. 2C), which is not accessible in 3D by other morphological/ histological methods (except with a 3D reconstruction based on serial sections). Further data analysis will eventually allow to analyse aspects of egg cell development. Additionally, in future studies we plan to investigate pairs in copula with SR-µCT in order to know the exact mode of interaction of female and male copulatory organ in these species.
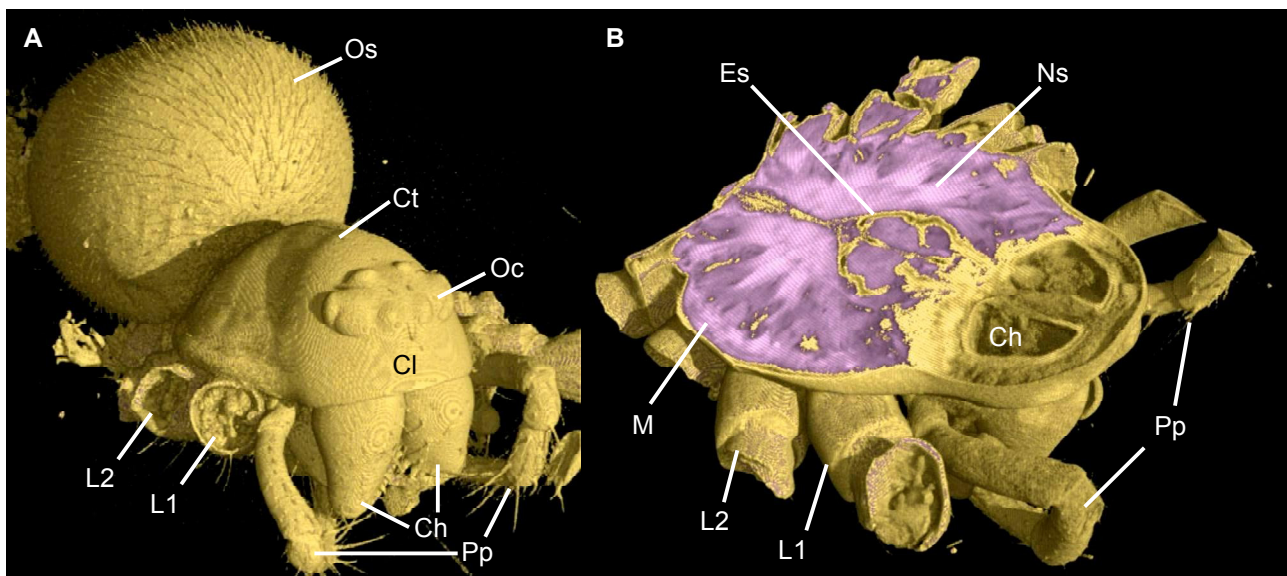
Figure 1: Reconstruction of the spider *O. retusus* based on SR *µ*CT data (2x binned). **A.** Whole animal (legs removed). Cephalothorax (Ct) with eyes (Oc). Setae, spines and sensory hair patterns on chelicerae (Ch), pedipalps and coxae of legs (L1, L2) as well as clypeus (Cl) and the whole opisthosoma (Os) is resolved by SR *µ*CT. B. Clipping of the cephalothorax, displaying muscles (M), the endosternite (Es) and part of the central nervous system (Ns). Rendered using VG Studio.
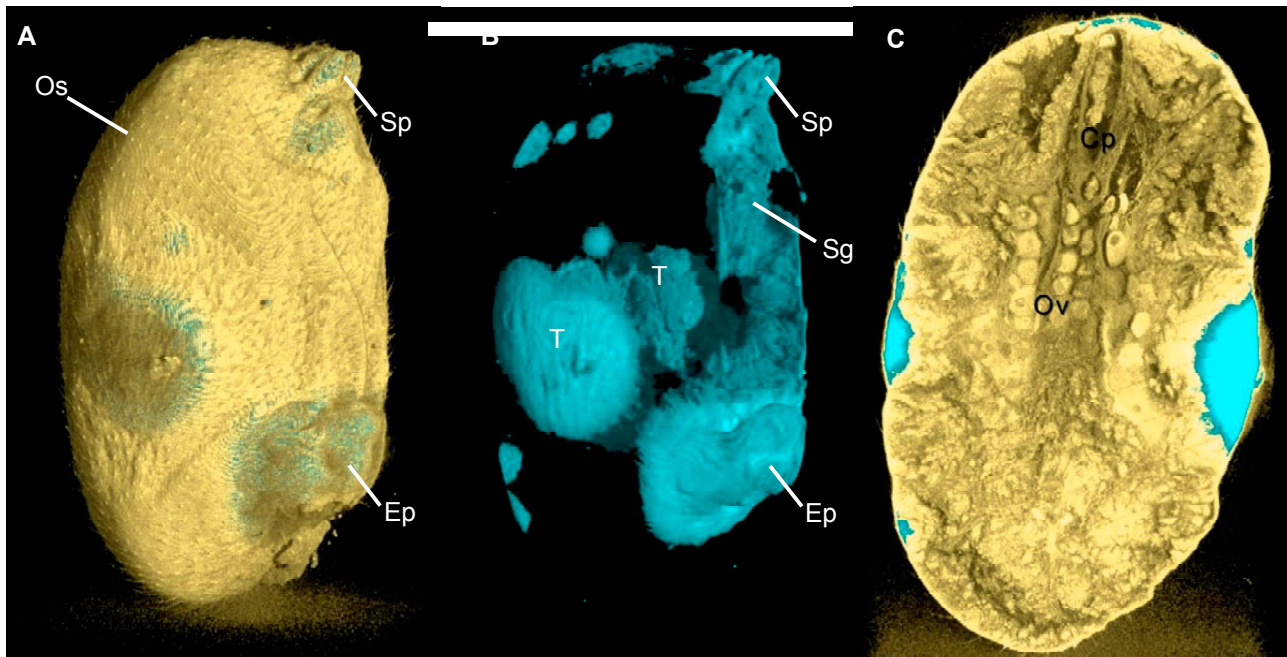
Figure 2: Reconstruction of the opisthosoma (Os) of the spider *O. retusus* based on SR *µ*CT data (2x binned). **A.** Latero-ventral view with spinnerets (Sp) and female genitalia (epigyne, Ep). **B.** Corresponding view, segmented for structures overstained by OsO$_4$: genitalia (Ep), spinnerets (Sp), spinning glands (Sg), book lungs (hidden behind genitalia) as well as artificial taps (T). **C.** Dorsal view of a clipping showing ovary structures (Ov) and and structures of the digestive trakt, e.g. the stercoral pocket (Cp). Rendered using VG Studio.

An important aspect of these dwarf spiders is the sexual dimorphism, i.e., the males possess special glandular structures in the prosoma [3,4]. These special glands are used during courtship/mating, but their exact function is still obscure (an influence on mating and paternity is assumed, but not revealed, e.g., for *O. retusus* according to recent studies by Uhl et al [personal communication]). For comparison, we investigated the female prosoma which lacks these glandular structures that are usually located in front or behind the eyes (depending on the species). In a next step we would like to investigate the male prosoma for a reconstruction of these glandular structures and use them as a basis for following studies on the fine structure of these special organs.

The 3D morphology of the spinning glands will be investigated in detail by segmentation of the datasets obtained within this study. Additionaly comparative studies on spinning gland 3D-morphology in relation to phylogenetic questions will be accomplished in future studies.

The methodology will have to be improved for future studies. Contrast enhancement, by osmium tetroxide, which worked well in other animal groups for SR µCT [5], resulted in overstaining of exposed structures and artificial taps of the opisthosoma (Fig. 2B). Except for muscles, the organ systems located within both the cephalothorax and the opisthosoma are characterized by a low x-ray absorbance. Eventually phase contrast µCT would help to resolve these structures better. Nevertheless, with our preliminary study we were able to demonstrate the value of SR µCT for morphological studies in spiders.

References

[1] B. A. Huber, J. Morphol. 267, 705 (2006)
[2] R. F. Foelix. Biology of Spiders. Oxford University Press (1996)
[3] U. Schaible and C. Gack. Verh. Naturwissenschaftl. Ver. Hamburg 29, 171 (1987)
[4] D. Vanacker, L. Maes, S. Pardo, F. Hendrickx, F. and J.-P. Malfait. J. Arachnol. 31, 309 (2003)
[5] M. Nickel, T. Donath, M. Schweikert & F. Beckmann, Zoomorphology 125, 209-223 (2006)

Microtomography of a human jaw segment

at the newly rebuilt W2 beamline

M. Dalstra, P.M. Cattaneo, T. Donath, J. Herzen and F. Beckmann[1]

Dept. of Orthodontics, University of Aarhus, Vennelyst Boulevard 9, 8000 Aarhus C, Denmark
[1]GKSS Research Center Geesthacht , Max-Planck-Str. 1, 21502 Geesthacht, Germany

The correct understanding of the load transfer from teeth via the periodontal ligament (PDL) and the alveolar bone to the rest of the jaw is a biomechanical challenge. Especially during orthodontic treatment, where external forces are applied to the teeth of a patient in order to move them to a new desired position, the choice of force is not evident. Due to the complex architecture of the jaw bones, the teeth are suspended in a thin cortical shell, the *lamina dura*, which in turn is supported by a loose network of trabeculae. In an on-going study we aim to scan a large number of human jaw segments using both conventional and synchrotron radiation-based microtomography (SRμCT) to assess the extent of individual anatomical variations and to use this data to generate more accurate finite element models of jaw segments to analyse the mechanical load transfer during orthodontic and physiological loading [1,2].

Due to the extensive rebuilding works at beamline W2, we have been unable to scan jaw segments for this project for the last two years. Although limited scanning was possible during this time at beamline BW2, the physical size of the jaw segments prevented this option as higher energies would have been required. In the Summer of 2006, work on beamline W2 had progressed such that the first pilot experiments could be performed there and in early November, while testing the scanning of large samples, it was finally the turn for one of our jaw segments.

The jaw segment was obtained at autopsy from the maxilla of a 49 year old female donor. It consisted of the left lateral incisor, canine and first premolar and the surrounding bone. Upon excision the segment was preserved in alcohol. Prior to scanning, the segment was dehydrated and embedded in a cylindrical block of methylmetacrylate ($\varnothing$ 28 mm, height 30 mm) to avoid decay.

The embedded jaw segment was measured with the SRμCT device of the GKSS at beamline W2 using the photon energy of 64 keV. The tomographical scan was performed by aquiring 720 X-ray attenuation projections equally stepped between 0 and π. As the width of the sample was larger than the field of view of the detector, a tomographic scanning technique was used. The detector was set to a field of view of 14.7 mm x 9.8 mm (width x height), pixel size 9.6 μm, and a measured spatial resolution of about 31.4 μm. The rotation axis was set near the border of the detector and the scan was performed obtaining radiograms between 0 and 2π. Before reconstruction the projections of $0..\pi$ and $\pi..2\pi$ were combined to built one tomographical scan from $0.. \pi$. This procedure had to be performed at seven slightly overlapping heights of the sample to cover its full length. Finally, a back-filtered projection algorithm was used to obtain the three-dimensional (3D) data of the X-ray attenuation for the entire sample.

The image quality is of the same high standard, if not slightly better, than those of the jaw segments scanned previously at the old W2 beamline [1,2]. The different mineralized tissues in the sample (bone, dentine, enamel and cementum) can clearly be distinguished. On the buccal side the alveolar bone is very thin; even to the extent that there is a fenestration with the apex of the root of the canine penetrating. Furthermore, a cortical shell at the cervical level of the roots is as good as absent, leaving only low density trabecular bone for support there (Figure 1). This might explain the presence of root resorptions at the exposed part of the root of the premolar, probably due to abrasion during repetitive tooth brushing over time. The roots of the teeth also display various degrees of root resorption on those parts which are fully covered by the alveolar bone. In these cases, the *lamina dura* seems to have adapted itself to conform with the changes on the root surface by maintaining the width of the PDL.
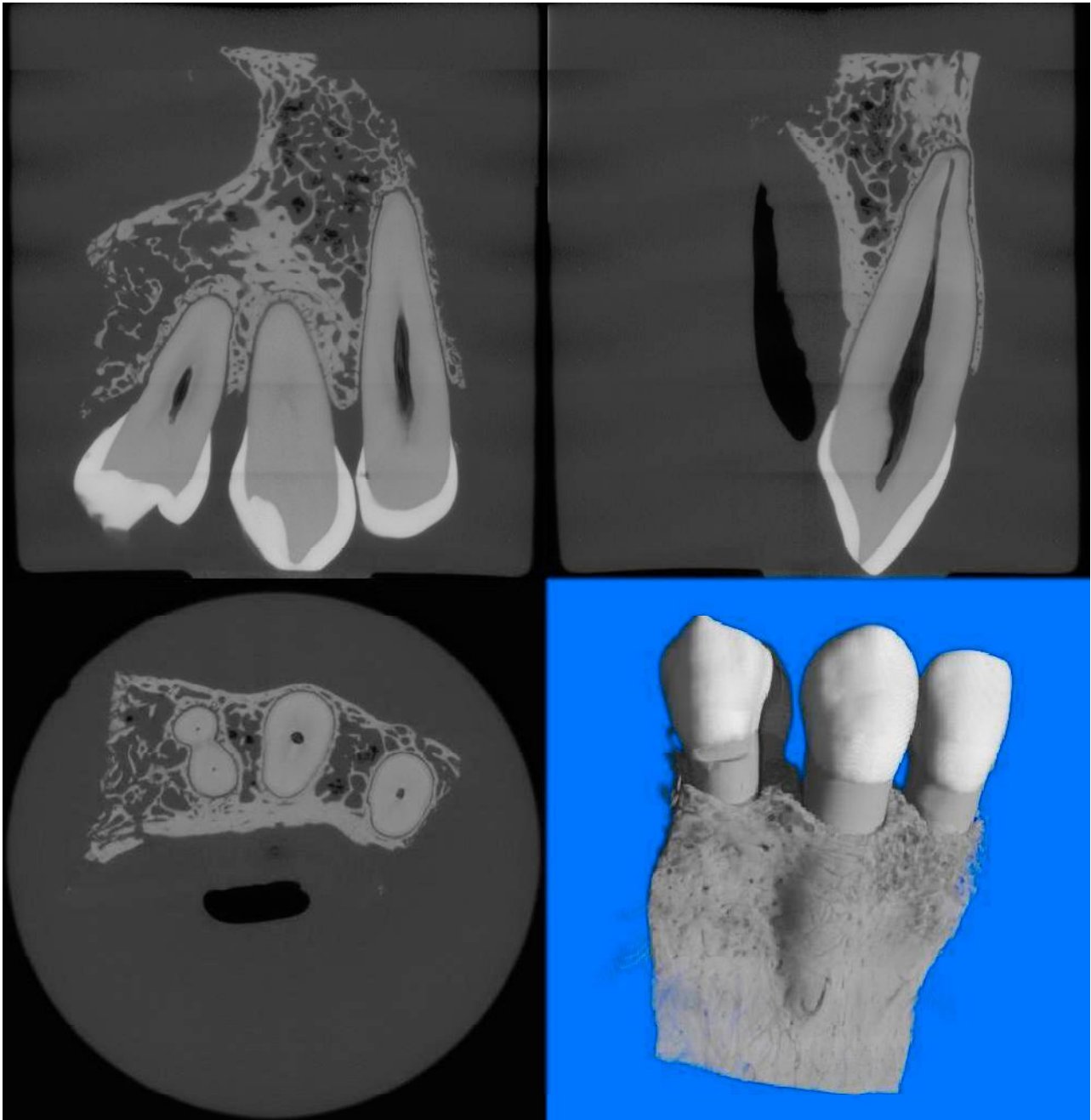
Figure 1: Mesio-distal (top left), bucco-lingual (top right) and transverse single-slice images (bottom left) of the jaw segment together with its rendered 3D reconstruction (bottom right). Note the fenestration at the apex of the root of the canine and the root resorption at the enamel-cementum junction on the root of the premolar.

References

[1] M. Dalstra, P.M. Cattaneo, F. Beckmann, M.T. Sakima, C. Lemor, M.G. Laursen, and B. Melsen, Developments in X-Ray Tomography V, 631804-1 (2006)

[2] M. Dalstra, P.M. Cattaneo, F. Beckmann, Orthod. Craniofac. Res. 9, 199 (2006)

Mikrotomographie an Biomineralien

Frank Neues,[a] Andreas Ziegler,[b] Tilman Donath,[c] Jens Fischer,[c,d] Felix Beckmann,[c] Matthias Epple [a,*]

[a] Universität Duisburg-Essen, Institut für Anorganische Chemie, Universitätsstraße 5-7,
45117 Essen., Germany
[b] Universität Ulm, Zentrale Einrichtung für Elektronenmikroskopie, Albert-Einstein-Allee 11,
89069 Ulm, Germany
[c] GKSS Forschungszentrum Geesthacht, Institut für Materialforschung, c/o GKSS am DESY,
Notkestrasse 85, 22607 Hamburg, Germany
[d] Klinik für Orthopädie, Medizinische Hochschule Hannover, Hannover, Germany.

Biomineralien sind anorganische Mineralen, die durch lebende Organismen gebildet wurden. Ihre Vorkommen in der Natur sind vielfältig. Sie werden beispielsweise benötigt, um die Stabilität zu verbessern (als Knochen oder als Exoskelett), als „Werkzeug" (z.B. Zähne) oder als Schutz vor natürlichen Feinden (Muschelschalen). Da Biomineralien von der Natur für ganz bestimmte Aufgaben synthetisiert werden, sind ihre Eigenschaften ebenso speziell. Knochen ist ein Kompositmaterial, bestehend aus Kollagen und Hydroxylapatit, das eine ausgewogene Kombination aus Flexibilität und Stabilität besitzt. Biomineralien stehen aus mehreren Gründen zunehmend im Blickpunkt der Wissenschaft: einerseits können durch das Studium des Aufbaus der biologischen Vorbilder biomimetische Werkstoffe entwickelt werden, andererseits ist das Verständnis der Mineralisationsvorgänge in Lebewesen wichtig in der Medizin, sei es in erwünschten Fällen (Knochen und Zähne), als auch in unerwünschten Fällen (Mineralisationsstörungen wie z.B. Osteoporose oder Arteriosklerose). Die Mikrocomputertomographie hat im Vergleich mit herkömmlichen mikroskopischen Methoden (z.B. der Rasterelektronenmikroskopie) mehrere günstige Eigenschaften. So ist es nicht nötig, die mineralisierten Gewebe aus dem sie umgebenden Weichgewebe zu isolieren, d.h. Hartgewebe können in ihrer natürlichen Umgebung untersucht werden (ohne Präparations-artefakte).
Im Folgenden werden mikrocomputertomographische Untersuchungen an zwei unter-schiedlicher Biomineralien vorgestellt: Das Skelett des Zebrafisches (*Danio rerio*) und die Kutikula einer Assel (*Porcellio scaber*).

Das Skelett des Zebrafisches
Der Zebrafisch ist in der biologischen Forschung ein Modellorganismus. Durch seine kurze Vermehrungszeit und die Transparenz der Embryonen ist er ideal für Laborversuche geeignet, insbesondere nach genetischer Manipulation. Knochen und Zähne des Zebrafisches sind vom Aufbau her den menschlichen Knochen und Zähnen ähnlich. Die Zähne vom Zebrafish sind im Schlund lokalisiert und erneuern sich fortlaufend. Die Krone der Zähne besteht aus einer dünnen Schicht Zahnschmelz (Enamel). Tubulares Zahnbein (Dentin) umschließt die Kammer mit Odontoblasten und Nervengewebe. In Abbildung 1 ist eine Übersicht über die Lage der Zähne gezeigt. Die Messung wurde am Messplatz BW2 bei einer Energie von 19 keV durchgeführt.

Die Kutikula von *P. Scaber*
Da die Kutikula (Exoskelett="Schale") der Assel *P. scaber* nicht mitwachsen kann, wird sie in mehreren Häutungsphasen ausgetauscht. Dieser Austausch erfolgt in zwei Schritten, da *P. scaber* sonst schutzlos ihren Feinden ausgeliefert wäre. Die Häutungsphase beginnt mit der Demineralisation (Abbau des darin enthaltenen Calciumcarbonats) der posterioren Kutikula. Das Calciumcarbonat wird dabei in vier sternalen Depositen der Assel zwischen gelagert. Nach dem Abwurf der posterioren Kutikula wird die neue Kutikula durch Material aus der Demineralisation der anterioren Kutikula und aus den sternalen Depositen wieder aufgebaut. Anschließend wird der anteriore Teil abgeworfen und ebenfalls wieder aufgebaut. In

Abbildung 2 ist *P. scaber* in zwei unterschiedlichen Häutungsphasen (*intermoult* und *premoult*) dargestellt. Die Messung wurde am Messplatz BW2 bei einer Energie von 17 keV durchgeführt.
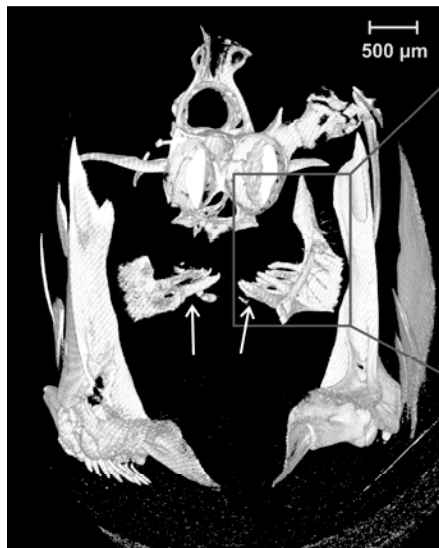
Abbildung 1: Frontaler Blick auf einen Kopfausschnitt des Zebrafisches in Richtung Schwanz. Die branchialen Knochen mit den Zähnen sind gut sichtbar (rechts: Vergrößerung eines Kieferknochens).
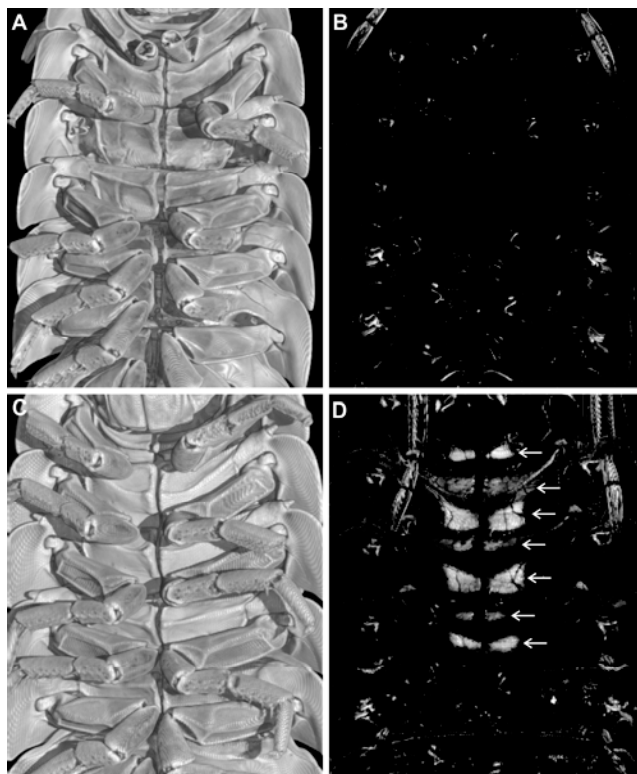
Abbildung 2: SRµCT von *P. scaber* mit Blick auf die ventrale Seite. A+C Intermoult Phase; B+D Premoult Phase mit Calciumcarbonat in den sternalen Depositen (Pfeile).

Literatur
1. F. Neues, W. H. Arnold, J. Fischer, F. Beckmann, P. Gängler, M. Epple, The skeleton and pharyngeal teeth of zebrafish (Danio rerio) as a model of biomineralization in vertebrates *Mat.-wiss. u. Werkstofftech.* **2006**, *37*, 426.
2. F. Neues, F. Beckmann, A. Ziegler, M. Epple; "The application of synchrotron radiation-based micro computer tomography in biomineralization" in: Handbook of Biomineralization Vol. 1: The Biology of Biominerals Structure Formation (Ed. E. Bäuerlein), Wiley-VCH, **2007**

Morphology of the endolymphatic space in the murine cochlea uncovered by micro computed tomography using synchrotron radiation

Anita Lareida[1,2], Felix Beckmann[3], Adrian Andronache[2], Wolfgang Freysinger[4], Annelies Schrott-Fischer[4], Rudolf Glückert[4] and Bert Müller[1,2]

[1]Biomaterials Science Center, University of Basel, c/o University Hospital, 4031 Basel, Switzerland
[2]Computer Vision Lab, ETH Zürich, Sternwartstrasse 7, 8092 Zürich, Switzerland
[3]GKSS-Research Center, c/o GKSS at DESY, Notkestrasse 85, 22607 Hamburg, Germany
[4]ORL University Clinics, Medical University Innsbruck, Anichstrasse 35, 6020 Innsbruck, Austria

The hearing organ belongs to the most complex structures in the human body. It is very important to recognize its morphology on the microscopic level, because already minor morphological deviations may result in crucial hearing deficiencies. Current methods such as histological sectioning are very powerful, but destructive, may lead to preparation artefacts and only provide the necessary spatial resolution in two dimensions. Consequently, it is highly desirable to complementarily apply a non-destructive, fully three-dimensional technique, as synchrotron radiation-based micro computed tomography (SRμCT).

For the feasibility test we have chosen the mouse cochlea, since it is known to be an appropriate model system for the human hearing organ. Furthermore, it is easier to investigate the mouse cochlea because it is smaller by a factor of two with respect to the human one. The preparation procedure includes explantation, removal of the Petrous bone, fixation in 1% OsO_4-solution and embedding in SPURR [1, 2]. The SRμCT measurements were performed at the beamline BW 2 (HASYLAB at DESY) using the standard set-up for tomography in absorption contrast mode. The photon energy was set to 10.8 keV. The spatial resolution corresponds to 5.2 μm at a pixel size of 2.8 μm [3]. Three tomograms out of 721 projections each and 1536 x 1024 pixels, respectively, were co-registered using a rigid registration algorithm [4].

Figure 1 shows the entire segmented endolymphatic space of the selected right murine labyrinth from different points of view. Because this space exhibits a lower absorption than the surrounding tissues, it can be easily segmented semi-automatically. The segmentation as well as the visualization of the endolymphatic space has been carried out by means of the software VG Studio Max (Volume Graphics, Heidelberg, Germany).

The endolymphatic space is a fluid-filled compartment that is rich of potassium. The positively charged ions lead to a potential difference between the endo-lymphatic and the surrounding peri-lymphatic compartment. As the reaction to mechanical stimuli the endolymphatic space is responsible for the deflection of the hair cells and the consecutive opening of ion channels. Consequently, it plays the key role in the transduction of mechanical to chemical-neuronal/electrical impulses. The endolymph is produced in the middle scale (stria vascularis). There is almost no way for the outflow except diffusion. Therefore, physiological and non-physiological constrains are of crucial importance. Minor deviations from the generic morphology can lead to severe consequences for the quality of hearing.

The upper parts of the four images in Figure 1 show the three semicircular canals. As easily recognized they are orthogonal to each another. The spiral cavity is the cochlear duct also termed the *scala media*. It is the part of the cochlea that is used to perceive the different acoustic impulses. In the images, a few artefacts are present, namely some missing volume on the posterior semicircular duct, especially visible in the second image, which results from a conglomeration of osmium particles. The tiny connections are hardly seen since they coincidence with the gate of the nerve fibres and the vascular structures. These structures have absorbed relatively high amounts of osmium and exhibit absorption values that make their differentiation from the endolymphatic space difficult. Nevertheless, the morphology of the endolymphatic space is imaged with equidistant

resolution in the three orthogonal directions and unattained precision. The SRμCT data are available to be presented as movie for teaching purposes.
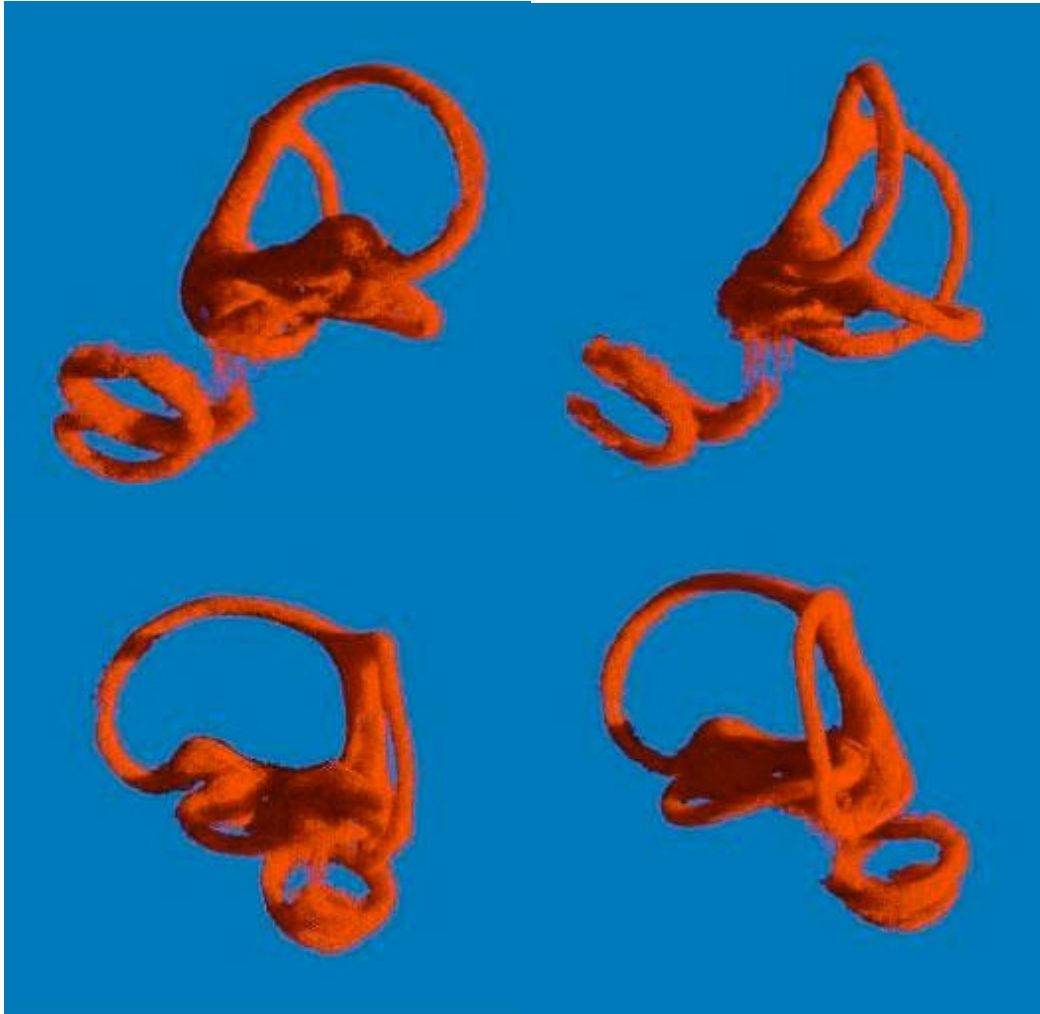
Figure 1: The four different three-dimensional representations show the details of the segmented endolymphatic space of the selected murine cochlea, namely the three orthogonal semicircular canals with their three ampullae, the saccule, the utricle, and the cochlear duct.

References

[1] H. Spoendlin and A. Schrott, Acta Otolaryngol. 105, 403 (1988)
[2] H. Spoendlin and A. Schrott, Hear Res. 43, 25 (1989)
[3] B. Müller et al., Proc. SPIE 4503, 178 (2001)
[4] B. Müller et al., Proc. SPIE 6318, 631805 (2006)

Neuroimaging with Synchrotron-based Methods

M. Kuehbacher[1], B. Gruenewald[2], G. Falkenberg[3], T. Donath[4],
J. Herzen[4], F. Beckmann[4] and A. Kyriakopoulos[1]

[1]*Hahn-Meitner-Institut Berlin, Department of Molecular Trace Element Research in the Life Sciences,*
Glienicker Str. 100, 14109 Berlin, Germany
[2]*Institut für Neurobiologie, Freie Universität Berlin, Königin-Luise-Str. 28-30, 14195 Berlin, Germany*
[3]*Hamburger Synchrotronstrahlungslabor HASYLAB at Deutsches Elektronen-Synchrotron DESY, Notkestr. 85,*
22603 Hamburg, Germany
[4]*GKSS-Research Center Geesthacht, Institute for Materials Research, Max-Planck-Strasse 1,*
21502 Geesthacht, Germany

Golgi and Ramón y Cajal established the anatomy of the central nervous system by neuroimaging with staining techniques on fixed tissue. The modern functional brain imaging techniques are non-invasive and are applied on living brains. Methods like functional magnetic resonance imagery, positron emission tomography, electroencephalography, event related potential, optical imaging, magnetoencephalography belong to the toolbox of neuroimaging. Synchrotron-based tomography is on its way to enlarge this toolbox. Synchrotron radiation x-ray fluorescence analysis (SRXRF) allows the determination of the metal distribution in cryosections of tissues. Microprobe-synchrotron radiation X-ray fluorescence (micro-SRXRF) has been applied to determine the distribution of several metals and metalloids in cryo-sections of 10 μm thin tissue sections by scanning with a focused beam of synchrotron radiation at beamline L. The third spatial dimension of the elemental distribution pattern can be investigated by tomographic techniques. The results of our study with synchrotron radiation-based computed microtomography (SRμCT) in absorption contrast mode at beamline BW2 shows the importance of the right choice of the used animal model for the development of new neuroimaging methods. Animals with small brains are particularly useful models. We used honeybees, because their neuroanatomy is studied in great detail and we can correlate our results with already published functional data.

The neurophysiological mechanisms underlying learning and memory formation within the brain of honeybees are well-understood [1] and the neuroanatomy of the brain of the bee is among the best investigated in the insect world. What is missing is a high-resolution live neuroanatomy to reveal the wiring between and inside specific brain regions. The majority of the classical investigations were solved by combined staining and 2D histological sectioning techniques [2]. Recently, a 3D atlas of the honeybee brain is available [3]. However, also this standard atlas is based upon brain sections from fixed tissues.
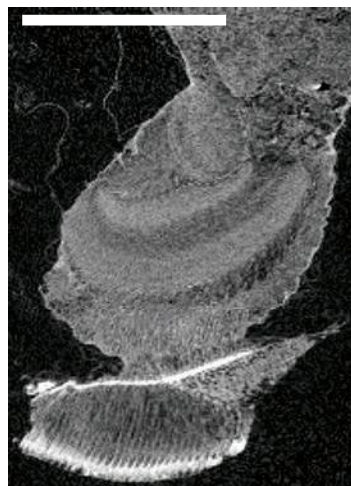

Figure 1: Visualized section of a part of the brain of a honeybee after tomographic reconstruction.

In our study the head as well as isolated brains of worker honeybees were investigated by synchrotron radiation-based computered microtomography (SRμCT) in absorption contrast mode at beamline BW2. The measurements were performed with photon energies of 8 and 10.5 keV. The voxel size was about 1.6 μm. Figure 1 shows a section through the visual areas of the honeybee brain.

In brain tissues, knowledge about the spatial distribution of certain metals, such as iron, copper, zinc, and manganese, may help to explain age-related changes in the central nervous system (CNS). A wide variety of neuropathological manifestations including elevations in protein oxidation, protein aggregation, and cytotoxicity may be the result of age-related alterations in the metal-homeostasis [4]. Although the causes for the neurodegenerative processes are different, protein aggregations caused by misfolded proteins are involved in most cases, which can settle in the brain and damage nerve cells. Neurons of the CNS are as old as the individual, because they usually do not divide and are not replaced. Their long persistence renders them susceptible to damages due to free radicals and oxidative stress, and trace elements are known to be involved in the production of free radicals as well as in the protective systems against these damages, the elucidation of the role of trace elements and their different binding forms in neurodegenerative diseases is of great interest [5].

One approach for investigating neurodegenerative processes is to test new concepts on animal models, in particular on mice mutants that are relevant for human diseases. These models are suitable because of the practicability of investigating cell death *in vivo* or *in vitro* preparations. Therefore, the aim is to use micro-SRXRF and micro-XANES for phenotyping different animal models, focusing on the mouse as the model animal species.

References

[1] R. Menzel, M. Giurfa, *Cognitive architecture of a mini-brain: the honeybee.* Trends in Cognitive Sciences 5, 2: 62-71 (2001)

[2] B. Grünewald, *Morphology of feedback neurons in the mushroom body of the honeybee, Apis mellifera.* J. Comp. Neurol. 404: 114-126 (1999)

[3] R. Brandt, T. Rohlfing, J. Rybak, S. Krofczik, A. Maye, M. Westerhoff, H.C. Hege, and R. Menzel, *Three-Dimensional Average-Shape Atlas of the Honeybee Brain and Its Applications.* The Journal of Comparative Neurology 492: 1-19 (2005)

[4] M. Kühbacher, G. Weseloh, A. Thomzig, H. Bertelsmann, G. Falkenberg, M. Radtke, H. Riesemeier, A. Kyriakopoulos, M. Beekes, D. Behne, *Analysis and localization of metal- and metalloid containing proteins by synchrotron radiation x-ray fluorescence spectrometry.* X-Ray Spectrometry 34, 2: 112-117 (2005)

[5] NE. Savaskan, AU. Bräuer, M. Kühbacher, A. Kyriakopoulos, O. Ninnemann, D. Behne, R. Nitsch, *Selenium deficiency increases susceptibility to glutamate-induced excitotoxicity.* FASEB J 17(1): 112-114 (2003)

Study of renal calculi structure

G.Taton, T.Rok, E. Rokita, A.Wrobel[1], F. Beckmann[2], T. Donath[2], J. Fischer[3], P. Thor[4]

Jagiellonian University Medical School, Department of Biophysics, Lazarza 16a, 30531 Cracow, Poland
[1]*Jagiellonian University, Institute of Physics, Reymonta 4, 30059*
[2]*GKSS-Research Center, Max-Planck-Straße 1, 21502 Geesthacht, Germany*
[3]*Hannover Medical School, Anna-von-Borries-Str. 1-7, 30625 Hannover, Germany*
[4]*Jagiellonian University Medical School, Chair of Pathophysiology, Czysta 18, 31-121 Cracow, Poland*

There is a type of renal calculi which are build mostly of uric acid. It is currently known that these calculi occur in 13 % of nephrolithiasis cases [1,2]. The macroscopic structure and the average elemental composition of the uric acid stones have been well established [1-3]. Results collected so far showed particularly wide variability of the Ca concentration [4]. The explanation of this observation remains unknown. The investigations concerning the renal calculi growth, their microscopic structure and elemental composition are still conducted.

Uric acid calculi can be divided into two groups. Type I stones develop by crystallization of uric acid from supersaturated solution with respect to uric acid anhydrous (UAA) or uric acid dehydrate (UAD). Their size ranges from several to a dozen or so millimeters. These stones have lamellar structure with small centrally located core composed of the UAA crystals. The layers develop due to variable supersaturation of urine. Thicker layers are formed slowly, when supersaturation and pH are lower, while thinner ones develop quickly, at strong urine supersaturation and high pH.

A characteristic feature of type II stones is the lack of any particular inner structure. Calculi of this type are formed by sedimentation of uric acid crystals that occurs at higher supersaturation of urine.

The pilot study of renal calculi observed in the recurrent nephrolithiasis was performed. To pieces of stones taken from the same patient but in the first and second nephrolitiasis episodes were scanned with the microtomography with the use of synchrotron radiation. The beamline BW2 equipped with microtomographic scanning system was utilized. The energy of 18 keV was applied. Achieved image resolution was about 6 μm. The 3D images of investigated samples were reconstructed.
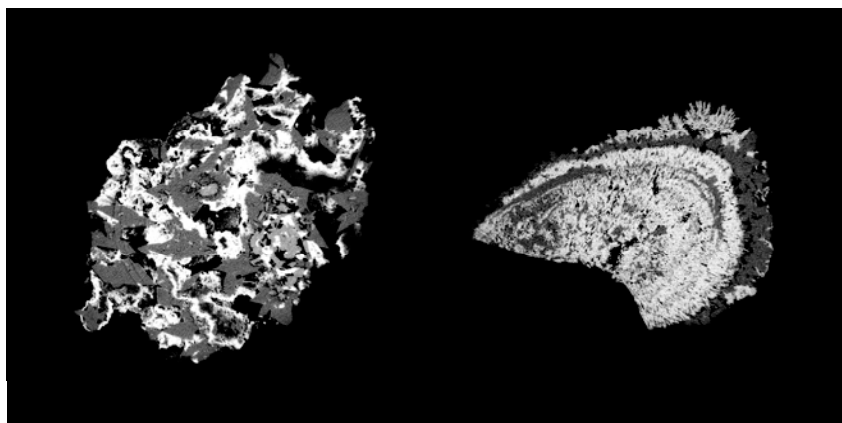

Figure 1: The cross-sections through the reconstructed 3D microtomographic images of two renal calculi samples. The sample collected during the first episode of recurrent nephrolithiasis is shown on the left while the sample cross-section of the second episode is presented on the right. Brighter areas represent regions characterised by higher densities.

The cross-sections through both stone samples are shown in fig. 1. The left-hand-site picture shows the cross-section through the stone collected in the first nephrolitiasis episode while the picture on the right represents the sample collected in the second nephrolitiasis episode. The structure visible inside the first sample suggest that it is of type II stone while the second is of type I calculi.

Our pilot studies led to an interesting conclusion. Calculi formed in the same patient in the first and second nephrolitiasis episodes were usually uric type with similar macroscopic structure and elemental composition. They differ with the inner structure. It is worth to emphasise that two investigated samples came from the same patient but in different nephrolitiasis episodes which suggests different mechanisms of stone development in both phases. The explanation of this fact remains unclear.

References

[1] F. Grases, A. Costa-Bauza, M. Ramis, V. Montesinos, A. Conte, Clinica Chimica Acta, 322, 29 (2002)

[2] F.Grases, A. Villacampa, A. Costa-Bauza, O. Sohnel, Clinica Chimica Acta, 302, 89 (2000)

[3] F. Grases, A. Costa-Bauza, M. Ramis, Advances in Colloid and Interface Science, 74, 169 (1998)

[4] A. Wrobel, E. Rokita, P, Thor, Trace Elements and Electrocytes, 4, 296 (2005)

Transformations of the vertebrate skull: How are skull anatomy and function correlated with the reproductive mode in caecilians (Lissamphibia: Gymnophiona)?

T. Kleinteich and A. Haas

University of Hamburg, Biozentrum Grindel und Zoologisches Museum, Martin-Luther-King-Platz 3, 20146 Hamburg

This project focuses on the skull anatomy and function in a particular group of amphibians; i.e. caecilians. Modes of reproduction in caecilians are oviparity with metamorphosis, oviparity with direct development, and viviparity [1]. The different reproductive modes have an impact on the feeding behaviour of early developmental stages (i.e. embryos, larvae, and fetuses). Feeding modes comprise suction feeding [2], peeling of the skin of the mother [3], and intrauterinal feeding [4]. The goal of this study is to understand the correlation between feeding mode during early development and head anatomy in caecilian amphibians.

We intend to use Synchrotron based radiation for micro computed tomography (μCT). The μCT method results in three dimensional datasets of caecilian skulls. Three dimensional images will give detailed insights on their cranial anatomy. The μCT technique is non-invasive. This makes imaging of precious material from zoological collections possible.

In July 2006 we scanned the heads of two specimens of the caecilian *Ichthyophis kohtaoensis*. This was the first attempt ever, to have μCT images of caecilian larvae. The first specimen (Figs. 1 A and B) was a larva at hatching stage; the second animal (Figs. 1 C and D) was an animal during metamorphosis to the adult.

The scans were performed at beamline W2 (GKSS at HASYLAB). The animals have been stored in 70% Ethanol for the scanning process. Scanning the animals in liquid resulted in a decrease of contrast in the final data set. However, drying the specimens would have had effected especially the soft tissues in the head (e.g. cranial musculature). We rely on specimens from zoological collections. In many cases there is only one specimen for our studies available. For this, we have to make sure that the specimens remain undamaged. The heads have been mounted in plastic tubes. This setup made it possible to store the animals in liquid for the scanning process. The 3D analysis of the scans was performed with VGStudio Max software at GKSS and the volume rendering software package Bitplane Imaris. Both software packages contained numerous tools to improve the contrast of the μCT Images.

Because of technical limitations only 2 mm of the length of the animal could be scanned in one go. The regions of interest in the studied specimens, however, comprised approximately 10 mm beginning with the tip of the snout. It was necessary to shift the adjustment after the scan was completed, and to start again for the next 2 mm. For both specimens this procedure was repeated four times.

Results of this scan are presented in figure 1. The cranial bones in the first specimen (Figs. 1 A and B) are barely calcified. However, using the different section planes (Fig. 1 B) they can easily be distinguished from soft tissues. Though the contrast is weak, it is possible to determine single cranial muscles in the scanned dataset. The cranial bones in the second specimen (Figs. 1 C and D) are more calcified than in the first animal. Increased calcification results in stronger radiation absorption by the skull. The contrast in the second dataset is much better than in the first; all cranial elements can be identified.

One objective of this scans was to test, whether the μCT technique can be used for our project on the head anatomy in caecilian larvae, how the specimens have to be prepared, and what adjustments have to be made for. Based on the positive results from this scan, we successfully applied for beamtime in 2007. It is planned to study different developmental stages of 11 species (18 specimens) using the μCT technique.
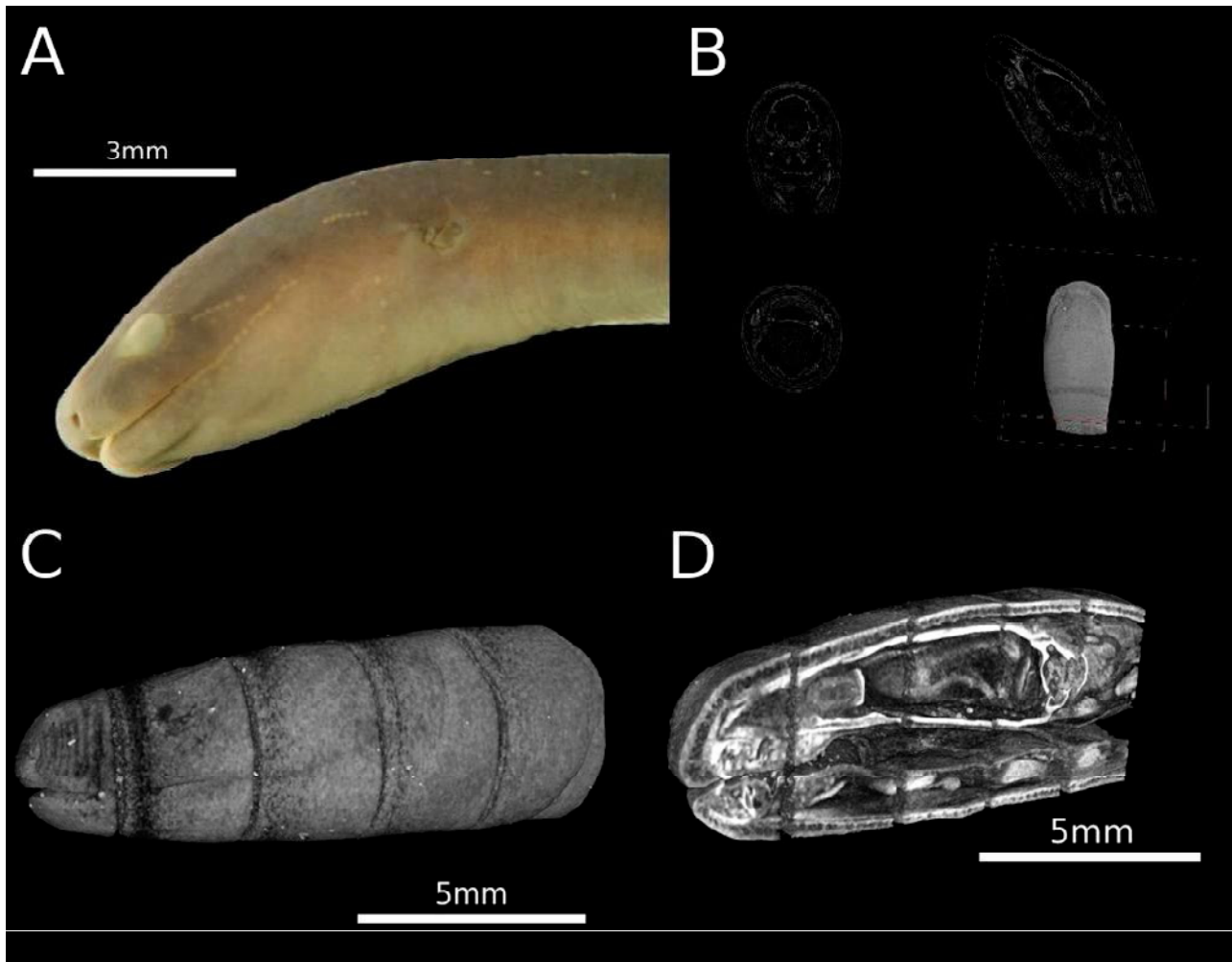
Figure 1: µCT images of caecilian heads. **A:** *Ichthyophis kohtaoensis*, larval specimen, hatching stage. Lateral view. **B:** Same specimen as in A, µCT dataset. Image stacks in different planes of section and 3D illustrations can be generated based on µCT datasets. Because µCT is a non-invasive technique, it is possible to study the anatomy of the specimens without destroying them. **C:** *I. kohtaoensis*, specimen during metamorphosis. µCT dataset, lateral view. The head region of the animal is presented. The segmentation of the animal in five segments is an artefact because of the shift of the adjustment after scanning 2 mm. **D:** Same specimen as C. µCT dataset, lateral view, clipping plane approximately along the midline of the animal. Different tissues can easily be distinguished. Bones are almost white, the cranial musculature is greyish.

References

[1] Wake MH. J. Exp. Zool. 266, 394-413 (1993)

[2] O'Reilly JC in Schwenk K (editor). Feeding: form function and evolution in tetrapod vertebrates. 149-166 (2000)

[3] Kupfer A, Müller H, Antoniazzi MM, Jared C, Greven H, Nussbaum RA, Wilkinson M. Nature 440, 926-929 (2006)

[4] Wake MH. J. Herpetol. 11, 379-386 (1977)

3D Bone Architecture

G.Taton, T.Rok, E. Rokita, Z. Tabor, M. Karwala-Szytula, F. Beckmann[1], T. Donath[1], J. Fischer[2]

Jagiellonian University Medical School, Department of Biophysics, Grzegorzecka 16a, Cracow, Poland
[1]GKSS-Research Center, Max-Planck-Straße 1, 21502 Geesthacht, Germany
[2]Hannover Medical School, Anna-von-Borries-Str. 1-7, 30625 Hannover, Germany

The bone mineralization process and its alterations is one of the fields of interest for contemporary medicine. There are open questions concerning it onset, dynamics and the mechanism of being influenced by different physical or chemical factors. The aim of the project is to investigate the influence of the extremely low frequency magnetic field (ELFMF) on the bone mineralization process [1]. We decided to rely on the three-dimensional (3D) bone architecture investigations with the use of microtomography. The 3D micro-tomographic data allow the calculations of bone architectural parameters describing its mechanical properties. It is believed that such parameters are more precise and reliable for the description of bone changes than the other parameters [2,3].

The rat bone model was used. Pregnant female rats were taken into consideration. One group was treated with ELFMF while the second stayed untreated as a control group. Magnetic field parameters typical for magnetotherapy in humans were utilized (frequency 15Hz, intensity 1mT). The rats breed was treated also with ELFMF after the labour. The young treated and control rats were killed in different age (10, 20 and 30 days). Their femoral bones were dissected and investigated.

12 bone samples dissected in different animals age were scanned with the microtomography with the use of synchrotron radiation. Only the femoral head was scanned due to the lack of trabeculae in the bone shaft. The beamline BW2 equipped with microtomographic scanning system was utilized. The energy of 18 or 24 keV was applied depending on sample sizes. Achieved image resolution was 6 μm - 10 μm depending on the sample size. The 3D scanning of single sample takes 5 to 13 hours depending on the sample size.

A set of parameters characterising the trabecular bone was calculated, e.g.: tissue volume (TV), bone volume (BV), trabecular thickness (TT), trabecular number (TN), trabecular separation (TS) and BV/TV. Also the trabecular thickness distribution and trabecular separation distribution were calculated.

The former project stage was concentrated on the best architectural parameters choice allowing the observations of subtle bone structure changes [4]. The ELFMF influenced and osteoporotic bones were investigated. Because of the large time-consumption of 3D microtomographic measurements only few bone samples were investigated: 20 and 30 days old animals treated with ELFMF and their control counterparts (4 samples) and two samples connected to the osteoporotic investigations. Since that the proper statistical analysis was not possible. Comparing the architectural parameters driven for investigated samples it was stated that some simple parameters could be taken into consideration [4] assuming that the parameter variability for particular individuals (individual variability –IV) is not higher than the differences caused by the investigated factors. In order to estimate IV additional bone samples treated with ELFMF (and their control counterparts) were scanned in the last project stage.

Despite more samples (12) were finally measured the proper statistical analysis is still impossible. The conclusions can be driven only on the basis of some simple results comparisons. As the estimator of IV the maximal observed parameter difference in the control or treated group (two samples in all cases) was taken. As the estimator of the parameter change (PCh) caused by the ELFMF the mean parameter values difference for both groups was taken (see formulas defined below):

$$IV = \max (|T1-T2|,|C1-C2|) ; \qquad PCh=|(T1+T2)/2-(C1+C2)/2|$$

where: T1, T2 – samples treated with ELFMF for particular age groups, C1, C2 – control samples. The calculated IV and PCh for three chosen architecture parameters are shown in Table 1. The results of structural parameters calculations are presented in Fig 1.

Table 1. The calculated estimators for individual parameter variability (IV) and parameter change (PCh) caused by the ELFMF for three chosen bone structure parameters. See text for abbreviations.

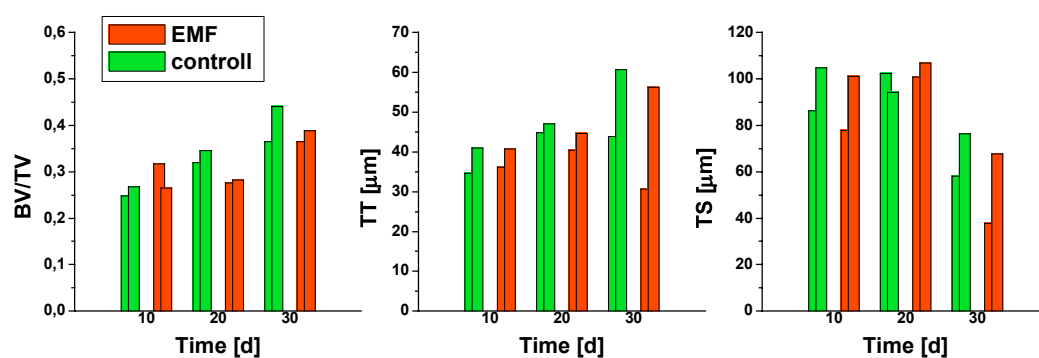| Age [d]			BV/TV	TT [μm]	TS [μm]
10	IV		0,052	6,75	24,78
	PCh		0,033	0,69	6,45
20	IV		0,026	4,49	8,69
	PCh		0,053	3,64	5,83
30	IV		0,075	27,18	31,68
	PCh		0,026	9,40	15,44

Fig. 1. Chosen bone architectural parameters calculated from 3D microtomographic measurements (see text for abbreviations).

As one can see in Table 1 the observed IV is in most cases larger than the parameter changes caused by the investigated physical factor. Also there is no clear dependence between the investigated parameter value changes and the influence of ELFMF (fig.1). Performed investigations did not confirm the influence of ELFMF on the trabecular bone structure.

It is possible that the influence of ELFMF could be observed if the larger data sets would be involved. The more sophisticated statistical analysis probably would discover logical behaviour of calculated parameters in larger populations allowing to minimize the IV importance. Such solution regards the changes in measurements procedure allowing faster sample scanning.

References

[1] C. Sert, M. Deniz, M. Zahair Duz, F. Aksen, A. Kaya, J Bone Miner Metab, 20, 345 (2002)
[2] M. Stenstrom, B. Olander, D. Letho-Axtelius, J. Madsen, L, Nordsletten, G. Carlsson, J Biomech 33, 289 (2000)
[3] M. Audran, D. Chappard, E. Legrand, H. Libouban, M. Basle, Calcif Tissue Int, 69, 214 (2001)
[4] G. Taton, T. Rok, E. Rokita, Z. Tabor, M. Karwala-Szytula, F. Beckmann, T. Donath, J. Fischer, Hasylab Annual Report, 2005, 1087-88

Acknowledgement

Automated Data Reconstruction for
X-ray Microtomography

T. Donath, F. Beckmann, A. Schreyer

GKSS-Research Center, Max-Planck-Straße 1, 21502 Geesthacht, Germany

The GKSS-Research Center operates a setup for x-ray microtomography at HASYLAB beamlines BW2 and W2 [1]. Further developments of the data-processing (reconstruction) software have been made that have enabled the automation of the tomographic data reconstruction. Especially, a method has been developed that allows for the precise determination of the center of rotation in the projection data [2,3].

The center of rotation is an important input parameter for the applied (filtered-backprojection) reconstruction algorithms [4]. Selection of a wrong center of rotation results in artifacts (tuning-fork artifacts) that mainly become visible as disturbing streaks in the reconstructed cross sections. As an example, a cross section through a bone sample containing a titanium implant is shown in Figures 1(a) and (b). This cross section was calculated for the correct center of rotation. Figure 1(c) shows a streak artifact that appears in the equivalent cross section calculated for a center of rotation that deviates by only 1.0 pixel from the optimal center of rotation. To avoid such artifacts, the determination of the center of rotation with sub-pixel precision is required.

So far the optimal center of rotation was found by performing test reconstruction for under variation of the center of rotation t_r. The quality of the reconstructions [as those in Figures 1(b) and (c)] was compared by a human scorer and the best reconstruction selected. This process could now be automated. Three image metrics Q have been developed that can be used for scoring of test reconstructions, where the metric value describes the quality of the calculated reconstructions. Figure 1(d) shows a plot of the metric Q_{IA} (IA = integral of absolute) as a function of the center of rotation for the displayed sample. A unique minimum is found at the optimal center of rotation.
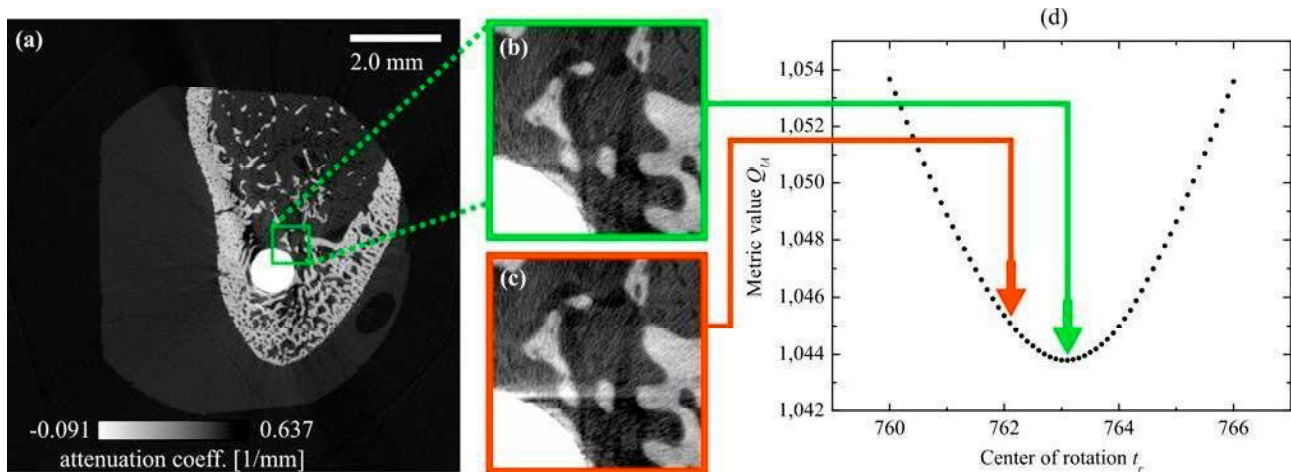

Figure 1: Demonstrating the effect of a wrong center of rotation. (a) Reconstructed cross section through a bone sample with titanium implant [investigator: R. Bernhardt, MBC, TU Dresden] , (b) cutout from the cross section, and (c) the equivalent cutout for a reconstruction with 1.0 pixel offset from the optimal center of rotation. (d) Value of the implemented metric as a function of the center of rotation at a resolution of 0.1 pixel. The optimal center of rotation results in the minimal metric value.
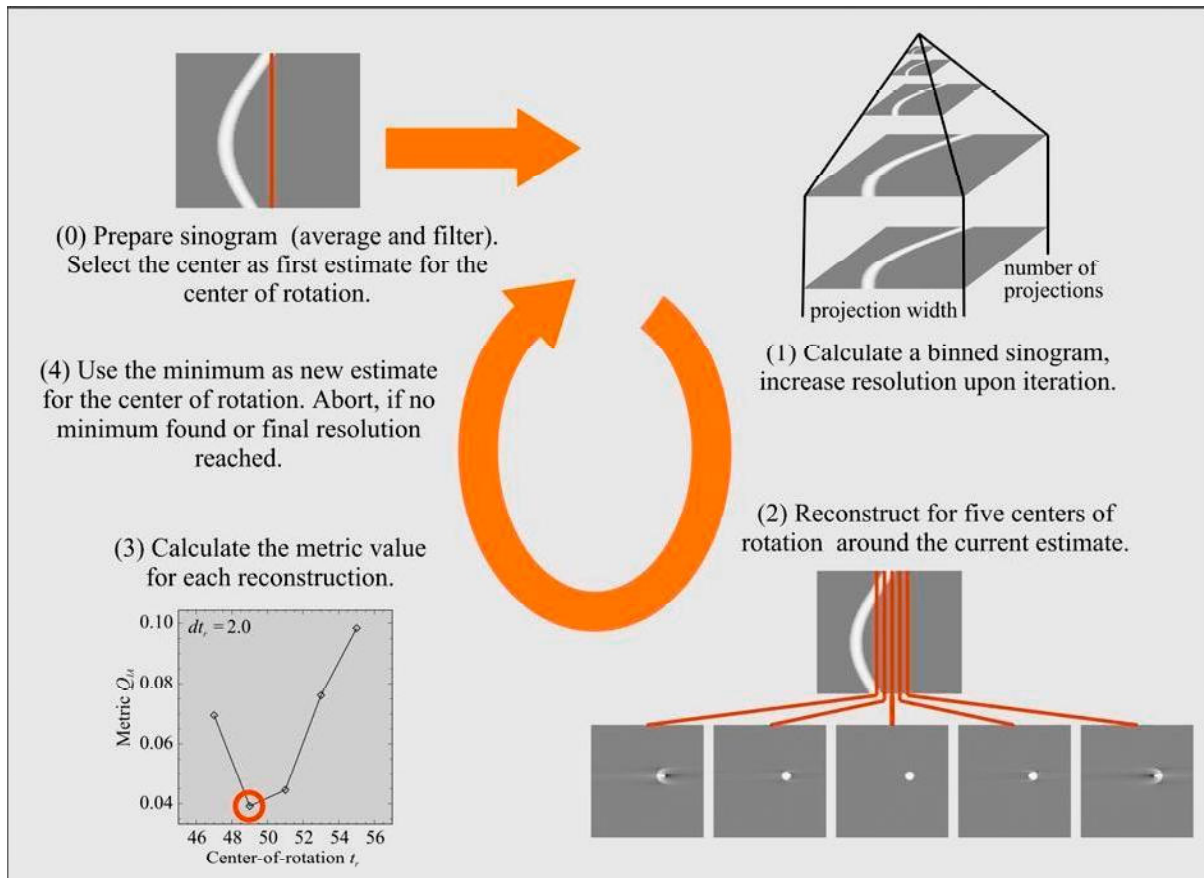
Figure 2: Scheme of the implemented optimization procedure. The center of rotation is determined iteratively using a multi-resolution approach.

In order to speed up the search of the optimal center of rotation, an iterative procedure was implemented that continuously increases the resolution of the sinogram before reconstruction. This so-called multi-resolution approach also prevents getting trapped at local minima and reduces the influence of noise. Figure 2 shows a schematic representation of the iteration procedure. The resolution (projection width) of the sinogram is increased upon iteration. For a resolution of $dt_r = 2^z$ in t_r, with z an integer number, the sinogram is binned by a factor of $b = dt_r$ for $dt_r > 1$. For $dt_r \leq 1$, the sinogram is used in its original size.

The iterative procedure in combination with metric Q_{IA} has been implemented into our reconstruction chain and is now routinely used to determine the center of rotation at 0.05 pixel resolution. Limits on the precision of the method were discussed by calculation of the metric signal and its noise level for a cylindrical sample [2]. Here it was shown that for typical count rates and resolutions used in microtomographic imaging, the method allows for the determination of the center of rotation with a precision of better than 0.06 pixel. In summary, the implemented method enables to determine the center of rotation in a robust, precise, and objective manner and, furthermore, enables full automation of the reconstruction process.

References

[1] T. Donath, F. Beckmann, and A. Schreyer, J. Opt. Soc. Am. A, 23(5):1048–1057 (2006)

[2] T. Donath, F. Beckmann, and A. Schreyer, Proc. SPIE Vol. 6318 (2006)

[3] F. Beckmann, T. Donath, J. Fischer, T. Dose, T. Lippmann, L. Lottermoser, R. V. Martins, and A. Schreyer, Proc. SPIE Vol. 6318 (2006)

[4] R. H. Huesman, G. T. Gullberg, W. L. Greenberg, and T. F. Budinger. RECLBL Library users manual, Lawrence Berkeley Laboratory, University of California, 1977.